CIRCULATION AND MIXING IN

A STRATIFIED RESERVOIR

Thesis submitted in accordance with the requirement of the

University of Liverpool for the degree of

Doctor in Philosophy.

By

M.R. Jaefarzadeh

July 1988

SUMMARY

The seasonal variation of temperature has a great influence on water quality in storage and service reservoirs.

Momentum jets have often been considered as an effective means of mixing and prevention of thermal stratification. Mixing processes in a reservoir are largely dependent on the flow patterns which are influenced by the reservoir's geometry, momentum inflows and the density of the receiving water.

In the present research some of these effects were studied theoretically and experimentally. Applicability of various theories suggested for the circulation in a homogeneous reservoir, was investigated. Predictions of these theories were compared with experiments. Circulation patterns were examined for various reservoir depths and inflow discharges.

The study was extended to the flow in a stratified reservoir. The slow moving interior flow within a large scale gyre was investigated. It was shown that the rotation of the upper layer may suck the lower layer and thereby enhance the mixing.

Jet forced circulation in a stratified reservoir was also studied experimentally. The inflow's discharge and the density of the lower layer were varied widely. The results of several experiments were compared with a corresponding one for a homogeneous reservoir. Substantial differences were observed.

A theoretical model was presented to calculate the velocities at different depths. The time variation of the interface was also calculated. The agreement between theory and experiment was encouraging.

CONTENTS

LIST OF FIGURES

LIST OF TABLES

ACKNOWLEDGEMENTS

The author wishes to express his sincere thanks to Dr. K.H.M. Ali Senior Lecturer in Civil Engineering, for his supervision of this research and for his continuing help and encouragement and constructive criticism throughout the period of this research.

Thanks are due to Professor R.A. Falconer (University of Bradford) for the useful comments regarding Chapter 4. I am also grateful to Dr. D. Yoo (Department of Civil Engineering) for the frequent discussions on the subject of finite difference methods and to Mr. J. Wilkinson (Senior Scientific Officer) for his assistance on computational matters.

The author is very grateful for the financial support of the Islamic Republic of Iran, without which this research would have been impossible. Appreciation is expressed to the British Council for supporting the author's last two years in the University of Liverpool. I also acknowledge the assistance of the Department of Civil Engineering for approving my attendance at a conference on mixing in estuaries.

I am indebted to the staff of the Workshop and Laboratory Technicians of this Department for their help in constructing the models and equipment. Thanks also to Mr. S. Glass for his photography and Mrs. Donna Eccles for typing this thesis with patience and speed.

Finally I thank my family and my wife for their unstinting encouragement, interest and support during this research, my fellow students for the pleasure of sharing with them the 7th Floor Research Room, and all my friends making this an unforgettable happy time.

CHAPTER 1

STATEMENT OF PROBLEM

1.1 INTRODUCTION

The growth of population and the industrialisation of societies increases the demand for water resource. Streams are known as an abundant and natural sources of water which can supply irrigation and hydro-electric projects as well as city waterworks.

However, due to the seasonal variation of the stream flows it may not always be possible to match the needs for consumption. Moreover, the quality of the river water may decline due to pollution discharged into the river upstream by industries, residential areas and agriculture. Usually raw (untreated) water involves a complex combination of chemical and biochemical substances which may develop an appropriate environment for the growth of bacteria and noxious micro-organisms.

Storage of water, on the other hand, permits the stabilisation of the supply, either by regulating a varying supply in a natural stream or by satisfying a varying demand by the ultimate consumers. Storage of raw water can also be regarded as a first stage (pre-purification) in the treatment of the water.

In the process of storage of water in a basin for a period of one month to several months, there will be a very great decrease in the numbers of bacteria of intestinal origin and the specific organisms of typhoid, and the disappearance of other water-borne diseases.

There are, however, some disadvantages in the prolonged storage of raw water due to the lack of mixing. Unfortunately large water masses are subject to complex meteorological and biological effects and the mixing processes are often either weak or unpredictable.

In most reservoirs in temperate climate, assuming they are more than about 10m deep in parts, thermal stratification occurs and persists for most of the year. In early spring the water warms up and the whole body of reservoir water becomes uniform. Water on the increase in temperature causes the upper layers of the reservoir to become warmer (lighter density) than the lower layers. Much colder water remains in the bottom part.

The upper and lower layers are known as the "epilimnion" and the "hypolimnion". In either of these layers the rate of change of temperature with depth is very small, probably less than one degree per metre. In between there is a zone with a relatively steep change from the higher temperature of the epilimnion to the lower temperature of the hypolimnion. This zone is called the "thermocline", Fig. (1.1).

In a reservoir of depth, say, 20m, the epilimnion can extend some 7-9m from the surface. The thermocline may be at least 2m in thickness, whilst the remaining 10m of the water form the third layer, the hypolimnion. This layer can be some 10°C colder than the epilimnion.

Basins with shallow depths, in mid-summer, can develop a weak stratification.

Stratification is a direct consequence of the density-temperature variation of the water (see Chapter 6). It resists any vertical motion specifically from the hypolimnion to the epilimnion and therefore prohibits vertical mixing.

1.2 FACTORS INFLUENCING THE STRATIFICATION OF RESERVOIRS

The process of the annual history of stratification for a typical reservoir cannot be generalised to all reservoirs and lakes. The major factors in thermal stratification of a basin can be categorised as:

1. The character of the catchment feeding the lake or reservoir.
2. The ratio of the average annual inflow/outflow to lake capacity.
3. The shape of the reservoir and the orientation of its great length.
4. In artificial reservoirs, the average depth and greatest surface length and the ratio of these dimensions.
5. In natural reservoirs, bottom bathymetry.
6. The geographical latitude, elevation and shelter by hills or mountains.
7. Variation of the climatic conditions, unusual cold winters or strong gales etc.
8. Functions of the reservoir.

1.3 STRATIFICATION AND WATER QUALITY

Algal growth in reservoirs usually takes place in the early part of spring due to suitable weather condition and the diffusion of plant nutrients. Waters which contain sufficient nutrient materials to support the prolific growth of plankton are usually described as "eutropic".

During the summer in a deep lake of moderate size, the hypolimnion water may remain in a stagnant condition for several months. Algal growth, then, is restricted to the zone of strong illumination near the surface. Organic debris, however, will sink down into the hypolimnion. The percentage of saturated oxygen in the epilimnion is usually normal because of free circulation and mixing caused by the wind. The hypolimnion, on the other hand, is almost isolated from the atmosphere and water movement is very much reduced. In a eutrophic reservoir decomposition of organic matter is largely derived from dead plankton. This deplets the store of oxygen available in the hypolimnion during the development of thermal stratification. At quite an early stage in the summer period, the hypolimnion water can in some cases become almost completely de-oxygenated, beginning at the bottom and extending progressively upwards.

At the same time, inorganic materials are liberated and accumulate in the hypolimnion. Observations made on some of the London reservoirs by Ridley (1964), show that when the dissolved oxygen content falls below 50 percent of saturation, the ammonical nitrogen concentration is likely to reach 0.5 ppm. In the 0 to 25 percent saturation range, the concentration is of the order of 1 to 2 ppm. In the strata where hydrogen sulphide is present, the ammoniacal nitrogen content may well exceed 5 ppm. These facts suggest that the bottom 4 to 6 metres of water in a stagnant reservoir some 16 metres in depth might be unacceptable on biochemical standards unless diluted with epilimnion water which is well oxygenated and contains minimal concentration of ammonia. This is not necessarily an economic solution, because the upper epilimnion at that time contains dense concentrations of

phytoplankton, and if dominant members are myxophyceae, the problem is even more complex.

In the worst circumstances, only about half of the total capacity of the reservoir would be of a quality immediately suitable for discharge to filtration works.

The subsequent redistribution which occurs when stratification breaks down in the autumn can also cause serious deterioration in the quality of the water. This process of events is well described in the works of Mortimer (1941) and Mortimer (1942). Further, undesirable consequences are pointed out by Steel (1972) who considered hypolimnetic anaerobism to cause a significant loss of available storage volume during the summer in King George VI reservoir. Internal seiches of 3 to 4m amplitude compounded the draw-off problems, since water from the epilimnion and hypolimnion, which varied greatly in quality, was being drawn off alternatively.

1.4 CONTROL OF WATER QUALITY - REMEDIAL METHODS

Since in eutropic waters it is usually the water above the thermocline that is most suitable for use, measures have been taken in recent years to control the stratification of a reservoir. Optimization of the quality of raw water before treating it can also be economically beneficial.

There are, however, two basic approaches towards the problem, remedial methods and preventive methods. In the remedial methods, measures are developed to minimise the effect of stratification on water quality. In the present section these methods are reviewed in brief.

1.4.1 Selective Withdrawal

When a reservoir is stratified vertical motion is inhibited, but the layers can still move horizontally. Selective withdrawal from an off-take structure, therefore, leads to a layered flow. The fluid above the outlet falls vertically to make up the deficit, the fluid in a thin layer adjacent to the orifice, flows horizontally towards the off-take and the fluid below the off-take remains essentially stagnant, Fig. (1.2). Thus, the quality of the water withdrawn at the outlet is determined by the quality of water immediately opposite the outlet level. By constructing an off-take with ports at multiple depths, water in any part of the reservoir may be sampled. In this way the water may be taken in the summer from just above the thermocline to avoid algae (particularly blue green algae, which is usually very buoyant). This method avoids the use of de-oxygenated hypolimnion water, that may have a bad taste and be less amenable to purification. The hypolimnion water may be discharged into a river below the reservoir.

Therefore, deficiency of oxygen can rapidly be improved when the hypolimnion water is in direct vicinity with the atmosphere. Because of nutrient in solution in such water both the flora and fauna of the river bed are likely to be richer, and fish food more abundant, than they would otherwise be, Thompson (1954).

Unfortunately, selective withdrawal is restricted to a relatively small portion of the stored water. However, the quality of the water in the reservoir and the overall mixing does not change very much. Moreover internal seiches may cause poor quality water from the other layers to leave the reservoir through the outlet. Selective

withdrawal can, however, give its ultimate gain in a pumped storage scheme, Imberger (1980).

1.4.2 Artificial Destratification by Vertical Mixing

Artificial destratification aims at redistribution of oxygen and other disolved gases, present in the reservoir, and helps to remove from the water body some of the unwanted metals in solution, thereby improving the general quality of the water.

To accomplish artificial destratification a number of techniques have been used in fairly large lakes and reservoirs. A review of the results of several of these studies can be found in the article by Symons et al. (1970) and Irwin et al. (1966). Different methods of destratification can be applied which use either "mechanical pumping" or "diffused-air pumping".

In the "mechanical pumping" method, fluid is withdrawn from the hypolimnion through a draft tube and discharged at the free surface. Brush and Rutgers (1970) pumped warm water from the epilimnion and jetted it into the hypolimnion in a laboratory tank to simulate artificial destratification.

The "diffused-air pumping" system usually involves the pumping of air into a set of ceramic diffusers located on the bottom of the lake or reservoir in an x-pattern causing a column (12m to 30m in diameter) of air bubbles to rise through the various diffusers, Irwin et al (1966). Other techniques involving air include "Aero-Hydraulics Gun" and the "Air Aqua System".

Generally, the capital and running costs of these methods are somewhat expensive.

Vertical mixing techniques remove many of the problems associated with thermal stratification. Sometimes, however, insufficient horizontal circulation may prevent the complete success of these techniques, Derby (1956).

1.5 CONTROL OF WATER QUALITY - PREVENTIVE METHODS

These methods are applied before any deterioration in water quality in order to prevent stratification and its subsequent effects.

1.5.1 The Multi-Inlet System

Judicious positioning of several inlets will prohibit the possibility of stagnation in a reservoir. This method is particularly applicable to long rectangular reservoirs, Robinson (1978). Inlets can also be located at various elevations in order to produce vertical circulation as well, Meyer (1982).

1.5.2 Momentum Jet Inlets

Provision of jetted inlets in a large pumped storage reservoir where there is a regular river flow can offer a method of preventing stratification and improving water quality.

In order to understand the role of inflows, it is useful to introduce two specific types of ideal flow relevant to reservoir behaviour. "plug flow" is that which moves from inlet to outlet at a uniform and constant velocity and in which there is no mixing or diffusion along the flow path. "Perfectly mixed flow" or "well mixed flow" occurs when the incoming fluid is instantaneously mixed throughout the entire

volume. In plug flow, it is easier to detect possible toxic pollution because of the lack of any mixing and dispersion with the ambient fluid. In the well mixed flow, however, the pollution can be diluted and loses its effect in the water body.

In practice, however, the objectives of the two ideal systems cannot be fully achieved.

The main purpose of using momentum jets is to produce a well mixed flow all over the reservoir. Therefore, the fluid should circulate in the longest possible path from the inlet to the outlet and sweep the greater part of the area of the reservoir. This in turn will discourage the establishment of algal reserves specifically at the peripheries. In the reservoirs of the Thames Water Authority, the inlets were placed near the floor and elevated upwards at about $22^{1}/_{2}°$. Therefore, the warm inflow was able to entrain a large volume of the ambient cold water and mix it thoroughly, ensuring that the reservoirs remained isothermal. The inclination of the jets to an optimum angle prevented the mixing of the deepest layers of the bottom and reduced the possibility of raising the muds and debris laying at the floor of the reservoir.

1.6 SCOPE OF THE PRESENT RESEARCH

Although it is about half a century that the problem of stratification in reservoirs has been studied, the subject still needs more investigation. Cooley and Harris (1954) conducted an extensive experimental work on laboratory models of the Walton and Queen Mary reservoirs and presented an approximate method for calculating the entrainment and thermocline variation.

Sobey and Savage (1974) studied, theoretically, the problem of circulation caused by a tangential jet in a homogeneous reservoir and obtained plots relating the geometrical characteristics of reservoir (aspect ratio), to the relative roughness and the dimensionless circulation discharge.

In the present research, an attempt is made to study the circulation caused by a tangential surface jet in a circular stratified reservoir. Chapter 2 gives details of the model and the various experimental techniques.

Chapter 3 reviews the characteristics of various turbulent jets in different situations. This chapter deals with jet action in homogeneous reservoirs. The results of a series of experiments were used to verify the workability of Sobey's (1973) mathematical model.

In Chapter 4, circulation caused by a wide radial inlet jet discharging into a homogeneous reservoir is investigated. The depth integrated hydrodynamic equations of motion have been solved by finite difference approximations following Falconer (1977), and the results are compared with related experimental studies.

In Chapter 5 the interior slow motion is studied and applied to the stratified reservoir.

In Chapter 6 circulation and mixing caused by a tangential turbulent jet in a stratified reservoir is studied experimentally and analytically.

In Chapter 7 general conclusions on the research are presented.

CHAPTER 2

EXPERIMENTAL ARRANGEMENTS

2.1 INTRODUCTION

Hydrodynamic mathematical models aim at simulating the actual flow in prototypes. Verification of these models requires considerable field information. Preparation of the field data, for example, for reservoirs and lakes is usually very expensive and time consuming. Moreover, there is a large number of unknown parameters which might greatly effect the final results.

Therefore, the use of hydraulic models as a means of preliminary investigation is fruitful. It is also possible to control the different parameters in these models. There are, however, some difficulties encountered in the modelling of reservoir circulation.

In a full size reservoir, the motion of the water will be turbulent, whereas in a small model with very small velocities laminar flow will usually occur. Therefore, the velocities in the model should be increased.

In thermal stratification experiments, the task of controlling the temperature is extremely difficult. Therefore a saline solution is often used for simulating the layered flow. At the same time to produce with reasonable accuracy the contrasting densities now required, these densities have to be increased. Fortunately, increasing the densities and the velocities may be met in the Richardson number:

$$R_i = F'^{-2} = \frac{\epsilon g h}{V^2}$$

where F' = densimetric Froude number

$\epsilon = \frac{\rho_2 - \rho_1}{\rho_1}$ = proportionate density defect

ρ_1, ρ_2 = the density of upper and lower layers of the flow

V = a characteristic velocity

h = a characteristic depth.

The final and most important factor is the effect of the aspect ratio and the likely vertical distortions on the circulation. This effect can be investigated by choosing different reservoir models with different aspect ratios.

Sharp (1981), on the other hand, assumed the following requirements for exact similarity between the model and prototype:

(1) Geometric similarity; no exaggeration.

(2) Reynolds number greater than approximately 2500.

(3) Equal Froude numbers, in model and prototype.

(4) Equal densimetric Froude numbers in model and prototype.

In the present research some of the above factors were investigated in an ideal model of a circular reservoir. Time limitations made it impossible to use more than one model.

2.2 MODEL ARRANGEMENTS

2.2.1 Outline of the Reservoir Pipework

To maintain steady flow in the model a constant head arrangement was used. This is shown in Fig. (2.1). The apparatus consisted essentially of two constant-head tanks one containing fresh water and the other salt water. In the experiments with a homogeneous reservoir, fresh water was used as inflow. Dyed water was stored in a small tank and, if necessary, was then mixed with fresh water. This was mainly used for the dye photography runs.

In the stratified reservoir experiments, saline solution was injected at the bottom of the reservoir through two holes connected to a distribution cylinder via a pipe. The distribution cylinder was fed by the saline head tank. A small pump was located downstream of the cylinder to pump the remaining saline solution (at the end of experiments) to waste or back to the saline solution tank.

A sump tank was provided for each constant head tank. Circulation of fluid between the constant head tanks and sump tanks was set up by pumping fluid from the sump tank to the constant head tank. The fluid then passed over the side weirs, through an outlet and returned to the sump tank under gravity, via a pipe. The saline solution was, therefore, stirred continuously and kept in circulation.

To provide the required rate of flow through the reservoir inlet, an inlet pump, a valve and a suitable flow measuring device were connected to the pipe running from the fresh water head tank to the reservoir's inlet.

The reservoir outlet consisted of a pipe running from a particular position in the reservoir to waste. The water discharged out of the reservoir by gravity.

2.2.2 Construction of the Reservoir Model

The experiments were carried out in a 0.92m diameter circular tank whose bed and walls were made out of perspex. A 0.9m square frame was constructed from four wooden beams. The frame was then screwed to the bottom of the reservoir.

The outlet which was located at the centre of the reservoir was made of a 22cm long perspex pipe having a 3cm external diameter. The bottom of the reservoir was painted matt black and a 10cm x 10cm grid was painted onto it. A grid of 1cm x 1cm was drawn on the wall of the reservoir for measuring the position of the interface and for locating the velocity probes. The side of the reservoir was cut and a tangential brass jet 1cm high and 0.2cm wide was installed and was supported by a frame.

The top of the jet was positioned 1.5cm below the water surface. The jet was fed by a 1.93cm diameter transparent polythene tubing.

In a series of experiments the depth of the reservoir was changed in order to examine the effect of the aspect ratio. Therefore, a circular base was made from perspex (1.3cm thickness) and mounted over three cylindrical supports of a given height which were fixed inside the reservoir. The base was then sealed to the wall by plasticine.

2.2.3 Preparation of the Stratified Reservoir Model

In the experiments on the stratified reservoir, saline solutions of different densities were used to simulate the hypolimnion. Two different methods were tried for simulating the stratification in the model reservoir.

(a) Filling the model with the saline solution to a certain depth and then gently forming a layer of fresh water on top of that.

(b) Filling the model with fresh water and injecting the saline solution from the bottom of the reservoir.

In cases where the concentration of the saline solution was high, method (a) saved time considerably. However, method (b) produced a sharper interface, because of less mixing and agitation compared to method (a). Therefore, method (b) was preferred.

The reservoir was first filled with fresh water the night before and left for a few hours to settle down. Saline solution of a given density was made in a storage tank and kept homogeneous using the head tank arrangement. This solution was then introduced gently through two small holes located at the bottom of the reservoir. The process was continued until the desired depth of the saline solution was reached. Meanwhile, the excess fresh water was discharging to waste through the outlet.

The lower fluid was dyed green with florescene. This enabled the position of the interface to be easily determined. The temperature of both layers and that of the fresh layer in the storage tank were

measured using thermometers. These values were later used for calculating the densities.

2.3 MEASUREMENT TECHNIQUES

2.3.1 Measurement of Velocities in the Horizontal Plane

Throughout the experimental work, the measurement of velocities was of prime importance. The magnitude of velocities, however, changed dramatically over a small distance from the reservoir's perimeter wall. For example, for a discharge of Q_0 = 30.83 cc/sec, the range of velocities covered in the experiment was from 0.5 cm/sec to about 100 cm/sec. Therefore, the chosen method or methods of velocity measurement must be capable of covering this range.

Special attention must be given to the range 0.0 to 10 cm/sec, as it encompasses most of the velocities in the reservoir. The miniature propeller meter, used in some of these experiments, covers the range 5 cm/sec to 150 cm/sec but is not very accurate at low velocities.

Stefan and Scheihe (1968) proposed a method of velocity measurement involving the measurement of the deflection of a wax sphere tethered to the channel or to the reservoir's bed. The disadvantage of this method, for application here, is that the device only measures point velocities. The setting up and the measurements were very time consuming and each sphere, unless absolutely identical, required new calibration.

S.J. Robinson and P. Minton (1979) developed a similar device for measuring depth averaged velocities in a model reservoir. Although the setting up of the probes was very time consuming and the subsequent analysis was complicated, the measurements were instantane-

ous and covered a large area through the use of photography. Robinson and Minton were not able to attain sufficient uniformity of the manufacture of the probes for individual calibration to be unnecessary.

White et al. (1955) recorded the movement of floats, travelling with the water particles, by photography. Each float appeared several times in a photograph, which was developed by superimposing at least four images, giving successive positions of the floats, at equal time intervals.

Ali and Pateman (1982) used illuminated surface floats with time lapse photography for the measurement of low velocities at the surface. The floats were made of alloy bottle tops, approximately 2cm in diameter, inverted and set to float on the water surface.

The illumination of the probes was achieved by attaching small birthday candles to the bottle tops. With the candles lit, and the probes placed on the moving water surface, it was possible to alternately open and close the camera shutter to record the movement of each probe over a known time interval.

Comparing the different methods, the illuminated floats technique is very simple and useful. It also illustrates the circulation pattern which is very important in understanding the mechanism of the motion.

For our small model, however, the kind of float was a major problem. The round alloy bottle tops floating over the surface were influenced by surface tension forces and were attracted to the wall of the reservoir. Moreover the candles burnt relatively quickly and their

brightness was not uniform. Surface velocities, however, could be quite different from the depth averaged velocities in a deep reservoir.

Taking account of these difficulties, a new kind of float was developed. This was made of perspex. It was cylindrical in shape, having an outside diameter of 1cm, height of 4cm and weight of 4gms. A small light-emitting diode (LED) was used and it was powered by a mercury button-cell. The simple circuit used in the system is shown in Fig. (2.4). A major advantage of the new float was its ability of being used at considerable depths below the water surface. Because of the length of the float, it was not possible to use it for water depths less than 4cm.

Surface floats, with candles, were used instead. The use of floats was restricted to the areas of low velocities, while the propeller meter was used in the big velocity zones (i.e. near to the jet and the perimeter wall).

2.3.2 Measurement of Velocities at Different Levels

The hydrogen bubble technique was used in some of the experiments to obtain the vertical distribution of small peripheral velocities.

In the stratification experiments, the problem of changes in densities and therefore conductivities was encountered. Conductivity of the saline solution was several times higher than that of fresh water. Therefore, the majority of the hydrogen bubbles were liberated from the lower portion of the wire which was positioned in the saline solution.

Moore and Long (1971) split the wire into four segments, each being supported by insulated needles. They then, applied separate voltages to each segment, thereby controlling the current in each portion.

Hino and Nguen (1983) connected the wire below the interface to a fine plastic wire to avoid violent hydrogen bubble generation.

In the present study the velocity profile of the heavy layer, below the interface, was not required. Therefore, the part of wire in the saline solution was insulated.

The propeller meter was used for the measurement of the variation of big velocities with depth near to the wall.

2.3.3 Effect of the Saline Solution on the Performance of the Propeller Meter

The 'Streamflo' propeller meter measures flow velocity in a fluid by sensing the rotation of a propeller rotor. The rotation is detected by sensing the change in impedance of the fluid as the rotor blades pass a gap between a gold tipped wire and a stainless steel supporting tube. Variation in the fluid conductivity, such as that produced by salinity, will alter the change in impedance. Later models of the instrument make automatic compensation for this effect, and provision is made for varying the range over which it operates.

In earlier models this facility was not provided, thus limiting the range of salinity in which they could operate. An experiment was conducted, in a flume, to study the effect of salinity on the performance of the propeller meter. The propeller was fixed in the flume and while the discharge was kept constant, the salinity of fluid

was increased gradually. For a critical salinity, the reading fell down quickly. The experiment was run for two different discharges and the results are shown in Fig. (2.2). The critical density was about 1028 kg/m^3 and apparently did not depend on the magnitude of the velocity.

Fortunately, in the stratification experiments, the density of the upper layer at the time of velocity measurement was usually less than the critical value except for a narrow zone near the interfacial zone (about 5mm).

2.3.4 Measurement of Densities

After preparing the two layered model and before starting the experiments, samples of fluid were abstracted by micropipette from different depths. The samples were measured later to determine the stratification curve of the model.

In all of the experiments the jet was placed in the fresh layer and very near to the surface. In some of the experiments, the lower layer extended up to the bottom of the jet. The inflow from the tangential jet caused agitation and mixing in the stratified reservoir and a consequent change in the density structure therein. Samples of fluid were taken simultaneously from different stations. The samples were collected in the bottles of a chamber, Fig. (2.3), and kept for analysis.

The total volume of saline solution removed from the model in sampling was small compared with the total volume of the reservoir. However, in some of the experiments a volume of saline solution equal to that

extracted in sampling was added to the reservoir through the bottom holes.

2.3.5 The Forty Probe Sampler

The sampler was designed to collect forty samples of fluid simultaneously so that the distribution of densities in the three coordinate directions could be measured in addition to the variation with time. The operating principle involved using suction to provide an equal discharge into a partially evacuated chamber through each of forty small bore polythene tubes.

2.3.5.1 The Pressure Chamber

The pressure chamber was made circular in plan, using a 5mm sheet steel base 700mm in diameter with 4mm sheet steel walls curved to form a circle, and welded to the base. To the top of the walls was attached a 40mm wide steel flange cut from 5mm sheet. The top of the chamber was made from 15mm perspex and bolted to the flange using 52 M8 steel bolts and nuts. A 3mm thick rubber gasket sealed with silicone grease was used over the whole of the flange to take up distortions.

The aim of the device was to collect fluid from forty probes simultaneously at a number of different times from the beginning of the experiment. A horizontal plywood tray drilled to hold sample bottles was placed inside the chamber. Bottles were placed radially on the tray in lines long enough to accommodate ten bottles. The tray was made to rotate about a vertical central axis, Fig. (2.5).

Sample tubes running from the model were attached to hose connectors screwed into the top of the chamber in such a manner that the fluid

issuing from them fell directly into bottles situated on the tray beneath.

The arrangement of the hose connectors was such that a small rotation of the tray presented a set of forty clean bottles beneath them. The vertical axle on which the tray revolved was of brass, bearing a ball seat braised to the cut of the base of the pressure chamber. A shoulder on the axle, situated 25mm below the top of the chamber supported a set of washers and a wooden disc to support the perspex top when the chamber was subjected to negative pressures. The axle then continued on through the perspex top to terminate with a handle with which the axle and tray could be rotated. The cross section of the pressure chamber, tray, axle and hose connectors is shown in Fig. (2.6).

The pressure chamber was reinforced against bending by welding four lengths of 35mm x 35mm angle section externally to the bottom. The pressure in the chamber was controlled through three tappings on the side of the pressure chamber just beneath the flange.

2.3.5.2 <u>The Vacuum Pump and Manometer</u>

One of the tappings was connected to a vacuum pump. A compton D/351 VM diaphragm pump was chosen, capable of producing a negative pressure of 0.5m head of mercury.

A vertical manometer open to the air was connected to one of the tappings to enable measurement of the pressure within the chamber. A $^{1}/_{4}$ inch B.S.P. gate valve was incorporated in the line between the chamber and the manometer to allow air to bleed into the system,

thereby regulating the pressure in the chamber and hence the discharge through the sample tubes.

2.3.5.3 The Fast Bleed Valve

The third tapping, in the chamber, was fitted with a $^1/_4$ inch B.S.P. butterfly valve to allow rapid restoration of atmospheric pressure in the chamber. A space beneath the bottle tray was required to contain spillage occurring when transferring from one set of forty bottles to the next, and also whilst waiting for the discharge from the sample tubes to become constant.

During the experiment the elapsed time between the two consecutive measurement was enough to repressurise the chamber, pump out the waste fluid in the bottom through a drain tap, and evacuate the chamber once more down to the correct pressure ready for the next measurement.

2.3.6 Analysis of the Density Results

Samples of saline solution were analysed using conductivity measuring bridge type M.C.3 for the range of low and medium densities ($\rho < 1050$ kg/m^3). The conductivity bridge was sensitive to the variation of temperature. Therefore its readings were calibrated using different concentrations of saline solutions at different temperatures. The variation was approximately linear and regression analysis was used to give the best fit line to the results, Table (2.1).

The density of saline solutions at different concentrations and different temperatures were obtained from International Critical Tables, Washburn (1929), Table (2.2). The value of concentration, at a certain temperature, obtained from Table (2.1) was used and related to the corresponding density from Table (2.2). All the calculations

were performed using a computer program that finally plotted the depth-density curves at different times.

For high densities of saline solution ($1050 < \rho < 1090$ kg/m^3), Density Meter DMA 35 was used. It gave the density and temperature of solution directly.

2.3.7 Measurement of Jet Expansion and Circulation Patterns

Circulation patterns inside the reservoir were obtained using dye photography. Photographs of dye mixing were taken at different time periods.

Expansion of the jet in the vertical direction was also recorded by dye photography.

CHAPTER 3

NOTATION

a	characteristic azymuthal velocity of reservoir
a'	an experimentally determined function of α
b_0	nozzle width
c	constant
C_0, C_1, C_1', C_2, C_*	experimental constants
d	diameter of nozzle
E	entrainment coefficient
f	function of similarity
f	friction factor
f_1	Coriolis parameter
F_r, F_θ, F_z	body forces in r, θ, z directions
F_r	jet Froude number
g	acceleration due to gravity
h	depth of reservoir
h_0	height of nozzle
I	kinematic moment of angular flux
J	slot momentum
k	constant
k_s	equivalent roughness height
K_0	kinematic jet momentum flux
ℓ	mixing length
L	a typical horizontal length of reservoir
L_0	potential core length
M_0	excess momentum
$p, \bar{p}$	pressure and mean pressure

p'	perturbation pressure
q	constant
Q	volume flux
$Q_c, \bar{Q}_c$	total volume flux and mean Q_c
Q_0	inlet discharge
r, θ, z	cylindrical polar coordinate system
R	radius
R_e	Reynolds number
s	constant
t	time
u,v,w	velocity componoents in three directions of a cartesian coordinate or cylindrical polar coordinate
$\bar{u},\bar{v},\bar{w}$	mean velaues of u,v,w or depth averaged values of u,v,w
u',v',w'	perturbation values of u,v,w
u_m	maximum velocity in x direction
u_{m0}	centerline maximum velocity
u_r	a reference velocity
u_*	shear velocity
U	$= u - U_1$ in co-flowing stream
U_c	a characteristic velocity
U_m	velocity scale in co-flowing stream
U_0	jet velocity in x direction
U_1	velocity of a co-flowing stream
v_m	maximum velocity in tangential direction in reservoir
v_0	inlet velocity in θ direction in reservoir

V	a characteristic azimuthal velocity in wall jet in reservoir
V_1	stream characteristic velocity
W_e	entrainment velocity
x,y,z	cartesian coordinate system
$\bar{x}$	the distance from virtual origin
x_o	distance from the jet and virtual origin
y_m	length scale in y direction
Y_m	length scale in y direction in co-flowing flow
y,y_m	distance from the wall towards the center of reservoir and length scale in that direction in reservoirs
z_m	length scale in z direction
Z_m	length scale in z direction in co-flowing flow
z'	constant
α	the ratio of jet velocity (U_0) to stream velocity (U_1)
α'	horizontal scale ratio
α_p	the growth rate of free jet in motionless surrounding
α_w	the growth rate of wall jet in motionless surrounding
β	constant
β'	vertical scale ratio
δ	characteristic width of wall jet in reservoir
δ_1	boundary layer thickness
ϵ	turbulent coefficient of kinematic viscosity
ϵ'	perturbation parameter
ζ	water surface elevation

η	y/y_m
θ	angle from the jet
θ_1	momentum thickness
θ_0	angle between the jet and virtual origin
λ	angle of growth in vertical direction
ν	laminar coefficient of kinematic viscosity
ρ	density
$\sigma_{i,j}$	stress component in plane nomral to i direction and directed in j direction for i and j = r, θ and z
σ_0, σ_1	constant
τ_ℓ	laminar shear stress
τ_t	turbulent shear stress
τ_0	wall shear stress
$\tau_{r\theta}{}^w$	side wall shear stress in reservoir
$\tau_{ze}{}^b$	bed shear stress in reservoir
φ	latitude of basin
Ω	angular speed of earth

CHAPTER 3

JET FORCED RESERVOIR CIRCULATION

3.1 INTRODUCTION

Reservoir circulation can be induced by many different parameters. The most important ones are throughflows, wind action and the earth's rotation.

Wind action does not always produce strong enough currents specially over the relatively small fetch of a service reservoir. Moreover, it is irregular and subject to various meteorological, climatological and topographical factors which might be specific to one site.

On the other hand, the roation of the earth and the coriolis forces acting over the circulation of the water body are normally weak. They are also a function of the geographical latitude and position of the reservoir.

Throughflows and specifically momentum jetting of the inlet water is the most important method for hydraulic and biological control of water supply reservoirs. The incoming jets impart their momentum to the reservoir and in so doing cause large scale circulations. Controlled circulatory currents reduce the development of stratification and layered flow.

The foundation for the development of models of fluid motion lies in the Navier-Stokes equations for the conservation of momentum. In addition, conservation laws for mass and energy are usually also required. The complete set of equations is without formal general

solutions, yet methods have been devised to obtain solutions for particular cases usually including the use of numerical methods.

The three components of velocity u,v,w and the pressure p are decomposed, according to Reynolds conceptualisation, into mean and fluctuating components, i.e.

$$u = \bar{u} + u', \quad v = \bar{v} + v', \quad w = \bar{w} + w', \quad p = \bar{p} + p'$$

The above expressions are usually substituted into the Navier-Stokes equations and time averaged.

In homogeneous flows with a relatively large area (e.g. reservoirs and lakes) the ratio of the horizontal scale to the vertical scale is usually very large. Therefore, the major flow is in the horizontal plane and the vertical velocity component is usually small.

The hydrostatic approximation is, then, justified i.e. the vertical component of acceleration is neglected compared with the gravitational acceleration. Moreover, the Navier-Stokes equations may be integrated over the depth to obtain simpler depth averaged relationships.

Usually, there are two methods for the solution of the Navier-Stokes equations:

(i) The integral method

(ii) The finite difference method.

The first method is the subject of the present chapter and the second one will be discussed in the next chapter.

The basic philosophy of the integral method is that the governing equations need not be satisfied at every point within a region of interest but ratehr in an average way throughout the entire region. This theory will later be discussed in detail. However, because of the important role of jets and their application in the development of the theory, a review of jet literature is presented first.

Also, a comprehensive series of experimental studies will finally be given.

Throughout this chapter, the study is restricted to homogeneous flows. The effect of density variation is dealt with in subsequent chapters.

3.2 TURBULENT JETS, A LITERATURE REVIEW

Jets are usually known as point sources of momentum. There is extensive work on the behaviour of turbulent jets. In the present study we start with the analysis of the two-dimensional jet and extend later to more complicated cases. This review will be more concerned with the results of the investigations rather than the derivation of the various relationships. These results will be applied later to our reservoir circulation problem.

3.2.1 Two-Dimensional Momentum Jet

The boundary-layer equation for a two-dimensional plane, turbulent jet of water issuing into a stationary body of water is, (Fig. 3.1a), Townsend (1976), Rajaratnam (1976):

$$u \frac{\partial u}{\partial x} + v \frac{\partial u}{\partial y} = \nu \frac{\partial^2 u}{\partial y^2} - \frac{\partial(\overline{u'v'})}{\partial y} - \frac{\partial}{\partial x}(\overline{u'^2} - \overline{v'^2}) \qquad (3.1)$$

The continuity equation is given by:

$$\frac{\partial u}{\partial x} + \frac{\partial v}{\partial y} = 0 \qquad (3.2)$$

The pressure, p, is assumed to be constant.

The last term in equation (3.1) is smaller than the other terms and could be dropped. Hence we obtain the reduced equation of motion:

$$u \frac{\partial u}{\partial x} + v \frac{\partial u}{\partial y} = \nu \frac{\partial^2 u}{\partial y^2} - \frac{\partial \overline{u'v'}}{\partial y} \qquad (3.3)$$

where u = mean velocity of the jet in x direction

v = mean velocity of the jet in y direction

u' = turbulent fluctuating velocity in x direction

v' = turbulent fluctuating velocity in y direction

ν = kinematic viscosity

(x,y) = axial direction of jet and normal to it respectively.

We could rewrite the last two terms of equation (3.3) as:

$$\frac{1}{\rho}\frac{\partial}{\partial y}\left(\mu\frac{\partial u}{\partial y}\right) + \frac{1}{\rho}\frac{\partial}{\partial y}\left(-\rho\,\overline{u'v'}\right) = \frac{1}{\rho}\frac{\partial}{\partial y}\left(\tau_\ell + \tau_t\right) \qquad (3.4)$$

where τ_ℓ = laminar shear stress

τ_t = turbulent shear stress

μ = coefficient of dynamic viscosity

ρ = density.

In free turbulent flows, due to the absence of solid boundaries, τ_t is much larger than τ_ℓ and hence it is reasonable to neglect τ_ℓ and rewrite equation (3.3) as:

$$\rho u\frac{\partial u}{\partial x} + \rho v\frac{\partial u}{\partial y} = \frac{\partial \tau_t}{\partial y} \qquad (3.5)$$

A plane turbulent jet issuing into a large stagnant environment and expanding under zero pressure gradient, conserves its axial momentum as there is no external force involved. This will be shown as follows:

The equation of motion may be integrated with respect to y,

$$\rho\int_{-\infty}^{+\infty} u\frac{\partial u}{\partial x}\,dy + \rho\int_{-\infty}^{\infty} v\frac{\partial u}{\partial y}\,dy = \int_{-\infty}^{+\infty}\frac{\partial \tau_t}{\partial y}\,dy \qquad (3.6)$$

The order of differentiating and integrating of the first term may be interchanged by noting:

$$u\frac{\partial u}{\partial x} = \frac{\partial}{\partial x}\left(\frac{u^2}{2}\right)$$

In addition, the second term may be integrated by parts,

$$\frac{\rho}{2}\frac{\partial}{\partial x}\int_{-\infty}^{+\infty} u^2\,dy + \rho uv\Big|_{-\infty}^{+\infty} - \rho\int_{-\infty}^{+\infty} u\frac{\partial v}{\partial y}\,dy = \tau_t\Big|_{-\infty}^{+\infty} \qquad (3.7)$$

If we use the continuity equation (3.2) for the third term on the left-hand side, it becomes identical with the first term. As $y \to \pm\infty$, u and its derivative with respect to y vanish, and also $\tau_t = 0$. Equation (3.7) may then be written as:

$$\rho\frac{\partial}{\partial x}\int_{-\infty}^{+\infty} u^2\,dy = 0 \qquad (3.8a)$$

and $$\int_{-\infty}^{+\infty} \rho u^2\,dy = \text{const.} \qquad (3.8b)$$

Equation (3.8b) states that the product of momentum per unit volume (ρu) and the volume per unit time (udy) i.e. the total momentum per unit time passing any section of the jet or the flux of momentum of the jet is constant and independent of x. The constant in equation (3.8b) may be evaluated from the momentum influx at x = 0, and hence, since the momentum per unit volume is ρU_0, the volume per unit time is ($b_0\ U_0$), where b_0 is the width of the slot and U_0 is the velocity of jet.

Now we can write:

$$\int_{-\infty}^{+\infty} \rho u^2 dy = \rho {U_0}^2 b_0 \qquad (3.9)$$

As shown in Figure (3.1), in the development of a plane jet there is a potential core of length L_0 in which the cnetre line velocity U_0 remains constant. This is the zone of flow establishment. For values of x greater than L_0 the jet is said to be fully developed and the maximum velopcity (u_m) is decreasing with the increase in x.

In the fully developed region of the jet both the maximum velocity, u_m, (the velocity scale), and the offset from the centerline, y_m (the length scale), may be expressed in terms of x to unknown exponents. Hence:

$$u_m \sim x^s \tag{3.10a}$$

$$y_m \sim x^q \tag{3.10b}$$

Moreover for the plane turbulent jet, the velocity distribution in the fully developed region is similar. That is:

$$\frac{u}{u_m} = f(\eta) \tag{3.11}$$

where $\eta = y/y_m$

y_m = the position at which $u = u_m/2$

$f(\eta)$ = a function independent of x.

Substitution of equation (3.11) into (3.8a) gives:

$$\frac{d}{dx}\,(y_m\, u_m^{\,2}) = 0 \tag{3.12a}$$

From (3.12a) we can say that $y_m\, u_m^{\,2}$ is independent of x. That is:

$$y_m \, u_m^2 \propto x^0 \tag{3.12b}$$

From (3.10a) and (3.10b), we obtain:

$$x^{q+2s} \propto x^0 \tag{3.13}$$

$$\text{and} \quad q + 2s = 0 \tag{3.14}$$

To evaluate s and q another equation should be developed. This equation can be obtained in a number of ways, for example by using the entrainment hypothesis.

If Q is the rate of (forward) flow, experiments show that Q/Q_0 is greater than unity and become very large for high values of x (Q_0 = jet discharge). That means, the jet entrains a considerable amount of the surrounding fluid as it travels forward. We can now write:

$$\frac{dQ}{dx} = 2 \frac{d}{dx} \int_0^\infty u dy = 2W_e \tag{3.15}$$

where W_e is the so-called entrainment velocity.

From dimensional considerations, we could write:

$$W_e \propto u_m \quad \text{or} \quad W_e = E \, u_m \tag{3.16}$$

where E is the entrainment coefficient. Thus:

$$\frac{d}{dx}\int_0^\infty u\,dy = E\,u_m \tag{3.17}$$

or

$$\frac{\frac{d}{dx}\,(u_m\,y_m)\int_0^\infty f(\eta)\,d\eta}{u_m} = E$$

Consequently:

$$\frac{\frac{d}{dx}\,(u_m\,y_m)}{u_m} \propto x^0 \tag{3.18}$$

That is:

$$s + q - 1 - s = 0 \quad \text{or} \quad q = 1 \tag{3.19}$$

Using (3.14), we obtain s = - 1/2. Therefore we get:

$$u_m \propto 1/\sqrt{x} \tag{3.20}$$

$$y_m \propto x \tag{3.21}$$

The theoretical evaluation of the velocity distributions (u and v) may be obtained by solving the equations of motion (3.5 and 3.2). This requires a closure euqation for the turbulent shear stress (τ_t). For this missing equation, Tollmien, utilized the prandtl mixing length theory and assumed that:

$$\tau_t = - \rho \ell^2 \left(\frac{\partial u}{\partial y}\right)^2 \tag{3.22}$$

where ℓ is the so-called mixing length, which is proportional to y_m:

$$\ell \propto y_m$$

or $$\ell = \beta\, y_m \tag{3.23}$$

or $$\ell = \beta C_1\, x$$

β and C_1 are constants of proportionality. Substituting for the turbulent shear stress and solving the system of partial differential equations, Tollmien obtained a numerical solution for the velocity distribution.

Goertler, on the other hand, used the second equation of Prandtl:

$$\tau_t = \rho \epsilon \frac{\partial u}{\partial y} \tag{3.24}$$

where ϵ is known as the turbulent coefficient of kinematic eddy viscosity and is assumed to be constant at any cross section. Goertler assumed that:

$$\epsilon \propto u_m\, y_m$$

or $$\epsilon = k\, u_m\, y_m \tag{3.25}$$

and obtained another numerical solution for the velocity distribution. A comparison between the above two solutions and other theoretical solutions is given in Figure (3.1b).

On the experimental side, a Gaussian curve was found to satisfactorily represent the velocity distributions. This expression is given by:

$$\frac{u}{u_m} = \exp(-0.693\ \eta^2) \tag{3.26}$$

where $\eta = y/y_m$.

The constants of proportionality in equations (3.20) and (3.21) have also been determined experimentally.

The general formulae for the variation of centreline velocity can be written as:

$$\frac{u_m}{U_0} = \frac{C_1'}{\sqrt{\dfrac{\bar{x} + C_* b_0}{b_0}}} \tag{3.27}$$

where $\bar{x}$ = the distance from virtual origin, which is not necessarily at the actual nozzle

C_1' = constant experimental results cover the range (3.12-3.78)

C_* = constant (0 - 2.4).

For all practical purposes we can use:

$$\frac{u_m}{U_0} = \frac{3.5}{\sqrt{\bar{x}/b_0}} \tag{3.28}$$

Concerning the length scale y_m, we have:

$$y_m = C_1 \, x \tag{3.29}$$

and $C_1 \approx 0.1$

3.2.2 The Axisymmetric Turbulent Jet

The axisymmetric or circular turbulent jet can be treated in an anlogous manner to the two-dimensional jet with the cylindrical coordinate r replacing the cartesian coordinate y. The simplified equations of motion are, (Rajaratnam (1976)):

$$u \frac{\partial u}{\partial x} + v \frac{\partial u}{\partial r} = \frac{1}{\rho r} \frac{\partial (r \tau_t)}{\partial r}$$

$$\frac{\partial (ru)}{\partial x} + \frac{\partial (rv)}{\partial r} = 0 \tag{3.30}$$

The integral momentum equation, then becomes:

$$\frac{d}{dx} \int_0^\infty 2\pi r \, dr \, \rho u^2 = 0 \tag{3.31}$$

Equation (3.31) states that the rate of change of the momentum flux in the axial direction is zero or that the momentum flux in the axial direction is conserved.

A similar procedure to that for the two-dimensional plane jet would give the following proportionalities for velocity and lengths scales.

$$u_m \propto \frac{1}{x}$$

$$y_m \propto x \qquad (3.32)$$

A collection of experimental results gives:

$$\frac{u_m}{U_0} = 6.39/(\frac{\bar{x}}{d} + 0.6) \qquad (3.33)$$

the virtual origin is located 0.6d behind the nozzle, and d is the diameter of nozzle. In a simplified form the velocity scale becomes:

$$\frac{u_m}{U_0} = 6.3/(x/d) \qquad (3.34)$$

For the length scale one could use the relation:

$$y_m = 0.1x \qquad (3.35)$$

which is the same as that for the two-dimensional plane jet. The velocity distribution for the circular turbulent jet could be presented by a Gaussian curve:

$$\frac{u}{u_m} = \exp(-\ 0.693\ (\frac{r}{y_m})^2) \qquad (3.36)$$

3.2.3 The Turbulent Wall Jet

A turbulent wall jet, Figure (3.2) consists of an inner boundary layer, for $y < \delta_1$, and an outer half jet, for $y > \delta_1$. Where δ_1 is the thickness of the boundary layer.

Using a coordinate system and notation similar to that for the plane free jet and following closely the previous arguments, we could show that the equations of motion of the plane turbulent wall jet are:

$$\begin{cases} u \dfrac{\partial u}{\partial x} + v \dfrac{\partial u}{\partial y} = \dfrac{1}{\rho} \dfrac{\partial \tau_t}{\partial y} \\ \\ \dfrac{\partial u}{\partial x} + \dfrac{\partial v}{\partial y} = 0 \end{cases} \tag{3.37}$$

Integrating with respect to y from zero to infinity, the integral momentum equation is:

$$\frac{d}{dx} \int_0^\infty \rho u^2 dy = - \tau_0 \tag{3.38}$$

where τ_0 is the wall shear stress.

It is also found that the variation with x of the maximum velocity, u_m, the length scale, y_m, and wall shear stress, τ_0, is given by:

$$\begin{aligned} u_m &\propto \frac{1}{\sqrt{x}} \\ y_m &\propto x \\ \tau_0 &\propto \frac{1}{x} \end{aligned} \tag{3.39}$$

The velocity distribution of the entire wall jet has been found to be similar, Sigalla (1958), Myers et al. (1961) and Schwarz and Cosart (1961). Verhoff (1963) obtained the following empirical equation to describe the velocity-distribution:

$$\frac{u}{u_m} = 1.48\ \eta^{1/7}\ [1 - \text{erf}\ (0.68\eta)] \tag{3.40}$$

Recent obersvations of Myers et al (1961) have shown that the velocity distribution in the boundary layer can be well described by the logarithmic law:

$$\frac{u}{u_*} = 5.6\ \log\ (\frac{yu_*}{\nu}) + 4.9 \tag{3.41}$$

with $u_* = \sqrt{\tau_0/\rho}$, shear velocity.

The outer flow has also been represented quite satisfactorily by the following Gaussian profile:

$$u = u_m\ \exp(-0.693\ (y - \delta_1)^2/(y_m - \delta_1)^2) \tag{3.42}$$

The ratio δ_1/y_m decreases with increasing Reynolds number ($R_e = u_m\ \delta_1/\nu$), but typically has a value around 0.15.

Rajaratnam and Subramanya (1967) have shown that the decay of the maximum velocity can be described by:

$$\frac{u_m}{U_0} = 3.5/\sqrt{x/b_0} \tag{3.43}$$

for x/b_0 at least up to 100, where b_0 is the width of the jet, Fig. (3.3a).

Schwarz and Cosart (1961) obtained:

$$\frac{u_m}{U_0} = 5.395 \left(\frac{x}{b_0} + 11.2\right)^{-0.555} \tag{3.44}$$

Indicating that the maximum velocity decays a little more rapidly than in the case of the plane free jet. This reflects a small momentum loss due to wall friction.

The growth rate (dy_m/dx) has been shown to be in a range of 0.056 to 0.085. Figure (3.3b) shows that a value of 0.068 is appropriate.

This reduction in the growth rate from the plane free jet would indicate that the prixmity of a wall could significantly reduce the entraining capacity of a reservoir inlet.

3.2.4 The Curved Wall Jet

The special case of a plane jet located at the inner side of a wall of constant radius R (Figure 3.4) has been studied by Guitton (1964). His experiments indicate that the curved wall further decreases the growth rate from that of straight wall jet. The growth law being presented in the form:

$$\frac{y_m}{x - x_0} = 0.065 - 0.32\, y_m/R \tag{3.45}$$

where $x = R\theta$, θ being the angular position

x_0 = distance from the jet and hypothetical origin.

Based on Guitton's analysis for the self preserving curves, (i.e. the cases where the radius of curvature is proportional to the distance from the jet). We can write:

$$u_r \propto x^{-1/2-\epsilon'(0.225)} \tag{3.46}$$

where u_r = a reference velocity which is proportional to the maximum velocity u_m.

ϵ' = perturbation parameter = $y_m/0.8812R$

The decay is, therefore, a little more rapid than in the case of the free jet.

For the case of non-self preserving flow (i.e. a circle with a constant radius, R), Guitton derived the following relationship:

$$\frac{\rho u_m{}^2 x}{J} = \frac{3}{2}\sigma_0\left[1 - \frac{|R|}{R}\left(\frac{2.32}{\sigma_0} + \frac{1}{\sigma_1}\right)\theta\right] \tag{3.47}$$

where ρ = the density

u_m = maximum velocity

J = the actual slot momentum

x = distance from the jet

σ_0, σ_1 = constants

θ = x/R

Kobayashi and Fujisawa (1983), conducted experiments on curved surfaces having curvature parameters of $y_m/R = 0.008$ to $y_m/R = 0.095$ (defined as the ratio of half width y_m to the radius) and obtained a linear variation of $(U_0/u_m)^2$ and y_m/b_0 with x/b_0 (Figure 3.5).

The gradient of the growth rate, however, reduces with the decrease in R. The range of jet velocity U_0 at the nozzle's exit was 32 m/sec to 48 m/sec and the jet width was $b_0 = 0.8$ cm.

3.2.5 Surface Jet

Rajaratnam and Humphries (1984) and Rajaratnam (1969), conducted a series of experiments on two-dimensional surface jets issuing into a stagnant pool, Figure (3.6). Based on the results of these experiments, it can be shown that the u velocity profiles are similar at different sections and can be well described by the exponential law equation (3.26).

The length scale z_m varies linearly with the longitudinal distance x, i.e.

$$\frac{dz_m}{dx} = 0.07 \tag{3.48}$$

This result is very close to that for the wall jet.

The velocity scale decays in the same manner as in the case of the plane free jet with the constant coefficient being somewhat smaller than that for the free jet.

$$\frac{u_m}{U_0} = \frac{3.1}{\sqrt{x}} \tag{3.49}$$

Maxwell and Pazwash (1967) investigated experimentally the influence of a free surface on a horizontally-oriented axisymmetric turbulent jet. They showed that the locus of the maximum velocity was attracted towards the free surface. The lower part of the velocity distribution closely resembled that for a deeply submerged jet but the upper part was affected by wave action and spread at an increased rate. In a subsequent study, to include the effect of a horizontal bed, a similar attraction and increased growth rate was observed at the solid boundary. Both the free surface and bed tend to attract the jet and both cause increased spreading of the flow but one boundary generally proved to be dominant, depending on the geometry.

3.2.6 Three-Dimensional Free Jet

Jets issuing from nozzles which are neither axisymmetric nor rectangular, with a very large aspect ratio b_0/h_0, where b_0 is the width and h_0 is the height, are referred as three-dimensional jets. In Figure (3.7) there are three regions for the (3-D) jet with an aspect ratio of say $b_0/h_0 = 20$. In the first region (0A), the centerline velocity of jet is constant. In the second region (AB) the centreline velocity decays with x (where x is the axial distance from a suitable virtual origin) at a rate roughly the same as that of a plane jet. In the third region (BC), u_{m_0} decays inversely with x. Region 2 could be referred to as the 'plane jet type decay region', and region 3 as the 'axisymmetric-type decay region'. For a jet with smaller aspect ratio ($b_0/h_0 \leqslant 5$), square or triangular jets, the potential core is followed by the axisymmetric decay region. The jets with three distinguished

regions are known as 'slender jets' while the ones with two regions are termed 'bluff jets'.

Decay of the maximum velocity and the length scale for 'slender jets' of various aspect ratios, in both directions (z,y), are given by Yevdjevich (1966). For the 'bluff jets', the maximum velocity decay follows the same curve for square, triangular, rectangular and elliptic nozzles, Rajaratnam (1976). The growth of length scale in the y and z directions are the same for square nozzles and is described by the equation:

$$\frac{y_m}{h_0} = \frac{z_m}{h_0} = 0.097 \frac{x}{h_0} \tag{3.50}$$

with the virtual origin located at the nozzle itself. For the other shapes of nozzles, the growth of the length scale in the z direction for the nozzles with aspect ratio up to about 10 is satisfactorily given by equation (3.50). It appears difficult to predict the variation of y_m when b_0/h_0 is larger than unity.

3.2.7 Three-Dimensional Wall Jet

Consider a rectangular jet of an aspect ratio of about 40 issuing tangentially on a smooth plate with the longer side of the nozzle parallel to the plate. The potential core of the jet is invaded by the boundary layer on the plate side and by shear layers on the other three sides. There are usually three different regions, very similar to those of the three-dimensional free jets.

In the first region or the potential core region, the maximum velocity remains constant and equal to the efflux velocity U_0.

In the next region the maximum velocity decays with the axial distance x similar to the plane wall jet case. This second region was termed the 'characteristic decay region' by Viets and Sforza (1966).

In the third region, the maximum velocity decays roughly as 1/x, i.e. similar to the case of a round jet.

For the bluff wall jets the decay of the maximum velocity is usually proportional to 1/x, after the first region.

The growth of length sacle in the y direction is given by Rajaratnam and Pani (1974) as:

$$\frac{y_m}{b_0} = 0.9 + 0.045 \frac{\bar{x}}{b_0} \tag{3.51}$$

and in the z direction, close to the jet, by:

$$\frac{z_m}{h_0} = 0.2 \frac{\bar{x}}{h_0} - 1.25 \tag{3.52}$$

where h_0 is the height of the nozzle (parallel to the wall). It is interesting to note that z_m grows about 4 to 5 times faster than y_m.

3.2.8 Bluff Surface Jet

Rajaratnam and Humphries (1982) conducted an experimental study on circular and bluff surface jets, Fig. (3.8). They verified the similarity of velocity profiles in both y and z directions.

The velocity decays less rapidly than in the case of a free circular jet. The rate of growth of length scale in the vertical direction can be approximated by:

$$\frac{dz_m}{dx} \cong 0.044 \tag{3.53}$$

which is essentially equal to the corresponding expansion rate for circular wall jets equation (3.51). The variation of length scale in the transverse direction is given by:

$$y_m = 0.09x \tag{3.54}$$

which is twice the value of z_m.

3.2.9 Momentum Jet in a Co-Flowing Stream

For a two-dimensional free jet in a co-flowing stream, Fig. (3.9a), the similarity form requires that:

$$\frac{U}{U_m} = f(\eta)$$

or $$u = U_1 + U_m f(\eta) \tag{3.55}$$

where $U = u - U_1$

U_1 = the velocity of the co-flowing stream

U_m = the velocity scale = $u_m - U_1$

$\eta = y/Y_m$

Y_m = the length scale where $U = U_m/2$.

The momentum integral equation for the two-dimensional jet is given by:

$$\frac{d}{dx}\int_0^\infty u(u - U_1)dy + \int_0^\infty (u - U_1)dy\,\frac{dU_1}{dx} = 0 \qquad (3.56)$$

Theoretically, there is no exact self-preservation even for the case of zero pressure gradient (U_1 constant). Utilizing the observations of Bradbury (1965) and Tani and Kubashi (1951) we may conclude that the velocity distribution is approximately similar.

For the case of constant co-flowing stream we have:

$$\frac{d}{dx}\int_0^\infty \rho u(u - U_1)dy = 0 \qquad (3.57)$$

Substituting (3.55) into the above equation and simplifying we have:

$$\frac{d}{dx}\left[Y_m \frac{U_m}{U_1}\int_0^\infty f\,d\eta + Y_m \left(\frac{U_m}{U_1}\right)^2 \int_0^\infty f^2 d\eta\right] = 0 \qquad (3.58)$$

In the above equation there are two terms, the integrals are roughly of the same order of magnitude. Depending upon the value of U_m/U_1 one term will be large, small, or of the same order as the other. Now we

are specifically interested in the case where $U_m/U_1 \gg 1$. This type of flow is sometimes referred to as the 'strong jet'. It usually occurs in the early portion of the region of fully developed flow. For this condition (3.58) reduces to:

$$\frac{d}{dx}\left[Y_m \left(\frac{U_m}{U_1}\right)^2 \int_0^\infty f^2 d\eta\right] \cong 0 \tag{3.59}$$

Using equation (3.59) in a similar manner to the free jet analyses we can prove that:

$$U_m \propto 1/\sqrt{x}$$

$$Y_m \propto x \tag{3.60}$$

A similar argument gives the following results for strong circular compound jets:

$$U_m \propto \frac{1}{x} \tag{3.61}$$

$$Y_m \propto x$$

We have seen that for the plane co-flowing jet, the excess momentum $M_0 = b_0 \rho U_0(U_0 - U_1)$ is preserved, equation (3.57). We could write:

$$U_m = f_1(M_0, \rho, x) \tag{3.62}$$

Using the Π-theorem, equation (3.62) reduces to:

$$\frac{U_m}{\sqrt{M_0/\rho x}} = \text{constant} \tag{3.63}$$

or $$\frac{U_m}{\sqrt{U_0(U_0 - U_1)}} = C_2/\sqrt{x/b_0} \tag{3.64}$$

Rajaratnam (1976) introduced a length scale defined by:

$$M_0 = \theta_1 \rho U_1^2 \tag{3.65}$$

where $\theta_1 = b_0\ \alpha\ (\alpha - 1)$ the so called 'momentum thickness'

and $\alpha = \frac{U_0}{U_1}$

Equation (3.64) could be written as:

$$U_m/U_1 = C_2\sqrt{x/\theta_1} \tag{3.66}$$

Bradbury (1965), using his experiments, found that the velocity distribution was similar, Fig. (3.9b), and could be described by the equation:

$$U/U_m = \exp[-0.6749\ \eta^2(1 + 0.027\ \eta^4)] \tag{3.67}$$

The experimental observations of Weinstein (1955), Bradbury (1965) and Bradbury and Reily (1967) resulted in the following relationship:

$$\frac{U_m}{\sqrt{U_0(U_0 - U_1)}} = \frac{3.41}{\sqrt{x/b_0}} \tag{3.68}$$

Equation (3.68) could also be written as:

$$\frac{U_m}{U_1} = 3.41/\sqrt{x/\theta_1} \tag{3.69}$$

Substituting the velocity scale into the integral momentum equation results in the following relationship for the length scale:

$$\frac{Y_m}{b_0} = 0.118\ \frac{x}{b_0}\ \frac{1}{1 + \frac{0.41}{\sqrt{\alpha(\alpha - 1)}}\ \sqrt{x/b_0}} \tag{3.70}$$

where $\alpha = U_0/U_1$.

Experiments show that equation (3.70) is acceptable for values of α up to about 6.25, Rajaratnam (1976). Another equation by Abramovich (1963) relates the growth of the jet in a co-flowing stream to that in still surroundings. He transformed the x coordinate such that it moved at a velocity U_c characteristic of the jet. The growth rate is analogous to the equation for the free jet in still surroundings:

$$\frac{dY_m}{dx} = \alpha_p\ (U_c - U_1)/U_c \tag{3.71}$$

where α_p is the growth rate in the motionless environment.

Abramovich chose $U_1 + {}^1/_2\ U_m$ for the characteristic velocity. Patel (1971), however, has shown that the choice of $U_1 + U_m$ for U_c gives a more satisfactory result, both theoretically and experimentally. The Abramovich/Patel equation is thus:

$$\frac{dY_m}{dx} = \alpha_p \frac{U_m}{U_1 + U_m} \tag{3.72}$$

where α_p is 0.104.

An important conclusion in the present context follows directly from equation (3.72), namely that the general effect of a co-flowing stream is to reduce the rate of entrainment. This conclusion is well supported by experiments, Newman (1967).

3.2.10 Wall Jet in a Co-Flowing Stream

In Section 3.2.3 turbulent wall jet in still surrounding environment was reviwed. In this section we consider the case where there is a uniform flow of the ambient fluid (U_1). The present analysis of the wall jet in a co-flowing stream is generally an extension of the motionless ambient fluid case. The analysis almost invariably involves the use of the momentum integral equation (3.57) together with two other equations in order to determine the three unknowns U_m, Y_m and δ_1.

The first two equations are normally integral momentum equations for the inner boundary layer from $y = 0$ to δ_1 and the outer mixing layer from $y = \delta_1$ to infinity where an average velocity profile must be assumed in both cases. Applying a method similar to that for the previous section (3.2.9), we can deduce that (for strong jets):

$$\begin{aligned} U_m &\propto \frac{1}{\sqrt{x}} \\ Y_m &\propto x \\ \delta_1 &\propto x \end{aligned} \tag{3.73}$$

The experimental observations of Kruka and Eskinazi (1964) show that:

$$\delta_1 = 0.0109\ \bar{x} \tag{3.74}$$

where $\bar{x}$ is measured from a virtual origin located roughly aobut $8b_0$ behind the nozzle.

Kruka and Eskinazi (1964) and Patel (1971) have proposed simple extensions to the method of Abramovich (1963) for the uniform co-flowing case. The former chose a characteristic velocity:

$$U_c = U_1 + (1 - a')U_m \tag{3.75}$$

where a' is an experimentally determined function of $\alpha = U_1/U_0$ and can be determined from:

$$a' = 1.06/(1 - 1/\alpha) - 0.5 \tag{3.76}$$

Patel extended his free jet proposal of $(U_1 + U_m)$ for the characteristic velocity to the wall jet case, giving a simple growth law of the form

$$\frac{dY_m}{dx} = \alpha_w \frac{U_m}{U_1 + U_m} \tag{3.77}$$

where α_w is the growth rate in still surroundings.

3.2.11 Circular Surface Jet in a Co-Flowing Stream

Rajaratnam (1984) studied the case of a circular surface jet of diameter d issuing with a velocity U_0 parallel to the surrounding stream flow of mean velocity U_1, Figure (3.10). Based on these experiments Rajaratnam concluded that the velocity-distributions were similar in both the vertical (z) and transverse (y) directions.

If α is the ratio of the jet velocity (U_o) to the mean stream velocity U_1, the range of variation of α in the experiments was from 1 to 20 and the stream velocity U_1 in the majority of the tests was about 13.5 cm/sec. Investigations of the growth of width in both vertical ($\bar{z}$) and transverse ($\bar{y}$) directions shows the high dependence of the rates of growth on α.

For the large values of α the growth rate of $\bar{z}$ with x is almost the same as that for a circular jet in stagnant surroundings for a considerable distance from the nozzle. In the transverse direction the dominant effect of α on the growth rate of $\bar{y}$ was also observed (Figure 3.11). These experiments give $\bar{z} = 2.5\ Z_m$ and $\bar{y} = 2.2\ Y_m$, where Z_m and Y_m are the length scales in the vertical and horizontal directions.

Rajaratnam also concluded that the velocity scale and the vertical length scale can be predicted from the results of submerged circular jets in co-flowing streams using the excess momentum thickness as the length scale. The transverse length scale and width, however, appeared to grow at a rate roughly equal to that of circular wall jets in co-flowing streams for some distance from the nozzle.

3.3 JET ACTION IN RESERVOIRS

3.3.1 The Integral Method - Sobey's Solution

Sobey (1973) obtained a mathematical model for the circulation of water inside a circular reservoir caused by a tangential jet.

Although his mathematical model is not very accurate in detail, it does, however, give a satisfactory solution for the overall circulation. In the model, the Navier-Stokes equations of motion are solved using an integral method similar to that of Karman-Pohlhausen momentum integral method for boundary layer analysis. The coordinate system used (Fig. 3.12) is the cylindrical polar coordinates (r, θ, z) system with time averaged velocity components (u, v, w). The origin of coordinates being the free water surface at the geometric centre of the basin. In this system the steady-flow equations for mass and momentum, written in conservation form and in terms of stresses, are:

$$\frac{1}{r}\frac{\partial}{\partial r}(ru) + \frac{1}{r}\frac{\partial v}{\partial \theta} + \frac{\partial w}{\partial z} = 0 \qquad (3.78)$$

$$\frac{\partial u}{\partial t} + \frac{1}{r}\frac{\partial}{\partial r}(ru^2) + \frac{1}{r}\frac{\partial}{\partial \theta}(uv) + \frac{\partial}{\partial z}(uw) - \frac{v^2}{r}$$

$$= -F_r + \frac{1}{\rho r}\left[\frac{\partial}{\partial r}(r\sigma_{rr}) + \frac{\partial}{\partial \theta}(\sigma_{\theta r}) + \frac{\partial}{\partial z}(r\sigma_{zr}) - \sigma_{\theta\theta}\right] \qquad (3.79a)$$

$$\frac{\partial v}{\partial t} + \frac{1}{r}\frac{\partial}{\partial r}(rvu) + \frac{1}{r}\frac{\partial}{\partial \theta}(v^2) + \frac{\partial}{\partial z}(vw) + \frac{uv}{r}$$

$$= -F_\theta + \frac{1}{\rho r}\left[\frac{\partial}{\partial r}(r\sigma_{r\theta}) + \frac{\partial\, \sigma_{\theta\theta}}{\partial \theta} + \frac{\partial}{\partial z}(r\sigma_{z\theta}) + \sigma_{r\theta}\right] \qquad (3.79b)$$

$$\frac{\partial w}{\partial t} + \frac{1}{r}\frac{\partial}{\partial r}(rwu) + \frac{1}{r}\frac{\partial}{\partial \theta}(wv) + \frac{\partial}{\partial z}(w^2)$$

$$= F_z + \frac{1}{\rho r}\left[\frac{\partial}{\partial r}(r\sigma_{rz}) + \frac{\partial \sigma_{\theta z}}{\partial \theta} + \frac{\partial}{\partial z}(r\sigma_{zz})\right] \qquad (3.79c)$$

in which σ_{ij} = the (laminar plus turbulent) stress components in the plane normal to the i direction and directed in the j direction.

The following assumptions are now introduced:

(a) Flow is steady, i.e. $\frac{\partial u}{\partial t} = \frac{\partial v}{\partial t} = \frac{\partial w}{\partial t} = 0$

(b) Body forces are $F_r = F_\theta = 0, \quad F_z = -g$

(c) Deviatoric normal stresses are neglected

i.e. $\sigma_{rr} = \sigma_{\theta\theta} = \sigma_{zz} = -p$

(d) The z pressure gradient is hydrostatic.

(e) The r pressure gradient is approximately centrifugal.

Under these assumptions equations (3.79a,b,c) become

$$-\frac{v^2}{r} = -\frac{1}{\rho}\frac{\partial p}{\partial r} \qquad (3.80a)$$

$$\frac{1}{r}\frac{\partial}{\partial r}(rvu) + \frac{1}{r}\frac{\partial}{\partial \theta}(v^2) + \frac{\partial}{\partial z}(vw) + \frac{uv}{r}$$

$$= -\frac{1}{\rho r}\left[\frac{1}{r}\frac{\partial}{\partial r}(r^2\sigma_{r\theta}) - \frac{\partial p}{\partial \theta} + \frac{\partial}{\partial z}(r\sigma_{z\theta})\right] \qquad (3.80b)$$

$$0 = -g - \frac{1}{\rho}\frac{\partial p}{\partial z} \qquad (3.80c)$$

In the subsequent depth integrations the water surface elevations, $\zeta(r,\theta)$, above the z datum have been assumed small with respect to the depth, h. The approximations:

$$\bar{v} = \frac{1}{h + \eta} \int_{-h}^{\zeta} v\,dz; \quad \overline{v^2} \cong \left[\bar{v} \right]^2 = \int_{-h}^{\zeta} v^2\,dz$$

have been made, and the over bars representing the average values have been dropped.

Depth integration of equation (3.80a) and (3.80b) results in:

$$\frac{v^2}{r} = \frac{1}{\rho} \frac{\partial p}{\partial r} \tag{3.81}$$

$$\frac{\partial}{\partial r} (r^2 vu) + r \frac{\partial}{\partial \theta} (v^2) = \frac{1}{\rho} \frac{\partial}{\partial r} (r^2 \sigma_{r\theta}) - \frac{r}{\rho} \frac{\partial p}{\partial \theta} - \frac{r^2}{\rho h} \tau_{z\theta}^{b} \tag{3.82}$$

In equation (3.82), $\tau_{z\theta}^{b}$ is the shear stress at the bed (z = -h) given by $\tau_{z\theta}^{b} = \rho f\, v^2/8$, where f is the friction factor.

Equation (3.82) is then integrated radially from the centre of the reservoir (r = 0) to the wall (r = R) to give:

$$\frac{d}{d\theta} \int_0^R rv^2 dr = \frac{1}{\rho} R^2\, \tau_{r\theta}^{w} - \frac{1}{\rho} \frac{d}{d\theta} \int_0^R rp\, dr$$

$$- \frac{1}{\rho h} \int_0^R r^2\, \tau_{z\theta}^{b}\, dr \tag{3.83}$$

where $\tau_{r\theta}^{w}$ is the shear stress at the wall, given by $\tau_{r\theta}^{w} = -\rho f\, v_m^2/8$ and v_m is the maximum velocity.

The friction factor can be obtained from conventional open channel resistance formulae, say Colebrook-White equation:

$$\frac{1}{\sqrt{f}} = -\,2 \log. \left(\frac{k_s}{14.83h} + \frac{2.52}{R_e\sqrt{f}}\right) \tag{3.84}$$

in which R_e = a Reynolds number

k_s = average bed roughness height

Using equation (3.81), the pressure term in equation (3.83) becomes:

$$\frac{1}{\rho}\int_0^R pr\, dr = \frac{1}{2} R^2 \int_0^R \frac{v^2}{r}\, dr - \int_0^R \frac{1}{2} rv^2\, dr \tag{3.85}$$

and the integral angular momentum equation (3.83) becomes:

$$\frac{d}{d\theta}\int_0^R \frac{1}{2}\left(r + \frac{R^2}{r}\right) v^2 dr = \frac{1}{\rho} R^2\, \tau_{r\theta}^{w} - \frac{1}{\rho h}\int_0^R r^2\, \tau_{z\theta}^{b}\, dr \tag{3.86}$$

Depth integration from -h to ζ and radial integration from 0 to R of the equation of continuity (3.78) would lead to:

$$\frac{Q_0}{2\pi h} + \frac{d}{d\theta}\int_0^R v\, dr = 0 \tag{3.87}$$

where Q_0 is the jet discharge.

The boundary conditions adopted for w and u are no flow through the bed:

$$w = 0 \quad \text{at} \quad z = -h$$

or through the side wall:

$$u = 0 \quad \text{at} \quad r = R$$

The central outlet has been assumed to extract fluid in the manner of a potential sink:

$$\lim_{r \to 0}(ru) = -\frac{Q_0}{2\pi h} \tag{3.88}$$

Sobey studied his experimental velocities and concluded that the tangential velocity profiles consist of a wall jet component superimposed on a low velocity circulation flow component. The circulating flow is in fact driven by the entraining action of the decaying wall jet.

Consequently, the tangential velocity (v) can be satisfactorily described by three parameters. It is convenient to use two parameters (a characteristic azimuthal velocity, V, and a characteristic radial width δ) to describe the jet development and to use one parameter (another characteristic azimuthal velocity a) to describe the forced circulation. Thus:

$$v = v(r, V(\theta), \delta(\theta), a(\theta)) \tag{3.89}$$

As a result there are three unknowns and three equations are, therefore, required to solve the system. The third equation, for closure, could be an entrainment equation in the manner of Abramovich (1963). Recalling equation (3.77), for the growth of wall jet in a co-flowing stream, we have:

$$\frac{d\delta}{dx} = \alpha_w \frac{V}{V_1 + V} \tag{3.90}$$

where V_1 = a characteristic stream velocity

V = wall (maximum) velocity.

It is convenient to generalise the equation for the case of wall jet within a curved surface of constant radius R, by substituting the appropriate coefficient of Guitton for still surrounding.

Guitton's equation (3.45) was:

$$\frac{y_m}{(x - x_0)} = 0.065 - 0.32\ y_m/R$$

assuming $x_0 \approx 0$ and $x = R\theta$

Rearranging and differentiating with respect to θ gives an expression for the growth rate α_w:

$$\alpha_w = \frac{1}{R} \frac{d\ y_m}{d\theta} = 0.065\ (1 + 0.32\ \theta)^{-2} \tag{3.91}$$

Therefore, the system of equation can be closed by the entrainment equation

$$\frac{d\delta}{dx} = 0.065\ (1 + 0.32\ \theta)^{-2}\ V/(V_1 + V) \qquad (3.92)$$

Based on his experiments, Sobey concluded that the circulating flow component of the v velocity profile (equation (3.89)) could be suitably represented by a triangular velocity distribution extending from a zero velocity at the half-radius point, r = R/2 to a velocity $a(\theta)$ at the wall (Fig. 3.13a). The flow velocities inside the half-radius point were observed to be very small except in the bottom boundary layer and in the immediate neighbourhood of the outlet. Sobey assumed that these small velocities contribute little to the mass and momentum fluxes. The jet component of the depth-averaged azimuthal velocity profile was observed to be rather similar to the standard two-dimensional, turbulent wall jet. The wall boundary layer was quite thin and wall shear was already incorporated in the model by using $\tau_{r\theta}{}^{w}$ of equation (3.83).

In this situation the simplest profile for the wall-jet component is a rectangular (top-hat) distribution of magnitude V and width δ (Fig. 3.13a). The combined velocity profile is then:

$$\begin{cases} v = 0 \quad \text{for} \quad r < \frac{R}{2} \\ \\ v = a(\frac{2r}{R} - 1) \quad \text{for} \quad \frac{R}{2} < r < R - \delta \\ \\ v = V + a\ (\frac{2r}{R} - 1) \quad \text{for} \quad R - \delta < r < R \end{cases} \qquad (3.93)$$

Substituting this profile into the integral angular momentum equation with:

$$\tau^{b}_{z\theta} = \rho \frac{f}{8} v^2 \tag{3.94}$$

$$\tau^{w}_{r\theta} = - \rho \frac{f}{8} (V + a)^2 \tag{3.95}$$

and completing the integration and subsequent differentiation gives an equation of the form:

$$A_{11} \frac{da}{d\theta} + A_{12} \frac{dV}{d\theta} + A_{13} \frac{d\delta}{d\theta} = B_1 \tag{3.96}$$

Similar substitution into the integral mass conservation equation and completing the integration and differentiation gives:

$$A_{21} \frac{da}{d\theta} + A_{22} \frac{dV}{d\theta} + A_{23} \frac{d\delta}{d\theta} = B_2 \tag{3.97}$$

The Reynold's number in the Colebrook-White formula for the friction factor, f, is defined by:

$$R_e = (V + a)h/\nu \tag{3.98}$$

The jet region is expected to be responsible for the majority of the frictional resistance.

The final equation (equation (3.92)) can also be written in a similar form:

$$A_{31} \frac{da}{d\theta} + A_{32} \frac{dV}{d\theta} + A_{33} \frac{d\delta}{d\theta} = B_3 \tag{3.99}$$

In the above equation a reasonable value for the surrounding velocity (V_1) would seem to be the magnitude of the underlying circulation at the edge, $r = R - \delta$ of the jet, giving:

$$V_1 = (1 - \frac{2\delta}{R})a \tag{3.100}$$

The coefficients A_{ij}, B_j are defined by Sobey (1973). The three equations of the integral method can be written as the matrix equation:

$$(A_{ij}) \left(\frac{da}{d\theta}, \frac{dV}{d\theta}, \frac{d\delta}{d\theta}\right)^T = (B_i) \tag{3.101}$$

in which the subscript, T, represents vector transposition. This can be transformed by matrix inversion to a simultaneous system of three, first-order, ordinary differential equations, which can be numerically integrated by standard techniques, but first require the specification of initial conditions at $\theta = 0$. The initial V and δ values follow directly from the specification of the inlet jet. The $a(\theta = 0)$ value is unknown but it can be computed in an iterative manner.

First an initial value is chosen and then the equations are integrated through 2π radians. The mass and momentum fluxes of the assumed co-flowing stream at the jet orifice and those computed after 2π radians must, match so that there are two independent conditions with which to determine $a(\theta = 0)$. Both the volume flux, $Q(\theta)$, and the

kinematic moment of angular momentum flux, $I(\theta)$, will increase with the parameter, a, so that the sum of their relative errors:

$$F(a) = \frac{Q(\theta = 2\pi) - Q(\theta = 0)}{Q(\theta = 0)} + \frac{I(\theta = 2\pi) - I(\theta = 0)}{I(\theta = 0)} = 0 \quad (3.102)$$

can be used to assist in the solution for $a(\theta = 0)$. An iterative solution of the above equation is accomplished by a half-interval method.

The volume flux:

$$Q(\theta) = h \int_0^R v dr \quad (3.103)$$

and the moment of kinematic angular momentum flux:

$$I(\theta) = h \int_0^R \frac{1}{2} (r + \frac{R^2}{r}) v^2 dr \quad (3.104)$$

to be used in equation (3.102) must first be evaluated in terms of the three parameters of the velocity profile by using equation (3.93).

To verify his mathematical model Sobey conducted two experiments with discharges $Q_0 = 560$ cc/sec and $Q_0 = 300$ cc/sec. A comparison between the theoretical predictions and the experiments was reported to be satisfactory, Fig. (3.13b), Sobey (1973). The predicted maximum velocities are quite close to the experimental results and are usually located in a narrow band near the wall. Predicted velocities at the interior region are rather different from the experimental values.

3.3.2 Dimensional Analysis and Scale Effects

Sobey and Savage (1974) used the total circulating volume flux, Q_c, as a suitable measure of the forced circulation. Using the Buckingham Π theorem and after some rearrangements, they obtained:

$$\frac{Q_c}{\sqrt{K_0}\, L} = \psi_1(\Pi_1, \Pi_2, \Pi_3, \Pi_4, \Pi_5, \Pi_6) \qquad (3.105)$$

where $\Pi_1 = \frac{1}{L}\left(\frac{K_0}{f_1^2}\right)^{1/4}$ a measure of the jet momentum coriolis balance

$\Pi_2 = \frac{\sqrt{K_0}\, L}{Q_0}$ representing jet geometry

$\Pi_3 = \frac{L}{h}$ representing reservoir geometry (aspect ratio)

$\Pi_4 = \frac{\sqrt{K_0}}{\nu}$ a jet Reynolds number (3.106)

$\Pi_5 = \frac{K_0}{Q_0\sqrt{gh}}$ a jet Froude number ($= v_0/\sqrt{gh}$)

$\Pi_6 = \frac{k_s}{h}$ representing the relative roughness of the reservoir

where K_0 = kinematic jet momentum flux = $\sum_{i=1}^{N} Q_i\, v_i$

(Q_i is the discharge and

v_i is the average velocity of separate inlet)

$Q_0 = \sum_{i=1}^{N} Q_i$ the reservoir through flow

$f_1 = 2\Omega \sin \varphi$ the coriolis parameter

L = a typical horizontal length of the reservoir

h = the average depth of the reservoir

k_s = the average bed roughness height

ν = the kinematic viscosity of the reservoir water

g = the local gravitational acceleration

In Sobey and Savage's mathematical model, the effect of rotation was not considered, so Π_1 was neglected. They also assumed that the forced circulation was independent of gravity waves, which elliminated the Froude number (Π_5).

The remaining four parameters were varied in a series of computational experiments. The results indicated a significant decrease in the non-dimensional circulating flow with the increase in both the aspect ratio and the relative roughness. Minor changes in $Q_c/\sqrt{K_0}L$ resulted from varying the jet geometry ratio (slight decrease) and the jet Reynolds number (slight increase).

Therefore, concluding that, Q_c depends predominantly on the aspect ratio, L/h, and relative roughness, k_s/h, Sobey and Savage (1974) produced a jet-forced circulation diagram, Fig. (3.14). Also given in Fig. (3.14) is a curve obtained from the experimental results of White et al (1955).

Fig. (3.14) clearly shows that $Q_c/\sqrt{K_0}L$ is very dependant on the aspect ratio L/h for a given value of k_s/h. This finding has an important

implication regarding the use of hydraulic models. Distorted hydraulic models where L/h is different for the model and prototype should therefore be avoided. Experimental results of various researchers showing the effects of L/h will be discussed later.

3.4 EXPERIMENTAL INVESTIGATIONS

3.4.1 Past Experimental Investigations on Tangential Jets

An extensive experimental study of jet forced reservoir circulation has been carried out in recent years.

In a majority of the experiments, the tangential velocity distribution was found to be reasonably similar.

Ali and Whittington (1979) plotted the experimental velocity distributions of Sobey in dimensionless form. His experiments were conducted in a circular reservoir having R = 252cm and depth = 6cm. The inlet jet was 0.2cm wide and 5cm high. Ali and Whittington fitted the following hyperbolic curve, suggested by Schwarz and Coasart (1961), to Sobey's results:

$$\frac{v}{v_m} = \text{sech}^2 \left(\frac{y}{y_m} - 0.14\right) \qquad (3.107)$$

where y is the distance from the wall towards the center of reservoir and y_m is the length scale in that direction.

Ali and Whittington performed several experiments on a smooth circular reservoir having a diameter of 3m. The tangential jet was 0.2cm wide and 2cm high. Input discharges were 4.7, 8.8, 11.2, 22.4, 28.4, 33.6 and 73.5 cc/sec. These discharges were used for reservoir water

depths of 2, 5, 10, 15 and 20cm. The values of h result in a range of L/h of 15-150. The dimensionless velocity-distributions were found to be similar. Near the wall, equation (3.107) fitted the experimental results. Away from the wall, however, the results were better represented by:

$$\frac{v}{v_m} = \exp\left[-0.693\left[\frac{y}{y_m}\right]\right] \tag{3.108}$$

The mean circulation discharge for Ali and Whittington's results was calculated from:

$$\frac{\bar{Q}_c}{Q_0} = 4.3\,\frac{h}{h_0}\,z' \tag{3.109}$$

where z' is given by:

$$z' = 1.702 + \frac{0.607 * 10^9}{R_e^{2.5}}$$

and

$$R_e = \frac{v_0\, h}{\nu}$$

where v_0 = inlet velocity.

Ali and Whittington assumed that the decay of the maximum velocity is given by:

$$\frac{v_m}{v_0} = A\left[\frac{R}{b_0}\,(\theta + \theta_0)\right]^B \tag{3.110}$$

where θ = angle from the jet

θ_0 = angle between the jet and virtual origin.

The coefficients A and B are constant. A similar relationship was assumed for the expansion of the jet half width (y_m) with θ. The values of A = 5.395, B = -0.555 (for v_m) and A = 0.625, B = 0.682 (for y_m) was given for Sobey's experiments.

Ali and Pateman (1981) conducted experiments on a large reservoir having a diameter of 7.35m. The inlet jet was 5cm high and 0.2cm wide. For a jet discharge of 615 cc/sec, reservoir water depths of 7, 12, 17, 22 and 28cm were used. Ali and Pateman demonstrated the similarity of their velocity distribution. They also obtained the following relationship for v_m:

$$\frac{v_m}{v_0} = \alpha_1 \ (\theta + \theta_0)^{\alpha_2} \qquad (3.111a)$$

where α_1 and α_2 are parameters obtained from their experiments and are given by:

$$\alpha_1 = 0.6 - 0.044 \ h/h_0$$

$$\alpha_2 = 0.0832 \ (h/h_0)^{0.744}$$

Fig. (3.15) shows Ali and Whittington's comparison between the classical wall jet relationship, equation (3.44) and the experimental results of Sobey. This figure also shows the experimental results of Ali and Pateman.

Fig. (3.16) shows Ali and Pateman's curves for the variation of y_m with θ for different reservoirs. These results are given for different aspect ratios and discharges. Based on the results of Fig. (3.16) the following expression was obtained for y_m

$$\frac{y_m}{R} = \alpha_3 \ \theta^{\alpha_4} \qquad (3.111b)$$

where

$$\alpha_3 = 0.138 \ (L/h)^{-0.147}$$

$$\alpha_4 = 0.222 \ (L/h)^{0.238}$$

Ali et al. (1978) constructed several hydraulic models of the Liverpool reservoirs at Prescot. They investigated systematically the relative importance of the various parameters in equation (3.105). Three models having horizontal scales of 1/500, 1/250 and 1/83.3 were built.

The vertical scale was changed systematically such that values of α'/β' of 1, 2, 3, 4, 5 and 6 were used (α' = horizontal scale ratio, β' = vertical scale ratio).

Ali et al (1978) plotted the dimensionless circulating discharge $Q_c/\sqrt{K_0}L$ versus the aspect ratio, for a constant Froude number. Their results together with the findings of other experiments on different reservoir models are plotted in Fig. (3.17). The following remarks may be concluded from this figure:

(a) The aspect ratio (L/h) has a dominant effect on circulation.

(b) The experimental results using the smooth (glass) circular reservoir (L = 3m) are very different from Sobey's predictions.

(c) The values of $Q_c/\sqrt{K_0}L$ for the same L/h and jet Froude number are very close for the different sizes of Prescot No. 4 models, thus confirming that the effect of jet Reynolds number is small for these experiments.

(d) The prototype values of $Q_c/\sqrt{K_0}L$ for the Silvola reservoir are much higher than those of its small model.

3.4.2 Present Experiments

The present experimental work was carried out in a homogeneous reservoir. The aim of these experiments was to verify the previous theories and also to compare the results with the experiments on a stratified reservoir (Chapter 6).

The reservoir characteristics, the system of inlet and outlet and the head tank arrangement have been mentioned in Chapter 2. The depth of water was variable but had a maximum value of 22.5cm.

Because of the similar nature of the experiments, the same procedure was used throughout. The inlet discharge was set up to the correct value, and the model was left to settle to a steady state conditions (usually after 5 to 10 minutes). Inlet discharges were checked regularly throughout the experiment. Velocity measurements were made using equipment appropriate for the range of velocities encountered.

The room was darkened in the time lapse photography experiment. A tape-recorder was used to announce the appropriate time steps.

A stop watch was used to record the experimental run time in the dye photography experiments. The start of time was when the dye first appeared at the jet inlet.

Table (3.1) gives a list of the various experiments. Each series was run at a certain depth and experiments were conducted at four different flow rates.

Table (3.2) gives the values of the dimensionless parameters (F_r, R_e, L/h) for the experiments of Table (3.1).

3.4.2.1 Experimental Results and Comparison with Theories

Fig. (3.18) shows dye photographs obtained using a jet discharge of 19.66 cm^3/s and a reservoir aspect ratio of 19.2, (h = 4.8cm).

Flow visualization in this case clearly defines the general characteristics of the flow pattern. The main flow is seen to be concentrated into a wall jet around the circumference of the model. The growth rate of this shear layer appears to decrease with distance from the inlet, and does not grow very much at all beyond π radians from the inlet. Dye gradually diffuses toward the central outlet in a symmetrical manner. After about 3 minutes, dye can be found all over the reservoir but at different concentrations.

Figs. (3.19 - 3.21) show dye photographs using a jet discharge of 5.75 cm^3/s and reservoir aspect ratios of 19.2, 7.7 and 4.1. Comparing Fig. (3.18) and Fig. (3.19) (same L/h, different discharges), clearly

the form of the expansion of the jet is different. For Q_0 = 5.75 cm^3/s, the expansion is not symmetrical about the centre. After some distance from the jet, the dye departs from the wall and moves towards the centre. Comparing Fig. 3.18 for t = 1 min 30 sec and Fig. 3.19 for t = 3 min, the degree of asymmetry in the latter is evident.

Clearly the momentum of the jet, for Q_0 = 5.75 cm^3/s, is not large enough to preserve a narrow shear layer as in the case of Q_0 = 19.66 cm^3/s. As a result frictional forces overcome the driving throughflow momentum and disperse the dye toward the inner zone. After 6 min dye is found all over the reservoir.

The experiment with Q_0 = 5.75 cm^3/s and maximum depth of 22.5cm shows more symmetry, Fig. (3.21). The circulation pattern is similar to that of the first run Q_0 = 19.66 cm^3/s. This clearly emphasises the dominant effect of L/h over the circulation pattern inside the reservoir. Bearing this case in mind the relative roughness k_s/h is also decreased considerably resulting in less friction. The experiment with Q_0 = 5.75 cc/sec and h = 12cm can be considered as an intermediate stage between the previous two runs and shows more or less both phenomena.

Fig. (3.22) shows time lapse photographs for a water depth of 4.8cm and for four inflow discharges. The lapse time for the first two discharges is 5 sec and is 3 sec for the last two flows. The tracks of the floats display a spiral motion in the interior zone for the smaller discharges. This indicates the lack of any dominant tangential flow in this region. On the other hand, the float path is circular for the stronger inflows.

Figure (3.23) shows time lapse photographs for a jet discharge of 5.75 cm^3/s and for water depths of 2.5, 4.8, 12 and 22.5cm. The quality of the photograph for the smallest depth (h = 2.5cm) is not good, as candles were used in this case instead of diods. The tracks of the candles are irregular, near the centre, showing that the circulation is very small in this zone. More symmetrical track are again obtained with the larger water depths.

Velocity distribution at different angles were calculated from the time-lapse photographs and are shown in Figs. (3.24 - 3.31). These velocity distributions are given for four reservoir water depths. For each depth, results are given for four discharges.

Theoretical velocities based on Sobey's model are also plotted in Figs. (3.24 - 3.31). The roughness height was assumed to be 0.5mm. Agreement between the theory and experiment is fairly good. Prediction is even better in the region far from the inlet.

Theoretical considerations show that when the water depth of reservoir increases the reservoir velocity (a) grows while the jet velocity (V) and its thickness (δ) decrease. As a consequence, the volume flux and circulating discharge increases considerably (equation (3.103)).

Detailed study of the Sobey's theoretical velocities, however, shows that they are not very realistic. Moreover, the assumption of zero velocity at 0.5R neglects any circulation in a very big area of the reservoir. This is justified for shallow depths, but it underestimates the circulation for big depths and discharges.

Figs. (3.24 - 3.31) also show the variation of v/v_m with y/y_m. In most cases these profiles are similar especially for big discharges.

On the other hand, big reservoir depths result in non-similar distributions especially for small values of θ, Fig. (3.29) and Fig. (3.30). This indicates the presence of an independent three dimensional flow in the interior region. The standard classical wall jet curve (equation (3.40)), is also plotted in Figs. (3.24 - 3.31). The measured velocities deviate considerably from this curve when y/y_m > about 2.5, indicating that the effect of the jet extends further in the circular reservoir than in the case of flat wall.

Wall velocities were measured using the propeller meter, for four different depths and for several discharges for each depth. Two examples are shown in Fig. (3.32a,b), where the dimensionless velocities are plotted against the angle from the jet for the minimum and maximum depths.

Although the jet Froude numbers ($v_0/\sqrt{gh}$) cover a wide range of each depth, the velocity distributions follow the same curve, implying that Froude number, F_r, has little effect on the maximum velocity distribution.

Therefore, for each depth an average curve was plotted and the results for the different depths are drawn in Fig. (3.33a). This figure shows the effect of aspect ratio on the maximum velocity distribution. Velocities are considerably reduced for the deeper reservoir. Another interesting result can be deduced if these velocities are plotted against the inverse square root of the distance from the jet, Fig.

(3.33b). It can be shown that there is a linear relationship for each depth, given by

$$\frac{v_m}{v_0} = C_0 \, (\theta + \theta_0)^{-0.5} \qquad (3.112)$$

where C_0 and θ_0 are different for each depth and $\theta = x/R$.

Equation (3.112) is very similar to the relationship of the maximum velocity suggested by Schwartz and Cosart for the classical wall jet, equation (3.44). Kobayashi and Fijisawa (1983), Fig. (3.6), have also reported the linear variation of $(v_0/v_m)^2$ with x.

A similar formula was also derived by Ali and Pateman (1981) for different reservoirs, equation (3.111a). Apparently even for water depths 20 times the jet height, the three-dimensional wall jet behaviour is similar to that of a two-dimensional jet and is quite different from the trends described by Sforza (1966), see Section (3.2.6).

On the other hand the maximum velocity tends to keep its two-dimensionality (equation (3.49)). This justifies the use of Sobey's model for reservoir depths bigger than the height of jet and the use of Guitton's two-dimensional growth law in that theory. These deductions will be used in extending Sobey's model to stratified reservoir flow.

The spread of the jet in the vertical direction was investigated for the maximum water depth. The growth of the jet with distance from

exit was studied using potassium permangenete, for two discharges, Fig. (3.34).

This figure shows that the rate of expansion of the jet is slightly greater for the smaller discharge. It might be due to the small co-flowing reservoir velocities for the small jet discharge. The jet is allowed to expand rapidly in this case. Tangential velocities were measured near the perimeter wall for various angular distances from the jet for various distances below the water surface and for three discharges. These results are given in Fig. (3.35). At the regions near to the inlet velocities are very high, but decrease sharply with the increase in depth from the surface. These velocities finally reach a constant value corresponding to the value for the co-flowing stream, see for example Fig. (3.35a), section x = 10.

The curves for x = 20 - 70cm are flatter than that for x = 10cm but they still exhibit an inflection near to the reservoir's stream. Finally at distances x > 140cm ($\theta > \pi$), the velocity distribution is monotonic and is almost uniform with depth. This clearly justifies the application of depth averaged models for the prediction of reservoir circulation.

Non-dimensional velocity distributions were plotted in Fig. (3.37) together with a Gaussian distribution curve. The measured velocities deviate from the curve at about $z/z_m > 2$, indicating the effect of co-flowing flow of the reservoir.

Using Figs. (3.35a - 3.35c), the growth rate of z_m was plotted versus the distance from the jet, Fig. (3.36). These results can be approximated by a linear relationship. Table (3.3) gives the various

velocities of jet and the streamflow. α is the ratio of the jet velocity to that of the surrounding flow. Recalling Rajaratnam's (1984) investigations and Fig. (3.11), Section (3.2.11), it has been shown that for α greater than about 10, the growth of the jet in the vertical direction in a co-flowing flow is similar to that of a jet in stagnant surroundings.

In the present investigations on the reservoirs, the co-flowing velocity was usually very much smaller than the velocity of the jet and the ratio α satisfied that condition to a good approximation. This probably explains why the growth of the jet is almost independent of the reservoir's stream.

From Fig. (3.36), the rate of growth can be approximated by

$$\frac{dz_m}{dx} = 0.2325 \qquad (3.113)$$

This gives a value for the angle of growth, λ, of about 13°.

This value is five times greater than that for bluff surface jets (equation 3.53) and three-dimensional wall jets (equation 3.51) and twice that of a three-dimensional free jets (equation 3.50).

The presence of the curve wall greatly inhibits the tangential jet from expanding in the r-direction. As a consequence the jet growth is less than that of an ordinary wall jet.

Recalling Fig. (3.16) which gives the variation of y_m/R with θ for various reservoir sizes, the above argument may be confirmed, (the

growth rate is between 0.016 to 0.0273). It is also clear from Guitton's equation (3.45) that for $y_m/R \cong 0.1$ to 0.15, the growth rate is 0.033 to 0.017, which is much smaller than that of a wall jet (about 0.068).

Moreover, in the present case where the inlet is a three-dimensional curved wall jet located near to the surface, the eccentricity, forces the jet to penetrate in the vertical direction more than in the case of ordinary surface jet. This results in a great expansion of jet in the z-direction.

CHAPTER 4

NOTATION

b_0	inlet width
c	Chezy coefficient
c'	non-dimensional Chezy number
c_1	constant
C_d	dimensionless weir coefficient
C_p	propagation velocity
C_s	constant
D	dispersion coefficient
E	subgrid eddy diffusion coefficient
f	Coriolis parameter
g	acceleration due to gravity
h	distance between the bed and the undisturbed water level
H	total water depth
ℓ	mixing length
n	time step level
p	pressure
q,Q	boundary discharge between two successive grid points
r	local radius of curvature
R'	constant
t	time
T_b	bed shear stress
T_{bx}, T_{by}	bed shear stresses in x and y directions respectively

T_{wx}, T_{wy}	wind shear stress in x and y directions respectively
u,v,w	time averaged velocity components in the x,y,z directions respectively
$\rho\overline{u'^2}, \rho\overline{u'v'}, \rho\overline{v'^2}$	turbulent (Reynolds) stresses
u_*	shear velocity
U,V	depth averaged velocity in x and y direction
U_d	the desired velocity for characteristic boundary relationship
U_m	maximum velocity
U_0	jet velocity
U_1	free stream velocity
x,y,z	horizontal lateral and vertical coordinates in cartesian system
z'	height above the bed
z_0	roughness height
$\alpha, \beta_1, \beta, \gamma, \gamma'$	coefficients for the non-uniformity of velocity profile
ϵ	effective eddy viscosity
η	water level elevation above or below mean depth
κ	von Karman constant
μ	Courant number
ν	kinematic viscosity
ρ	density
$\tau_{i,j}$	Reynolds stresses acting in x_i direction on x_j plane
φ	geographical latitude
ω	vorticity
Ω	angular velocity of the earth's rotation

CHAPTER 4

FINITE DIFFERENCE MODELS

4.1 STATEMENT OF THE PROBLEM

4.1.1 Depth Averaged Equations

Mathematical models of free surface flows exist at various levels of sophistication. Detailed description of flow phenomena is best accomplished in a three dimensional spatial frame work. However the complexity of a formulation in three dimension often requires tremendous amount of computational effort. Where valid, the simplification to a two dimensional representation can offer a considerable reduction in complexity and expense. This involves an integration of the three-dimensional equations of fluid dynamic over the flow depth.

Hansen (1962) is credited for being the first to outline the depth-averaged two dimensional formulation. Using the Eulerian cartezian system, Fig. (4.1), the basic equations representing an incompressible turbulent flow on a rotating earth can be written (Lamb (1932)) as:

$$\frac{\partial u}{\partial t} + \frac{\partial u^2}{\partial x} + \frac{\partial uv}{\partial y} + \frac{\partial uw}{\partial z} - fv + \frac{1}{\rho}\frac{\partial p}{\partial x}$$

$$- \frac{1}{\rho}\left(\frac{\partial \tau_{xx}}{\partial x} + \frac{\partial \tau_{xy}}{\partial y} + \frac{\partial \tau_{xz}}{\partial z}\right) = 0 \qquad (4.1a)$$

$$\frac{\partial v}{\partial t} + \frac{\partial vu}{\partial x} + \frac{\partial v^2}{\partial y} + \frac{\partial vw}{\partial z} + fu + \frac{1}{\rho}\frac{\partial p}{\partial y}$$

$$- \frac{1}{\rho} \left(\frac{\partial \tau_{yx}}{\partial x} + \frac{\partial \tau_{yy}}{\partial y} + \frac{\partial \tau_{yz}}{\partial z}\right) = 0 \qquad (4.1b)$$

$$\frac{\partial w}{\partial t} + \frac{\partial wu}{\partial x} + \frac{\partial wv}{\partial y} + \frac{\partial w^2}{\partial z} + \frac{1}{\rho} \frac{\partial p}{\partial z}$$

$$- \frac{1}{\rho} \left(\frac{\partial \tau_{zx}}{\partial x} + \frac{\partial \tau_{zy}}{\partial y} + \frac{\partial \tau_{zz}}{\partial z}\right) = 0 \qquad (4.1c)$$

where x,y,z = coordinates of a right handed system with z upwards

u,v,w = time averaged velocity components in the x,y,z directions respectively

t = time

h = distance between the bed and the undisturbed water level

η = distance between the undisturbed water level and the water surface elevation

p = pressure

g = acceleration due to gravity

ρ = fluid density

f = Coriolis parameter = $2\Omega \sin(\varphi)$ where Ω = angular velocity of the earth's rotation and φ = geographical latitude

τ_{ij} = shear stresses acting in the i direction and on the j plane, where i = x,y,z and j = x,y,z

The equation of continuity for an incompressible flow is:

$$\frac{\partial u}{\partial x} + \frac{\partial v}{\partial y} + \frac{\partial w}{\partial z} = 0 \qquad (4.2)$$

In any predominantly horizontal flow the vertical accelerations due to hydrodynamic processes are generally regarded as being small in comparison with gravity effects. Consequently in equation (4.1c) the vertical accelerations and shear stresses can be neglected so that in the vertical direction a hydrostatic pressure distribution results:

$$\frac{\partial p}{\partial z} + \rho g = 0 \tag{4.3}$$

In determining the two dimensional depth-averaged equations, use is made of the kinematic boundary conditions. The free surface boundary condition is:

$$\frac{\partial \eta}{\partial t} + u_\eta \frac{\partial \eta}{\partial x} + v_\eta \frac{\partial \eta}{\partial y} - w_\eta = 0 \tag{4.4}$$

and at the bed

$$u_{-h} \frac{\partial(-h)}{\partial x} + v_{-h} \frac{\partial(-h)}{\partial y} - w_{-h} = 0 \tag{4.5}$$

where u_η, v_η and w_η are the respective velocity components at the surface and u_{-h}, v_{-h}, w_{-h} are the velocity components at the bed.

If F is the mean value of the parameter f, then this can be defined by:

$$F(x,y) = \frac{1}{h + \eta} \int_{-h}^{\eta} f(x,y,z)dz$$

The equations for the depth-averaged, two dimensional flow are obtained by integrating Equations (4.1a and 4.1b) and equation (4.2) from the bottom to the surface, using the kinematic boundary conditions, Vreugdenhil (1973). The integrated equations in final form are:

$$\frac{\partial HU}{\partial t} + \frac{\partial HU^2}{\partial x} + \frac{\partial HUV}{\partial y} - fHV + gH \frac{\partial \eta}{\partial x}$$

$$- \frac{1}{\rho} (T_{wx} - T_{bx}) - \frac{1}{\rho} \frac{\partial HT_{xx}}{\partial x} - \frac{1}{\rho} \frac{\partial HT_{xy}}{\partial y} = 0 \qquad (4.6a)$$

$$\frac{\partial HV}{\partial t} + \frac{\partial HVU}{\partial x} + \frac{\partial HV^2}{\partial y} + fHU + gH \frac{\partial \eta}{\partial y}$$

$$- \frac{1}{\rho} (T_{wy} - T_{by}) - \frac{1}{\rho} \frac{\partial HT_{xy}}{\partial x} - \frac{1}{\rho} \frac{\partial HT_{yy}}{\partial y} = 0 \qquad (4.6b)$$

$$\frac{\partial \eta}{\partial t} + \frac{\partial HU}{\partial x} + \frac{\partial HV}{\partial y} = 0 \qquad (4.7)$$

where H $= h + \eta$ = total depth of flow

T_{bx}, T_{by} = components of bottom shear stress

T_{wx}, T_{wy} = components of surface shear stress (due to wind)

T_{xx}, T_{xy}, T_{yy} = effective stresses in vertical planes.

In the present study the effect of wind action is neglected. The bottom stresses have to be related to other parameters by empirical relations. The usual assumptions for the bottom stresses are (i) that they have the same magnitude as in steady, uniform flow, and (ii) that they are in the same direction as the depth-averaged velocity. The

Chezy equation together with the relationship for uniform flow results in the following expressions:

$$T_{bx} = \rho g U(U^2 + V^2)^{1/2}/c^2 \tag{4.8a}$$

$$T_{by} = \rho g V(U^2 + V^2)^{1/2}/c^2 \tag{4.8b}$$

Where c is the Chezy's coefficient. The effective stresses T_{xx}, T_{xy}, T_{yy} by definition read:

$$T_{xx} = \frac{\rho}{H} \int_{-h}^{\eta} \{2\nu \frac{\partial u}{\partial x} - \overline{u'^2} - (u-U)^2\} dz \tag{4.9a}$$

$$T_{xy} = \frac{\rho}{H} \int_{-h}^{\eta} \{\nu(\frac{\partial u}{\partial x} + \frac{\partial v}{\partial y}) - \overline{u'v'} - (u-U)(v-V)\} dz \tag{4.9b}$$

$$T_{yy} = \frac{\rho}{H} \int_{-h}^{\eta} \{2\nu \frac{\partial v}{\partial y} - \overline{v'^2} - (v-V)^2\} dz \tag{4.9c}$$

Where ν is the kinematic coefficient of viscosity and $\overline{\rho u'^2}$, $\overline{\rho u'v'}$ and $\overline{\rho v'^2}$ indicate the turbulent (Reynolds) stresses. Each of the expressions for T_{xx}, T_{yy} and T_{xy} in Eqs. (4.9) contains three contributions. The first contribution (a) is due to the vertical mean viscous stress. At sufficiently high values of the Reynolds number it may be neglected. The more important second part (b) is formed by the turbulent stresses acting in vertical planes. These will be of the same order of magnitude as the bottom shear stress. The third contribution (c), in equation (4.9) is the most important one, it describes the momentum flux due to the non-uniform velocity distributions, i.e. to large-scale circulations extending over the

entire water depth. In comparison, the same influence on the flow is exerted by stresses (b) and (c) via the effective stresses T_{xx}, T_{yy}, while via T_{xy} opposite influences are possible. The order of magnitude of both stresses depends on the location in the flow, the location of main interest, herein, being the transition region between the main flow and the circulating flow.

4.1.2 Secondary Flow - Vorticity Equation

In order to understand the mechanism by which secondary flow can be maintained, it is necessary to study the transfer of vorticity in depth-averaged flow. The basis for the argument is the vorticity equation derived by Kuipers and Vreugdenhil (1973) and restated here:

$$\underbrace{\frac{\partial H\omega}{\partial t}}_{1} + \underbrace{\frac{\partial H\omega U}{\partial x} + \frac{\partial H\omega V}{\partial y}}_{2} + \underbrace{H(\omega - f)\left(\frac{\partial U}{\partial x} + \frac{\partial V}{\partial y}\right)}_{3}$$

$$\underbrace{- H\left[\frac{\partial}{\partial y}\left(\frac{T_{wx}}{\rho H}\right) - \frac{\partial}{\partial x}\left(\frac{T_{wy}}{\rho H}\right)\right]}_{4}$$

$$\underbrace{+ H\left[\frac{\partial}{\partial y}\left(\frac{T_{bx}}{\rho H}\right) - \frac{\partial}{\partial x}\left(\frac{T_{by}}{\rho H}\right)\right]}_{5}$$

$$\underbrace{- \frac{H}{\rho}\frac{\partial}{\partial y}\left[\frac{1}{H}\left[\frac{\partial (HT_{xx})}{\partial x} + \frac{\partial (HT_{xy})}{\partial y}\right]\right]}_{6}$$

$$\underbrace{+\frac{H}{\rho}\frac{\partial}{\partial y}\left[\frac{1}{H}\left[\frac{\partial(HT_{xy})}{\partial x}+\frac{\partial(HT_{yy})}{\partial y}\right]\right]}_{7}=0 \qquad (4.10)$$

where $\omega = (\partial U/\partial y - \partial V/\partial x)$, the so-called vorticity, all the other parameters have been defined before. Consideration of different terms in the above equation can give the following conclusions:

(i) The time rate of change of vorticity is represented by term 1.

(ii) Vorticity is convected by the mean flow (term 2).

(iii) Vorticity is generated by convergence or divergence of the mean-velocity field (term 3).

(iv) The fourth term shows that vorticity is generated by the wind stress if it has a non-vanishing curl.

(v) Bottom stress acts as a dissipation of vorticity, term 5.

(vi) The net moment of the stresses T_{xx}, T_{xy}, T_{yy}, relative to a vertical axis (i.e. terms 6 and 7), can generate vorticity in either direction.

Neglecting the wind stress, it follows that a body of water within a closed stream line can acquire vorticity either by divergence/convergence of the flow or by the action of the effective stresses on the circumference of the body of water. Examination of the energy balance equation, also shows that the bottom stresses only dissipate energy, Flokstra (1976), therefore energy has to be transferred to the circulating flow to be able to maintain this flow. In other words shear stresses can supply this mechanism. Flokstra (1976) concluded that circulating flows computed without these stresses show only a numerical effect. The recognition of these

stresses is necessary but not a sufficient condition to guarantee circulation. Kuipers and Vreugdenhil (1973) observed numerically that circulatory flows are suppressed too, by the omission of the convective terms.

4.1.3 Closure of the Equations

As mentioned before effective stresses consist of three parts. The contribution of turbulent (Reynolds) stresses (part b) and the non-uniformity of vertical velocity (part c), may be considered as the major parts.

In the literature much attention has been paid to the closure problem of the Reynolds stresses in the turbulent momentum equations derived from the Navier-Stokes equations for both two and three-dimensional problems. The closure propositions vary from simple eddy viscosity approaches to the more extended models, describing the Reynolds stresses by additional differential equations. Review of these models are given by Launder and Spalding (1972) and Rodi (1980).

The terms resulting from non-uniformity of the vertical velocity, however have nothing to do with turbulence because they are solely a product of the depth averaging process; accordingly, models describing these terms are not turbulence models. Considering the computational time required to solve a problem, it is preferable to use a simple model.

In the literature a presentation of the horizontal stress gradients by a diffusive term has occasionally been used. This would amount to the assumption:

$$T_{xx} = 2\rho\epsilon \frac{\partial U}{\partial x} \tag{4.11a}$$

$$T_{xy} = \rho\epsilon \left(\frac{\partial U}{\partial x} + \frac{\partial V}{\partial y}\right) \tag{4.11b}$$

$$T_{yy} = 2\rho\epsilon \frac{\partial V}{\partial y} \tag{4.11c}$$

where ϵ = effective eddy viscosity.

Substitution of these expressions into equations (4.6a and 4.6b) and simplifying leads to the form:

$$\text{x-direction } \epsilon H\left(\frac{\partial^2 U}{\partial x^2} + \frac{\partial^2 U}{\partial y^2}\right) \tag{4.12a}$$

$$\text{y-direction } \epsilon H\left(\frac{\partial^2 V}{\partial x^2} + \frac{\partial^2 V}{\partial y^2}\right) \tag{4.12b}$$

instead of the last two terms in equations (4.6a and 4.6b). The above expressions have the correct tensor properties of symmetry and invariance to rotation of the coordinate system. However by definition T_{xx}, T_{yy} (equations (4.9a and 4.9c)) are always negative which is not the case in equations (4.11a and 4.11c). These equations will, therefore, not be satisfactory as a meaningful description. Moreover an estimate of ϵ is not simple. In any analogy with the dispersion of matter in turbulent flow, the dispersion coefficient can be estimated from:

$$D = 6H \sqrt{\frac{\overline{T_b}}{\rho}} \cong 6H\sqrt{\overline{g(U^2 + V^2)}}/c \tag{4.13}$$

where T_b is the bottom shear stress.

This expression was based on a concentration profile, determined from the approximate two-dimensional diffusion equation (see Elder (1959)). It could be expected that the effective eddy viscosity ϵ is of the same order of magnitude as D. There is, however an important difference between the two cases, because momentum can be transferred by pressure gradients, where as there is no comparable mechanism for mass transfer.

Falconer (1977) utilized the mixing length theory for open channel flow and obtained the following expression for the mixing length:

$$\ell = \kappa(h + z)(1 - \frac{h + z}{H})^{1/2} \qquad (4.14)$$

where κ = von Karman constant

and obtained:

$$\epsilon = \beta_1 \frac{\sqrt{g}}{c} H(U^2 + V^2)^{1/2} \qquad (4.15)$$

where $\beta_1 = \kappa/6$.

For the non-uniformity of velocity in depth he applied a similar approach to that of Vreugdenhil (1973), equation (4.13). Combining the two effects, he obtained:

$$\text{in x-direction} \quad - \frac{6H\rho\sqrt{g}}{c} \left[|U| \frac{\partial^2 U}{\partial x^2} + |V| \frac{\partial^2 U}{\partial y^2} \right] \tag{4.16a}$$

and

$$\text{in y-direction} \quad - \frac{6H\rho\sqrt{g}}{c} \left[|U| \frac{\partial^2 V}{\partial x^2} + |V| \frac{\partial^2 V}{\partial y^2} \right] \tag{4.16b}$$

for the last two terms in Eqs. (4.6a and 4.6b). These two terms accounted for the effective shear stresses.

Abbot and Rasmussen (1979) stated that circulating patterns were a direct consequence of the resistance effects dominating the inertial effects. They categorized the shear stress process as 'rolling dispersion' and 'advective dispersion'. The former is associated with secondary flow and the latter is due to deviation from a constant velocity profile in depth. Both processes were studied using an elementary mixing length approach. In the case of 'rolling dispersion' the result that is based on circulatory flow field, as described by Engelund (1974), is:

$$\epsilon = \frac{c'^3}{18} (H/r)^2 \, V \, H \tag{4.17}$$

where c' = the non-dimensional Chezy number $\cong 10$

V = the depth averaged velocity $= \frac{1}{H} \int_0^H v \, dz$

H = water depth

r = local radius of curvature.

For the case of 'advective dispersion' their result is:

$$\epsilon = \frac{\gamma - \gamma'^2}{2} cVH \tag{4.18}$$

$$\gamma = \frac{\int_0^H v^3 \, dz}{V^3 H}$$

$$\gamma' = \frac{\int_0^H v^2 \, dz}{V^2 H}$$

The value of ϵ given by equation (4.18) is close to the one derived by Elder (1959) for the dispersion of matter in uniform channel flow.

In all of the above models, the effective stresses were expressed in fully diffusive form (Boussinesq approximation). Flokstra (1976) has, however, suggested a convective interpretation of the stresses as:

$$\begin{aligned} T_{xx} &= \alpha U^2 \\ T_{xy} &= \alpha UV \\ T_{yy} &= \alpha V^2 \end{aligned} \tag{4.19}$$

In which α is a suitable constant. In this form energy will not be dissipated by these terms, and T_{xy} will be of primary importance.

Falconer (1980) assumed a logarithmic velocity profile. The correction factor (β) which allows for the non-uniformity of the velocity profile was given by:

$$\beta = 1 + \alpha = 1 + \frac{g}{c^2 \kappa^2} \tag{4.20}$$

For the turbulent eddy viscosity he used the same form of equation (4.15).

Lean and Weare (1979) modelled the eddy formed on the down stream side of a breakwater. In, (Fig. 4.2) a large eddy is separated from the main flow by an expanding region of intermittent turbulence emanating from the breakwater's tip. Within this mixing zone, momentum is transferred laterally between the main stream and the eddy through two processes, i.e. turbulence and the secondary flow induced by the curvature of the streamlines. The turbulence in the mixing zone is a combination of the turbulence generated at the bed and the turbulence produced by the horizontal velocity gradient between the main flow and the eddy. The latter is usually termed "shear layer turbulence", see Townsend (1956). If x is the distance downstream from the origin of the shear layer turbulence, and y is the distance transverse to the mean streamline then the mean velocity is observed to have a universal profile given by:

$$U = \frac{1}{2} U_1 \{1 + \text{erf}[\frac{y}{x} (R'/2)^{1/2}]\} \qquad (4.21)$$

in which U_1 = free stream velocity and R' is a constant parameter ($\cong$ 288). The corresponding mean eddy viscosity over the shear layer is approximately:

$$\epsilon = \frac{1}{2} U_1 \frac{x}{R'} \qquad (4.22)$$

The depth averaged lateral eddy viscosity corresponding to the shear velocity at the bed can be represented (assuming the Reynolds analogy) by:

$$\epsilon = 0.16 u_* H \tag{4.23}$$

where $u_* = \frac{T_b}{\sqrt{\rho}}$ is the shear velocity and in this case becomes:

$$u_* = \frac{1}{2} U_1 \sqrt{g/c}$$

Comparing equations (4.22 and 4.23) we may deduce that the mixing due to shear layer will dominate when:

$$\frac{x}{H} > 46 \frac{\sqrt{g}}{c} \tag{4.24}$$

On the other hand comparing the rate of production of turbulence energy per unit mass of the shear layer and of the bed-generated turbulence, the latter will be re-established when:

$$\frac{x}{H} > \frac{2}{\pi} \frac{c^2}{g} \tag{4.25}$$

In addition to the turbulence mixing processes previously considered, momentum can also be exchanged through secondary currents.

Along the mean curved streamlines, Lean and Weare (1979) assumed that the variation of velocity with depth was logarithmic and given by:

$$u = \frac{u_*}{\kappa} \ell n \left(\frac{z'}{z_0}\right) \tag{4.26}$$

in which κ = van Karman's constant = 0.4

z' = height above bed

z_0 = roughness height

u_* = shear velocity.

The transverse velocity component (see Rozovskii (1957)) then becomes:

$$v = \frac{H}{r} \frac{u}{\kappa^2} \left(F_1 - \frac{\sqrt{g}}{\kappa C} F_2\right) \tag{4.27}$$

where F_1 and F_2 are certain functions defined by Rozovskii. This secondary flow give rise to an effective lateral shear stress of:

$$T_{xy} = \frac{\rho}{H} \int_{z_0}^{h} (u - U)(v - V)\, dz$$

$$\cong - \rho \frac{H}{r} \frac{U^2}{\kappa^3} \frac{\sqrt{g}}{C} \left(0.8 - 0.4 \frac{\sqrt{g}}{\kappa C}\right) \tag{4.28}$$

Again shear mixing layer will dominate when the radius of curvature is such that:

$$\frac{r}{H} > 250\ \sqrt{g}/c \tag{4.29}$$

4.2 FINITE DIFFERENCE MODELS

4.2.1 The Presentation of the Model

Numerical modelling of depth-averaged two dimensional flow has been presented by several researchers, see Abbott (1981). In general most of these models include an implicit finite difference form of the equations of motion, with all but the non-linear convective accelerations being fully centered in time. A Fourier stability analysis of the linear terms of the finite difference equations shows that the corresponding numerical scheme is unconditionally stable, Leendertse (1967). However, if the imperfectly time-centered convective accelerations are quasi-linearized and included in the stability analysis, the presence of a weak instability can readily be shown, Wear (1976). Under normal estuarine flow conditions where the influence of the convective accelerations is relatively small, this weak instability is controlled by the stabilizing effect of the frictional resistance terms. In the modelling of flows in reservoirs, harbors and estuaries where a narrow entrance exists, the influence of the convective acceleration terms is no longer small and the stabilizing effect of the frictional resistance term may be insufficient to avoid an explosive growth of non-linear instabilities.

The occurrence of non-linear instabilities in many of the difference schemes used to solve the shallow water-wave equations is explained by Phillips (1956) in terms of the physical process of transferring turbulent energy from large to small scales. Energy is generally fed into the flow at large scales of motion and is transferred by non-linear interactions, to smaller and smaller scales to be finally dissipated by viscous friction. In the numerical representation of this process, energy cannot be transferred to scales smaller than twice the grid size and, for this reason, tends to accumulate at the

corresponding wave length, i.e. $2\Delta x$. This results in an accumulation of oscillations that, after some time, can completely swamp the true numerical solution. The usual approach for damping the growth of non-linear instabilities has been achieved by introducing an artificial viscosity-type energy dissipation process. This process has the effect of simulating the transfer of turbulent energy to scales smaller than twice the grid size by artificially smoothing the numerical solution. The simplest procedure adopted for this purpose is to spatially average the computed velocities at the end of each time step, by using a predetermined weighting factor. However, there are two basic disadvantages with using such a method. Firstly there is the difficulty in determining the appropriate value of weighting factor itself, secondly it is almost impossible to determine what proportion of the smoothing function is being used in damping the growth of non-linear instabilities as compared to diffusing the small-scale energy. In a three time level implicit model, an attempt has been made to remove the non-linear instability by centering the advective terms, Falconer (1977). The stability analysis, however, indicate that the time centered non-linear convective acceleration terms impose a stability constraint of the form:

$$\beta \frac{\Delta t}{\Delta x} |U_m| < 1 \qquad (4.30)$$

Moreover, the presentation of the second derivatives of the depth-averaged effective stresses is in the three-level Du-Fort and Frankel explicit scheme, Richtmyer and Morton (1967). This in turn, has the disadvantage of not being consistent with the original differential equations when Δx and Δt tend to zero at the same rate. So care has to be taken in choosing the values of both the time step

and the grid size. This model has a truncation error of approximately $0(\Delta t, \Delta x^2)$, most of which is a phase error.

Recently, a central implicit scheme, involving a double iterative technique has been applied by many investigators, including Leendertse (1984). The approach is similar to the one firstly suggested by Pearson (1965). In the following this model, which is chosen for the simulation of reservoir circulation, will be explained in brief.

Application of the difference scheme to the two dimensional depth averaged flow Eqs. (4.6a and 4.6b) and equation (4.7) yields a set of finite difference equations, which allow the prediction of the velocity field throughout the model domain. The solution procedure makes use of the Alternating Direction Implicit approach (see Roache (1976)) where for each computing cycle, two successive time level operations are performed. During the first operation, from time $n\Delta t$ to $(n+1/2)\Delta t$, all components, involving U and η, of Eqs. (4.6a) and (4.7) are expressed in an implicit form while those relating to V are expressed explicitly. Similarly, during the second operation, from time $(n+1/2)\Delta t$ to $(n+1)\Delta t$, all the components involving V and η of Eqs. (4.6b) and (4.7) are expressed implicitly, while the previous implicit U values are now expressed explicitly. The position of the different variables on the computational grid is illustrated in Fig. (4.3). Referring to this figure, each variable can be represented uniquely by a set of subscripts and superscripts of the following form:

$$\eta^{n}_{j,k} = \eta(j\Delta x,\ k\Delta x,\ n\Delta t)$$

$$\bar{\eta}^{x}_{j,k} = \frac{1}{2}\,(\eta_{j+1/2,k} + \eta_{j-1/2,k})$$

$$\bar{\eta}^{y}_{j,k} = \frac{1}{2}\,(\eta_{j,k+1/2} + \eta_{j,k-1/2})$$

$$\bar{\bar{\eta}} = \frac{1}{4}\,(\eta_{j-1/2,k-1/2} + \eta_{j-1/2,k+1/2} + \eta_{j+1/2,k-1/2} + \eta_{j+1/2,k+1/2})$$

Using the above notations the depth averaged continuity and momentum equations may be re-written in the following finite difference form, for the first operation and in the x-direction:

$$(\eta^{n+1/2}_{j,k} - \eta^{n}_{j,k}) + \frac{\Delta t}{2\Delta x}\,[(\bar{h}^{y} + \bar{\eta}^{x})_{j+1/2,k}\,U^{n+1/2}_{j+1/2,k} - (\bar{h}^{y} + \bar{\eta}^{x})_{j-1/2,k}\,U^{n+1/2}_{j-1/2,k}]$$

$$+ \frac{\Delta t}{2\Delta x}\,[(\bar{h}^{x} + \bar{\eta}^{y})_{j,k+1/2}\,V^{n}_{j,k+1/2} - (\bar{h}^{x} + \bar{\eta}^{y})_{j,k-1/2}\,V^{n}_{j,k-1/2}] = 0 \qquad (4.31)$$

and

$$(U^{n+1/2}_{j+1/2,k} - U^{n-1/2}_{j+1/2,k}) + \beta\,\frac{\Delta t}{\Delta x}\,[(\overline{UM}^{x}_{j+1,k})^{2} - (\overline{UM}^{x}_{j,k})^{2}]$$

$$+ \beta\,\frac{\Delta t}{\Delta x}\,[UM_{j+1/2,k+1/2+p}\,(\bar{V}^{x}_{j+1/2,k+1/2})^{n}$$

$$- UM_{j+1/2,k-1/2+q} (\overline{V}^{x}_{j+1/2,k-1/2})^{n}]$$

$$+ \frac{g\Delta t}{2\Delta x} (\eta^{n+1/2}_{j+1,k} + \eta^{n-1/2}_{j+1,k} - \eta^{n+1/2}_{j,k} - \eta^{n-1/2}_{j,k})$$

$$- f\Delta t \, \bar{V}^{n}_{j+1/2,k}$$

$$+ \frac{g \frac{\Delta t}{2} [(UM_{j+1/2,k})^2 + (\overline{\bar{V}}^{n}_{j+1/2,k})^2]^{1/2} (U^{n+1/2}_{j+1/2,k} + U^{n-1/2}_{j+1/2,k})}{(\overline{h}^{y} + \overline{\eta}^{x})_{j+1/2,k} (\overline{c}^{x}_{j+1/2,k})^2}$$

$$+ \epsilon_{xx} \frac{\Delta t}{\Delta x^2} (UM_{j+3/2,k} - 2UM_{j+1/2,k} + UM_{j-1/2,k})$$

$$+ \epsilon_{xy} \frac{\Delta t}{\Delta x^2} (UM_{j+1/2,k+1} - 2UM_{j+1/2,k} + UM_{j+1/2,k-1}) = 0 \qquad (4.32)$$

where $p = (\frac{-\overline{V}^{x}}{2|\overline{V}^{x}|_{j+1/2,k+1/2}})$ and $q = (\frac{-\overline{V}^{x}}{2|\overline{V}^{x}|_{j+1/2,k-1/2}})$

and likewise for the second operation in y-direction:

$$(\eta^{n+1}_{j,k} - \eta^{n+1/2}_{j,k}) + \frac{\Delta t}{2\Delta x} [(\overline{h}^{y} + \overline{\eta}^{x})_{j+1/2,k} U^{n+1/2}_{j+1/2,k}$$

$$- (\overline{h}^{y} + \overline{\eta}^{x})_{j-1/2,k} U^{n+1/2}_{j-1/2,k}]$$

$$+ \frac{\Delta t}{2\Delta x} [(\overline{h}^{x} + \overline{\eta}^{y})_{j,k+1/2} V^{n+1}_{j,k+1/2}$$

$$- (\overline{h}^{x} + \overline{\eta}^{y})_{j,k-1/2} \; V^{n+1}_{j,k-1/2}] = 0 \qquad (4.33)$$

and

$$(V^{n+1}_{j,k+1/2} - V^{n}_{j,k+1/2}) + \beta \frac{\Delta t}{\Delta x} [(\overline{VM}^{y}_{j,k+1})^2 - (\overline{VM}^{y}_{j,k})^2]$$

$$+ \beta \frac{\Delta t}{\Delta x} [VM_{j+1/2+p,k+1/2} (\overline{U}^{y}_{j+1/2,k+1/2})^{n+1/2}$$

$$- VM_{j-1/2+q,k+1/2} (\overline{U}^{y}_{j-1/2,k+1/2})^{n+1/2}]$$

$$+ \frac{g\Delta t}{2\Delta x} [\eta^{n+1}_{j,k+1} + \eta^{n}_{j,k+1} - \eta^{n+1}_{j,k} - \eta^{n}_{j,k}]$$

$$+ f \, \overline{\overline{U}}^{n+1/2}_{j,k+1/2}$$

$$+ \frac{\frac{g\Delta t}{2} [(\overline{\overline{U}}^{n+1/2}_{j,k+1/2})^2 + (VM_{j,k+1/2})^2]^{1/2} (V^{n+1}_{j,k+1/2} + V^{n}_{j,k+1/2})}{(\overline{h}^{x} + \overline{\eta}^{y})_{j,k+1/2} (\overline{c}^{y}_{j,k+1/2})^2}$$

$$+ \epsilon_{yx} \frac{\Delta t}{\Delta x^2} (VM_{j+1,k+1/2} - 2VM_{j,k+1/2} + VM_{j-1,k+1/2})$$

$$+ \epsilon_{yy} \frac{\Delta t}{\Delta x^2} (VM_{j,k+3/2} - 2VM_{j,k+1/2} + VM_{j,k-1/2}) = 0 \qquad (4.34)$$

where $p = (\frac{-\overline{U}^{y}}{2|\overline{U}^{y}|})_{j+1/2,k+1/2}$ and $q = (\frac{-\overline{U}^{y}}{2|\overline{U}^{y}|})_{j-1/2,k+1/2}$

Each operation involves a double iteration. During the first iteration the components UM and VM describe the corresponding terms at the lower time level, giving:

$$UM = U^{n-1/2}_{j+1/2,k}$$

$$VM = V^{n}_{j,k+1/2}$$

whereas during the second iteration these components represent the terms in the form:

$$UM_{j+1/2,k} = \frac{1}{2}\left(U^{n-1/2}_{j+1/2,k} + U^{.n+1/2}_{j+1/2,k}\right)$$

$$VM_{j,k+1/2} = \frac{1}{2}\left(V^{n}_{j,k+1/2} + V^{.n+1}_{j,k+1/2}\right)$$

where $U^{.n+1/2}_{j+1/2,k}$ and $V^{.n+1}_{j,k+1/2}$ are the implicit velocities obtained at the end of the first iteration of the first and second operations respectively.

The terms which need more explanation are the convective accelerations expressing the lateral transport of momentum in the x and y directions respectively, i.e. the UV products. These terms are represented in such a way that their spatial locations are dependent upon the direction of the velocity component perpendicular to the direction of the axis being considered. This scheme allows the momentum fluxes ρU, and similarly ρV, to be evaluated more nearly at the position where it originates. Thus, momentum is more rigorously conserved in the finite

difference sense, Williams and Holmes (1974). As will be shown later, the values of the effective stresses are described in different ways (either in a diffusive form or in an advective form), therefore the coefficients β and ϵ will be determined later. The inclusion of wind action has not been considered in this study, so the wind stresses are not shown in finite difference form.

All the terms of the finite difference equations (4.31 to 4.34) are centered in space with a truncation error of (Δx^2), with the exception of the cross-product advection terms which have a truncation error of $0(\Delta x)$. In addition, the difference scheme is second order accurate with respect to time, that is all of the terms have a truncation error of $0(\Delta t^2)$.

In order to solve the finite difference equation and determine the velocity field in the problem area, the prescription of the initial and boundary conditions is necessary. For the initial conditions, all the variables should be given to start the calculations. This could be, for example, a "cold start" i.e. horizontal surface and zero velocity everywhere. With regard to the boundary conditions, for closed boundaries, two different cases can be examined, namely "free slip boundary" and "no slip boundary". For a "free-slip boundary" the exterior tangential velocity component is assumed to have the same value as the corresponding interior image velocity component and the exterior normal velocity component is the negative of the interior image value. For a "no-slip boundary", on the other hand, the exterior tangential velocity component is the negative of the interior image velocity component, and the exterior normal velocity component has the same value as the interior image velocity component. Further details can be found in Falconer (1977) and Williams and Holmes

(1974). For the case of open boundaries, velocities should be given at the boundaries. They can be specified in terms of the inflow discharges for reservoirs. Discharges can be most suitably included in the mathematical model by expressing them in terms of the mean velocity across corresponding grid spacing, Kuipers and Vreugdenhil (1973). For a known lower boundary discharge Q between the grid points j+1/2, k+1/2 and j+1/2, k-1/2 the relationship used reads:

$$U^{n+1/2}_{j+1/2,k} = Q^{n+1/2}_{j+1/2,k} \Big/ \frac{\Delta x}{2} \left[\left(h_{j+1/2,k+1/2} + h_{j+1/2,k-1/2} \right) \right.$$

$$\left. + \frac{1}{2} \left(3\eta^{n}_{j+1,k} - \eta^{n}_{j+2,k} + \eta^{n}_{j+1,k+1} + \eta^{n}_{j+1,k-1} \right) \right] \qquad (4.35)$$

and for the upper boundary:

$$U^{n+1/2}_{M+1/2,k} = Q^{n+1/2}_{M+1/2,k} \Big/ \frac{\Delta x}{2} \left[\left(h_{M+1/2,k+1/2} + h_{M+1/2,k-1/2} \right) \right.$$

$$\left. + \frac{1}{2} \left(3\eta^{n}_{M,k} - \eta^{n}_{M-1,k} + \eta^{n}_{M,k+1} + \eta^{n}_{M,k-1} \right) \right] \qquad (4.36)$$

Finite difference equations (4.31 to 4.34) make a number of simultaneous equations which need to be solved on the domain of problem. The method of Gauss elimination and backward substitution can be applied to solve the system. Falconer's original computer program (1977) was modified based on the latter scheme by the present author. That program was based on the model used by Leendertse et al. (1971).

4.2.2 Application of the Model

Pateman (1982) conducted a series of experiments on a circular reservoir fed by radial jets of various widths. The widest inlet of those experiments was chosen for comparison with the numerical model. Characteristics of the physical and mathematical models are given in Table 4.1.

The experimental velocity distributions are shown in Fig. (4.4). The corresponding numerical model consisted of a 19x19 grid points with an equidistant grid spacing of 13 cm. The jet inlet was represented at the central grid space of the x-direction upper boundary, while the weir outlet was represented at the diametrically opposite three adjacent grid spaces of the lower boundary. This model is similar to the case of a river discharging radially into a reservoir. The circular configuration of the reservoir was approximated on the square grid in a manner similar to that used by Kuipers and Vreugdenhil (1973) and Falconer (1977).

The open boundary conditions were read in as steady discharges. The weir outflow water level was determined by using the sharp crested weir equation given by Henderson (1966):

$$\eta^{n+1/2}_{M,k} = \left[\frac{3\, q^{n+1/2}_{M+1/2,k}}{2\sqrt{2g}\ \Delta x\ C_d} \right]^{2/3} \qquad (4.37)$$

where $q^{n+1/2}_{M+1/2,k}$ = the lower boundary discharge between the grid points M+1/2, k+1/2 and M+1/2, k-1/2

Δx = grid spacing

C_d = the dimensionless weir dicharge coefficient $\cong$ 0.6.

The rate of convergence from rest to the final numerical solution, will be accelerated by introducing the downstream open boundary condition in characteristic form, see Wurtele et al. (1971).

For a boundary with a positive propagation velocity, that is directed out of model, this relation reads, Kuipers and Vreugdenhil (1973) and Falconer (1977):

$$U - U_d = \frac{g}{C_p} (\eta - \eta_d) \tag{4.38}$$

where C_p = the propagation velocity = $\sqrt{g(h+\eta)}$

U_d = the desired velocity

η_d = the desired water level

This equation can be combined with the weir equation to give the finite difference approximation of the downstream as:

$$U^{n+1/2}_{M+1/2,k} = \left[\frac{g}{\overline{h}^{y}_{M+1/2,k} + \eta^{n}_{M,k}} \right]^{1/2} \left[\eta^{n+1/2}_{M,k} - \left[\frac{3}{2} \frac{q^{n+1/2}_{M+1/2,k}}{2\sqrt{2g}\ \Delta x\ C_d} \right]^{2/3} \right] + \left[\frac{q^{n+1/2}_{M+1/2,k}}{\overline{h}^{y}_{M+1/2,k} + \eta^{n}_{M,k}} \right] \tag{4.39}$$

The computational process was started from an initial state of rest with:

$$\eta_{j,k} = U_{j+1/2,k} = V_{j,k+1/2} = 0 \tag{4.40}$$

An initial disturbance was introduced to the program. The disturbance was followed by a steady flow of constant input discharge. The steady state situation for the computations was reached after approximately 125 secs, at which time the initial disturbance had disappeared. As the effect of the earth's rotation was not included in the hydraulic model, the Coriolis parameter was set equal to zero, as was the wind velocity. Due to the implicit form of the finite difference equations, from the stability point of view, there is no limitation on the maximum time step. However, as was noticed by Vreugdenhil and Voogt (1975) an upper limit of approximately $\mu = 5$ may be imposed on the solution ($\mu = \Delta t\sqrt{gh}/\Delta x$, the Courant number). And yet, this limit should not be considered as a firm restriction and depending on the set of data, it could be very conservative, Mardapitta Hadji - Pandeli (1985).

Weare (1979) discussed the errors arising from irregular boundaries in ADI schemes of the shallow-water equations and suggested a severe restriction of $\mu = 2$ for the accuracy of the scheme.

In the present study, however, comparison of velocities for Courant numbers of $\mu = 1$ and $\mu = 5$ revealed no significant difference. Therefore a maximum of $\mu = 5$ with a corresponding time step of 1 sec. was considered for all computations.

The computations which will be described later were aimed at determining the velocity field accurately. Different mathematical models were used to study the effects of the following:

(a) turbulent shear stresses

(b) non-linearity

(c) closed boundaries.

In the first model (case A), the following assumptions were made:

1. The eddy coefficient is given by equation (4.13)

2. Free-slip condition at the boundary.

Fig. (4.5) shows the theoretical and experimental velocities along the centreline and at different sections. Good agreement between the theory and experiment can be observed. The whole pattern of the velocity field is shown in Fig. (4.6). It can be seen that the general circulation have been computed reasonably well, however, the magnitude of the velocities in the symmetrical counter-rotating gyres are noticeably different from the experiment. In the experiments the maximum velocities are usually at the wall, while the numerical velocities are maximised at a position close to the centre of gyres.

The discrepancy between the measured and the computed velocities may be attributed to the large grid size of the mathematical model. On the other hand, reduction of grid size will increase computational expenses which is not desirable. Therefore the consideration of a subgrid eddy coefficient might solve the problem. According to Love and Leslie (1977), Smagorinski (1963) and Lilly (1966) suggested a subgrid eddy term as follows (using tensor notation):

$$E = - C_s^2 (\Delta x)^2 \left(\frac{\partial u_i}{\partial x_j} \cdot \left(\frac{\partial u_i}{\partial x_j} + \frac{\partial u_j}{\partial x_i}\right)\right) \qquad (4.41)$$

where u_i is the grid scale velocity component, C_s is a constant, and Δx is the grid spacing. Equation (4.41) can be written in terms of depth averaged velocities U and V (Larsen et al. (1987)) as:

$$E = - c_1^2(\Delta x)^2 \left[\left(\frac{\partial U}{\partial x}\right)^2 + \frac{1}{2}\left(\frac{\partial U}{\partial y} + \frac{\partial V}{\partial x}\right)^2 + \left(\frac{\partial V}{\partial y}\right)^2\right] \qquad (4.42)$$

where $c_1 \cong 0.18$, Love and Leslie (1977).

The momentum equation subgrid terms are:

$$\text{in the x-direction} \quad H\left[\frac{\partial}{\partial x}\left(E\,\frac{\partial U}{\partial x}\right) + \frac{1}{2}\,\frac{\partial}{\partial y}\left(E\left(\frac{\partial U}{\partial y} + \frac{\partial V}{\partial x}\right)\right)\right] \qquad (4.43a)$$

$$\text{in the y-direction} \quad H\left[\frac{1}{2}\,\frac{\partial}{\partial x}\left(E\left(\frac{\partial U}{\partial y} + \frac{\partial V}{\partial x}\right)\right) + \frac{\partial}{\partial y}\left(E\,\frac{\partial V}{\partial y}\right)\right] \qquad (4.43b)$$

Assuming $\partial U/\partial y \cong \partial V/\partial x$, the equations (4.43a,b) can be written as:

$$HE\left[\frac{\partial^2 U}{\partial x^2} + \frac{\partial^2 U}{\partial y^2}\right] \qquad (4.44a)$$

$$HE\left[\frac{\partial^2 V}{\partial x^2} + \frac{\partial^2 V}{\partial y^2}\right] \qquad (4.44b)$$

which are very similar to equation (4.16a,b).

Implementation of the subgrid eddy model and further tests shows that this coefficient is mostly strong around the center line close to the inlet, and yet it is one order of magnitude less than dispersion. Consequently its over all effect on the circulation is still negligible, Case B, Fig. (4.7).

In the next trial (Case C) the effect of diffusion of the jet was studied. Remembering the Goertler's assumption for constant eddy viscosity (see Section 3.2.1), one can show that downstream of a jet, Rajaratnam (1976):

$$\frac{\epsilon}{U_m x} \cong 0.003 \tag{4.45}$$

where x = the distance downstream of the jet.

U_m = the maximum velocity.

For a two-dimensional jet, U_m is given by, equation (3.43):

$$\frac{U_m}{U_0} = \frac{3.5}{\sqrt{x/b_0}} \tag{3.43}$$

where U_0 = jet velocity

b_0 = jet width.

Substituting the equation (3.43) into equation (4.45) we obtain:

$$\epsilon \cong 0.0105\ U_0\ \sqrt{b_0\ x} \tag{4.46}$$

This equation can be applied in the velocity region of $0.05\ U_m < U < U_m$. The turbulence generated by the bed has also been included into the model (see equation (4.23)). The results are shown in Fig. (4.8), where it is seen that the centres of gyres have shifted to a position closer to the inlet. This could be accounted for by the effect of the jet's eddy diffusitivity, which causes the inflow

momentum to be diffused very quickly. It is also responsible for the fast decay of the centre line velocity of the jet.

In another trial (Case D1) a rolling dispersion coefficient similar to the one suggested by Abbot and Rasmussen (1979) equation (4.17) was applied. The radius of curvature was assumed to be 1/4 of the radius of the reservoir and constant over the whole field. The results (Fig. 4.9) reveal more diffusion of the momentum jet and a faster decay of the centre line velocity than in the previous run, Fig. (4.8). Reduction of r to (1/10th of the radius of the reservoir decreases the vorticity's strength (Case D2, Fig. 4.10) even more.

In Case E, Fig. (4.11) the sum of all the previous eddy coefficients was applied. The simulation is very similar to the Case D1.

Fig. (4.12) shows variation of eddy viscosity, obtained using the various methods, against distance from the jet. It can be seen that the eddy coefficient of dispersion and of circulation are maximised at the vicinity of the inlet.

The jet eddy coefficient increases gradually with x, equation (4.46). The subgrid eddy viscosity is, however, very small and is at least one order of magnitude less than the other coefficients.

As was mentioned before effective shear stresses could be expressed in nonlinear forms, (for example equation (4.19) by Flokstra, equation (4.20) by Falconer and equation (4.28) by Lean and Weare). This form of presentation of circulation will increase the coefficient β by not more than 5%. In the present study, however, an increase of 20% was

assumed for β in order to examine the effect of non-linearity on the velocity field.

The diffusive coefficients were kept the same as in Case A. The resulting circulation is shown in Case F, Fig. (4.13). Comparing this figure with Fig. 6 (Case A) it can be seen that the velocities in the gyres are marginally increased. Also, the position of the stagnation areas of the gyres are moved away from the jet.

Summing up the previous results, it may be concluded that Case A, i.e. the assumption of a dispersive momentum jet, shows the most realistic circulatory patterns. Therefore, simulation (A) was chosen for investigating the effects of the different terms in the two-dimensional depth-averaged flow. At first (Case A1) the nonlinear terms were excluded ($\beta = 0$). Omission of these terms caused the suppression of vorticity, although the effective stresses were still present in the model (Fig. 4.14). This may seem to contradict the primary importance of the effective stresses in producing the circulatory flow, Folokstra see Section (4.1.3). However, for bigger shear terms (say increasing by a factor of 10) there appears two weak vortices, Case A2, Fig. (4.15). On the other hand, removal of shear stresses eliminates the vortices in the flow field, Case A3, Fig. (4.16).

In case A4 the nonlinear terms were kept in the model while the shear stresses were excluded. Surprisingly, the results (Fig. 4.17) appear to remain unchanged with a small reduction of velocities around the centre line. Flokstra (1977) has argued that this kind of circulation is a numerical effect. Lean and Weare (1979) concluded that this numerical effect can be of diffusive (refer to amplitude errors) or

dispersive (refer to phase errors) type. The latter is due to the finite spatial resolution of the numerical scheme (numerical dispersion) and is inherent in any discretised solution. The numerical tests of Ponce and Yabusaki (1981), on the other hand, indicated that the reproduction of circulation was not a result of numerical dispersion as evidenced by the undiminished presence of the circulation, in spite of the increased grid resolution.

In a review of accumulated evidence on the generation of circulation in depth averaged numerical models, Abbott et al. (1985) have shown such circulations to be physically realistic in spite of the exclusion of the lateral effective stresses. The explanation as to how these numerical circulations can arise in a physically realistic manner remains, however to be answered.

The effect of closed boundary condition on the generation of vorticity was also examined by changing the boundary condition from free slip to no slip. This alteration did not show any noticeable effect on the velocity field, as can be seen on comparing Case A5, Fig. (4.18) and Case A, Fig. (4.6).

It was thought that the errors introduced into the numerical model by representing the curved boundary on a square grid, may have caused the maximum velocity of the gyre to shift away from the curved boundary wall. Therefore the shape of the reservoir was totally changed to a square. The numerical results, Case A6, Fig. (4.19), show an improvement in the wall velocities, but no change in the position of the maximum velocity.

To study the effect of friction on the circulation, two further trials were made with the latter configuration. In Case A7, the frictional terms were completely removed from the Navier-Stokes equation. The results are virtually indistinguishable except near the inlet jet, where the velocities are slightly increased, Fig. (4.20). In Case A8 the effect of friction was increased 10 times. Fig. (4.21) shows that the central position of gyres are notably changed and velocities are greatly reduced, showing the importance of dissipation caused by the resisting terms, Kuipers and Vreugdenhill (1973). In fact merely including the convective inertia terms in the mathematical model will not ensure the generation of secondary flow. Even with the additional stipulation that the effective stresses and all other quantities be precisely described. Circulation may yet be inhibited by frictional effects. In every case where secondary flow does not occur, the resistance term is significant and becomes larger than the convective inertia terms, Ponce and Yabusaki (1981).

CHAPTER 5

NOTATION

F,G,H	dimensionless functions
F',G',H'	first derivative of F,G,H
F",G",H"	second derivative of F,G,H
F_i, G_i, H_i	i=1 F,G,H for upper layer i=2 F,G,H for lower layer
F_i', G_i', H_i'	first derivation of F_i, G_i, H_i
$F_i", G_i", H_i"$	second derivative of F_i, G_i, H_i
g	acceleration due to gravity
g'	acceleration due to densimetric gravity
h_c	the maximum height of dome
J_i, K_i	dimensionless functions
n_1	constant
p	pressure
P	dimensionless function of pressure
p_i	i=1 p for upper layer i=2 p for lower layer
P_i	i=1 P for upper layer i=2 P for lower layer
Q_s	swirling discharge
Q_o	jet discharge
r, φ, z	cylindrical polar coordinate system
R	$\sqrt{\mu_2 \rho_2 / \mu_1 \rho_1}$
u,v,w	velocities in three directions of the system of coordinates
u_i, v_i, w_i	i=1 u,v,w for upper layer i=2 u,v,w for lower layer

U	free stream velocity
x,y	cartesian system of coordinates
x_i,y_i	i=1 x,y for upper layer
	i=2 x,y for lower layer
y_s,y_s'	two dimensional boundary layer thickness
δ_i	three dimensional boundary layer thickness
	i=1 for upper layer i = 2 for lower layer
δ_1	a characteristic length
ϵ	$\frac{\rho_2 - \rho_1}{\rho_1}$ proportionate density defect
ζ	dimensionless vertical axe
ζ_i	i=1 ζ for upper layer i=2 ζ for lower layer
ν	kinematic viscosity
μ	dynamic viscosity
μ_i	i=1 μ for upper layer i=2 μ for lower layer
ρ	density
ρ_i	i=1 ρ for upper layer i = 2 ρ for lower layer
$\tau_{\varphi z}$	shear stress acting in φ direction and on z plane
τ_i	i=1 τ for upper layer i=2 τ for lower layer
ψ	stream function
ω	angular velocity of disk or surrounding fluid

CHAPTER 5

LARGE SCALE FLOW IN A STRATIFIED RESERVOIR

5.1 INTRODUCTION

Formation of large scale gyres caused by a momentum jet is a major feature of reservoir circulation. The action of the jet is restricted to a relatively narrow zone at the periphery of the gyre. The flow in that region is very fast.

The interior flow, on the other hand, is slow compared to the thin banded surrounding. The order of magnitude of velocities is not more than a few millimetres per second. Therefore, it is likely to be laminar. The lateral extent of this laminar flow is of the order of half the basin's width, which covers a considerable area.

This interior circulation is three dimensional and very similar to Boedewadt flow, Schilichting (1971).

Boedewadt (1940) treated the steady laminar flow over a stationary infinite disk with the outer flow in solid-body rotation. The flow in the boundary layer is radially inwards and the axial flow is away from the disk.

In reservoirs, this inward flow plays a significant role in the process of interior mixing.

In a stratified reservoir if the jet is located in the upper layer and discharges water into that layer, the interface prevents the transfer of momentum to the lower layers. When the motion of flow is small

enough, the upper layer circulates over the lower layer without mixing. If the interface is assumed to remain horizontal, it can be shown that the motion of the upper layer is very similar to Boedewadt's flow over a smooth plane. The surface of separation, however, rotates in a similar fashion to that of a rotating disk in a stationary fluid, (von Karman flow).

In the present research, this type of flow is studied. A review of the relative topics for the von Karman and Boedewadt flows is presented and applied to laminar circulation of a stratified reservoir.

The writer's work will show that the motion of the upper layer produces a suction over the interfacial plane.

5.2 THE ROTATION OF A HOMOGENEOUS FLUID

5.2.1 Flow Near a Rotating Disk

Consider a disk of infinite radius which rotates about an axis perpendicular to its plane with a uniform angular velocity (ω). An incompressible viscous liquid occupies the semi-infinite region on one side of the disk and the motion is rotationally symmetric. The layer near the disk is carried by it through friction and is thrown outwards owing to the action of centrifugal forces. This is compensated for by particles which flow in an axial direction towards the disk to be in turn, carried and ejected centrifugally. Using the cylindrical polar coordinate system, the velocities u, v, w, are assumed to be in radial (r), circumferential (φ) and axial (z) directions, respectively. An axonometric representation of this flow field is shown in Fig. (5.1) where the disk is assumed to be at $z = 0$. The Navier-Stokes equations can be written as:

$$u \frac{\partial u}{\partial r} - \frac{v^2}{r} + w \frac{\partial u}{\partial z} = - \frac{1}{\rho} \frac{\partial p}{\partial r} + \nu [\frac{\partial^2 u}{\partial r^2} + \frac{\partial}{\partial r} (\frac{u}{r}) + \frac{\partial^2 u}{\partial z^2}] \qquad (5.1a)$$

$$u \frac{\partial v}{\partial r} + \frac{uv}{r} + w \frac{\partial v}{\partial z} = \nu [\frac{\partial^2 v}{\partial r^2} + \frac{\partial}{\partial r} (\frac{v}{r}) + \frac{\partial^2 v}{\partial z^2}] \qquad (5.1b)$$

$$u \frac{\partial w}{\partial r} + w \frac{\partial w}{\partial z} = - \frac{1}{\rho} \frac{\partial p}{\partial z} + \nu [\frac{\partial^2 w}{\partial r^2} + \frac{1}{r} \frac{\partial w}{\partial r} + \frac{\partial^2 w}{\partial z^2}] \qquad (5.1c)$$

The continuity equation is

$$\frac{\partial u}{\partial r} + \frac{u}{r} + \frac{\partial w}{\partial z} = 0 \qquad (5.2)$$

where p = pressure

ν = kinematic viscosity of the fluid

The no-slip condition at the wall gives the following boundary conditions:

$$z = 0: \quad u = 0, \quad v = r\omega, \quad w = 0. \qquad (5.3a)$$

and at infinity:

$$z = \infty: \quad u = 0, \quad v = 0. \qquad (5.3b)$$

In order to integrate the system of equations it is convenient to introduce a dimensionless distance from the wall given by

$$\zeta = z\sqrt{\omega/\nu} \qquad (5.4)$$

Further, the following assumptions are made for the velocity components and pressure

$$u = r\omega F(\zeta) \tag{5.5a}$$

$$v = r\omega G(\zeta) \tag{5.5b}$$

$$w = \sqrt{\nu\omega}\, H(\zeta) \tag{5.5c}$$

$$p = p(z) = \rho\nu\omega\, P(\zeta) \tag{5.5d}$$

Inserting these equations into equations (5.1a,b,c), and equation (5.2), we obtain a system of four simultaneous ordinary differential equations for the functions F, G, H and P:

$$F^2 + HF' - F'' - G^2 = 0 \tag{5.6a}$$

$$2FG + HG' - G'' = 0 \tag{5.6b}$$

$$2F + H' = 0 \tag{5.6c}$$

$$P' + HH' - H'' = 0 \tag{5.6d}$$

The boundary condition can be calculated from equations (5.3a,b) and are:

$$\zeta = 0 : \quad F = 0, \quad G = 1, \quad H = 0, \quad P = 0. \tag{5.7a}$$

$$\zeta = \infty : \quad F = 0, \quad G = 0. \tag{5.7b}$$

The system of equations (5.6a,b,c,d) and (5.7a,b) was first derived and solved by von Karman (1921), using the integral method he invented. Later, Cochran (1934), refined the solution and obtained more accurate results by numerical integration of the equations. The results are plotted in Fig. (5.2). It is to be noted from the solution that when $\sqrt{\nu/\omega}$ is small, the velocity components u and v have appreciable values only in a thin layer of thickness $\delta \cong \sqrt{\nu/\omega}$.

The velocity component w, normal to the disk is, at any rate, small and of the order $\sqrt{\nu\omega}$.

5.2.2 Rotating Flow Near a Disk

Boedewadt (1940) considered the laminar boundary layer developed at a stationary infinite flat plate by an otherwise unbounded viscous fluid that is rotating at a constant angular speed ω at infinity about the normal plane, Fig. (5.3). In order to formulate the mathematical problem, the Navier-Stokes equations should again be written in polar coordinates, equations (5.1a,b,c). The boundary conditions for the Boedewadt flow are no-slip and no-normal flow at the infinite plate:

$$\text{at} \quad z = 0: \quad u = 0, \quad v = 0, \quad w = 0. \tag{5.8a}$$

and rigid body rotation normal to the plate at infinity:

$$z = \infty: \quad u = 0, \quad v = r\omega. \tag{5.8b}$$

Following von Karman, Boedewadt introduced similarity forms for the velocity components and a non-dimensional parameter (equation (5.4)

and equations (5.5)). The radial pressure gradient can be computed for the frictionless flow at a large distance from the wall from the infinity condition as:

$$\frac{1}{\rho}\frac{\partial p}{\partial r} = r\omega^2 \tag{5.9}$$

In the frame work of the boundary-layer theory it is assumed that the same pressure gradient acts in the viscous layer near the wall. Introducing equation (5.4) and equations (5.5) with the boundary conditions (5.8a,b) into the Navier-Stokes equations (5.1a,b) and equation (5.2) we obtain a system of ordinary differential equations which is analogous to Eqs. (5.6a,b,c), as:

$$F^2 + HF' - F'' - G^2 + 1 = 0 \tag{5.10a}$$

$$2GF + HG' - G'' = 0 \tag{5.10b}$$

$$2F + H' = 0 \tag{5.10c}$$

with the boundary conditions:

$$\zeta = 0: \quad F = 0, \quad G = 0, \quad H = 0. \tag{5.11a}$$

$$\zeta = \infty: \quad F = 0, \quad G = 1. \tag{5.11b}$$

The system of equations (5.10a,b,c) with the boundary condition (5.11a,b) was solved and the results for the functions F, G, H are shown in Fig. (5.4). It can be concluded that the axial velocity component does not depend on the distance from the axis of revolution

but only on the distance from the plate (Eq. 5.5c), with an order of magnitude smaller than the velocity scales of the u and v components equation (5.5a,b). So that flow near the plate is predominantly in the horizontal plane. A vector representation of the predicted flow near the wall is plotted Fig. (5.5) and clearly illustrates the swirling inflow which is the predominant feature of this flow. The motion is induced by an imbalance between the radial pressure gradient and the centrifugal force in the boundary layer. Continuity dictates the compensating vertical outflow from the boundary layer. It is worth noting that the boundary layer extends considerably higher than in the case of the disk rotating in a fluid at rest. If the boundary layer thickness δ is defined as the height at which the deviation of the peripheral velocity is equal to 2 percent, we shall obtain $\delta = 8\sqrt{\nu/\omega}$ as against $\delta = 4\sqrt{\nu/\omega}$ for the stationary fluid.

Further studies by Batchelor (1951) developed the investigation to a family of rotationally symmetric flows whose members were distinguished by the ratio of the angular velocity of the fluid at infinity to that of the disk. For positive values of this ratio, Rogers and Lance (1960) solved the flow equations numerically. The effects of suction through the disk were considered by Stuart (1954), Rogers and Lance (1960), Evan (1969), Ockendon (1972) and Bodonyi (1975).

5.3 IMPLICATIONS OF SWIRLING FLOW IN RESERVOIRS

The requirement of an infinite reservoir at infinite radius inherent in the assumption of Boedewadt flow can never be achieved in reality. Rogers and Lance (1964) investigated boundary layer development in a rotating fluid over a stationary finite disk in order to examine the validity and predictions of the Boedewadt solution. Their procedure was to obtain a numerical solution using a sufficiently large number

of terms in a series expansion given by Stewartson (1957). This solution was valid near the outer edge of the disk, so that an adequate representation of the flow was obtained at smaller radii, say r = 1/2. This series solution was then compared to the similarity solution for the infinite plate which presumably held at least near the very centre of the disk. The comparison confirmed that the Boedewadt solution was a good approximation over the inner half of the disk.

It may be concluded that the boundary layer flow in the central region depends essentially on the local inviscid flow field and has completely 'forgotten' the manner in which it originated at the edge of the disk. Consequently, in the central zone of reservoirs, where flow at the interior region is circulating by the transfer of momentum from the exterior shear layer, Boedewadt flow should be applicable. The most important property of the Boedewadt flow in the reservoir context is the swirling inflow induced by the boundary layer. The radially inward growth of the Boedewadt layer drives fluid particles into the middle zone and causes a slight mixing through the processes of convection. The total volume of the swirling inward flow through a cylinder of radius r around the z axis can be calculated from:

$$Q_s = 2\pi r \int_0^\infty u\,dz = -\pi r^2 \sqrt{\omega\nu}\, H(\infty)$$

$$Q_s = -1.387\, \pi r^2 \sqrt{\omega\nu} \qquad (5.12)$$

5.4 LAMINAR STRATIFIED FLOWS

In stratified flows where the effect of density gradient is noticeable, buoyancy forces act to inhibit the vertical motion. Therefore, the mechanism of mixing is completely different. In particular, for the ideal case of two separate layers with different densities, the upper layer can flow with little effect over the motionless lower one. In laminar flow, velocities are so small that the surface of separation (interface) remains sharp, steady and distinct. Therefore, a laminar boundary layer may be developed to transfer the momentum by viscosity.

The boundary layer developed by the motion of the top layer of a two layered flow in a straight channel was studied by Kuelegan (1949). This analysis will be discussed briefly and will then be extended to laminar circulatory flows.

5.4.1 Laminar Flow at the Interface of Two Liquids

Consider a liquid of infinite height and having an initial uniform velocity U, positioned flows over a stationary liquid of an infinite depth. In general the two liquids have different physical characteristics, that is, their velocities and densities are not the same. If the pressure is everywhere hydrostatic, the interface or surface of separation is a horizontal plane. When U is sufficiently small the narrow region on both sides of the interface is a region of viscous laminar flow. Every particle of liquid on the interface moves with a constant velocity u_0. The thickness of the viscous boundary layer in the two liquids is initially zero and increases with the distance downstream, Fig. (5.6). Take the sets of coordinates (x_1,y_1) for the upper liquid and (x_2,y_2) for the lower one, such that the x-axis of the two sets coincide and lie in the plane of separation of the two

liquids, the positive sense being in the direction of U. The point at which the two liquids first come into contact will be taken as the origin. In the upper liquid, positive y is directed upward; in the lower liquid, positive y is directed downward. The density, viscosity and the kinematic viscosity of the upper liquid will be denoted by ρ_1, μ_1 and ν_1 respectively, and the corresponding properties of the lower liquid will be ρ_2, μ_2 and ν_2. The parameter, R, is defined as:

$$R = \sqrt{\mu_2 \rho_2 / \mu_1 \rho_1} \tag{5.13}$$

Kuelegan wrote Prandtl's boundary layer equations for two dimensional flow of an incompressible fluid, together with the continuity equation for each layer:

$$u_1 \frac{\partial u_1}{\partial x_1} + v_1 \frac{\partial u_1}{\partial y_1} = \nu_1 \frac{\partial^2 u_1}{\partial y_1^2} - \frac{1}{\rho_1} \frac{\partial p_1}{\partial x_1} \tag{5.14a}$$

$$\frac{\partial u_1}{\partial x_1} + \frac{\partial v_1}{\partial y_1} = 0 \tag{5.14b}$$

$$u_2 \frac{\partial u_2}{\partial x_2} + v_2 \frac{\partial u_2}{\partial y_2} = \nu_2 \frac{\partial^2 u_2}{\partial y_2^2} - \frac{1}{\rho_2} \frac{\partial p_2}{\partial x_2} \tag{5.14c}$$

$$\frac{\partial u_2}{\partial x_2} + \frac{\partial v_2}{\partial y_2} = 0 \tag{5.14d}$$

Where u_1 and v_1 (u_2 and v_2) are the components of velocity in the x_1 and y_1 (x_2 and y_2) directions, and p_1 (p_2) is the hydrostatic pressure. At the interface, normal velocities are assumed to be zero, i.e.

$$v_1 = v_2 = 0 \tag{5.15}$$

and shearing stresses are continuous:

$$\tau_{1xy} = \tau_{2xy}$$

or

$$\mu_1 \frac{\partial u_1}{\partial y_1} = \mu_2 \frac{\partial u_2}{\partial y_2} \tag{5.16}$$

In the upper liquid for $y_1 = \infty$:

$$u_1 = U \tag{5.17}$$

and in the lower liquid for $y_2 = \infty$:

$$u_2 = 0 \tag{5.18}$$

The system of four partial differential equations (5.14a,b,c,d) was reduced to a system of two partial differential equations by satisfying the continuity equation and by the introduction of the stream functions ψ_1 and ψ_2. Considering the upper layer we have:

$$u_1 = - \frac{\partial \psi_1}{\partial y_1} , \quad v_1 = \frac{\partial \psi_1}{\partial x_1} \tag{5.19}$$

and a similar equation can be assumed for the lower layer. Equations (5.14a,b) become:

$$- \frac{\partial \psi_1}{\partial y_1} \frac{\partial^2 \psi_1}{\partial x_1 \partial y_1} + \frac{\partial \psi_1}{\partial x_1} \frac{\partial^2 \psi_1}{\partial y_1^2} = \nu_1 \frac{\partial^3 \psi_1}{\partial y_1^3} \tag{5.20}$$

where $\partial p_1/\partial x_1$ is assumed to be zero. This can be changed into an ordinary differential equation by adopting the concept of similarity of the flow. Choosing a characteristic length δ_1, which is to be regarded as a function of x_1 only, the new dimensionless variables for y_1 and the stream function ψ_1 are:

$$\eta_1 = n_1 \, y_1/\delta_1$$

$$H_1(\eta_1) = - \psi_1/U\delta_1 \tag{5.21}$$

where n_1 is a dimensionless numerical constant. Substituting for η_1 and H_1 from equation (5.21) into equation (5.20), we obtain:

$$U \frac{d\delta_1}{dx_1} H_1 \frac{d^2 H_1}{d\eta_1^2} + n_1 \frac{\nu_1}{\delta_1} \frac{d^3 H_1}{d\eta_1^3} = 0 \tag{5.22}$$

Thus, if we select δ_1 to satisfy the relation:

$$\delta_1 \frac{d\delta_1}{dx_1} = n_1 \frac{\nu_1}{U}$$

or

$$\delta_1^2 = 2n_1 \frac{\nu x_1}{U} \tag{5.23}$$

then equation (5.22) becomes:

$$\frac{d^3H_1}{d\eta_1^3} + H_1 \frac{d^2H_1}{d\eta_1^2} = 0 \qquad (5.24)$$

which is the 'Blasius Equation' for the laminar boundary layer when the pressure is independent of x.

A similar relationship can be derived for the lower layer. The boundary conditions (5.15 to 5.18) can now be written in terms of the new variables. Kuelegan solved the system of ordinary differential equations by a method of approximation of a series of polynomials. Fig. (5.7a) shows plots of dimensionless velocities for $R^2 = 1$ (i.e. upper and lower layers having the same density and viscosity). Fig. (5.7b) gives the results for $R^2 = 10$. The dimensionless vertical scale, y/y_s was used (y_s the boundary layer thickness). It can be seen from these Figures that the variation of density (and consequently R) has a great influence on the interfacial velocity distribution.

For the vertical velocities v_1 and v_2, Kuelegan obtained appropriate expressions and concluded that although there was no normal velocity at the interface there existed a weak current moving normally upward towards the interface. In a sense the boundary of the upper liquid acted as a pump, raising small portion of the lower liquid to the level of the interface, then causing these portions to move horizontally.

5.4.2 Laminar Flow at the Interface of a Rotating Liquid

5.4.2.1 Derivation of the Equations

Consider a liquid of density, viscosity and kinematic viscosity of ρ_1, μ_1 and ν_1 rotating with a constant angular velocity (ω) over a motionless liquid of ρ_2, μ_2 and ν_2, where the depths of both liquids are infinite. Now if the velocities are so small that a laminar boundary layer is maintained at the interface, then "Boedewadt flow" can be established in the upper layer. Momentum will then be transferred by viscosity to the plane of separation and will cause it to rotate as well.

Therefore, for the lower liquid, the interface can be assumed to be a smooth rotating disk in an otherwise stationary fluid (Similar to von Karman flow). We take the origin (0) of the two sets of polar system of coordinates (r, φ, z) at the interfacial plane and the normal axis of the first set (z_1) coincident with the axis of rotation (perpendicular to the plane of interface and upward) and the axis (z_2) in the opposite direction for the lower liquid (Fig. (5.8)). If the flow is sufficiently slow, the variation of the pressure at the interface will be negligible, therefore we can assume the interface to remain horizontal. The Navier-Stokes equations of motion and the continuity equation in polar coordinates are the same as equations (5.1a,b,c and 5.2) for both liquids. The boundary conditions at the interface are that of no normal flow; i.e.

$$w_1 = w_2 = 0 \tag{5.25}$$

and no radial flow:

$$u_1 = u_2 = 0 \tag{5.26}$$

while the velocities and shear stresses will remain continuous in the tangential direction.

$$v_1 = v_2 \tag{5.27}$$

$$(\tau\varphi_z)_1 = (\tau\varphi_z)_2$$

or

$$\mu_1 \frac{\partial}{\partial z_1} (v_1) = \mu_2 \frac{\partial}{\partial z_2} (v_2) \tag{5.28}$$

For the present study it is convenient to use the angular velocity of the fluid at infinity as a reference velocity. Denoting this by (ω) a dimensionless coordinate is defined for the upper layer as:

$$\zeta_1 = z_1(\omega/\nu_1)^{1/2} \tag{5.29a}$$

and similarly for the lower layer:

$$\zeta_2 = z_2(\omega/\nu_2)^{1/2} \tag{5.29b}$$

The velocity and pressure components for the upper layer are:

$$u_1 = r\omega\, F_1(\zeta_1) , \qquad v_1 = r\omega\, G_1(\zeta_1) ,$$

$$w_1 = \sqrt{\nu_1\omega}\, H_1(\zeta_1) , \qquad \frac{1}{\rho_1} \frac{\partial p_1}{\partial r} = r\omega^2 \tag{5.30}$$

and for the lower layer:

$$u_2 = r\omega\, F_2(\zeta_2) , \qquad v_2 = r\omega\, G_2(\zeta_2)$$

$$w_2 = \sqrt{\nu_2\omega}\, H_2(\zeta_2) , \qquad p_2 = \rho_2\nu_2\omega\, P_2(\zeta_2) \tag{5.31}$$

Substituting the similarity equations (5.30) and (5.31) into the Navier-Stokes equations, the following set of ordinary differential equations will be obtained for the upperlayer:

$$F_1^2 - G_1^2 + H_1F_1' - F_1'' + 1 = 0$$

$$2F_1G_1 + G_1'H_1 - G_1'' = 0 \tag{5.32}$$

$$2F_1 + H_1' = 0$$

and:

$$F_2^2 - G_2^2 + H_2F_2' - F_2'' = 0$$

$$2F_2G_2 + H_2G_2' - G_2'' = 0 \tag{5.33}$$

$$2F_2 + H_2' = 0$$

for the lower layer.

The derivatives in equations (5.32) are with respect to ζ_1 and in equations (5.33) they are with respect to ζ_2. However, by definition:

$$\zeta_2 = -\zeta_1 \tag{5.34}$$

thus if we change ζ_2 to $-\zeta_2$ in the system of equations for the lower layer, it can be solved simultaneously with the upper layer. Consequently we can write:

$$
\begin{aligned}
&F_1^2 - G_1^2 + H_1 F_1' - F_1'' + 1 = 0 \\
&2F_1 G_1 + G_1' H_1 - G_1'' = 0 \\
&2F_1 + H_1' = 0 \\
&F_2^2 - G_2^2 - H_2 F_2' - F_2'' = 0 \\
&2F_2 G_2 - H_2 G_2' - G_2'' = 0 \\
&2F_2 - H_2' = 0
\end{aligned}
\qquad (5.35)
$$

where the derivatives are all with respect to ζ_1. The boundary conditions at the interface ($\zeta_1 = 0$) are:

$$
\begin{aligned}
&F_1 = F_2 = 0 , \qquad H_1 = H_2 = 0 \\
&G_1 = G_2 , \qquad G_1' = - R\, G_2'
\end{aligned}
\qquad (5.36)
$$

where

$$
R = \sqrt{\mu_2 \rho_2 / \mu_1 \rho_1} \qquad (5.37)
$$

and at infinity ($\zeta_1 = \infty$):

$$F_1 = 0 , \quad G_1 = 1 , \quad F_2 = 0 , \quad G_2 = 0 \tag{5.38}$$

5.4.2.2 **Method of Solution**

It is more convenient to reduce the order of the system of equations (5.35) from two to one, by introducing a set of four new functions J_1, K_1, J_2 and K_2 such that

$$\begin{aligned}
F_1' &= J_1 \\
J_1' &= F_1^2 - G_1^2 + H_1 J_1 + 1 \\
F_2' &= J_2 \\
J_2' &= F_2^2 - G_2^2 - H_2 J_2 \\
G_1' &= K_1 \\
K_1' &= 2F_1 G_1 + H_1 K_1 \\
G_2' &= K_2 \\
K_2' &= 2F_2 G_2 - H_2 K_2 \\
H_1' &= -2F_1 \\
H_2' &= +2F_2
\end{aligned} \tag{5.39}$$

with the boundary condition at the interface:

$$\zeta_1 = 0: \qquad F_1 = F_2 = 0 , \quad G_1 = G_2 = b , \quad H_1 = H_2 = 0$$

$$J_1 = a \ , \quad J_2 = d \ , \qquad K_1 = c \ , \qquad K_2 = - \frac{c}{R} \tag{5.40}$$

and at the infinity:

$$\zeta_1 = \infty: \qquad F_1 = F_2 = 0 \ , \quad G_1 = 1 \ , \quad G_2 = 0$$

$$J_1 = J_2 = 0 \ , \quad K_1 = K_2 = 0 \tag{5.41}$$

In equations (5.40) the assumed values of a, b, c and d are unknowns and should be determined in such a manner in order to satisfy the boundary conditions at infinity.

Equation systems of this type with missing initial conditions compensated by asymptotic boundary conditions at infinity are integrated using a method presented by Nachtsheim and Swigert (1965). A further description is given in Appendix A.

5.4.2.3 Results and Discussion

The system of ordinary differential equations was solved for values of R of = 0.0, 0.01, 0.1, $\sqrt{0.1}$, 1, $\sqrt{10}$, 10, 100 and ∞, where $R = \sqrt{\mu_2 \rho_2 / \mu_1 \rho_1}$. The results are shown in Fig. (5.9a-i). It can be seen that the values of (R) cover two different ranges: $0 < R < 1$ and $1 < R < \infty$.

The case of liquid of infinite viscosity turning over a liquid of finite viscosity is represented by R = 0. Mathematically this is identical with the problem of a solid disk rotating on a still liquid, see Section (5.2). On the other hand, for the intermediate value of R

= 1, both layers have the same density and viscosity, thus the fluid is homogeneous. Therefore the range of variation of $0 < R < 1$ resembles the rotation of a denser liquid on a stationary light one, which is physically unstable. Figs. (5.9a-5.9e) represent this range of R.

At the lower end, R = 0.0, the upper layer has a constant tangential velocity of solid body rotation (G = 1 and F = H = 0 at $\zeta = 0$). This rotation transfers to the lower layer by viscosity. At infinity ($\zeta = -\infty$) there is a weak constant upward motion without any radial or tangential component (H = 0.88, F = G = 0).

When viscosity of the upper layer decreases the solid body rotation at infinity reduces to an interfacial motion with three non zero components of u, v and w in both layers.

At R = 1, i.e. homogeneous fluid, the non-dimensional tangential velocity component (G) has a continuous slope at the interface ($G_1' = G_2'$). The radial velocity component has an opposite sign in the upper and lower layers and the vertical velocity component is upward in both layers.

The case of a liquid of a finite viscosity rotating over a liquid of an infinite viscosity is represented by $R = \infty$, which is equivalent to Boedewadt flow. In this case, rotation of the upper layer has no influence on the lower layer and it remains motionless because of high density and viscosity (F = G = H = 0), Fig. (9i). Therefore, the second range of variation of R (i.e. $1 < R < \infty$) is related to the rotation of a lighter liquid over a denser one which is stable and

practical, Fig. (9f-9i). The radial velocity for the upper layer near the interface is inward while that for the lower layer is outward.

The vertical velocities (w_1, w_2) for both layers are upward. This implies that in the process of rotation, the upper liquid is gently sucking the lower liquid. Obviously this can either demolish the interface and produce more mixing (for the case of a miscible liquid) or build a dome like interface (for the case of an immiscible fluid), provided that the angular speed of rotation is relatively high, (see next section).

Variation of the interfacial shear stress can be obtained from:

$$\tau_i = \mu_i \frac{\partial v_i}{\partial z} = \mu_i \frac{\partial v_i}{\partial \zeta} \cdot \frac{\partial \zeta}{\partial z} = r\omega\sqrt{\omega\mu_i\rho_i}\, G_i'(0) \qquad (5.42)$$

where i = 1 refers to the upper layer and i = 2, to the lower one. Due to the continuity of the shear stress at the interface we can write:

$$\tau_1 = \tau_2$$

In non-dimensional form we have:

$$\frac{\tau_1}{r\omega\sqrt{\omega\mu_1\rho_1}} = G_1'(0)$$

and

$$\frac{\tau_2}{r\omega\sqrt{\omega\mu_2\rho_2}} = G_2'(0) \qquad (5.43)$$

The above ratios are not equal and depend on the various values of R.

Fig. (5.10) shows the variation of dimensionless shear stresses ($G_1'(0)$ and $G_2'(0)$) for the upper and lower layers. In the first range ($0 < R < 1$) at very small values of R($R \cong 0$), the value of $G_1'(0)$ is very small while $G_2'(0)$ has a constant value. By increasing R, $G_1'(0)$ increases and $G_2'(0)$ decreases monotonically.

For the case of a homogeneous fluid, R = 1, the values of $G_1'(0)$ and $G_2'(0)$ are identical.

In the second range ($1 < R < \infty$), $G_1'(0)$ approaches a constant value and $G_2'(0)$ becomes very small (Boedewadt flow).

The non-dimensional curves of asymptotic values of vertical velocities $H_1(\infty)$ and $H_2(\infty)$ are plotted in Fig. (5.11), where it can be seen that the uplift velocity in both layers is highly dependent on R. It can be shown that the vertical velocity does not depend on the horizontal distance from the axis of rotation z, (w_1 and w_2 in equations (5.30) and (5.31)). Its magnitude, however, is at least one order less than that of the horizontal velocities (u,v).

The velocities in the laminar boundary layers approach the limiting values in an asymptotic manner. Therefore, a boundary layer thickness can be defined as a height where the peripheral velocity does not change by more than 2 percent. This is plotted for the upper and lower layers in Fig. (5.12). The variation of the boundary layer thickness for the lower layer is not highly dependent on R.

On the other hand, the boundary layer thickness for the upper liquid (δ_1), is sensitive to the values of R. The range of variation of δ_2 is usually limited from (4 to 6) while that for δ_1 is from (0 to 8).

5.4.2.4 Limitation of the Model

Due to the rotation of the upper layer there is a change of pressure at the interface which is responsible for the curvature of the surface. The radial pressure gradient can be obtained by the assumption of centrifugal flow, equation (5.9). The effect of this pressure over the interface is balanced by the weight of the paraboid of fluid, Fig. (5.13), see also Gill et al (1979).

If h_c is the maximum height of the dome, then equating the gravity and centrifugal forces we have:

$$h_c = \frac{\omega^2 r^2}{2g'} \tag{5.44}$$

where $g' = \epsilon g = \frac{\rho_2 - \rho_1}{\rho_1} g$

The condition for h_c to be negligible is:

$$\frac{h_c}{\delta} = \frac{\omega^2 r^2}{2g'\delta} \ll 1 \tag{5.45}$$

where δ is the minimum thickness of the boundary layer.

For a gyre with the angular period of 2 days, the radius of 400m (Sobey (1972)), ϵ of 0.1% and a boundary layer δ of the order of magnitude of $\sqrt{\nu/\omega}$, equation (5.45) is satisfied.

In cases where the curve of stratification is continuous, if the angular velocity increase and the boundary layer decreases then equation (5.45) will not remain negligible. As a result, the denser liquid mixes and rises up into the upper layer.

CHAPTER 6

NOTATION

a	characteristic azimuthal velocity of reservoir
a'	amplitude of the internal waves
A	total area of reservoir or tank
A_p	area of part p
B	buoyancy
c', C, C_1	constants
C_e	phase velocity
d	diameter of nozzle
d_0	height of nozzle
E	entrainment coefficient
E_*	entrainment coefficient based on shear velocity
f, f_1	function
f_i	interfacial coefficient of friction
F'	a characteristic densimetric Froude number
F_0'	jet densimetric Froude number
F_1', F_2'	densimetric Froude numbers of the upper and lower layer
g	acceleration due to gravity
g'	acceleration due to densimetric gravity
h	a characteristic depth
h	depth of stirred layer
h_t	turbulent integral length scale
h_1, h_2	depth of upper and lower layers respectively
H	total depth
k	wave number
K	interfacial Keulegan parameter

K_c	critical value of K
K_u	constant for interfacial mixing
n	constant
N	frequency
P_e	peclet number
q	volume withdrawn per unit time
Q_e, Q_e', Q_e, Q_{ep}	entrianment discharge
Q_m	flux of mass per unit area
Q_0	jet discharge
r, θ, z	cylindrical polar coordinates
R_e	
R_{e_1}, R_{e_2}	Reynolds number of the upper and lower layer
R_{h_1}, R_{h_2}	hydraulic radius of the upper or lower layer
R_{h_0}	hydraulic radius of the whole cross section
R_i	overall Richardson number
R_{i*}	Richardson number based on shear velocity
R	radius of reservoir
S	the axial distance from the jet along the trajectory
t	time
T	temperature
T_m	scale for excess temperature
u	velocity in x direction
u_t	root mean square value of the velocity u
U	a characteristic mean velocity in x direction
U_c	critical velocity of mixing
U_m	maximum velocity in x direction
U_1, U_2	mean velocity of the upper or lower layer in x direction

U_*	shear velocity
v	depth average velocity in tangential (θ) direction
v_i	interfacial velocity in θ direction
v_p	depth average velocity in tangential direction of a subdivision p
V	characteristic azimuthal velocity in tangential jet in a reservoir
V_o	jet velocity
W_d	channel width
W_e	entrainment velocity
W_{ep}	entrainment velocity of subdivision p
w'	velocity perturbation in z direction
x,y,z	rectangular cartesian coordinate axes
y_m	length scale in y direction
z_m	length scale in z direction
z_1	the depth of jet
δ	characteristic radial width of tangential jet in a reservoir
ϵ	proportionate density defect
ϵ_t	turbulent eddy viscosity
λ	angle of jet growth in z direction
λ'	length of the internal waves
ν	kinematic viscosity
ν_e	effective viscosity
ν_m	molecular diffusivity
ν_1, ν_2	kinematic viscosity of upper and lower layers
ρ, ρ'	a characteristic density and perturbation density
ρ_1, ρ_2	density of upper and lower layers
$\Delta\rho = \rho_2 - \rho_1$	density difference
τ	surface shear stress

τ_i	interfacial shear stress
ψ	Iwasaki-Keulegan parameter
ψ_c	critical values of ψ
ψ_0	jet dimensionless parameter
ψ_*	Iwasaki-Keulegan parameter based on shear velocity
ω	angular velocity

CHAPTER 6

CIRCULATION IN STRATIFIED RESERVOIRS

6.1 INTRODUCTION

6.1.1 Thermal Stratification

Thermal stratification is the term applied to the segregation of the water of a lake or reservoir into horizontal layers exhibiting differences of temperature, and consequently density and viscosity. The specific relationship between the temperature and density of water, the low thermal conductivity of water, the limited penetration of radiant heat and light and the fact that stream inflows in late spring and early summer tend to be warmer than the reservoir surface waters account for the primary cause of thermal stratification. In Fig. (6.1) the curve of temperature-density is plotted from 0°C to 25°C, and also the differential of that curve. It can be seen that the curve is approximately parabolic and that the gradient curve is nearly linear.

The maximum density of water occurs at 4°C, and the more departure from that, the greater are the buoyancy forces. These forces cause the warm water to float at the surface and the cold water to sink down to the lower layer, producing a system of stable stratification. When fully developed in summer, stratification of a deep lake produces three distinct layers, Fig. (6.2). The upper layer, which may extend 6-10m below the surface is known as "epilimnion" and has a high and fairly uniform temperature. Below this layer there is a zone of steep temperature gradient, which is called the "thermocline". Below the thermocline there is a layer of nearly uniform and low temperature which extends to the bottom of reservoir. This layer is known as the

"hypolimnion". Mathematically, the thermocline is defined as the plane of the point of inflexion on the vertical temperature profile:

$$\frac{\partial^2 T}{\partial z^2} = 0 \qquad (6.1)$$

where T is the temperature of water.

6.1.2 Annual Thermal Cycle of Reservoirs

If we assume the beginning of the spring season as the time when the ice cover of reservoir or lake melts, then the temperature of the surface will be 0°C. Below the surface, the temperature will be higher, say up to 4°C, extending down to the bottom.

As the sunlight becomes stronger, the air temperature rises and the surface water warms up. By the time its temperature approaches 4°C it becomes denser and sinks. The lower cooler layers come to the surface to be warmed in turn. The temperature difference all over the depth diminishes and even moderate winds produce a thorough circulation which will be able to bring the bottom water to the surface.

This state of full and complete mixing in the lake or reservoir is referred to as the "spring overturn". At the time of "spring overturn" the temperature of the lake is approximately about 4°C throughout. The increase in sunlight results in the surface water becoming warmer and lighter, while the lower layers remain at a temperature of perhaps 6°C - 7°C. The surface water continues to heat up and if the weather is calm, a shallow thermocline begins to form. A period of moderate winds increases the depth of the epilimnion and

deepens the thermocline. The bottom layers, however, remain at much the same temperature as before and constitutes a definite hypolimnion.

In the temperate region of the northern hemisphere, the epilimnion water reaches its maximum temperature during June, July or August, and the thermocline becomes best defined. It acts like a barrier and prohibits the energy of the circulation of the epilimnion generated by the wind, to reach the hypolimnion. The stratification is so stable that the inflow of warm water will float over the surface and cold water inflows will sink to the deepest parts of the lake without mixing with the water above.

By the end of August, the strength and duration of solar radiation decreases and air temperature decreases gradually. The epilimnion water cools, becomes dense and sinks down. Again, wind can demolish the thermocline and remove it. Depending on the weather conditions, the stratification disappears about October. The "autumn overturn" makes the reservoir relatively uniform and moderate wind helps in its full circulation. As autumn passes into winter, air temperature falls, and sunlight fades and becomes less and less effective in heating the surface of the lake or reservoir.

In a mild winter, water temperature may never become as low as 4°C. But in cold winters and relatively shallow reservoirs or lakes, the surface water may freeze while the lower layers have a higher temperature and an "inverted stratification" occurs, Thompson (1954).

6.1.3 The Use of Jetted Inflows for the Prevention of Stratification

Probably, one of the most effective methods in the prevention of stratification in reservoirs is the application of momentum jets, to circulate the stagnant body of water.

The first serious investigation was carried out by Cooley and Harris (1954) and White, Cooley and Harris (1955) in simulating the reservoirs of the Metropolitan Water Board (recently part of the Thames Water Authority). Their tests were performed on different scale models of the Walton and Queen Mary Reservoirs. The case of spring inflow was simulated by jetting the incoming warm water into a uniformly cold reservoir water.

The inlets were made to discharge horizontally near the floor of the reservoir and several pipe diameters were tried.

The case of water flowing into an already stratified reservoir was simulated by discharging a warm jet into a two-layered reservoir model. The resulting upward curving jet was found to become so diluted by the cold water, before reaching the upper layer, that by the time it did so it no longer had the sufficient buoyancy to penetrate far into it. Thus the jet entrained a small amount from the upper layer, which however, remained separate from the rest of the water in the reservoir. To overcome this difficulty inclined jets were installed at a level below the floor of the reservoir.

Cooley and Harris (1955) computed the total volume of entrained water and the variation of thermocline by using an expression, they derived, for the shape of the trajectory of the rising jet. Their analysis was

very approximate and the errors were magnified in subsequent time steps.

Steel (1975) utilised the densimetric jet Froude number:

$$F_0' = \frac{V_0}{\sqrt{\epsilon g d}}$$

where V_0 = jet velocity

d = diameter of nozzle

$\epsilon = \frac{\Delta\rho}{\rho}$ = proportionate density defect.

for describing the trajectories of the jets. The jet was located near the bottom of the reservoir in cold water ambient.

In order to achieve the optimum mixing it was necessary to produce the longest trajectory in the deepest water masses. The trajectory should be such as to allow the mixture eventually to rise to the surface without any local recirculation.

Based on these constraints, for a given density defect and jet dimension, it was possible to obtain a desirable densimetric Froude number by using an appropriate velocity, if that was practicable and economically acceptable.

Steel (1972) gave the following approximate relationship for the estimation of S/d in Queen Elizabeth II reservoir when the jets were horizontal:

$$\frac{S}{d} \cong 3(F_0')^{0.63} \left(\frac{z_1}{d}\right)^{0.38} \qquad 10 < F_0' < 200 \qquad (6.2a)$$

where S = the axial distance from the jet

z_1 = the depth of the jet.

It was then possible to estimate the entrainment discharge, Q_e from:

$$Q_e \cong Q_0 \left(0.3 \frac{S}{d}\right) \qquad (6.2b)$$

where Q_0 = jet discharge.

Given a known relationship between the depth of water and the impounded volume, it was possible to use such jet relationships as the basis for estimating the effect of jetting on the stratification characteristics of the reservoir.

Cooley and Harris (1955) performed one experiment to answer the question, how much of the mixing was due to circulating currents and how much to entrainment by jets. Water was discharged horizontally into the reservoir near its surface, the stored water being uniform and heavier (colder). In this way the jet remained near the surface causing a circulation therein. Cooley and Harris argued that the jet remained buoyant and the deepening of the thermocline was attributed to the circulation of the reservoir water body. Unfortunately, they did not use a rigorous analysis to distinguish between the effect of the jet's entrainment and the reservoir's circulation.

Based on the investigations described in Chapter 3, an impressive theory for circulation in water supply reservoirs was that developed by Sobey and Savage (1974). The analysis was, however, restricted to homogeneous reservoirs.

In the present research the mixing and circulation caused by a surface buoyant jet in a stratified reservoir has been studied analytically and verified experimentally. On the experimental side, stratification was simulated by resting a layer of fresh water over a layer of a saline solution. Fresh water was then introduced to the reservoir through a tangential surface jet which produced the circulation therein.

On the theoretical side, the analysis of Sobey and Savage, for homogeneous reservoirs, was extended to the case of stratified ones. The dimensional analysis of Chapter 3, for homogeneous reservoirs, revealed relationships between the jet discharge and the reservoir's geometric characteristics, (aspect ratio and bottom relative roughness). An attempt was made in the present study to correlate the jet discharge to the stratification characteristics of the reservoir. Before the presentation of the author's analysis, important topics dealing with reservoir, stability, entrainment and interfacial shear need to be reviewed.

6.2 STABILITY IN STRATIFIED FLOW

6.2.1 Preliminary Observations

Consider a long channel with a layer of fluid of uniform density ρ_1 flowing over a layer of density ρ_2. In a stable stratified flow the density of the lower layer is greater than that of the upper layer, i.e. $\rho_2 > \rho_1$. The interface is assumed to be a streamline separating the two fluids and coincident with the density discontinuity.

At low velocities, the interface is smooth, sharp and distinct and laminar motion develops on the two sides of it. When the velocity of the flow increases to some definite value (depending on the density and the viscosity of the two fluids), the separating surface becomes rough and covered with surface waves travelling in the direction of the flow. These waves usually have a velocity slightly smaller than the velocity of the upper current. The waves are long-crested, that is, the length of the crests normal to the direction of motion is greater than the spacing between the crests, and the crest lines are parabolic in their configuration. The waves are stable and travel with no deformation, except the tendency to grow slightly larger during their motion, Keulegan (1949).

When the velocity of the upper current exceeds a "critical velocity", the waves become sharp-crested and the crests shorten. The waves no longer are stable, that is portions of the crests break away from the waves and are thrown into the upper current, Fig. (6.3). These portions move forward and upward. When the velocity of the current is increased, the rate of mixing increases. At this stage of the flow, the wave length is not affected by changes of velocity, but the height of the sharp crested waves, the size of the eddies emanating from the crests, and the frequency of departure of the eddies are augmented.

These are the qualitative results of the observations made in laboratory channels and reported by several researchers.

6.2.2 Instability of Stratified Flow

The question of what constitutes the critical velocity of mixing has been the subject of various investigations. This, in a way, is related to the theories of instability in stratified flows that will be reviewed briefly.

The specific type of the interfacial waves that were discussed in the previous section are named "progressive waves". In a stratified flow when the two layers are motionless and deep compared with the wave length, progressive waves travel with the phase velocity, C_e, Lamb (1932).

$$C_e = \frac{\omega}{k} = \left(\frac{g}{k} \cdot \frac{\rho_2 - \rho_1}{\rho_2 + \rho_1}\right)^{1/2} = \left(\frac{g\lambda'}{2\pi} \cdot \frac{\rho_2 - \rho_1}{\rho_2 + \rho_1}\right)^{1/2} \qquad (6.3)$$

where ω = angular velocity

k = wave number

$\lambda' = 2\pi/k$ = wave length

If the two deep layers move with velocities U_1 and U_2, the phase velocity can be written as:

$$C_e = \frac{\omega}{k} = \frac{\rho_1 U_1 + \rho_2 U_2}{\rho_1 + \rho_2} \pm \left\{\frac{g}{k}\frac{\rho_2 - \rho_1}{\rho_2 + \rho_1} - \frac{\rho_1 \rho_2}{(\rho_1 + \rho_2)^2}(U_2 - U_1)^2\right\}^{1/2} \qquad (6.4)$$

which reduces to equation (6.3) when $U_1 = U_2 = 0$.

In equation (6.4), the first term is a weighted mean velocity of the layers, and the waves move relative to this with a phase speed related to the shear across the interface.

Stability of the interfacial waves depends on the character of the second term in equation (6.4). Instability occurs when the square root is imaginary (i.e. disturbances are exponentially growing and stationary relative to the mean velocity, rather than oscillatory). Therefore:

$$(\Delta U)^2 = (U_1 - U_2)^2 > \frac{g}{k} \frac{\rho_2^2 - \rho_1^2}{\rho_1 \rho_2} \qquad (6.5)$$

and if $\rho_1 \cong \rho_2$ and $g' = g \frac{\Delta\rho}{\rho_1}$ we can write:

$$\frac{(\Delta U)^2}{g'\lambda'} > \frac{1}{\pi} \qquad (6.6)$$

where the left hand side is written in the form of a critical internal Froude number, based on the wave length of the disturbance.

Analysis has been extended to more realistic velocity and density profiles. For example, Goldstein (1931) assumed a linear variation of velocity and density across the interface layer, Fig. (6.4a), and presented an approximate solution. Later on Miles and Howard (1964) obtained a more complete solution to that problem. Their stability diagram is shown in Fig. (6.4b), and is based on the variation of overall Richardson number, $R_i = g\ \Delta\rho/\rho\ h_i/(U_1 - U_2)^2$ against the

non-dimensional wave number, $\alpha = 1/2\ kh_i$. It can be seen that above $R_i = 1/4$ small disturbances of all wave numbers are stable.

Using numerical methods, calculations have been carried out for other profiles of smoothly varying density and velocity, see Hazel (1972).

It must be noted that all of these calculations concerning the instability of the stratified flows were based on the linearisation of the Navier-Stokes equations. The effect of viscosity, however, was not included explicitly. Viscosity was only considered through its effect on the velocity distribution, Turner (1979).

Keulegan (1949), on the other hand, carried out an extensive and much quoted series of experiments, using a pool of sugar solution with a laminar or turbulent flow of fresh water above it. He invoked viscosity to interpret his results. From dimensional reasoning it is possible to obtain a stability parameter involving the effect of viscosity. Given a velocity U_1 (the mean velocity of the upper layer) and the kinematic viscosity ν_2, of the lower fluid, only one non-dimensional parameter:

$$\psi = \frac{1}{K} = U_1^{\,3}/(\nu_2\ g\ \frac{\Delta\rho}{\rho_1}) \qquad (6.7)$$

can be formed. Keulegan's experimental results defined the following criterion for mixing:

laminar flow	$\psi_c = 500$	$R_{e_1} < 450$
turbulent flow	$\psi_c = 180$	$R_{e_1} > 450$

(6.8)

where $R_{e_1} = U_c R_{h_1}/\nu_1$,

ψ_c = critical values of ψ

R_{h_1} = hydraulic radius of the cross section of the upper layer

U_c = the critical velocity of mixing

significantly, $R_{e_1} \cong 450$ is also the Reynolds criterion that separates the regime of turbulent flow from the regime of laminar flow.

The case of sub-surface flow was studied by Ippen and Harleman (1952). For a two-dimensional flow with the depth of the lower layer, h_2, taken as the characteristic length in the Reynolds number. The stability criterion (Eq. 6.7) is readily transformed into:

$$K = \frac{1}{(F_2')^2 R_{e2}} \tag{6.9}$$

where

$$F_2' = \frac{U_2}{\sqrt{g \frac{\Delta\rho}{\rho} h_2}} \quad , \qquad R_{e2} = \frac{U_2 h_2}{\nu_2}$$

The critical values of stability are defined by:

Laminar flows (lower layer) $K_c = \frac{1}{R_{e2}}$

Turbulent flow (lower layer) $K_c = 0.18$ (6.10)

No mixing should occur for flows with K values greater than K_c. The transition to turbulent flow begins at a Reynolds number of approximately 1000, Harleman (1961).

It is interesting to point out that even after the interfacial waves began to break, the amount of lower-layer fluid entrained in the upper layer was relatively small. Ultimately this type of mixing process tends to form a new layer, with a density intermediate to that of the original layers.

6.3 INTERFACIAL MIXING

6.3.1 The Concept of Entrainment

In stratified flow, entrainment is defined as the process of mass transport across a density interface. Mass transport is generated by highly turbulent fluid motion on one side of the interface from a low velocity or almost quiescent layer to the turbulent one. If the flux of mass transfer per unit area is denoted by Q_m we can write:

$$Q_m = \nu_m \frac{\overline{d\rho}}{dz} - \overline{w'\rho'} \qquad (6.11)$$

where ν_m = molecular diffusivity

w', ρ' = velocity and density perturbations.

If the motion is statistically steady and if mean quantities do not vary horizontally the value of Q_m is constant in time and space.

In turbulent flow in which ν_m is small, it may be assumed that the molecular fluxes can be neglected. Now, it is usual to relate the

mass flux per unit area, Q_m, to the density difference of the two layers $\Delta\rho$, and the entrainment velocity W_e by:

$$Q_m = W_e . \Delta\rho \tag{6.12}$$

The entrainment coefficient, E, is defined by

$$E = \frac{W_e}{U} \tag{6.13}$$

where U is a characteristic velocity of the turbulent layer.

Initially, it can be assumed that the mixing process represents a balance between the gravity and inertia forces and is, therefore, a function of the overall Richardson number.

$$E = f(R_i) \tag{6.14}$$

where $R_i = \dfrac{g \dfrac{\Delta\rho}{\rho} h}{U^2} = (F'^{-1})^2$

F' = densimetric Froude number.

A number of laboratory experiments have been conducted to obtain the form of the function in Eq. (6.14).

Table 6.1 gives a review of the various experimental studies dealing with interfacial mixing and entrainment. The majority of the empirical data in Table (6.1) were obtained from laboratory experiments. The results can, however, be applied to the problem of mixing across a thermocline in an ocean, lake or reservoir.

6.3.2 Experiments Without Shear

Rouse and Dodu (1955) used a vertically oscillating grid of solid bars in two layers of liquid of different densities, Fig. (6.5). Observations were made of the entrainment velocity W_e, which is, in this case, the downward velocity of propagation of the interface. They found that turbulent eddies on the grid side of the interface entrained fluid across the interface from the quiescent layers into the stirred layer. The eddies eroded the other layer continuously. The change of density at the interface had a damping effect on the turbulence. The interface, however, moved away from the stirrer gradually, Rouse and Dodu assumed that the entrainment velocity was equal to the velocity with which the interface moved and was given by:

$$W_e = \frac{dh_1}{dt} \tag{6.15}$$

Cromwell (1960) performed an experiment to simulate the pycnocline similar to the above experiment.

Turner (1968), however, obtained a thorough experimental data, using two different experiments. In the first the lower layer was stirred by an oscillating grid with a frequency of N, and the fluid was withdrawn from the stirred layer at a rate adjusted to keep the interface at the same distance from the grid. The entrainment velocity, W_e, was given by:

$$W_e = \frac{q}{A} \tag{6.16}$$

where q = volume withdrawn per unit time

A = cross sectional area of the tank.

In the second experiment, both layers were stirred by two grids and the interface stayed at the mid-level. The entrainment velocity was obtained from the rate of change of the density difference:

$$W_e = \frac{\bar{h}}{\Delta\rho} \frac{d\Delta\rho}{dt} \tag{6.17}$$

where $\bar{h}$ = depth of stirred layer.

It has been shown that the integral length scale h_t and the root mean square value, u_t, of the horizontal turbulent velocity component are characteristics of the fluid motion near the interface, Thompson (1969).

Turner (1973) utilized these length and velocity scales and expressed the general results of his experiments with the oscillating grids as:

$$E = \frac{W_e}{u_t} \propto \left(\frac{u_t^2}{g \frac{\Delta\rho}{\rho} h_t}\right)^n = R_i^{-n} \tag{6.18}$$

where n = 1 if the density difference is produced by temperature and n = 3/2, when it is generated by the salt, Fig. (6.6). Turner concluded that the difference in the value of n is due to the influence of the relatively large molecular diffusivity. He introduced a dimensionless parameter, namely the 'Peclet number' as:

$$P_e = \frac{u_t \, h_t}{\nu_m} \tag{6.19}$$

where ν_m = molecular diffusitivity.

In Turner's experiments, the major change in P_e was due to the change in ν_m (ν_m for heat is about 100 times greater than ν_m for salt). Therefore, equation (6.14) can be replaced by:

$$E = f_1(R_i, P_e) \tag{6.20}$$

Crapper and Linden (1974) suggested a critical or threshold value of $P_e \cong 200$.

The dependence of E on the Reynolds number was studied by Wolanski (1972) who varied R_e by a factor of 3 and found a very weak dependence. Consequently for large values of P_e and R_e and for strong stability the law of n = 3/2 was found to apply, Turner (1973).

Long (1975) stated that the n = 1 law is more fundamental and that the n = 3/2 behaviour is based on erroneous interpretation of the experimental data. Long showed that u_t was proportional to $\omega^{4/3}$ (instead of proportional to ω which was used by Turner).

6.3.3 Experiments with Shear

Several experiments have been carried out on turbulent shear flows, to investigate the mechanism of entrainment. Keulegan (1949), suggested an empirical formula for the mixing from the lower layer to the upper layer:

$$E = \frac{W_e}{U_1} = K_u(1 - 1.15\ U_c/U_1) \qquad (6.21)$$

where U_c = the critical velocity of mixing

$K_u = 3.5 \times 10^{-4}$ for channel flow, Keulegan (1949)

$K_u = 2.14 \times 10^{-4}$ for salt wedges, Keulegan (1966)

Ellison and Turner (1959) studied the flow of a two dimensional surface buoyant jet in quiescent surroundings. Their results indicate that unlike an ordinary non-buoyant jet which expands linearly with the distance from the source, the buoyancy of the efflux tends to decrease the entrainment rate. If the Richardson number is defined by:

$$R_i = \frac{g(\rho_2 - \rho_1)}{\rho_2} h_1/U_1^2$$

where ρ_1, U_1 and h_1 are the mean density, mean velocity and thickness of the jet at any section and ρ_2 is the density of the ambient fluid, a smooth curve can fit the experimental results, Fig. (6.7). Koh (1971a) fitted the following formula to Ellison and Turner's results:

$$\begin{cases} E = 0.075 \left[\dfrac{2}{1 + \dfrac{R_i}{0.85}} - 1 \right]^{1.75} & 0 < R_i < 0.85 \\ E = 0 & \text{otherwise} \end{cases} \qquad (6.22)$$

Equation (6.22) shows that if $R_i = 0.85$, no further mixing takes place.

Ellison and Turner also studied the flow of a layer of heavy saline solution down a sloping channel under a deep layer of fresh water at rest. If h_2 and U_2 are the depth and mean velocity of the underlayer, their overall Richardson number becomes:

$$R_i = g \frac{\Delta\rho}{\rho} h_2/(U_2)^2$$

For a range of $R_i < 1$ their results are consistent with:

$$E = \frac{W_e}{U_2} \sim R_i^{-1} \tag{6.23}$$

Lofquist (1960) investigated the flow of a horizontal layer of salt under a still fresh water layer using the overall Richardson number for the underlayer. For $R_i > 1$, his data are in reasonable agreement with equation (6.23), see Fig. (6.8a). A comparison between the experiments of Ellison and Turner and those of Lofquist is shown in Fig. (6.8b).

The quasi-steady wind driven deepening of the ocean surface mixed layer was simulated first by Kata and Phillips (1969) and then by Kanta, Phillips and Azad (1977), (hereafter KP and KPA respectively). All of the experiments were conducted in the same annular tank, Fig. (6.9a), and followed identical procedures. A constant shear stress τ was applied at the surface of a stratified fluid by a rotating screen. Variation of the depth of the mixed-layer, h_1, in time was recorded. The degree of entrainment was also observed. The KP and KPA experiments differed only in the form of the density stratification. KP used a linear stratification, KPA used a two-layer stratification.

Viscosity was assumed to be unimportant at the relatively high Reynolds numbers achieved in the experiments.

Defining the friction velocity as $U_* = (\tau/\rho)^{1/2}$ where τ is the applied (constant) surface stress and ρ is a reference density, it is convenient and desirable to express experimental results in terms of external parameters:

$$E_* = \frac{h_1'}{U_*} = f\ (R_{i*},\ \frac{h_1}{W_d}) \tag{6.24}$$

where $h_1' = \frac{dh_1}{dt} = W_e$

$$R_{i*} = \frac{\rho_2 - \rho_1}{\rho_1}\ \frac{gh_1}{U_*^2}$$

W_d = channel width

ρ_1, ρ_2 = density of fresh and salt water

In the case of no side wall effect (i.e. $h_1/W_d \to 0$), KP fitted the following formula:

$$E_* = 2.5\ R_{i*}^{-1} \tag{6.25}$$

to their data, Fig. (6.9c).

The slope of -1 was interpreted as showing a simple proportionality between the rate of turbulent energy dissipation ($\propto U_*^3$) and the rate of work against buoyancy ($\propto \rho_2-\rho_1/\rho_1\ gh_1'$). This interpretation of

the experimental results has been widely applied to modelling the energy of entrainment in the atmosphere and in the ocean, see Turner (1973).

KPA on the other hand, reported no simple relationship between the entrainment E_* and R_{i*} in the range of their experiments.

Price (1979) and Thompson (1979), however, re-examined the KP- and KPA-data, and concluded that the influence of side wall friction was not always negligible.

Price showed that conservation of momentum leads to:

$$E_* = \frac{h_1'}{U_*} = n(0.6)^{1/2} R_{i*}^{-1/2} \qquad (6.26)$$

where $n = 1/2$ and $n = 1$ for the KP and KPA cases respectively, provided that $h_1/W_d \to 0$. In the range of $0.5 < R_i < 1$, which includes nearly all of KP and KPA data,

$$E \cong 5 \times 10^{-4} R_i^{-4} \qquad (6.27)$$

where $R_i = \dfrac{g \dfrac{\Delta\rho}{\rho} h_1}{U_1^2}$

h_1, U_1 = depth and velocity of the mixed layer respectively.

Moore and Long (1971) performed a series of experiments in a steady state shearing flow in a cylindrical continuous tank of rectangular cross-section, Fig. (6.10a,b). Salt water was injected at an angle of 5° to the horizontal from right to left at the channel's bottom from

slits spaced 30cm apart. An equal volume of (slightly less salty) water was withdrawn from a large number of holes at the bottom of the channel and returned to the brine storage tank.

Salt was added continuously to this tank to maintain a constant density. At the top of the channel, fresh water was injected from left to right from a similar set of slits and an equal volume of (slightly salty) water was extracted from a large number of 5mm holes and pumped to waste. Because of the mixing at the interface some salt transported to the upper layer. This mass of salt was calculated from the known mass of salt added to the brine storage tank. It was thus possible to determine the vertical flux of salt.

Due to the flow which was injected at the boundaries, two homogeneous layers were formed and were separated by a thin interface. These layers moved uniformly in opposite directions. Using the velocity difference ΔU, as the velocity scale and the total depth (H) as the length scale, Moore and Long showed that:

$$E = \frac{W_e}{\Delta U} = C_1 \left(\frac{g \frac{\Delta\rho}{\rho} H}{\Delta U^2}\right)^{-1} = C_1 \, R_i^{-1} \qquad (6.28)$$

For the range of $1 \leqslant R_i \leqslant 30$, C_1 had a value of approximately 8×10^{-4} with an uncertainty of ±20%, see also Fig. (6.10c).

Moore and Long also conducted experiments on thermally stratified fluid ($1 \leqslant R_i \leqslant 5$). The results were in agreement with equation (6.28) although viscosity was different.

In their time varying experiments, they found that the entrainment depth, h_1, varied with time, t, according to the relationship:

$$h_1^3 \propto t \tag{6.29}$$

Ashida and Egashira (1977) conducted several experiments in a long stratified flume (23m length), in which warm water was moving over a layer of cold water. They measured the variation of the interface, velocity and density with time. Fig. (6.11) shows their experimental results together with the data of other investigators. It can be seen that almost all the results are consistent with equation (6.28), with a slightly different constant. The results of Ellison and Turner (1959) are, however, a little greater than the others.

Wu (1973) conducted experiments in which wind was flowing over a flume containing two layers of water of different density. Using the friction velocity in water and the density of water, we have:

$$\frac{W_e}{U_*} = 0.234 \frac{U_*^2}{g \frac{\Delta\rho}{\rho} h_1} = 0.234 \, R_{i*}^{-1} \tag{6.30}$$

The coefficient of proportionality in equation (6.30) is a factor of 10 smaller than that of Kato and Phillips, equation (6.25).

Suga and Takahashi (1976) obtained the following relationship, from large scale laboratory experiments and from field observations of saline wedges in natural rivers:

$$E = \frac{W_e}{U_1} = 2 \times 10^{-3} \, R_i^{-3/2} \tag{6.31}$$

6.4 INTERFACIAL SHEAR STRESS AND FRICTION

A key factor in the modelling of stratified flow systems is the interfacial shear stress, τ_i, and the corresponding friction coefficient, f_i, Schijf and Schoenfeld (1953). The study of the latter and its dependence on the pertinent gross flow parameters and relative density difference has been the subject of numerous experimental investigations. The basic assumptions, the methodology of approach, and the range of variation of the controlling parameters varied widely in these investigations.

In general, the interfacial shear stress in a laminar flow is defined as:

$$\tau_i = \rho\nu \left(\frac{\partial u}{\partial z}\right)_i \tag{6.32}$$

where

ν = kinematic viscosity

$\left(\frac{\partial u}{\partial z}\right)_i$ = vertical gradient of horizontal velocity component at the interface

In the case of turbulent flow the effect of eddy viscosity ϵ_t and entrainment momentum must also be included, thus:

$$\tau_i = \rho(\nu + \epsilon_t) \left(\frac{\partial u}{\partial z}\right)_i + \overline{w'\rho'}\, U \tag{6.33}$$

where w', ρ' = velocity and density perturbations.

In practice, however, it is very common to express τ_i as

$$\tau_i = \frac{f_i}{8} \rho_{1,2} (U_1 - U_2)|U_1 - U_2| \tag{6.34}$$

where f_i = interfacial coefficient of friction

$\rho_{1,2}$ = ρ_1 or ρ_2

U_1, U_2 = average velocities of the upper or lower layer

In the earlier studies, attempts were made to correlate the friction factor f_i to the Reynolds number of the moving layer when the flow is laminar. For turbulent flows, relationships similar to the "Blasius formula" were used.

Ippen and Harleman (1951) derived the following expression for the average friction coefficient at the interface of laminar density underflow:

$$\bar{f}_i = \frac{35}{R_{e2}} \tag{6.35}$$

where

$$R_{e2} = \frac{U_2 h_2}{\nu_2}$$

U_2 = mean velocity of the underflow

h_2 = lower layer depth

ν_2 = kinematic viscosity of the lower layer

The form of the equation presented by Bata and Knezevich (1953) was similar to that of equation (6.35) with a different constant.

Georgiev Borislav (1972) studied the case of uniform underflow in a two-layered system and determined the Reynolds stresses at the interface by direct measurements with a hot film. His experimental data satisfy the relationship:

$$f_i = \frac{0.275}{R_{e2}^{0.276}} \tag{6.36}$$

The values of R_{e2} (= $U_2 R_{h2}/\nu_2$) ranged from 10^3 to 10^4. R_{h2} is the hydraulic radius of the underflow.

An extensive literature survey was conducted by the Delft Hydraulic Laboratory (1974). The result of different experimental and theoretical studies, for the cases of upper flow and lower flow were plotted and compared. These results are given in Fig. (6.12) and Fig. (6.13).

It can be seen from these figures that equations (6.35) and (6.36) are only valid in a very limited range and that the data are generally scattered.

Harleman and Stolzenbach (1972) reviewed the results of several researchers and gave the following equation:

$$\frac{1}{\sqrt{f_i}} = 2.1\log\,(R_e\sqrt{f_i}) - 0.8 \tag{6.37}$$

The experimental points were scattered for the turbulent zone of their graph.

Keulegan (1949) assumed that interfacial friction is caused by energy dissipation due to the interfacial waves. Extending this idea, Shi-igai (1965) derived a theoretical formula for the interfacial friction coefficient. He computed the velocity field of internal waves for a non-viscous two-layered flow. Shi-igai then introduced the viscosity to obtain the energy dissipation rate from which the interfacial friction coefficient was derived as a function of the Keulegan number:

$$f_i = \frac{8\tau_i}{\rho_1 U_1^2} = 32\ \pi^2\ (\frac{a'}{\lambda'})^2\ \frac{1}{\psi} \qquad (6.38)$$

where a' = amplitude of the internal waves

λ' = length of the internal waves

$\psi = R_{e1}\ F_1'^2$

$R_{e1} = U_1\ h_1/\nu_1$

$F_1' = U_1/\sqrt{g\Delta\rho/\rho\ h_1}$

The subscript denotes the upper moving layer. Calibration of f_i against the field data gave the following relationship

$$f_i = \frac{48}{\psi} \qquad (6.39)$$

Iwasaki et al. (1962) also suggested a power law relation for the friction coefficient and the non-dimensional coefficient ψ, as:

$$f_i = C\ \psi^{-n} \tag{6.40}$$

where

$$\psi = R_{e_1}\ R_i^{-1} = R_{e_1}(F_1')^2$$

Kaneko (1966) proposed the following relationship:

$$f_i = 0.8\ \psi^{-0.5} \tag{6.41}$$

Equation (6.41) gives good agreement with many experimental results, Fig. (6.14).

Dermissis and Partheniades (1984) determined the average interfacial friction coefficient (f_i) for the working section of a closed rectangular duct. Their values were best correlated with the number:

$$R_{e_1}\ F_1^{\,2} = \frac{4\ U_1^{\,3}}{\nu_1 g} \cdot \frac{R_{h_1}}{R_{h_0}} \tag{6.42}$$

where R_{h_0} = hydraulic radius of the entire cross section

R_{h_1} = hydraulic radius of the upper moving layer

The results of Dermissis and Partheniades are given in Fig. (6.15).

Csanady (1978) described the relationship between the interfacial shear stress and the velocity gradient in terms of an effective viscosity defined by:

$$\frac{\tau_i}{\rho} = (\nu + \epsilon_t) \frac{du}{dz}\bigg|_{z=i} = \nu_e \left(\frac{du}{dz}\right)_i \tag{6.43}$$

and if:

$$\tau_i = \rho U_*^2 \tag{6.44}$$

$$\text{then} \quad \nu_e = \frac{U_*^2}{\left(\frac{du}{dz}\right)_i} \tag{6.45}$$

Using Lofquist's data (1960) for the lower layer flow, Csanady showed that:

$$\frac{\nu_e}{\nu} = 7.3\ \psi_*^{1/2} \tag{6.46}$$

where ψ_* is an interfacial Keulegan parameter defined by:

$$\psi_* = \frac{U_*^3}{\nu \frac{\Delta\rho}{\rho} g}$$

where U_* = shear velocity at the interface.

Ura et al. (1984) conducted a series of experiments in a flume of stratified flow, with a moving upper layer. Their results fitted the following formulae:

$$\frac{\nu_e}{\nu} = (1 + 40\psi_*)^{1/2} \tag{6.47}$$

Nakano et al. (1985) performed similar experiments with a moving lower layer and with different bottom roughness. They obtained yet a different formulae:

$$\frac{\nu_e}{\nu} = 1 + 6.5\psi_*^{3/4} \tag{6.48}$$

Equations (6.46), (6.47) and (6.48) are all plotted in Fig. (6.16) and compared with the different experimental data.

Based on field data at large Reynolds numbers, the Delft Hydraulic Laboratory (1974) suggested the following relationships:

$$\begin{aligned} &\text{streaming upper layer} \quad f_i = 3.2 * 10^{-3} \\ &\text{streaming under layer} \quad f_i = 1.2 * 10^{-3} \\ &\text{counter flow} \quad\quad\quad\quad f_i = 5.6 * 10^{-3} \end{aligned} \tag{6.49}$$

6.5 BUOYANT JETS

Before studying the action of jets in stratified service reservoirs, it is appropriate to review the behaviour of surface buoyant jets. The problem is originally connected with the study of the discharge of a less dense water into the ambient. For example, the horizontal surface discharge of warm water from a power plant into a cooling pond, or heated water discharge from a channel into a deep lake or reservoir. Surface buoyant jets can be two or three dimensional.

6.5.1 Two-Dimensional Buoyant Surface Jets

The turbulent entrainment characteristics of two-dimensional surface buoyant jets were first studied experimentally by Ellison and Turner (1959), in which they related the entrainment coefficient to the overall Richardson number. Later studies by Wilkinson and Wood (1971), Koh (1971b), Stefan (1972) and Chu and Vanvari (1976) showed that the entrainment characteristics of the flow were in general influenced by the upstream and down-stream conditions in a very similar manner to that of free surface flow in open channels. Specifically a "density jump" analogous to the open-channel hydraulic jump has also been observed. The regime of flow upstream of the jump is "super critical" or "jet-like" and is characterised by turbulent mixing and entrainment similar to that of a neutral wall jet. Downstream of the jump, the flow is "subcritical" and can be characterised by a sharp interface with negligible entrainment.

Mixing in the region of the density jump is more complicated. Reverse flow has been observed near the interface, where entrainment is characterised by the breaking of internal waves, Fig. (6.17a).

The velocity distribution in the jet-like part can be very well described by the Gaussian distribution, Chu and Vanvari (1976).

$$\frac{u}{U_m} = \exp(-\ 0.693\ (\frac{z}{z_m})^2) \qquad (6.50)$$

where U_m = maximum velocity

z_m = the point where $u = 1/2\ u_m$

See Fig. (6.17b).

The longitudinal variation of jet width z_m is also shown in Fig. (6.17c). The growth of the jet at the initial stages is very similar to that of the neutral wall jet. Far from the jet, however, entrainment ceases and no further growth is observed. The buoyancy B (= g $\Delta\rho/\rho$) varies linearly with depth, Fig. (6.17d).

6.5.2 Three-Dimensional Buoyant Surface Jets

Three-dimensional buoyant surface jets, Fig. (6.18), have been studied by many researchers including Tamai et al. (1969), Jen et al. (1964), Hayashi and Shuto (1967) and Pande and Rajaratram (1977). The latter used the technique of similarity analysis to integrate the equations of motion. They showed that the surface discharges of warm water into cold ambient could be divided into three regimes depending on the value of the Richardson number defined by:

$$R_i = \frac{g \frac{\Delta\rho}{\rho} d_0}{V_0^2}$$

where d_0 = the height of jet

V_0 = jet velocity

The three regions could be referred to as surface discharges with small ($R_i < 0.01$), moderate ($0.01 < R_i < 0.6$)and large ($R_i > 0.6$) Richardson number. Further, it was found that for "small R_i":

$$U_m \propto \frac{1}{x} \; ; \quad T_m \propto \frac{1}{x} \; ; \quad y_m \propto x \; ; \quad z_m \propto x \qquad (6.51a)$$

For "moderate R_i", if $z_m \propto x^\circ$ i.e., far field with no more vertical expansion:

$$U_m \propto \frac{1}{x^{2/3}} \; ; \quad T_m \propto \frac{1}{x^{2/3}} \; ; \quad y_m \propto x^{4/3} \tag{6.51b}$$

For "large R_i" if ($z_m \propto x^\circ$)

$$U_m \propto \frac{1}{x^{1/3}} \; ; \quad T_m \propto \frac{1}{x^{2/3}} \; ; \quad y_m \propto x \tag{6.51c}$$

where U_m is the velocity scale, T_m is the scale for excess temperature, y_m and z_m are the length scales in the lateral (y) and z direction respectively, Fig. (6.18).

6.6 PRESENT EXPERIMENTAL WORK IN A STRATIFIED RESERVOIR

The experimental work was carried out in the same reservoir that was described in Chapter 3. The reservoir was stratified by using a saline solution for simulating the heavier layer and fresh water for the lighter layer.

Experiments were conducted for various jet discharges and degrees of stratification. Densities and peripheral velocities were measured at various sections in the reservoir. Circulating patterns were obtained using floats and dye photographs.

The experimental results, for the top layer, were compared with those for homogeneous reservoirs.

An analysis was developed for predicting the distribution of peripheral velocity in the top layer. This analysis was later used for predicting the time variation of the level of the interface. Good agreement was obtained with experiment.

6.6.1 Experimental Observation and Results (Densities)

An experiment was conducted to examine the effect of "molecular diffusion" on the initial density profile. The stratified reservoir was left for a few days and the variation of density with elevation above the bed was recorded and plotted, Fig. (6.19). It can be seen that although molecular diffusion has smeared the initial stratification curve, the interface is still well defined after three days. Therefore, molecular diffusion is very small and can be neglected in the calculations of the stratification curve especially when a strong turbulent jet is present.

Fig. (6.20) shows a buoyant jet discharging into the stratified reservoir. The interface acts like a barrier and prevents further expansion of the jet compared with its behaviour in a homogeneous reservoir. It also reveals that the hypolimnion can confine the momentum of the jet in the upper layer.

One series of experiments was run to observe the initial disturbances and instability of the interface caused by the turbulent jet. Sodium fluorescein (green) was added to the saline solution to make two layer distinct and the interface visible. Photographs of the progressive waves are shown in Fig. (6.21a,b,c) for different jet discharges. At low velocities the interfacial waves were smooth, though not uniform because of the variation of velocity in tangential direction. Further increase in discharge resulted in sharp-crested waves, but without

mixing Fig. (6.21b). When the velocity of the upper layer exceeded a critical value, the lower layer entrained into the upper one, Fig. (6.21c).

Increasing the jet velocity enhanced the mixing rate with the critical zone being near the point of intersection of the jet with the interface. Downstream of the jet, interfacial waves became smooth, long crested and travelled with no mixing. Because of the high rate of mixing the colour of the fresh layer became greenish gradually. The process of entrainment of the lower layer continued and the depth of the interface below the water surface went down to the position where further mixing ceased all over the reservoir. The greenish colour of the upper layer faded away gradually.

There are several different factors influencing the degree of mixing. These factors are usually combined in the dimensionless Richardson number:

$$R_i = \frac{g \frac{\Delta\rho}{\rho} h}{v^2}$$

where $\Delta\rho$ = density difference

h = a characteristic length

v = depth-averaged tangential velocity.

A series of experiments was carried out in which the above parameters were changed systematically. The proportionate density defect in

these experiments was $\epsilon \cong 1\%$ to 9% and discharges varied from 5.75 cc/sec to 49.5 cc/sec. The data for those experiments are given in Table (6.2).

In the majority of the experiments, samples were taken from several different stations located at various parts of the reservoir, Fig. (6.22). This was done in order to test the assumption that the circulation may tilt the interface at sections far from the jet in a manner similar to that of wind action on a stratified lake or reservoir. However, in all the experiments described herein, it was found that the interface remained approximately horizontal.

The curves for the variation of density with elevation above the bed for eight stations in a single experiment, number (2), are given in Fig. (6.24). It can be seen that the curves are fairly similar. The initial curves of stratification are shown by the dashed lines. At a period of 3.5 min after the start of the experiment, the density structure of the reservoir changed dramatically. The density difference between the upper and lower layer decreased by about 50% because of the high rate of entrainment. At the same time, the level of the interface dropped markedly, showing the penetrative effect of the momentum jet. This effect was more pronounced near the perimeter wall where the velocities were large.

In the subsequent times the entrainment rate decreased with the increment in Richardson number. The density of the upper layer gradually approached its initial value because of its mixing with the jet's fresh water. The interface was re-established at a lower position, but it continued to go down gradually. After about 3 hours,

the depth of the lower layer was about 7cm, which was approximately one-third of the initial depth.

Fig. (6.23) and Figs. (6.25-6.32) show the variation of density with time for different elevations but at one station. Experiment number (2,4,8,9,10) with discharges of 30.83, 19.66, 12.38, 9.71 and 5.75 cc/sec were performed in order to examine the effect of the jet discharge on the stratification structure of the reservoir. In these experiments the parameters h_1 and ϵ were kept almost constant. It can be seen from the corresponding figures that large jet momentum caused a rapid decrease in the depth of hypolimnion (experiment number (2) and (4) Figs. (6.24) and (6.26)). On the other hand, small jet momentum (experiment number 10, Fig. (6.32)) did not change the density structure even after about 2 hours.

Experiments 3, 4, 5, 6 and 7, (Table 6.2) were conducted to study the effect of ϵ for a constant jet discharge. The dominant effect of the density of the lower layer on the stratification can be clearly deduced. For example:

(1) Experiment (3) - Fig. (6.25), $\epsilon \cong 1.28\%$. Half of the hypolimnion was removed after only 50 minutes.

(2) Experiment (7) - Fig. (29), $\epsilon \cong 9.11\%$. Quarter of the hypolimnion volume was removed after about 2 hours.

The density-time curves mentioned above will later be used for verifying the theoretical analysis.

Fig. (6.33) shows the variation of density with time for a section 45° from the jet (distance from the wall = 3cm, ϵ = 2.1%, Q_0 = 19.66 cc/sec - experiment 4).

It can be seen that the density of the epilimnion reached a maximum (because of entrainment) at t = 3-15 minutes and then fell down to its initial value at bigger values of t. Figure (6.33) shows that jet action was deepening the upper layer and causing the density of the lower layers to approach that of the upper layer monotonically. The lower parts of the hypolimnion (Depth = 10.7 cm), however, remained unchanged.

Fig. (6.34) shows the variation of density with θ (angle from the jet position) for various depths and times. These results are for experiment 8 (Q_0 = 12.383 cc/sec, ϵ = 2.2%). These figures show that at the early stages of the experiment marked changes in density occurred at some stations. At later times the variation in density, at different positions became much smaller because of the decrease in the entrainment process and the drop in the level of the interface.

Fig. (6.35) shows the variation of density with distance from the wall for θ = 45°. These results are given for different depths and times (Experiment (9), Table (6.2)). It can be deduced that away from the wall the interface is relatively flat and horizontal at different times.

Fig. (6.36) shows the variation of the outlet density with time for experiment (7), Table (6.2). The values of density at the surface of the reservoir near the jet (θ = 45°) and 3cm from the wall are also given. The density of the outflow was generally higher than that of

the surface layer. This was mainly due to the effect of local vortex flow which was active near the outlet. The strength and action of the vortex varied with time and did not follow a specific curve.

Fig. (6.36) also gives the outlet results for an experiment conducted on a different occasion (for the same Q_0 and ϵ). Clearly the two outlet curves do not show any simple or well defined variation of density with time. This is undoubtedly caused by the erratic behaviour of the vortex.

6.6.2 Experimental Results (Velocities)

Several experiments were conducted to measure tangential velocities in the r, θ and z directions, and a summary of the experiments is given in Table (6.3).

A series of experiments was run to obtain the variation of tangential velocity with z using the hydrogen bubble technique. The primary aim of these experiments was to test the depth averaging assumption which usually simplifies any analytical solution considerably. Figs. (6.38a,b), show hydrogen bubble tracks for a station far from the jet (θ = 315°, distance from the wall = 2mm) for the same discharge (Q_0 = 8.83 cc/sec) and ϵ = 4.3% and 9% respectively. These tracks suggest that the velocities are reasonably uniform over the depth of the fresh layer except in the vicinity of interface.

Fig. (6.39) shows hydrogen bubble tracks for a station near to the jet (θ = 45°, Q_0 = 7.15 cc/sec, ϵ = 8.9%). Because of agitation and mixing by the turbulent jet, the columns of bubbles are not parallel or uniform. The eddies, however, were not strong enough to break up the bubble lines.

Fig. (6.40) shows bubble tracks for Q_0 = 19.66 cc/sec and θ = 315° (experiment 14 Table 6.3). Although the flow looks turbulent, nevertheless the tracks are reasonably parallel.

The second aim of the hydrogen bubble experiments was to verify the similarity assumption for the velocity profile near to the interface from Monin-Obukhov theory. This theory assumes a log + linear relationship for the velocity distribution on the diabatic atmospheric surface layer and has been well established in the field of atmospheric turbulence.

Hino and Nguyen (1983) applied the theory to the case of salt wedge flow. They were able to represent the velocity profiles either by the log + linear or by the bi-log laws.

The results of the present study gives a bi-log velocity profile at the narrow interfacial boundary layer for some of the experiments, Fig. (6.37). It was not possible, however, to prove a similarity profile for the velocity distribution and deduce the same conclusions of Hino and Nguyen. The method was rather sensitive to the accurate location of the interface as the origin in the vertical direction.

An experiment was conducted to study the variation of tangential velocity, near the perimeter wall, with elevation above the bed for the "quasi steady state" condition, (t ≅ 90 minutes). The jet discharge was 19.66 cc/sec and ϵ = 2.1%. During this period, the depth of the fresh layer changed from its original value of 2.5cm to 9cm. The final depth of the saline layer was 13.5cm. The resulting velocity-distributions are given in Fig. (6.41).

This figure also shows results obtained using a homogeneous reservoir for the same jet discharge. The total water depth was 22.5cm. For every section, the velocities in the top layer of the stratified reservoir are higher than those for the homogeneous reservoir at the same elevation.

Fig. (6.41) also shows that, near the jet, velocities decrease markedly with the distance below the free surface for both experiments ($x = R\theta$ = 10, 20 and 30cm, θ = 12.5°, 25° and 37.5°). Far from the jet (x = 90cm), velocities are almost constant over the depth.

Fig. (6.42) shows variation of tangential velocity, near the wall, with elevation above the bed at one station (x = 30cm, distance from the wall = 0.6cm) in the stratified reservoir (Q_0 = 19.66 cc/sec, ϵ = 2.1%). These results are given for 40 and 90 minutes respectively. The corresponding depth of the fresh layer was 7 and 9cm. Fig. (6.42) shows that, as expected, velocities are generally higher in the case of the shallower upper layer.

Fig. (6.43) shows variation of maximum tangential velocities at the surface with θ for a stratified reservoir (Q_0 = 19.66 cc/sec, ϵ = 2.1%, distance from the wall = 0.6cm). These results are for t = 90 minutes and a corresponding depth of fresh layer of 9cm. This figure also shows the results for a homogeneous reservoir (Q_0 = 19.66 cc/sec, distance from the wall = 0.6cm) at the surface.

Fig. (6.43) shows that near the jet, the velocities are almost identical for the same θ in both experiments. For $\theta > 0.5$ radians,

velocities in the stratified reservoir are higher than those in the homogeneous reservoir.

Fig. (6.44) shows the dimensionless velocities of Fig. (6.43) plotted against $1/\sqrt{x}$ ($x = R\theta$). The variation is almost linear and is consistent with the results of Chapter 3, equation (3.112).

The results of the time lapse photography experiments are shown in Fig. (6.45) for experiments (17) and (18), Fig. (6.46) for experiments (14) and (15) and Fig. (6.47) for experiment (19), (Table 6.3). Also given in these figures are the experimental results obtained from a homogeneous reservoir using the same depth and jet discharge.

The tracks of floats were considerably different in two layer flow. In homogeneous reservoir circulation velocities in the middle zone were small and almost negligible compared to the wall velocities. On the other hand, in the stratified reservoir the tracks were longer in the central region indicating a faster circulatory motion. In other words, in the two layered flow, the momentum of the jet was transferred to the inner area with less dissipation at the outer layers. Consequently, the internal stagnant area was removed due to a stronger circulation.

Around the outlet the motion of floats was irregular and the tracks were crossing. This can be attributed to the local vortex generated by the outlet.

Photographs of dye expansion give visual and qualitative information of circulation. Fig. (6.48) shows spread of the dye in stratified and homogeneous reservoirs at different times (experiment 19, Table 6.3).

In both experiments the density, jet discharge and the depth of moving fluid (top layer) were the same. Mixing was negligible in the stratified reservoir. The circulation patterns, however, were noticeably different.

In the case of little or negligible mixing, the interface acted as a smooth bed for the motion of the upper layer. In the homogeneous reservoir, the roughness of the bed is effective in dissipating the vorticity by the momentum jet.

In summary, the various experimental results demonstrate the dominant effect of bed friction on the overall circulation.

The tangential velocities calculated from Fig. (6.47) for a stratified reservoir, are plotted in Fig. (6.49). Also shown are velocities obtained in a homogeneous reservoir for the same water-depth and jet discharge.

Fig. (6.49) shows that velocities in the stratified reservoir are always higher than those in the homogeneous reservoir. Far from the wall in the middle zone, however, the velocity profile drops drastically for the case of the homogeneous reservoir. This again confirms the previous discussion about the mechanism of the transfer of momentum and its dissipation due to friction.

One experiment was run to measure the velocity in both the surface and near to the interface. The depth of the fresh layer was 10.5cm, the proportionate density defect was $\epsilon \cong 8.9\%$ and the discharge was $Q_0 = 19.66$ cc/sec. At the time of the experiment no mixing happened and the fresh layer circulated over the saline solution.

The results are shown in Fig. (6.50). The red (grey) tracks were produced by the interfacial floats and the yellow (white) tracks were the result of the surface floats. Fig. (6.50) shows that the circulation patterns for the surface and the interface were circular.

Fig. (6.51) shows velocity-distributions calculated from Fig. (6.50). As expected the calculated surface velocities were much bigger than the interfacial ones. Using these velocities, the approximate relationship between the average upper layer and interface velocities is:

$$\frac{v_i}{v} = 0.6 \tag{6.52}$$

where v_i = interfacial velocity, v = upper layer velocity.

Table (6.4) gives the values of the above ratio obtained by various investigators, Nakano et al. (1985). It can be seen from this table that this ratio varies from 0.4 to 0.6 for a moving upper layer flow and from 0.5 to 0.8 for a moving lower layer.

As was mentioned before, in the majority of the experiments in this chapter the characteristics of the moving layer were varying with time (densities, velocities and depth). The variation of density and initial depth with time was investigated and the results were reported previously. The variation of velocity with time at a point with $\theta = 45°$ from the jet was conducted in experiment (18), Table (6.3).

Fig. (6.52) shows the results for a total time of 2 hours and 20 minutes. The velocity was zero at the start of the experiment and reached its maximum value a few minutes later. In the subsequent times the velocity decreased gradually because of the increase in the depth of the upper layer. After the steady state (about 80 min) the rate of fall of velocity was about 1 cm/sec/hr for the last hour. A corresponding theoretical velocity (see next section) has also been plotted on the same figure for comparison with the experiment.

6.7 THEORETICAL CONSIDERATIONS

6.7.1 Presentation of the Method

The results of the hydrogen bubble experiments showed that, far from the jet, the velocity of the upper layer was reasonably uniform over the depth of the layer. Therefore, two-dimensional depth-averaged models can be extended to the case of the stratified reservoir.

Amongst the various models which have been examined by the writer, the most appropriate one, for the present study seems to be the Integral Momentum Method suggested by Sobey (1972). That model, however, is not directly applicable to the present problem. It requires some new assumptions and modifications to be made.

Fig. (6.53) shows the mechanism of mixing, in the stratified reservoir, near the inlet. It is assumed that the majority of mixing takes place in the vicinity of the inlet. The depth of the epilimnion is h_1 and the jet is assumed to lie just over the hypolimnion at the interfacial plane. At the start of the experiment (time t), the turbulent jet discharges into the reservoir and entrains the lower stagnant layer to the upper moving layer.

The most crucial region for mixing is around point A. In subsequent times the depth of the upper-layer increases and the interface goes down. Consequently, point A moves away from the jet's position with a corresponding reduction in velocities near this point. Consequently, the overall Richardson number increases and mixing decreases.

The position of point A can be approximately determined from the intersecting the line defining the locus of the vertical length scale, z_m, with the interfacial line, (z_m is the depth where $v = v_m/2$, v_m = maximum surface velocity).

Chapter (3) gives the rate of growth for a surface jet discharging inside a curved wall containing a co-flowing stream. When the ratio of the velocity of the jet to that of the co-flowing stream is high then we have:

$$\tan(\lambda) = \frac{dz_m}{dx} = 0.2325 \qquad (3.113)$$

or:

$$\lambda \cong 13°$$

In general, $\tan(\lambda)$ is a function of the radius of the reservoir. However, the author could not find any relationship similar to equation (3.113), in the literature, applicable to three-dimensional concave curved wall jet taking into account the effect of curvature.

Assuming that the exchange of mass and momentum between the upper and lower layers is negligible then the interface will act as a smooth

bottom for the upper circulating flow. Therefore, Sobey's mathematical model can be used to predict the velocities of the epilimnion (depth = h_1) with the following modifications:

(a) That coefficient of shear stress at the interface, is given by the expression suggested by Iwasaki and calibrated by Kaneko, equation (6.41):

$$\tau_i = \rho \frac{f_i}{8} v^2$$

$$f_i = 0.8 \, \psi^{-0.5} \qquad (6.41)$$

$$\psi = R_e \, R_i^{-1}$$

The various parameters were defined previously. This equation replaces the Colebroke-White formula which was used by Sobey for calculating the friction factor for the bed of the reservoir.

(b) That the azimuthal velocity profile is shown in Fig. (6.54a) and is based on the extensive velocity measurements conducted by the writer. Based on this velocity profile we can write:

$$v = \begin{cases} \frac{ar}{R_0} & 0 < r < R_0 \\ a & R_0 < r < R_0 - \delta \\ a + V & R - \delta < r < R_0 \end{cases} \qquad (6.53)$$

where R_0 = 1/2 R and R is the radius of reservoir.

This velocity profile contains the three unknowns $a(\theta)$, $V(\theta)$ and $\delta(\theta)$ which need to be determined at each angle.

Substitution of this new velocity profile into the integral angular momentum equation (3.86), the continuity equation (3.87) and the growth rate equation (3.92) gives new coefficients A_{ij} and B_j for the matrix equation (3.101). These coefficients are given in Appendix (B).

The azimuthal velocities were, next, calculated for depth h_1 using the modified Sobey's solution. The next step is the calculation of the entrainment and for that purpose, the equation of Moore and Long (1971) was used which is given by:

$$E = \frac{W_e}{v} = c' \, R_i^{-1} \qquad (6.28)$$

$$R_i = \frac{\epsilon g \, h_1}{v^2}$$

The value of the constant c' is half that given by Moore and Long, because h_1 in the present case represents the depth of the moving layer.

The azimuthal velocity varies all over the reservoir and as a consequence, the entrainment velocity, W_e, will be different at every point. Therefore, for calculating the entrainment discharge, Q_e, the reservoir was discretised to n portions, Fig. (6.54b). The total Q_e was obtained by summing up over the whole area, i.e.

$$Q_e = \sum_{p=1}^{n} Q_{ep} = \sum_{p=1}^{n} W_{ep} A_p \qquad (6.54)$$

where A_p = the area of subdivision;

$$W_{ep} = c' v_p R_{ip}^{-1}$$

The next step in the calculations is to increase the depth of the circulating layer by an amount of Δh. New velocities are obtained and new entrainment discharge, Q_e', is calculated. At the end of this stage an average entrainment discharge $\bar{Q}_e$ is obtained from:

$$\bar{Q}_e = \frac{Q_e + Q_e'}{2} \qquad (6.55)$$

This value of $\bar{Q}_e$ accounts for the main entrainment discharge required to remove the increased volume, Δvol, where:

$$\Delta vol = A.\Delta h \qquad (6.56)$$

A = total area of reservoir.

The time step Δt requires to entrain this volume was computed from:

$$\Delta t = \frac{\Delta vol}{\bar{Q}_e} \qquad (6.57)$$

Calculations proceed by increasing the depth of the upper layer and computing the entrainment time. The total time requires to reach a certain depth is assumed to be the summation of each time step Δt_i, i.e.

$$t_n = \sum_{i=1}^{n} \Delta t_i \qquad (6.58)$$

6.7.2 Comparison Between the Theoretical and Experimental Results

Wall velocities obtained from experiment (17), Table (6.3) were plotted in Fig. (6.55) together with the theoretical ones. This figure shows excellent agreement between experiment and theory.

The same theoretical velocities are plotted and compared with the theoretical velocities for a homogeneous reservoir of the same depth (of fresh layer) and discharge, Fig. (6.56). It can be seen that for homogeneous reservoir, frictional effects caused by the solid bed reduce the velocities considerably.

Azimuthal velocities of experiments (17) and (18) were obtained from the time lapse photographs and are plotted in Fig. (6.57) for the quasi-steady state situation. The velocity profiles obtained from the computer program are also plotted on the same figure. Comparison between the theory and experiment shows reasonable agreement in the shear layer around the perimeter wall. At the inner zone, the predictions are within a maximum of +25% accuracy. Bearing in mind that the mechanism of circulation and entrainment in stratified flow are much more complex than in the case of homogeneous flow, then these predictions are acceptable.

6.7.3 Variation of the Level of Interface with Time

The method of Section (6.7.1) can be directly applied to determine the variation of the level of the interface with time. The computer program was run for the experiments detailed in Table (6.2). In these experiments, the variation of density with time was obtained for various levels.

The program was started from the initial depth (h_1) and proceeded by a depth step (Δh). The time (Δt) required to entrain a volume of saline of (Δvol) was calculated and stored.

The Richardson number at point A, Fig. (6.53), was calculated at each time step. The process of computation may be interrupted after a certain time, depth or Richardson number.

In order to compare theory with the experiment, Figs. (6.23-6.32) corresponding to Table (6.2), were used for calculating the variation of interface level with time.

Determining the position of the interface accurately, proved to be difficult, not least because of the different definitions used by various researchers. For example, Suga and Takahashi (1976) defined it as the plane at which the fluid density is equal to 90% of the lower density. Most other researchers, use either visual interface (see Stefan (1972)) or density interface (see Ura et al (1984)).

The interface, in this study, was assumed to be the plane whose density was the average of that of the upper and lower layers. Because of entrainment, the density of the upper layer was changing with time. Therefore, the density of interface was also changing with time.

Figs. (6.58-6.66) show variation of the theoretical and experimental levels of the interface, measured from the water-surface, with time for the various runs. these results show reasonable agreement, in most cases, between theory and experiment.

In some of these figures the theoretical curve underestimated the level of the interface. This could be due to approximations made in the analysis such as the estimation of the value of the constant (c') in the entrainment coefficient formula. Another undesirable influence was that of the outlet which was drawing out saline solution by the action of weak vortices formed around the outlet.

The profile suggested for the azimuthal velocity distribution was composed of two different parts. The first part was due to the effect of the jet and the second contribution was that of the reservoir's circulation. Each part may entrain the lower layer. Fig. (6.67) corresponding to experiment number (6) of Table (6.2) shows variation of the entrainment discharge with time for each contribution separately.

It can be seen that at the early stages of the experiment (less than 5 mins), mixing by jet action is very high. Later on, the amount of jet entrainment discharge reduces quickly and approaches the value of the reservoir's entrainment discharge.

6.7.4 Dimensional Considerations

Based on the definition of the entrainment discharge, we had:

$$Q_e = \sum_{p=1}^{n} W_{ep} \, \Delta A_p \tag{6.54}$$

By substituting for the entrainment velocity, equation (6.28), we can write:

$$Q_e = \sum_{p=1}^{n} \frac{c' \, v_p^{\,3}}{\epsilon g h_1} \Delta A_p \tag{6.59}$$

where v_p is the velocity over the p^{th} part of the discretised reservoir. If it can be assumed that this velocity is related to the jet velocity explicitly, then we will have:

$$\frac{v_p}{V_0} \cong f(r, \theta, z, \epsilon, t, \ldots) \tag{6.60}$$

where f is a function that depends on the position, time and degree of stratification.

Substituting the above equation into equation (6.59) we get:

$$Q_e = \frac{c' \, V_0^{\,3}}{\epsilon g \nu} \sum_{p=1}^{n} \frac{f^3 \nu \, \Delta A_p}{h_1} \tag{6.61}$$

Now if we define:

$$\psi_0 = \frac{V_0^{\,3}}{\epsilon g \nu} \tag{6.62}$$

we can conclude that there might be a relationship between ψ_0 and entrainment discharge.

The computer program was run for the set of data given in Table (6.5). In the choice of the data, an attempt was made to include various jet discharges and proportionate density defects. The order of data in Table (6.5) is based on the average entrainment discharge at the start of the numerical experiment (i.e. t = 0).

The results of the variation of depth of the upper layer against time, for different runs, are plotted in Fig. (6.69). It can be seen that after some time most of the curves are linear and parallel. The variation of the depth of the upper layer, h_1, with t is very closely given by:

$$h_1^3 \propto t \tag{6.63}$$

A similar conclusion has already been obtained by Moore and Long (1971).

Fig. (6.68) shows variation of the initial Q_e with ψ_0 in a logarithmic scale. The results of this figure are well represented by:

$$Q_e = 0.0177\ \psi_0^{1.287} \tag{6.64}$$

Equation (6.64) shows that the power of ψ_0 is changed from 1, as predicted by equation (6.61) to 1.287. This slight change might be due to the approximations inherent in equation (6.60).

Assuming the jet velocity and proportionate density defect, it is possible to calculate the average initial Q_e and thereby plot the appropriate curve for the variation of depth with time using Fig. (6.69).

CHAPTER 7

CONCLUSIONS

Jet forced circulation in homogeneous and stratified reservoirs was studied in this research. In the following some conclusive remarks concerning various aspects of the research are presented.

7.1 HOMOGENEOUS RESERVOIR CIRCULATION (CHAPTER 3)

1. Comparison between the theoretical and experimental velocities shows reasonable agreement in the circulation patterns but not in the absolute magnitude.

2. The distributions of tangential velocities in the outer layers is similar and can be presented by a standard formula (for example a Gaussian curve).

3. The effect of aspect ratio (L/h) and relative roughness (ks/h) on reservoir circulation and flow patterns is very important.

4. Effect of the variation in jet Froude number, for a given reservoir, on the decay of v_m/V_0 (maximum velocity/jet velocity) is negligible. Aspect ratio, however profoundly effects v_m/V_0.

5. The assumption of depth averaging is reasonable far from the inlet or outlet. Near the inlet, however, the flow is strongly three dimensional.

6. Decay of the maximum velocity is proportional to the inverse root of the distance from the inlet.

7. Effect of co-flowing stream, on the growth of the jet, is negligible provided that the ratio of the jet velocity to the stream velocity is very high.

8. The growth rate of the tangential surface jet in the transverse direction is smaller than that of an ordinary wall jet. In the vertical direction, however, the growth rate is several times bigger than that for a surface jet. This may be attributed to the curvature of wall in the lateral direction.

7.2 RESERVOIR CIRCULATION CAUSED BY A WIDE RADIAL JET (CHAPTER 4)

The depth averaged hydrodynamic equations of motion were written in finite difference form and solved in the manner of an ADI scheme. The computer program was run for several different models to show the effects of shear stresses, boundary conditions, bottom roughness and geometric configurations.

1. The general theoretical circulation patterns are fairly good but the magnitude of velocities, at the boundaries, are underestimated.

2. The shear stress terms are necessary and important. However, they must be represented as accurately as possible as they are capable of changing the position of the centre of the gyre and decrease or increase the velocities.

3. Omission of the convective terms suppresses the circulation. Therefore, in cases where the circulatory flow is important they

should be included and presented in a realistic finite difference form.

4. The jagged boundary assumption reduces the velocities therein. A better resolution or even a different mesh configuration, see Johnson (1980), may remove the problem.

5. The effect of friction, in the model, was not very marked. This conclusion contradicts the findings of the integral method and the experimental results of Chapter Three.

7.3 SLOW MOTION WITHIN A LARGE SCALE GYRE IN A TWO-LAYERED STRATIFIED RESERVOIR (CHAPTER 5)

1. The nature of the flow is three dimensional in both layers. At the interface, the azimuthal velocities and tangential shear stresses are continuous.

2. Bodewadt flow can simulate the rotation of the upper layer and von Karman flow can simulate that of the lower flow. physically the stable case is when

$$R = \sqrt{\frac{\mu_2 \rho_2}{\mu_1 \rho_1}} > 1$$

3. Above the interface there is a gentle inward flow and below it the flow is outward. Far from the interface the vertical velocities in both layers approach their asymptotic upward values. Consequently, the rotation of the upper layer may produce a suction pressure over the lower layer.

4. Because of this suction the shape of the interface may be simulated by a paraboloid of revolution. However, if the maximum height of the dome is small enough compared to the depth of the boundary layer, the interface can be assumed to be flat.

7.4 JET FORCED CIRCULATION IN A STRATIFIED RESERVOIR (CHAPTER 6)

1. The effect of molecular diffusion in the experiments with saline solution was, as expected, small and negligible.

2. Because of the density difference the majority of the momentum of the jet was confined to the upper layer. Therefore, this layer rotated almost independently over the lower layer.

3. Sobey's theory was successfully modified and applied to the motion of the upper layer. Good agreement was obtained between the theoretical and experimental tangential velocities for the top layer of the stratified reservoir.

4. Shear stresses at a solid boundary of a homogeneous reservoir are considerably greater than those at the interface of a stratified reservoir. Therefore the velocities and flow patterns for homogeneous and stratified reservoirs are quite different. This demonstrates the dominant effect of relative roughness on the circulation.

5. Measurement of velocities at the interface showed that they were much smaller than the velocities at the upper layer. This was due to the negligible transfer of momentum from the epilimnion to the hypolimnion.

6. Form and shape of the interface is greatly influenced by the jet's discharge and by the relative density of the reservoir. These parameters can be combined in the non-dimensional Richardson number.

7. The lower layer entrains and mixes with the upper layer provided that the Richardson number is small. The analysis for the variation of the depth of the interface with time was in reasonable agreement with the experimental results. Majority of the mixing happened near the jet.

8. The entrainment discharge was found to be nearly proportional to the dimensionless Keulegan-Iwasaki jet number. It was also shown that the depth of the epilimnion was approximately proportional to the $^1/_3$ power of time.

APPENDICES

APPENDIX A

METHOD OF SOLUTION OF THE BOUNDARY LAYER DIFFERENTIAL EQUATIONS

In Section (5.4.2.2), the system of non-linear partial differential equations, for the boundary layer of a rotating fluid of density, ρ_1, over a stationary fluid with a density of ρ_2 was reduced to a system of non-linear ordinary differential equations by the assumption of similarity, equations (5.35). The non-linear system of six ordinary differential equations was then changed to a linear system of 10 equations by the use of four new assumed functions J_1, K_1, J_2 and K_2, equations (5.39).

Introduction of these four new functions resulted in four unknown initial boundaries (a, b, c and d in equations (5.40)), to be determined in the process of integration in a manner to satisfy the asymptotic boundary conditions at infinity. Nachtsheim and Swigert (1965) gave an algorithm for the solution of this type of equations.

All numerical integrations are performed using the Adams-Moulton integration scheme with initial passes using the Runge-Kutta scheme. Initial estimates are assumed for the unknown initial conditions a, b, c and d and the equations are integrated out to a specified ζ where the corrections Δa, Δb, Δc and Δd are determined from a least squares solution of the following matrix equation. These corrections are made to the estimated values of a, b, c and d.

$$\begin{bmatrix} F_{1a} & F_{1b} & F_{1c} & F_{1d} \\ G_{1a} & G_{1b} & G_{1c} & G_{1d} \\ F_{2a} & F_{2b} & F_{2c} & F_{2d} \\ G_{2a} & G_{2b} & G_{2c} & G_{2d} \\ J_{1a} & J_{1b} & J_{1c} & J_{1d} \\ K_{1a} & K_{1b} & K_{1c} & K_{1d} \\ J_{2a} & J_{2b} & J_{2c} & J_{2d} \\ K_{2a} & K_{2b} & K_{2c} & K_{2d} \end{bmatrix} \begin{bmatrix} \Delta a \\ \Delta b \\ \Delta c \\ \Delta d \end{bmatrix} = \begin{bmatrix} - F_1 \\ - (G_1 - 1) \\ - F_2 \\ - G_2 \\ - J_1 \\ - K_1 \\ - J_2 \\ - K_2 \end{bmatrix} \qquad \text{(A-1)}$$

The subscripted a, b c and d denote partial differentiation with respect to the named variable. The values of the partial derivatives F_{1a}, G_{1a}, F_{2a}, G_{2a}, J_{1a}, K_{1a} and K_{2a} are determined from integration of the perturbation equations:

$$\begin{aligned}
F_{1a}' &= J_{1a} \\
J_{1a}' &= 2F_1 F_{1a} - 2G_1 G_{1a} + H_{1a} J_1 + H_1 J_{1a} \\
F_{2a}' &= J_{2a} \\
J_{2a}' &= 2F_2 F_{2a} - 2G_2 G_{2a} - H_{2a} J_2 - H_2 J_{2a} \\
G_{1a}' &= K_{1a} \\
K_{1a}' &= 2F_{1a} G_1 + 2F_1 G_{1a} + H_{1a} K_1 + H_1 K_{1a} \\
G_{2a}' &= K_{2a} \\
K_{2a}' &= 2F_{2a} G_2 + 2F_2 G_{2a} - H_{2a} K_2 - H_2 K_{2a} \\
H_{1a}' &= -2F_{1a} \\
H_{2a}' &= 2F_{2a}
\end{aligned} \qquad \text{(A-2)}$$

with the initial condition

$$\zeta = 0 : \quad F_{1a} = F_{2a} = 0 \qquad G_{1a} = G_{2a} = 0$$
$$H_{1a} = H_{2a} = 0 \qquad K_{1a} = K_{2a} = 0$$
$$J_{1a} = 1 \qquad J_{2a} = 0 \qquad \text{(A-3)}$$

Similar perturbation equations can be obtained by differentiation of the primary system of equations (5.39) and its corresponding initial conditions, equations (5.40) with respect to b, c and d.

The resulting four systems of perturbation equations are linear and can be solved simultaneously with the primary system, equations (5.39), giving a system of fifty simultaneous first order ordinary differential equations.

The process of integration to a specified ζ_{end} and the computing of new estimates for a, b, c and d is repeated until the least squares residue:

$$E = F_1^2 + (G_1 - 1)^2 + F_2^2 + G_2^2 + J_1^2 + J_2^2 + K_1^2 + K_2^2 \qquad \text{(A-4)}$$

at ζ_{end} is within a specified limit E_{test}.

New values of E_{test} and ζ_{end} are then chosen to progress the integration further towards infinity. The whole process being repeated until the asymptotic boundary conditions at infinity have been satisfied.

A computer program based on the above algorithm was written and successfully run. The results are shown in Fig. (5.9a-i). The accuracy of the method was highly dependent on the chosen values of

ζ_{end}, because very small errors introduced in the initial conditions a, b, c and d were capable of inducing instabilities in the solution at large ζ.

APPENDIX B

COEFFICIENTS OF THE EQUATIONS OF THE INTEGRAL MOMENTUM METHOD

The coefficients A_{ij} and constants B_i of the momentum equation and continuity equation and the growth rate equation based on the new velocity profile are:

$$A_{11} = a[R^2 - \frac{1}{4} R_0^2 + R^2 \ell n(R/R_0)] + V[\frac{1}{2} (R^2 - (R - \delta)^2)$$

$$+ R^2 \ell n(R/(R - \delta))]$$

$$A_{12} = (V + a)[\frac{1}{2} (R^2 - (R - \delta)^2) + R^2 \ell n(R/(R - \delta))]$$

$$A_{13} = \frac{V^2 + 2aV}{2} [(R - \delta) + \frac{R^2}{R - \delta}]$$

$$A_{21} = 0.0$$

$$A_{22} = 0.0$$

$$A_{23} = 1.0$$

$$A_{31} = R - \frac{1}{2} R_0$$

$$A_{32} = \delta$$

$$A_{33} = V$$

$$B_1 = -\frac{f_i}{8h_1}\left[a^2\left(\frac{R^3}{3} - \frac{2}{15}R_0^3\right) + \frac{V^2 + 2aV}{3}\left(R^3 - (R - \delta)^3\right)\right]$$

$$- f_w \frac{R^2}{8}(V + a)^2$$

$$B_2 = 0.065\,(1 + 0.32\,\theta)^{-2}\,\frac{VR}{V + a}$$

$$B_3 = -\frac{Q_0}{2\pi h_1}$$

where $R_0 = \frac{1}{2}R$

f_i = interfacial coefficient of friction

f_w = coefficient of wall friction

h_1 = depth of upper layer.

The kinematic angular momentum flux per unit depth and the volume of the circulating flow at angular position θ are:

$$\frac{I(\theta)}{h_1} = \frac{a^2}{2}\left[R^2 - \frac{R_0^2}{4} + R^2 \ell n\left(\frac{R}{R_0}\right)\right]$$

$$+ \frac{V^2 + 2aV}{2}\left[\frac{1}{2}\left(R^2 - (R - \delta)^2\right) + R^2 \ell n\left(\frac{R}{R - \delta}\right)\right]$$

$$Q(\theta) = h_1\left[a\left(R - \frac{1}{2}R_0\right) + V\delta\right]$$

FIGURES AND TABLES

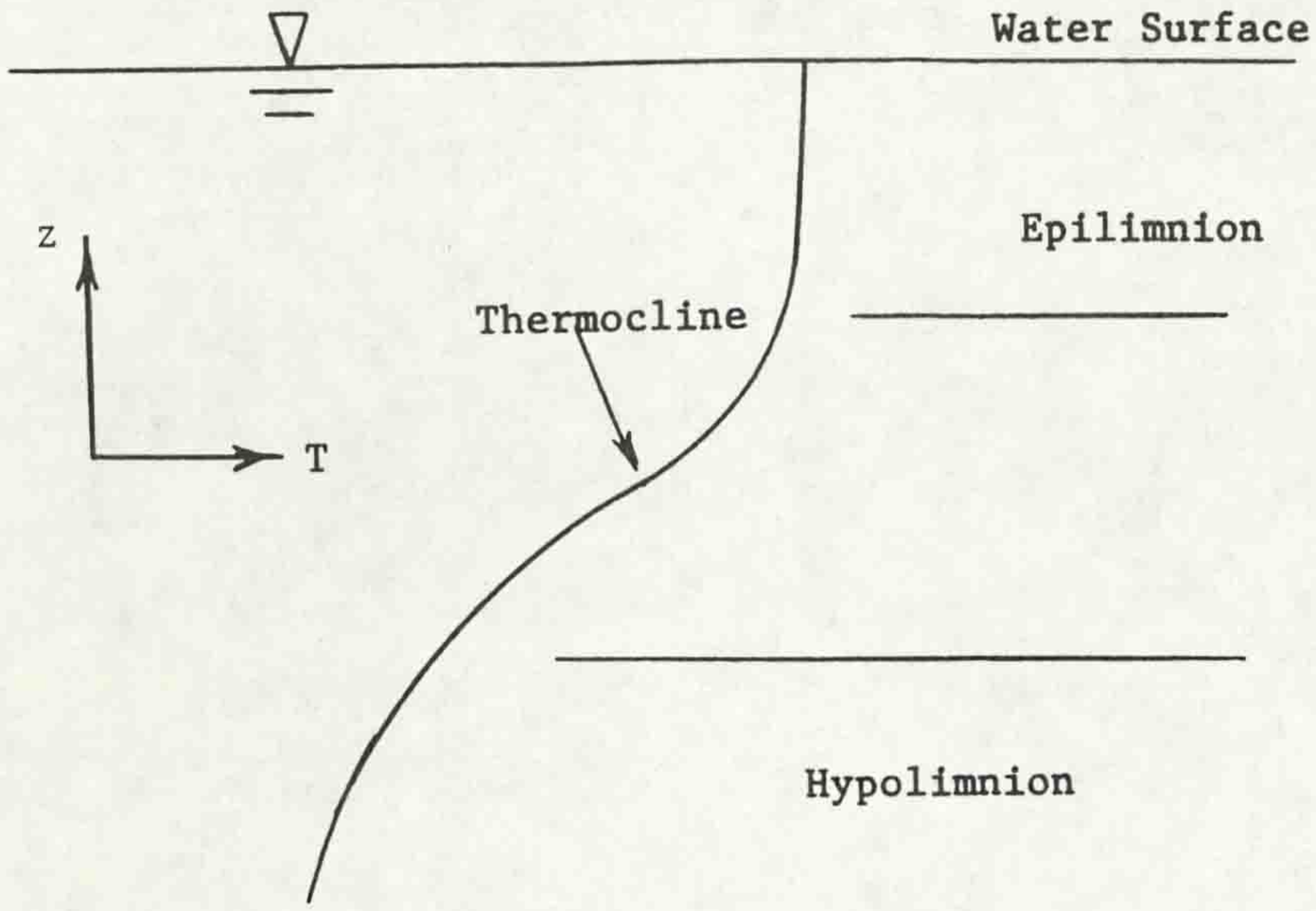

Fig. (1.1) Definition of regions of a reservoir.

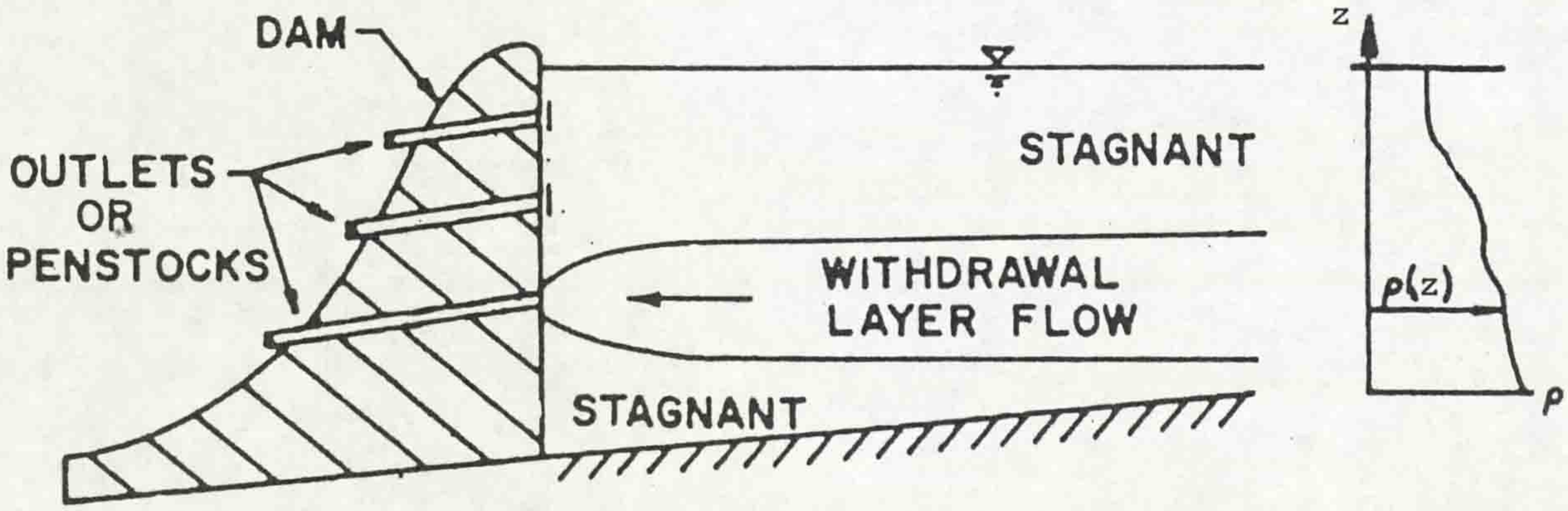

Fig. (1.2) Selective withdrawal from reservoir through one of several outlets at various levels in a dam.

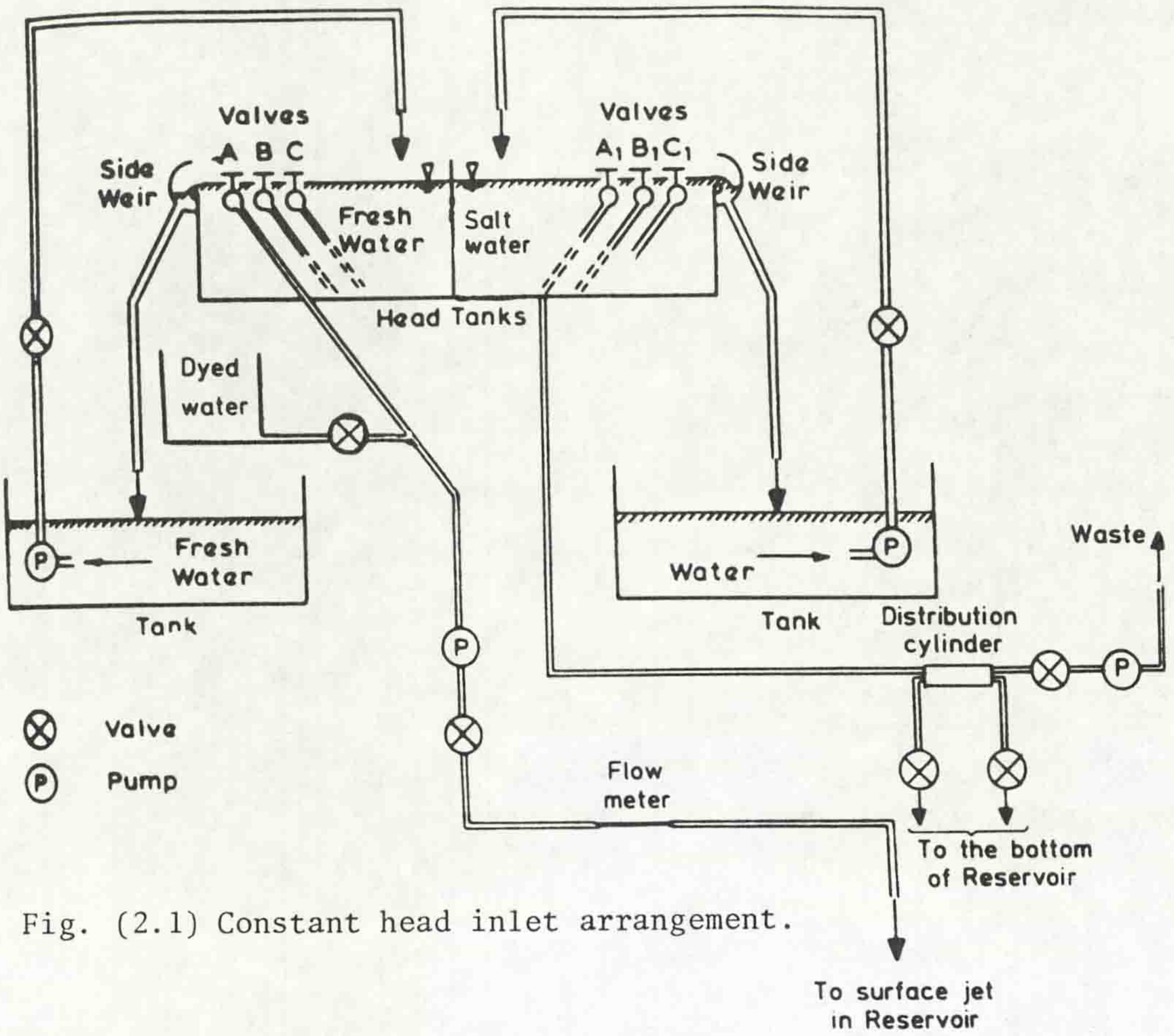

Fig. (2.1) Constant head inlet arrangement.

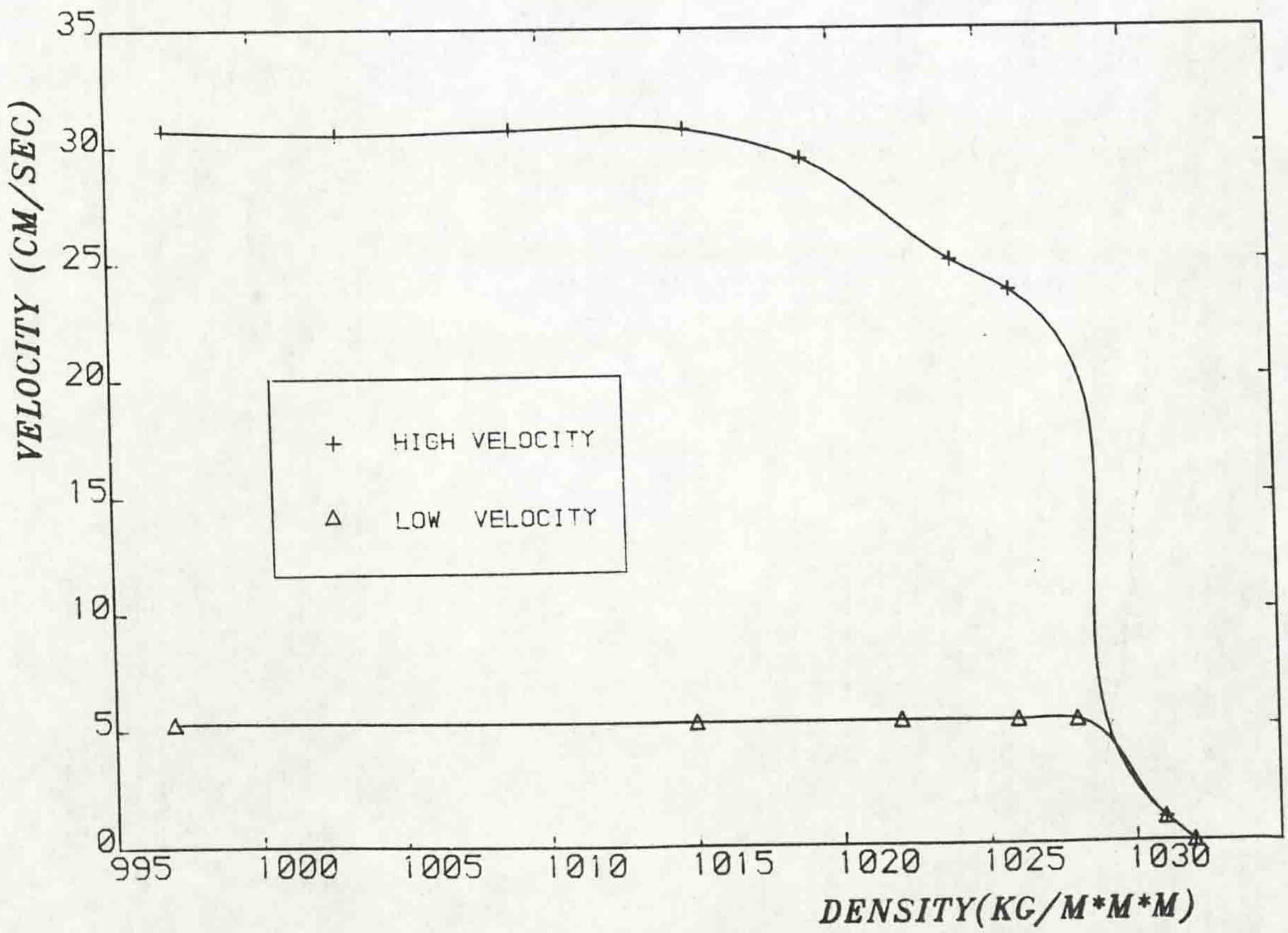

Fig. (2.2) The effect of salinity on the performance of the propeller meter.

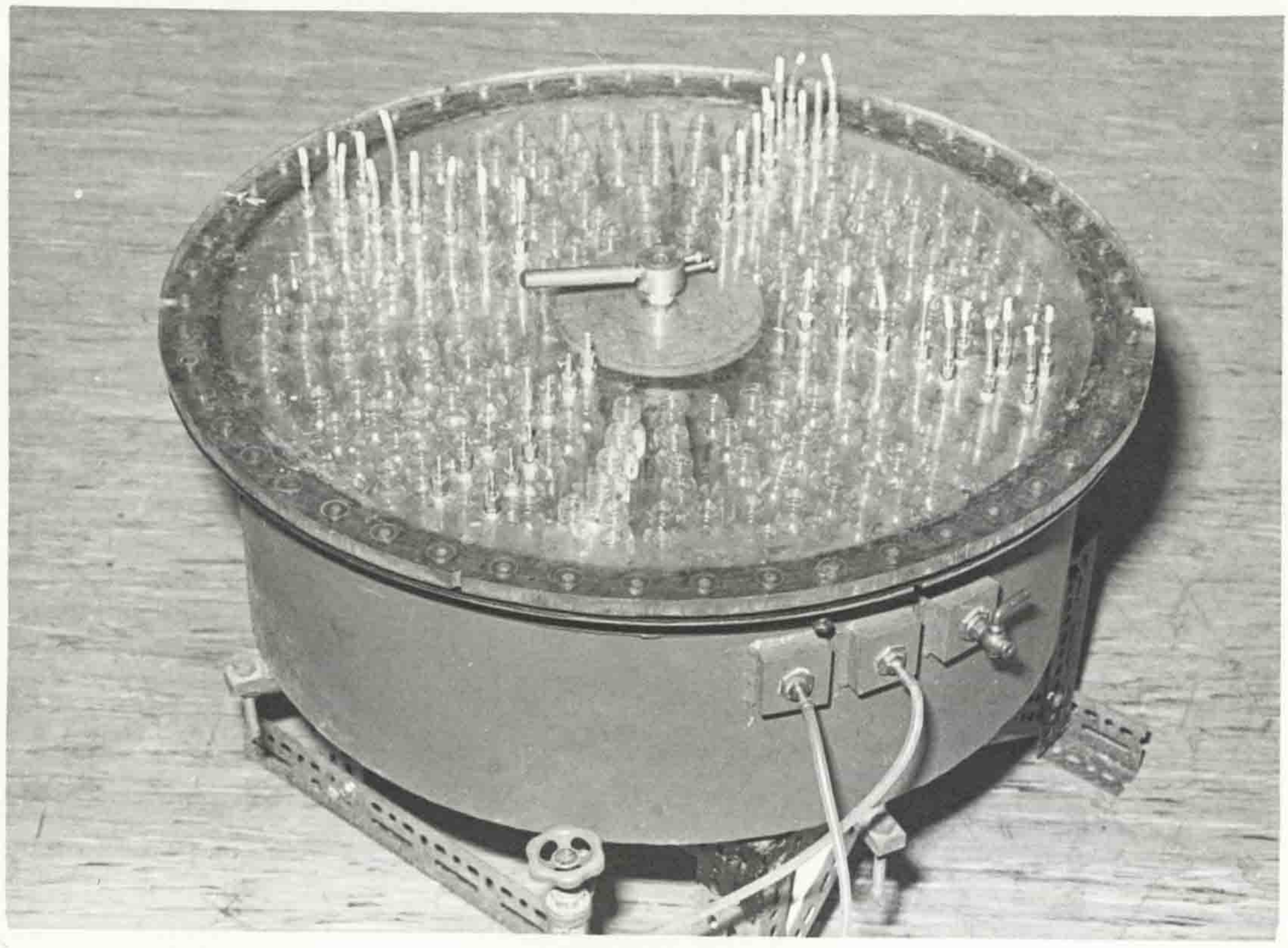

Fig. (2.3) The forty probe sampler.

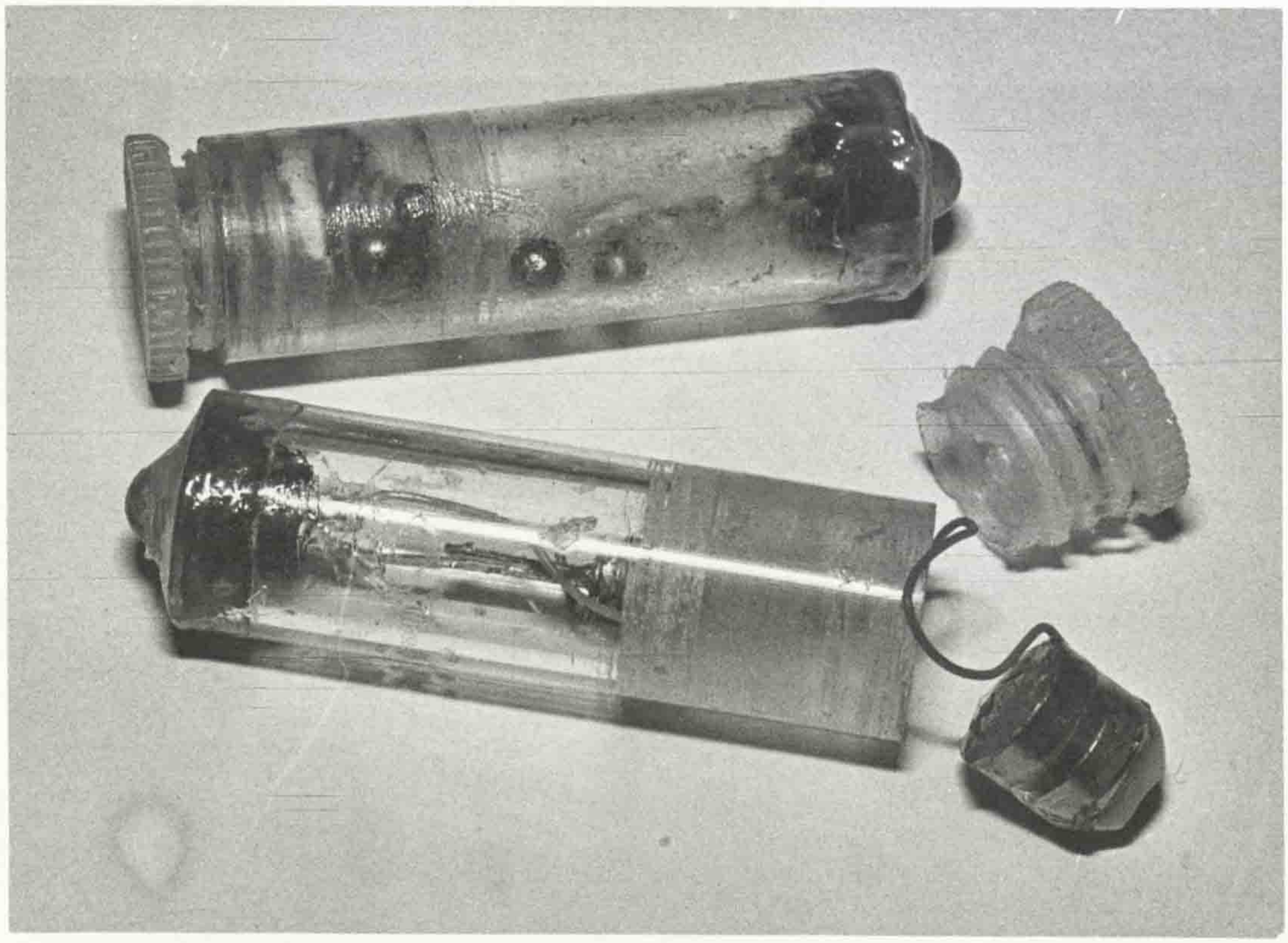

Fig. (2.4) The illuminated floats.

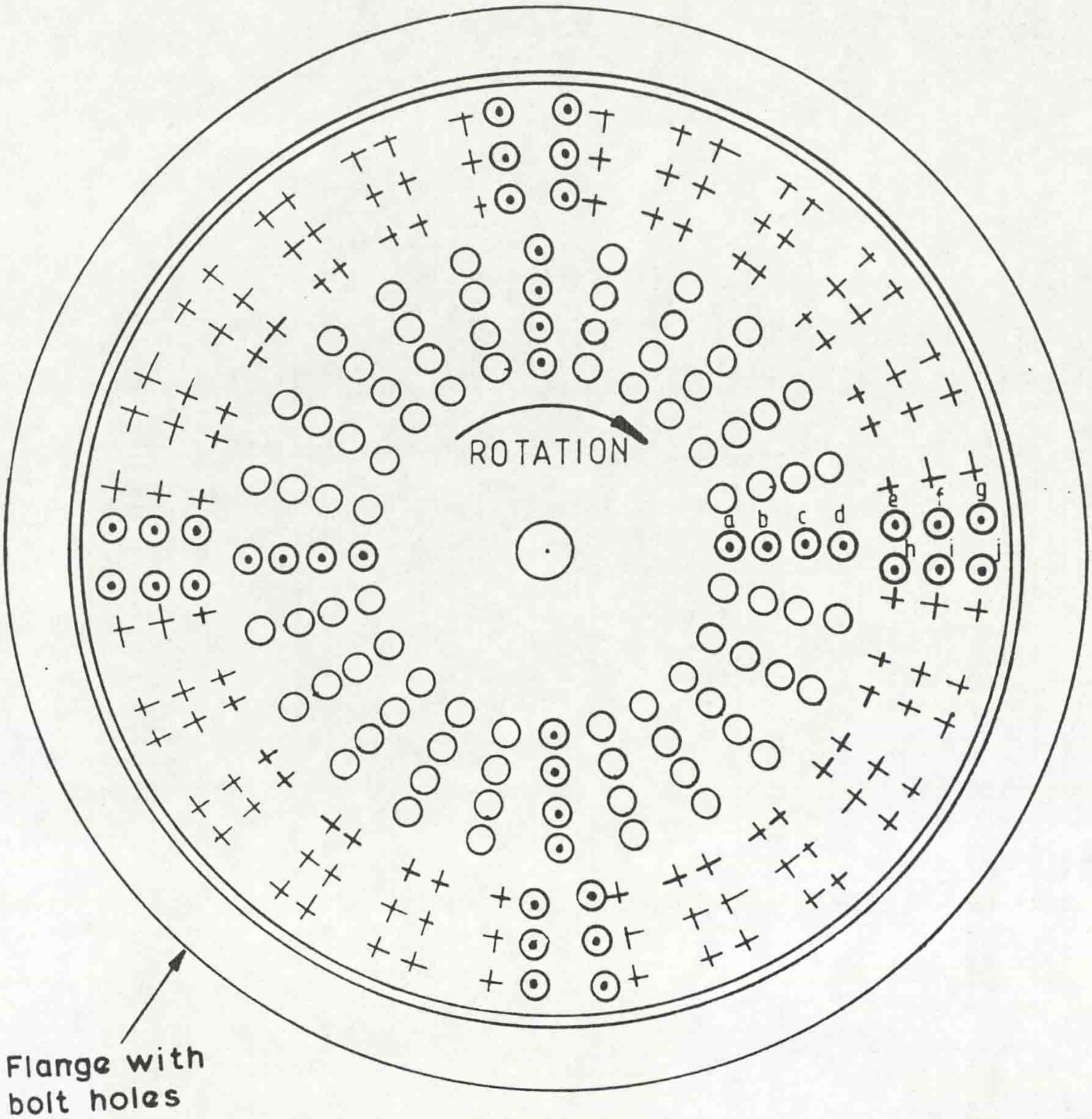

Fig. (2.5) Arrangement of bottles and tubes in the forty probe sampler.

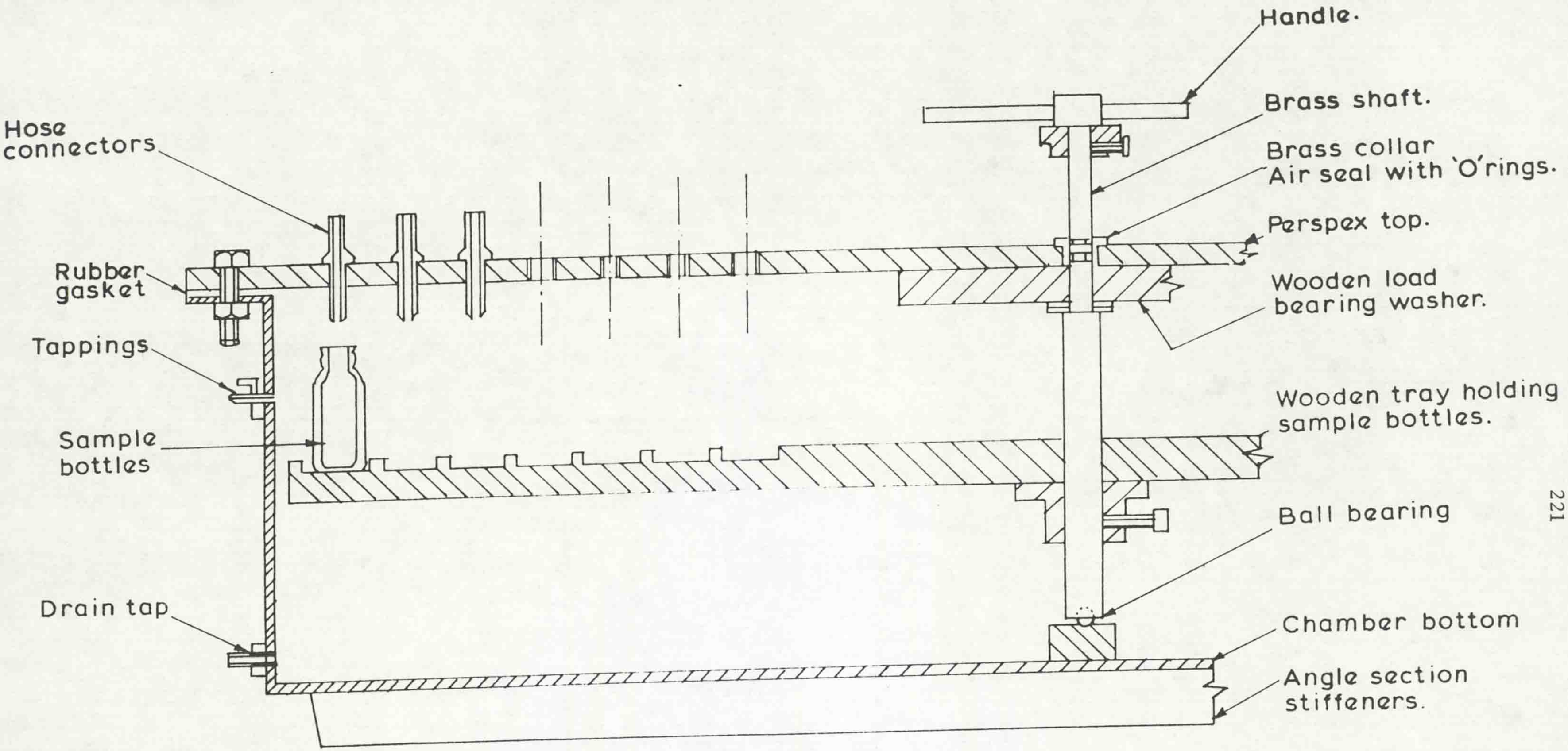

Fig. (2.6)

Cross section of the forty probe sampler.

Range of Reading (R)	Temperature °C	Regression Curve	Concentration gm/lit
R < 1430	10	C = 7.2727 x 10^{-4} R - 0.04	
1430 < R < 6500	10	C = 7.97 x 10^{-4} R - 0.265	
6500 < R < 42000	10	C = 9.49 x 10^{-4} R - 1.19	
42000 < R	10	C = 1.095 x 10^{-4} R - 4.51	
R < 1775	15	C = 5.5749 x 10^{-4} R + 0.01	
1775 < R < 7750	15	C = 6.7783 x 10^{-4} R - 0.298	
7750 < R < 49000	15	C = 8.5088 x 10^{-4} R - 2.106	
49000 < R	15	C = 9.8346 x 10^{-4} R - 7.098	
R < 2140	20	C = 4.5977 x 10^{-4} R + 0.016	
2140 < R < 8250	20	C = 6.3498 x 10^{-4} R - 0.58	
8250 < R < 54000	20	C = 7.7509 x 10^{-4} R - 1.901	
54000 < R	20	C = 8.548 x 10^{-4} R - 6.302	

Table (2.1) Regression Lines for the Variation of Concentration with Conductivity Bridge's Reading (R) for Various Temperatures

Concentration gm/lit	10°C	15°C	20°C	25°C
0	999.73	999.13	998.23	997.07
10	1007.2	1006.3	1005.3	1004.06
20	1014.21	1013.39	1012.29	1010.97
30	1021.29	1020.41	1019.22	1017.79
40	1028.37	1027.35	1026.07	1024.61
50	1035.32	1034.25	1032.88	1031.33
60	1042.25	1041.05	1039.6	1038.04
70	1049.07	1047.83	1046.32	1044.66
80	1055.87	1054.4	1052.92	1051.16

Table (2.2) Density (kg/m^3) of Water at Different Concentrations of Saline (gm/cc) and Temperatures.

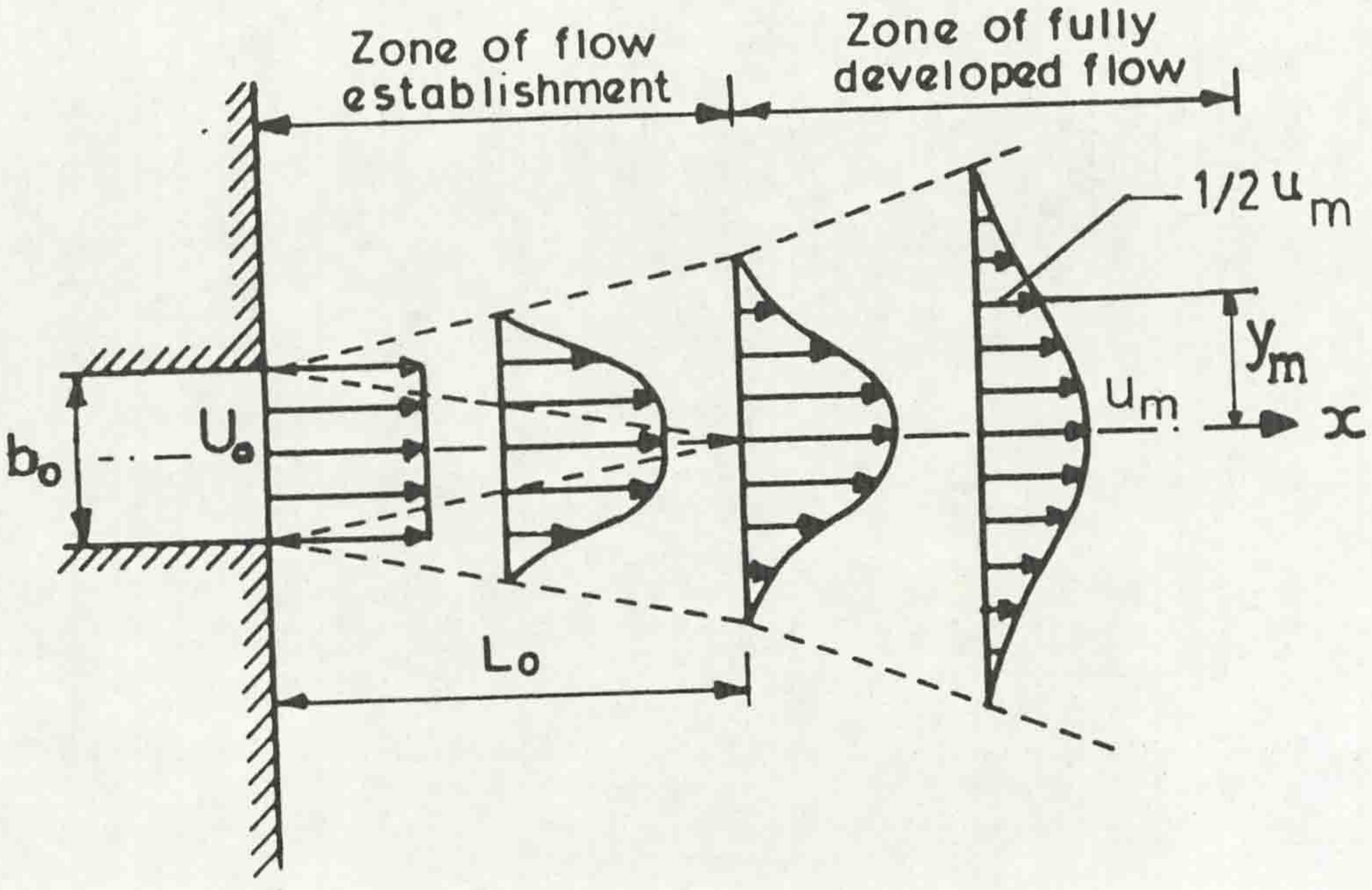

Fig. (3.1a)

Development of similar velocity profiles in a plane jet.

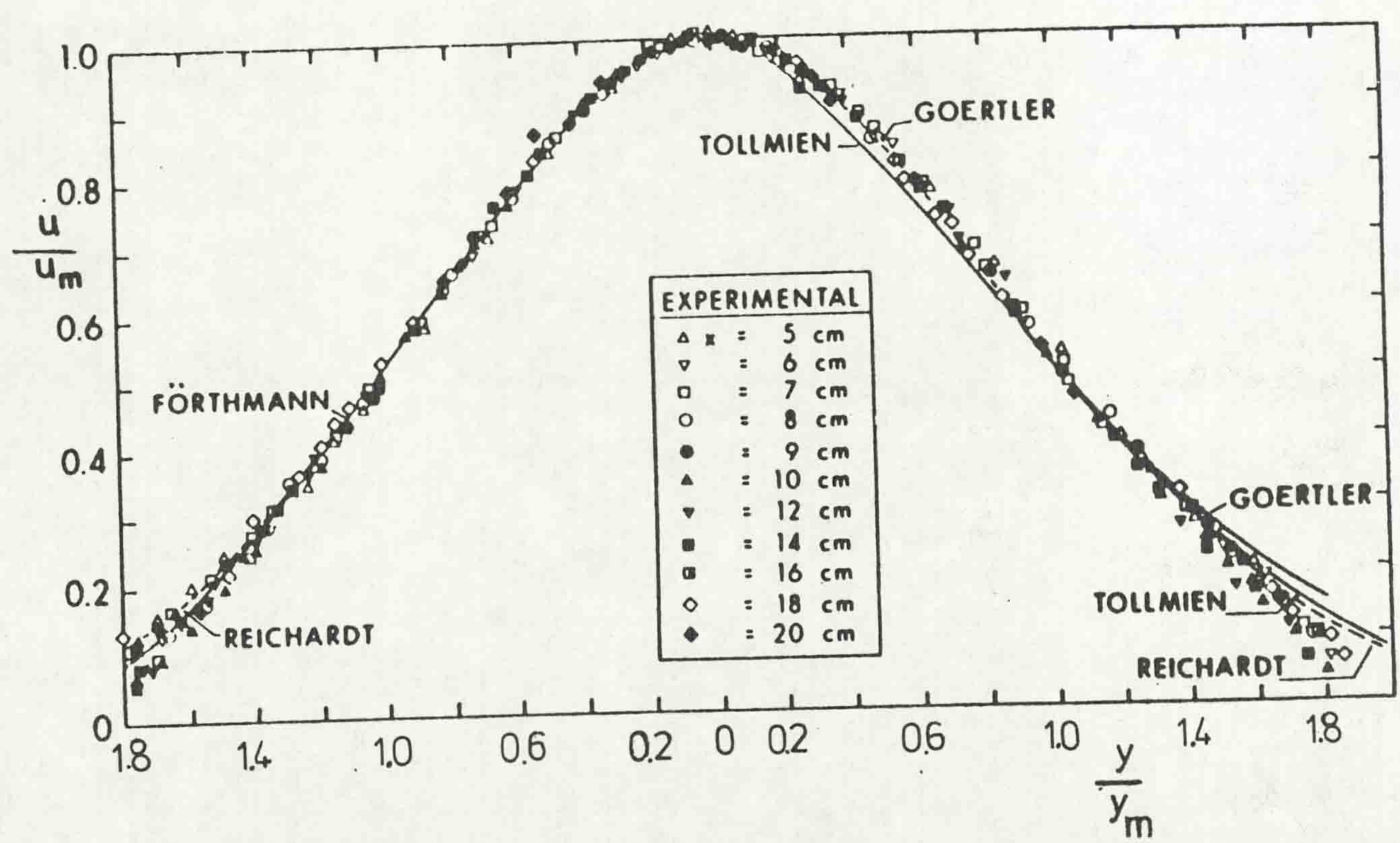

Fig. (3.1b)

Velocity distribution for plane free jet (Rajaratnam, 1976).

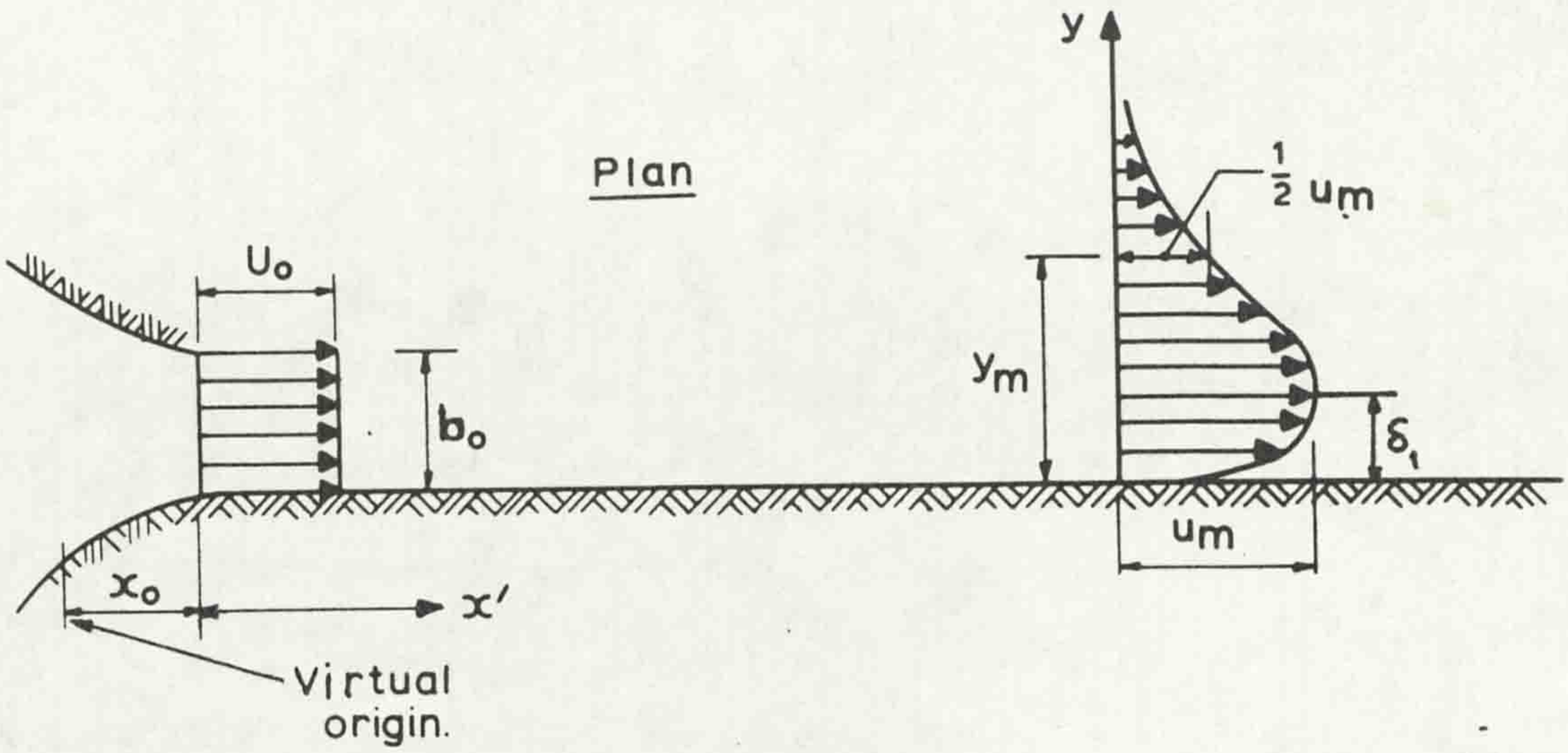

Fig. (3.2) Definition sketch for tangential wall jet.

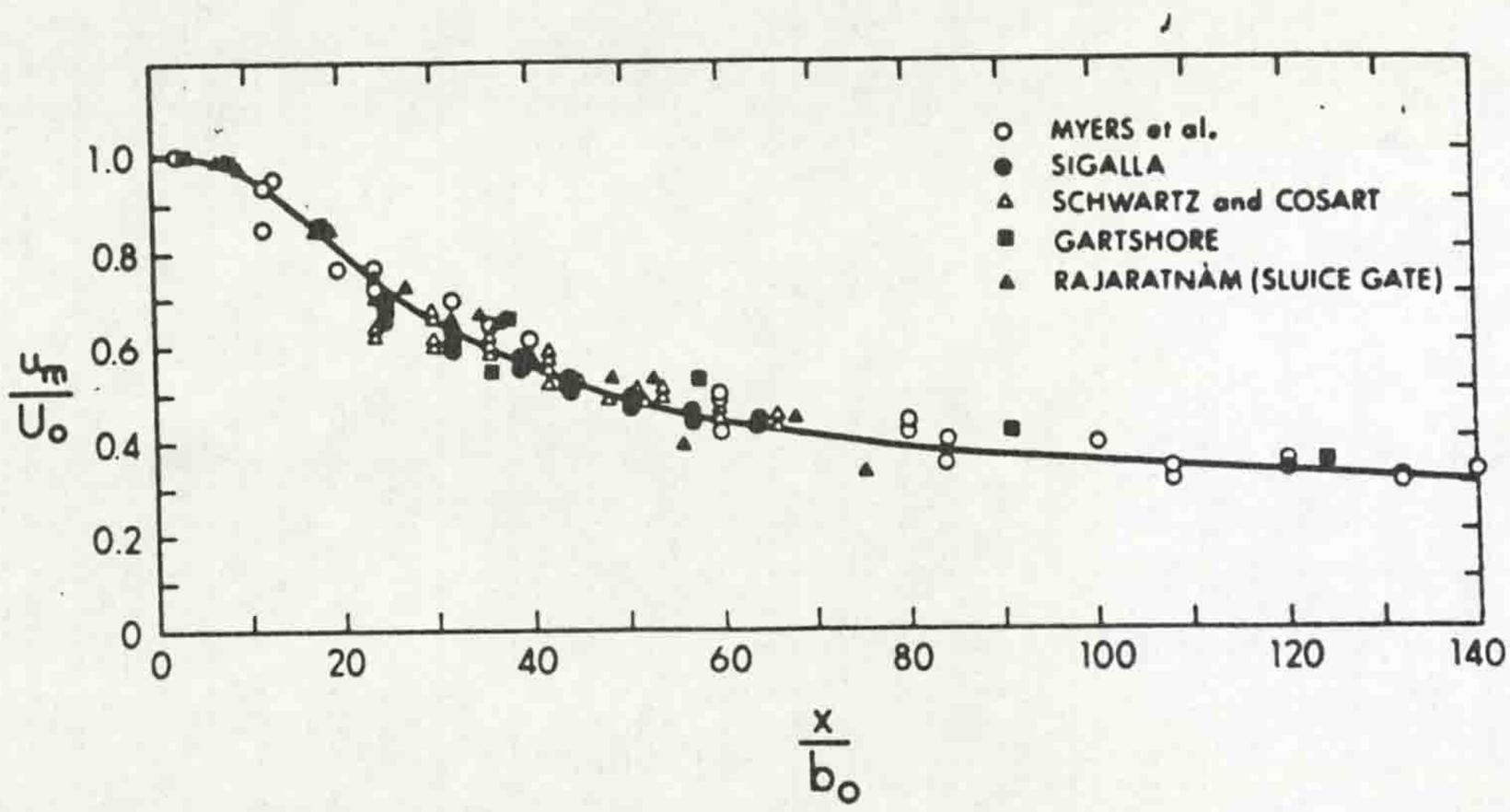

Fig. (3.3a) Correlation of the velocity scale for plane wall jet (Rajaratnam et al, 1967).

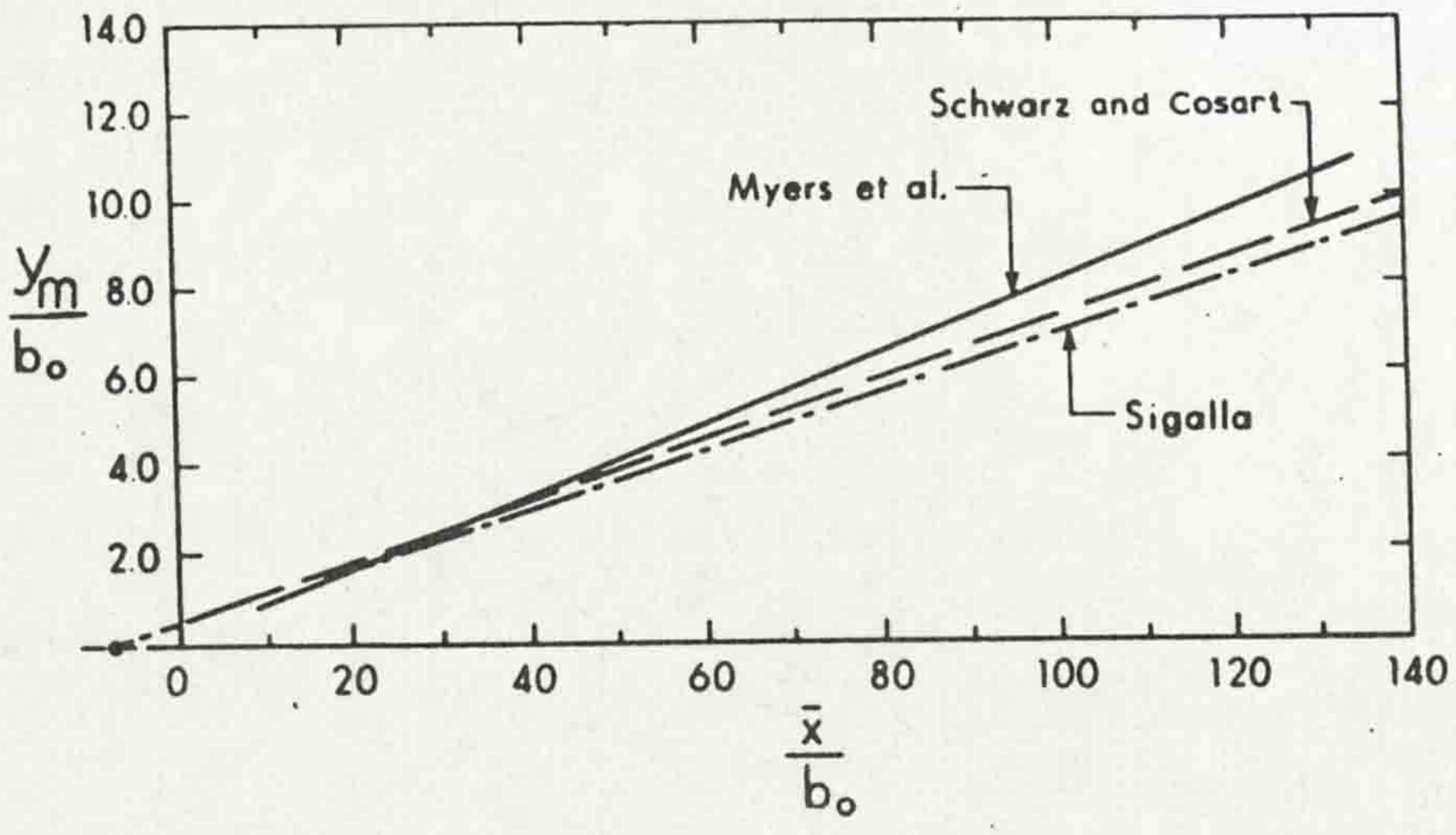

Fig. (3.3b) Growth of the length scale for plane wall jet (Rajaratnam et al, 1976).

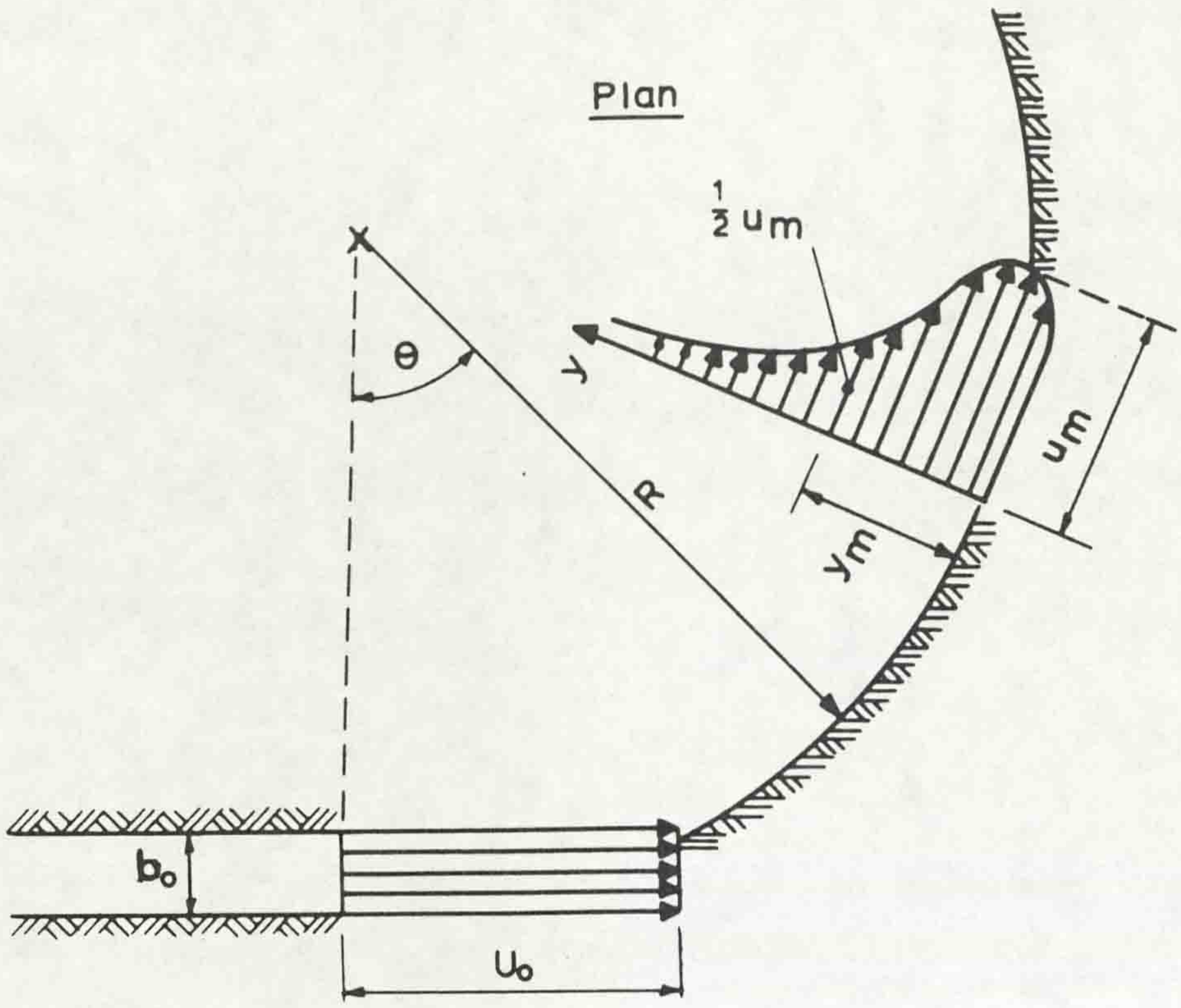

Fig. (3.4) Two-dimensional tangential wall jet on inside of circular cylinder.

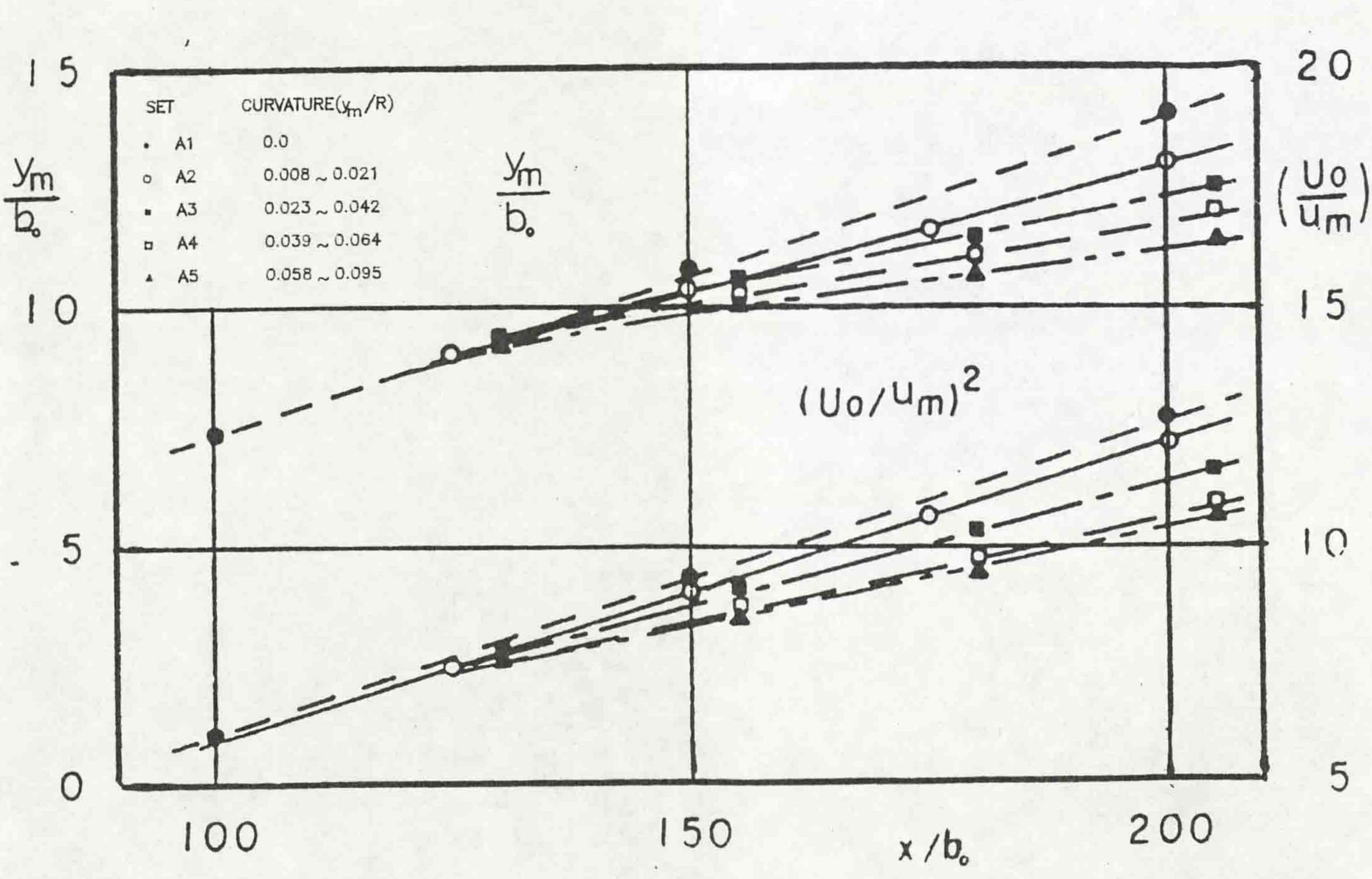

Fig. (3.5)

Variation of y_m/b_o and $(U_o/u_m)^2$ in the x direction for different sets of experiments (after Kobayashi et al, 1983).

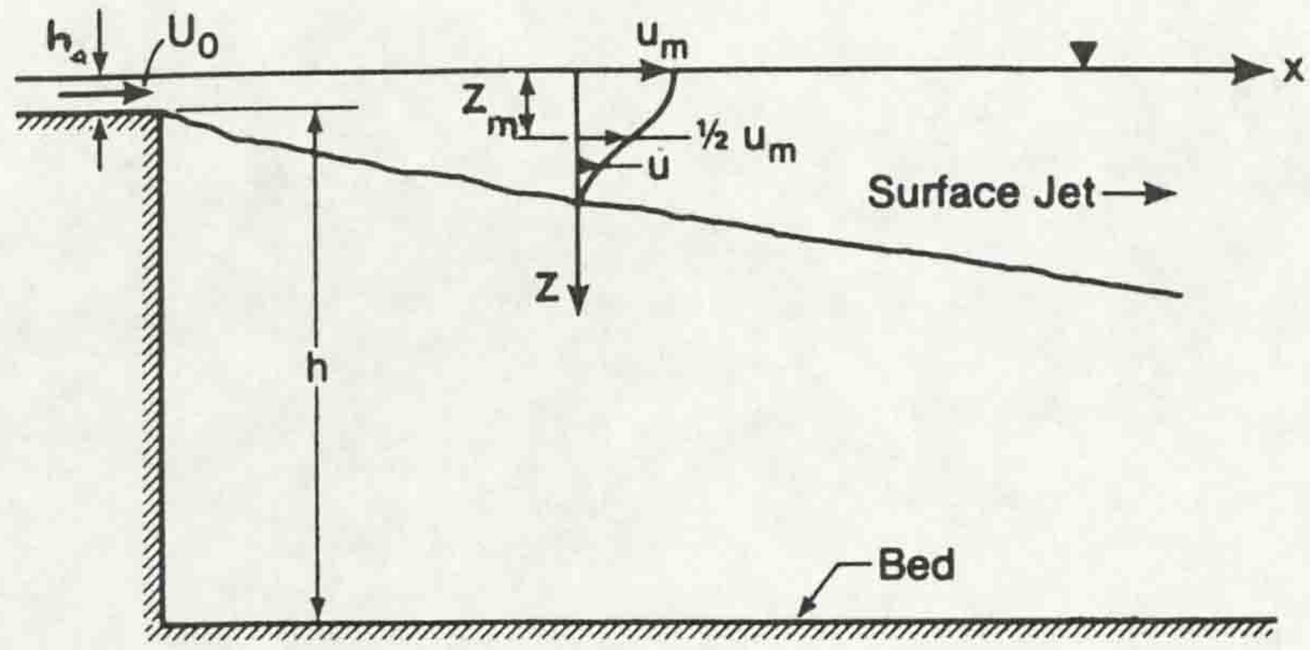

Fig. (3.6) Definition sketch for plane surface jet.

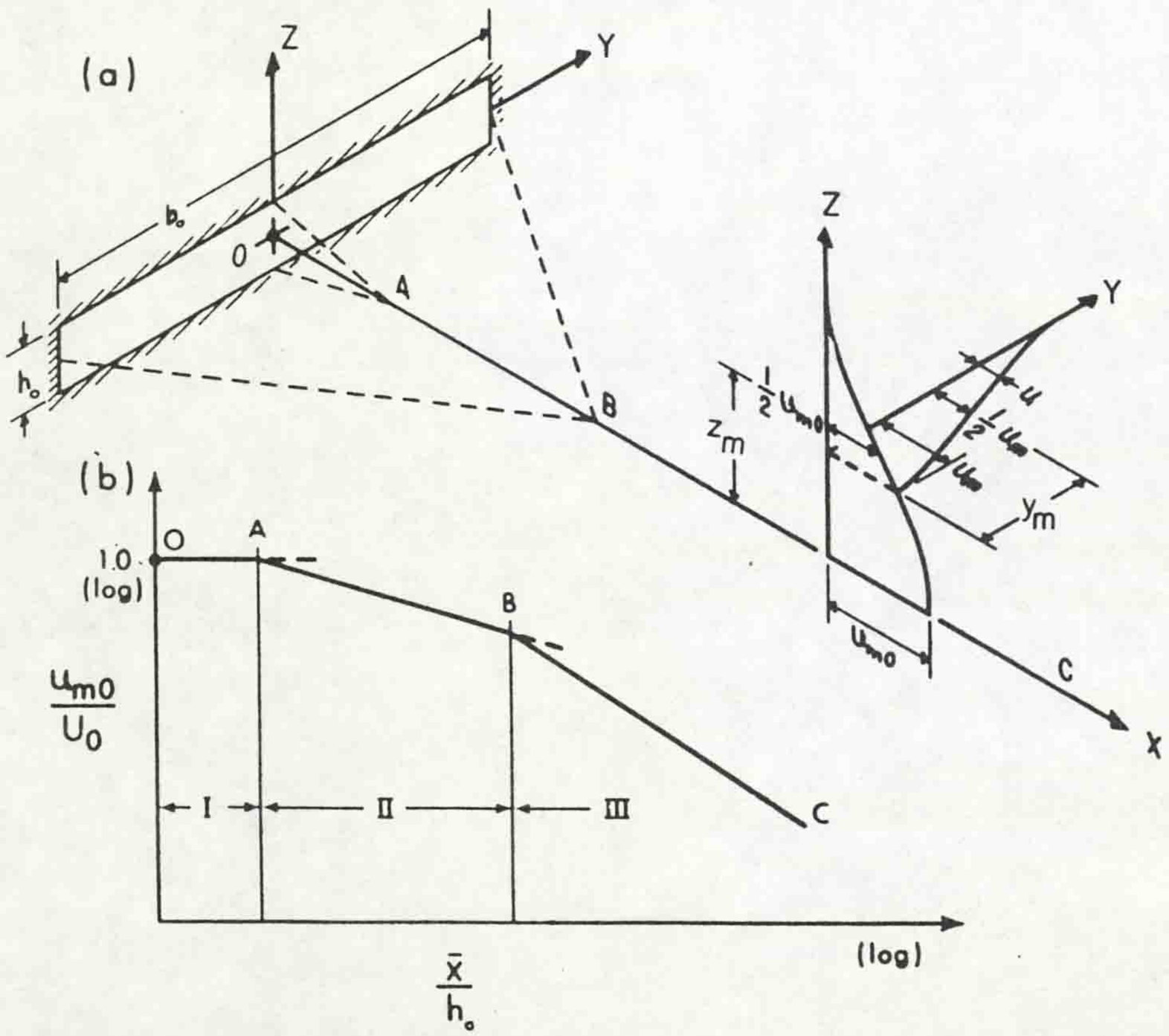

Fig. (3.7) Definition sketch for a three-dimensional free jet.

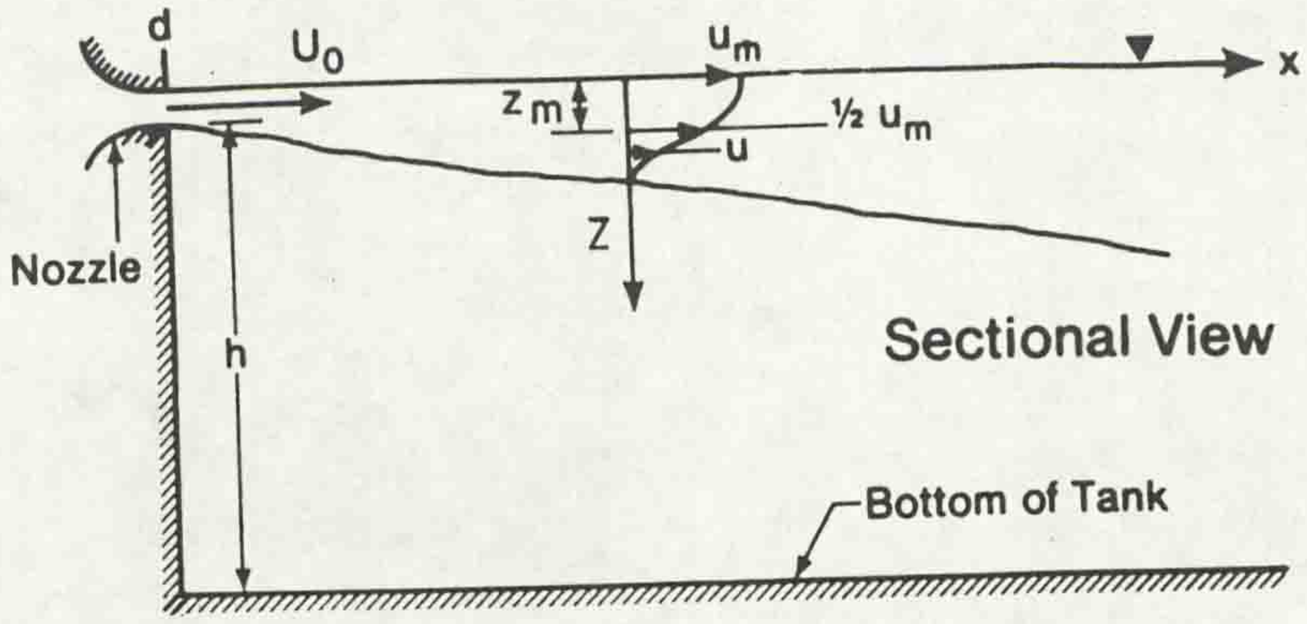

Fig. (3.8) Definition sketch for circular surface jet.

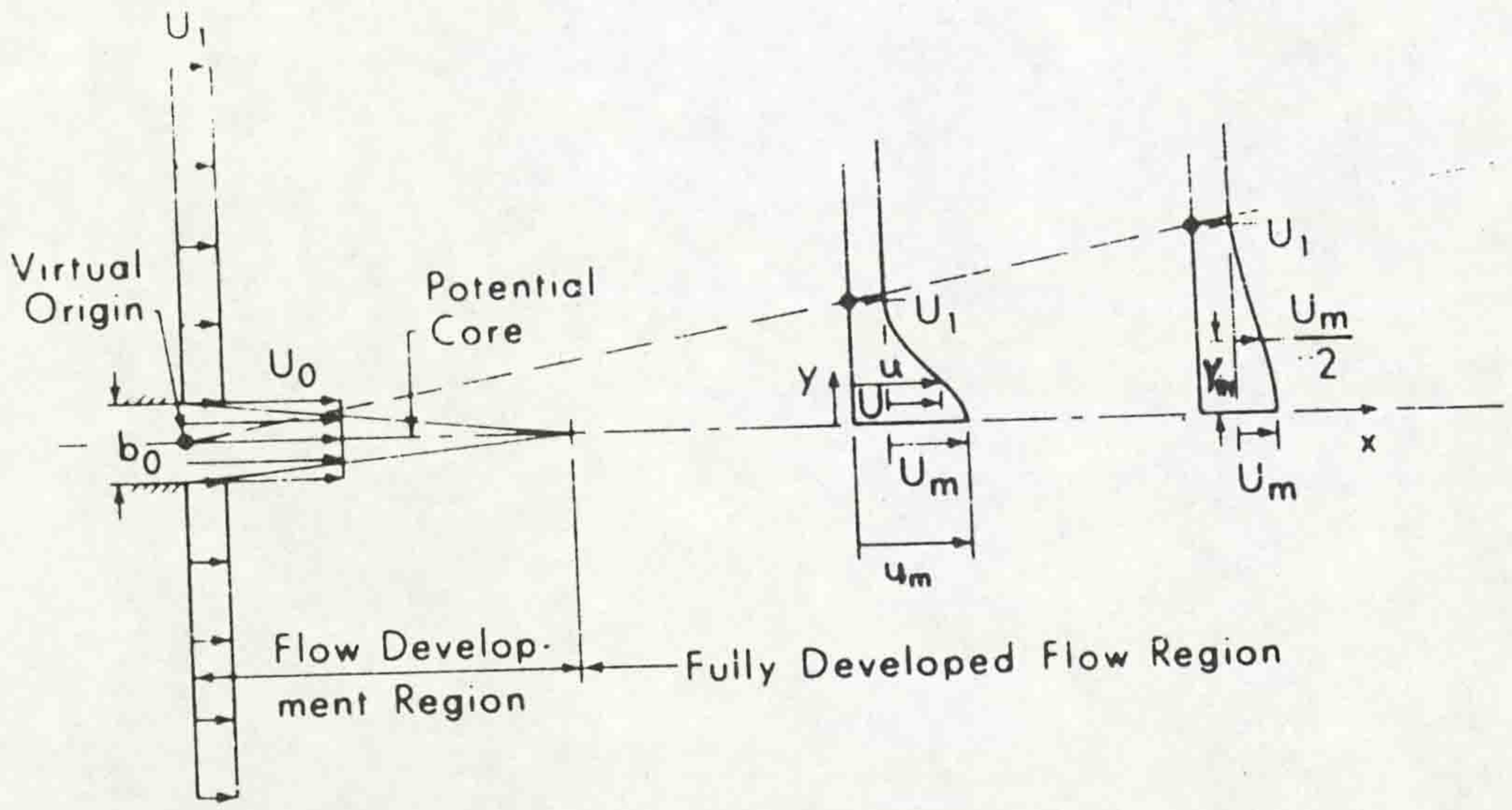

Fig. (3.9a) Definition sketch for a jet in co-flowing stream.

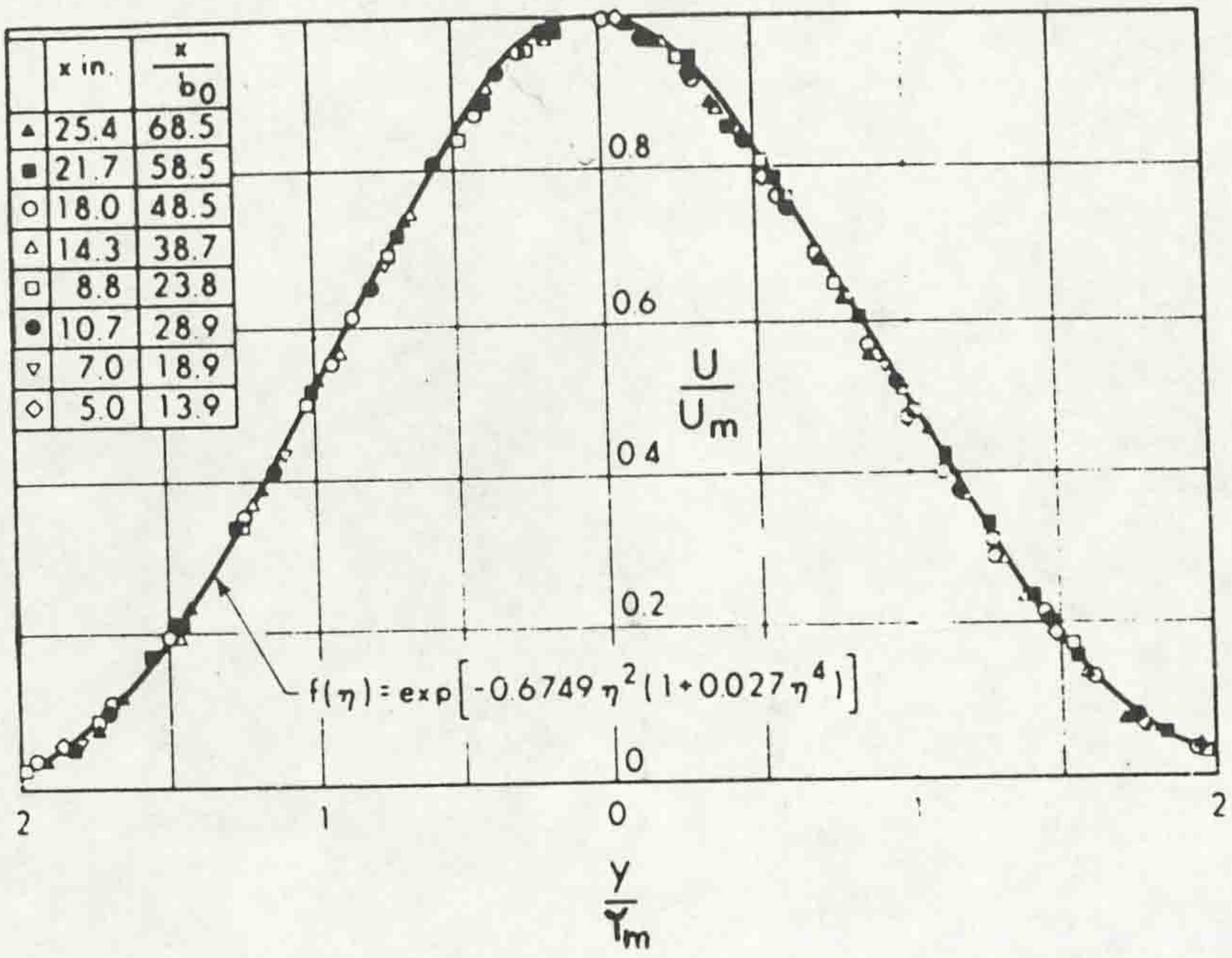

Fig. (3.9b) Similarity of velocity profiles for plane jet in co-flowing stream (Bradbury, 1965).

Fig. (3.10) Circular surface jet in co-flowing stream.

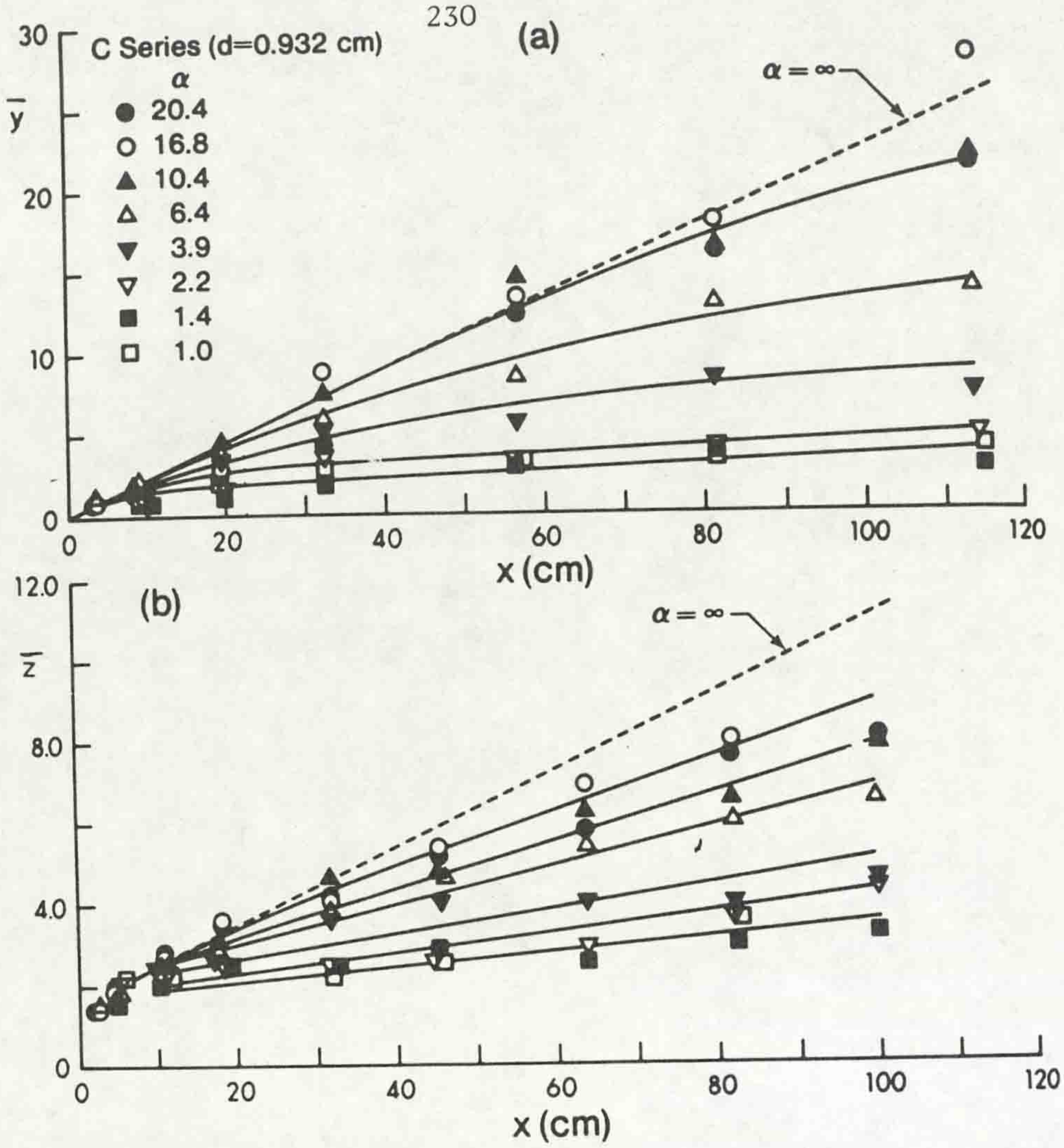

Fig. (3.11) Growth of width and thickness of a surface jet in co-flowing stream.

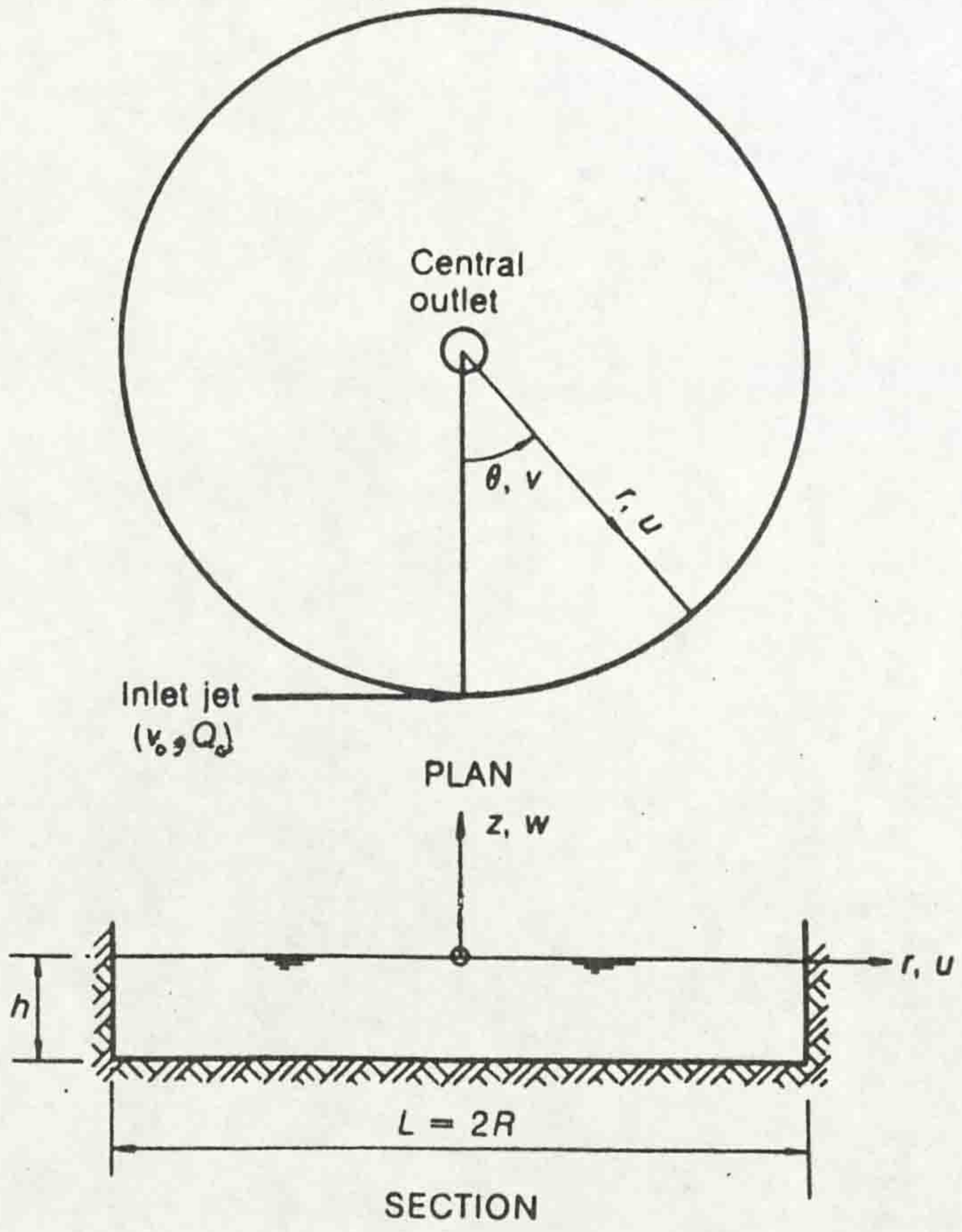

Fig. (3.12) Definition sketch for a jet-forced circulation in a reservoir.

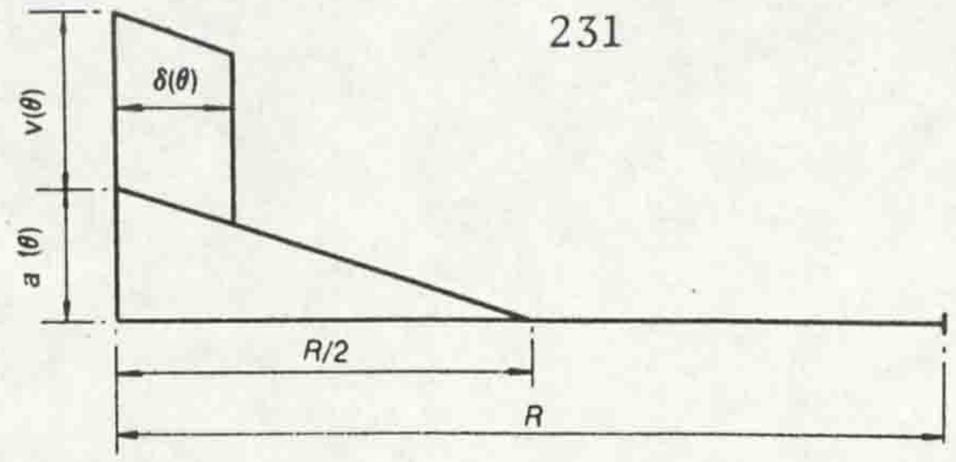

Fig. (3.13a) Sobey's assumed velocity distribution.

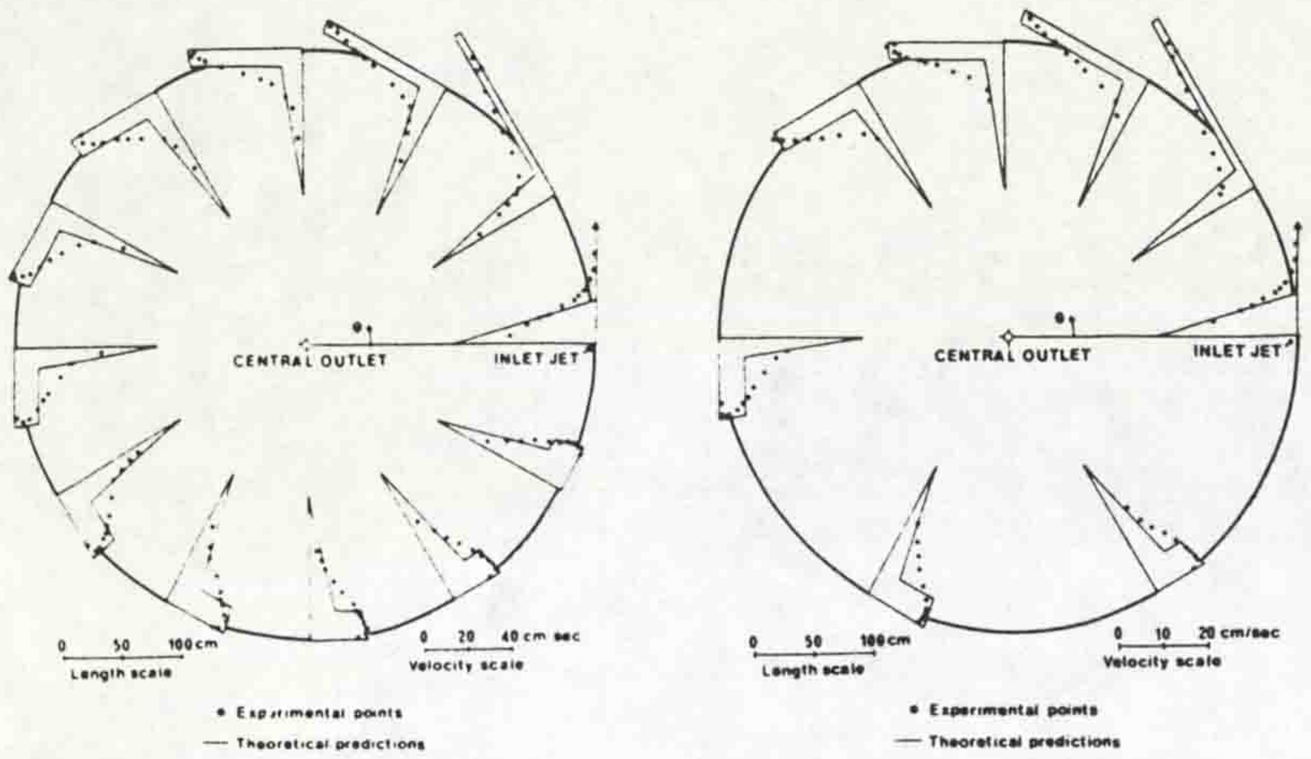

Fig. (3.13b) Sobey's experimental and theoretical results.

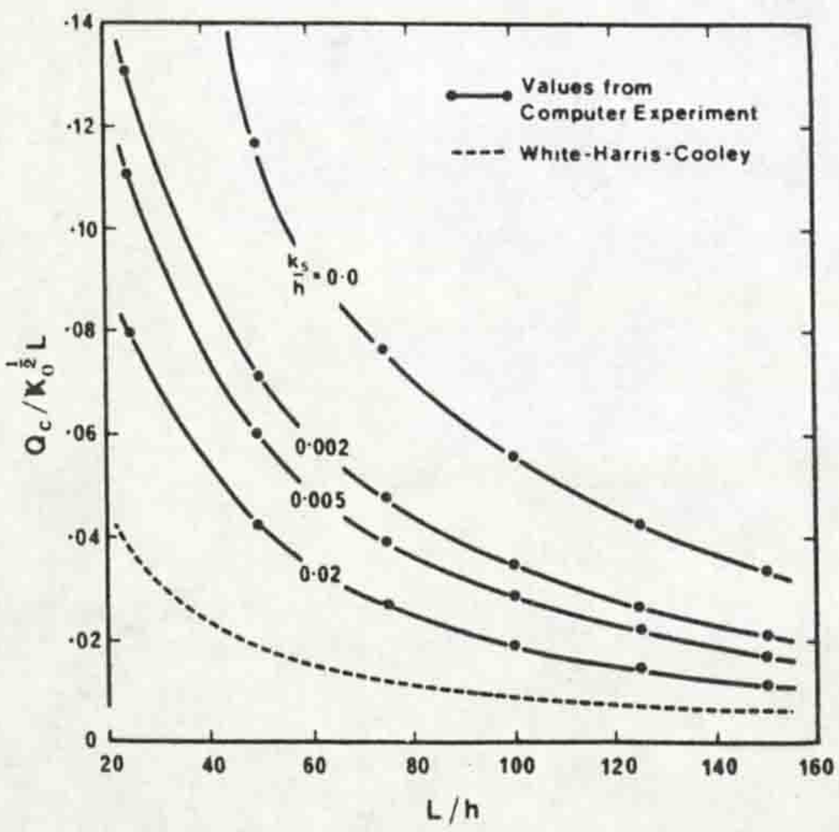

Fig. (3.14) Jet force circulation diagram (after Sobey, 1972).

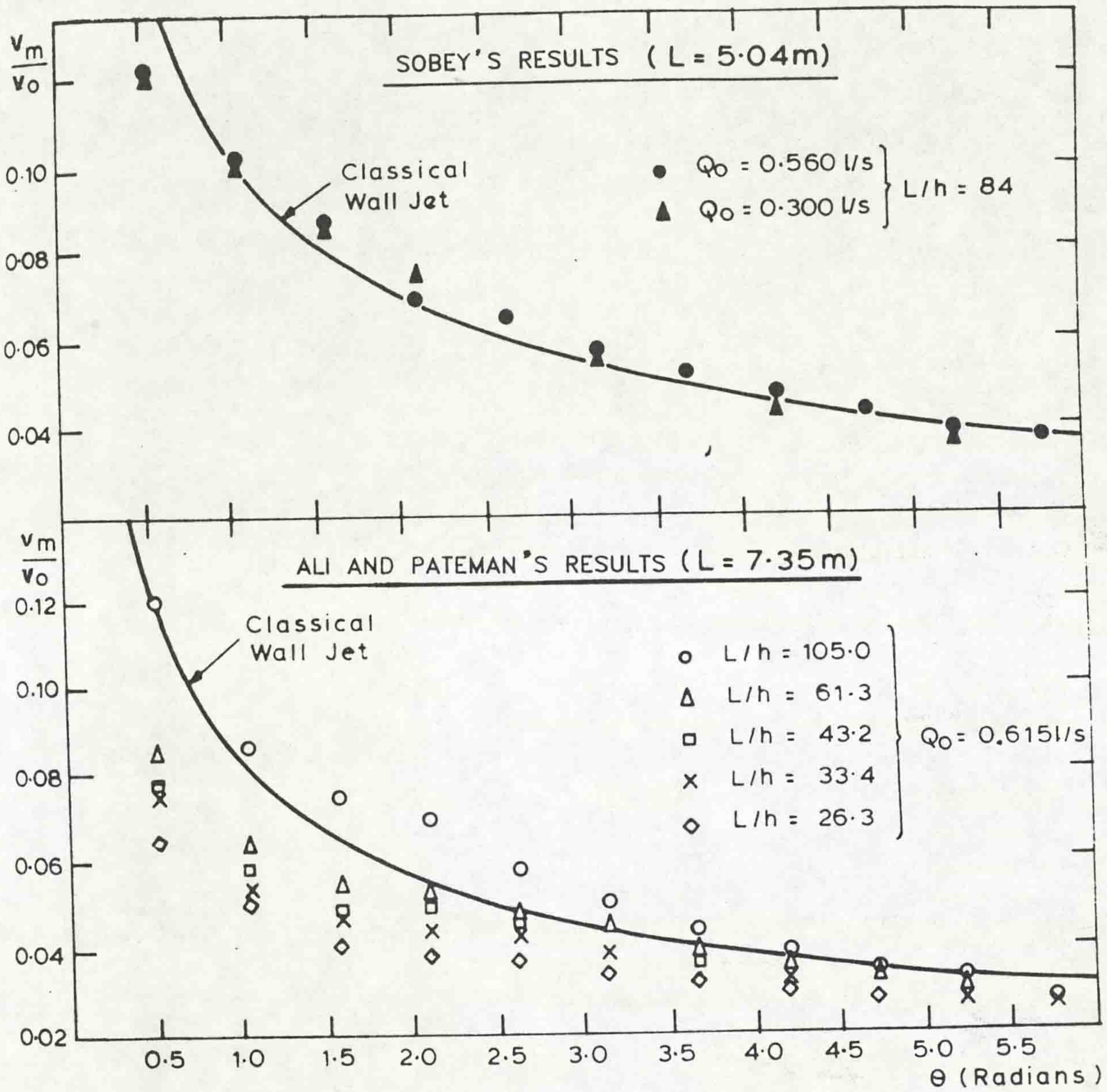

Fig. (3.15)

Variation of v_m with θ for various jet discharges and reservoir aspect ratios for different models (after Pateman, 1982).

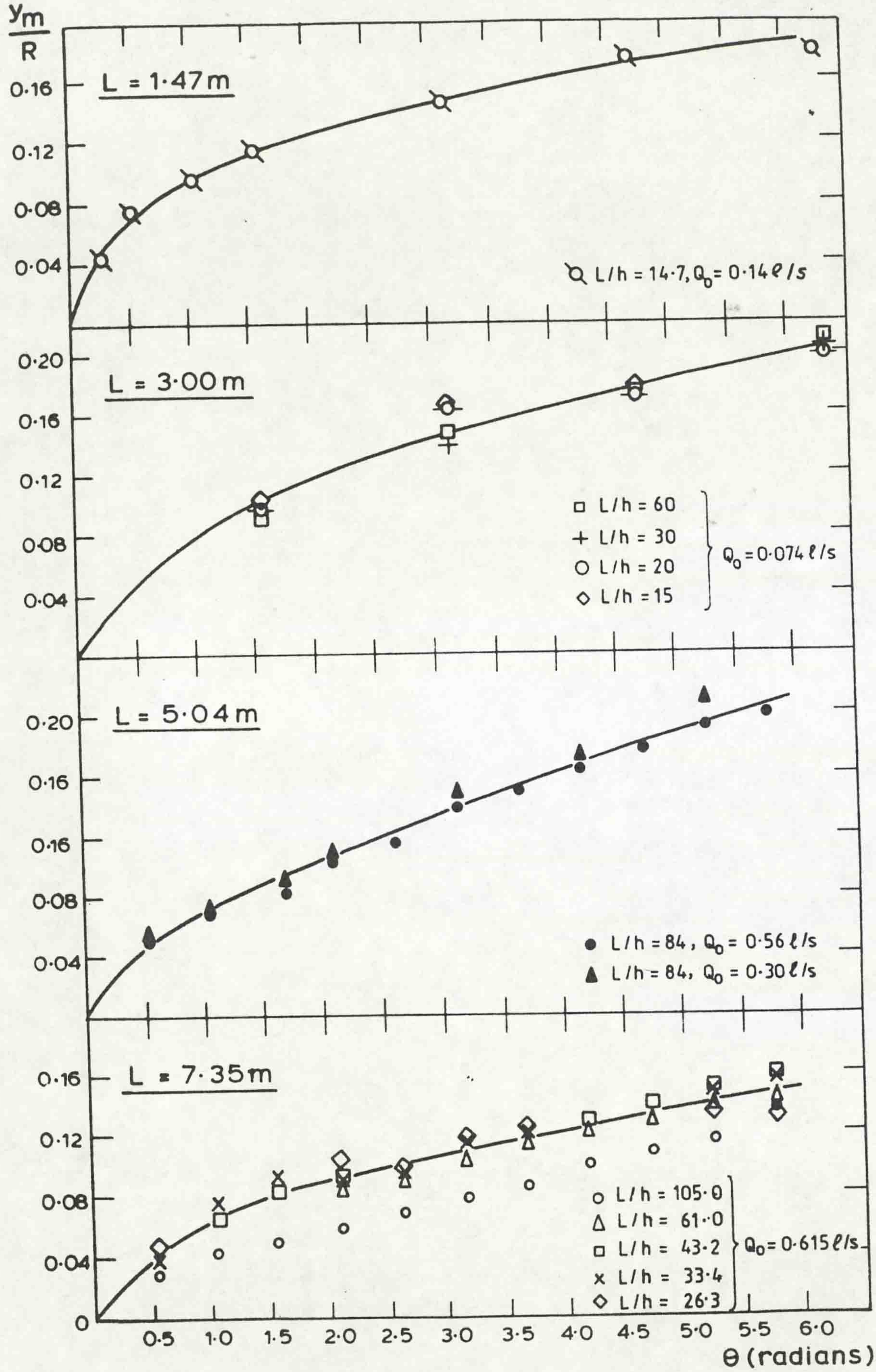

Fig. (3.16)

Variation of y_m/R with θ for various reservoir sizes (after Pateman, 1982).

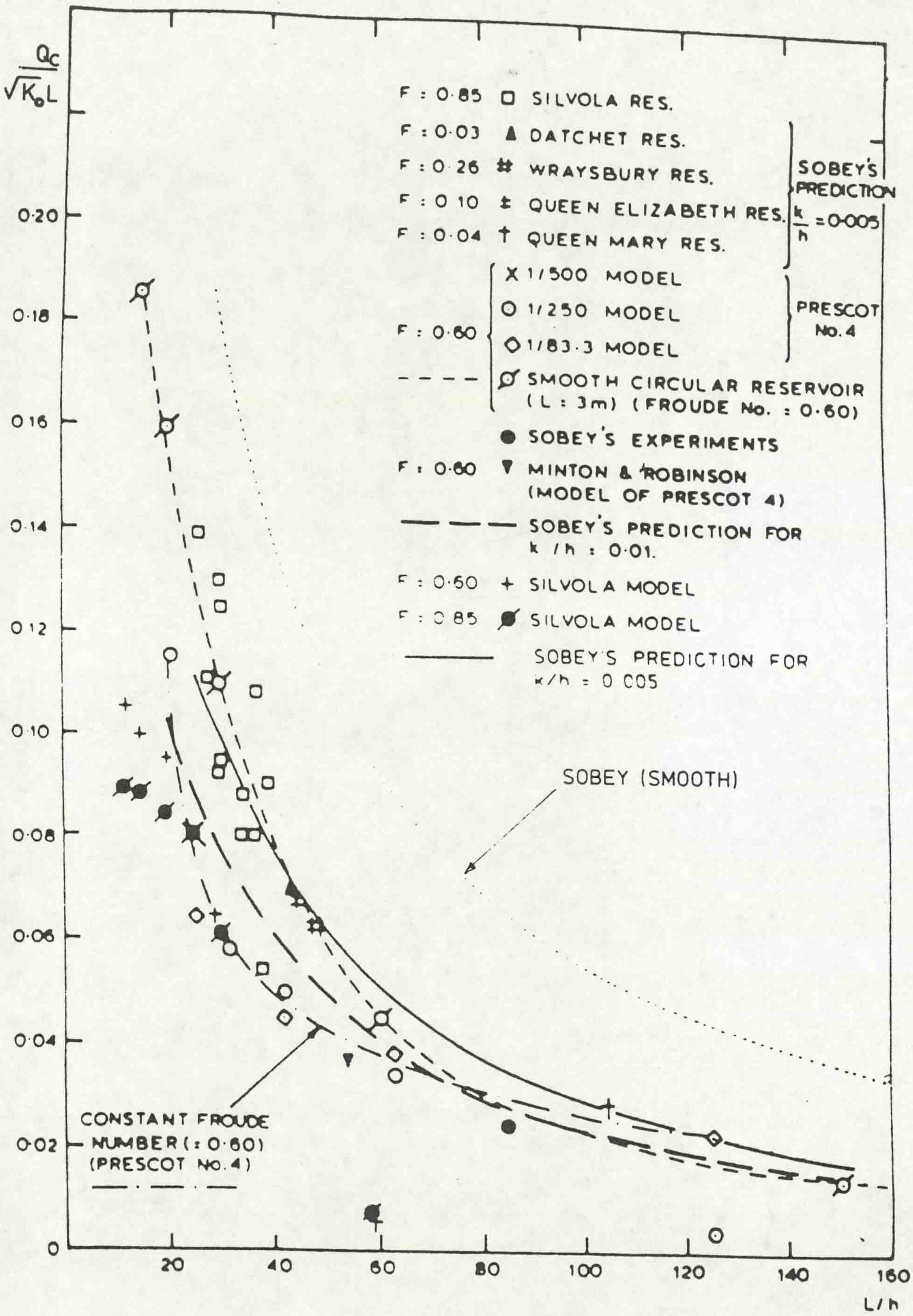

Fig. (3.17)

Variation of $Q_c/\sqrt{K_o L}$ with aspect ratio (L/h)
(after Pateman, 1982)

Series/ Run	Discharge cc/sec	Depth cm	Time Lapse Photography	Wall Velocity	Dye Photography	Velocity in Depth	Photography in Depth	Remarks
1/1	49.5	22.5	-	✓	-	✓	✓	
1/2	30.833	"	✓	✓	-	✓	-	L = 92 cm
1/3	19.66	"	✓	✓	-	✓	✓	
1/4	12.383	"	✓	✓	-	✓	-	Tangential
1/5	5.75	"	✓	✓	✓	-	-	jet
2/1	30.83	12.	✓	✓	-	-	-	b_0 = 0.2 cm
2/2	19.66	"	✓	✓	-	-	-	
2/3	12.383	"	✓	✓	-	-	-	h_0 = 2. cm
2/4	5.75	"	✓	✓	✓	-	-	
3/1	30.83	4.8	✓	✓	-	-	-	
3/2	19.66	"	✓	✓	✓	-	-	
3/3	12.383	"	✓	✓	-	-	-	
3/4	5.75	"	✓	✓	✓	-	-	
4/1	30.83	2.5	✓	✓	-	-	-	
4/2	19.66	"	✓	✓	-	-	-	
4/3	12.383	"	✓	✓	-	-	-	
4/4	5.75	"	✓	✓	-	-	-	

Table (3.1) Details of Experiments Carried Out in Homogeneous Reservoir Model

Series/ Run	Discharge cm^3/sec	v_0 cm/sec	$\frac{L}{h}$	F_r	R_e	Remark
1/1	49.5	247.5	4.1	1.67	11069	Tangential jet
1/2	30.83	154.15	"	1.04	6894	$A_{jet} = 0.2\ cm^2$
1/3	19.66	98.33	"	0.66	4397	
1/4	12.38	61.9	"	0.42	2768	
1/5	5.75	28.75	"	0.19	1286	$F_r = \frac{v_0}{\sqrt{gh}}$
2/1	30.83	154.15	7.7	1.56	6894	
2/2	19.66	98.33	"	0.99	4397	$R_e = \frac{\sqrt{K_0}}{\nu}$
2/3	12.38	61.9	"	0.62	2768	
2/4	5.75	28.75	"	0.29	1286	
						L = 92. cm
3/1	30.83	154.15	19.2	2.25	6894	
3/2	19.66	98.33	"	1.43	4397	
3/3	12.38	61.9	"	0.9	2768	
3/4	5.75	28.75	"	0.42	1286	
4/1	30.83	154.15	36.8	3.11	6894	
4/2	19.66	98.33	"	1.99	4397	
4/3	12.38	61.9	"	1.25	2768	
4/4	5.75	28.75	"	0.58	1286	

Table (3.2) Dimensionless No. Related to the Experiments of Table 3.1

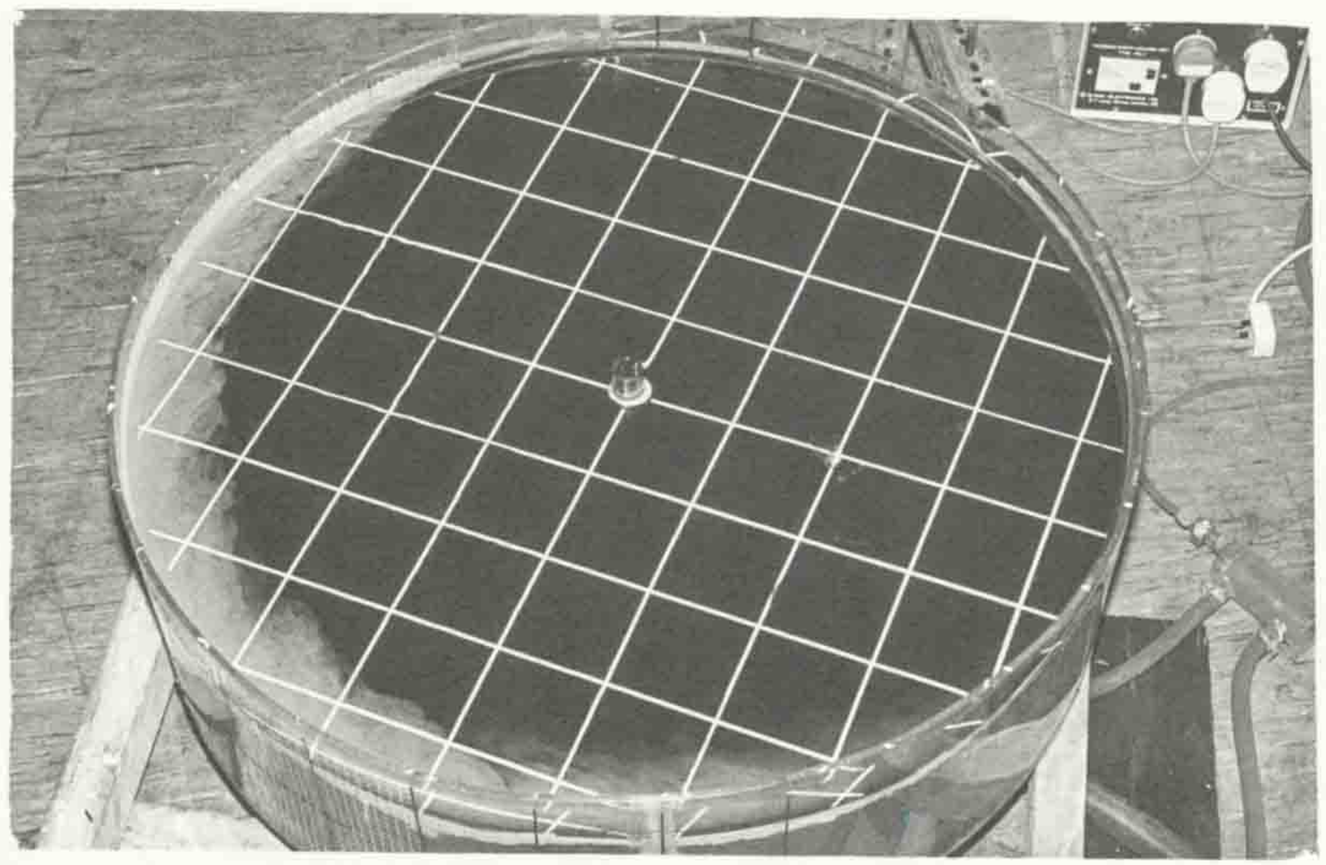

a) 10 sec.

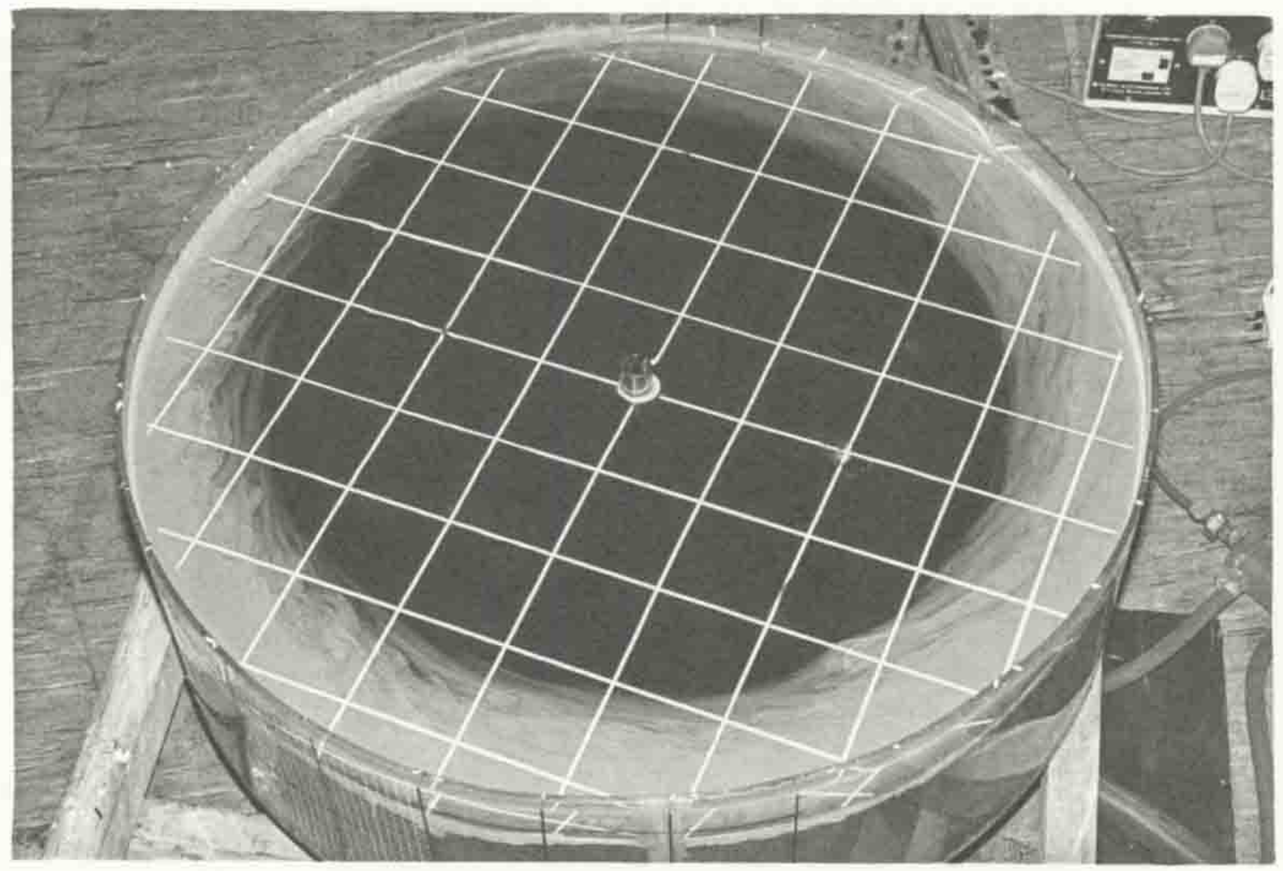

b) 30 sec.

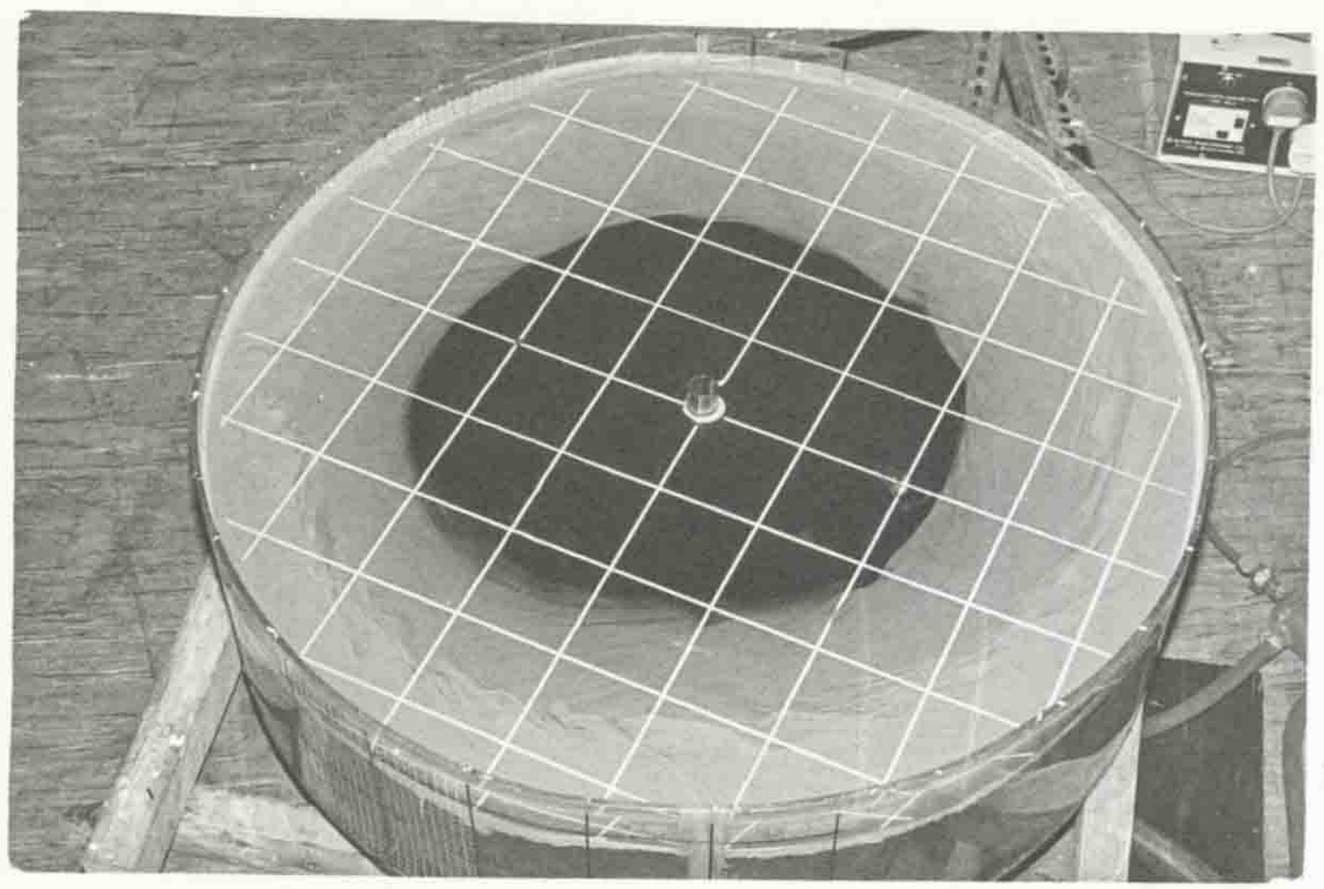

c) 1 min.30 sec.

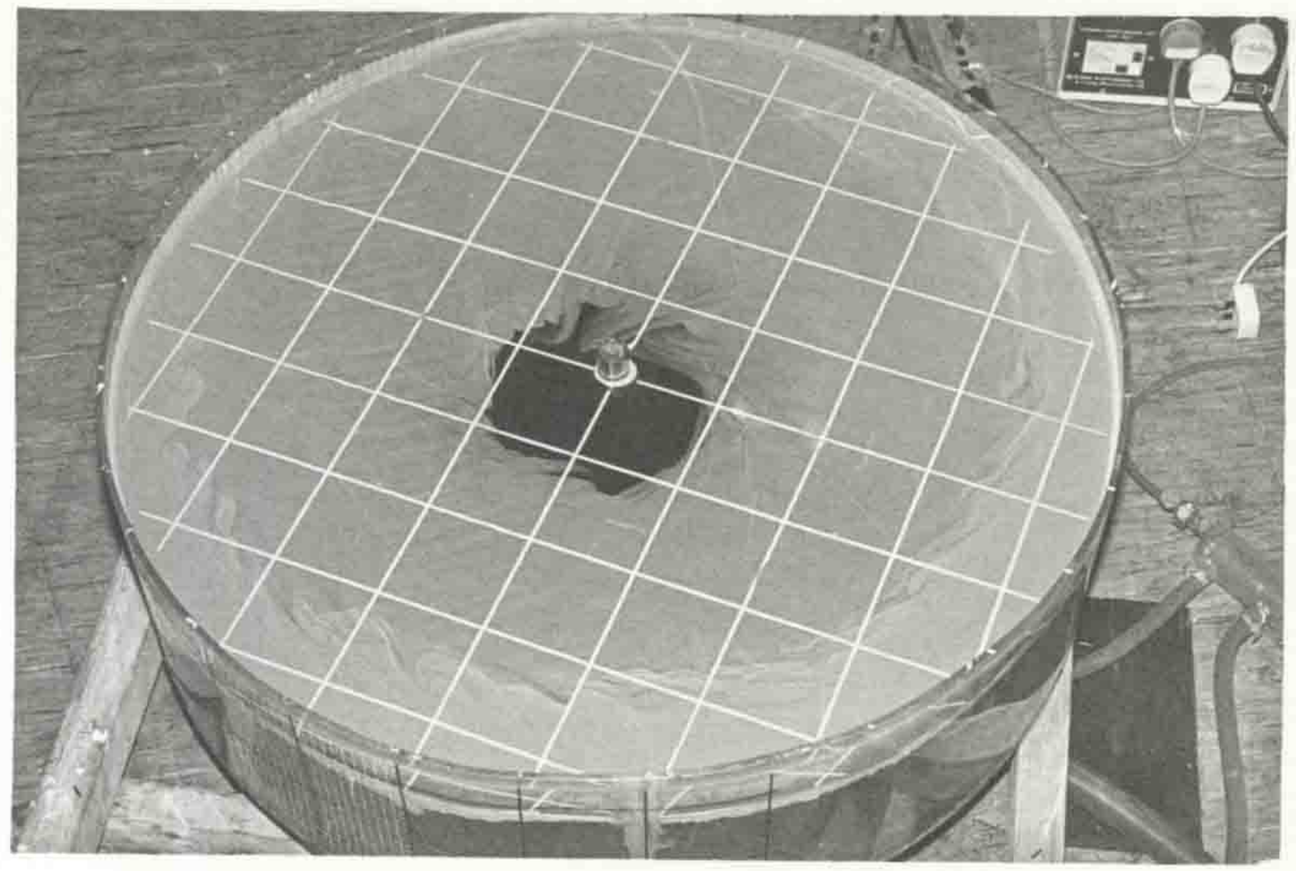

d) 2 min. 50 sec.

Fig. (3.18) Flow patterns in various times ($\frac{L}{h}$ = 19.2, h = 4.8 cm, Q_o = 19.66 cc/sec).

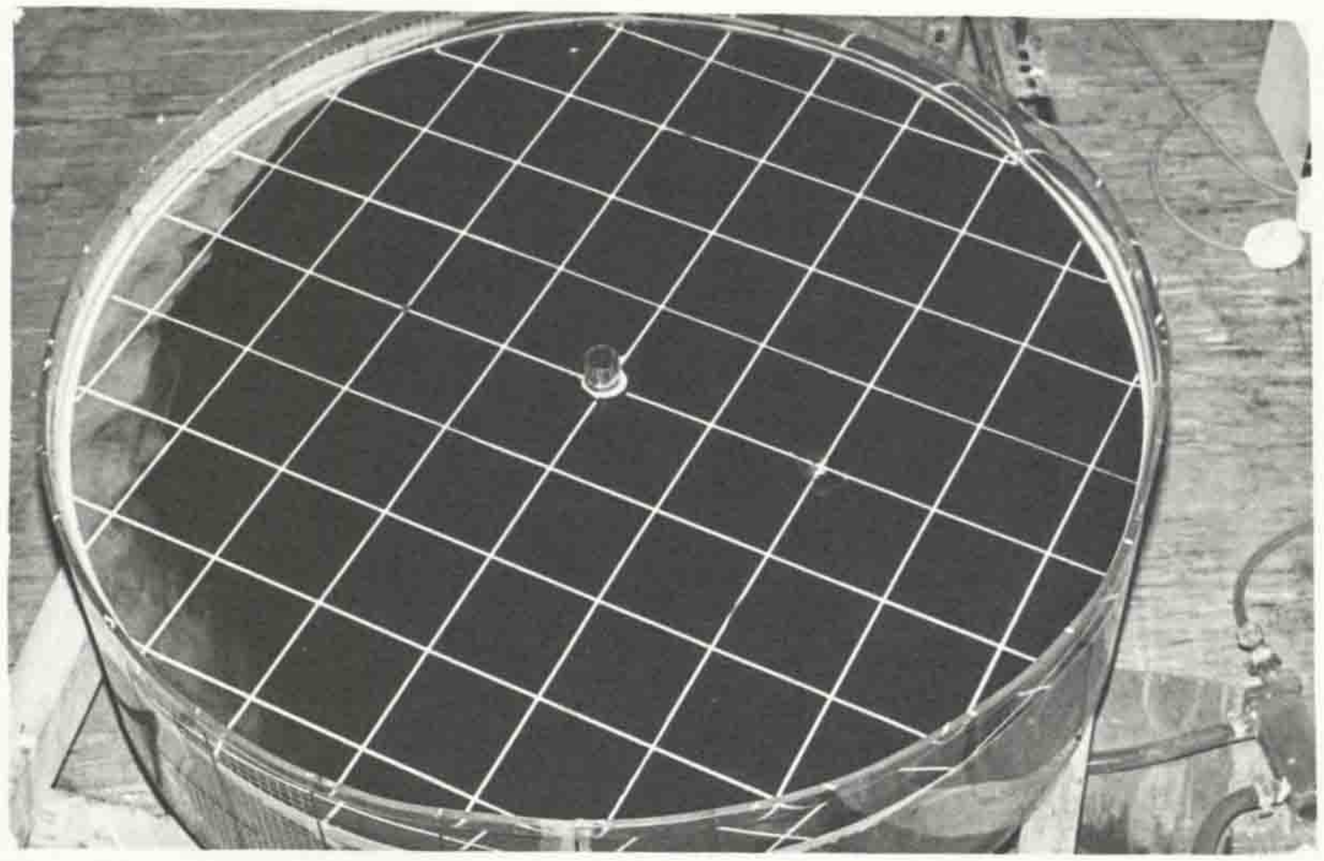

a) 40 sec.

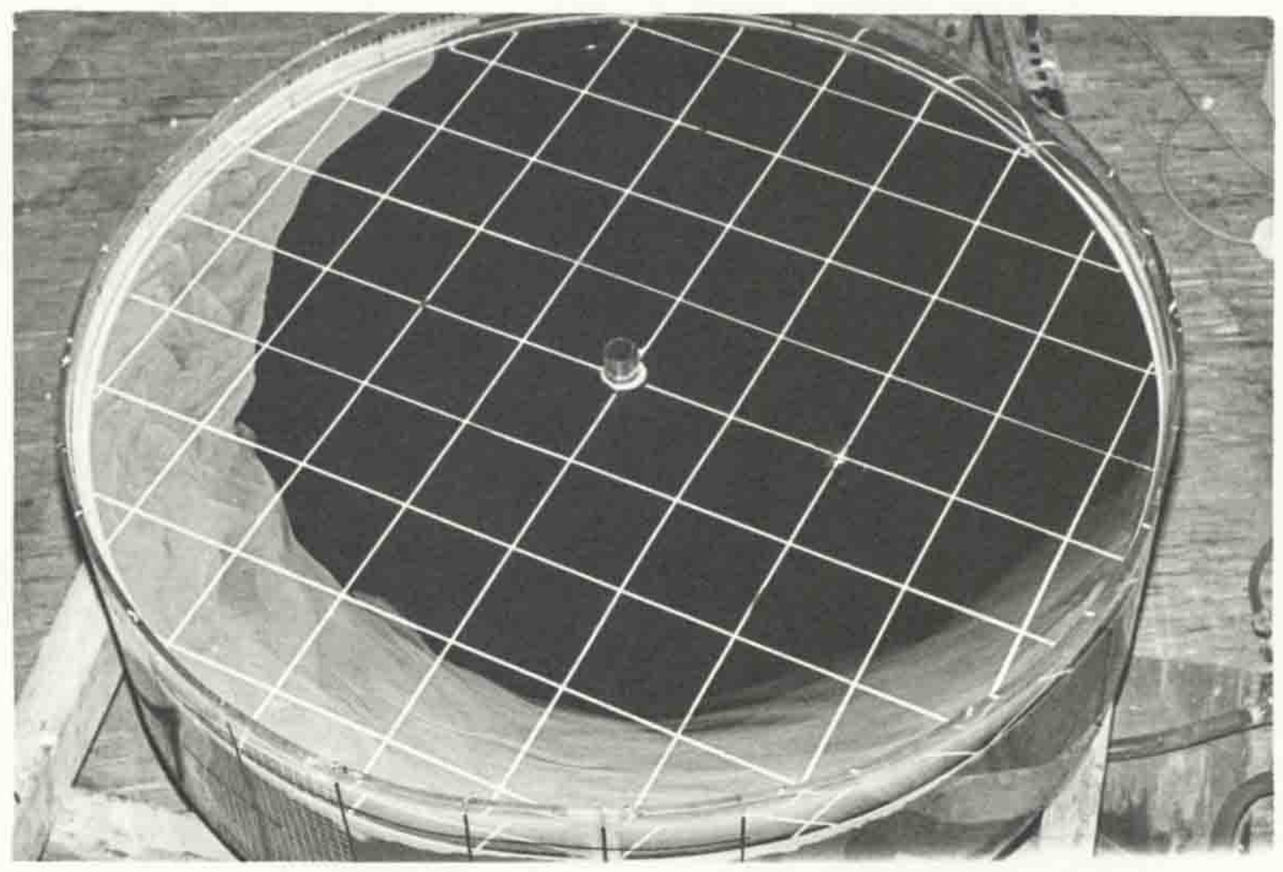

b) 1 min. 40 sec.

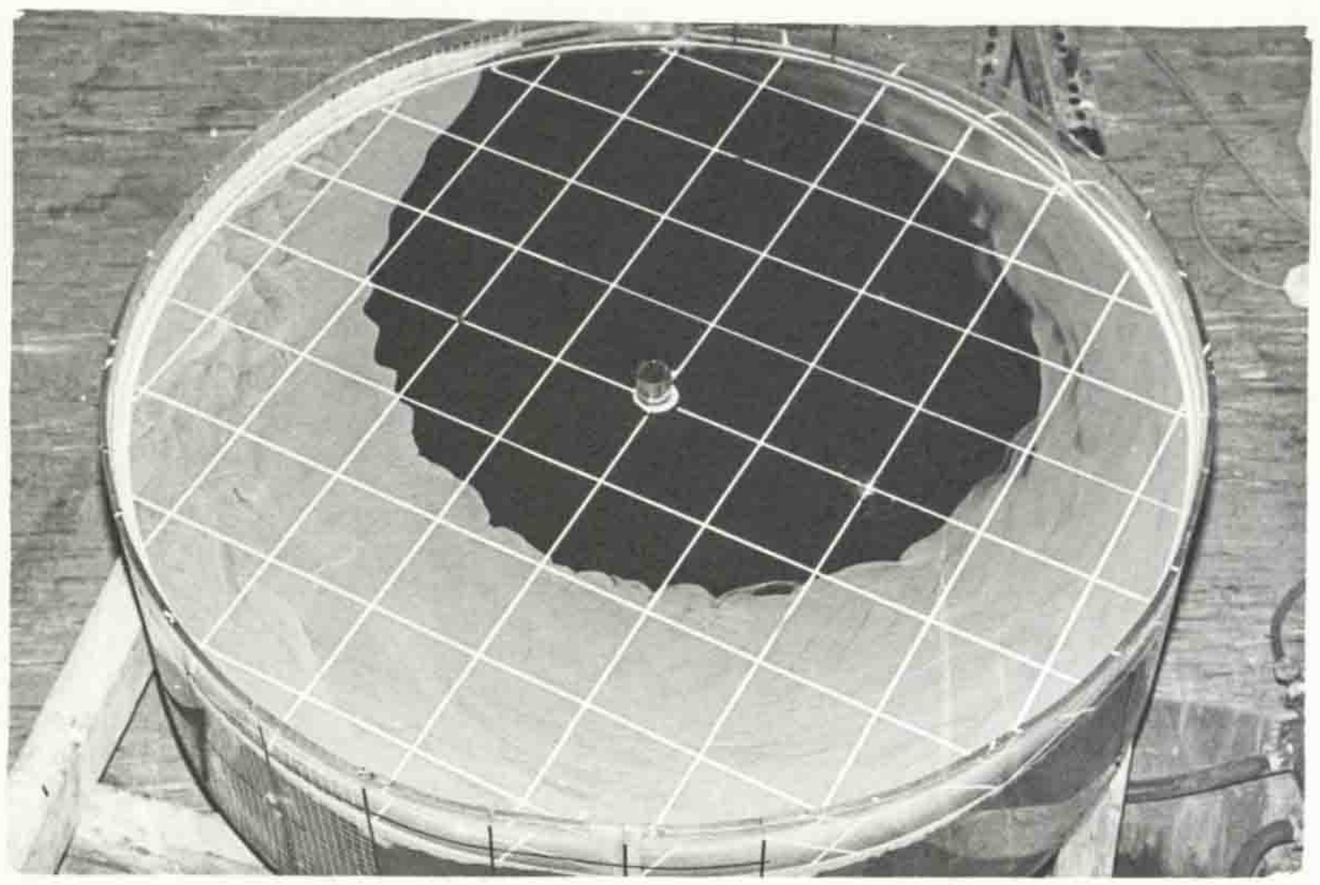

c) 3 min.

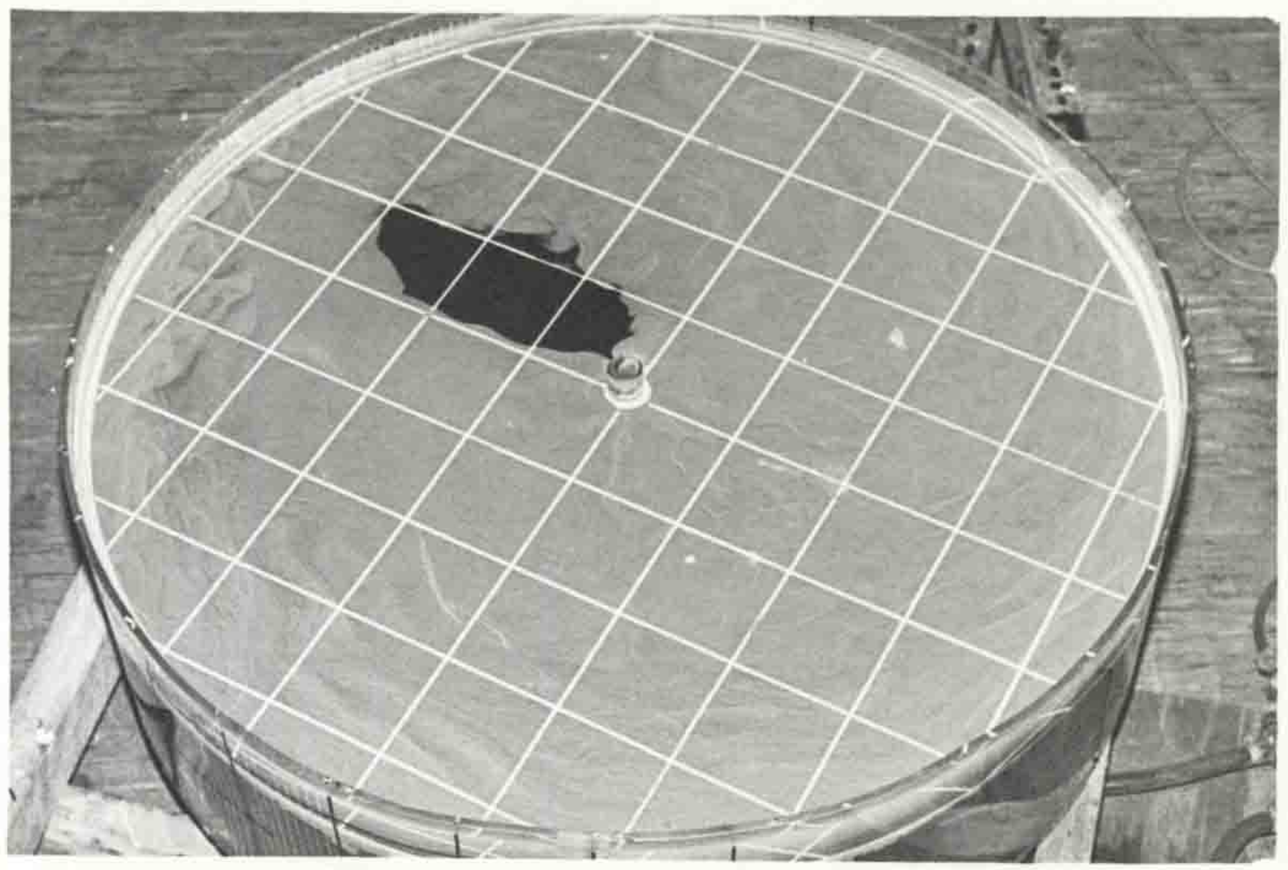

d) 6 min.

Fig. (3.19) Flow patterns in various times ($\frac{L}{h}$ = 19.2, h = 4.8 cm, Q_o = 5.75 cc/sec).

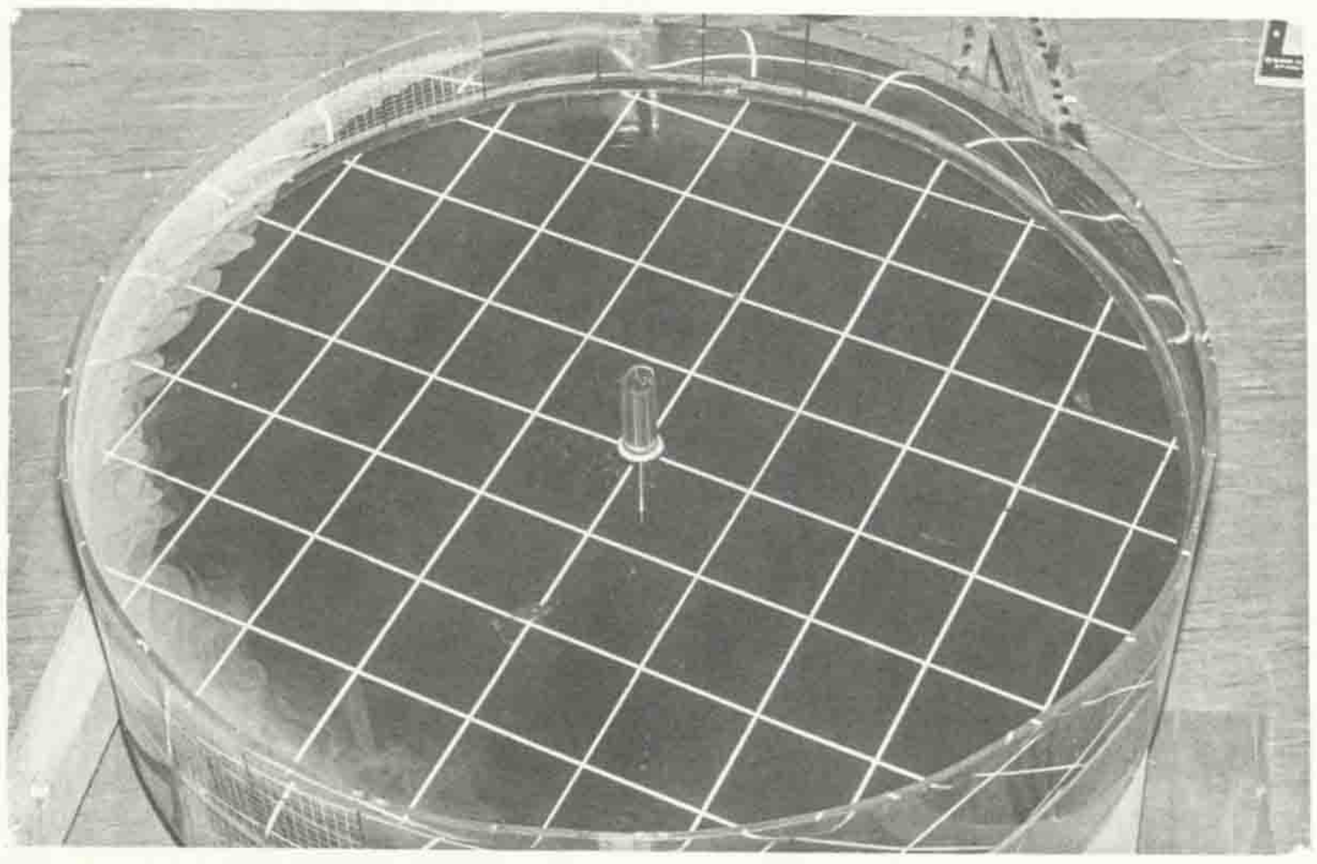

a) 40 sec.

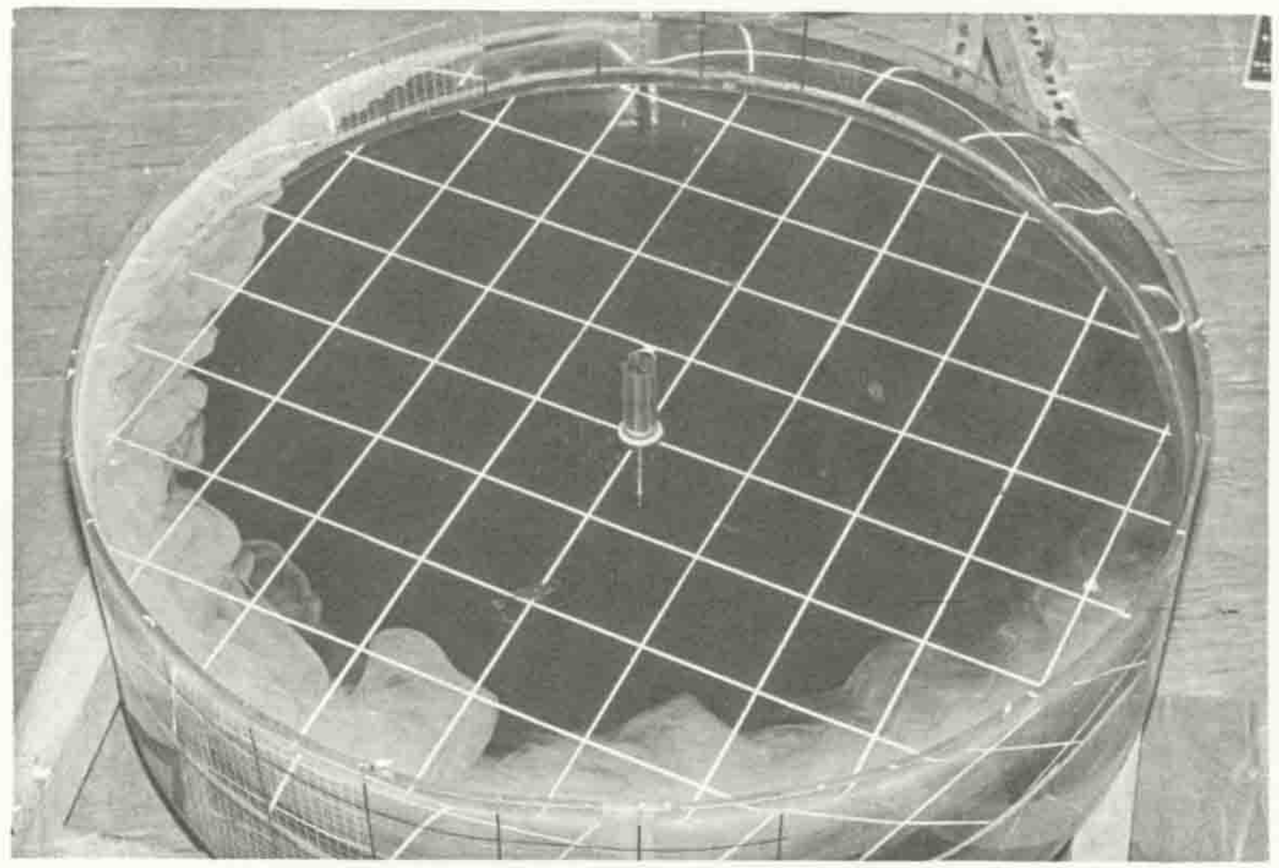

b) 1 min. 20 sec.

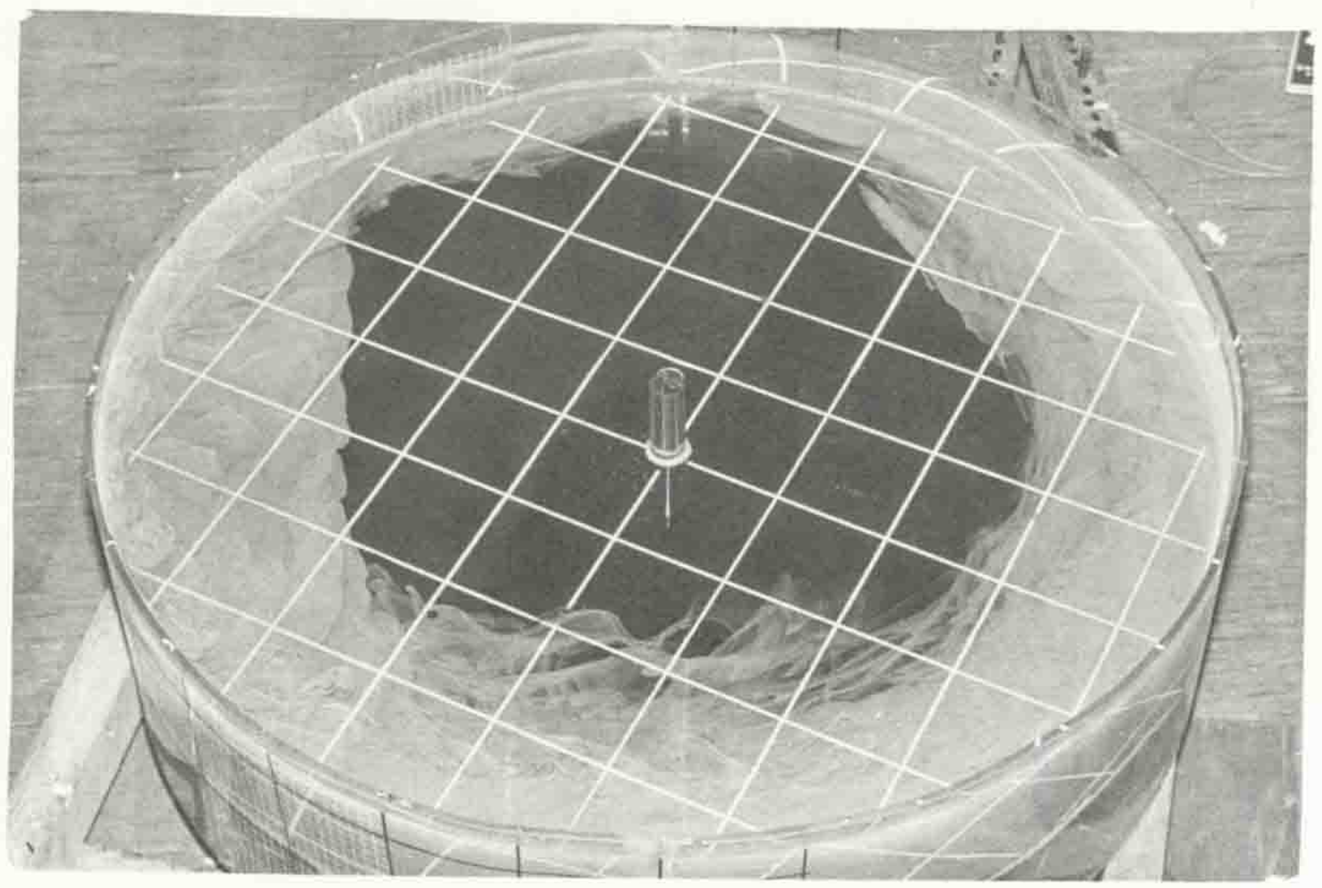

c) 3 min. 10 sec.

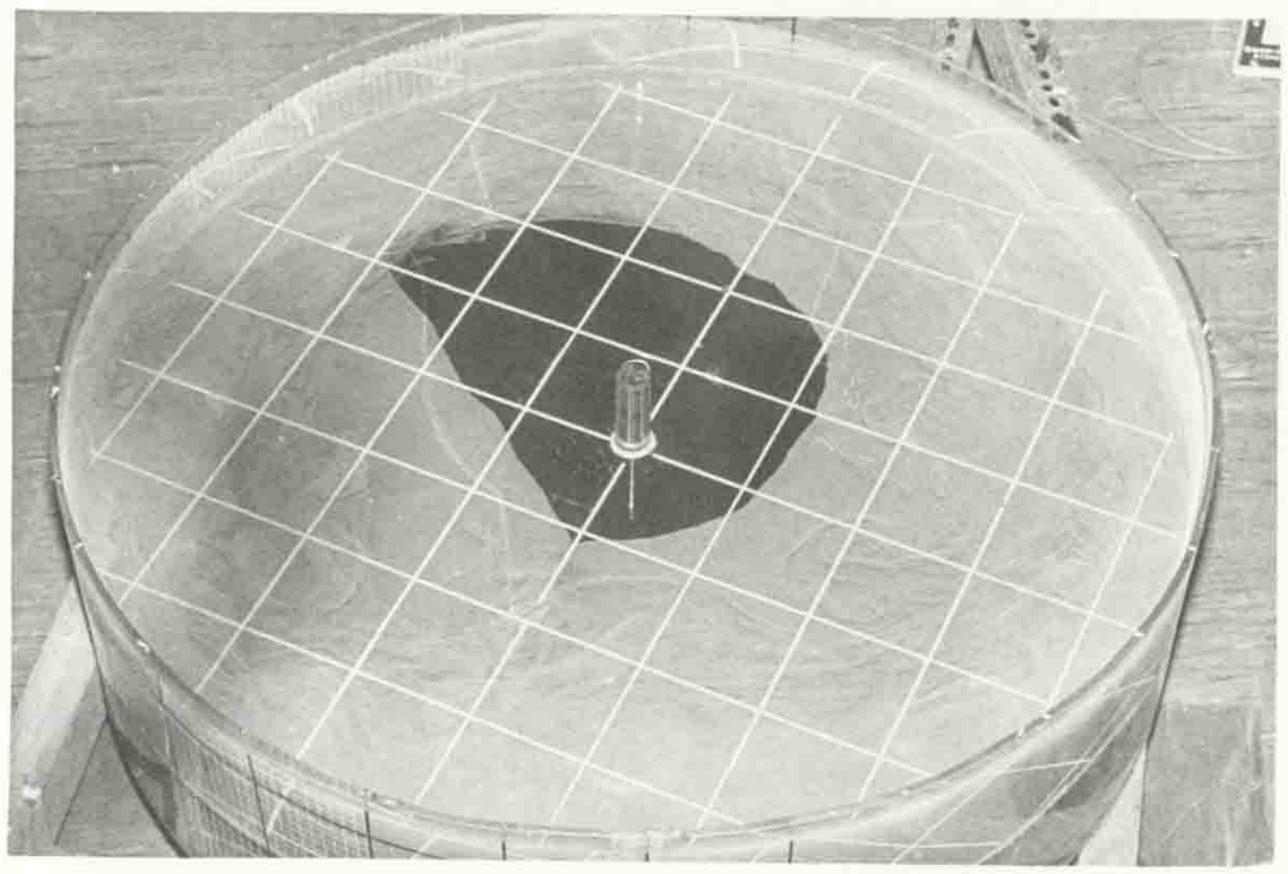

d) 6 min.

Fig. (3.20) Flow patterns in various times ($\frac{L}{h}$ = 7.7, h = 12 cm, Q_o = 5.75 cc/sec).

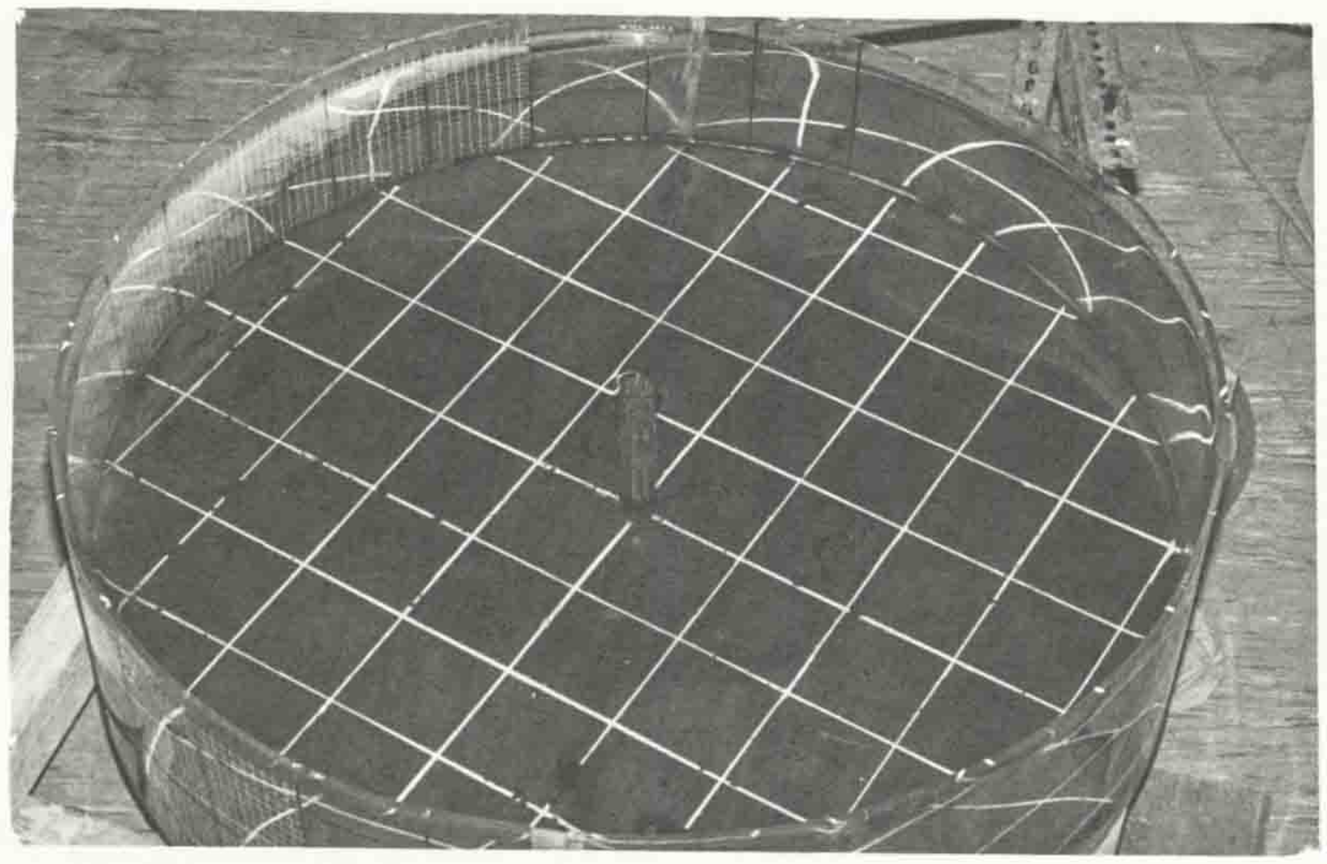

a) 40 sec.

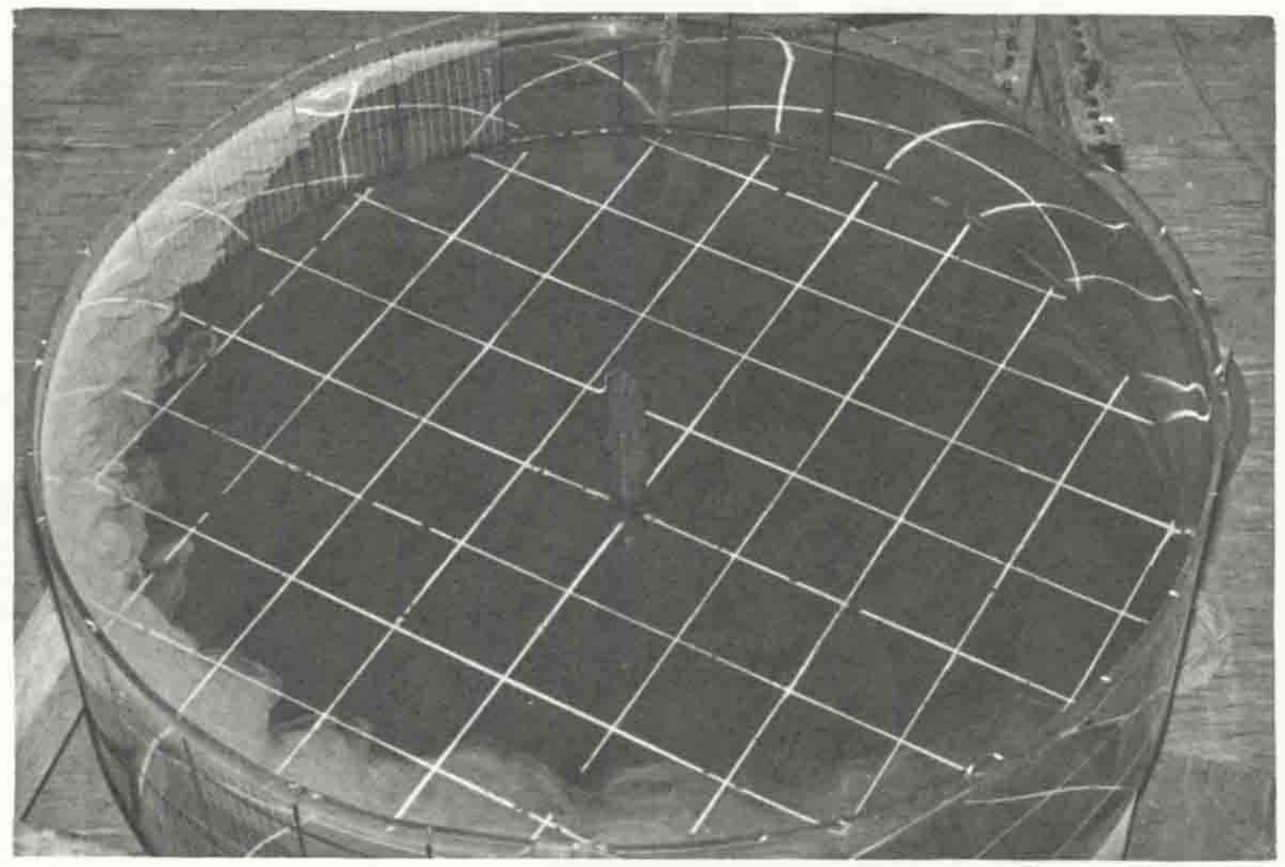

b) 1 min. 30 sec.

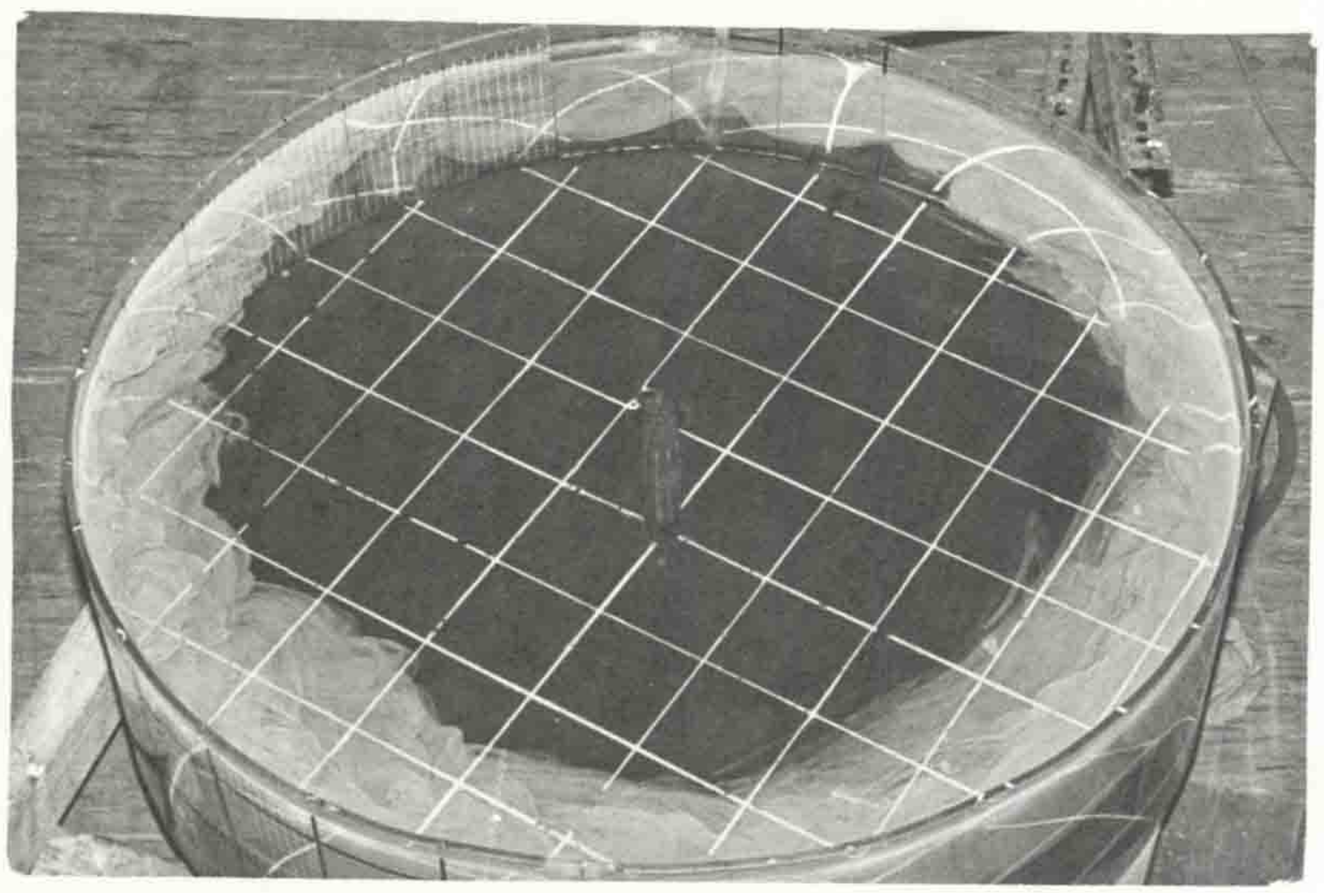

c) 3 min.

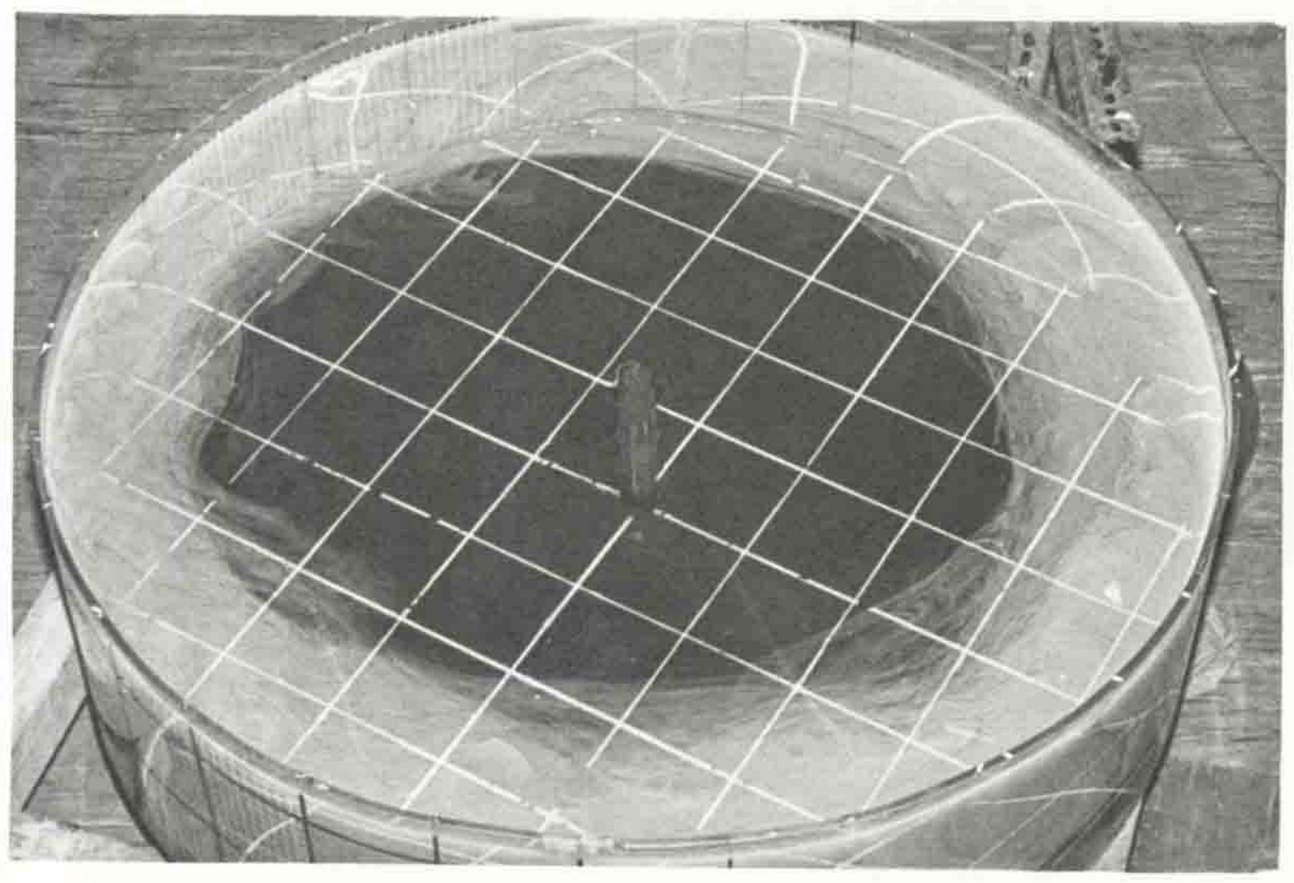

d) 6 min.

Fig. (3.21) Flow patterns in various times ($\frac{L}{h}$ = 4.1, h = 22.5 cm, Q_o = 5.75 cc/sec)

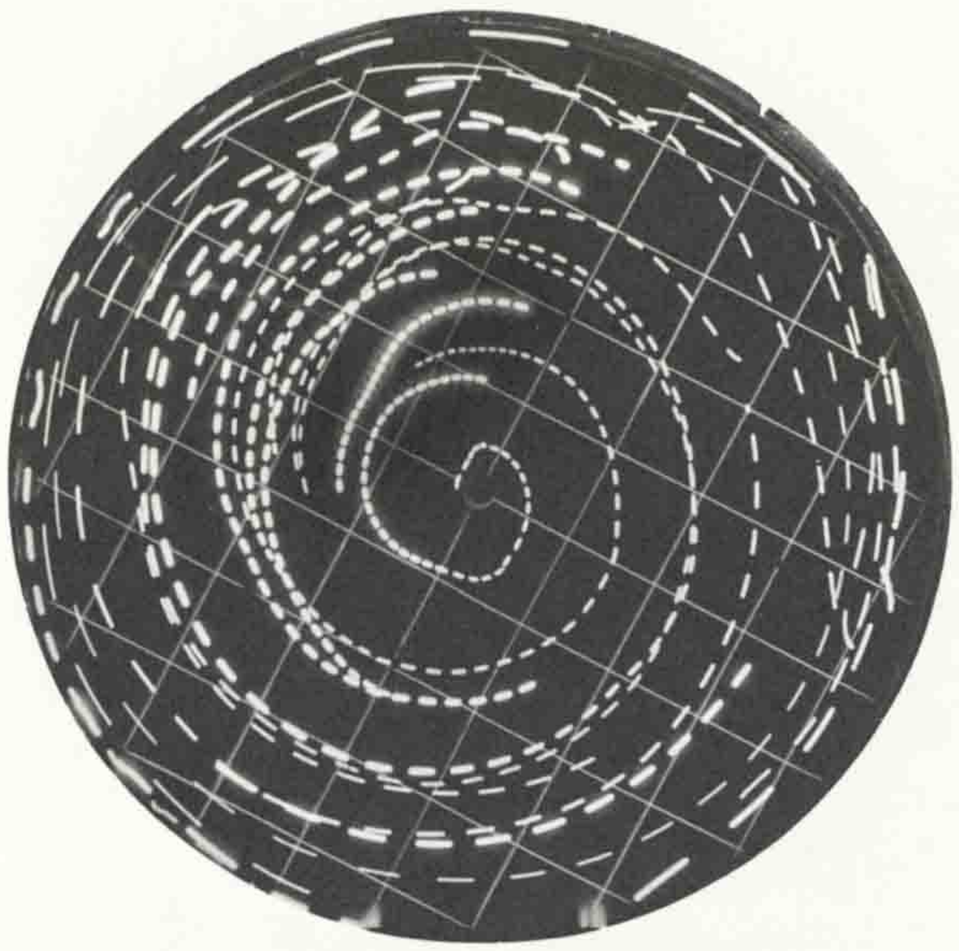

Q_o = 5.75 cc/sec.
lapse time = 5 sec.

Q_o = 12.383 cc/sec.
lapse time = 5 sec.

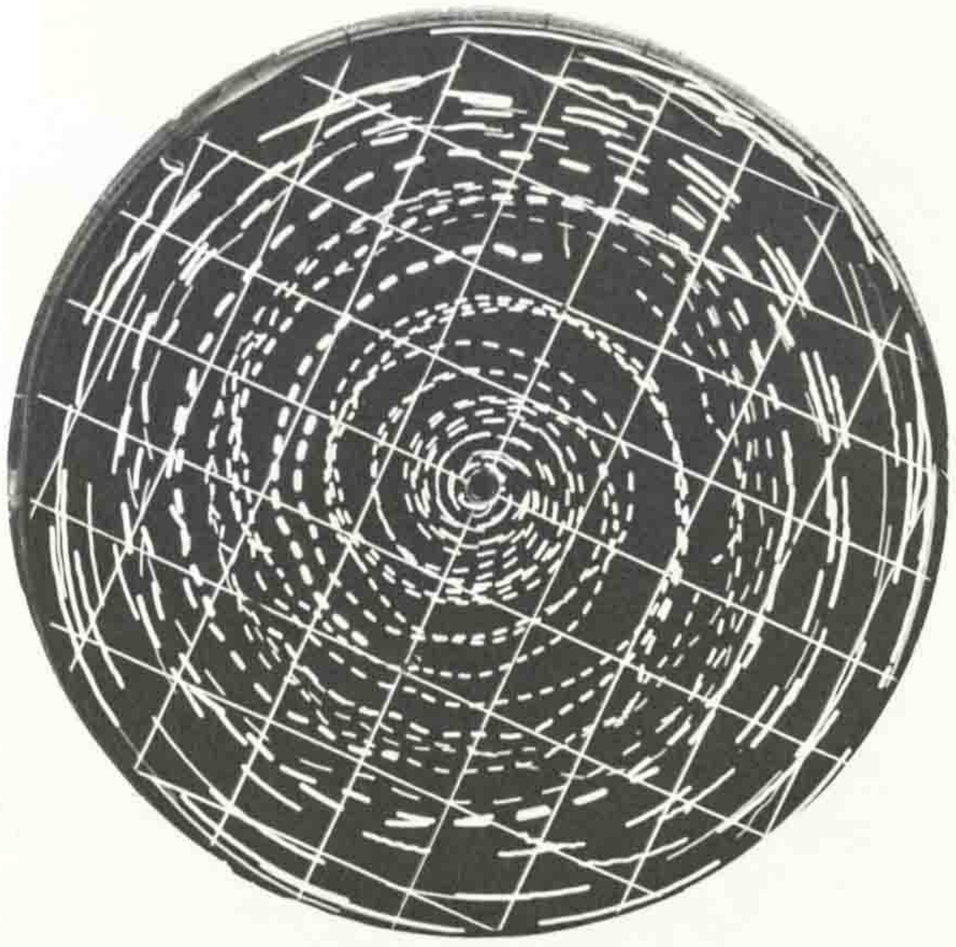

Q_o = 19.66 cc/sec.
lapse time = 3 sec.

h = 4.8 cm
L = 92 cm

Q_o = 30.83 cc/sec.
lapse time = 3 sec.

Fig. (3.22) Circulation patterns illustrated by illuminated floats for various discharges and the same aspect ratio.

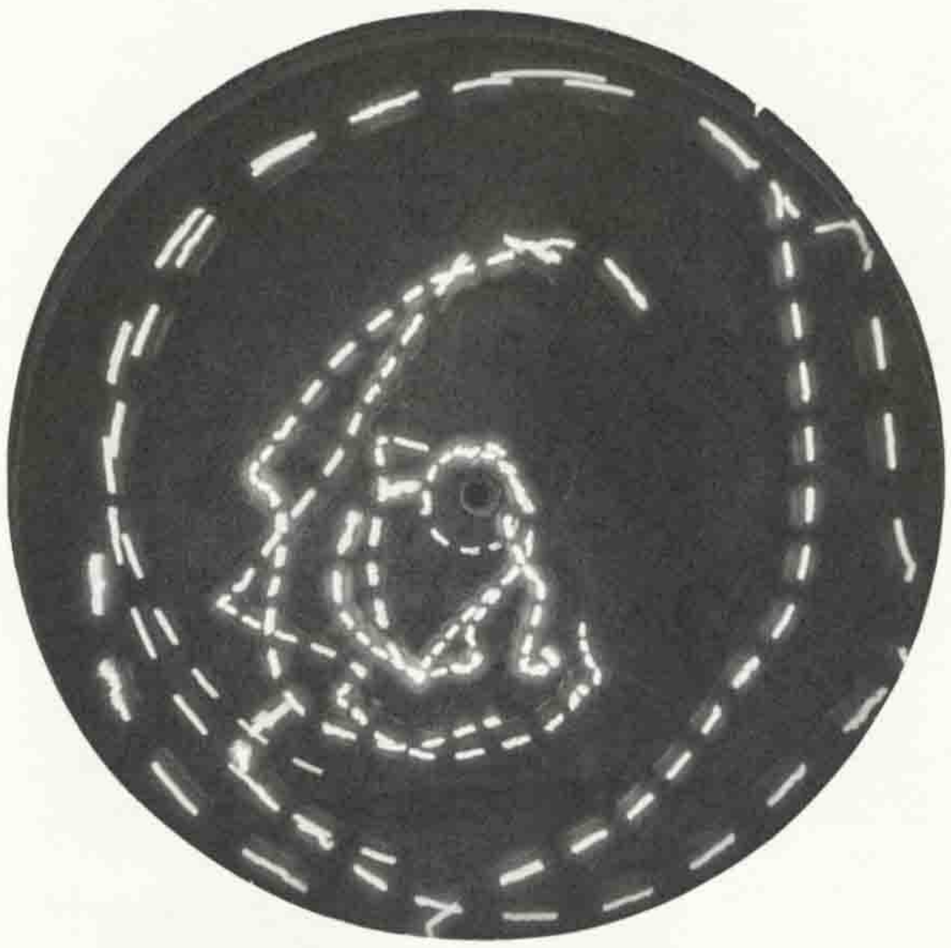

h = 2.5 cm

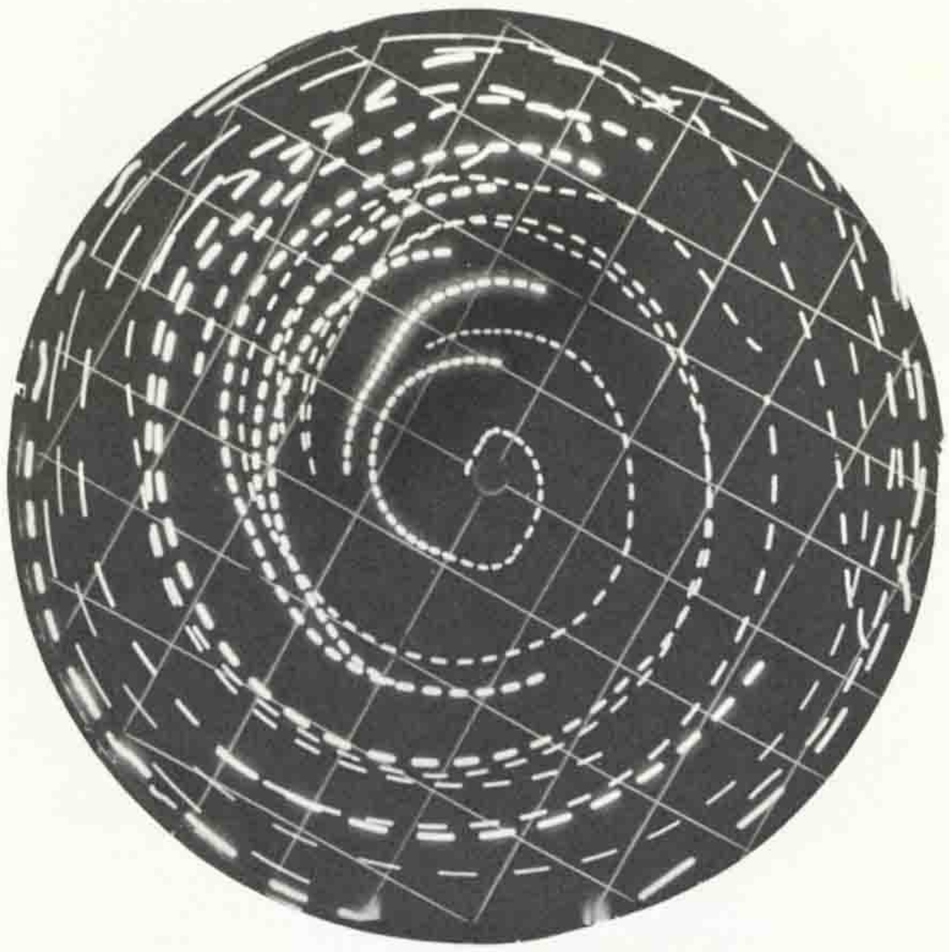

h = 4.8 cm

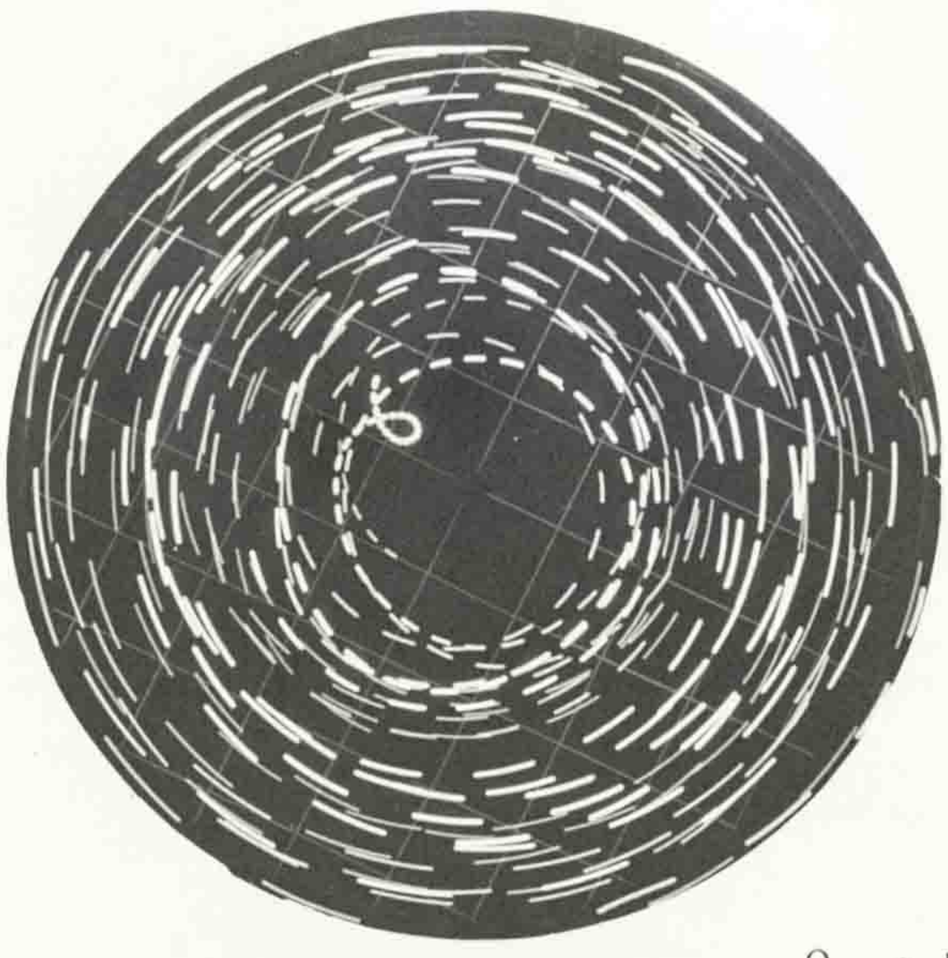

h = 12 cm

Q_0 = 5.75 cc/sec.
L = 92 cm
lapse time = 5 sec.

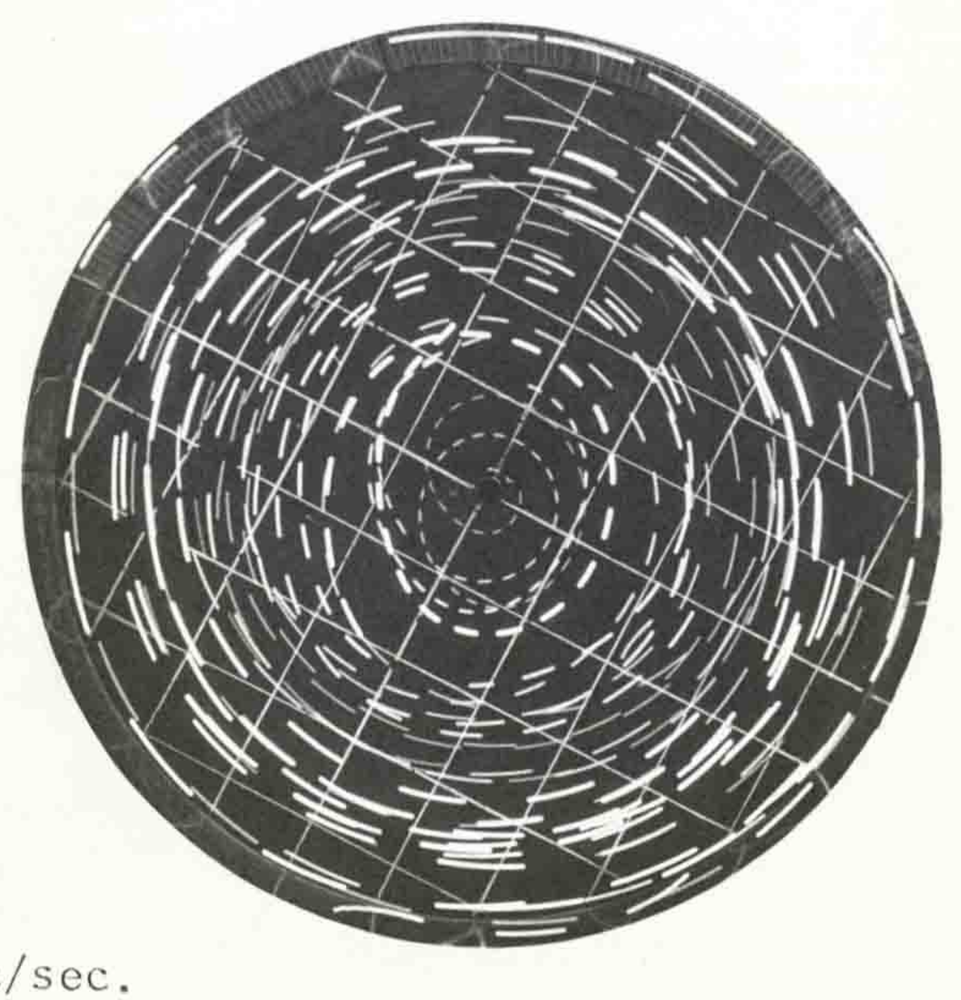

h = 22.5 cm

Fig. (3.23) Circulation patterns illustrated by illuminated floats for various depths and the same discharge.

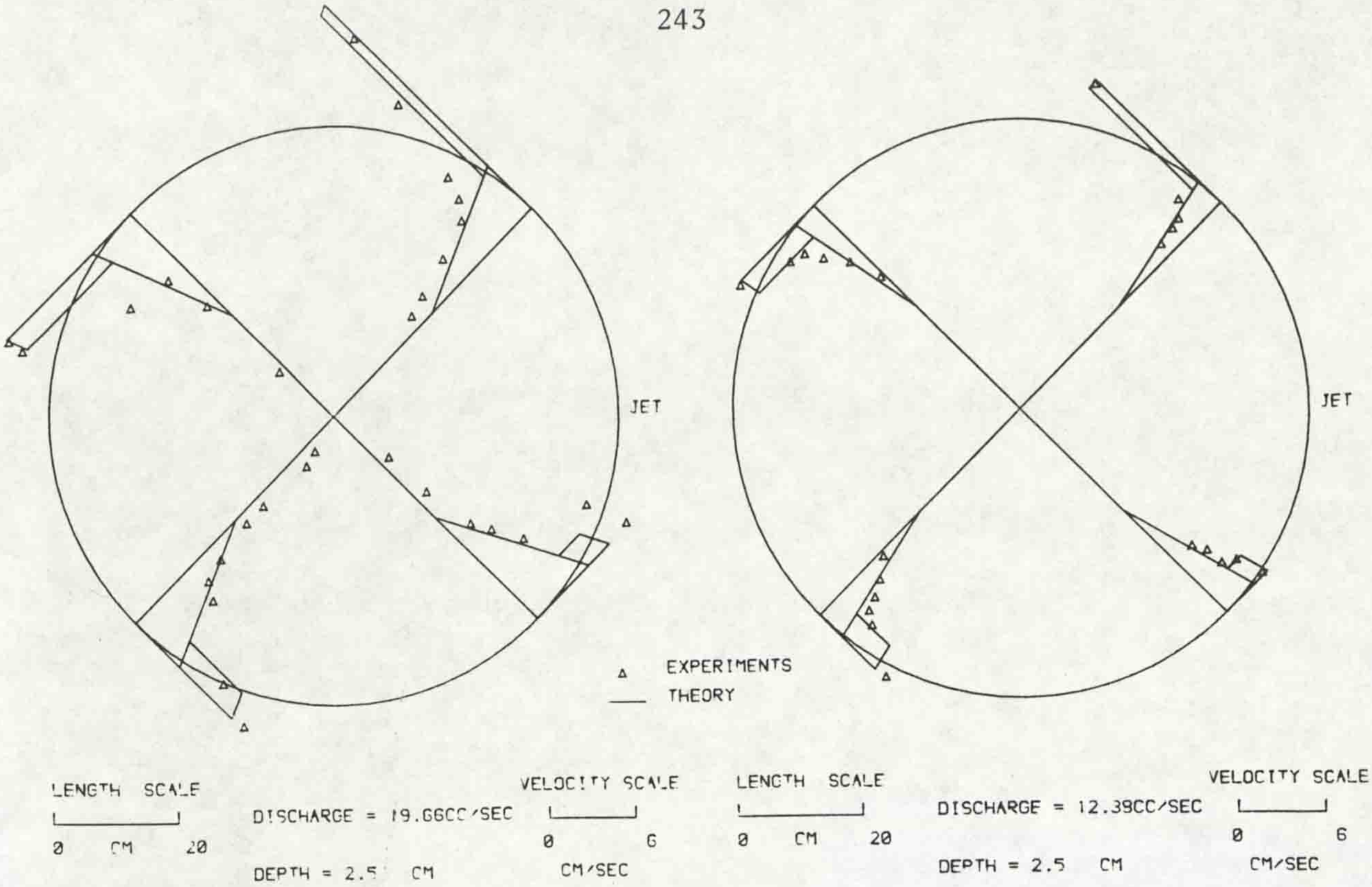

Fig. (3.24a) Measured velocities and comparison with theory for the same depth and various discharges.

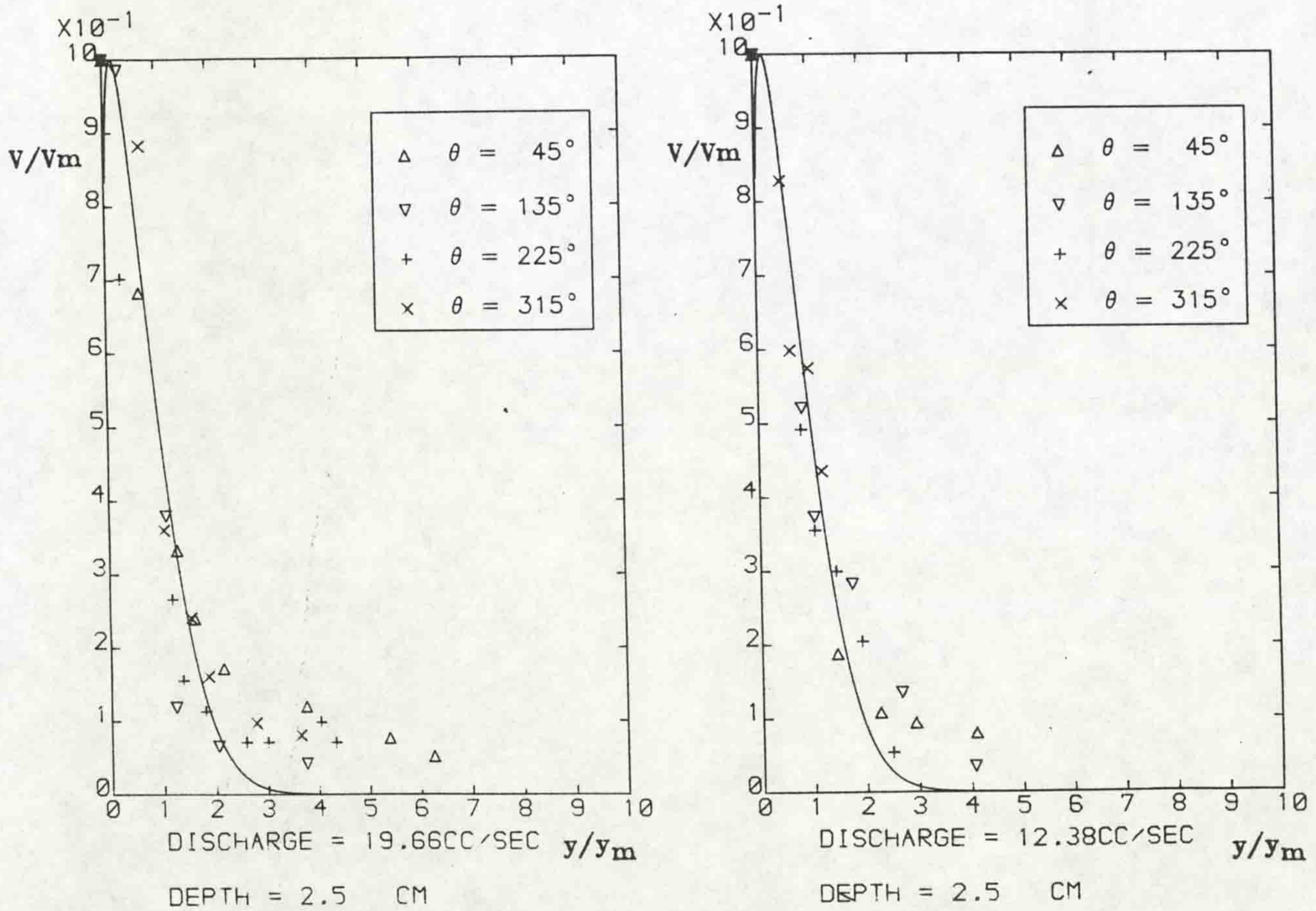

Fig. (3.24b) Dimensionless velocity distribution for the same depth and various discharges.

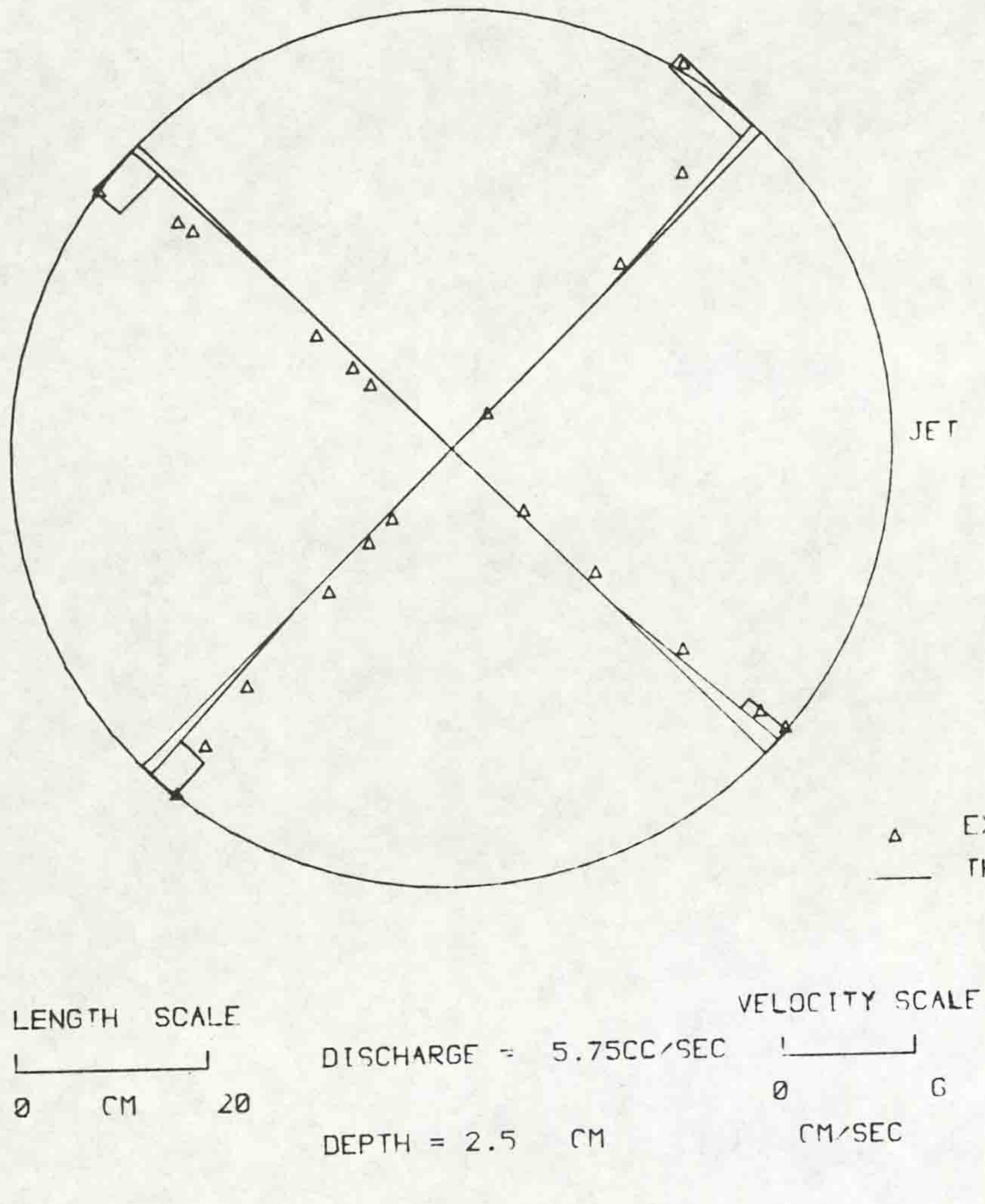

Fig. (3.25a) Measured velocities and comparison with theory.

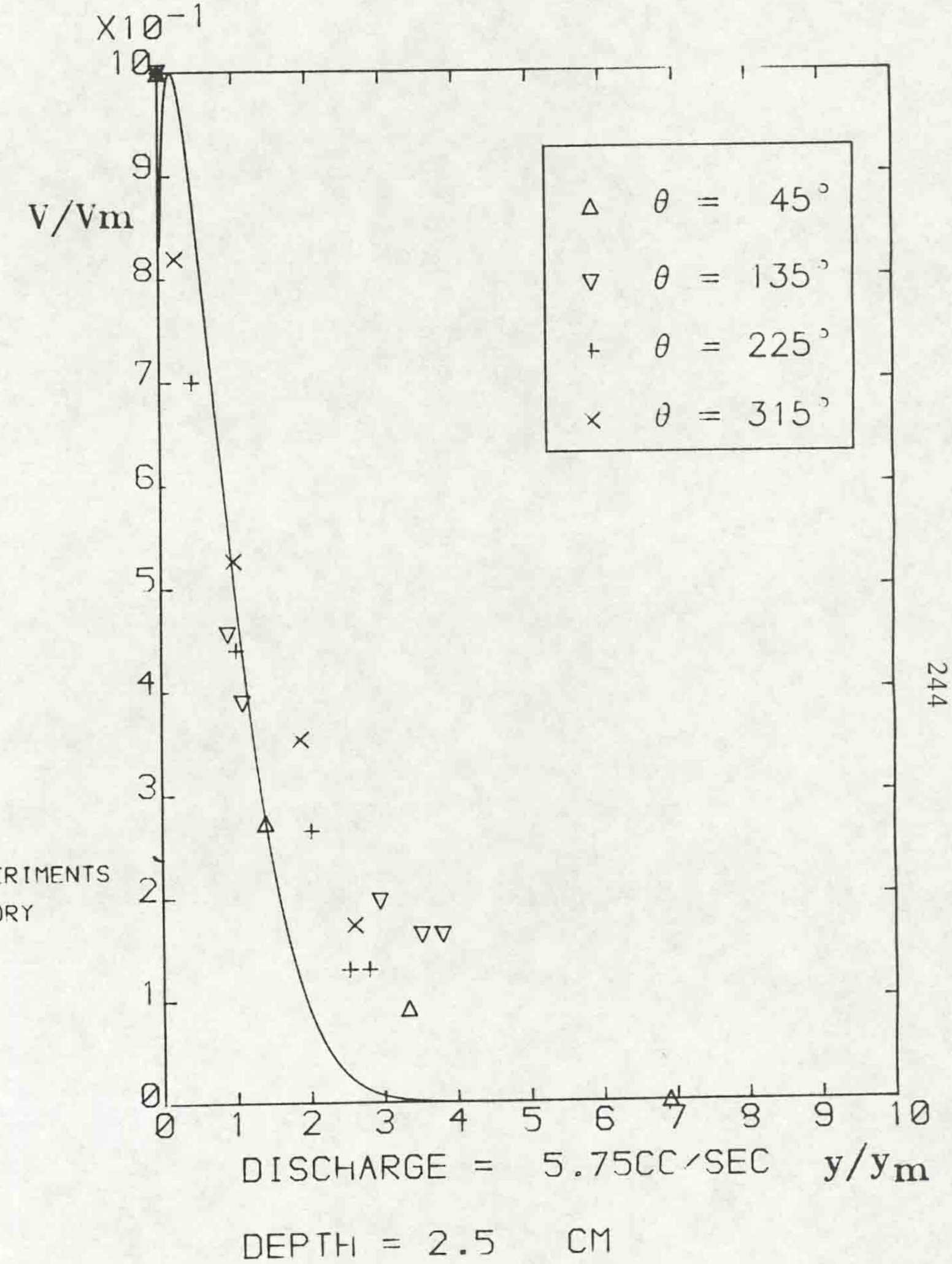

Fig. (3.25b) Dimensionless velocity distribution.

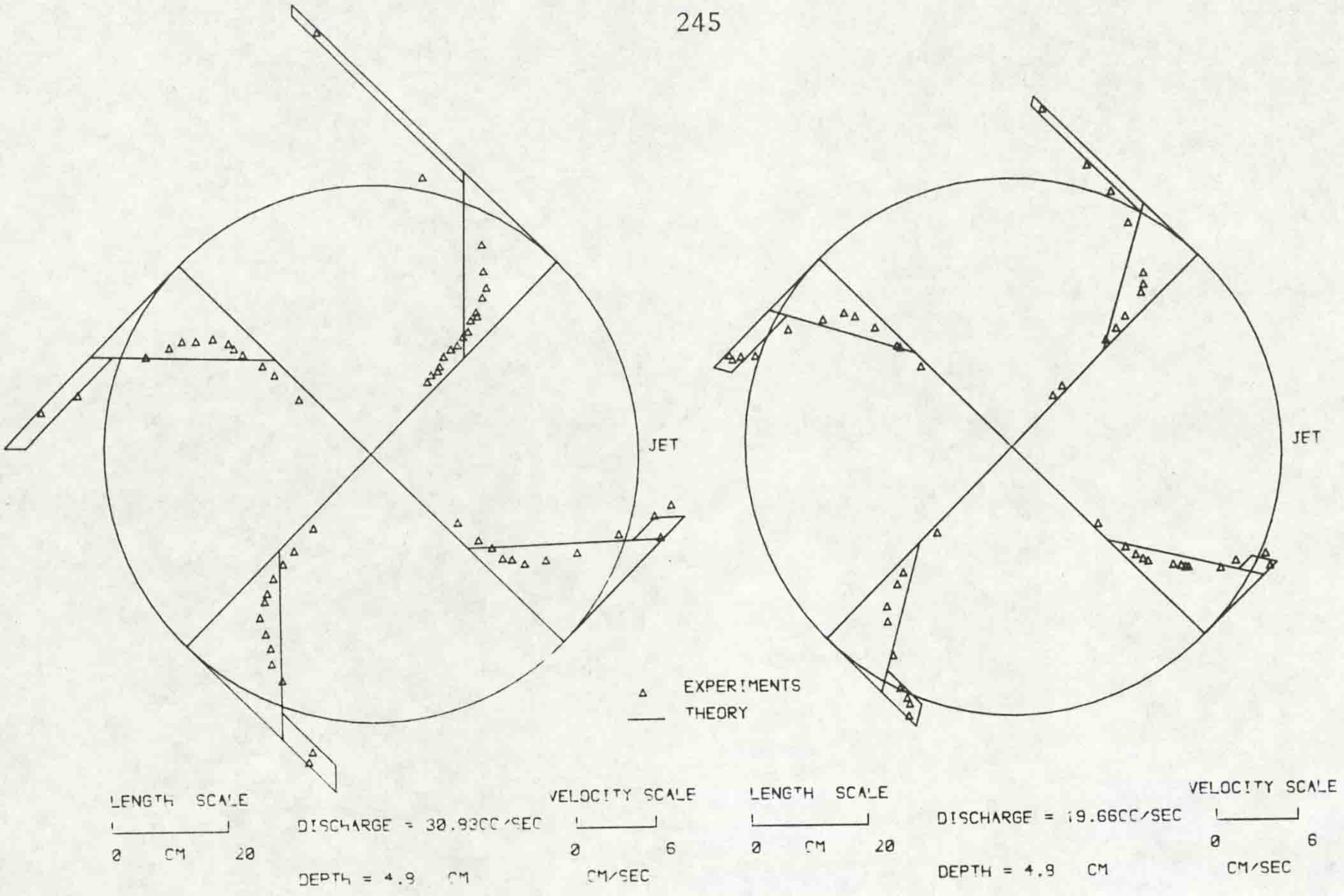

Fig. (3.26a) Measured velocities and comparison with theory for the same depth and various discharges.

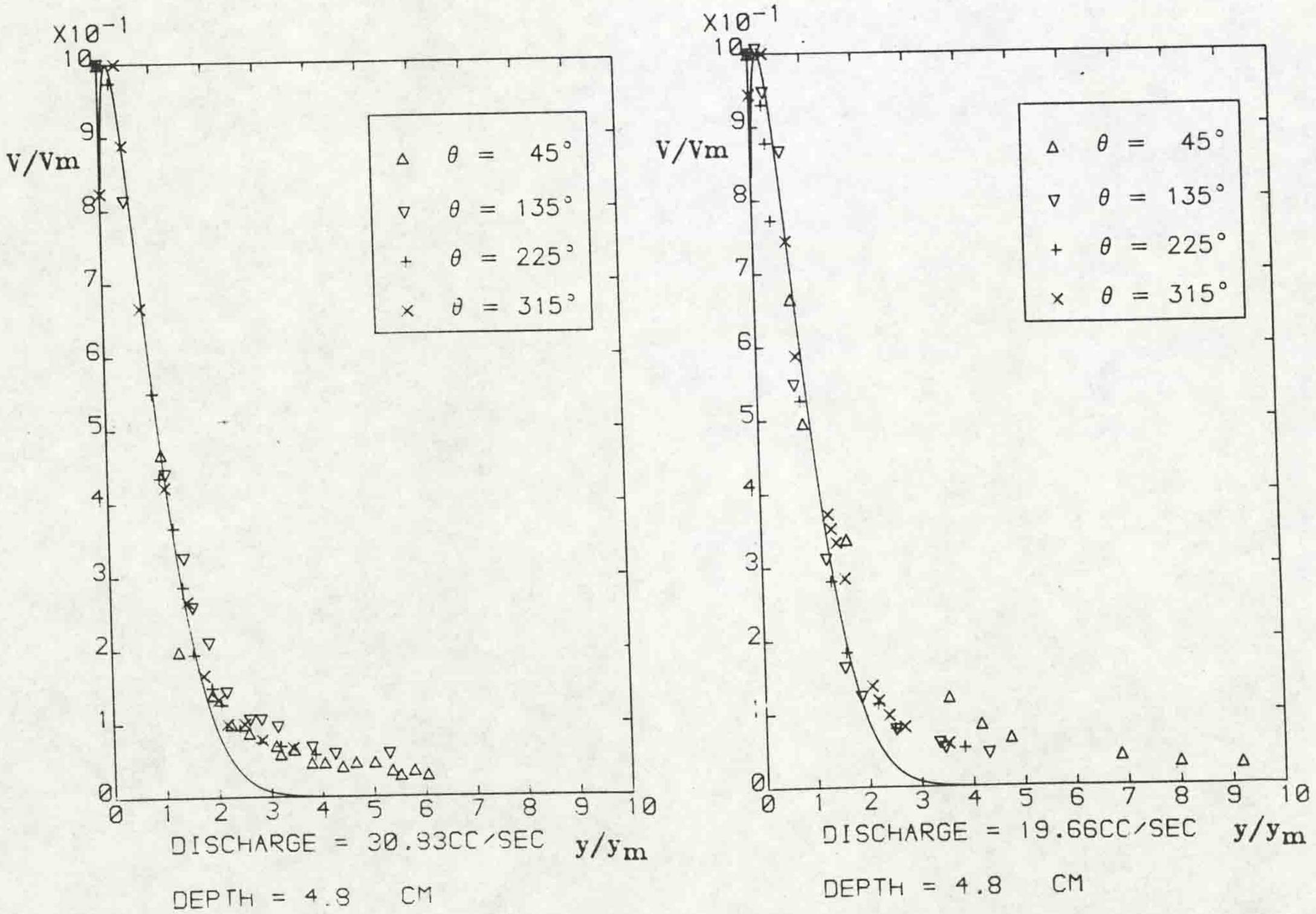

Fig. (3.26b) Dimensionless velocity distribution for the same depth and various discharges.

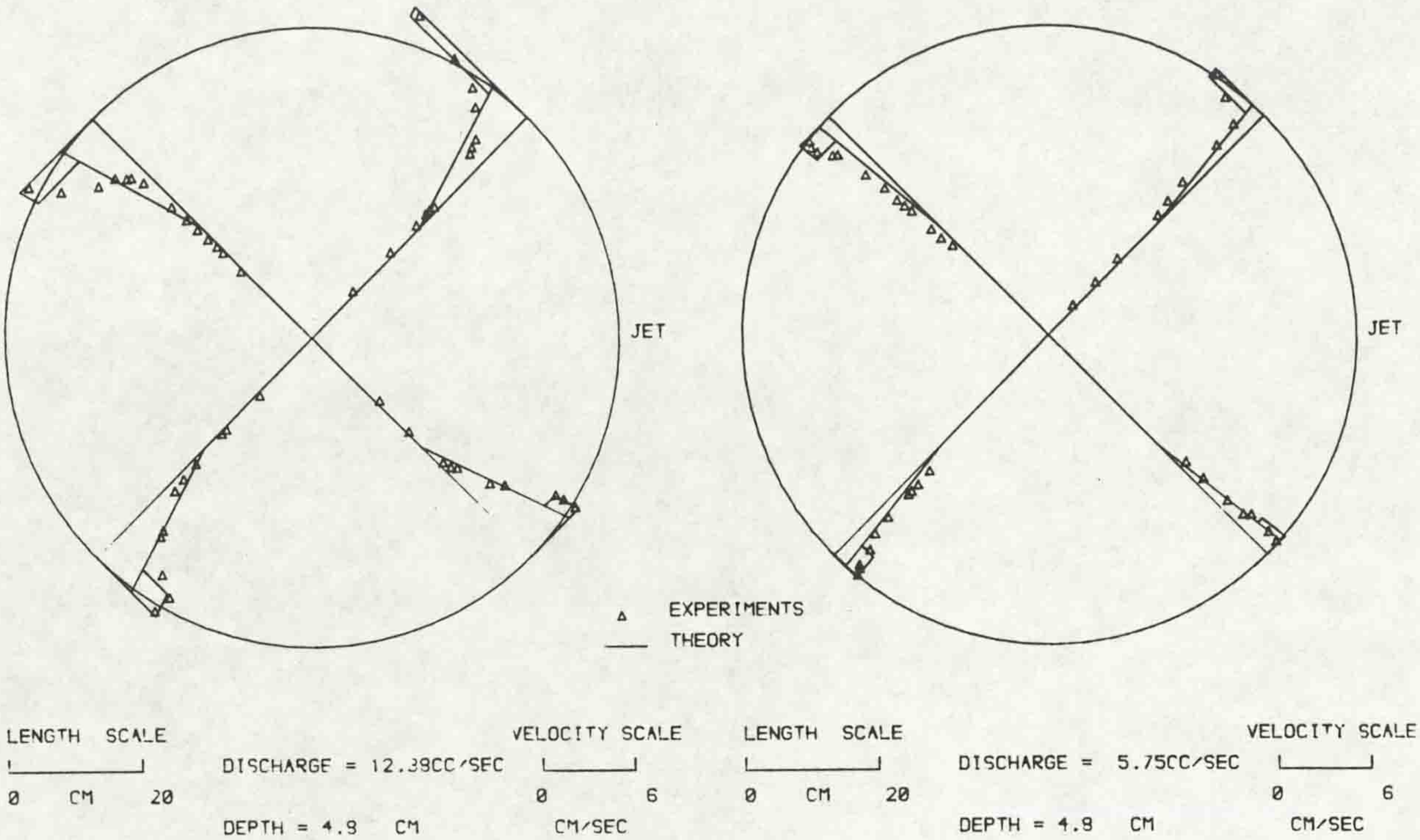

Fig. (3.27a) Measured velocities and comparison with theory for the same depth and various discharges.

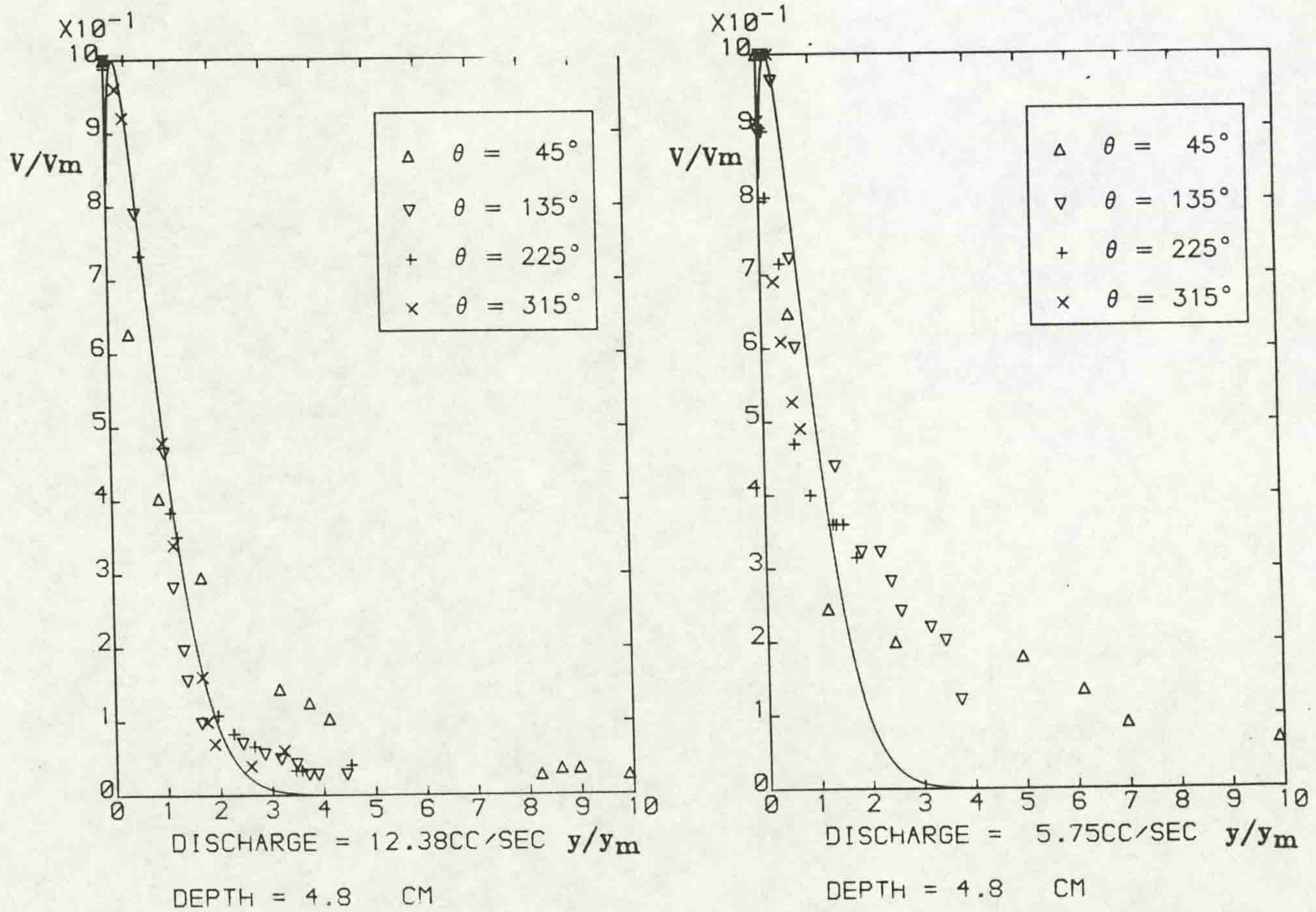

Fig. (3.27b) Dimensionless velocity distribution for the same depth and various discharges.

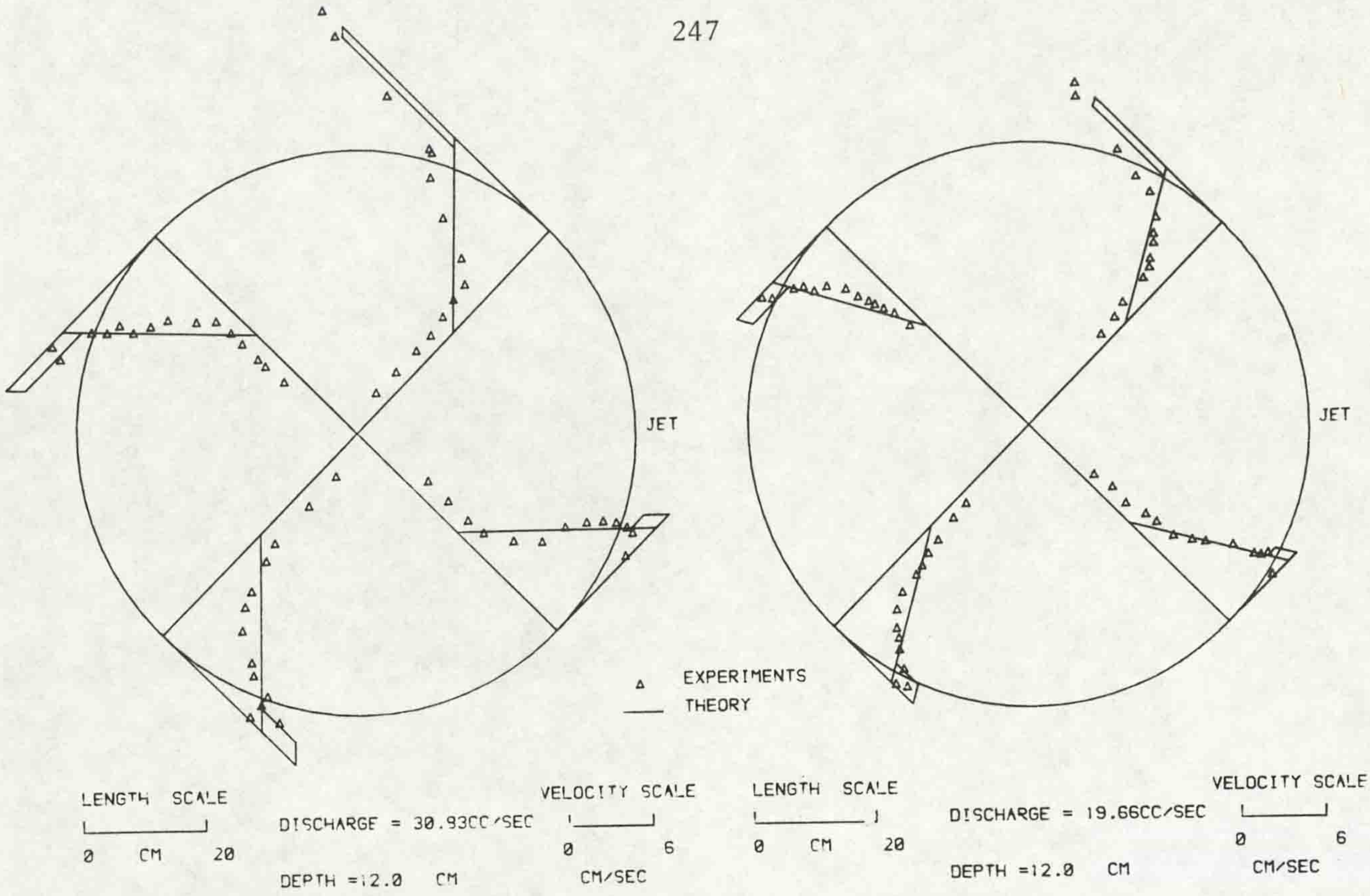

Fig. (3.28a) Measured velocities and comparison with theory for the same depth and various discharges.

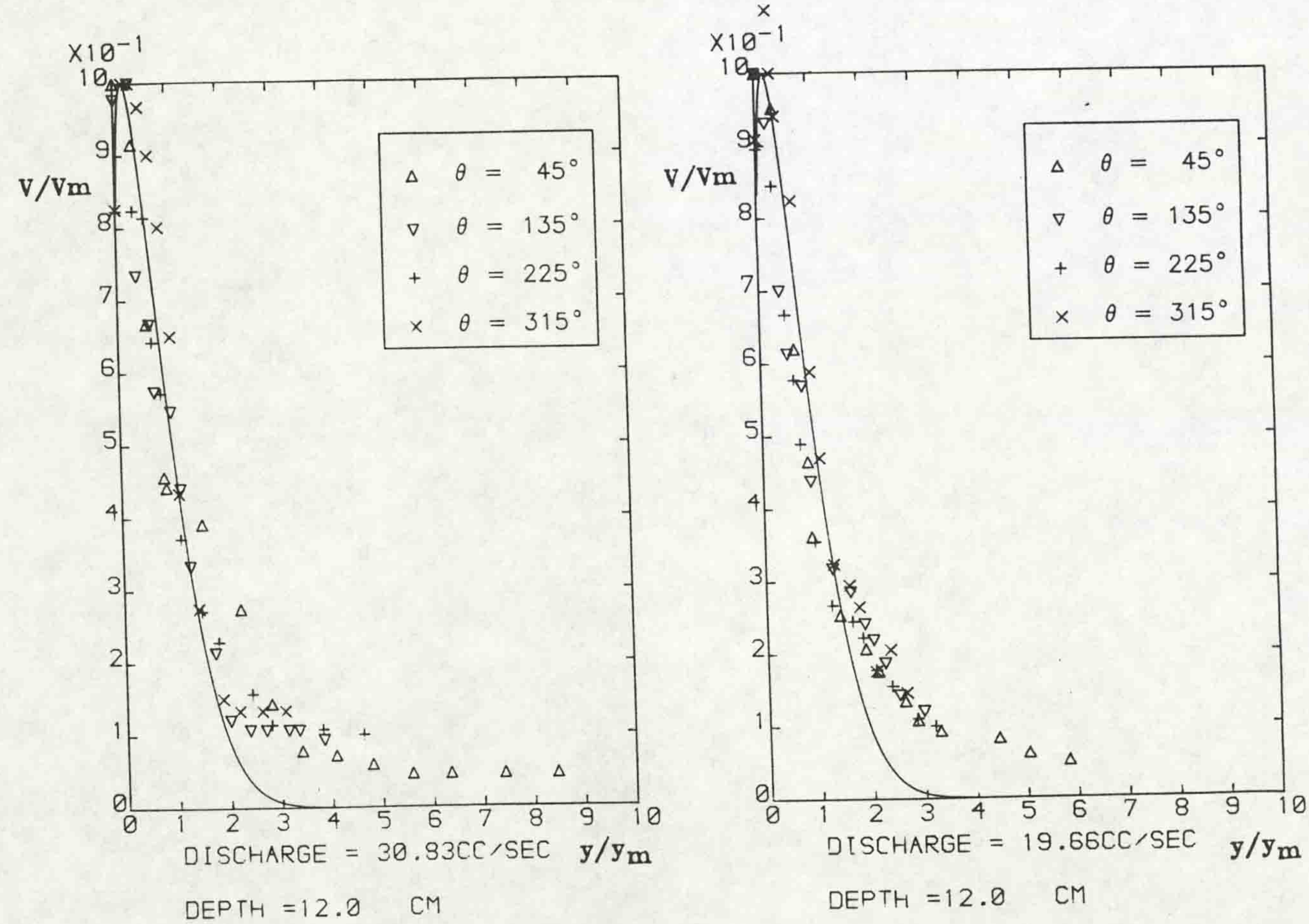

Fig. (3.28b) Dimensionless velocity distribution for the same depth and various discharges.

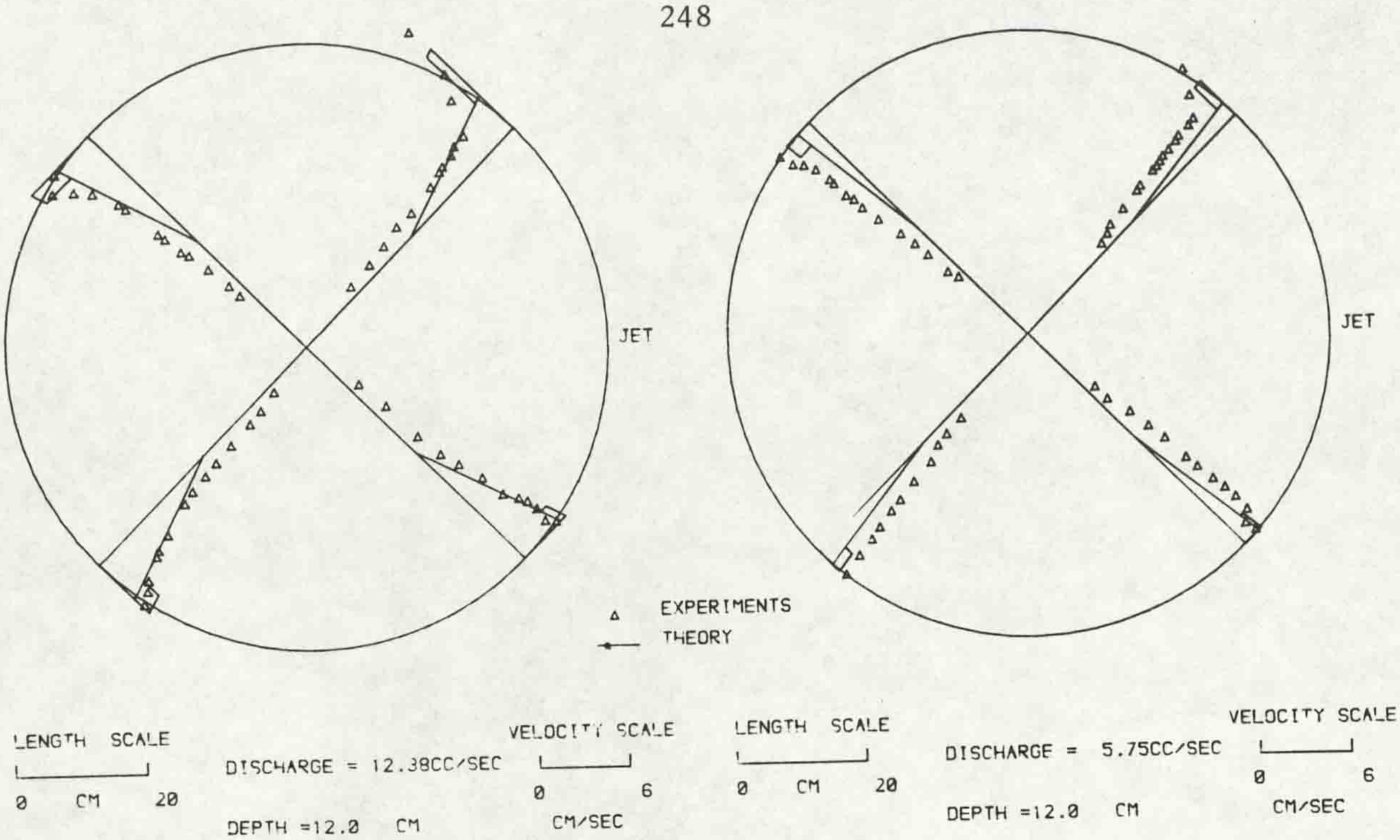

Fig. (3.29a) Measured velocities and comparison with theory for the same depth and various discharges.

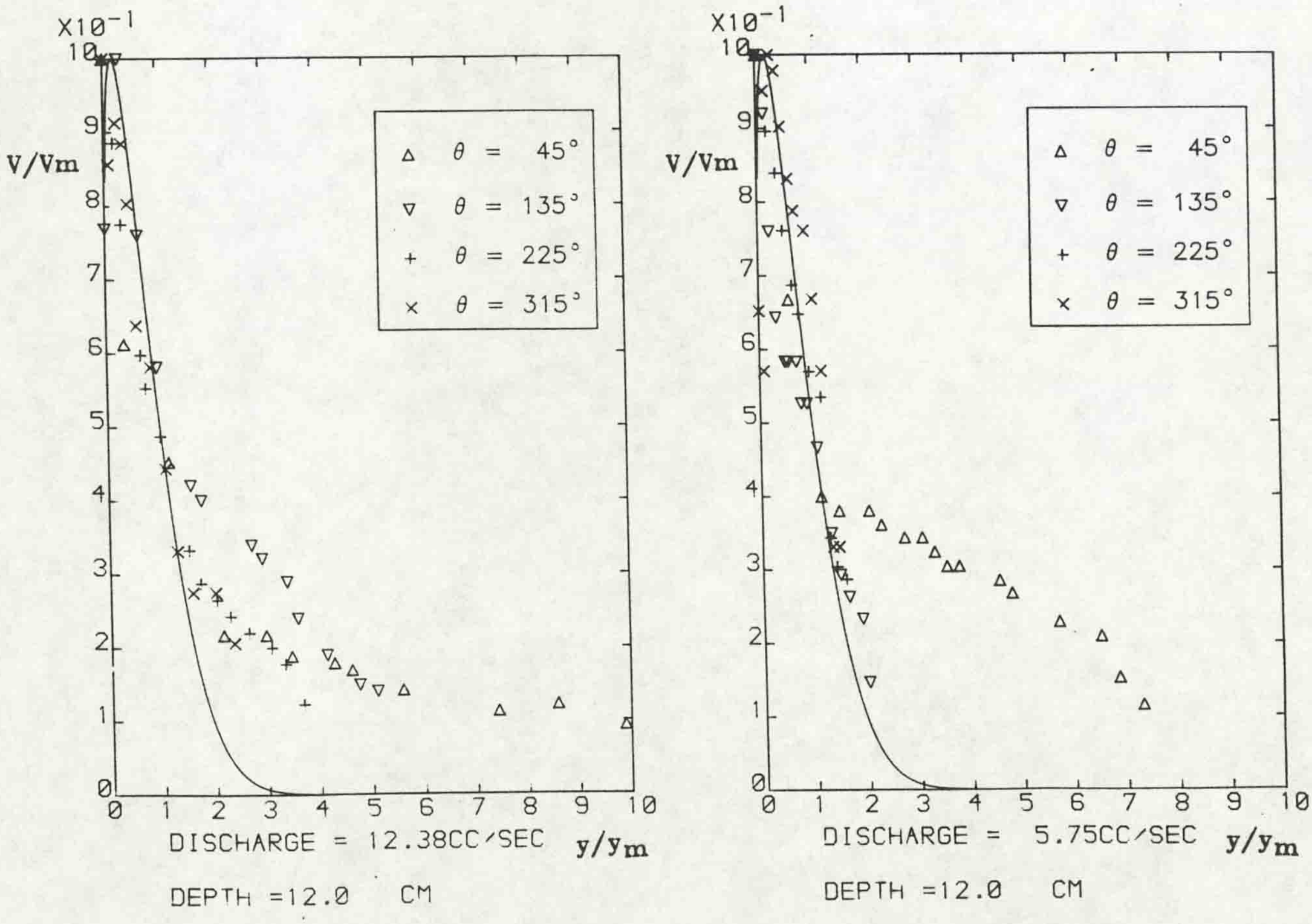

Fig. (3.29b) Dimensionless velocity distribution for the same depth and various discharges.

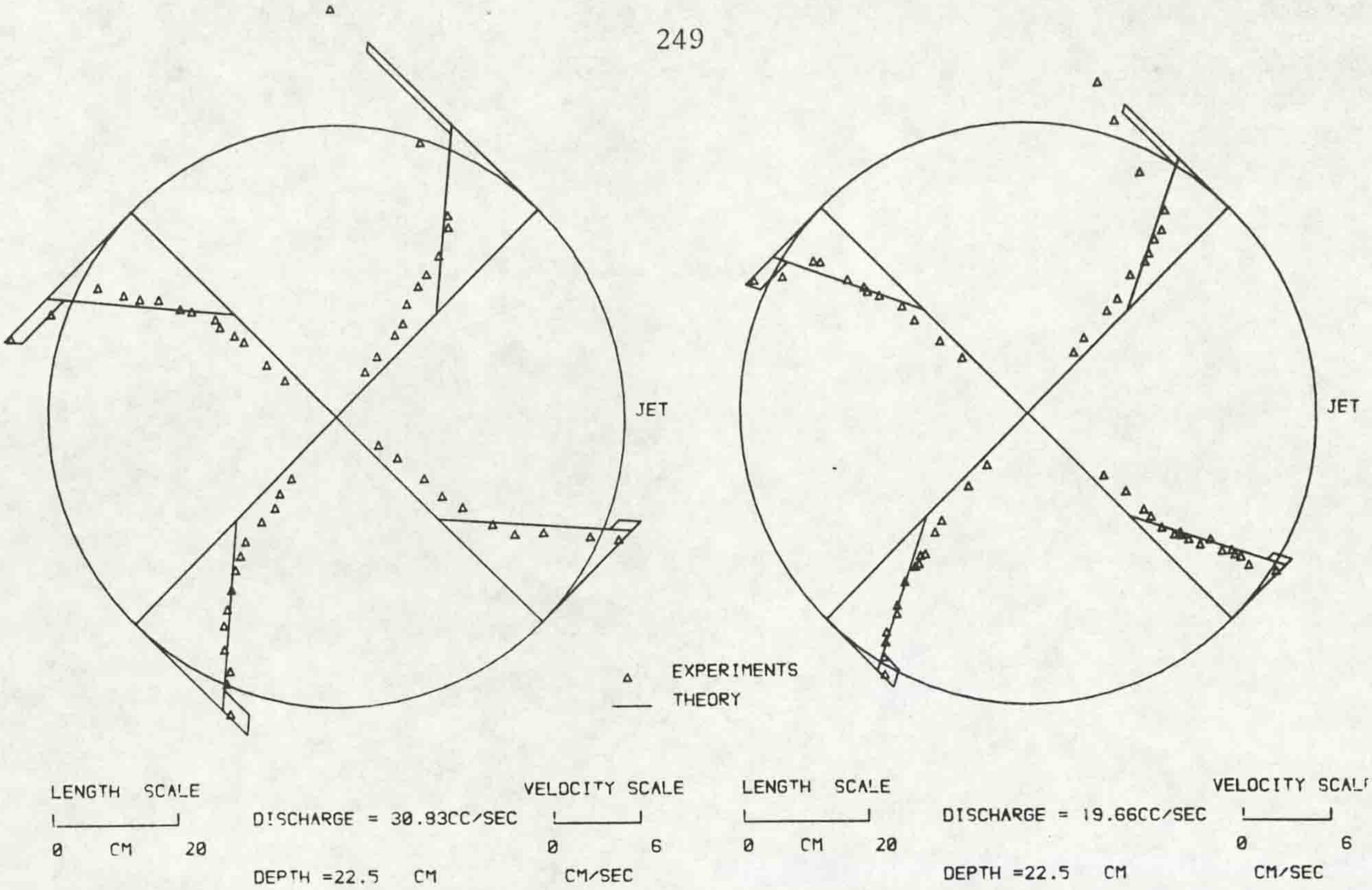

Fig. (3.30a) Measured velocities and comparison with theory for the same depth and various discharges.

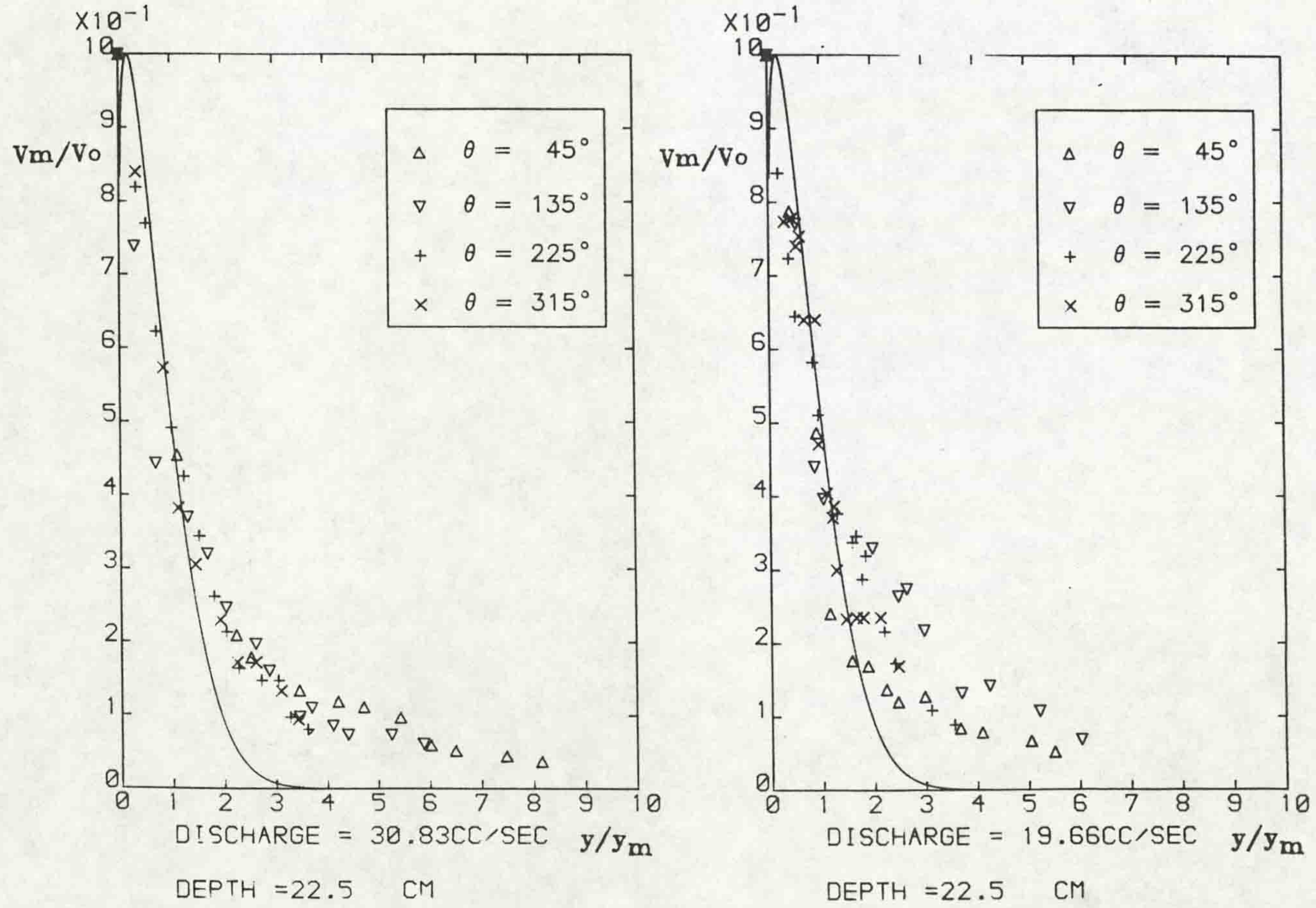

Fig. (3.30b) Dimensionless velocity distribution for the same depth and various discharges.

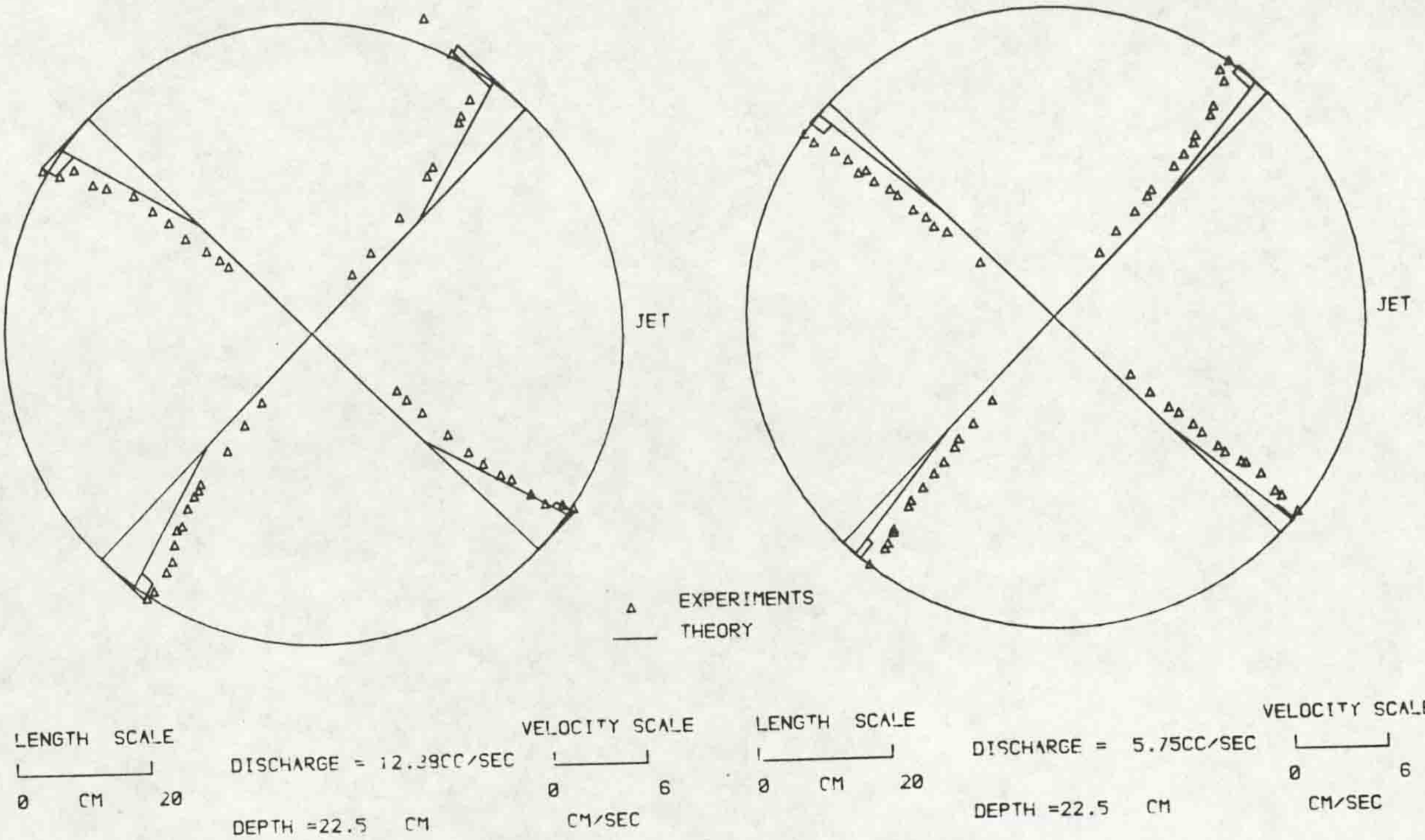

Fig. (3.31a) Measured velocities and comparison with theory for the same depth and various discharges.

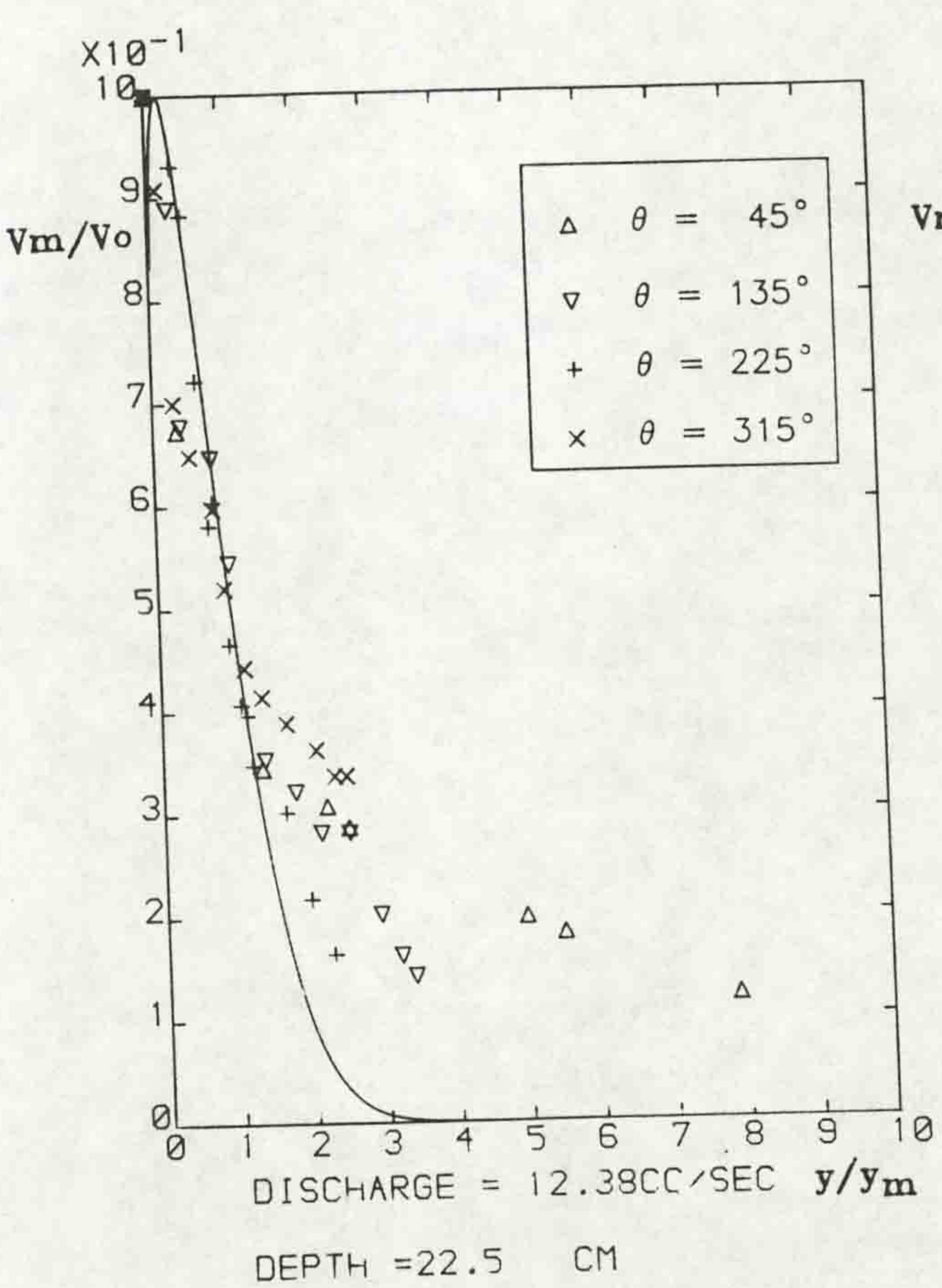

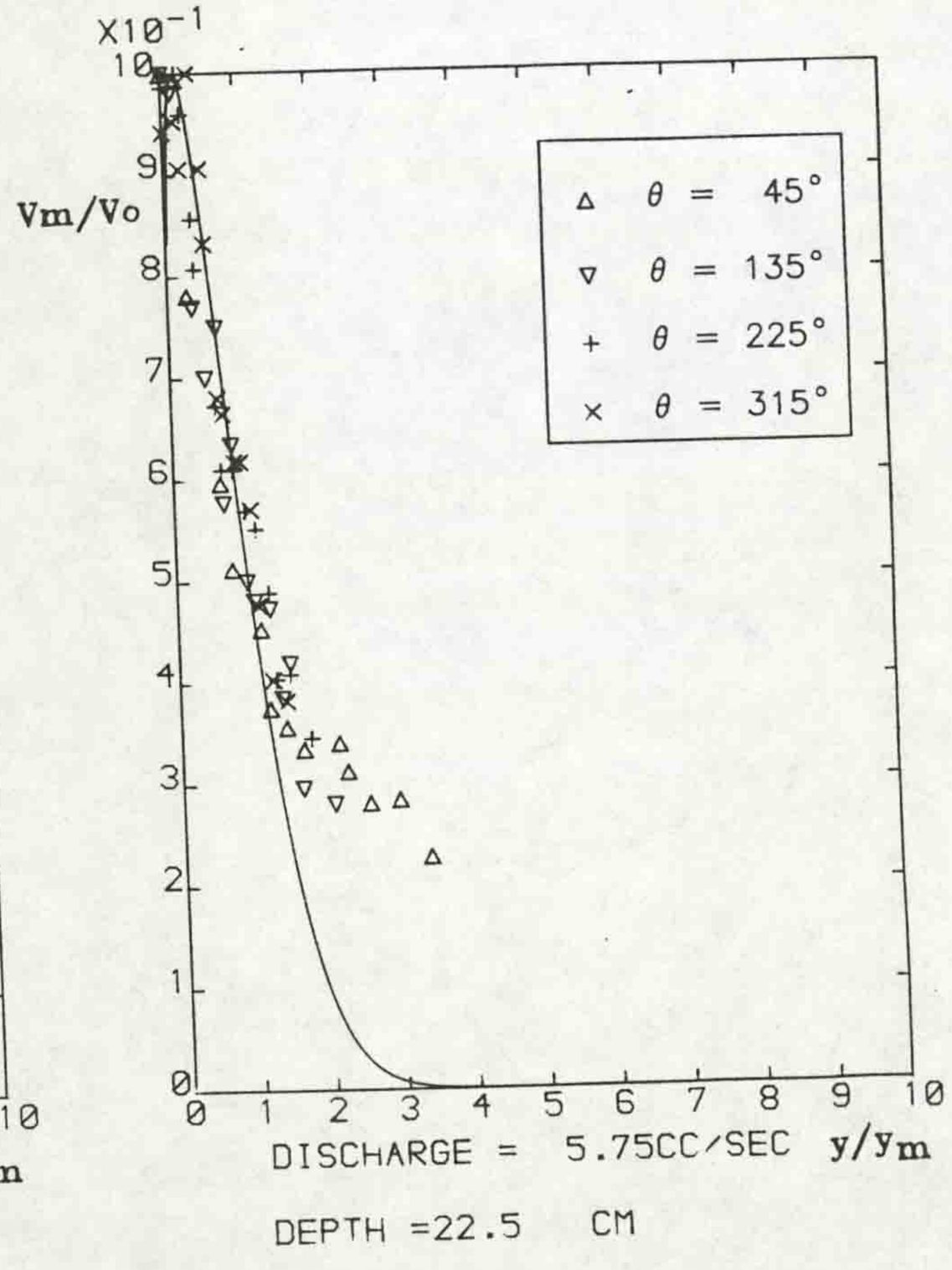

Fig. (3.31b) Dimensionless velocity distribution for the same depth and various discharges.

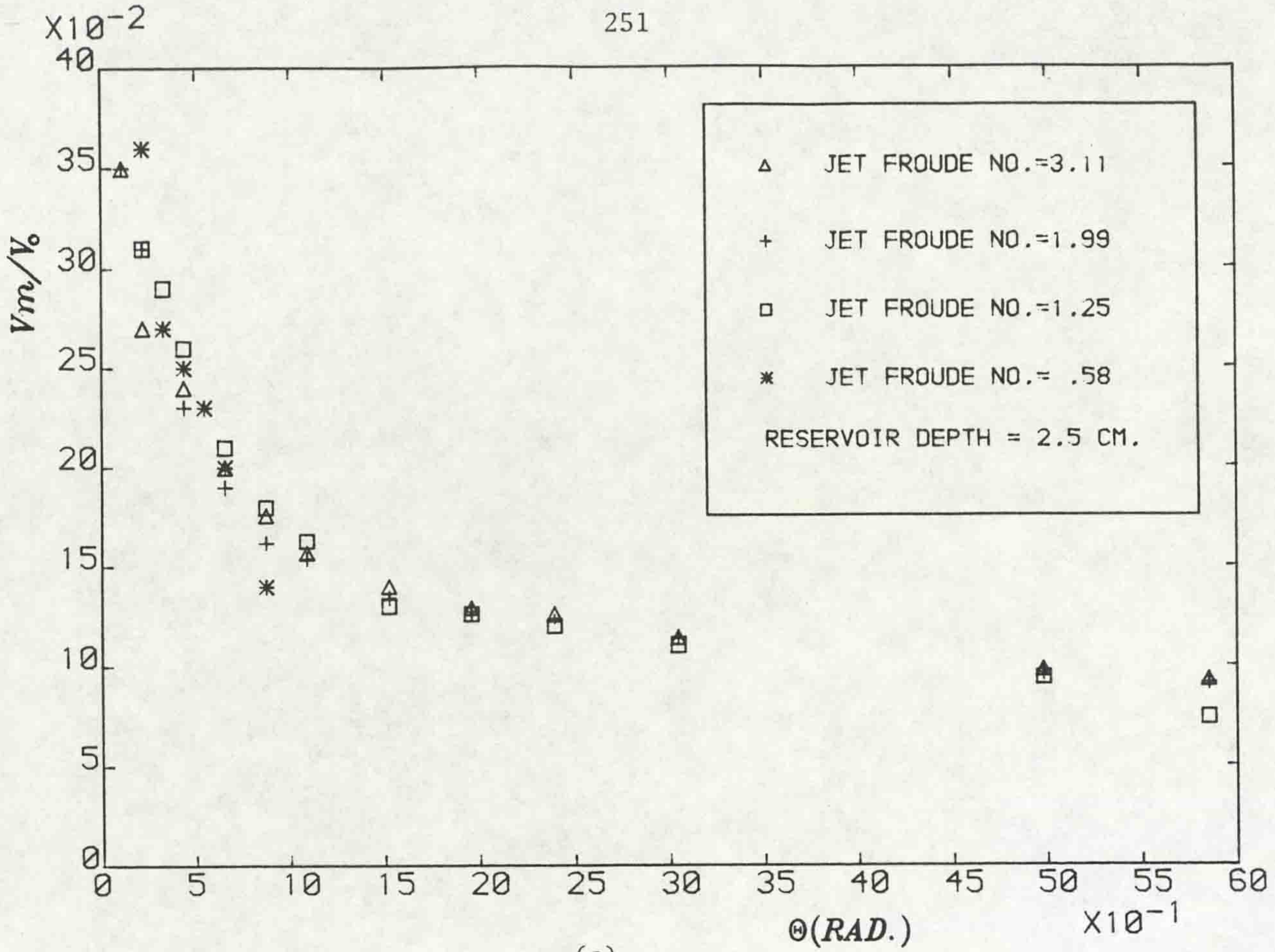

(a)

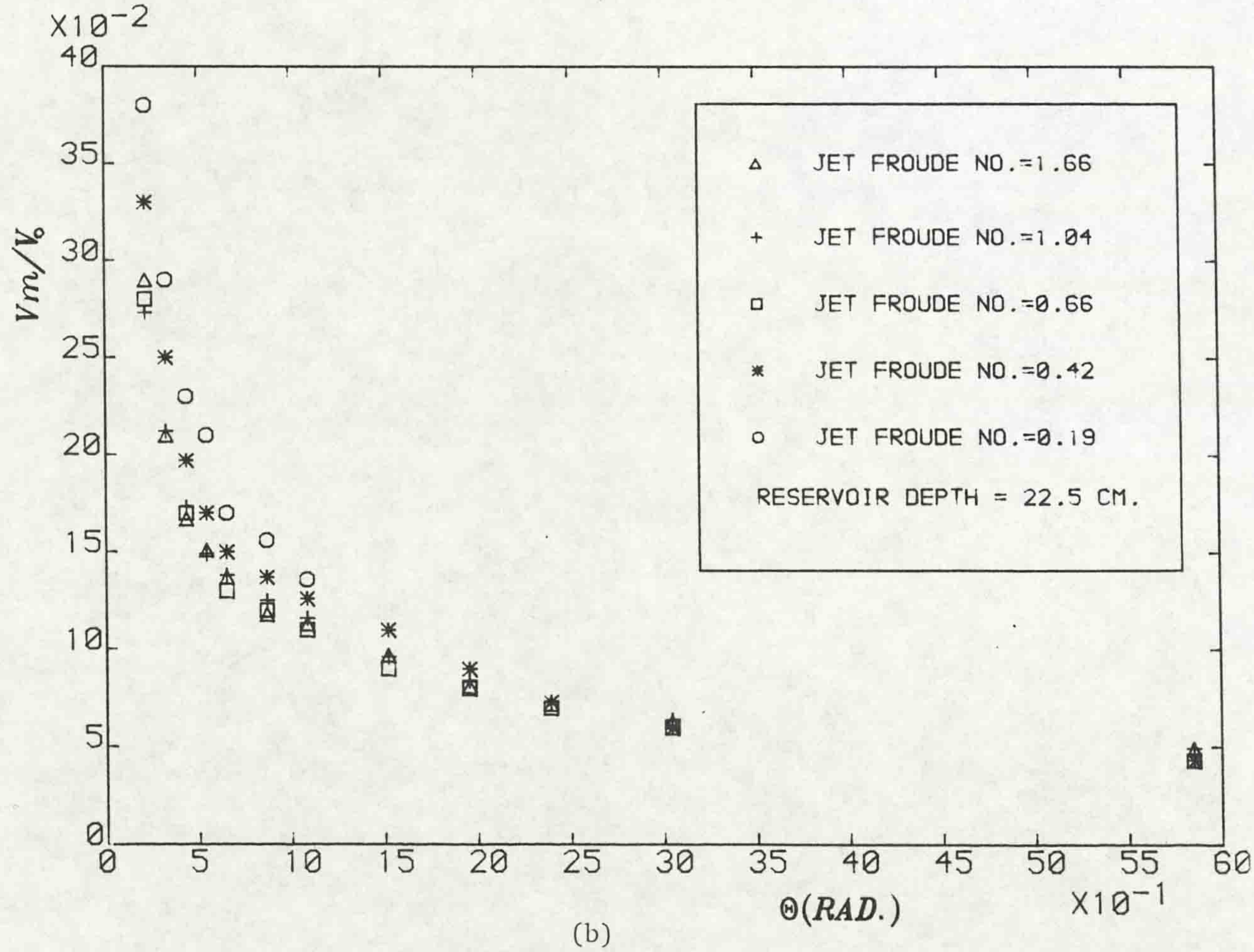

(b)

Fig. (3.32a,b) Variation of wall velocity with θ for the minimum and maximum depth and different jet Froude numbers.

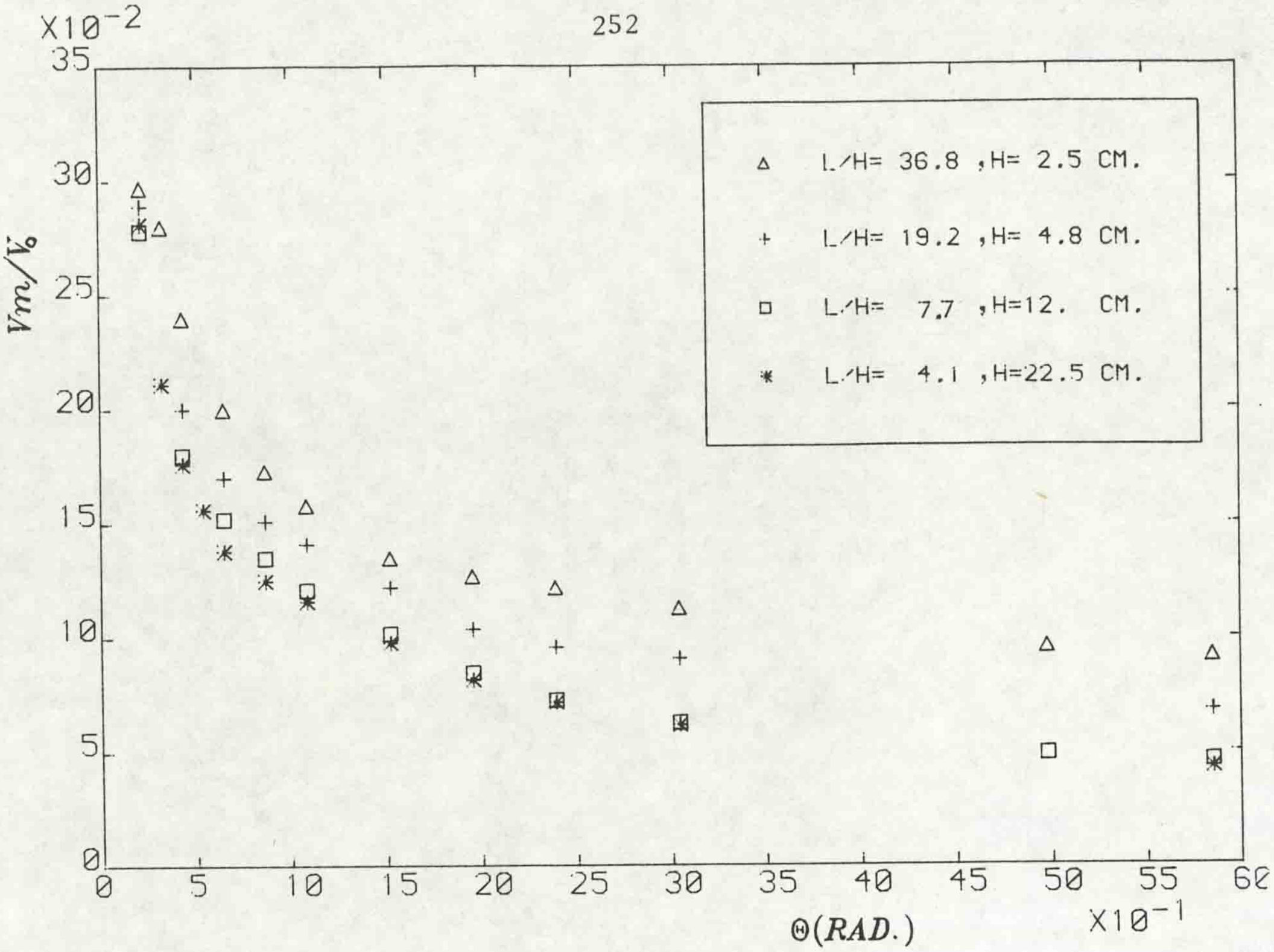

Fig. (3.33a) Variation of wall velocities with θ for various depths.

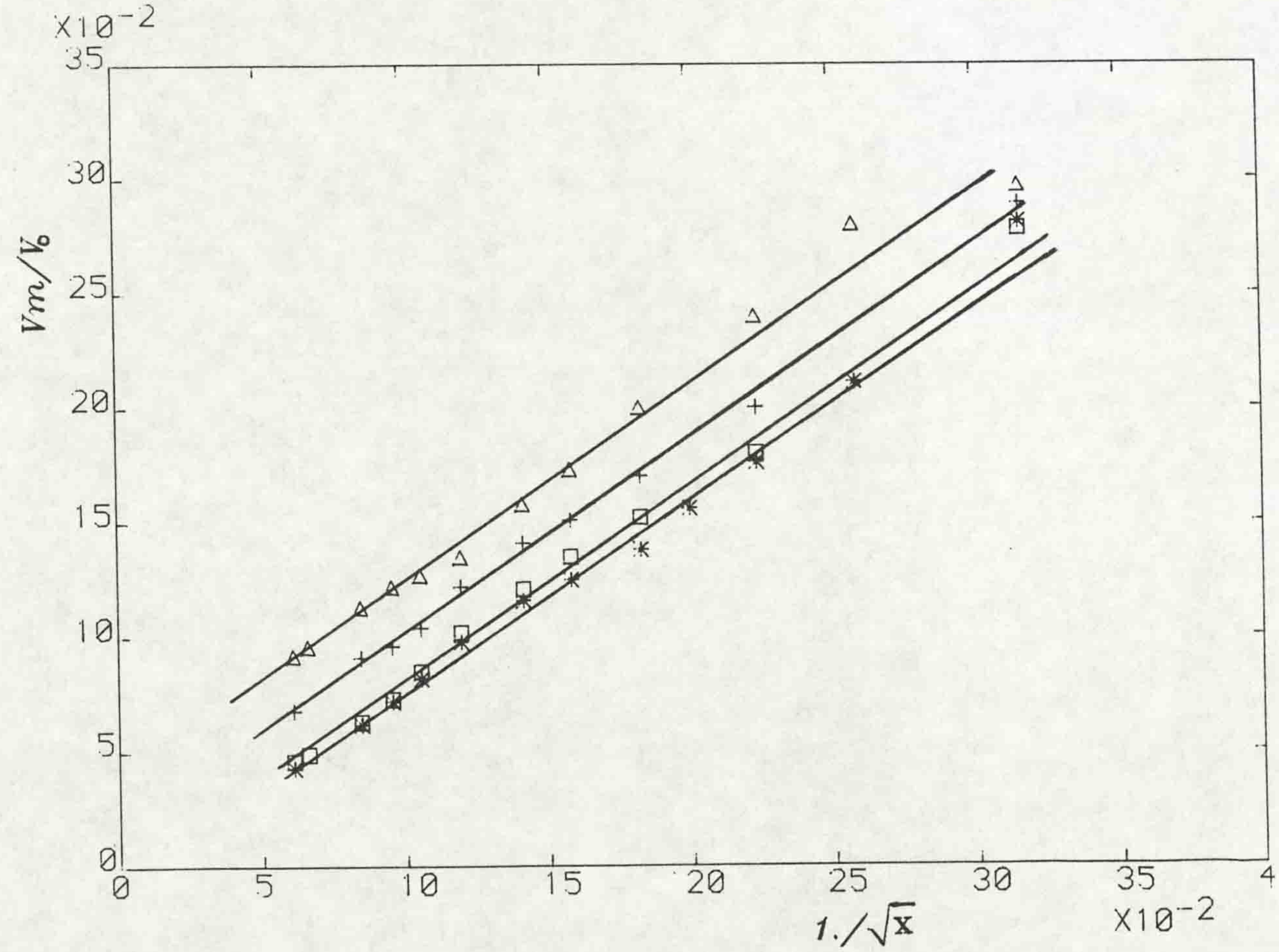

Fig. (3.33b) Dimensionless velocities in reservoir vs. $1/\sqrt{x}$ for various depths.

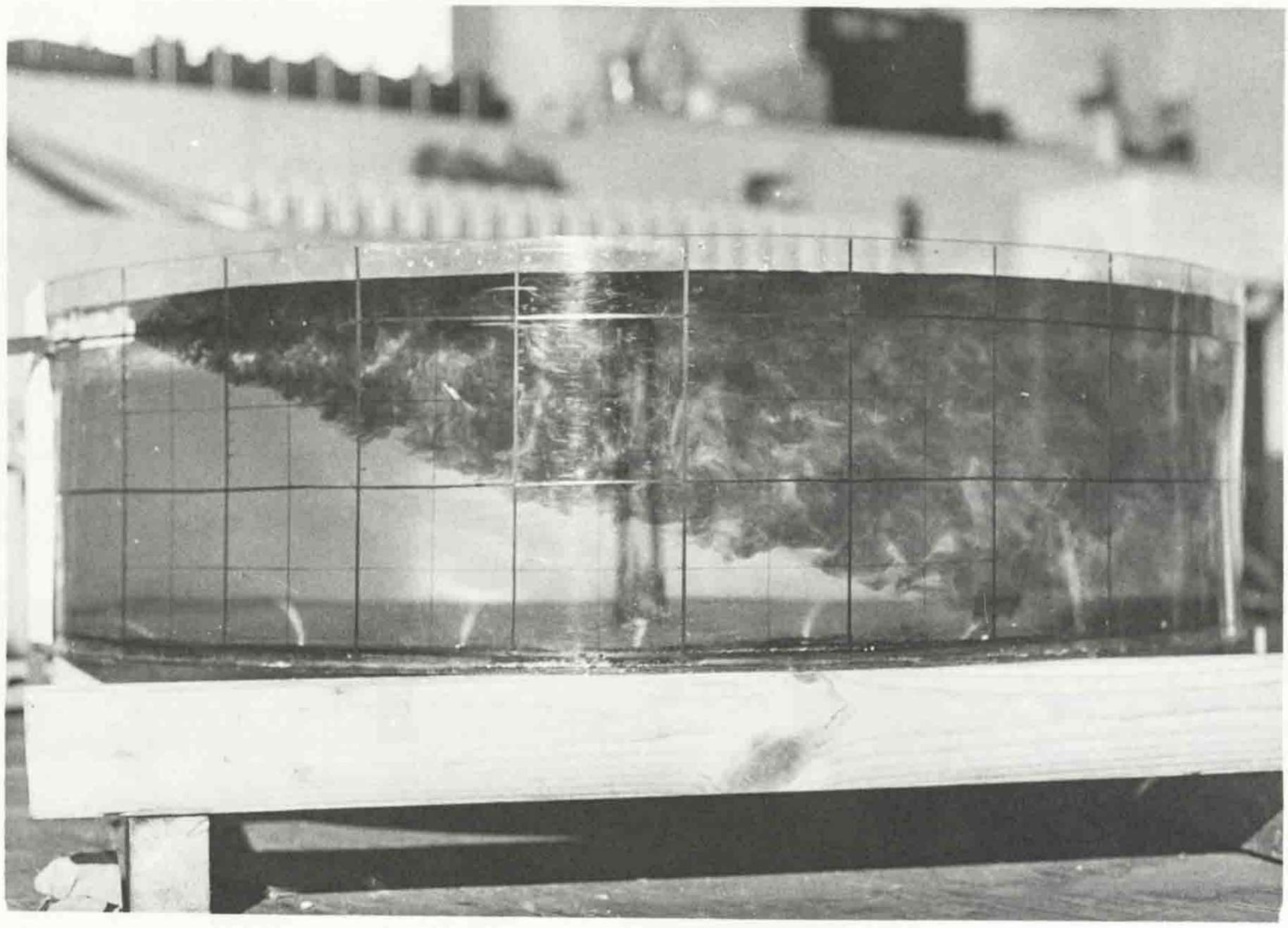

a) Q_o = 19.66 cc/sec.

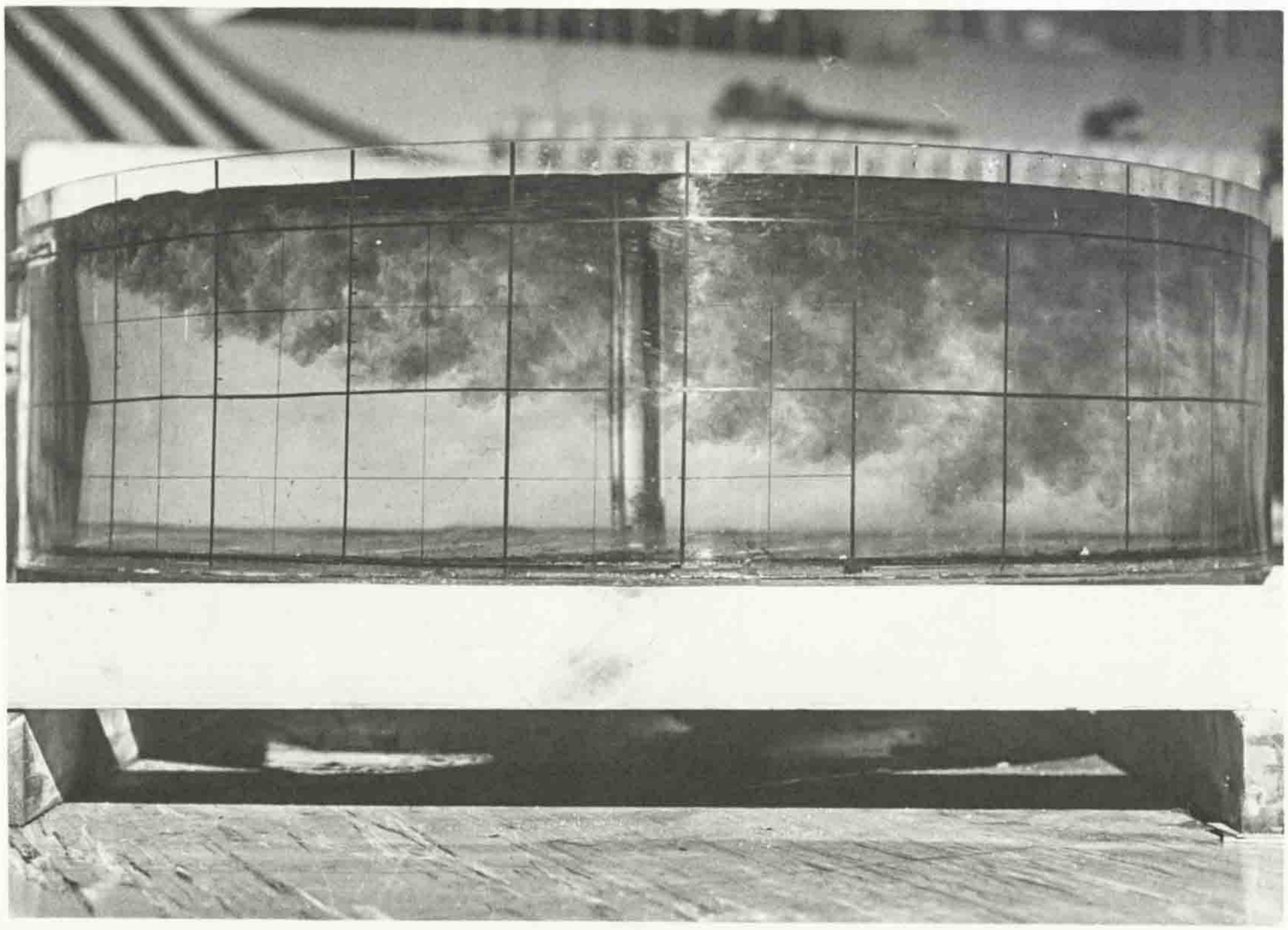

b) Q_o = 49.5 cc/sec.

Fig. (3.34) Diffusion of surface jet in reservoir h = 22.5 cm.

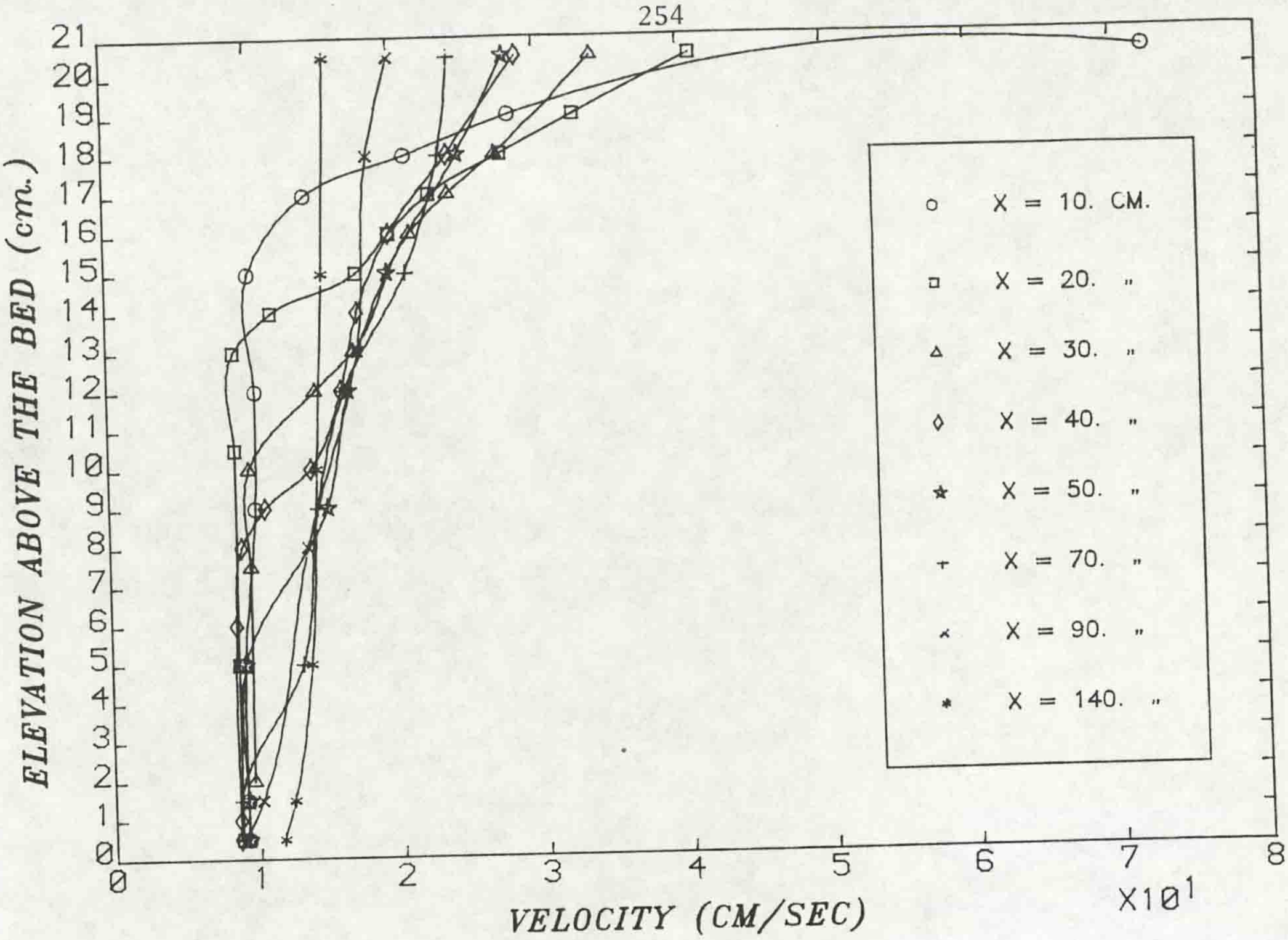

a) Q_o = 19.66 cc/sec.

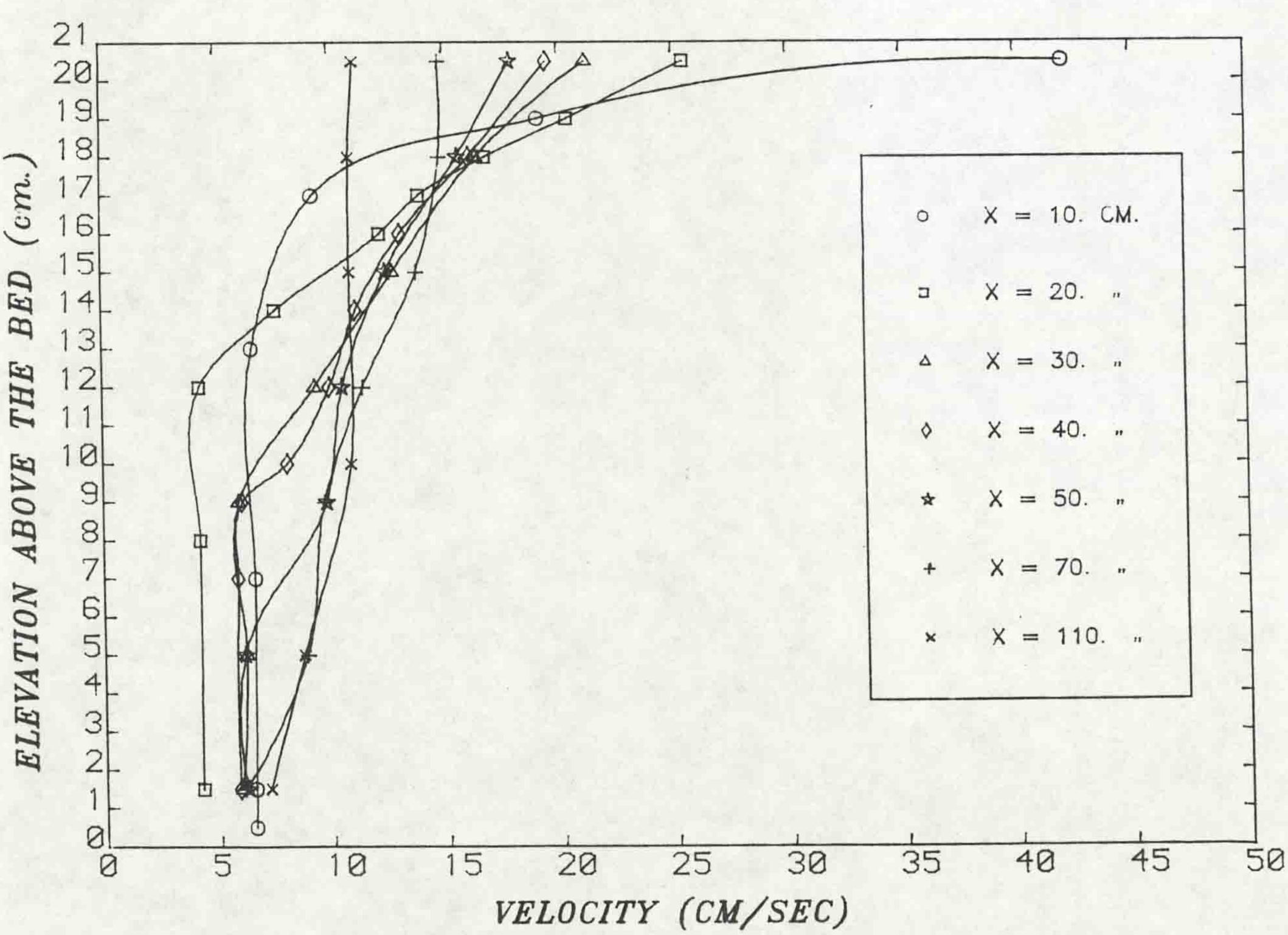

b) Q_o = 30.83 cc/sec.

Fig. (3.35a,b) Variation of wall velocities in depth at different stations for various discharges.

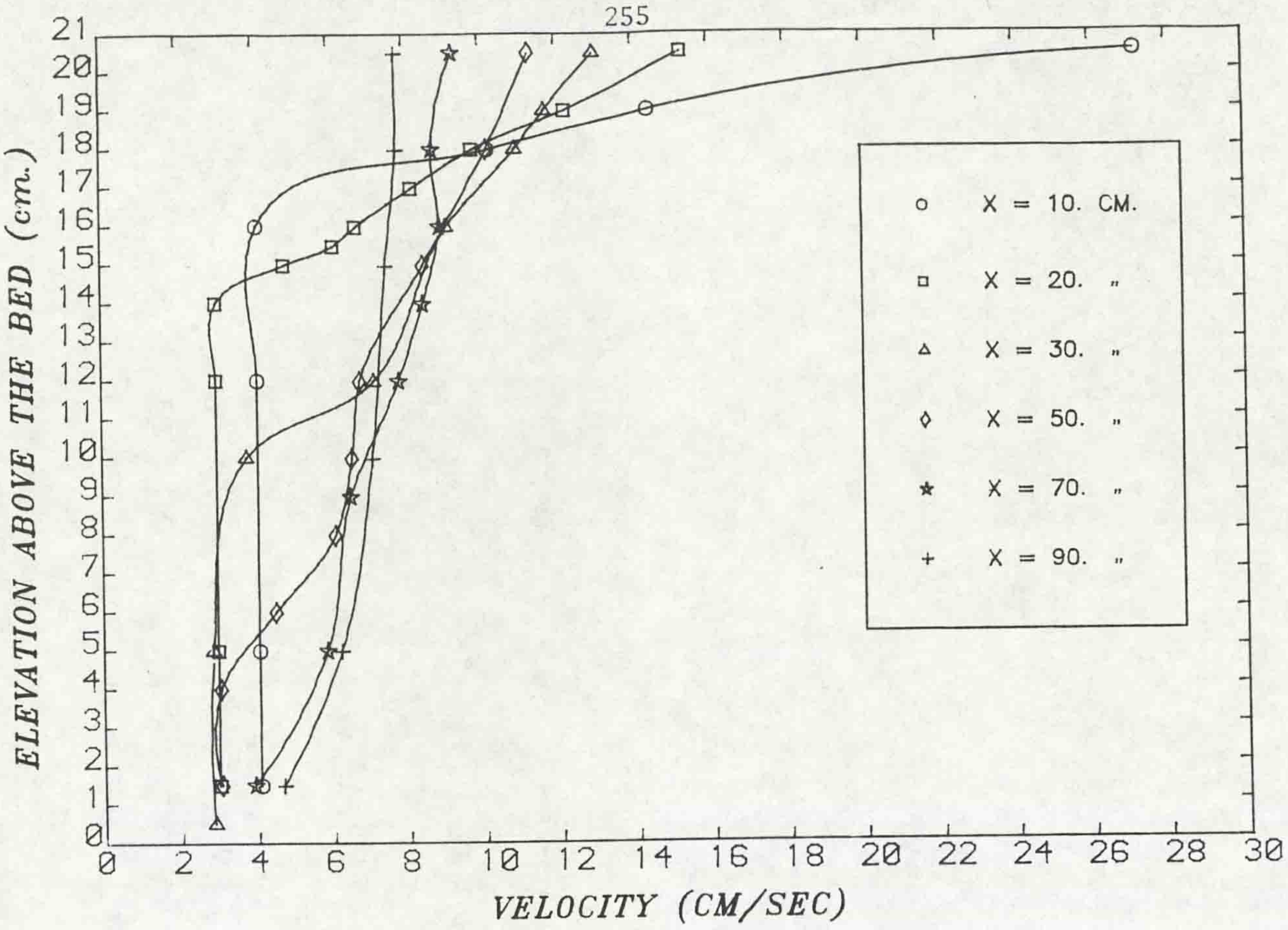

c) Q_o = 49.5 cc/sec.

Fig. (3.35c) Variation of wall velocities in depth at different stations.

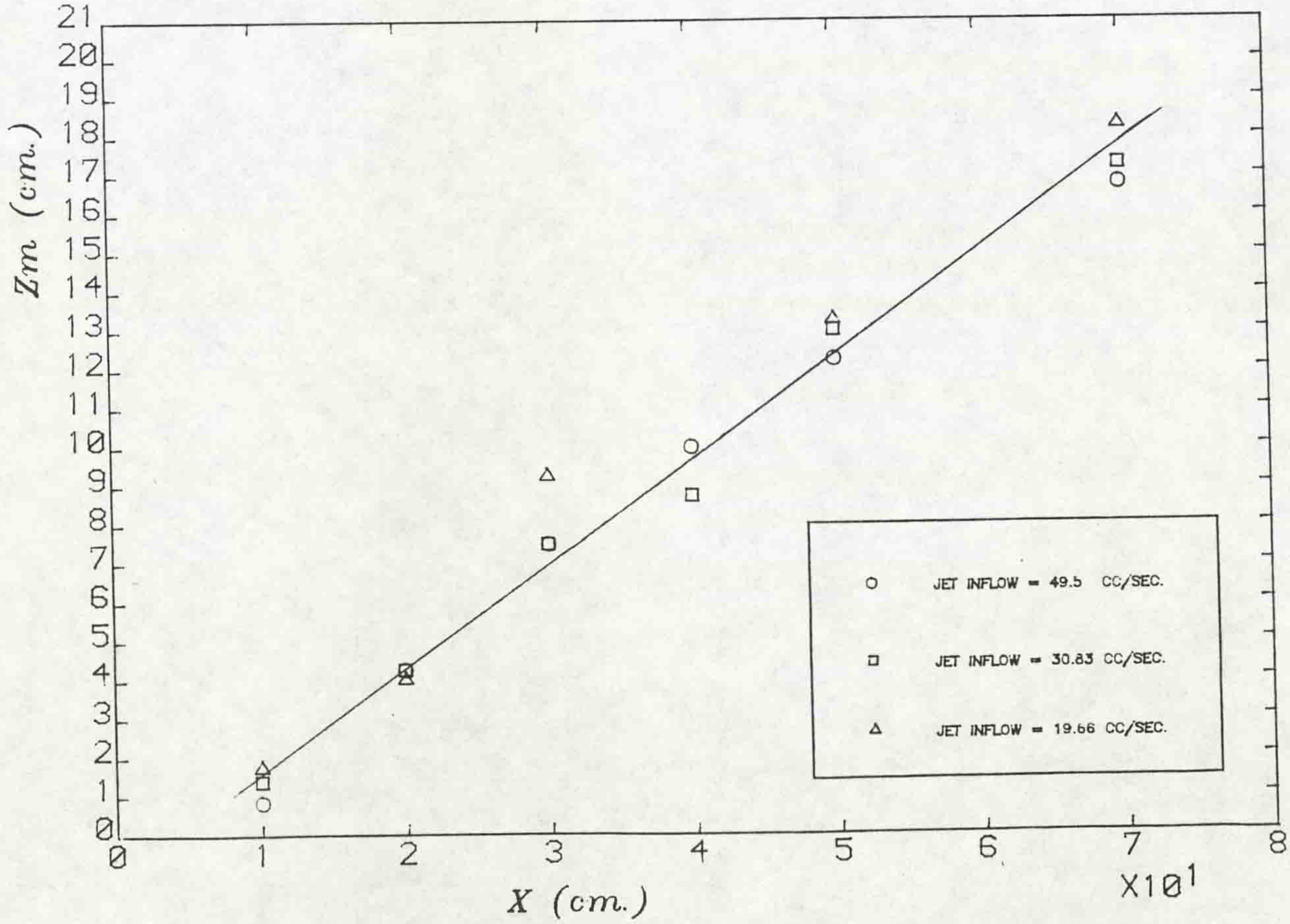

Fig. (3.36) Growth of z_m vs. the distance from the inlet for various discharges.

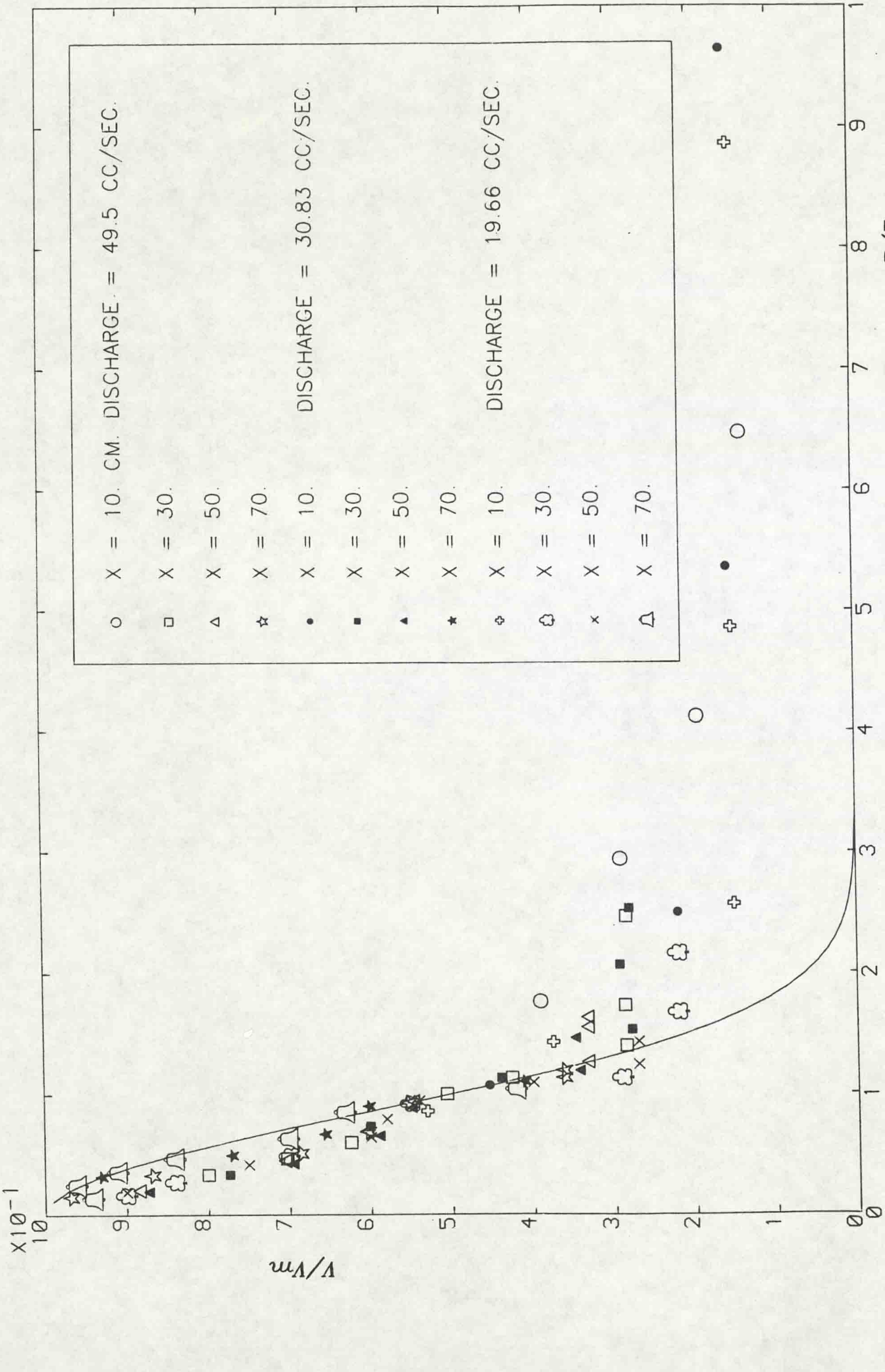

Fig. (3.37) Variation of dimensionless wall velocities in depth for different discharges and at various stations from the inlet.

Series/ Run	v_0 cm/sec	v_{stream} cm/sec	$\alpha = \frac{v_0}{V_s}$	Remarks
1/1	247.5	12.1	20.5	h = 22.5 cm
1/2	154.2	7.5	20.6	L = 92. cm
1/3	98.33	4.2	23.4	
1/4	61.92	< 3.	> 20.	
1/5	28.75	< 3.	> 10.	

Table (3.3) The Ratio of the Jet Velocity to the Stream Velocity for the Different Experiments.

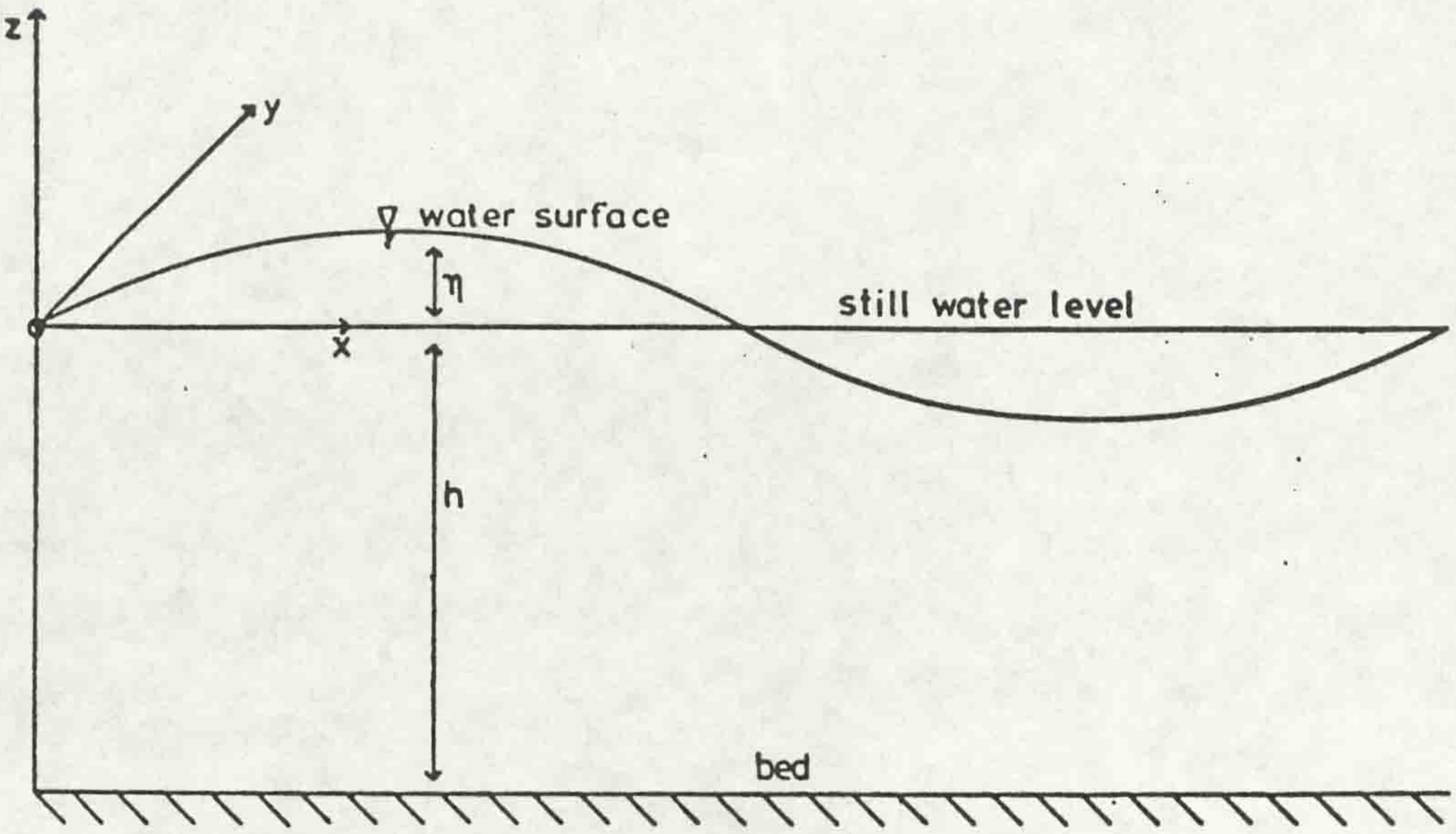

Fig. (4.1) Definition sketch for the system of coordinates.

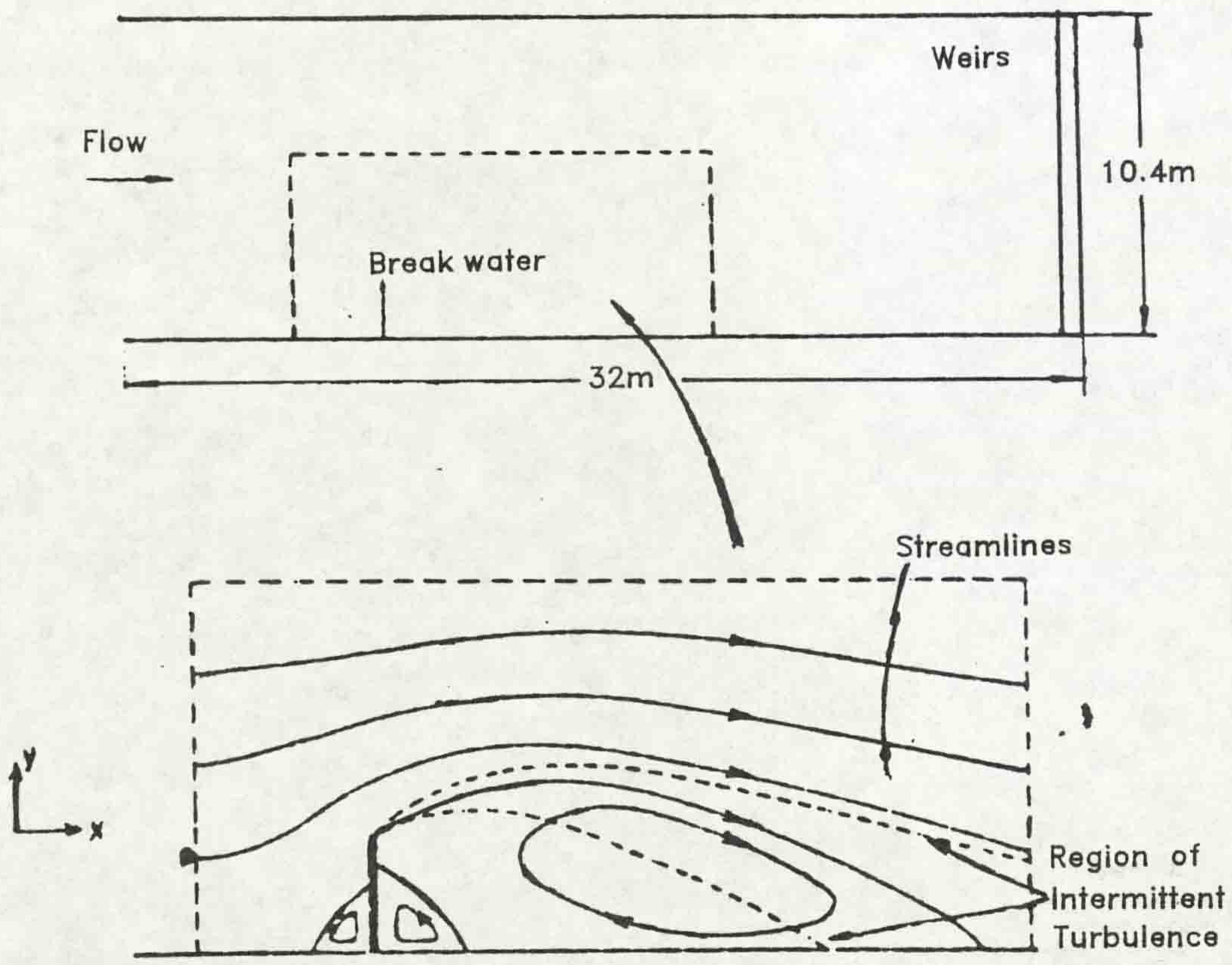

Fig. (4.2) The eddy after the breakwater.

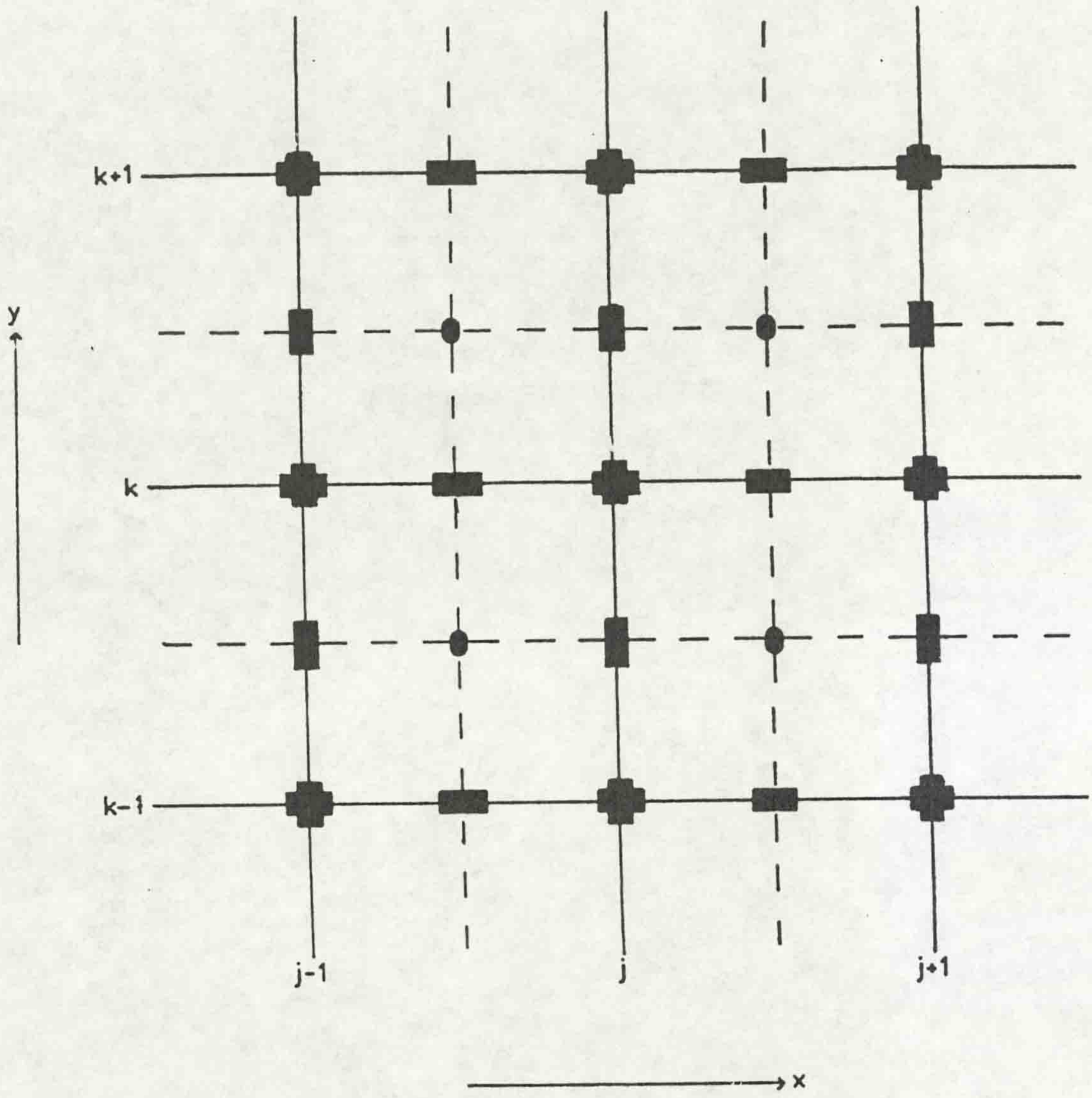

Water Level (η) and Chézy Coefficient (C)

Depth (h)

U velocity (U)

V velocity (V)

Fig. (4.3) The computational grid.

Characteristics	Experimental Model	Numerical Model
Reservoir diameter	243.8 cm	247. cm
Water depth	4.6 cm	4.6 cm
Inlet width	13. cm	13. cm
Outlet width	38. cm	39. cm
Jet inflow	192 cm^3/sec	192 cm^3/sec
Weir outflow	192 cm^3/sec	192 cm^3/sec
Depth of inlet	0.8 cm	0.8 cm

Table (4.1) Details of Experimental and Numerical Models

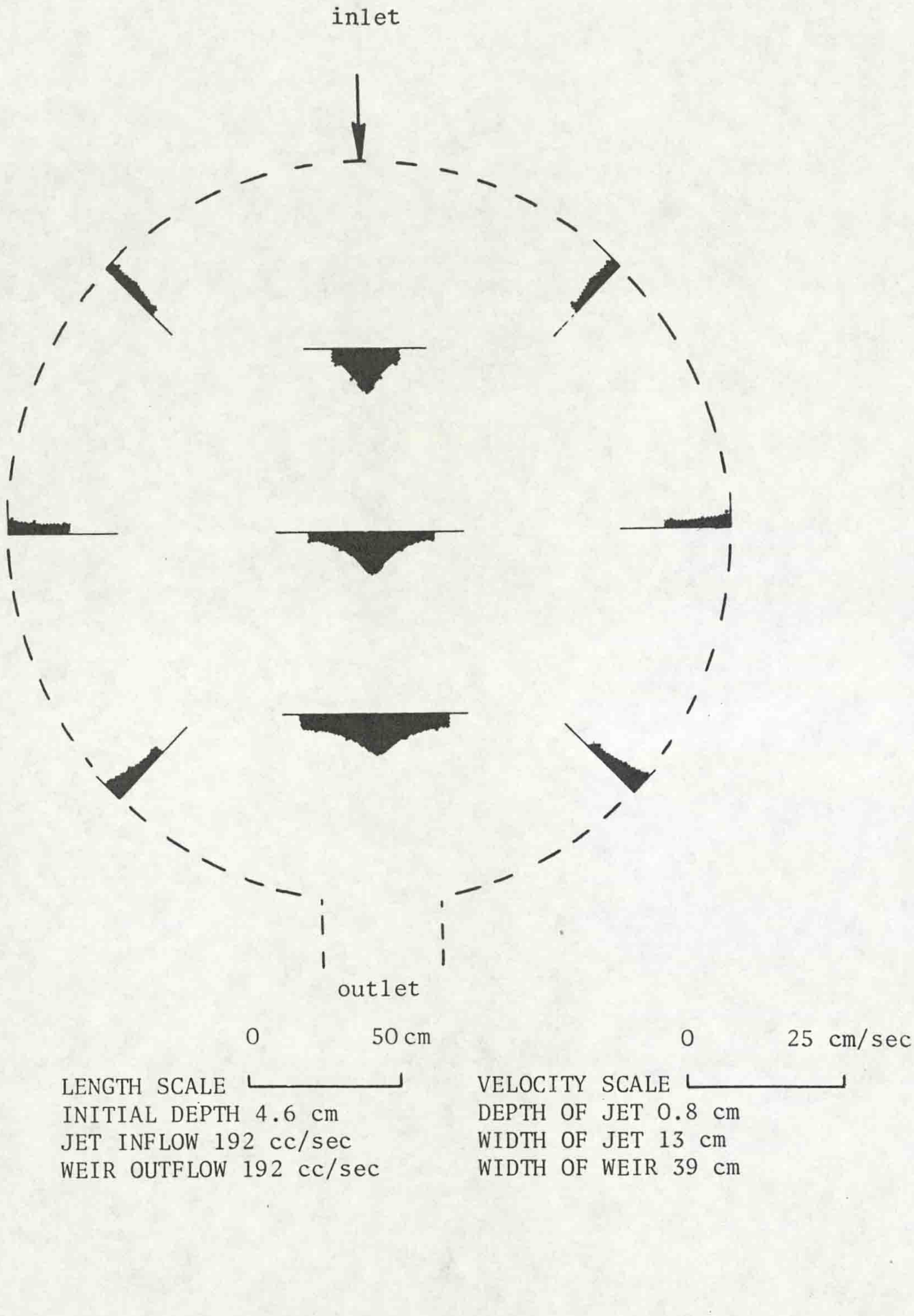

Fig. (4.4) The experimental velocity distribution (after Pateman, 1982).

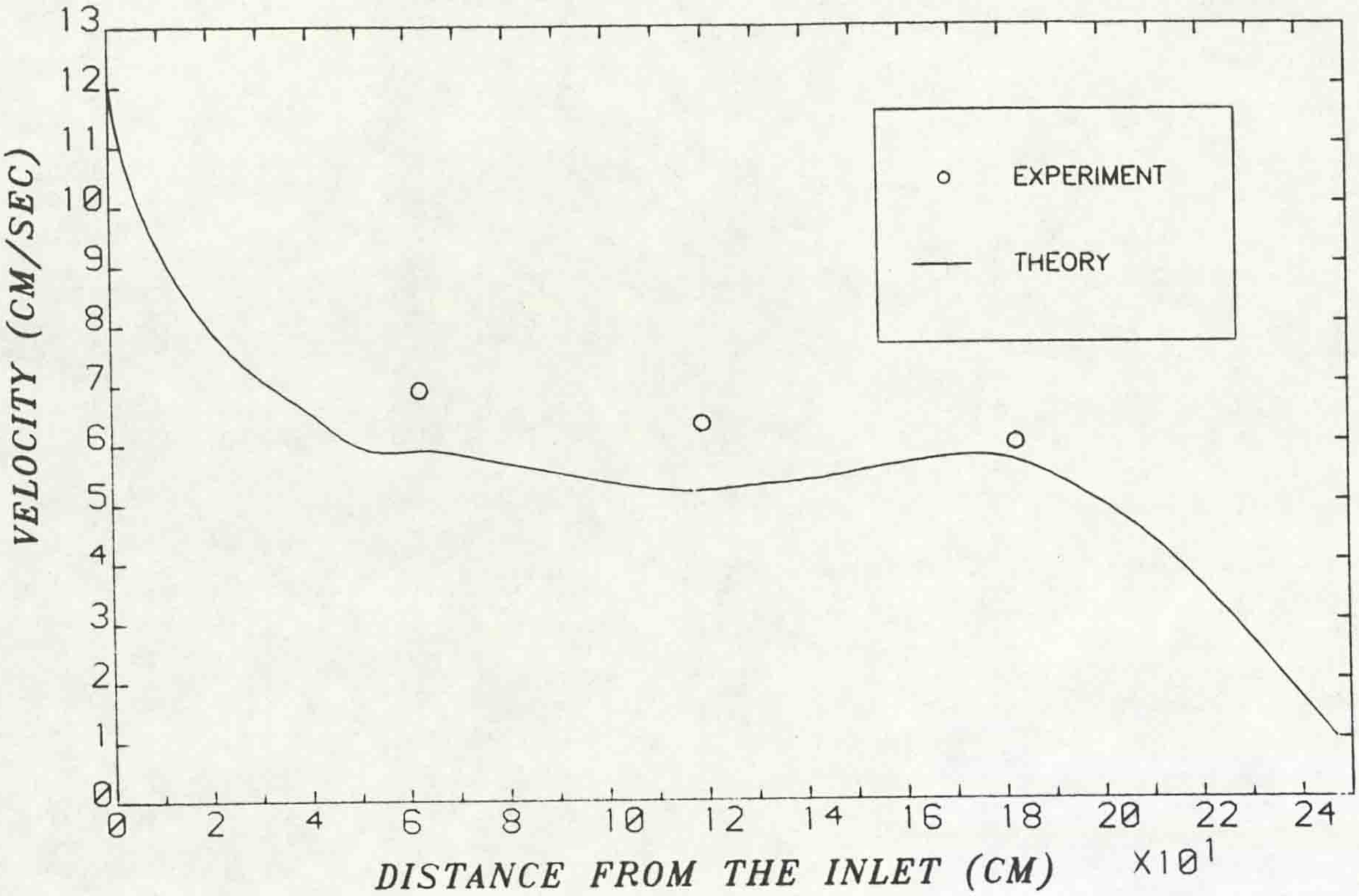

Fig. (4.5a) Computational and experimental velocities along the centreline.

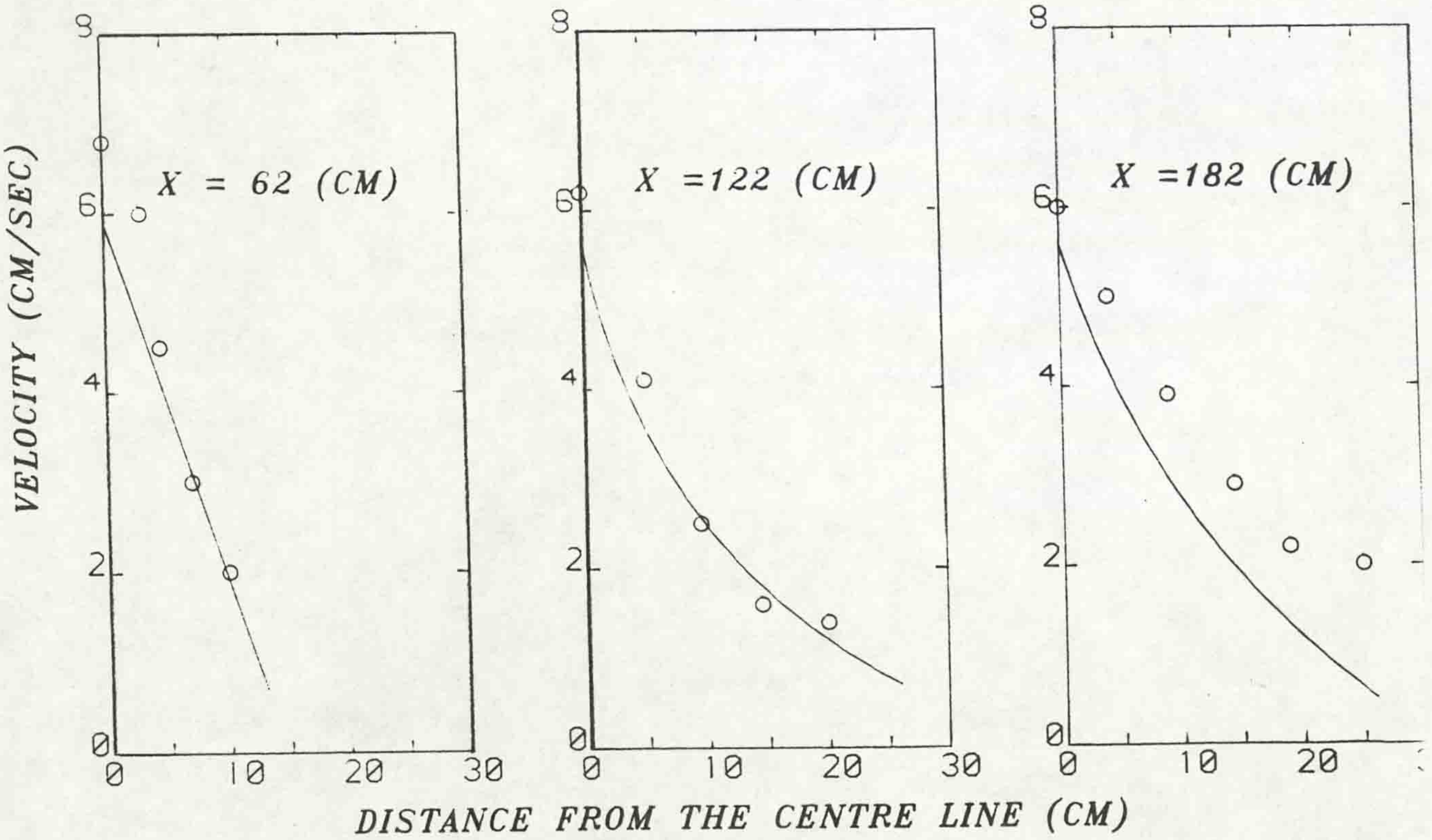

Fig. (4.5b) Computational and experimental velocities at different sections of centreline.

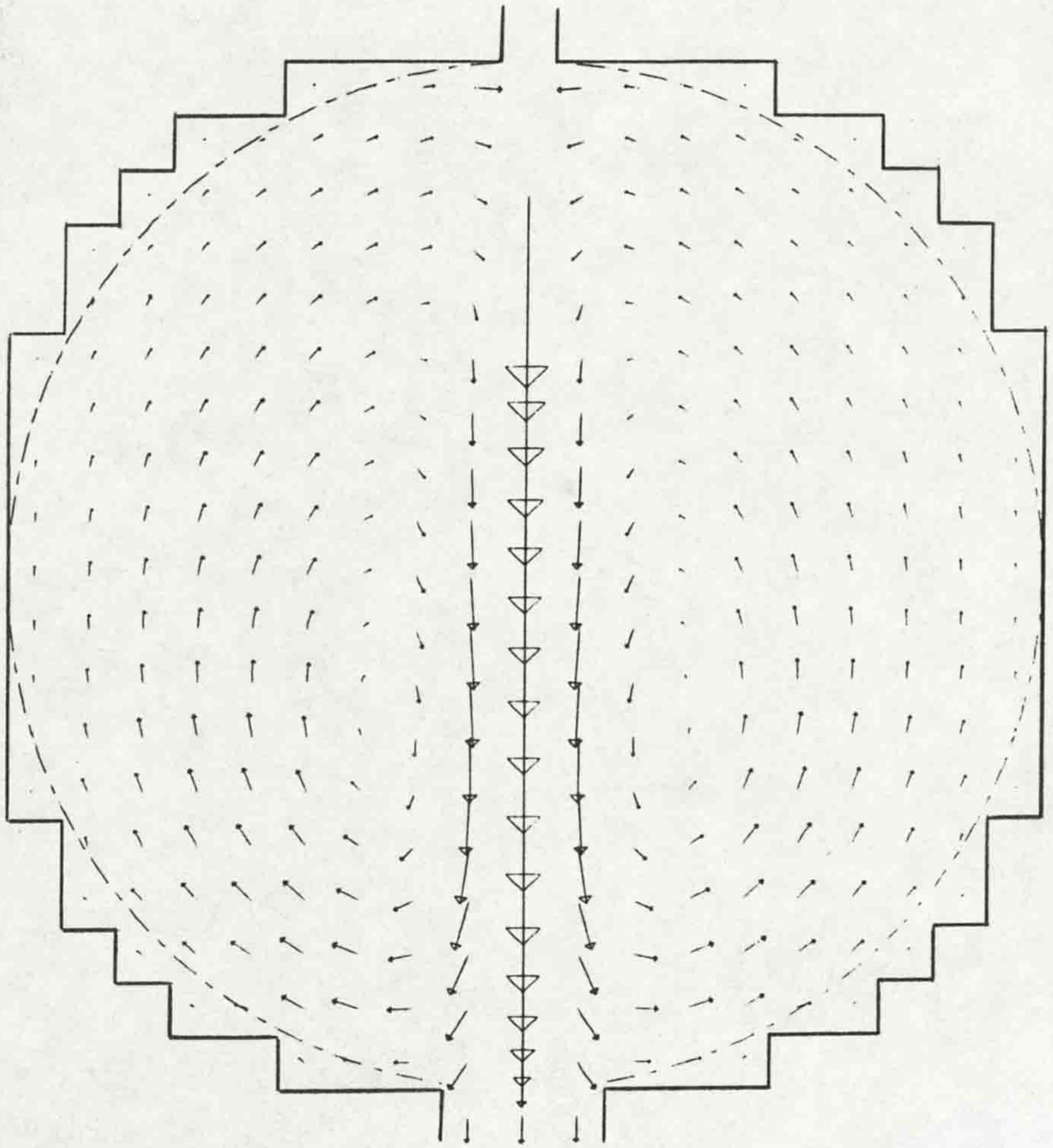

Fig. (4.6) Computational velocity field for case (A).

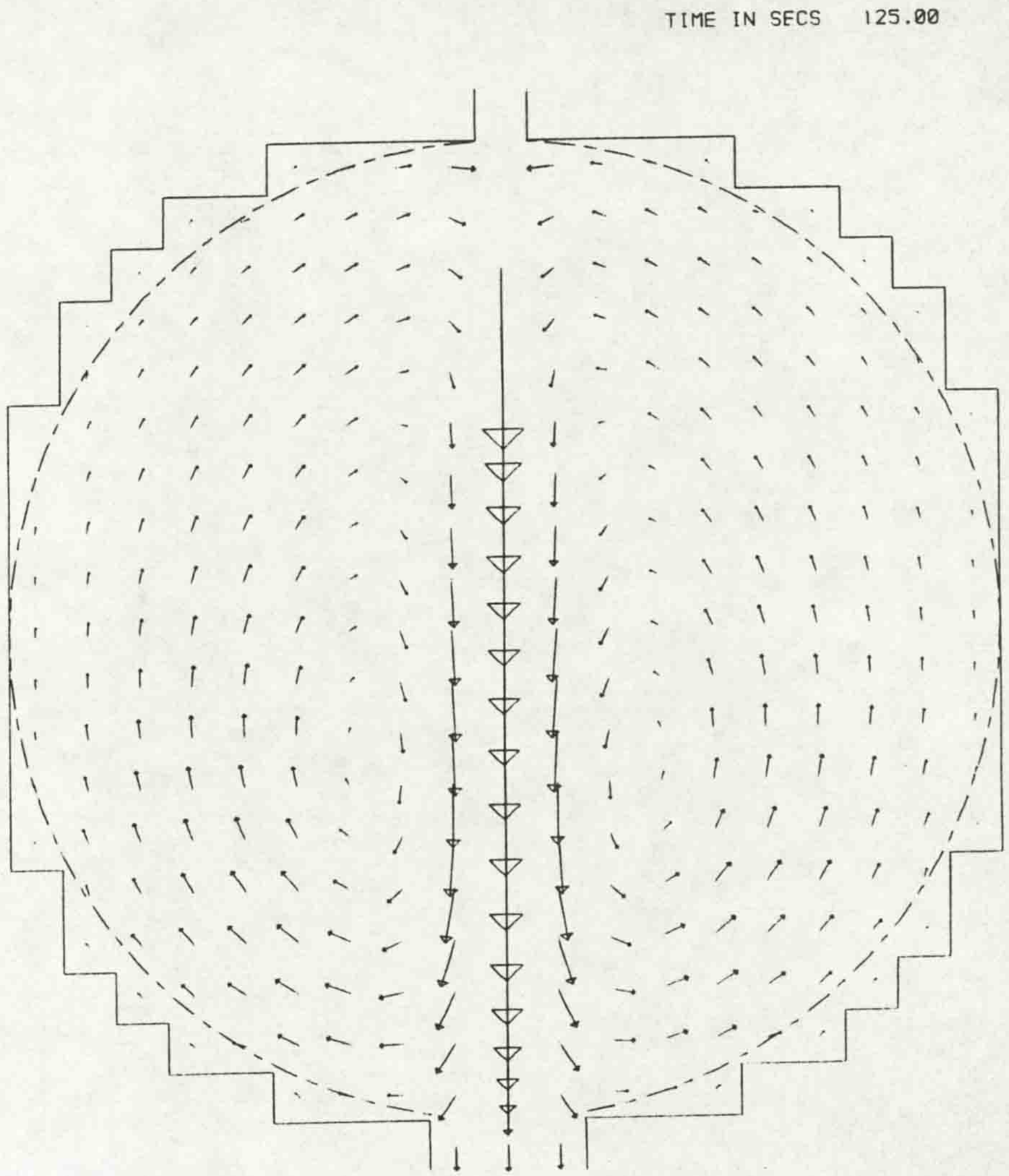

Fig. (4.7) Computational velocity field for case (B).

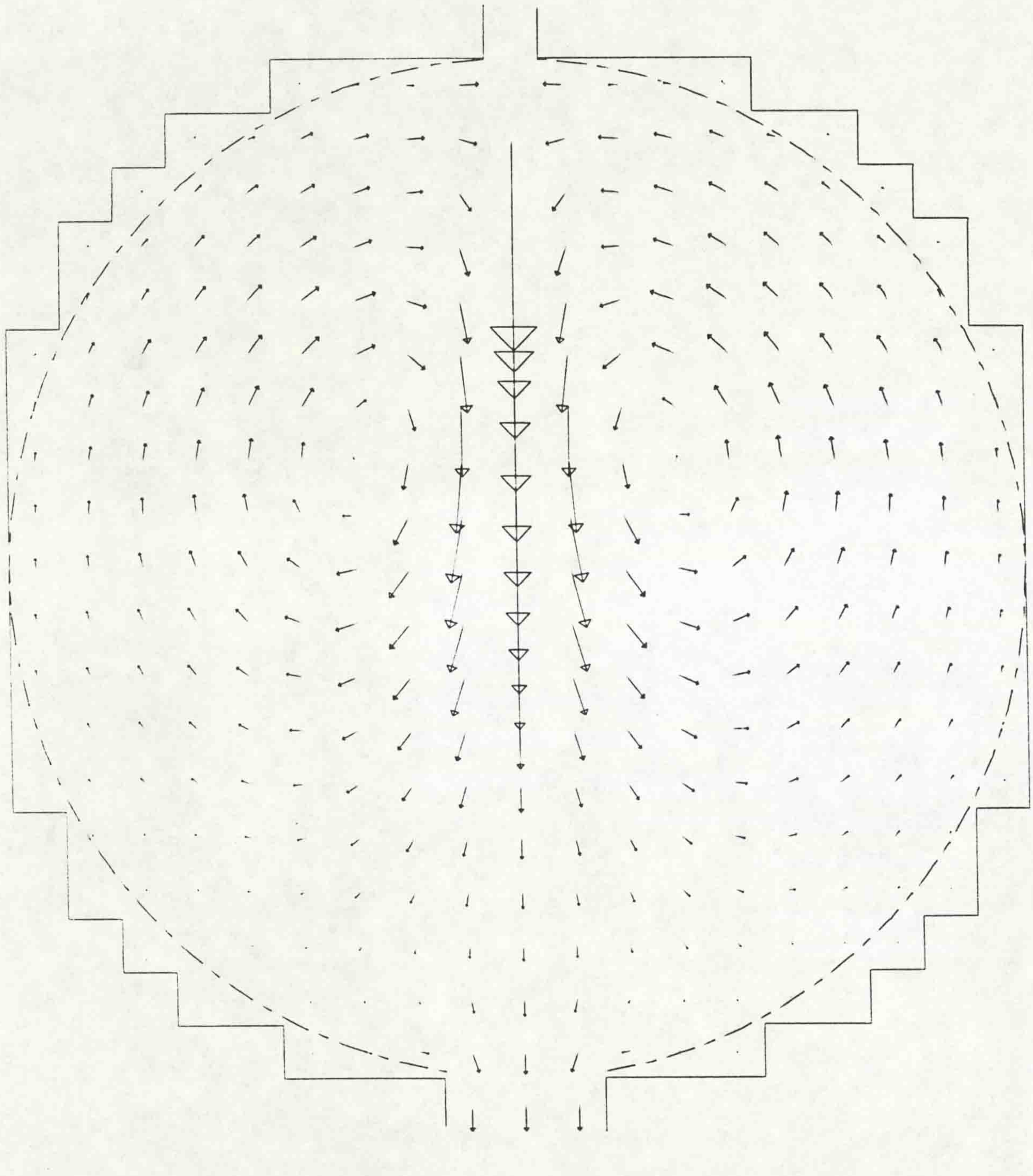

Fig. (4.8) Computational velocity field for case (C).

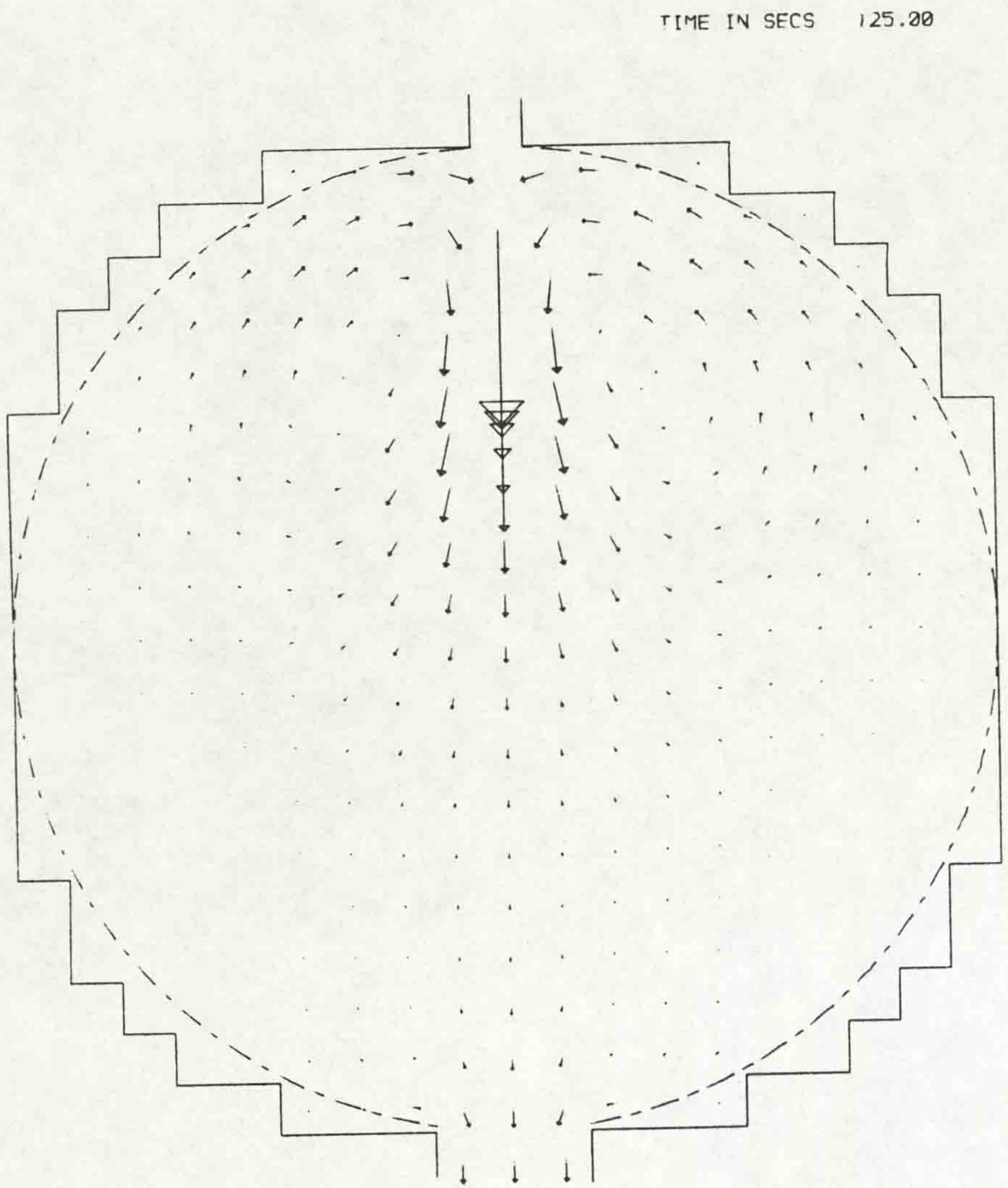

Fig. (4.9) Computational velocity field for case (D1).

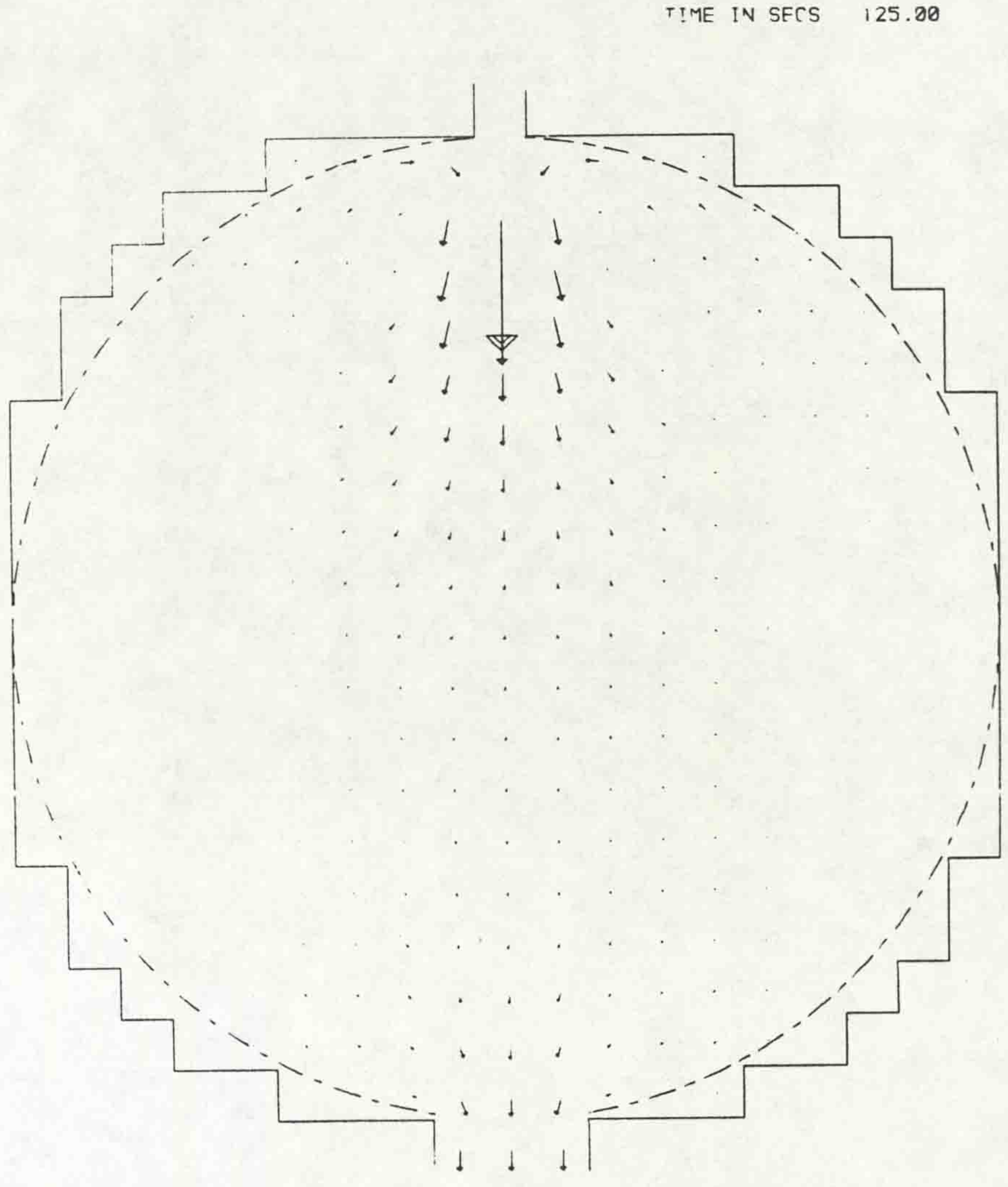

Fig. (4.10) Computational velocity field for case (D2).

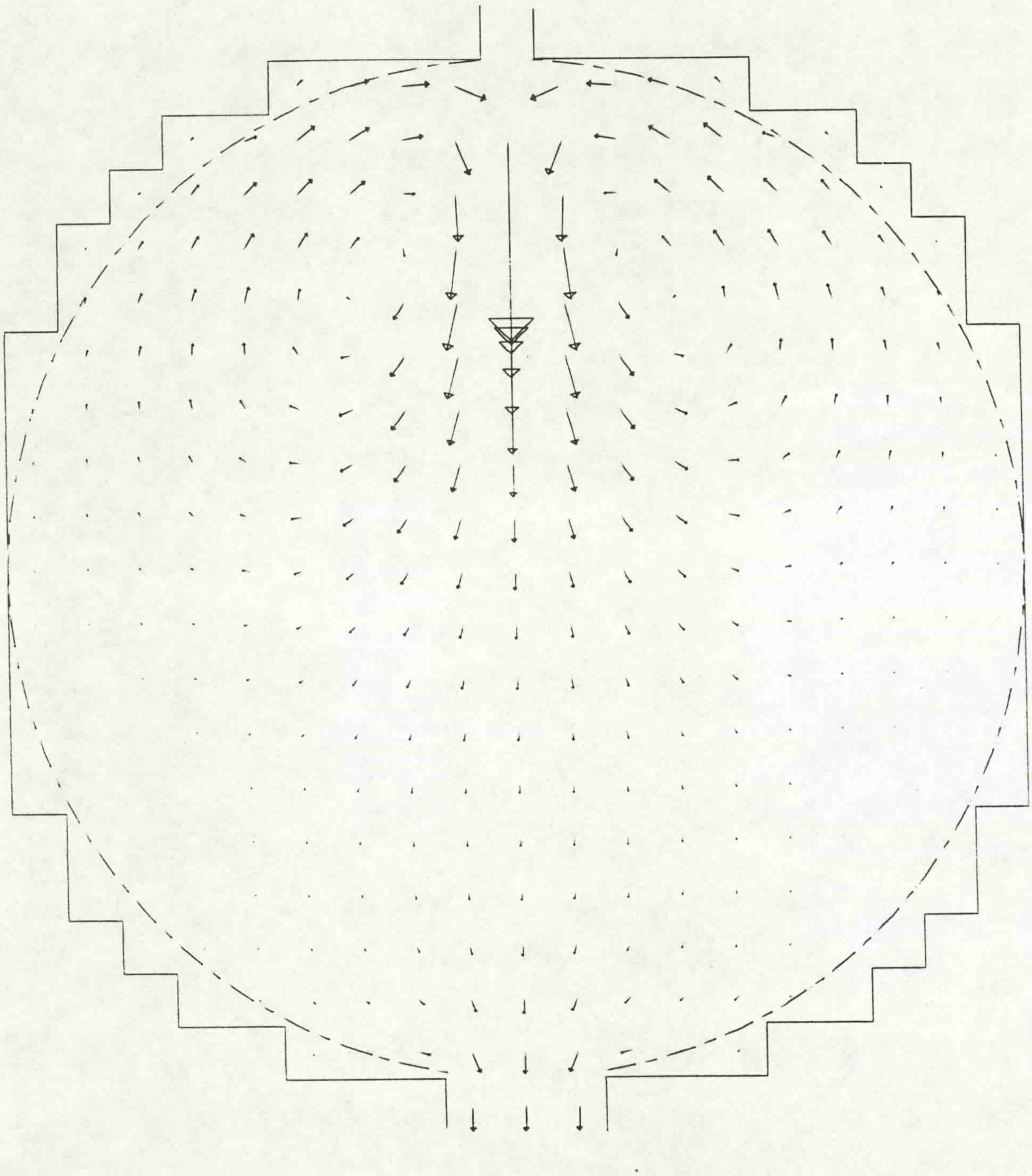

Fig. (4.11) Computational velocity field for case (E).

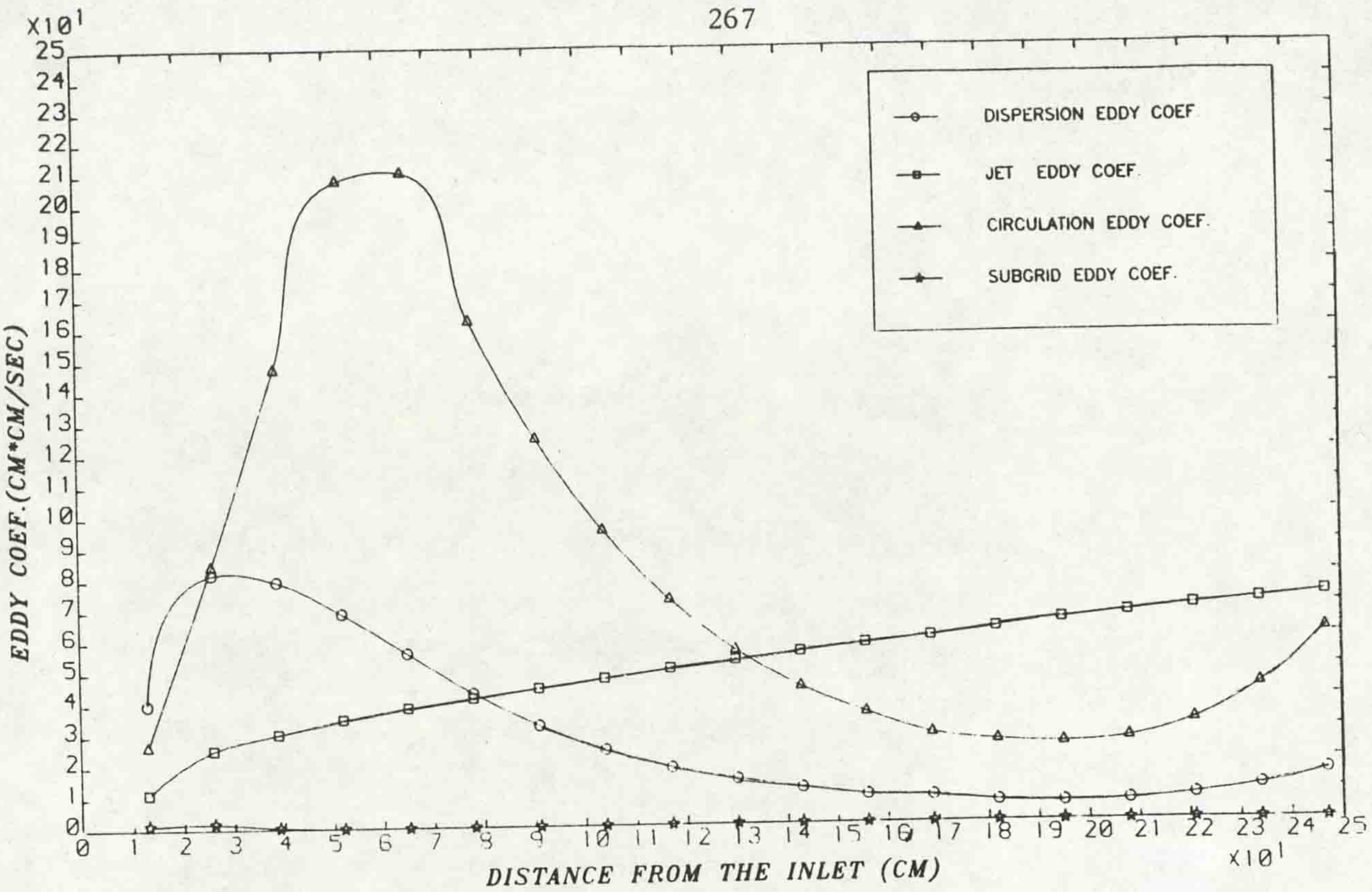

Fig. (4.12) Variation of eddy coefficients along the centreline.

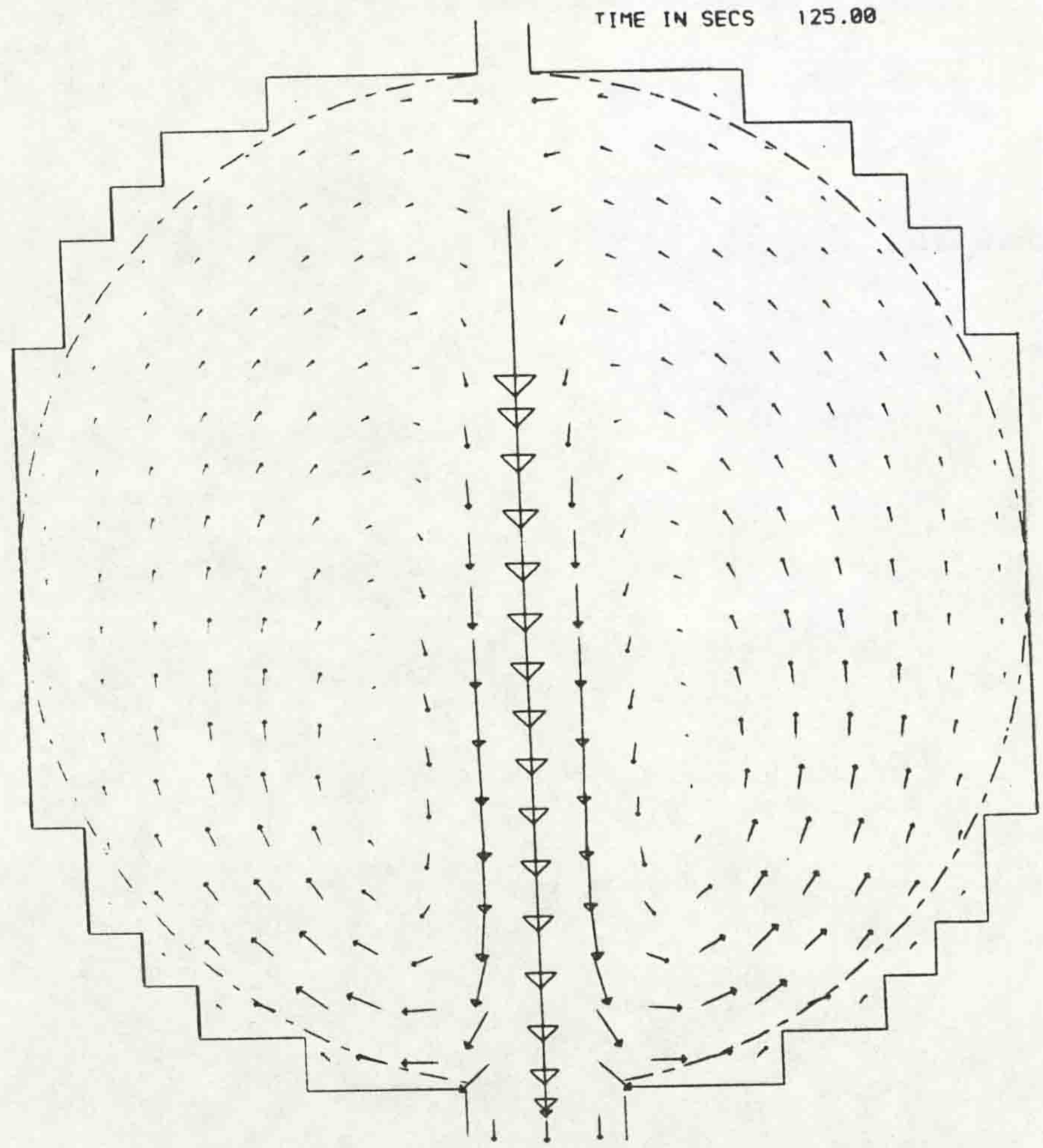

Fig. (4.13) Computational velocity field for case (F).

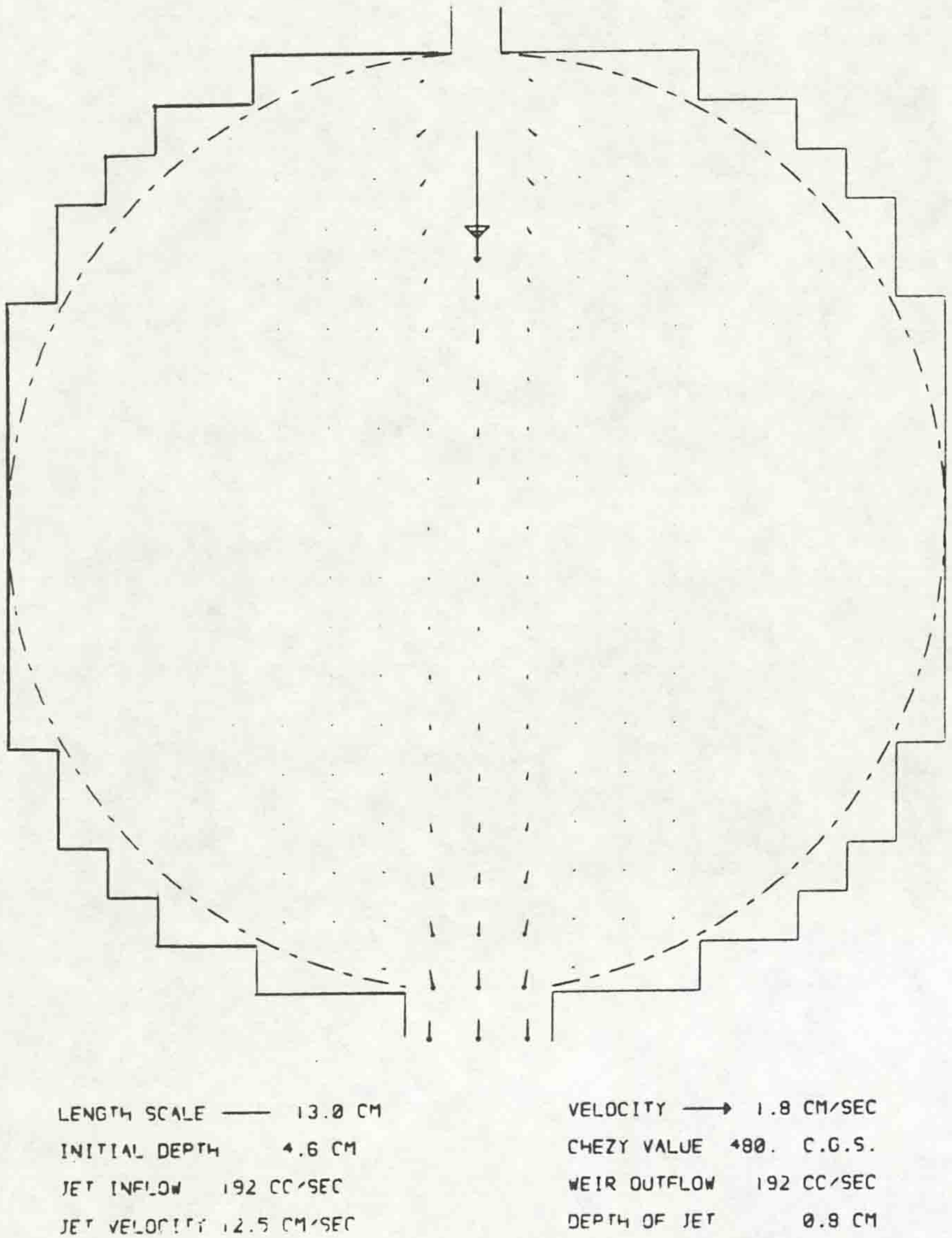

Fig. (4.14) Computational velocity field for case (A1).

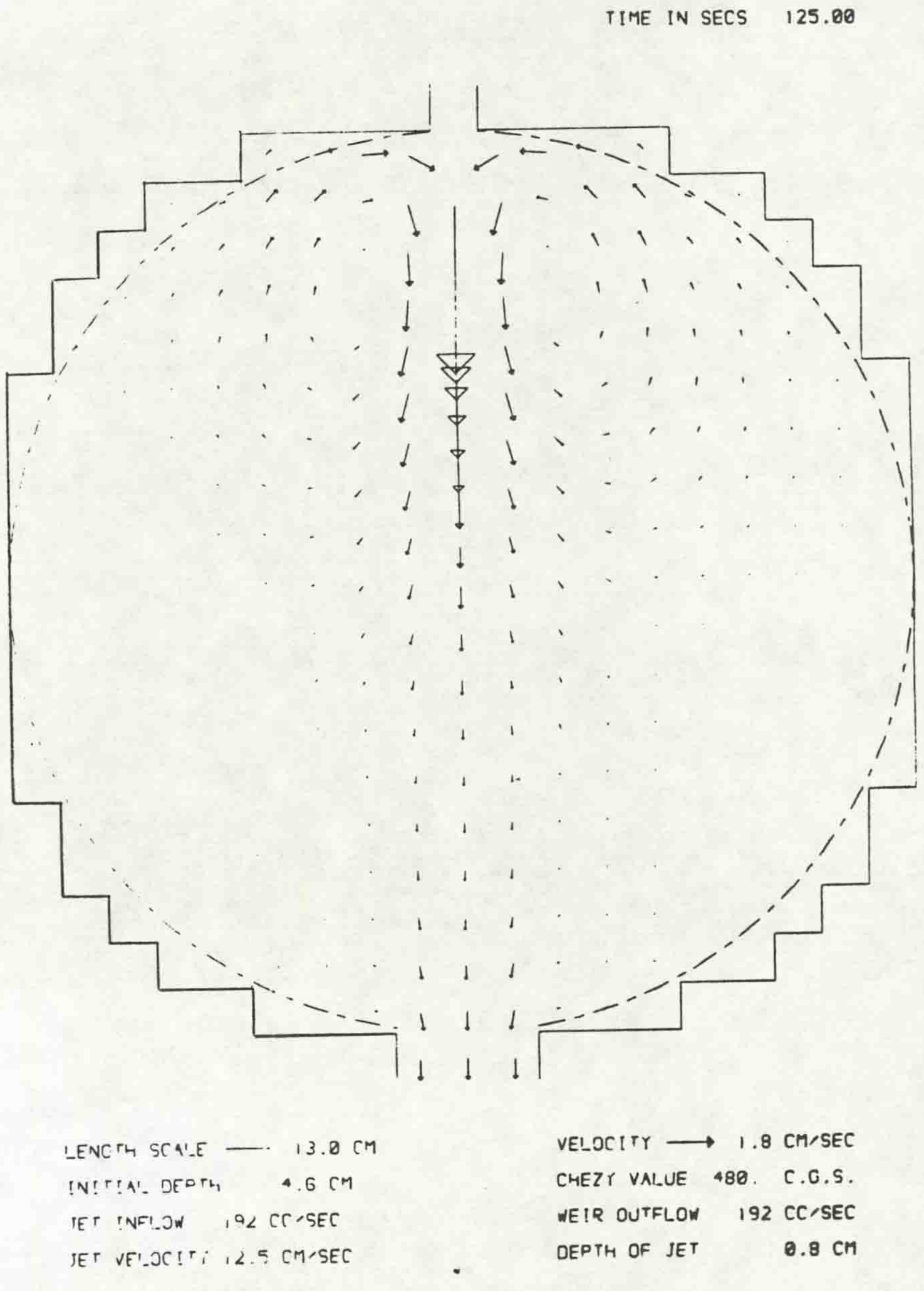

Fig. (4.15) Computational velocity field for case (A2).

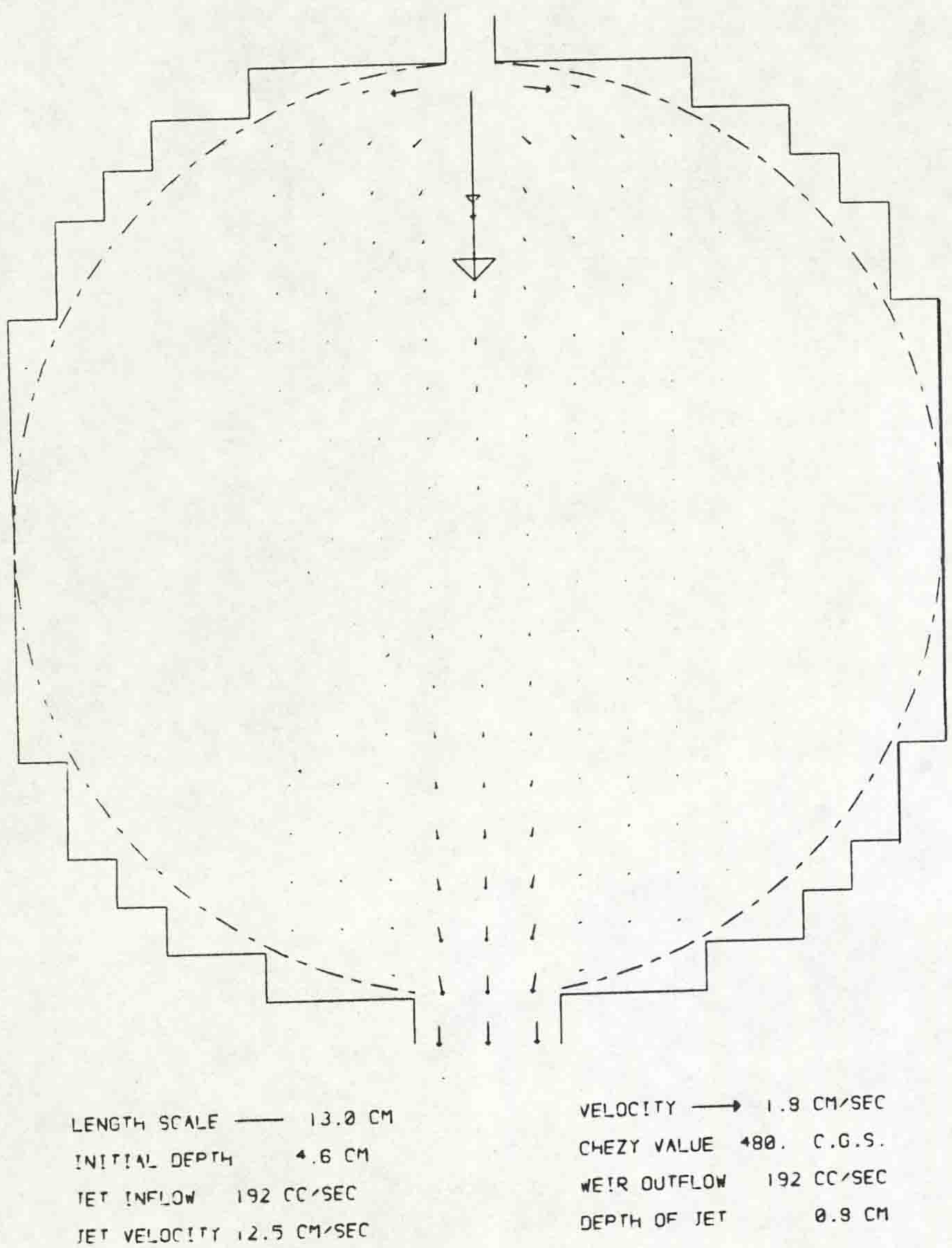

Fig. (4.16) Computational velocity field for case (A3).

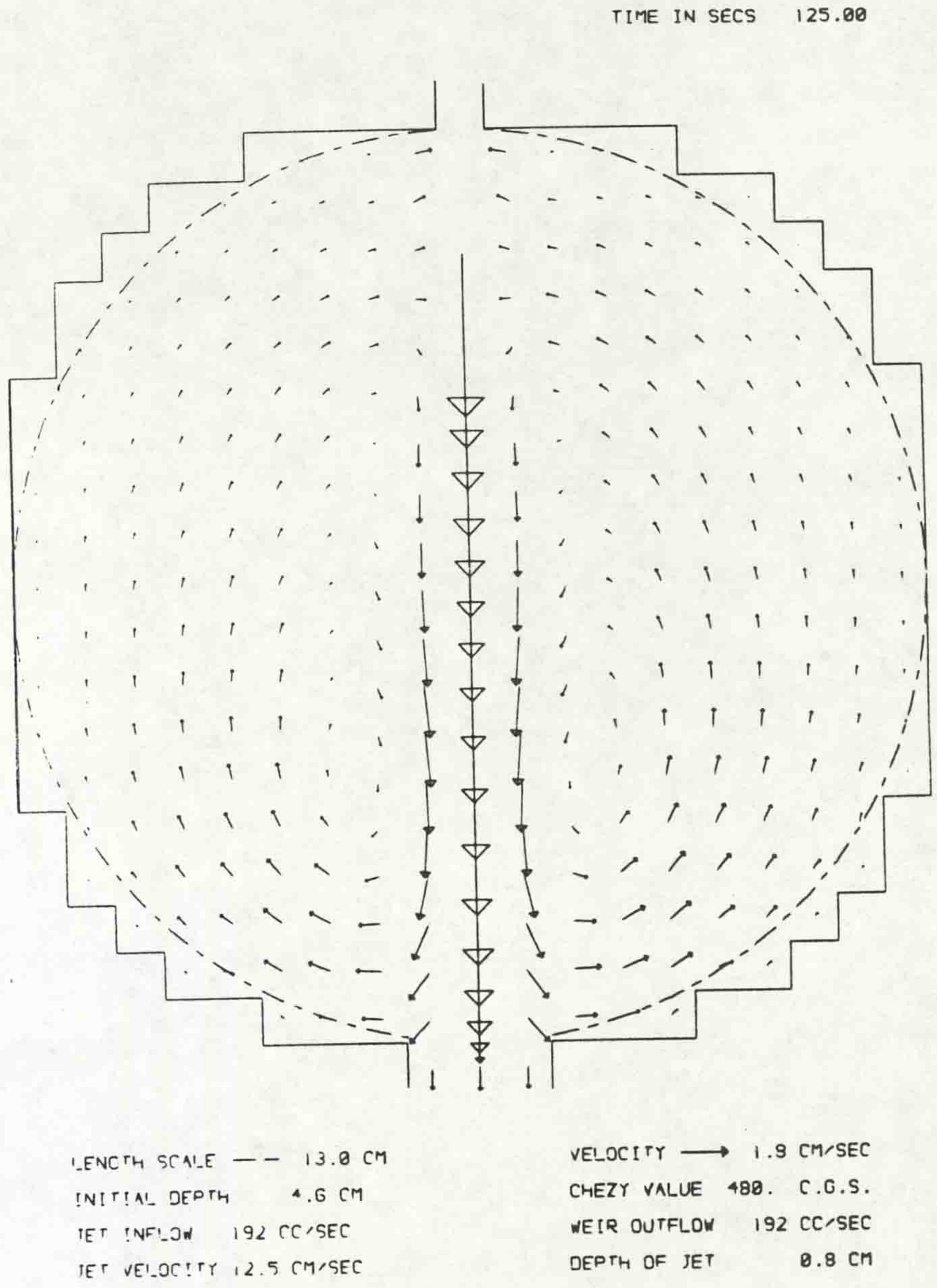

Fig. (4.17) Computational velocity field for case (A4).

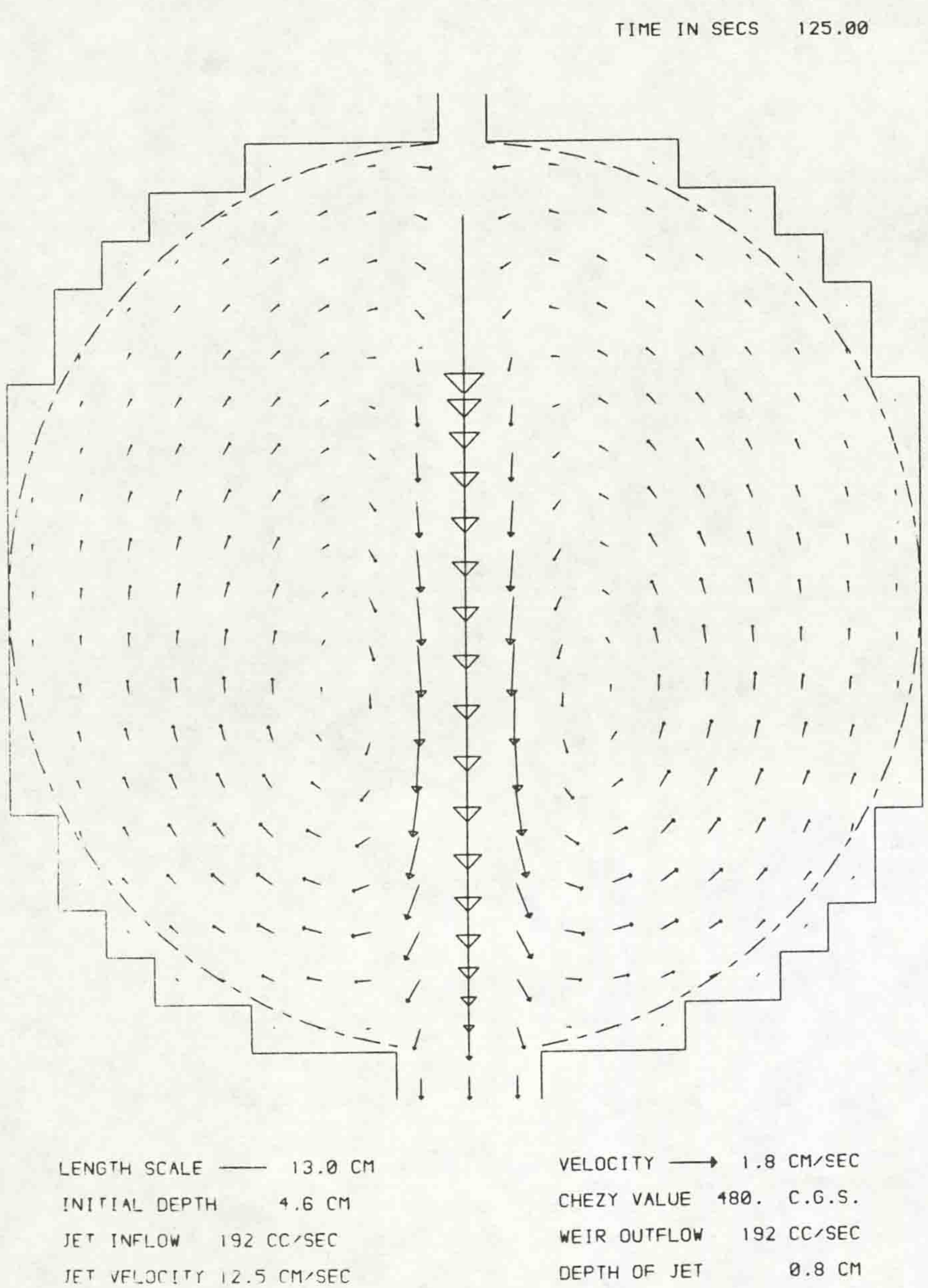

Fig. (4.18) Computational velocity field for case (A5).

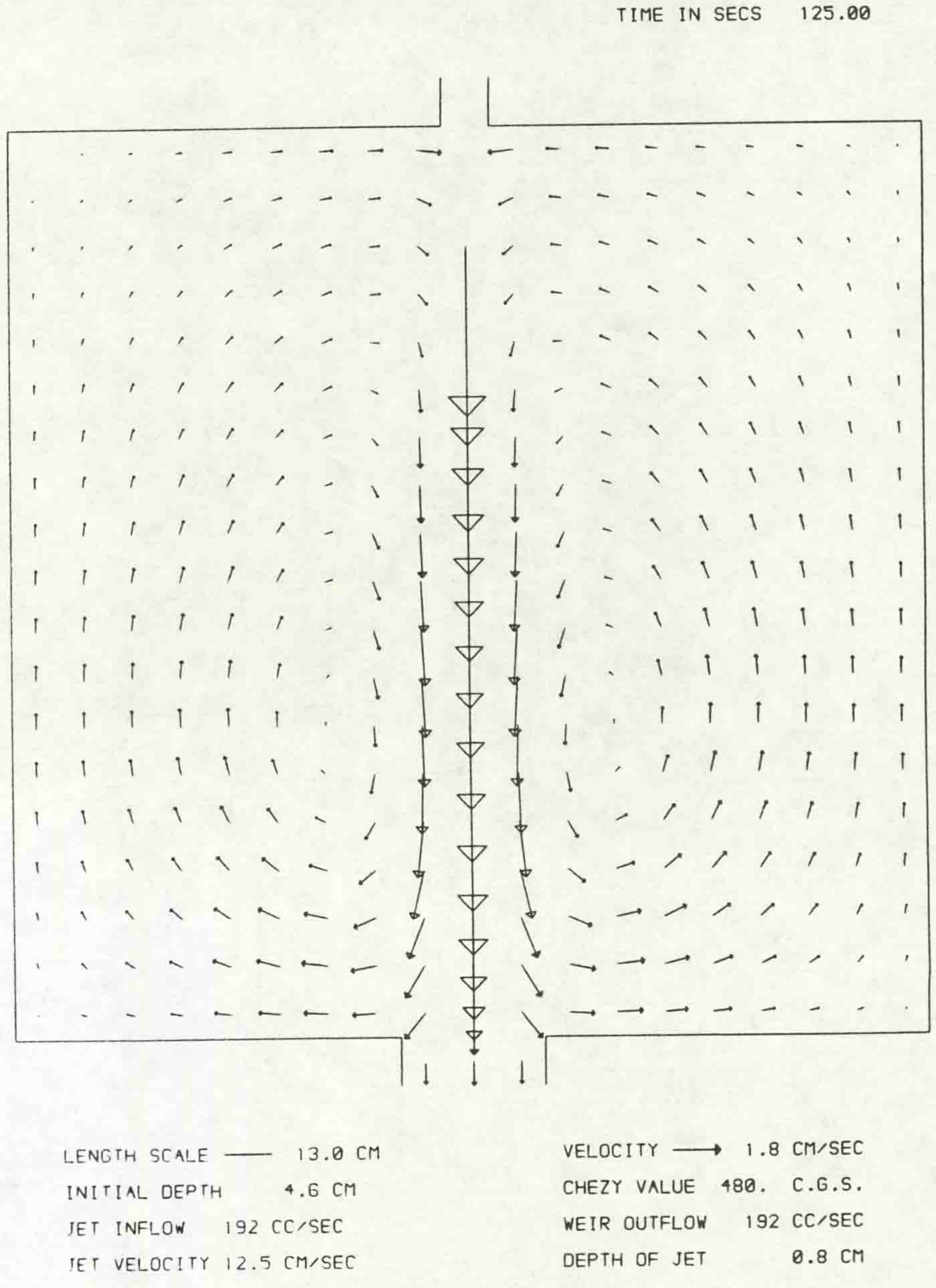

Fig. (4.19) Computational velocity field for case (A6).

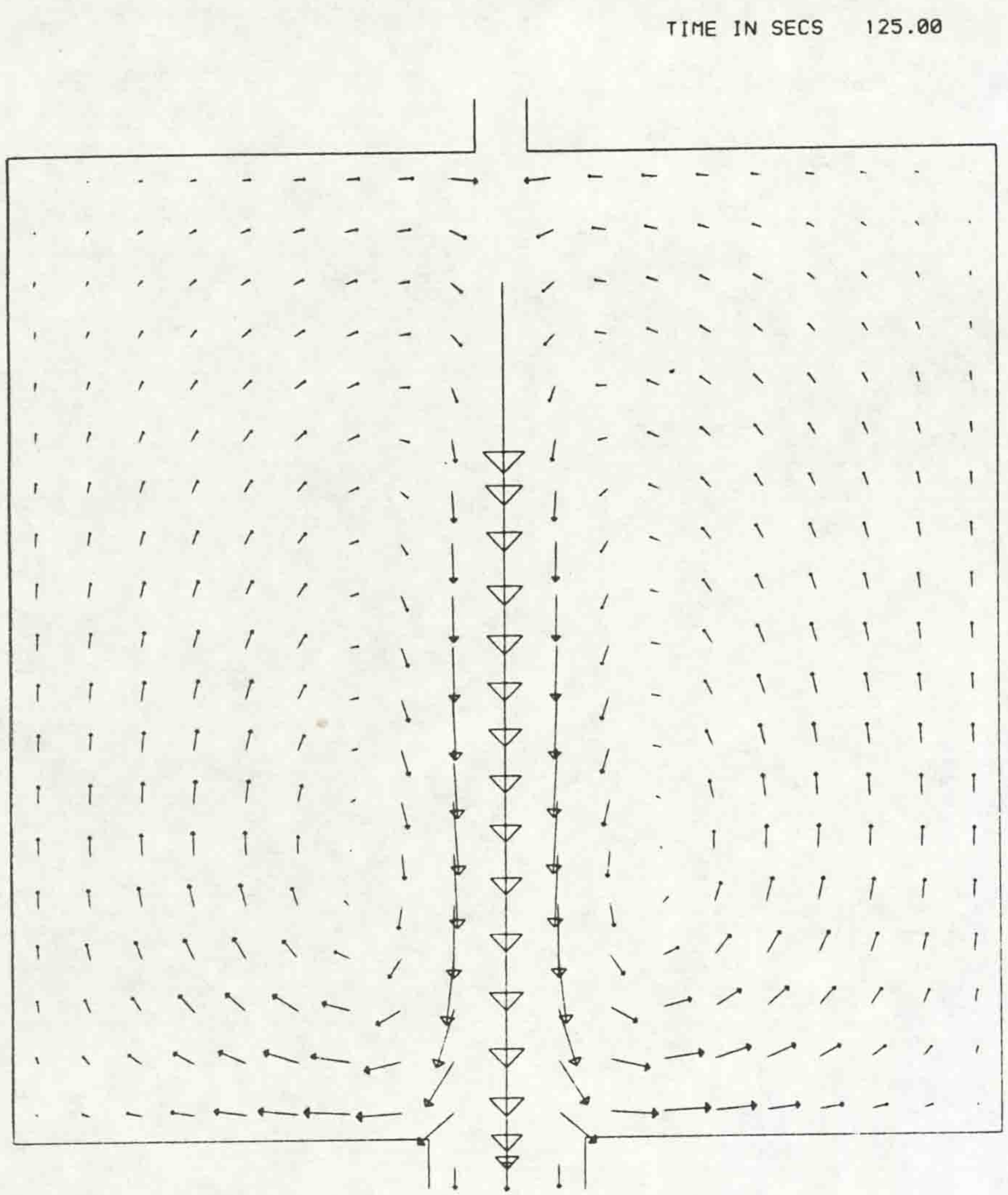

Fig. (4.20) Computational velocity field for case (A7).

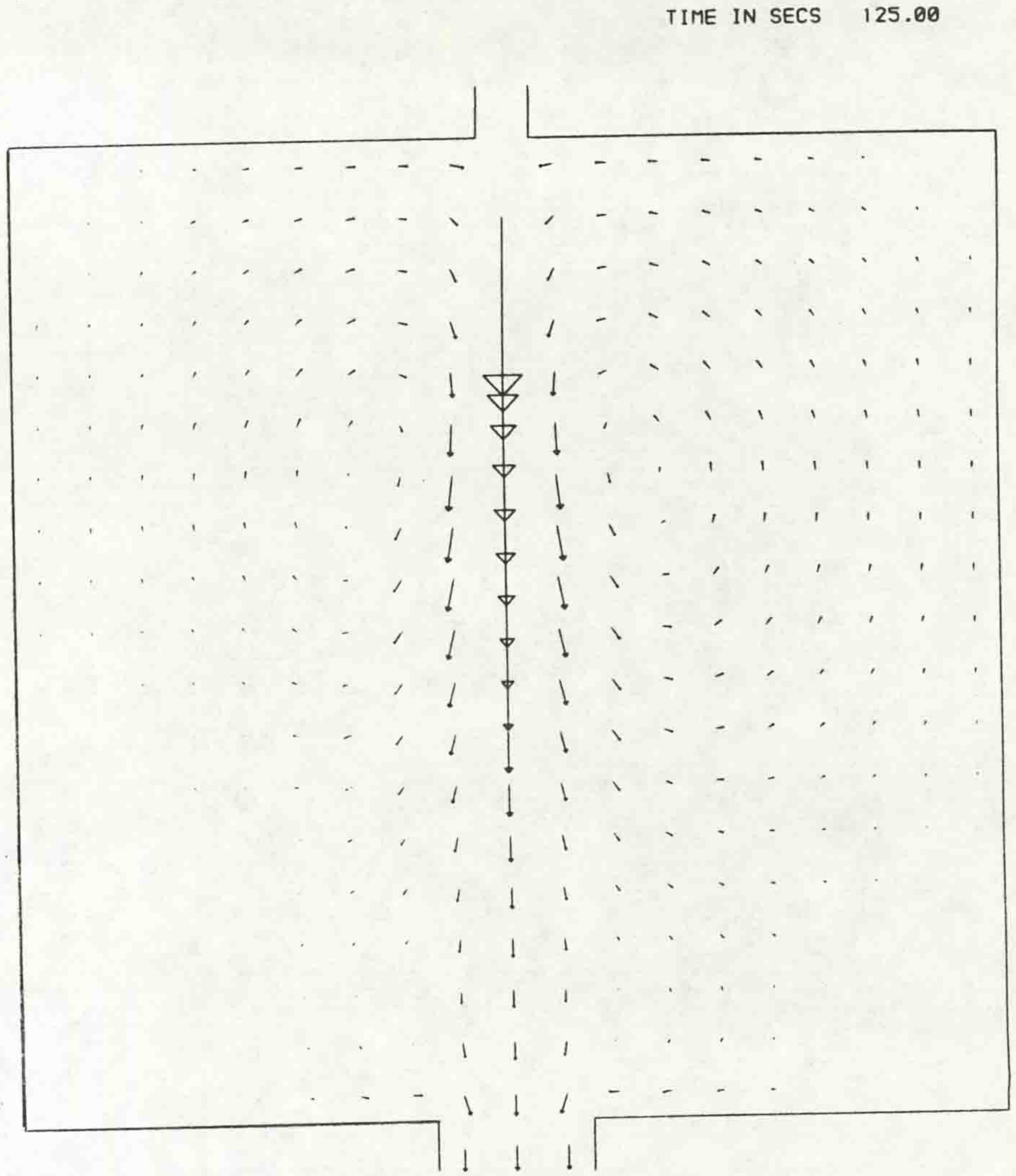

Fig. (4.21) Computational velocity field for case (A8).

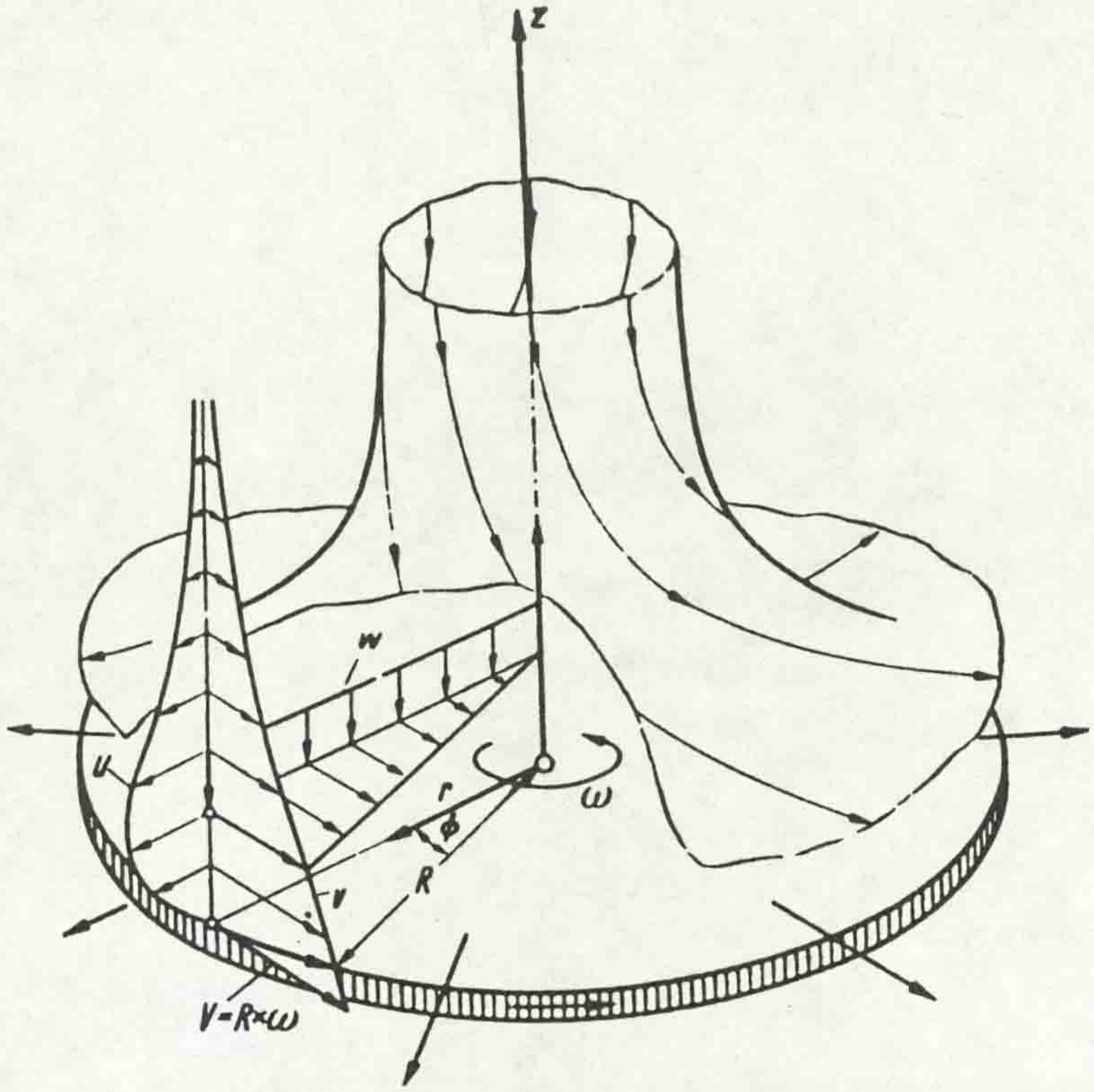

Fig. (5.1) Flow in the neighbourhood of a disk rotating in a fluid at rest.

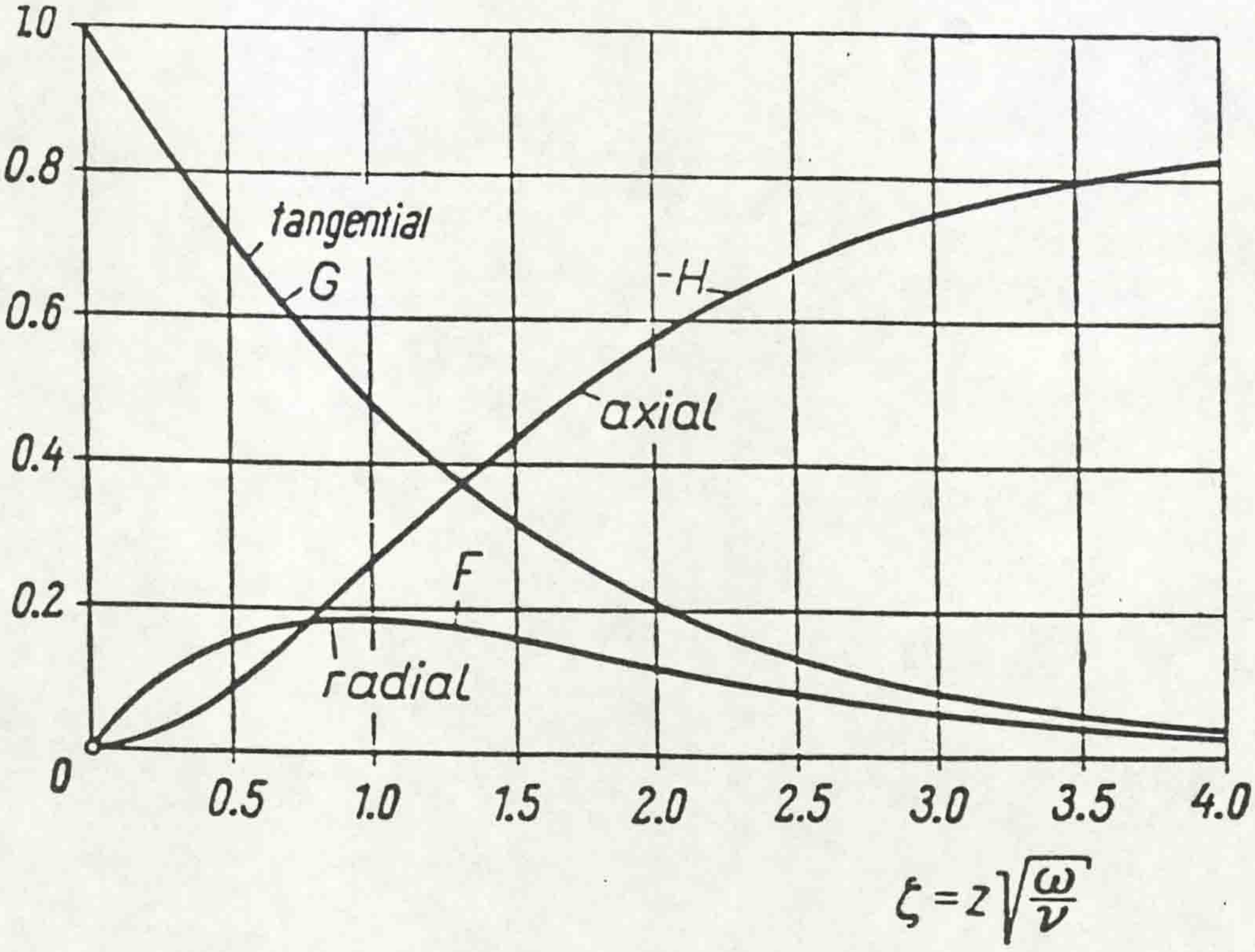

Fig. (5.2) Velocity distribution near a disk rotating in a fluid at rest.

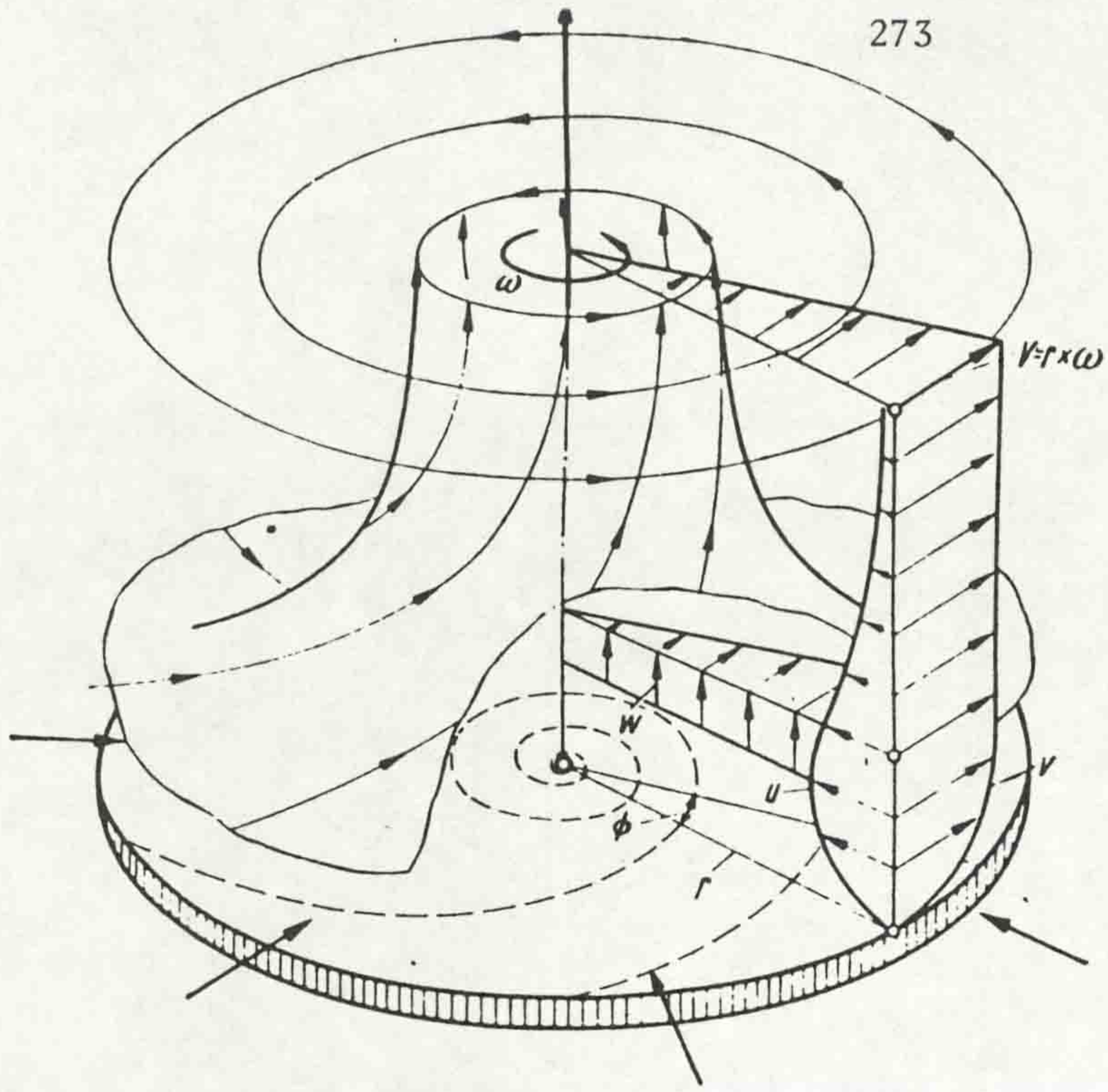

Fig. (5.3) Rotation of flow near a disk.

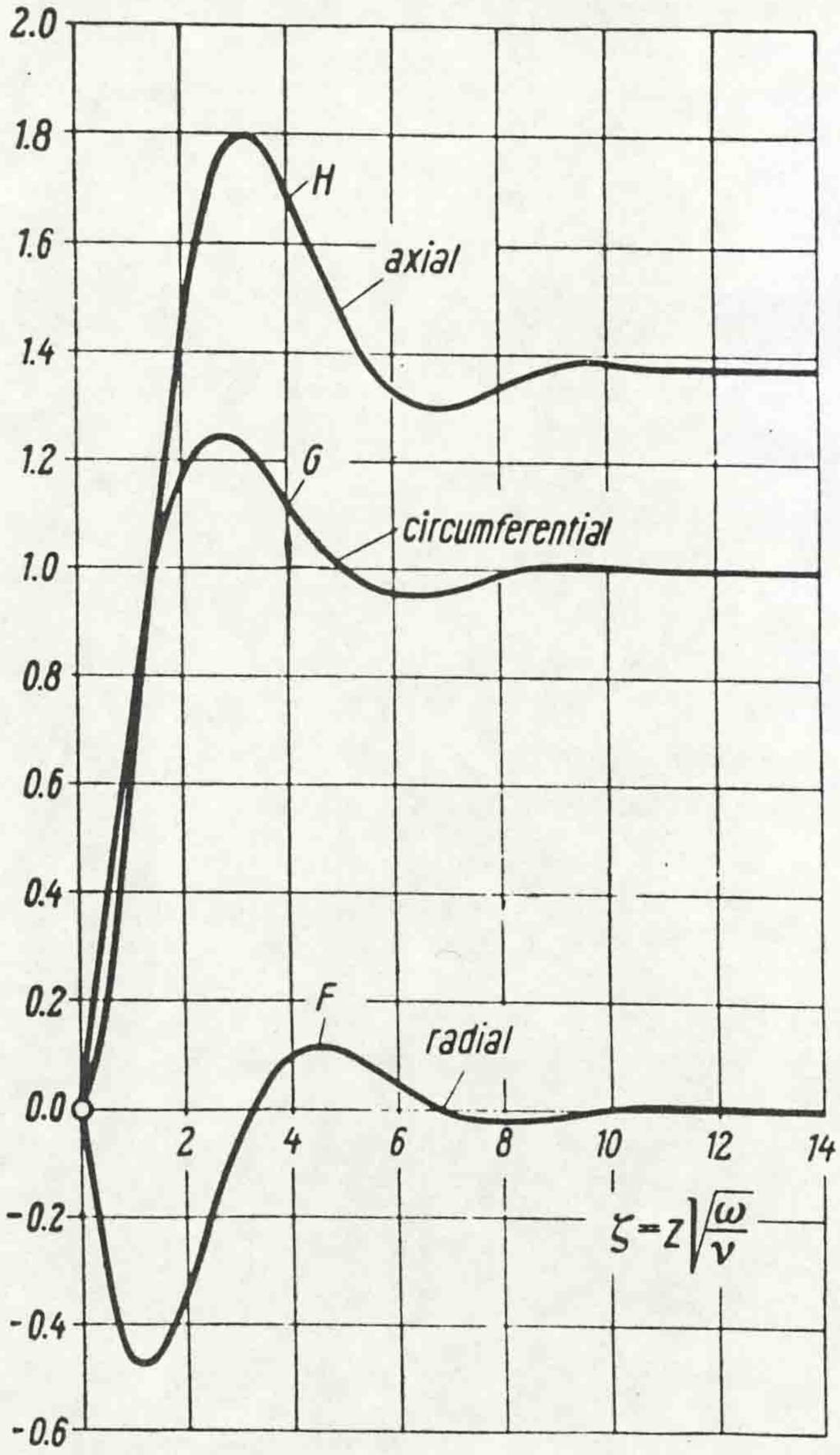

Fig. (5.4) Velocity distribution in the boundary layer.

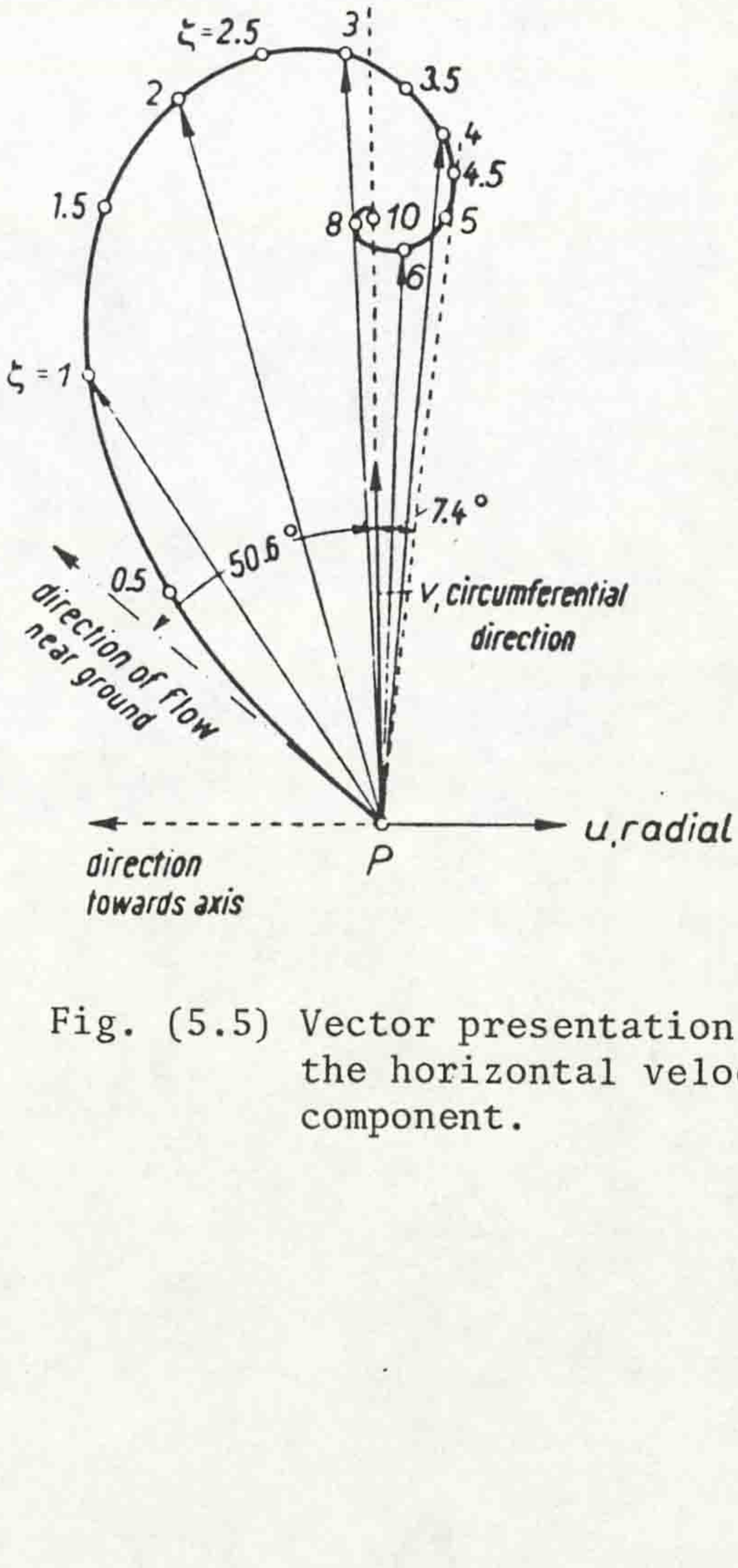

Fig. (5.5) Vector presentation of the horizontal velocity component.

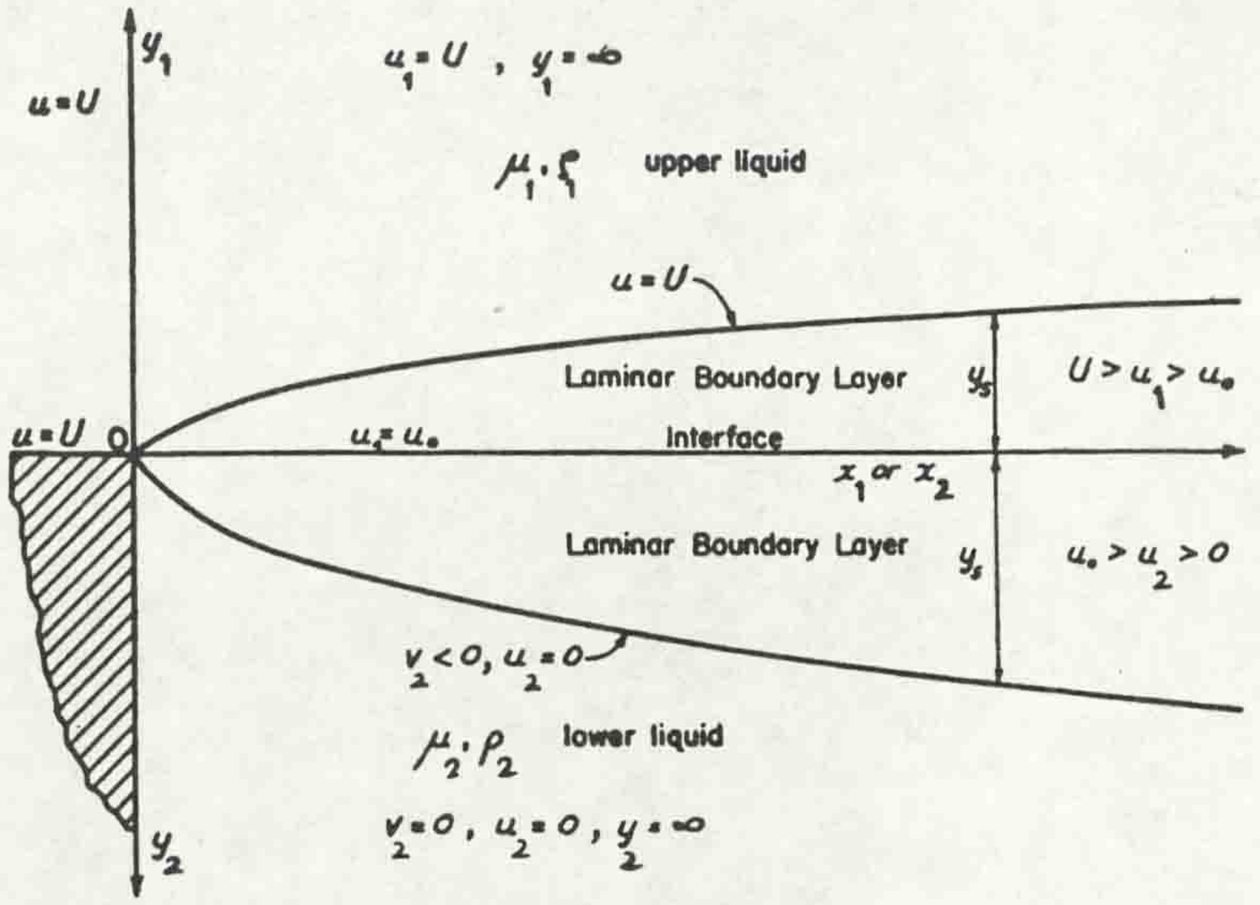

Fig. (5.6) Definition sketch for the laminar boundary layers at the interface of two liquids.

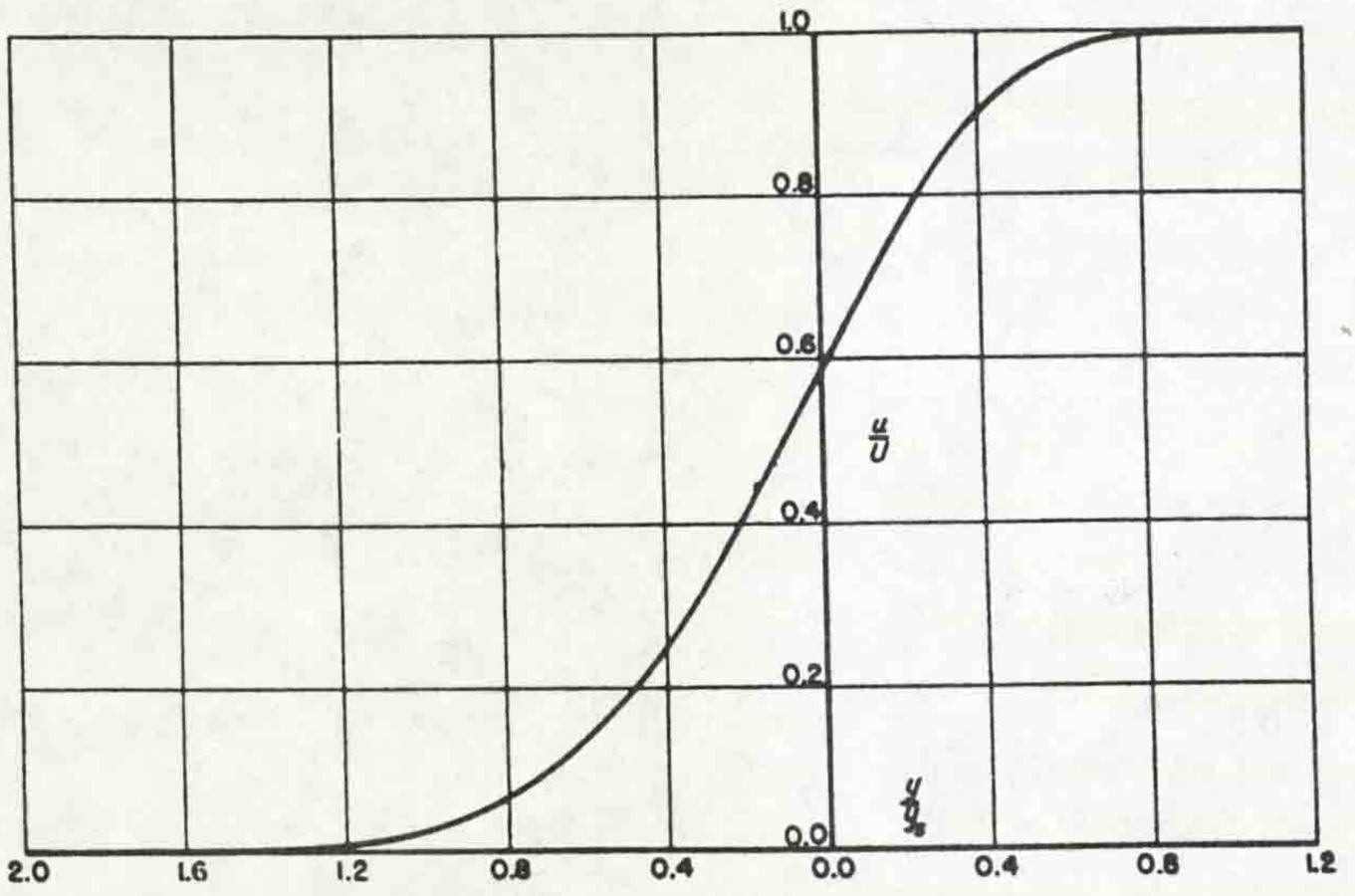

Fig. (5.7a) Interfacial laminar velocity distribution for $R = \sqrt{\mu_2 \rho_2 / \mu_1 \rho} = 1$.

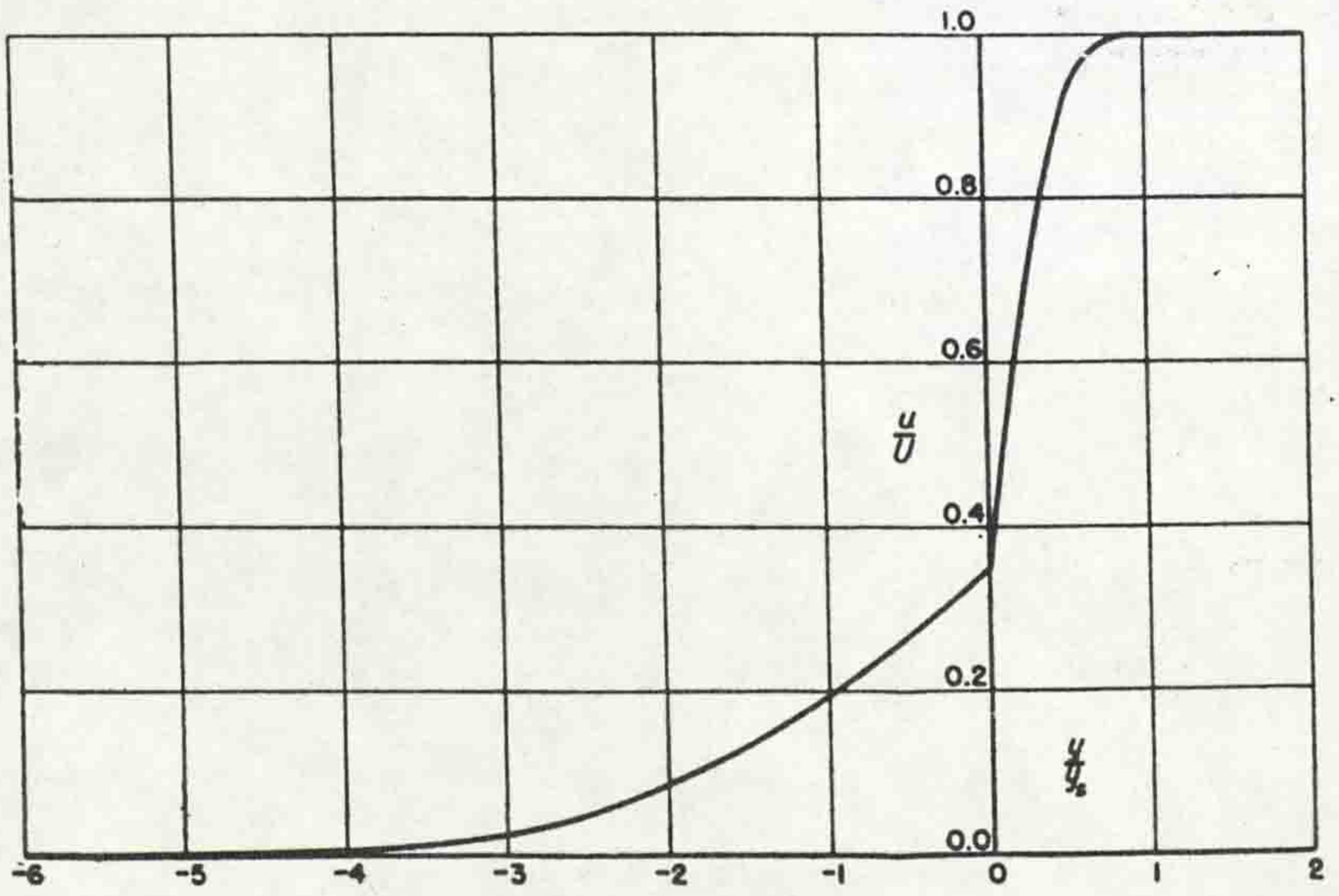

Fig. (5.7b) Interfacial laminar velocity distribution for $R = \sqrt{10}$.

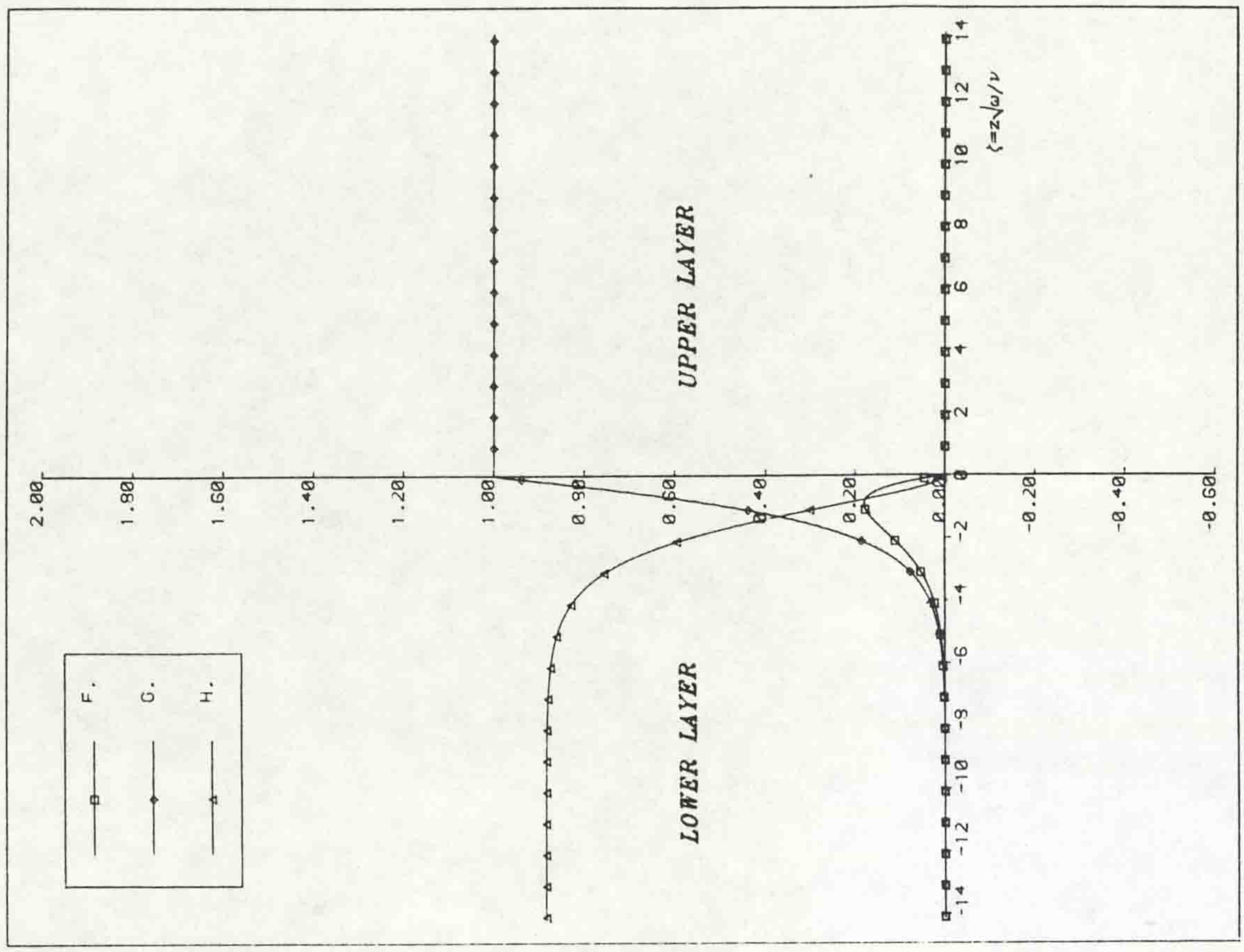

Fig. (5.9a) Interfacial velocity distribution for $R = \sqrt{\mu_2 \rho_2 / \mu_1 \rho_1} = 0.$

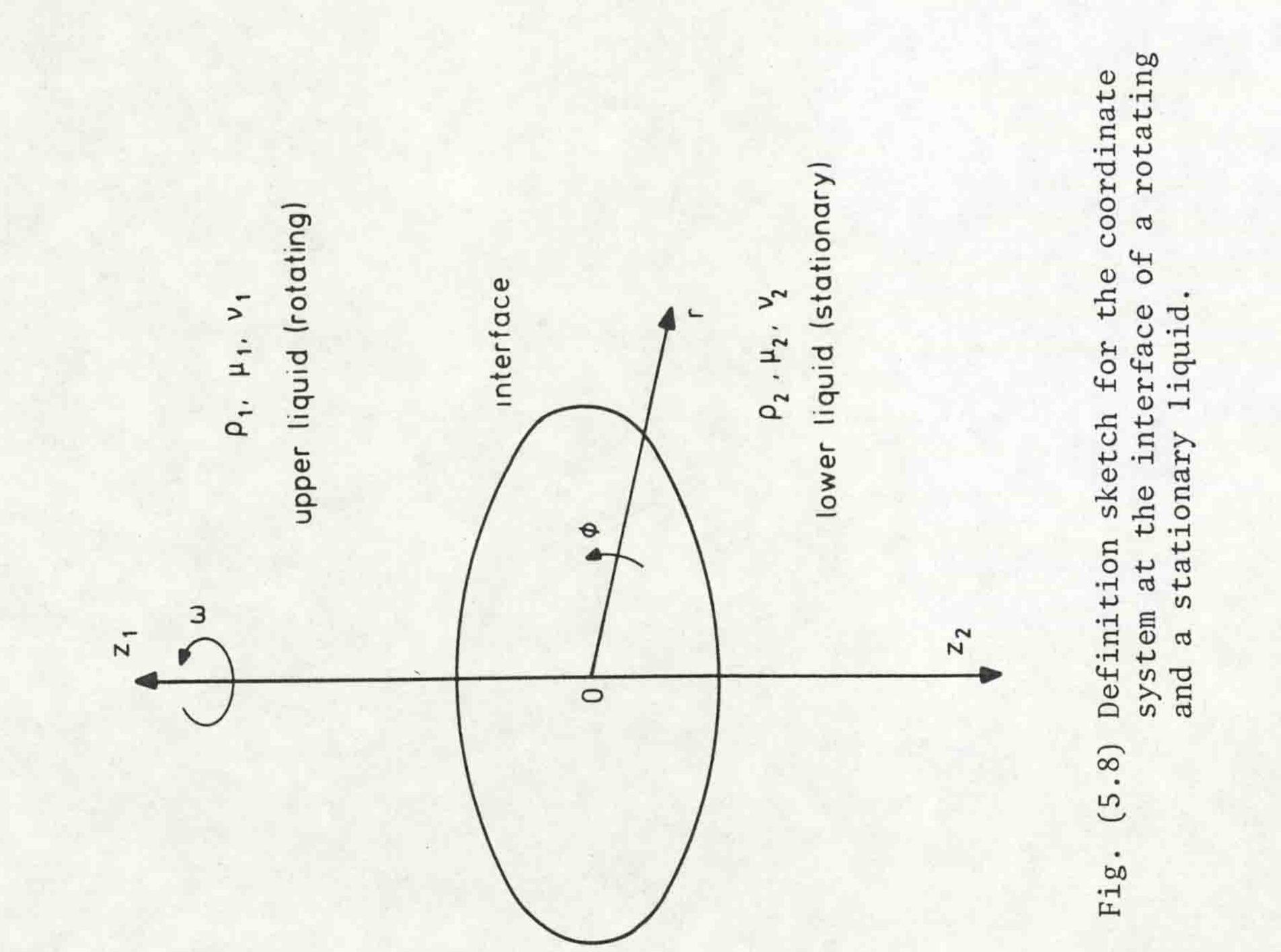

Fig. (5.8) Definition sketch for the coordinate system at the interface of a rotating and a stationary liquid.

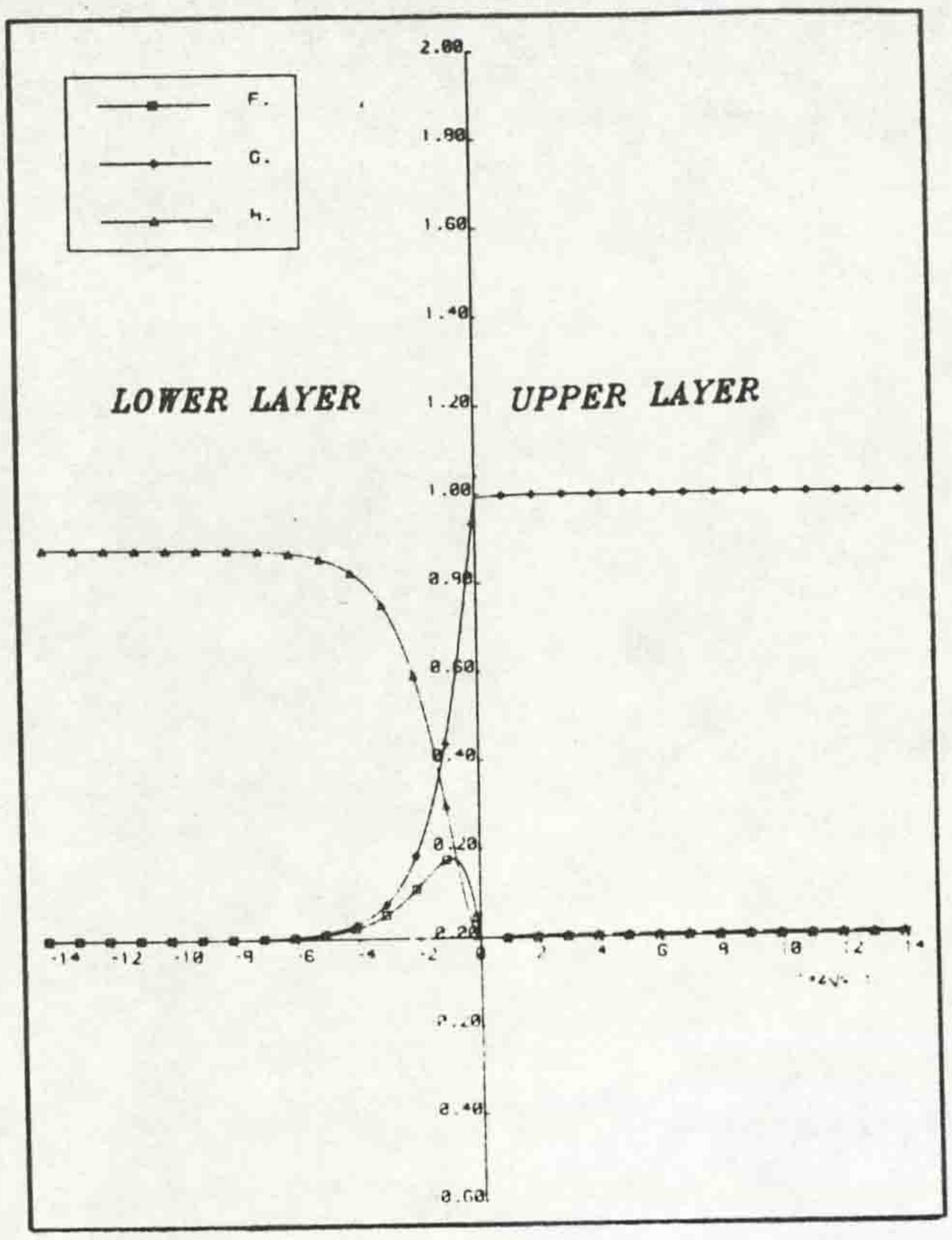

(b)

R = 0.01

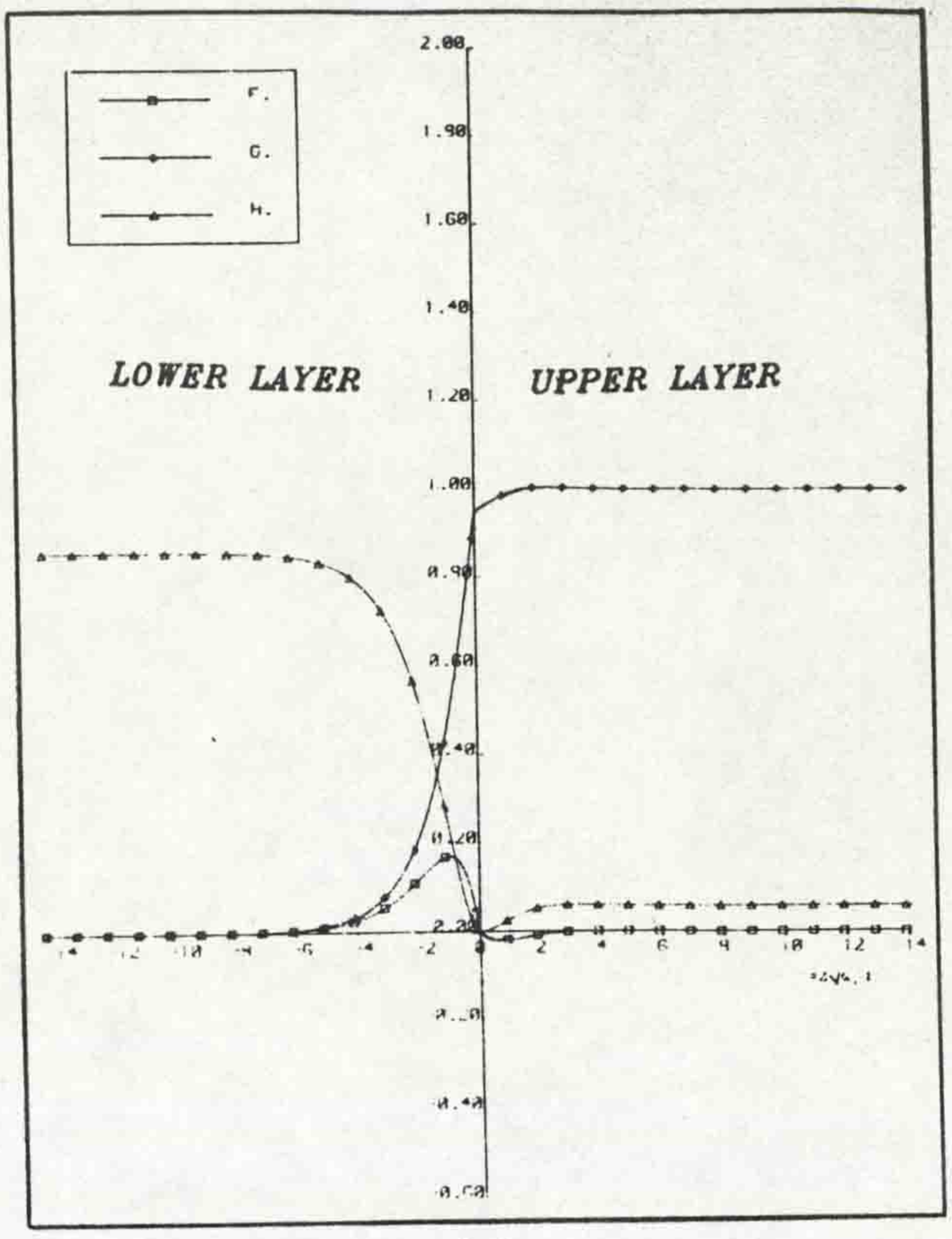

(c)

R = 0.1

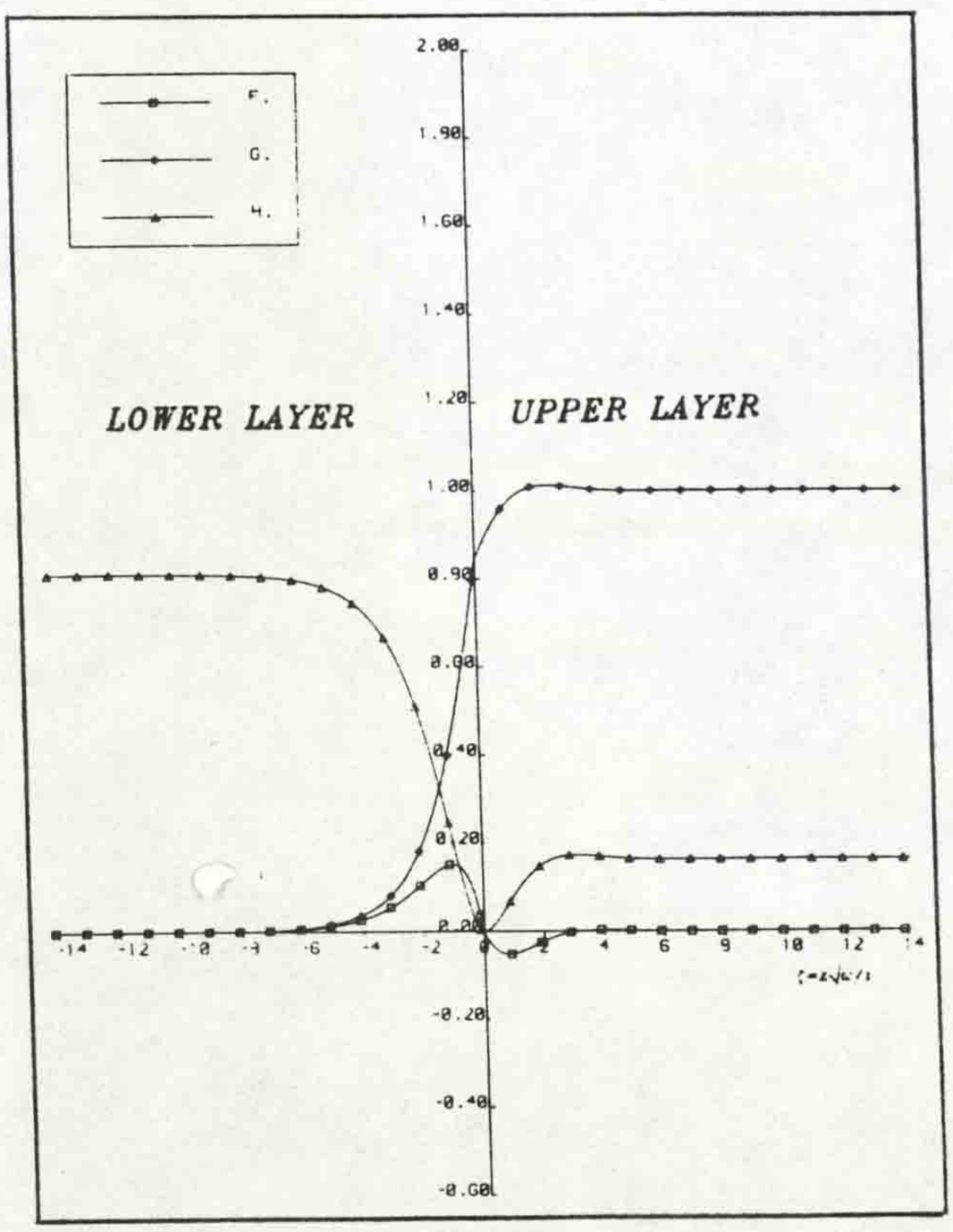

(d)

R = $\sqrt{0.1}$

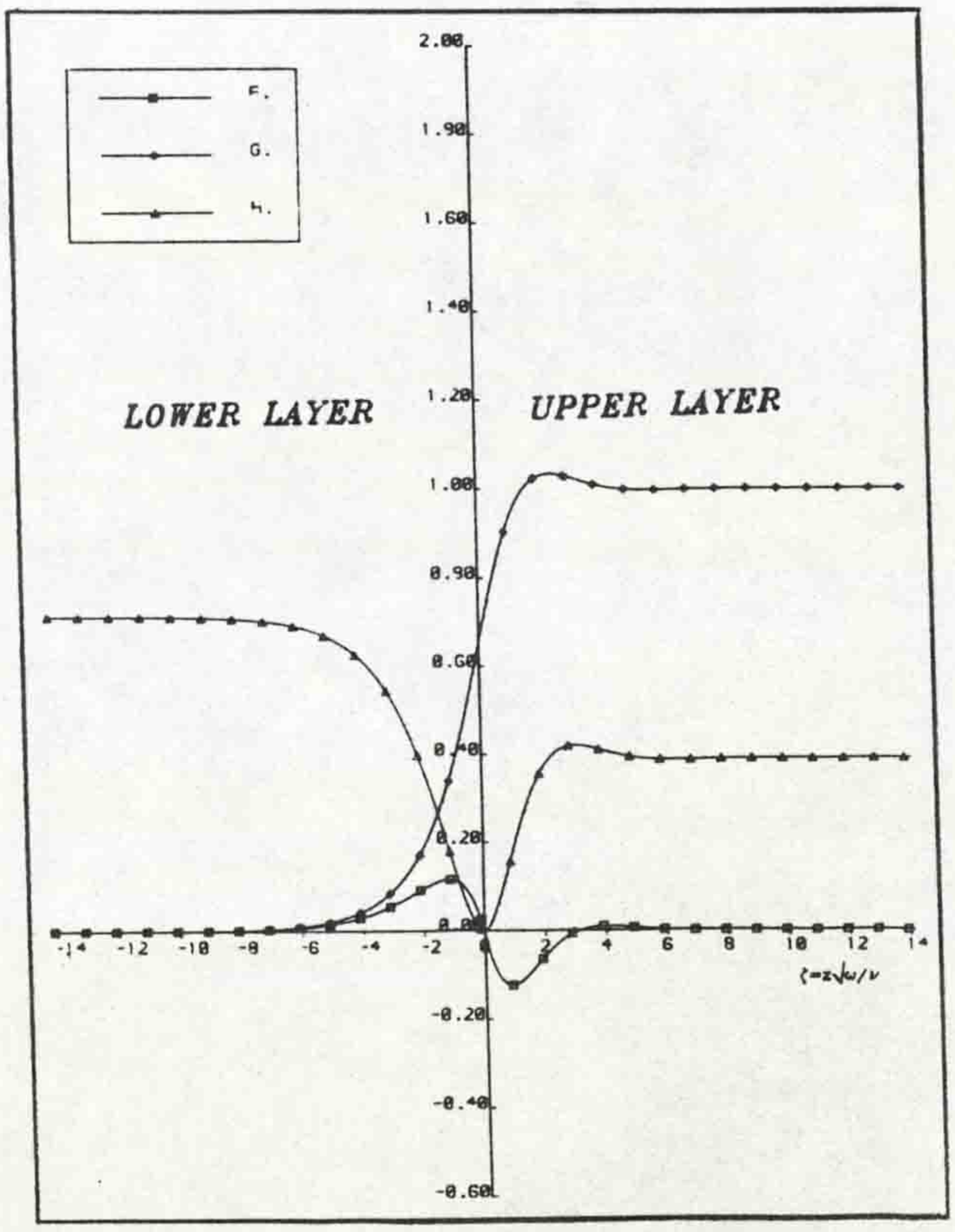

(e)

R = 1

Fig. (5.9b-e) Interfacial velocity distribution for different values of $R = \sqrt{\mu_2\rho_2/\mu_1\rho_1}$.

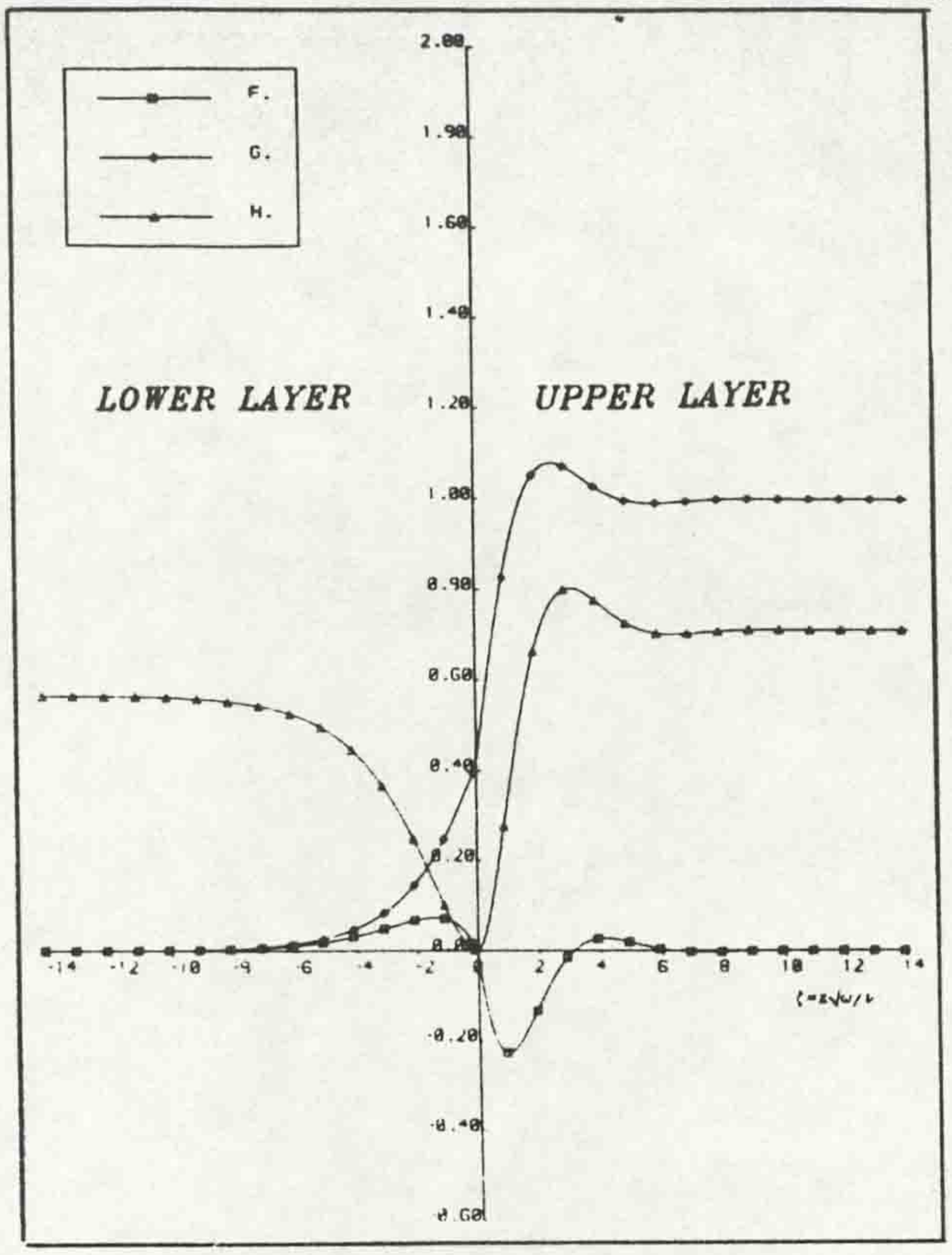

(f)

$R = \sqrt{10}$

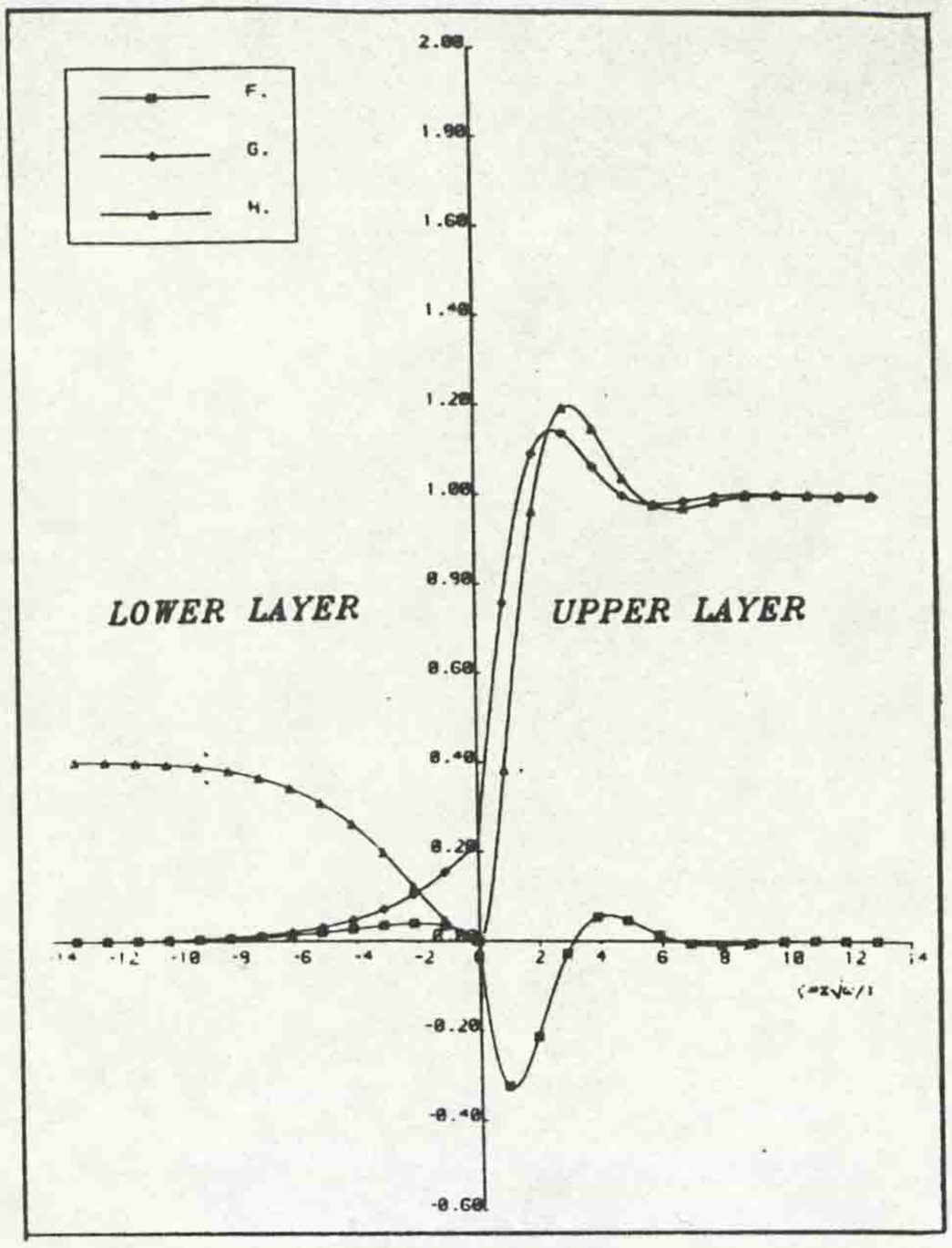

(g)

$R = 10$

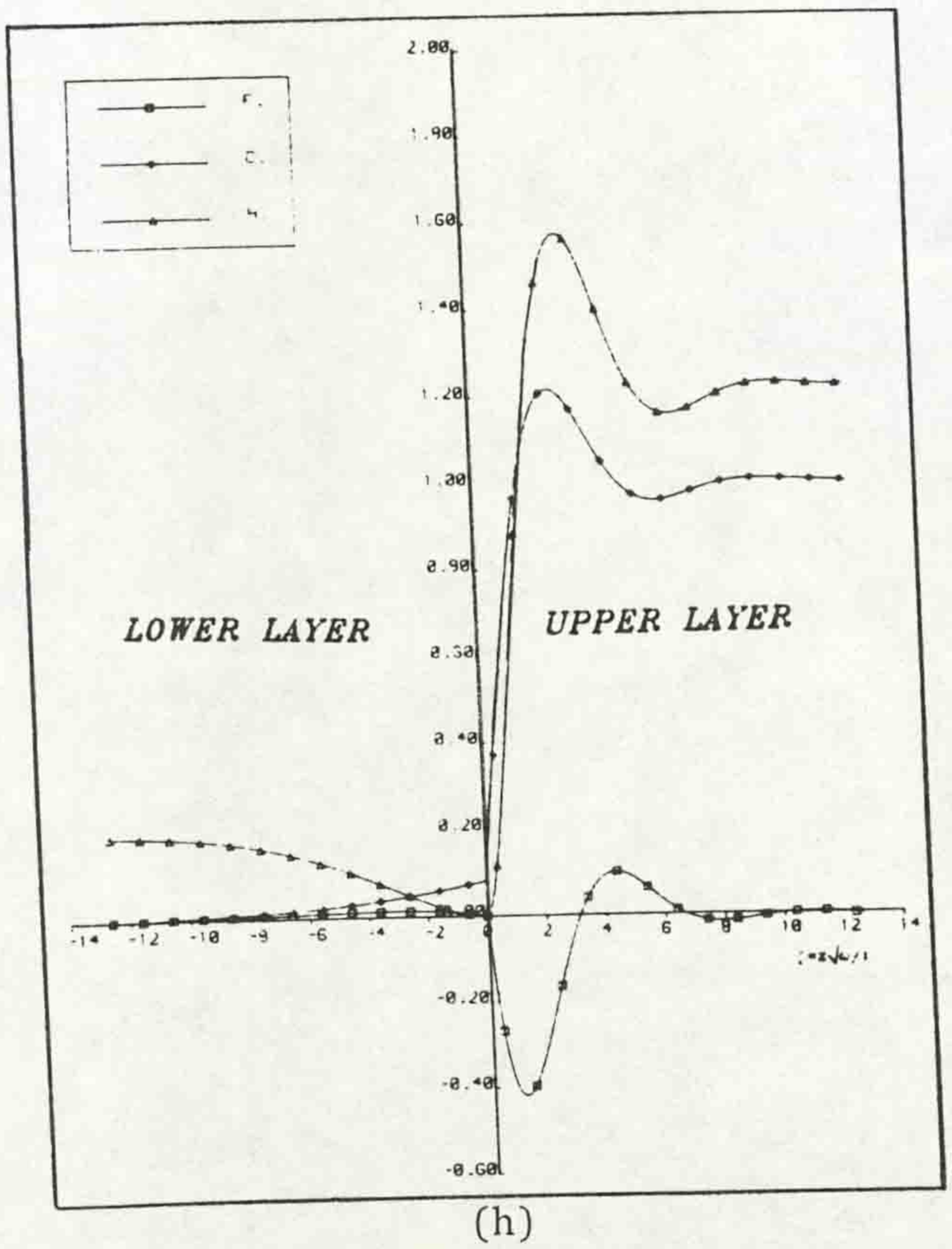

(h)

$R = 100$

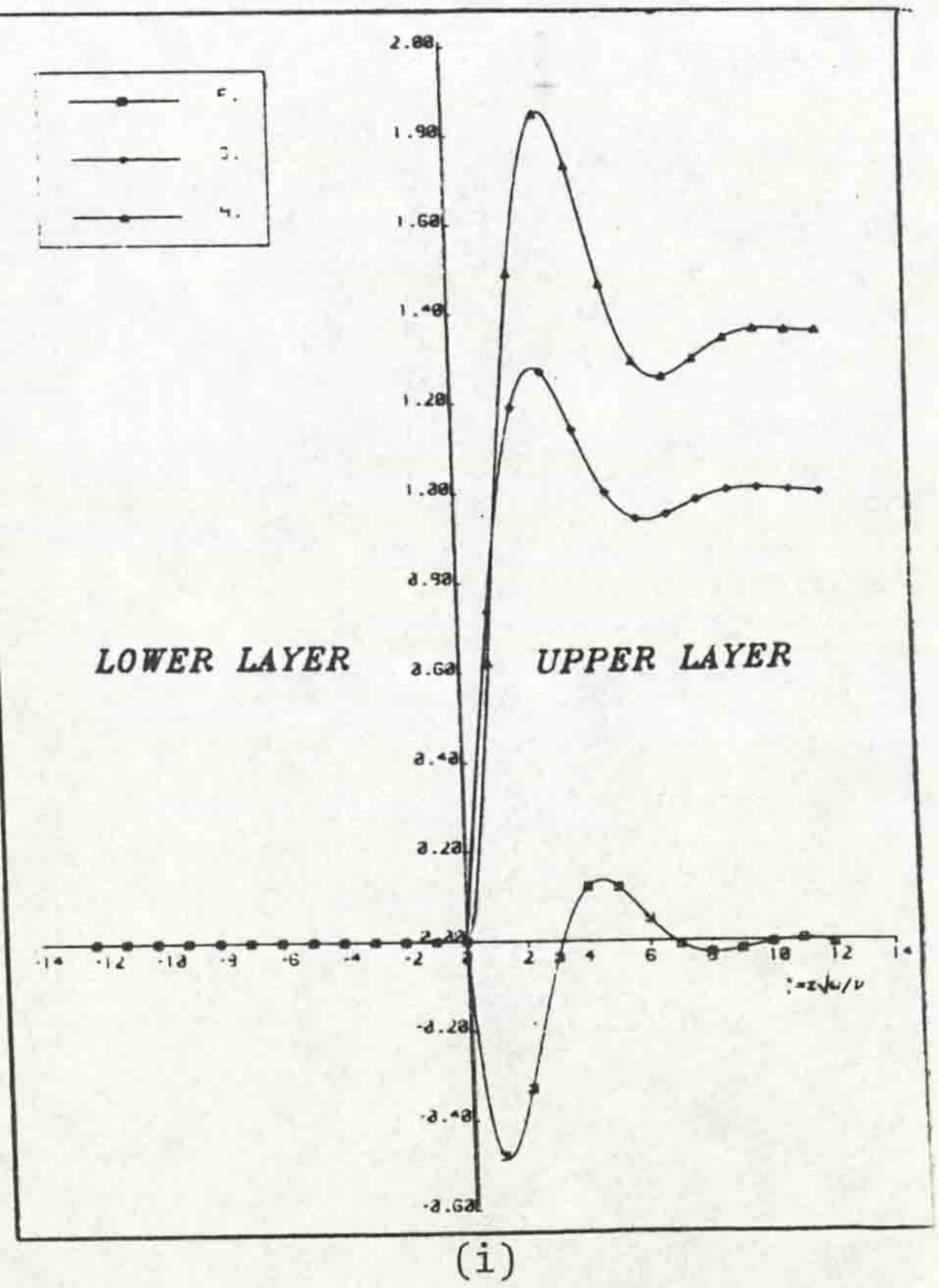

(i)

$R = \infty$

Fig. (5.9f-i) Interfacial velocity distribution for different values of $R = \sqrt{\mu_2\rho_2/\mu_1\rho_1}$.

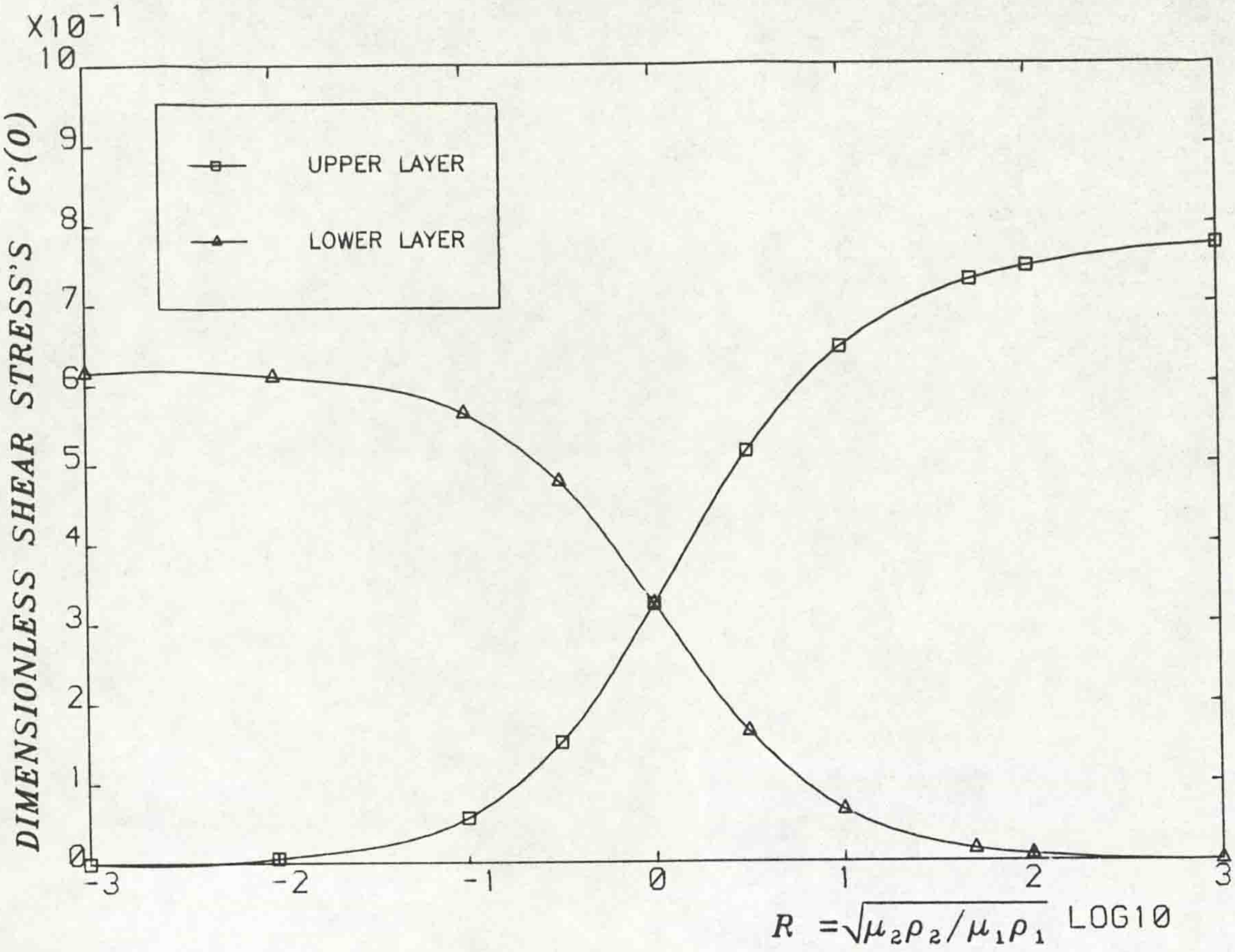

Fig. (5.10) Variation of dimensionless shear stresses versus R.

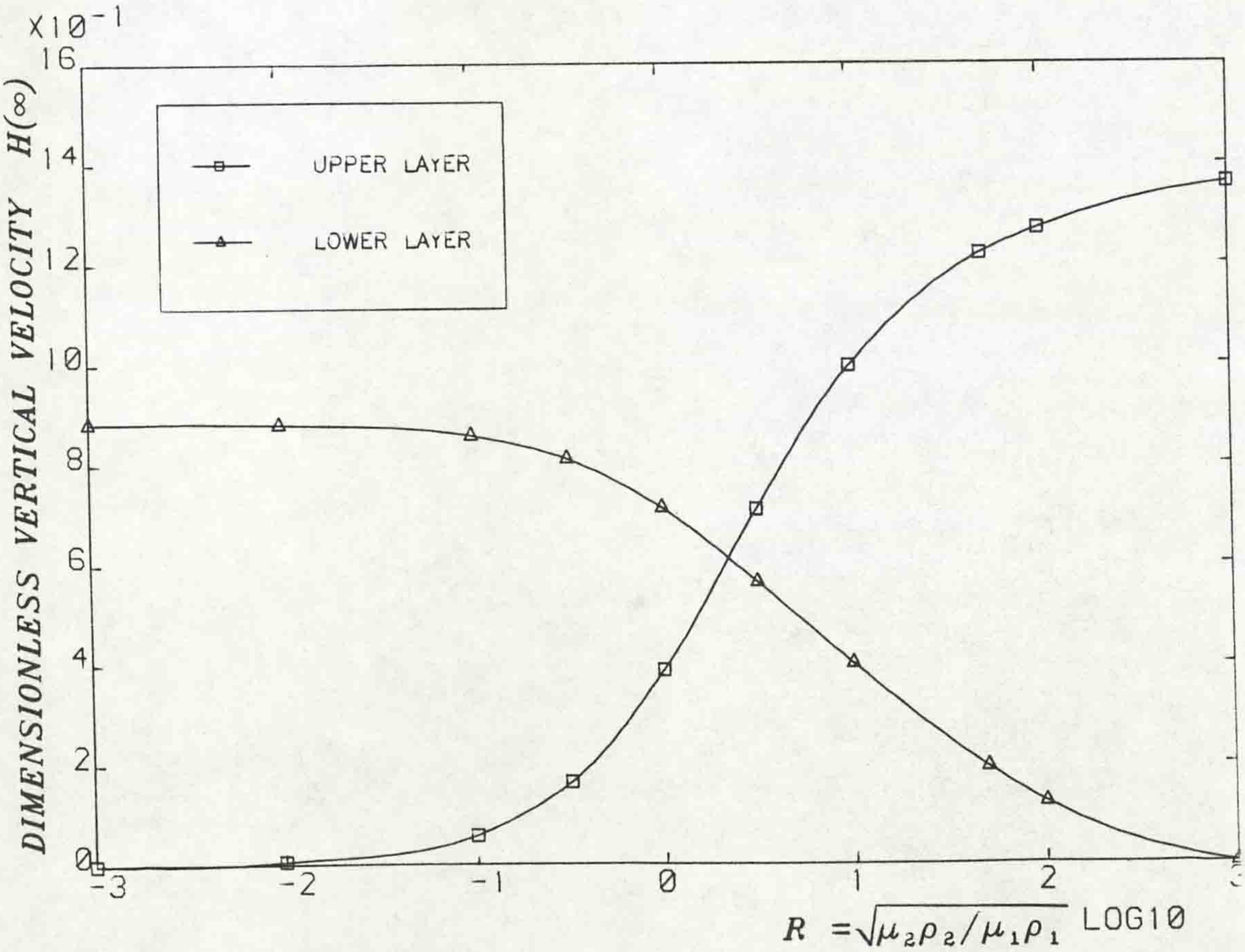

Fig. (5.11) Variation of asymptotic dimensionless vertical velocities versus R.

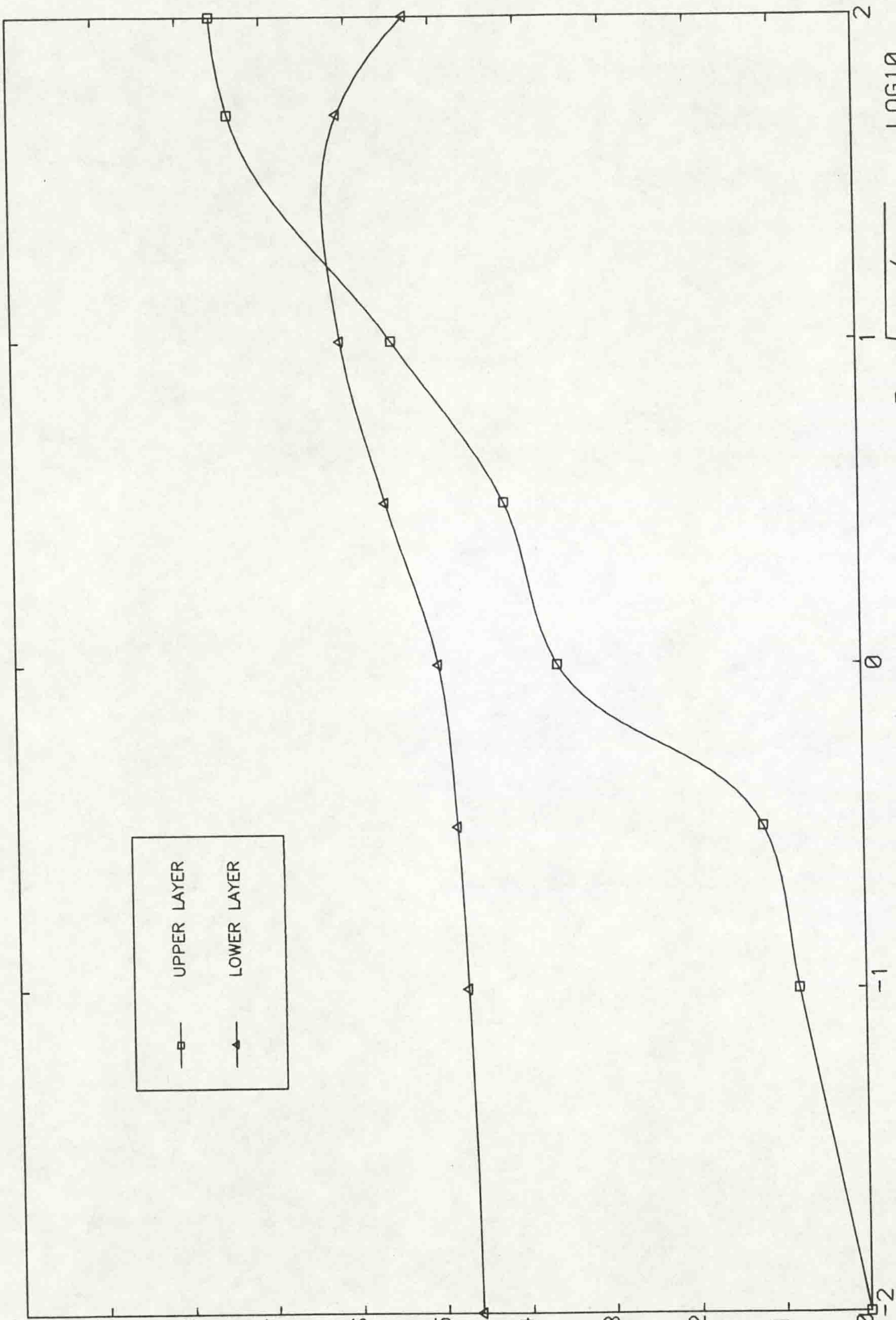

Fig. (5.12) Variation of dimensionless boundary layer thicknesses versus R.

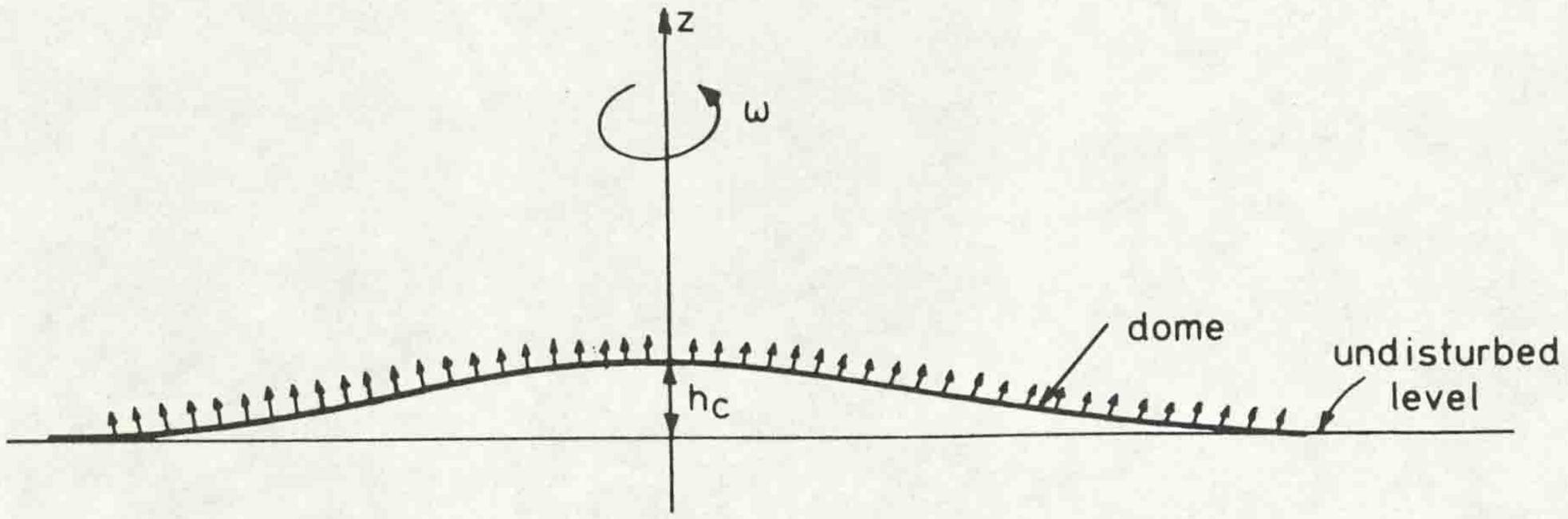

Fig. (5.13) Deformation of the shape of interface due to rotation of the upper layer.

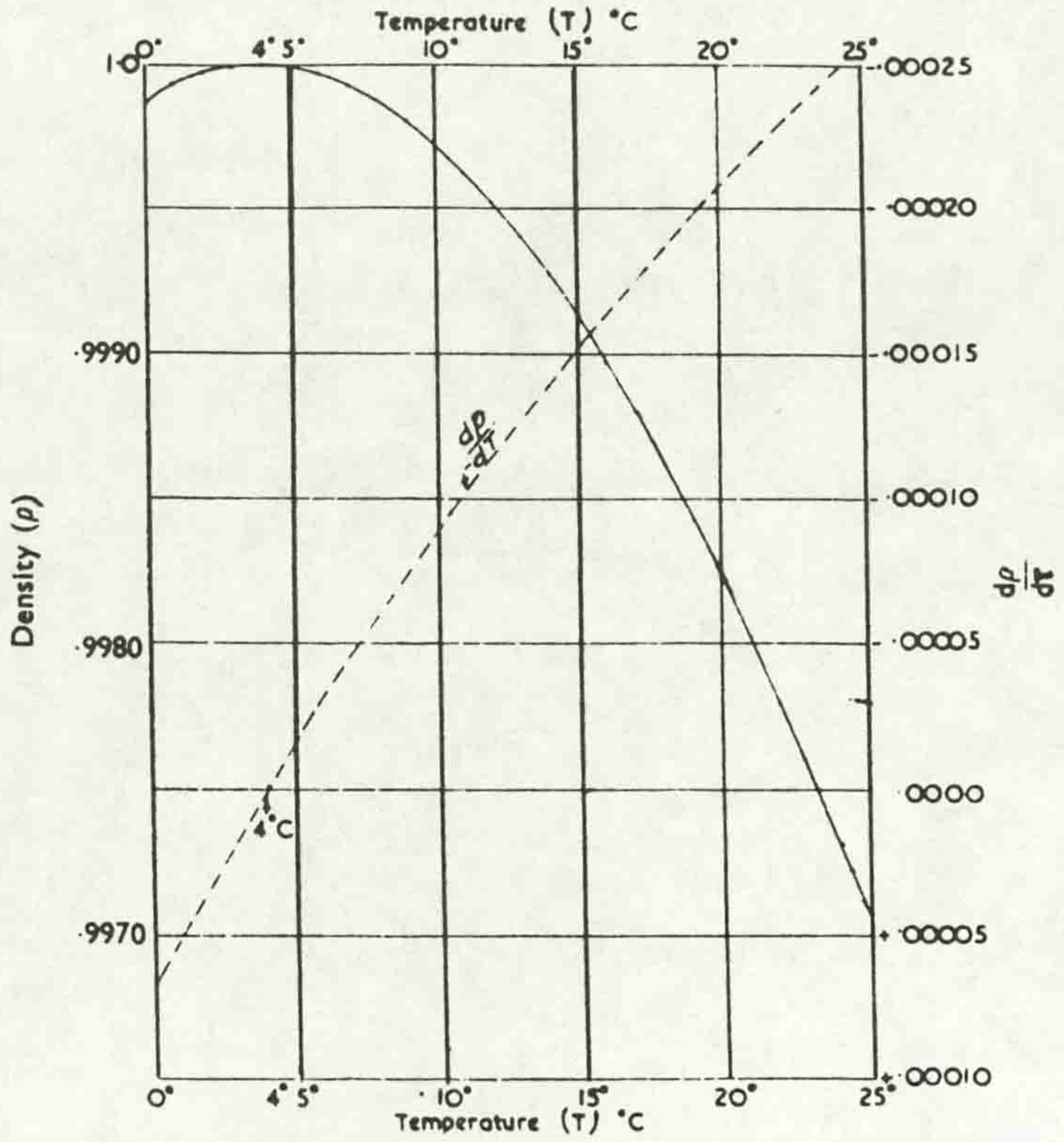

Fig. (6.1) Temperature - density relations for pure water.

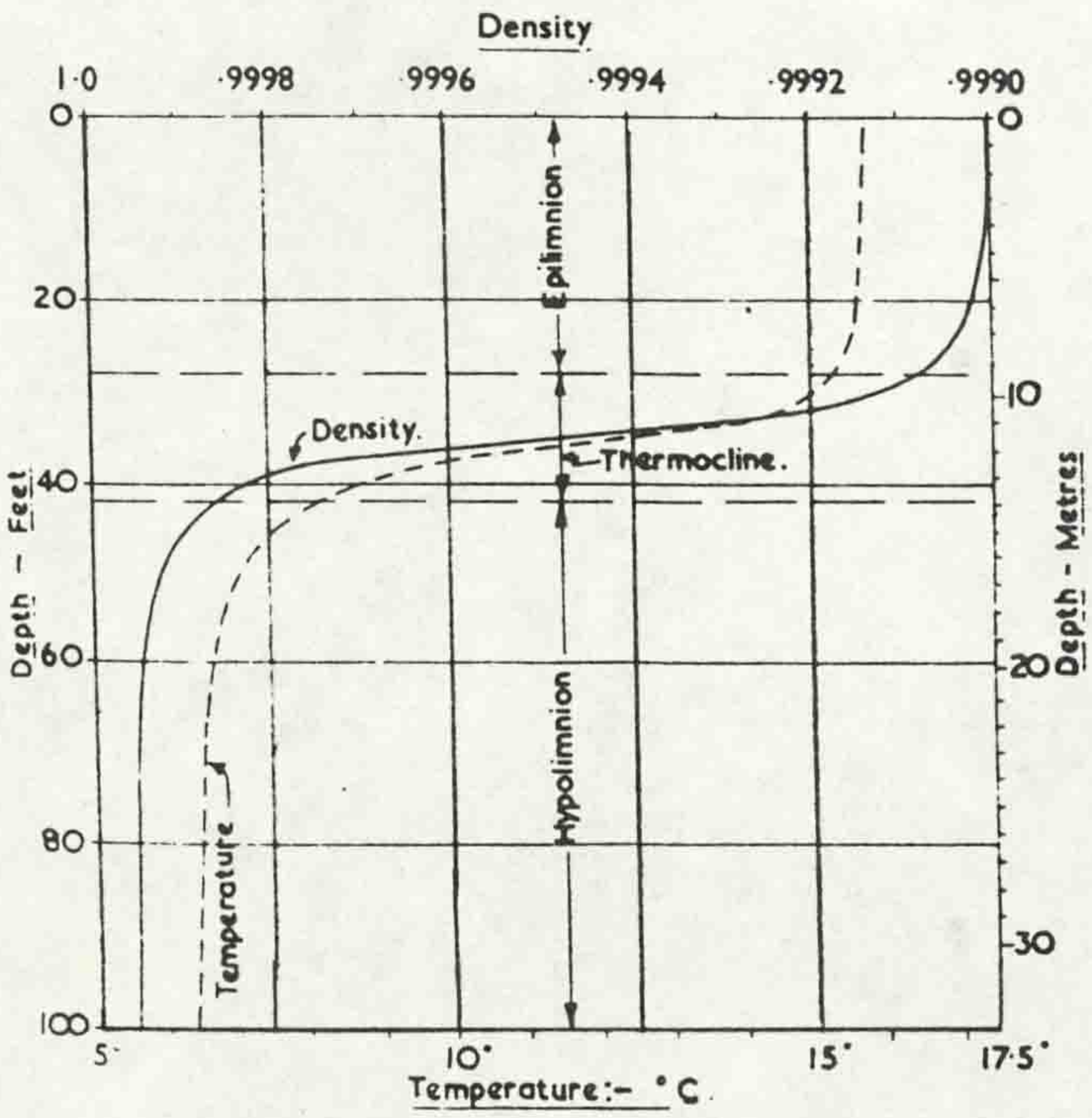

Fig. (6.2) Typical summer stratification in a reservoir.

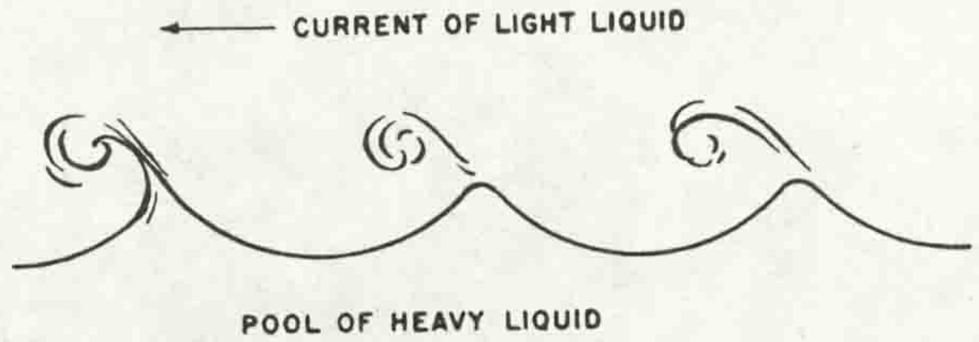

Fig. (6.3) Instability of the interfacial waves.

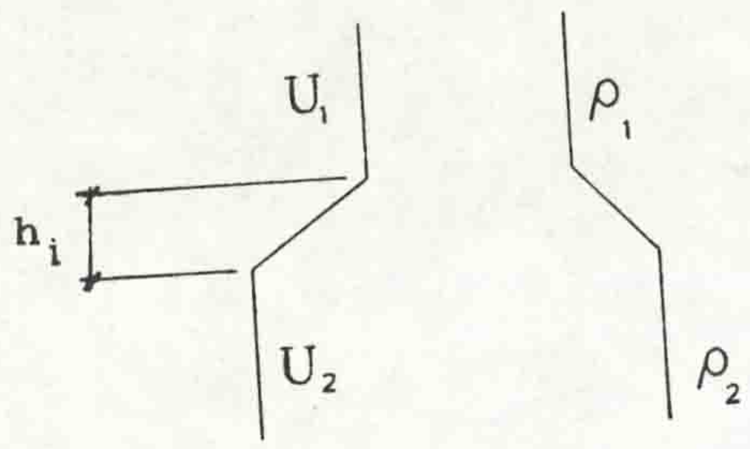

Fig. (6.4a) Velocity and density profiles for the interfacial stability calculations.

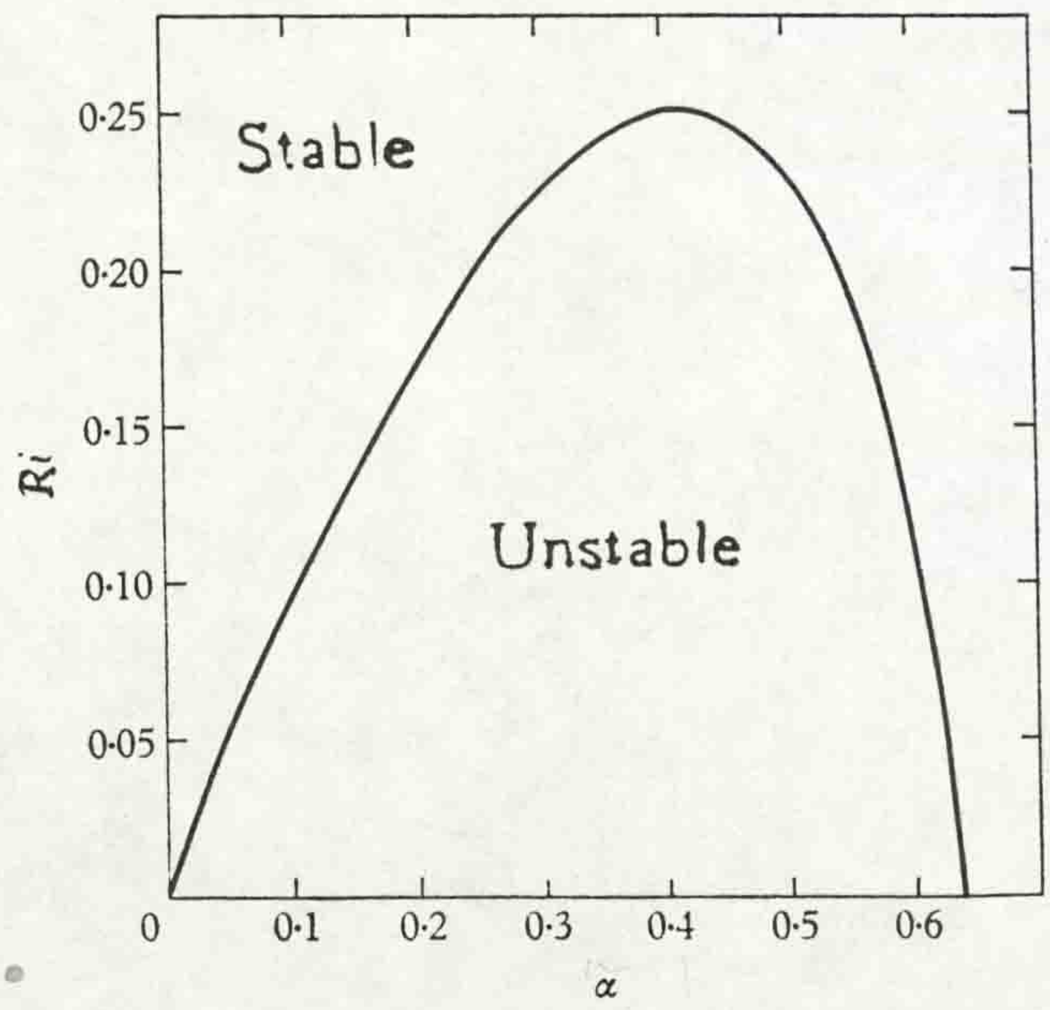

Fig. (6.4b) Variation of Richardson number (R_i) versus wave number (α).

Author	Type of Experiment	Measured in	Measured Flux	U	h	Range of R_i	Comments
Rose/Dodu	Stirring in a tank	Laboratory	Salt	-			Entrainment without shear
Cromwell	" " " "	"	Sea water	-			" " "
Turner	" " " "	"	Salt/heat	-		> 1	" " "
Crapper/Linden	" " " "	"	Salt/heat	-		> 1	" " "
Ellison/Turner	Upper flow	"	Salt	U_1	h_1	< 1	Entrainment with shear
Kato/Phillips	Flow induced by moving surface plate	"	Salt	U_*	h_1	> 1	" " "
Kanta/Phillips/Azad	Flow induced by moving surface plate	"	Salt	U_*	h_1	> 1	" " "
Keulegan	Upper flow	"	Sugar	U_1	h_1		" " "
Lofquist	Under flow	"	Salt	U_2	h_2	> 1	" " "
Moore/Long	Flow induced by surface and bottom jets	"	Salt/heat	ΔU	h	> 0.7	" " "
Ashida/Egashira	Upper flow	"	Heat	U_1	h_1	> 0.2	" " "
Suga/Takahashi	Saline wedge	Laboratory and Field	Salt	U_1	h_1		" " "
Wu	Flow induced by wind	Laboratory	Salt	U_*	h_1	60-400	" " "
Delft Hydraulics Laboratory	Flow induced by wind	"	Salt	U_*	h_1	40-400	" " "

Table (6.1) Studies Dealing with Experiments of Entrainment (with or without shear)

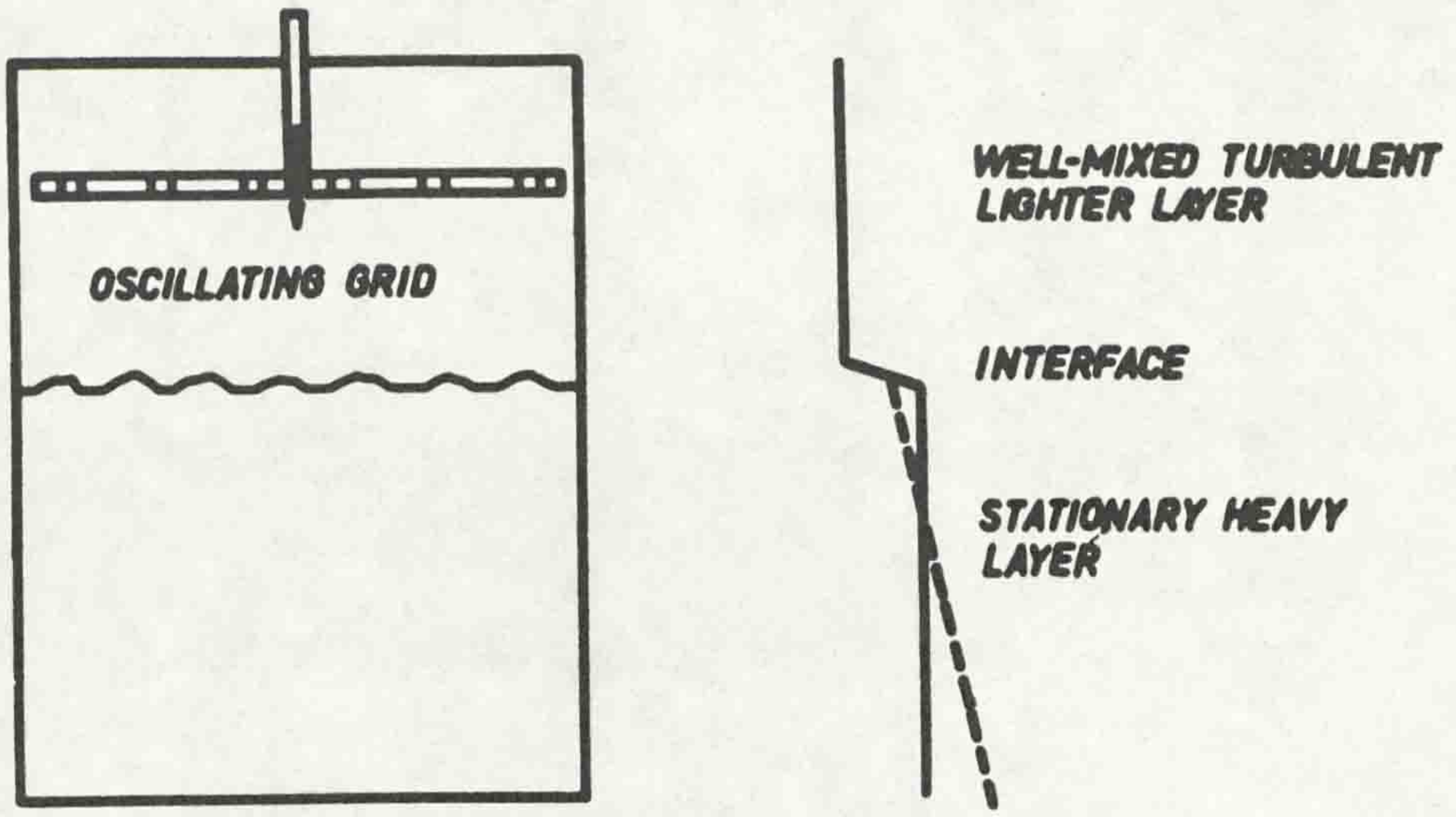

Fig. (6.5) Sketch of the experimental tank and stirring grid and the density distribution produced by stirring.

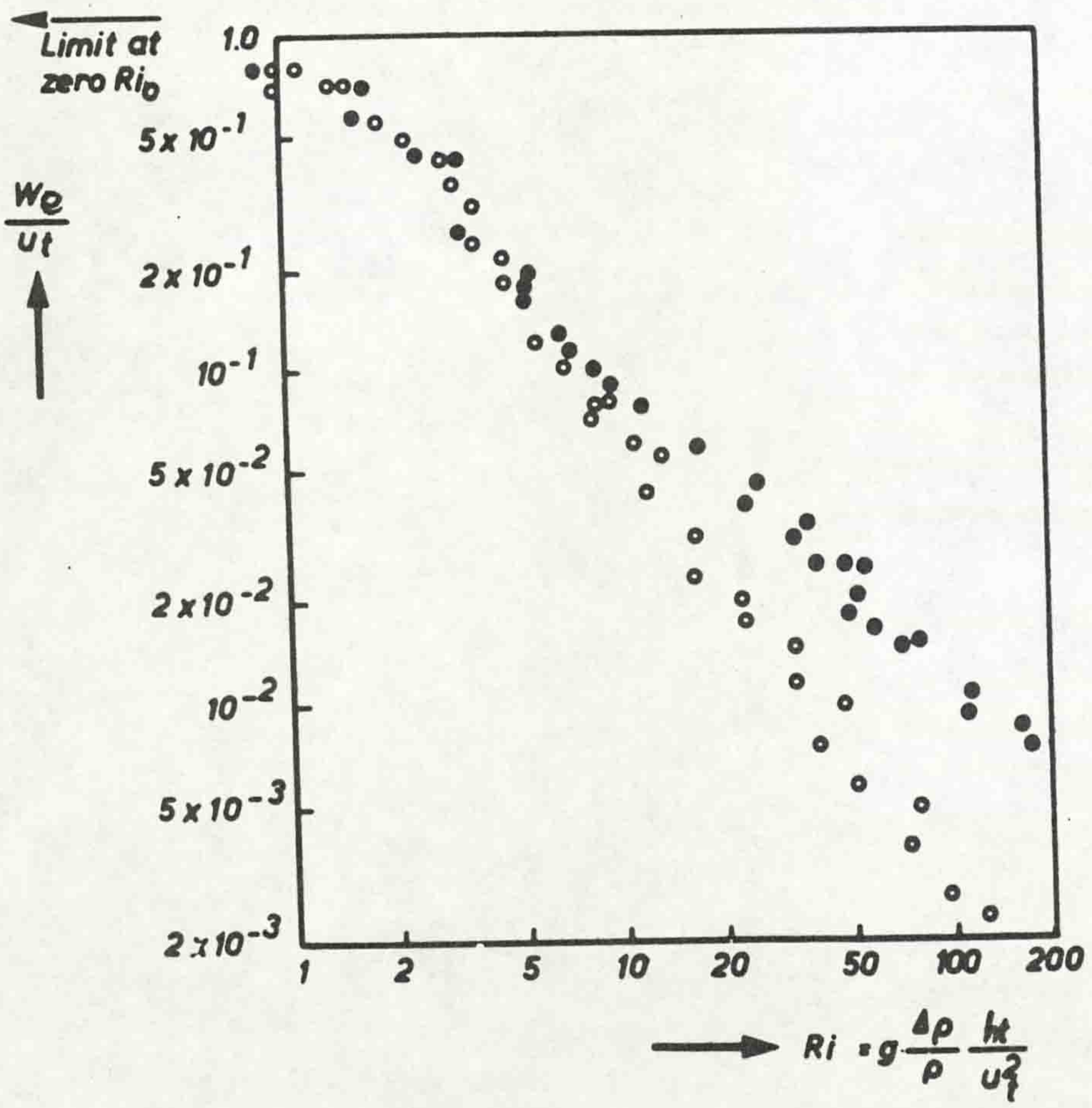

Fig. (6.6) Density difference with • temperature difference
o salinity difference.

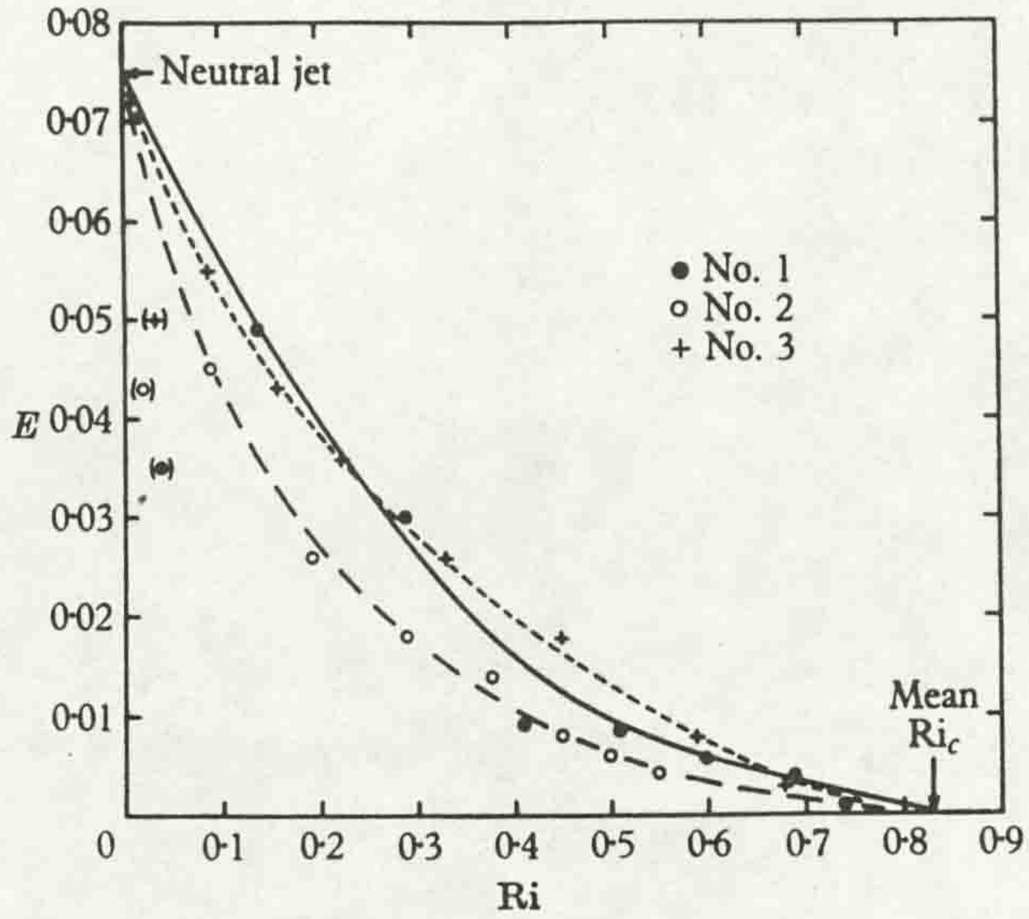

Fig. (6.7) Entrainment coefficient, E, as a function of Richardson number for three experiments on surface jet (after Ellison and Turner, 1959).

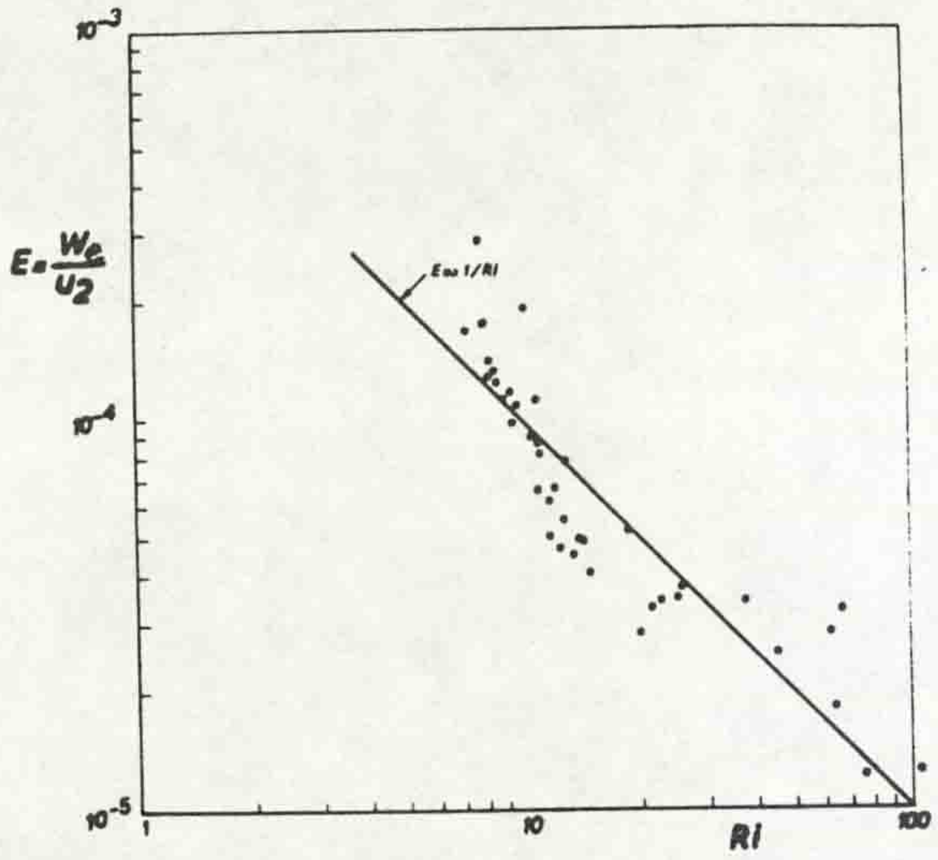

Fig. (6.8a) Entrainment E, as a function of R_i for lower layer flow (after Lofquist, 1960).

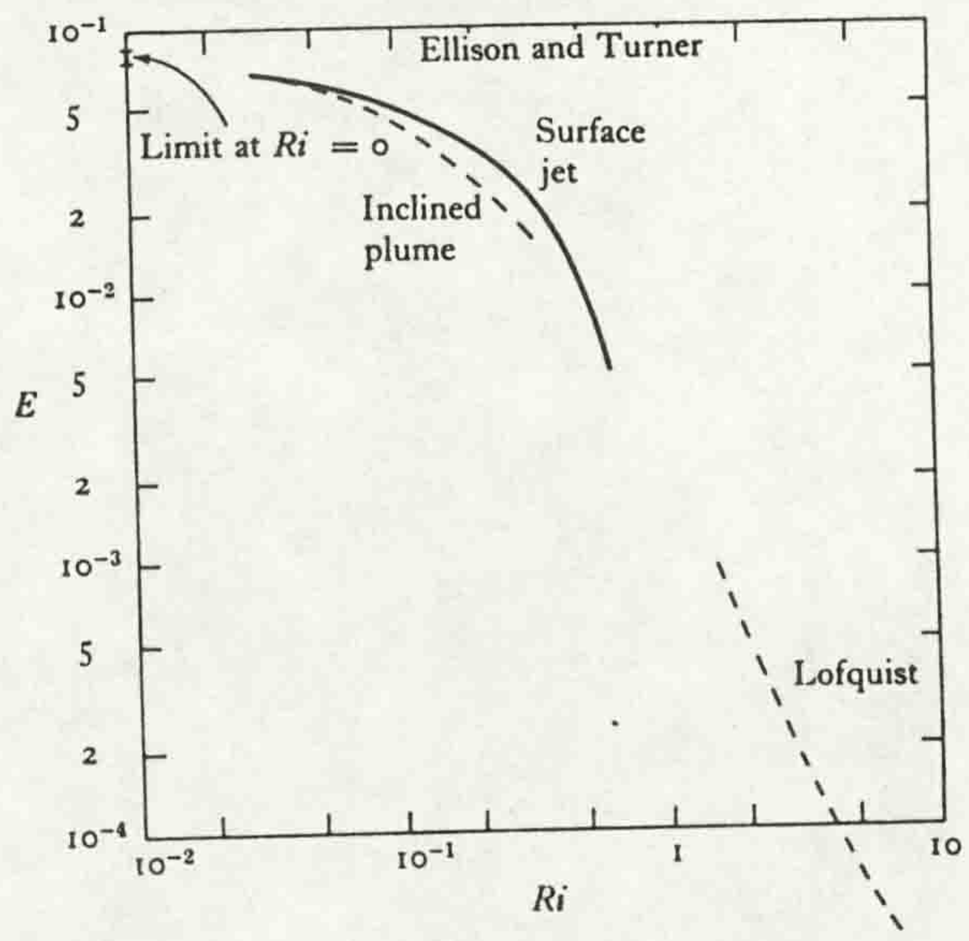

Fig. (6.8b) Comparison between the Ellison and Turner (1959) and Lofquist (1960) results.

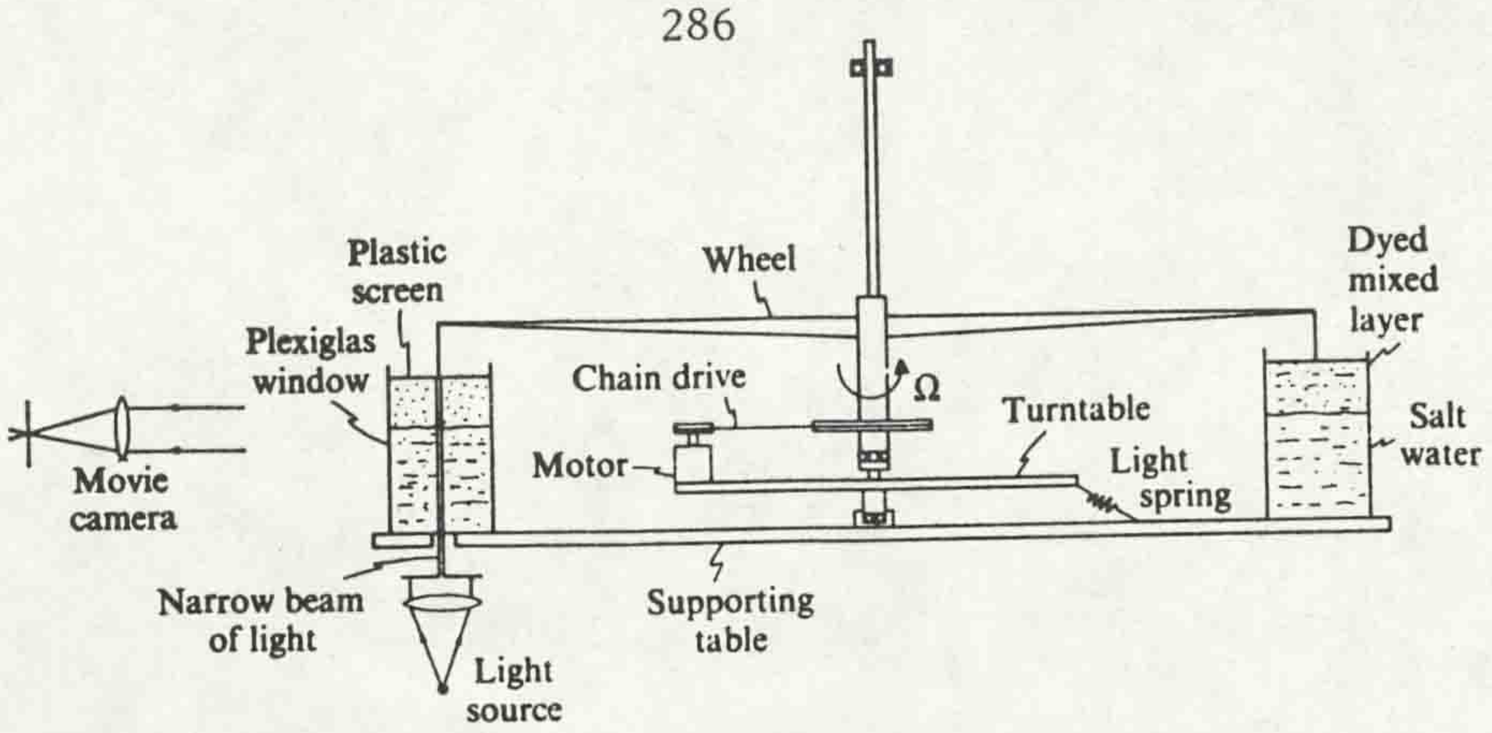

Fig. (6.9a) A cross sectional sketch of the experimental apparatus of KP (1969) and KPA (1977).

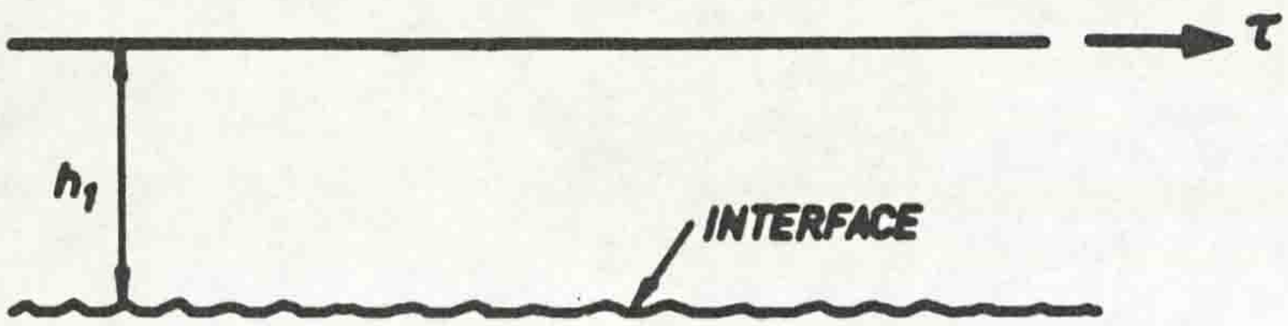

Fig. (6.9b) Sketch of mixing process in KP (1969) experiment.

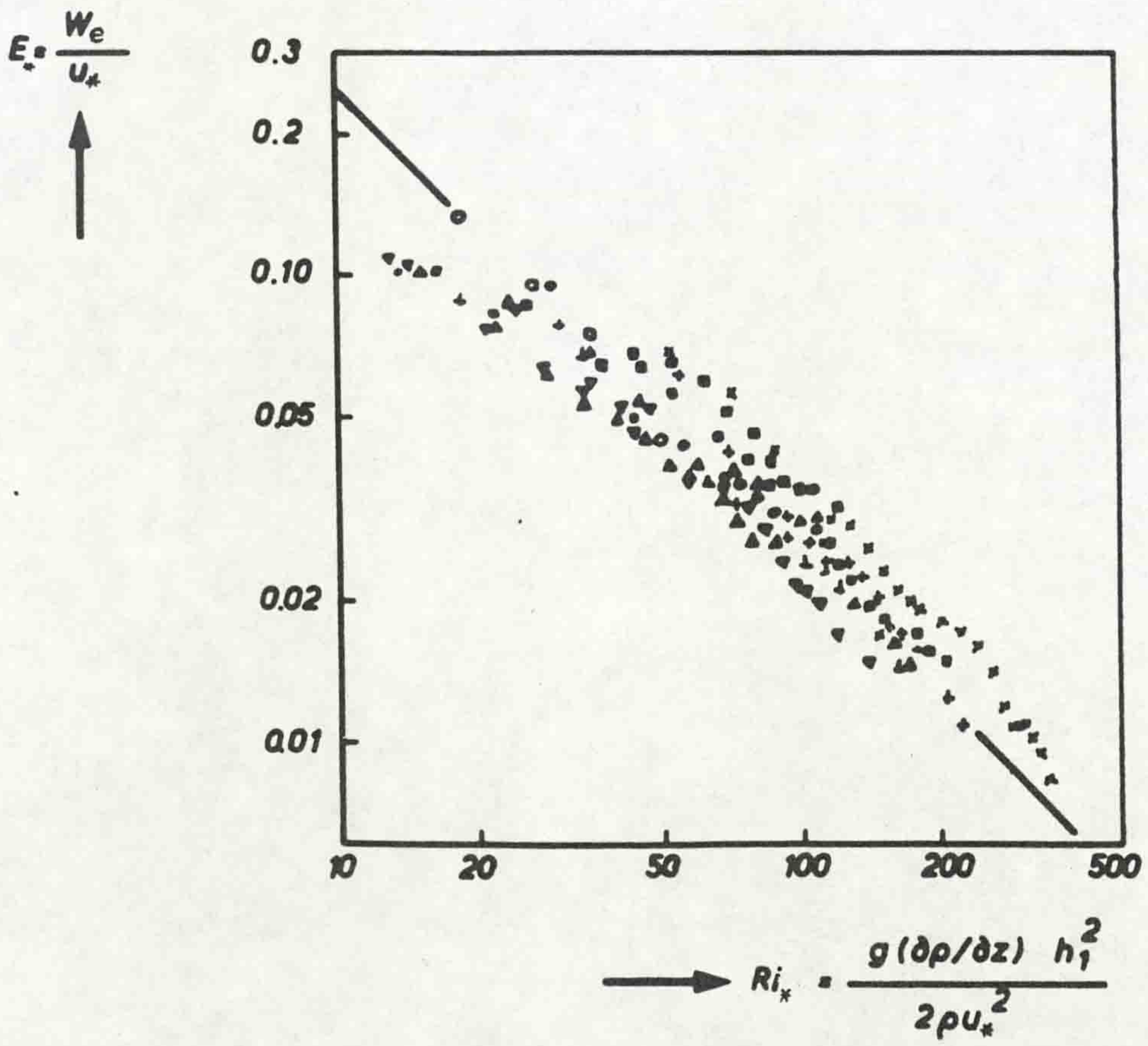

Fig. (6.9c) Entrainment coefficient, E_*, versus the Richardson number, R_{i*} in KP (1969) experiment.

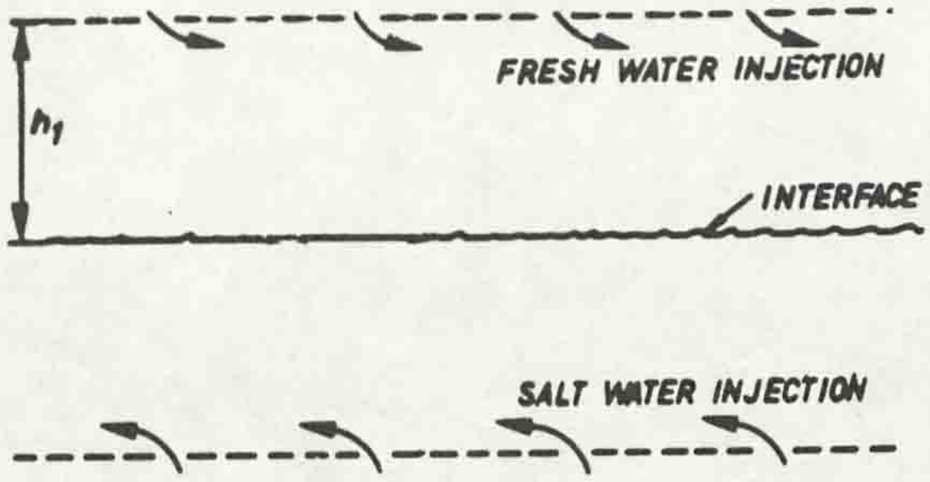

(a)

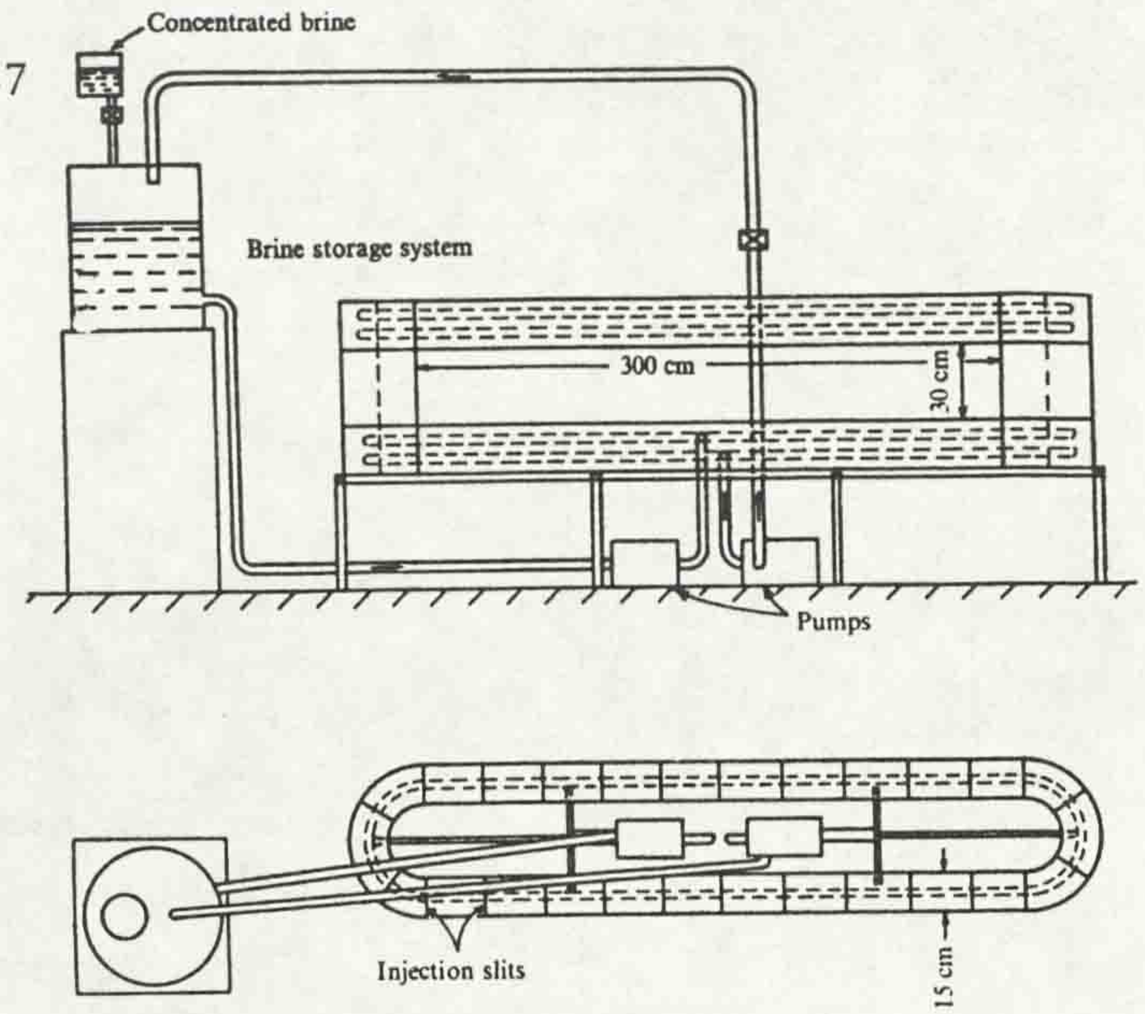

(b)

Fig. (6.10a,b) Sketch of mixing process and experimental apparatus in Moore/Long (1971).

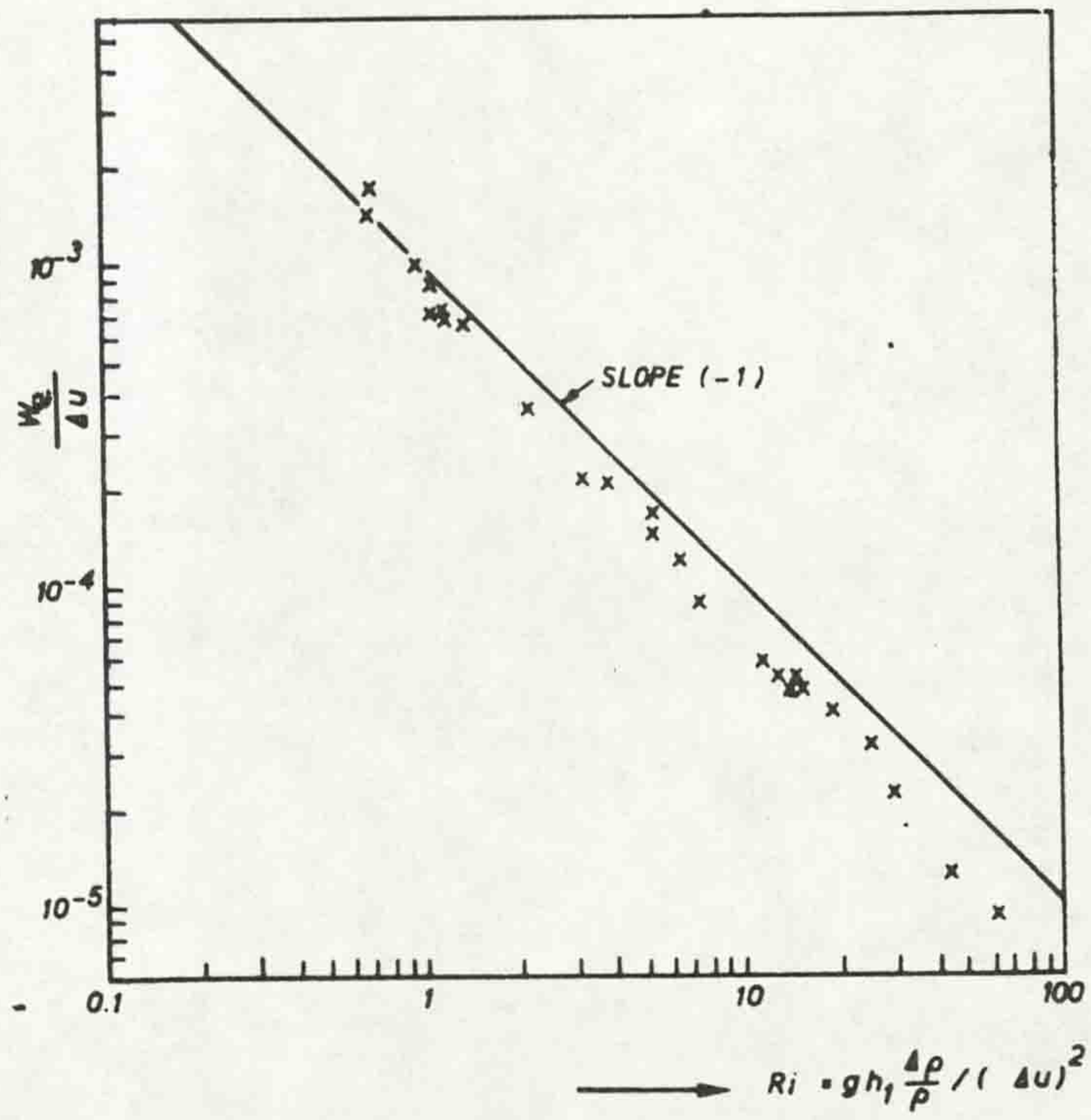

Fig. (6.10c) Entrainment coefficient, E, versus Richardson number (after Moore/Long, 1971).

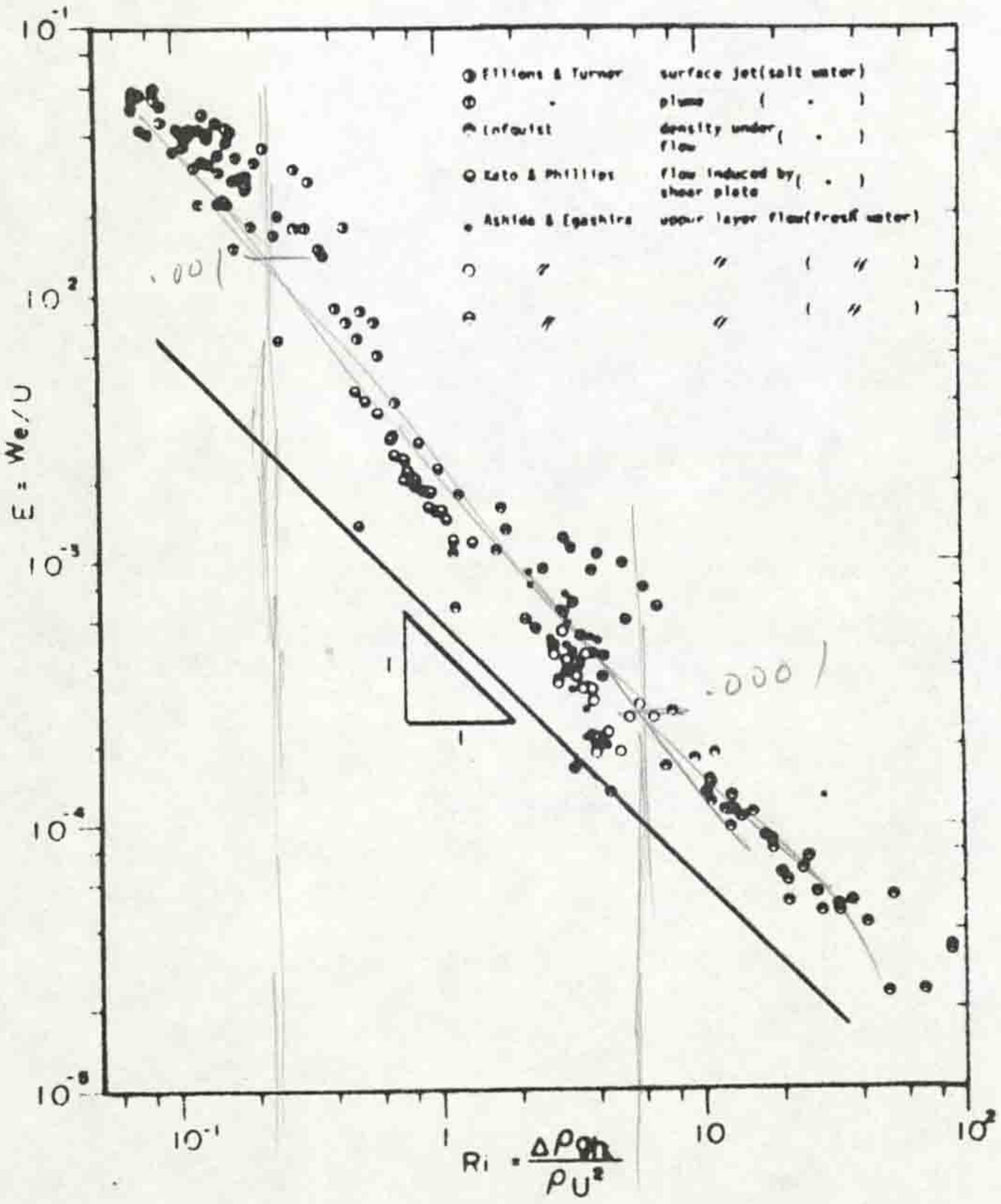

Fig. (6.11) Entrainment coefficient, E, versus Richardson number (after Ashida and Egashira, 1977).

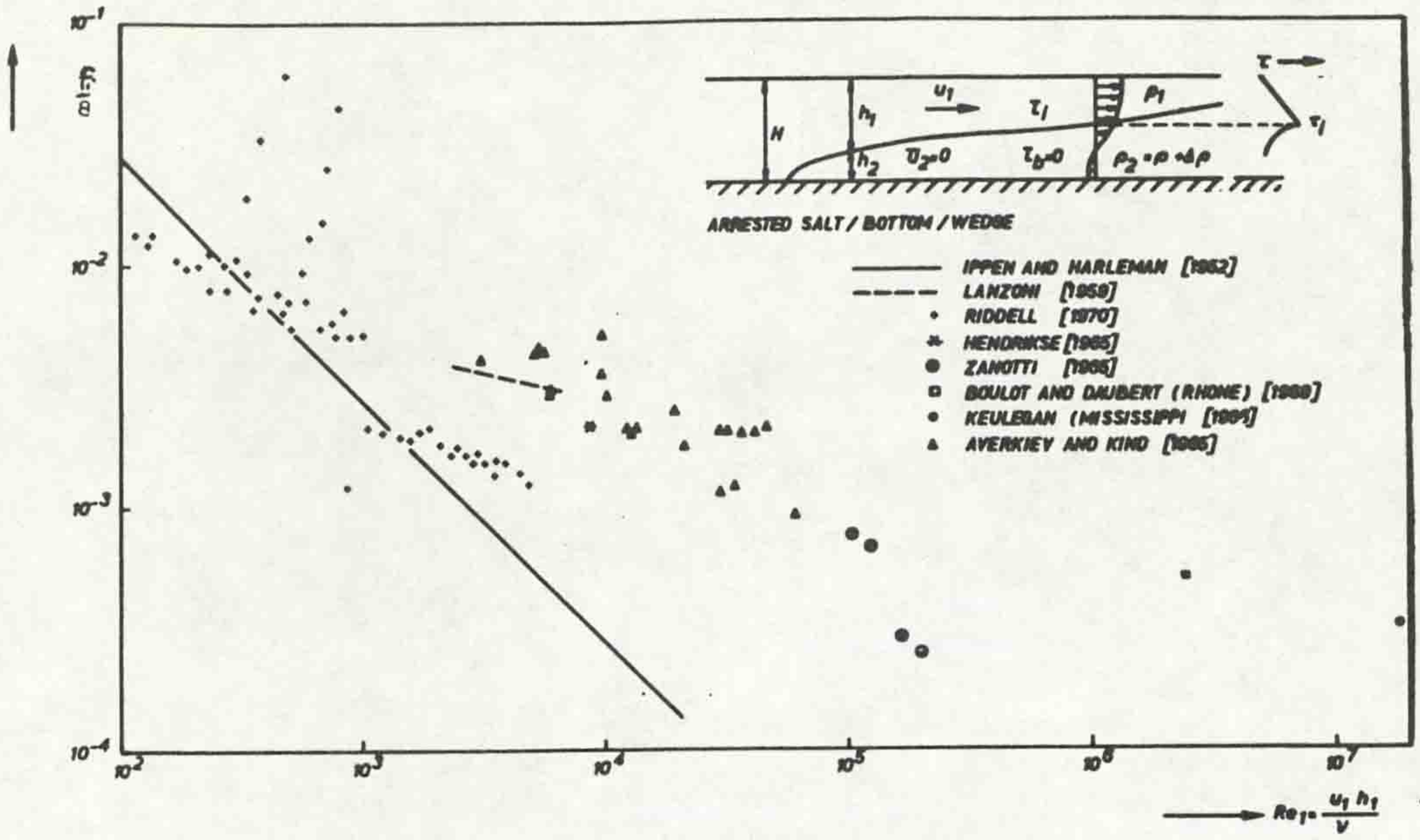

Fig. (6.12) Variation of the interfacial friction coefficient, f_i, in two layered stratified upper flow (after Delft Hydraulics Lab, 1974).

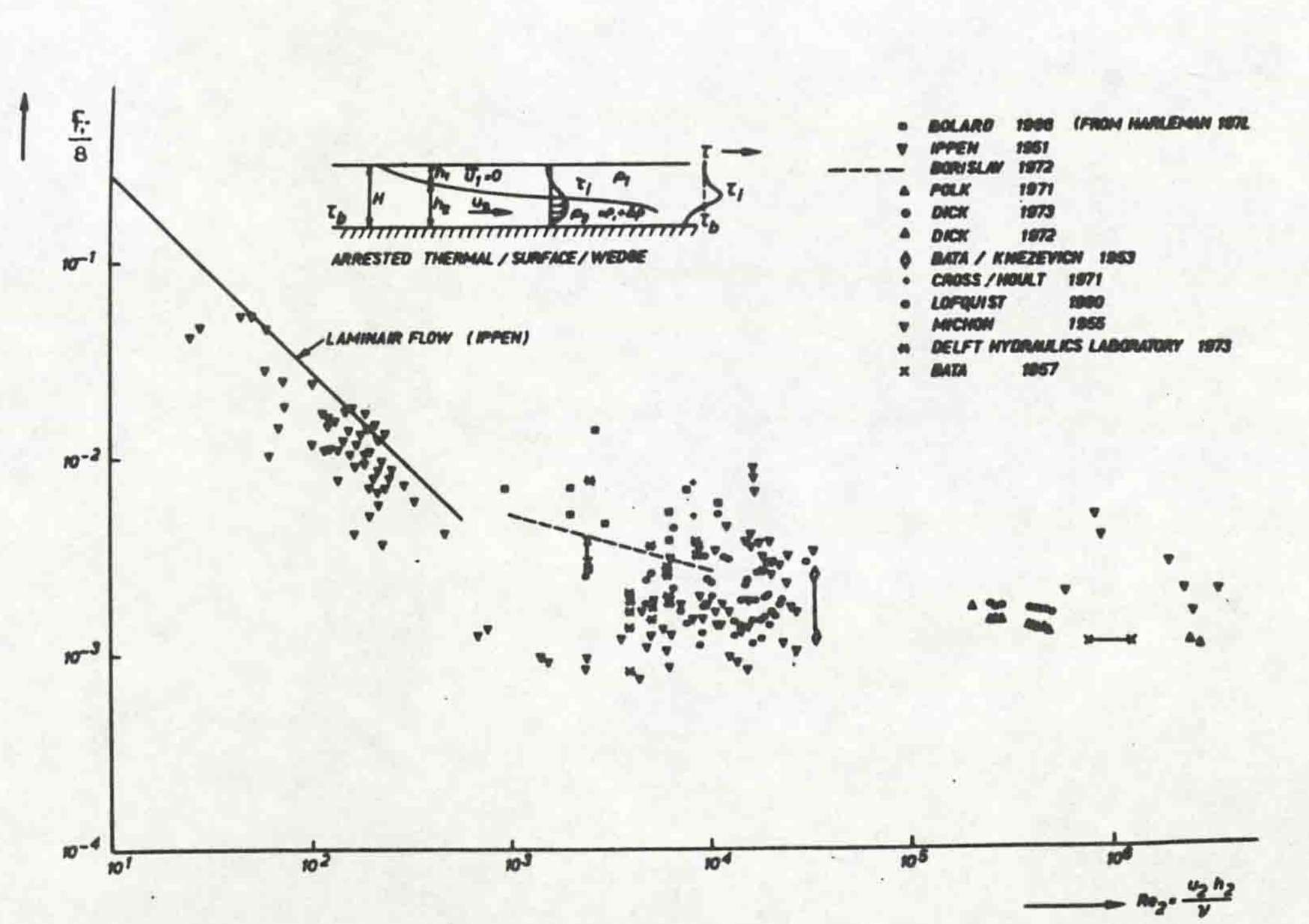

Fig. (6.13) Variation of the interfacial friction coefficient, f_i, in two layered stratified under flow (after Delft Hydraulics Lab, 1974).

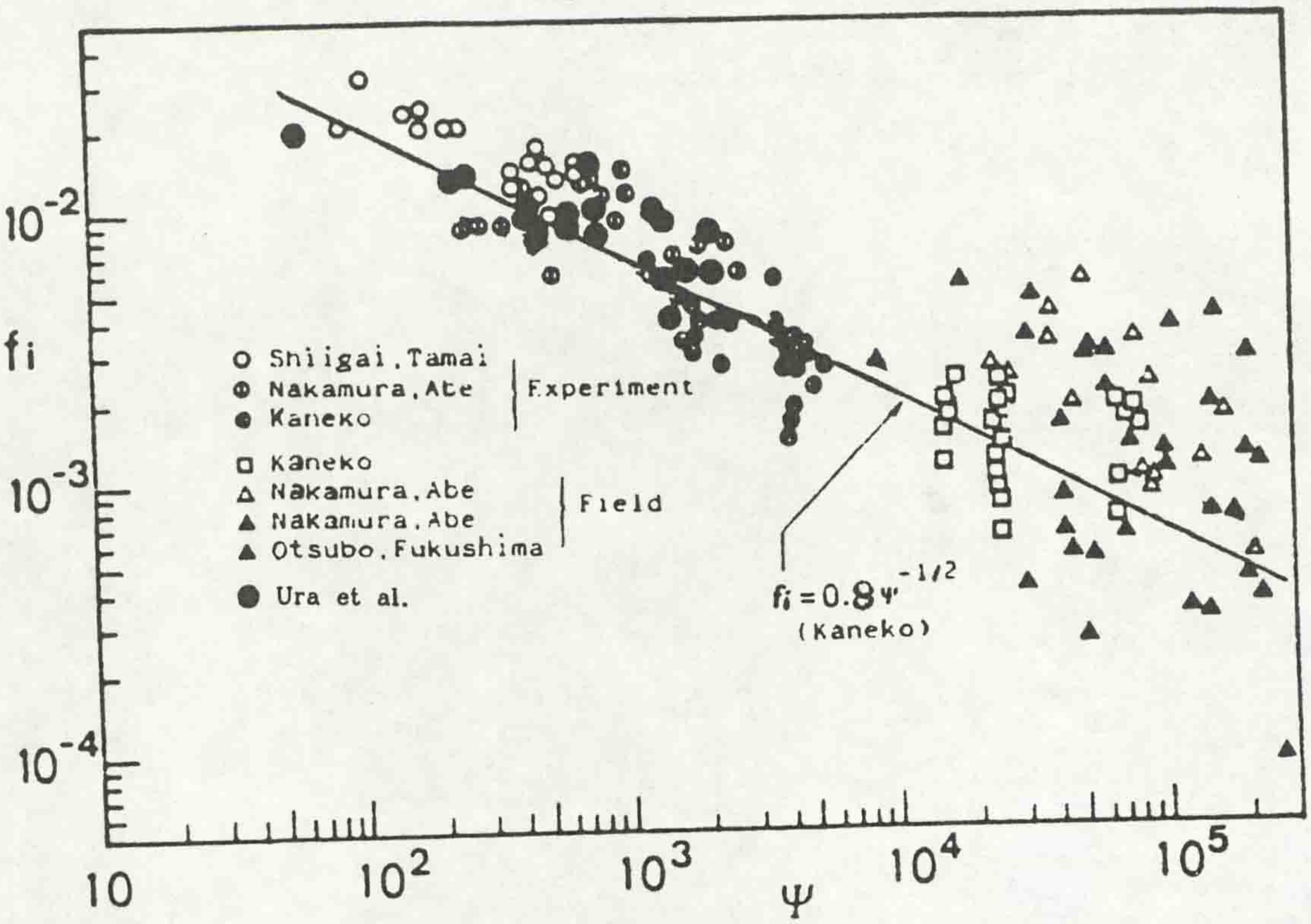

Fig. (6.14) Relationship between f_i and ψ (after Ura et al, 1984).

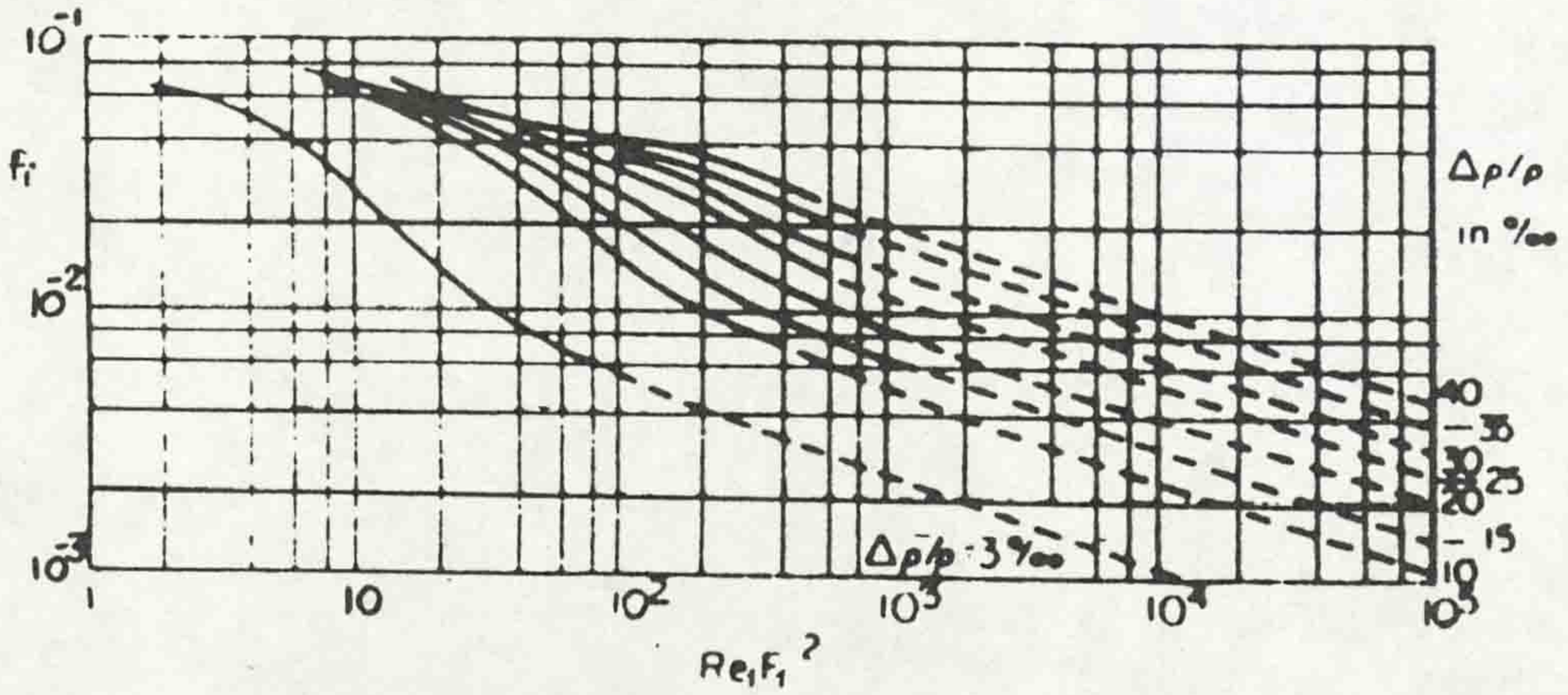

Fig. (6.15) Extrapolation of the results of experiments of interfacial friction coefficient (after Dermissis and Partheniades, 1984).

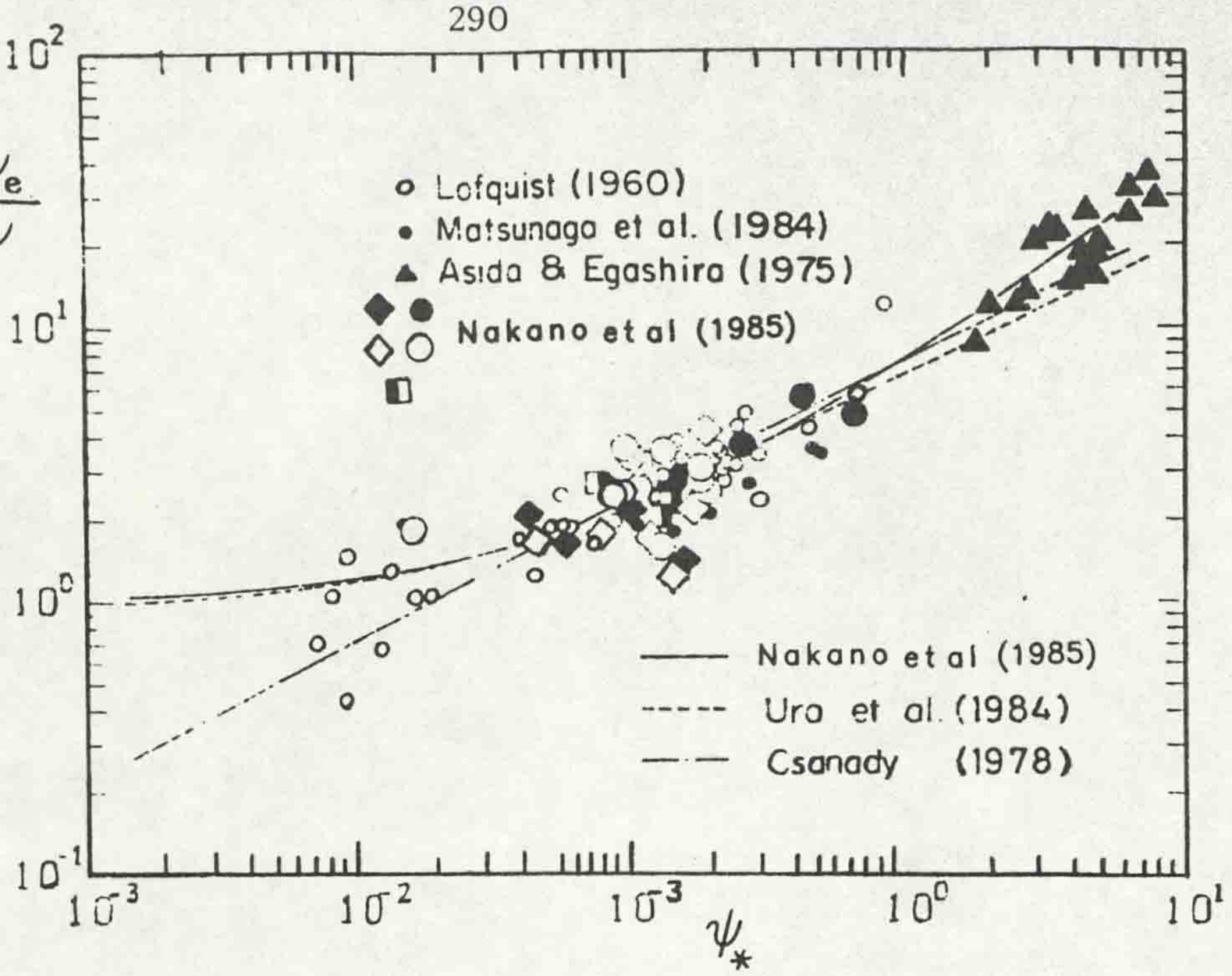

Fig. (6.16) Variation of effective viscosity, ν_e, versus ψ_* (after Nakano et al, 1985).

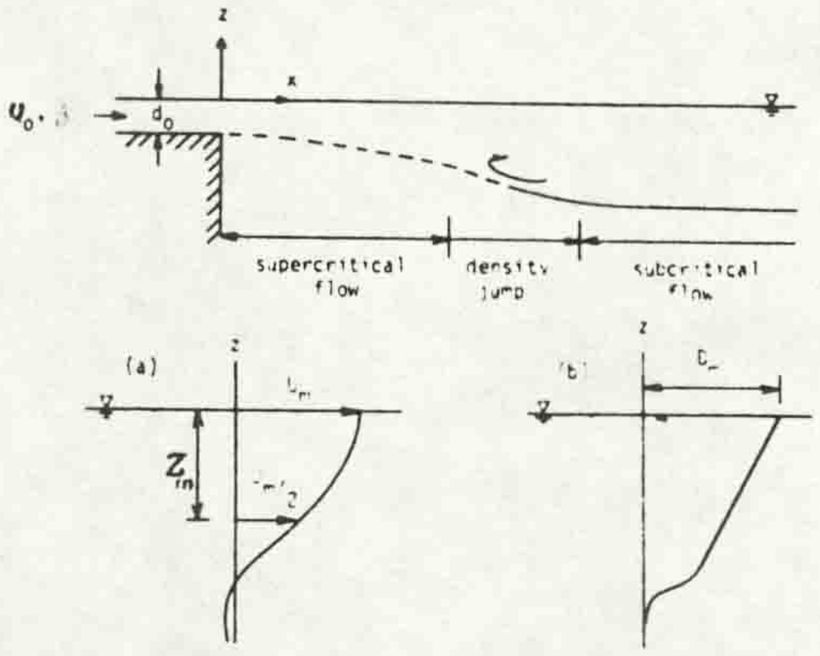

Fig. (6.17a) Schematic diagram of a typical two-dimensional buoyant jet.

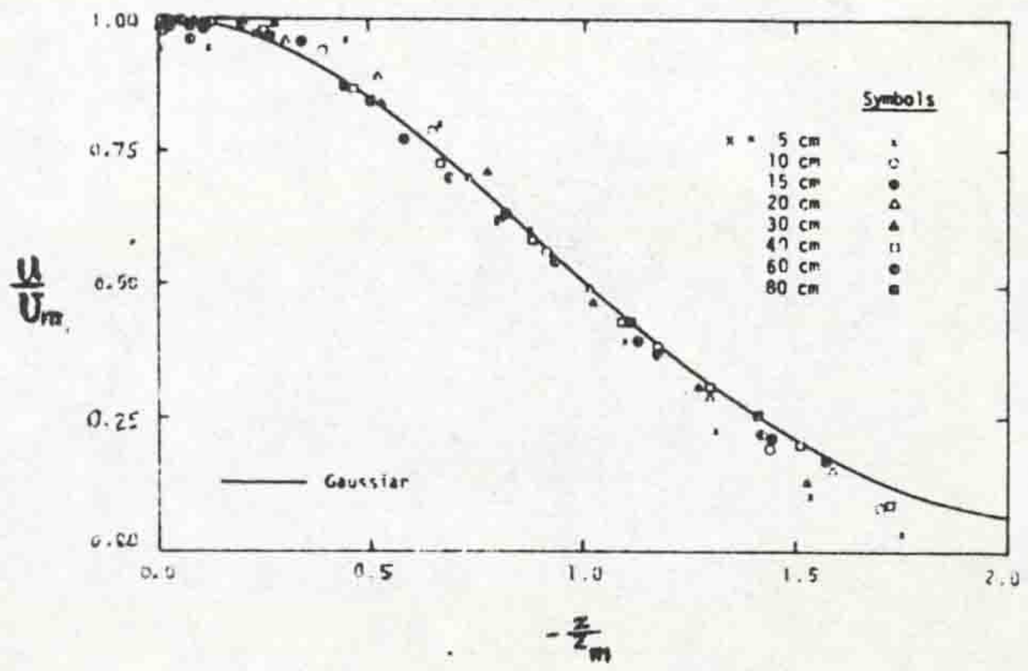

Fig. (6.17b) Dimensionless velocity distribution (after Chu and Vanvari, 1976)

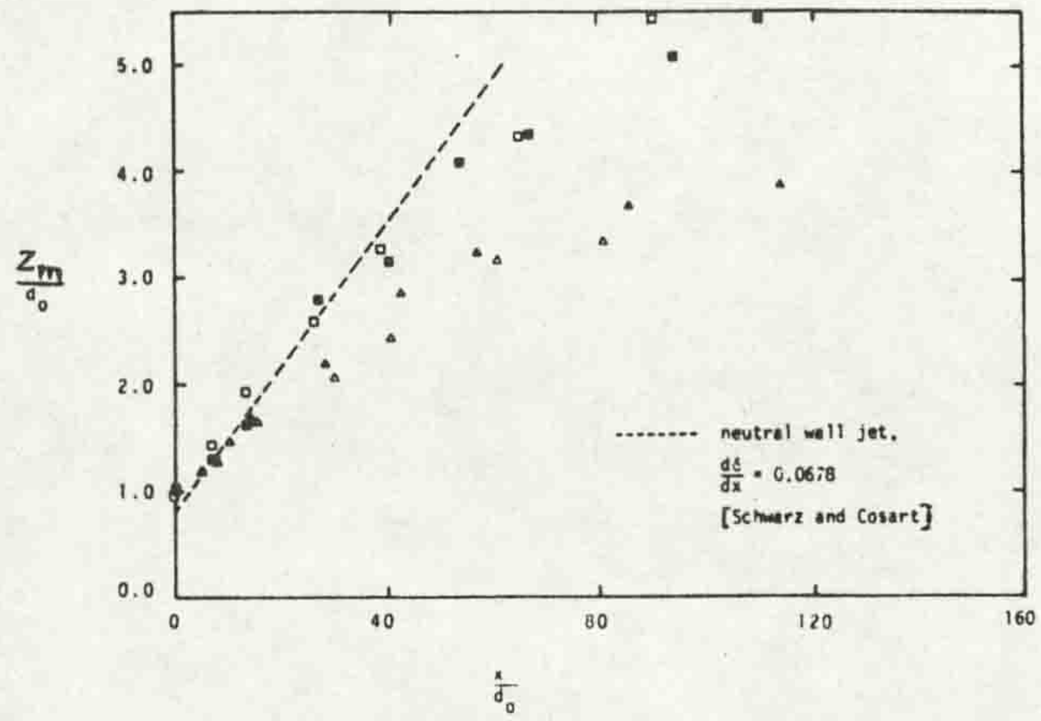

Fig. (6.17c) Jet width (after Chu and Vanvari, 1976).

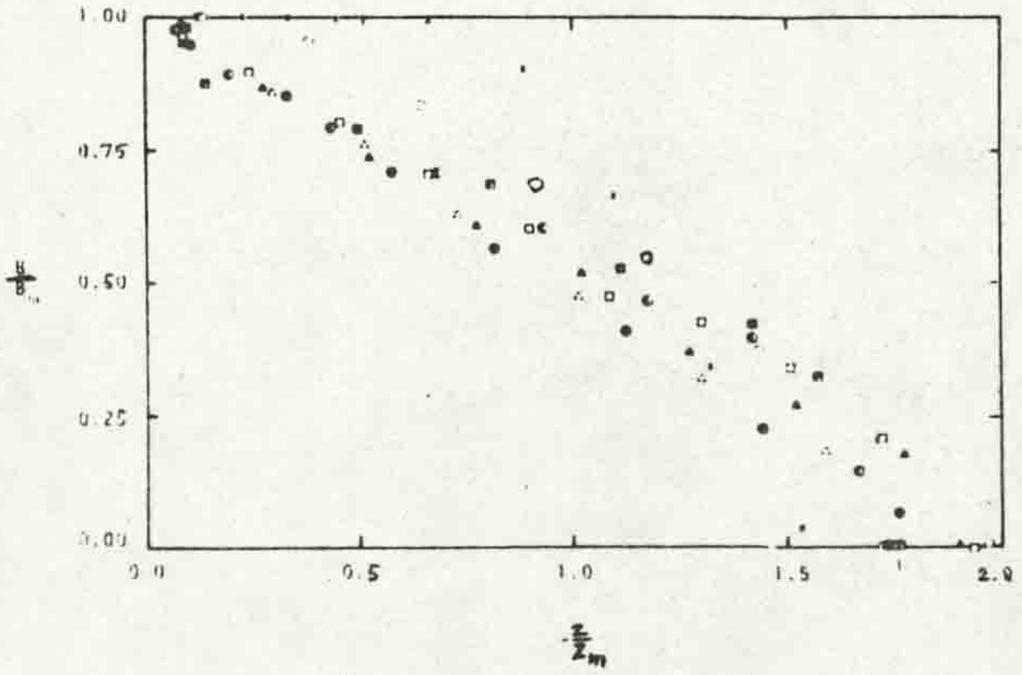

Fig. (6.17d) Buoyancy profiles (after Chu and Vanvari, 1976).

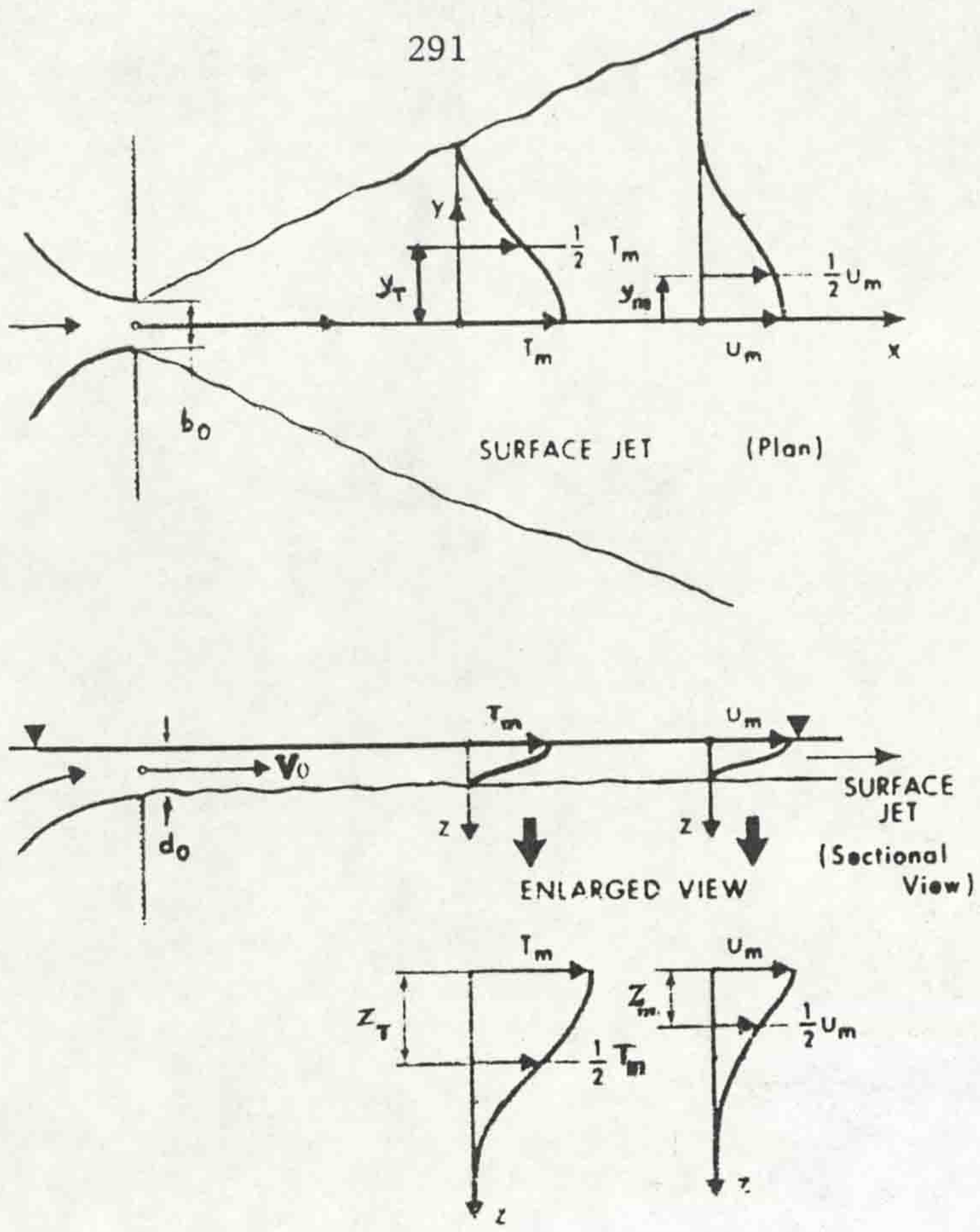

Fig. (6.18) Definition sketch for bluff buoyant surface jet.

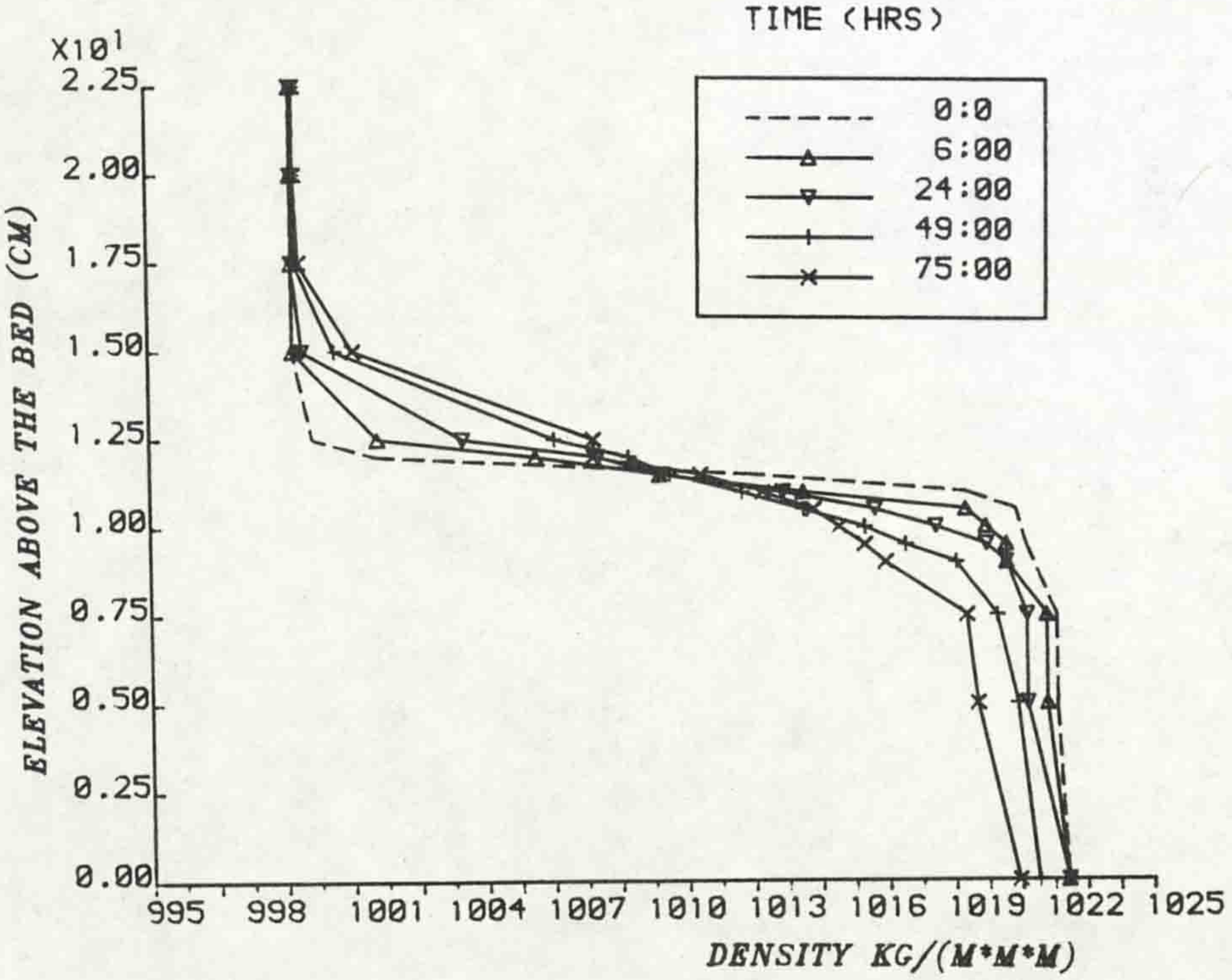

Fig. (6.19) The effect of saline molecular diffusion at the interface of a stratified reservoir.

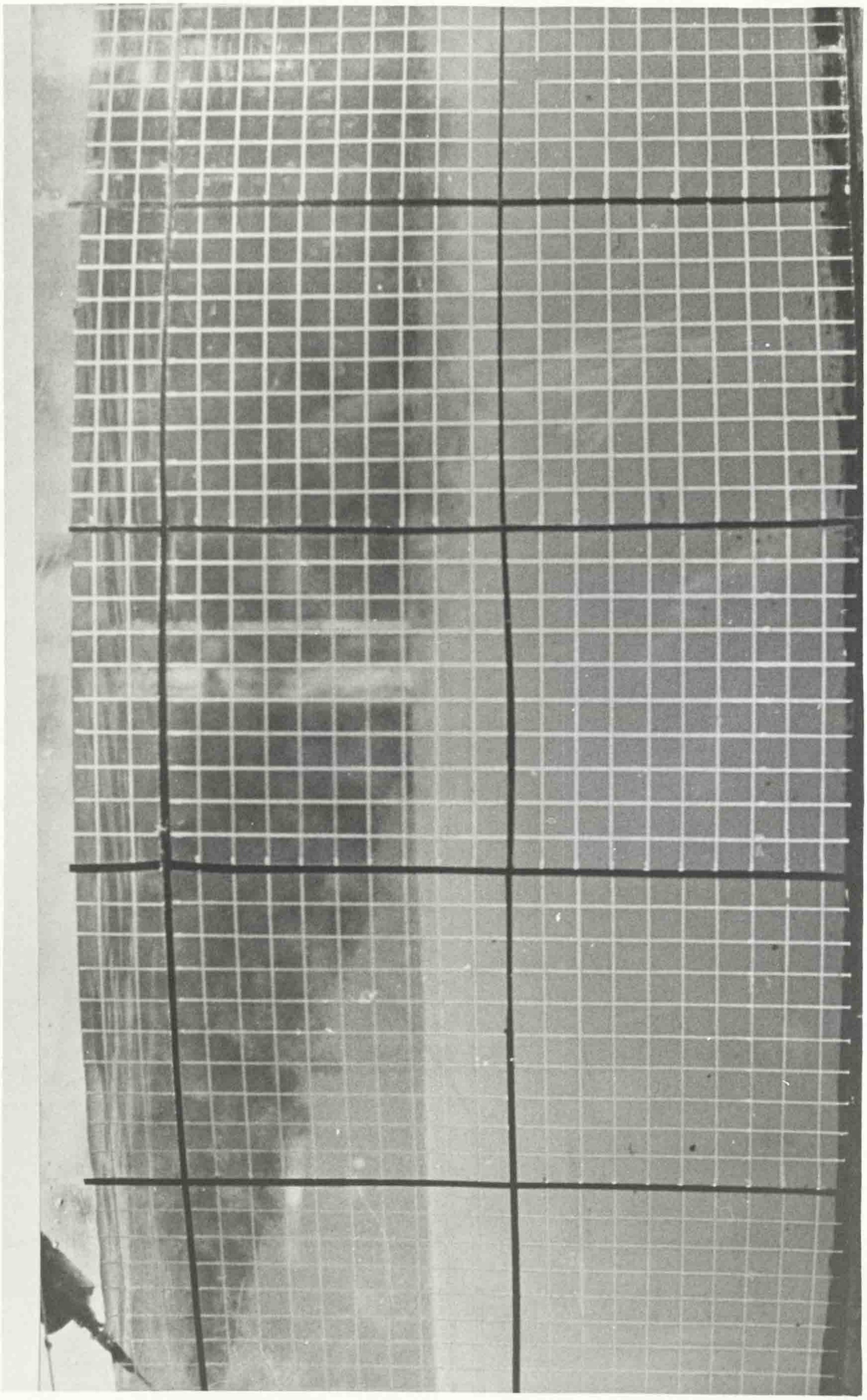

Fig. (6.20) Diffusion of surface jet in stratified reservoir.

Experiment No.	Discharge cc/sec	Depth of Fresh Water cm	Depth of Saline cm	Density of Fresh Water kg/m^3	Density of of Saline kg/m^3	Duration of Experiment min.
1.	49.5	12.5	10.	998.9	1011.2	50.
2.	30.88	2.5	20.	998.9	1018.8	170.
3.	19.66	2.5	20.	998.9	1011.7	50.
4.	19.66	2.5	20.	999.1	1020.2	100.
5.	19.66	2.5	20.	999.3	1042.8	325.5
6.	19.66	2.5	20.	998.3	1051.2	150.5
7.	19.66	2.5	20.	999	1090.	125.5
8.	12.383	2.5	20.	998.9	1020.8	100.
9.	9.71	2.5	20.	998.9	1020.	160.
10.	5.75	2.5	20.	998.9	1022.2	100.

Table (6.2) Details of Density Measurement Experiments in Stratified Reservoir

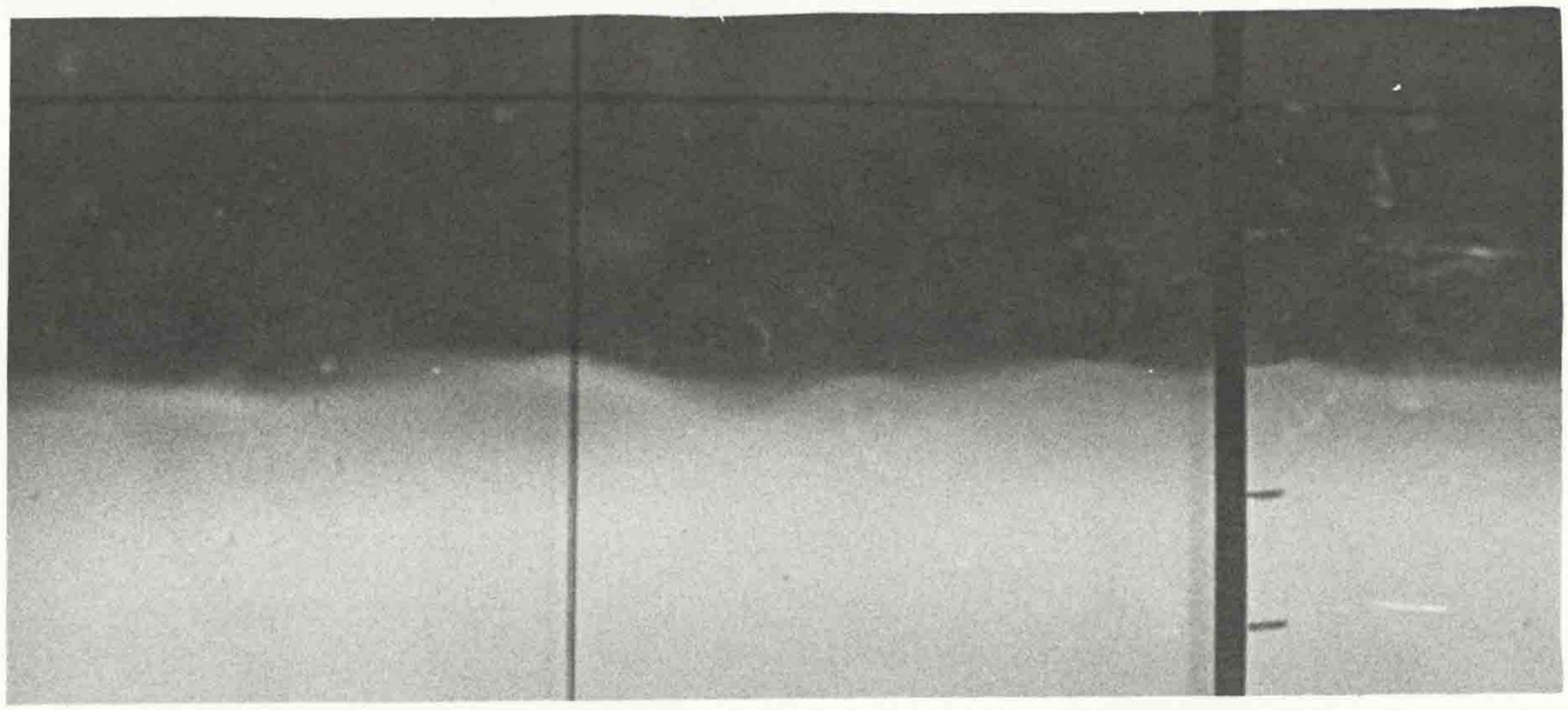

a) Q_o = 10.5 cc/sec, ε = 2.1%

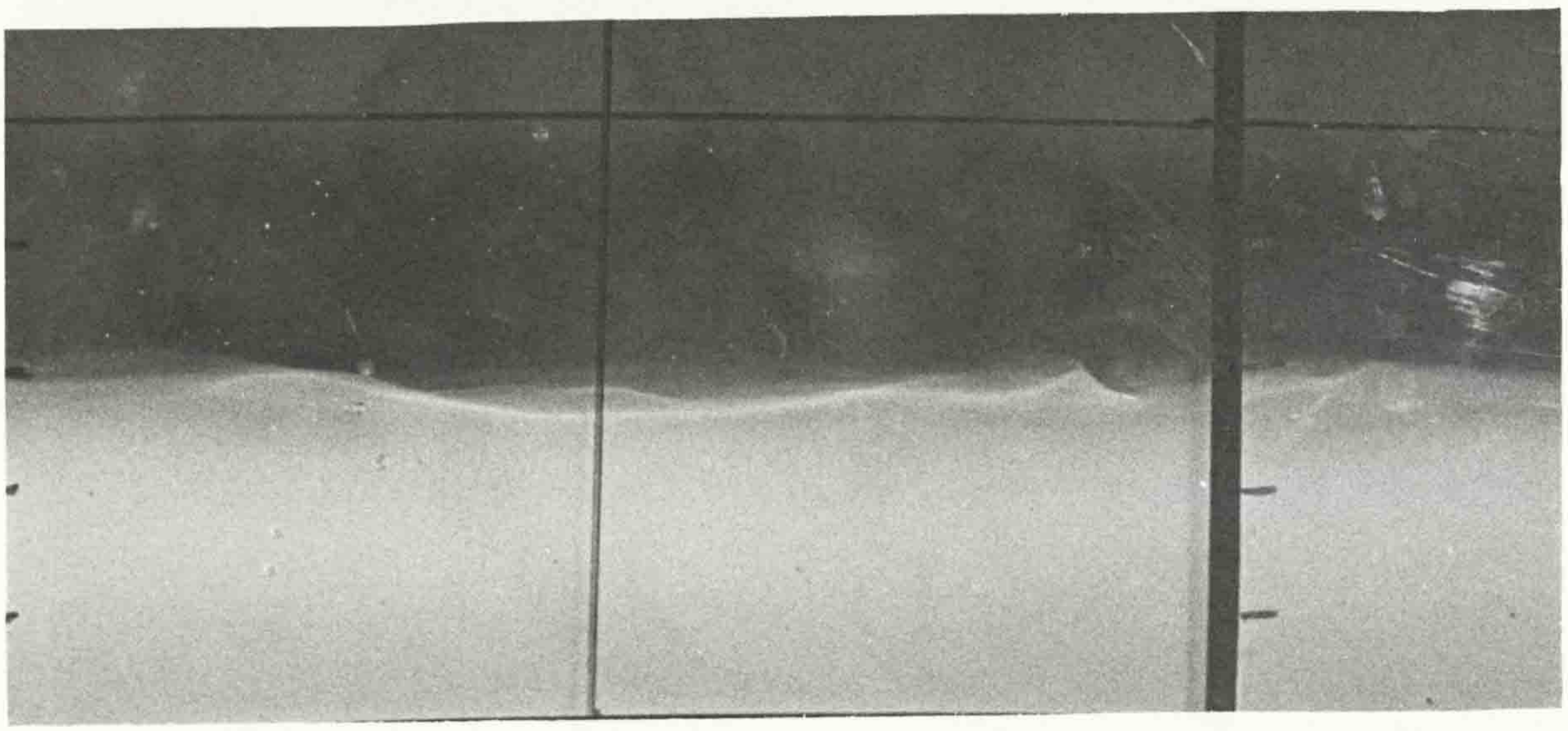

b) Q_o = 12.5 cc/sec, ε = 2.1%

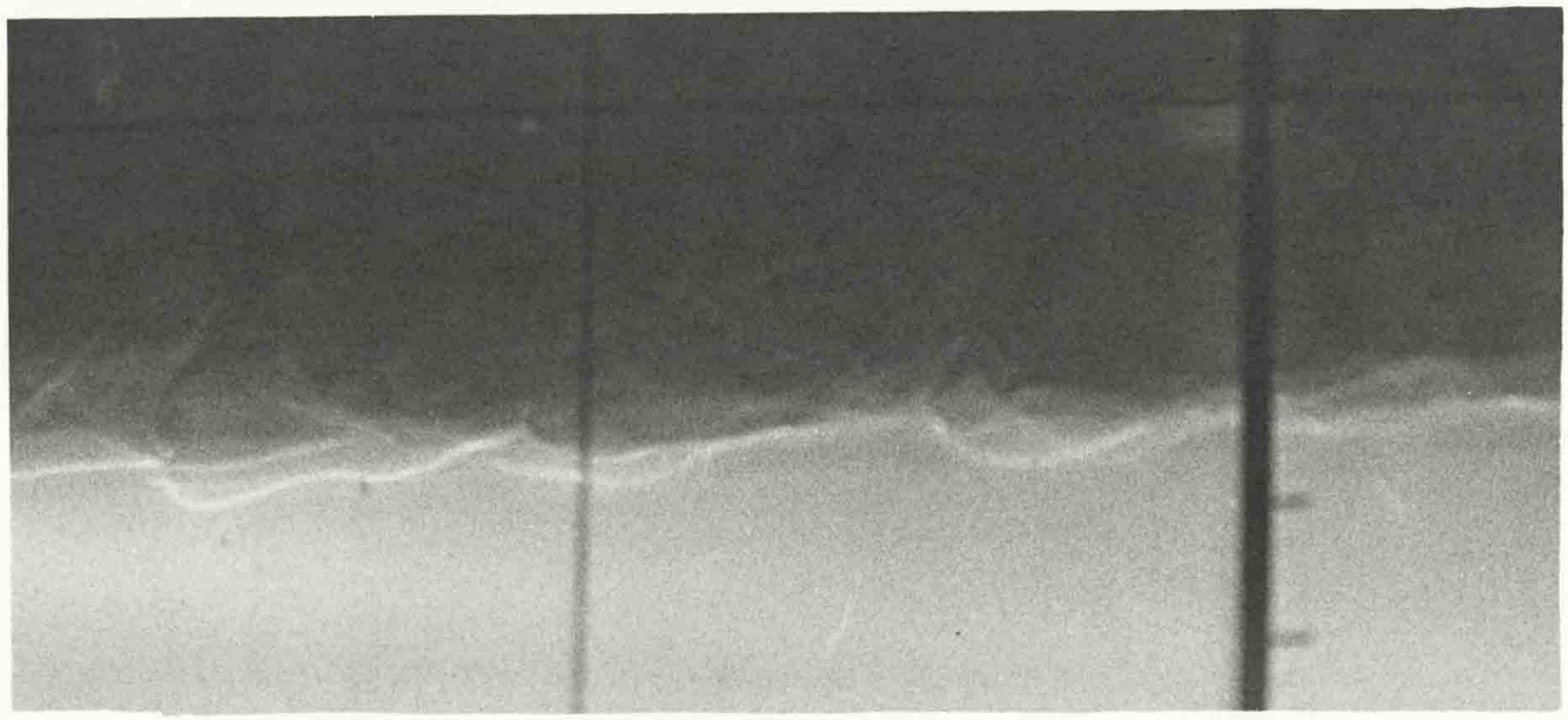

c) Q_o = 16.2 cc/sec, ε = 2.1%

Fig. (6.21) Interfacial progressives waves at different jet discharges, depth of upper layer = 9.5 cm, depth of lower layer = 13 cm.

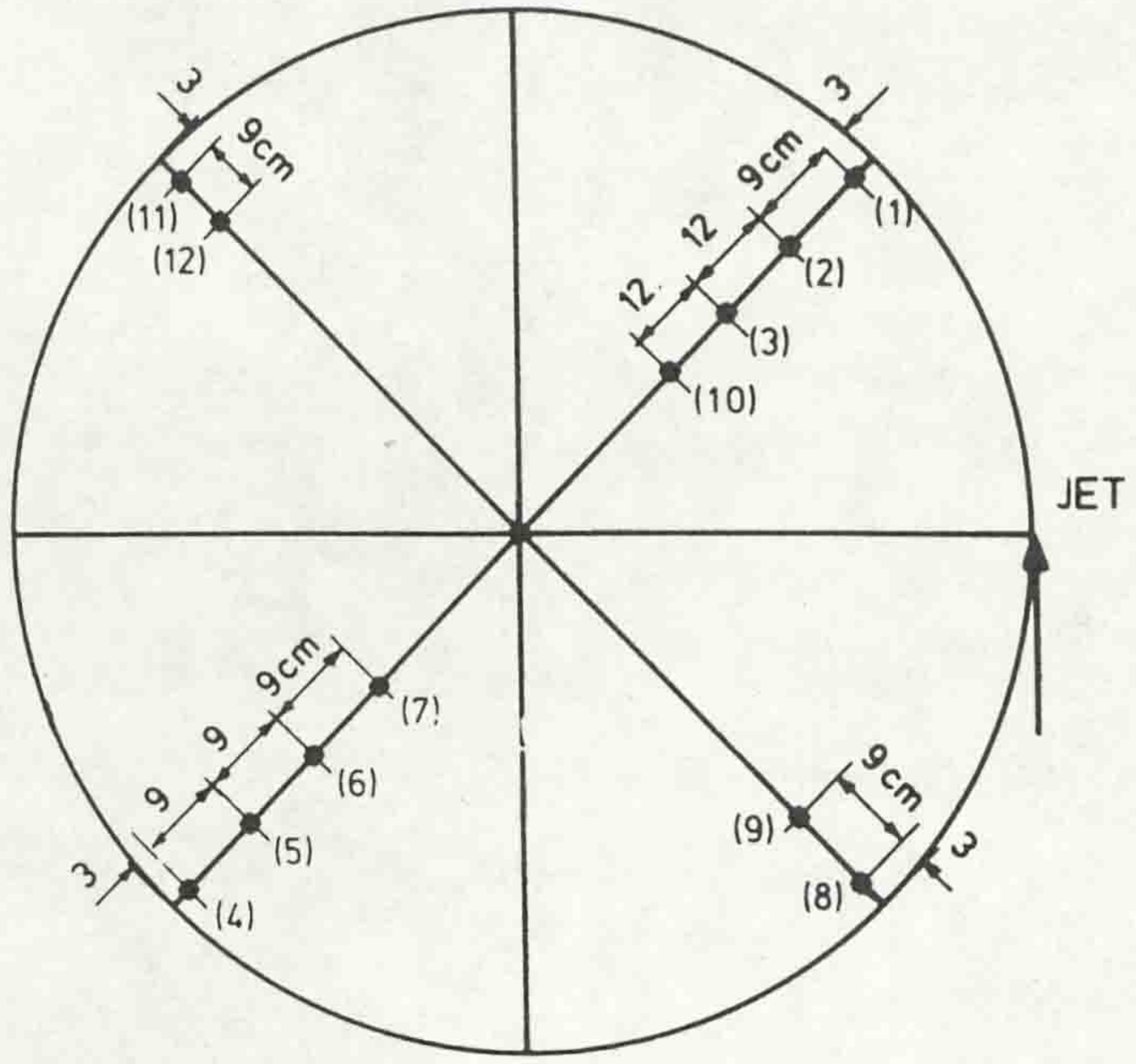

Fig. (6.22) Position of various stations.

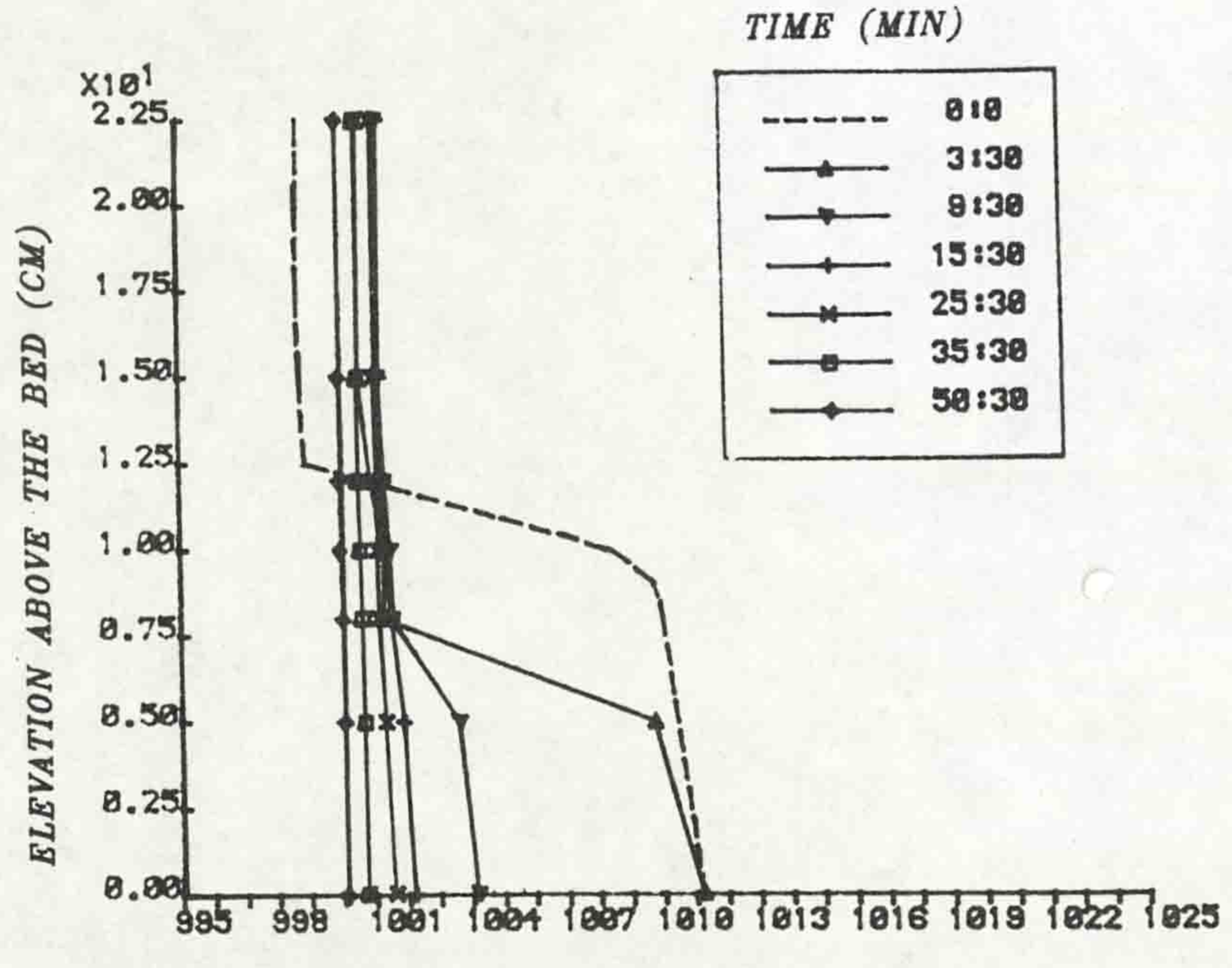

Fig. (6.23) Variation of density with elevation above the bed for station number 1, experiment number 1, Table (6.2), (Q_o = 49.5 cc/sec, ε = 1.2%, h_1 = 12.5 cm).

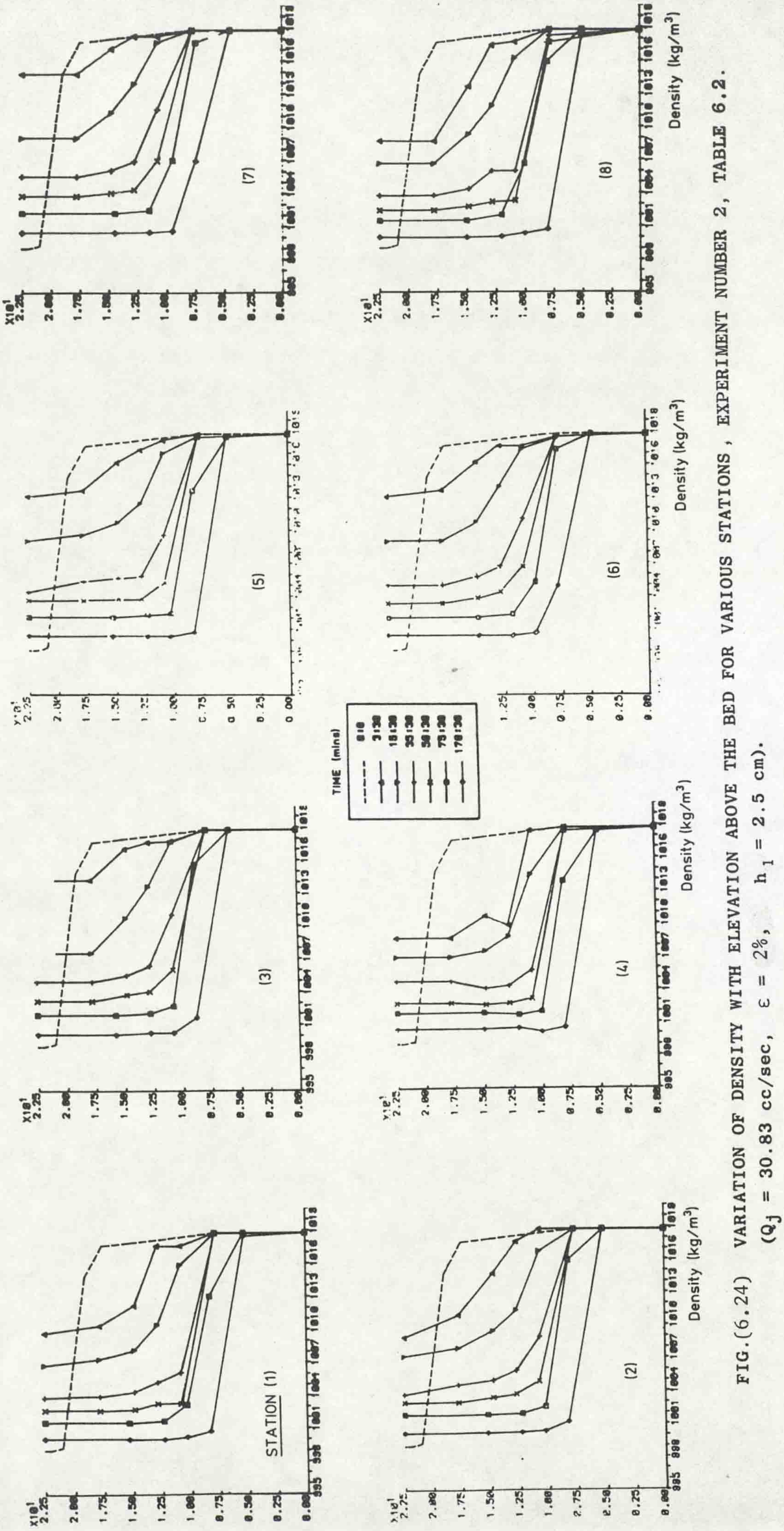

FIG.(6.24) VARIATION OF DENSITY WITH ELEVATION ABOVE THE BED FOR VARIOUS STATIONS, EXPERIMENT NUMBER 2, TABLE 6.2.
(Q_j = 30.83 cc/sec, ε = 2%, h_1 = 2.5 cm).

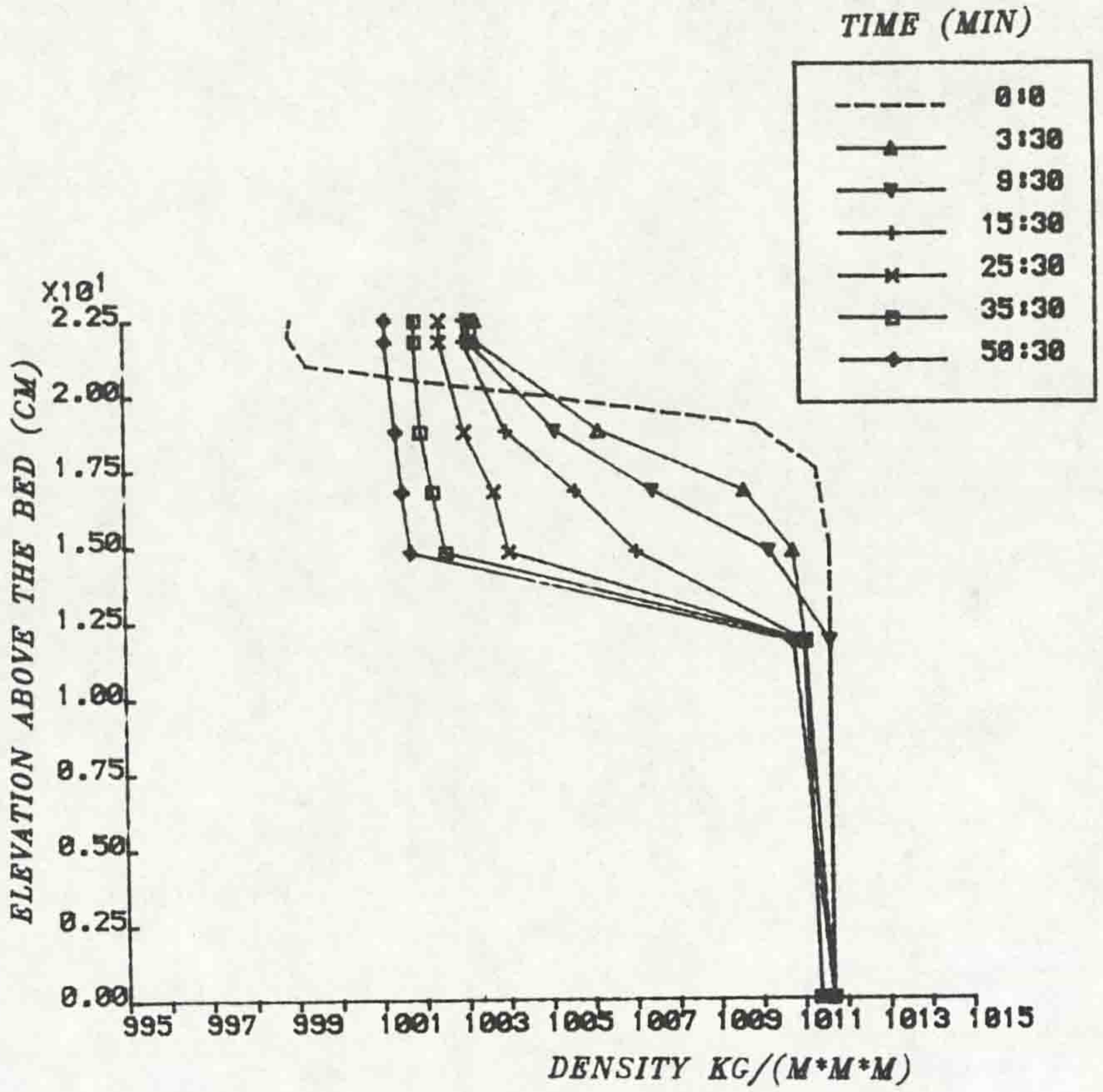

Fig. (6.25) Variation of density with elevation above the bed for station number 1, experiment number 3, Table (6.2), (Q_o = 19.66 cc/sec, ε = 1.28%, h_1 = 2.5 cm).

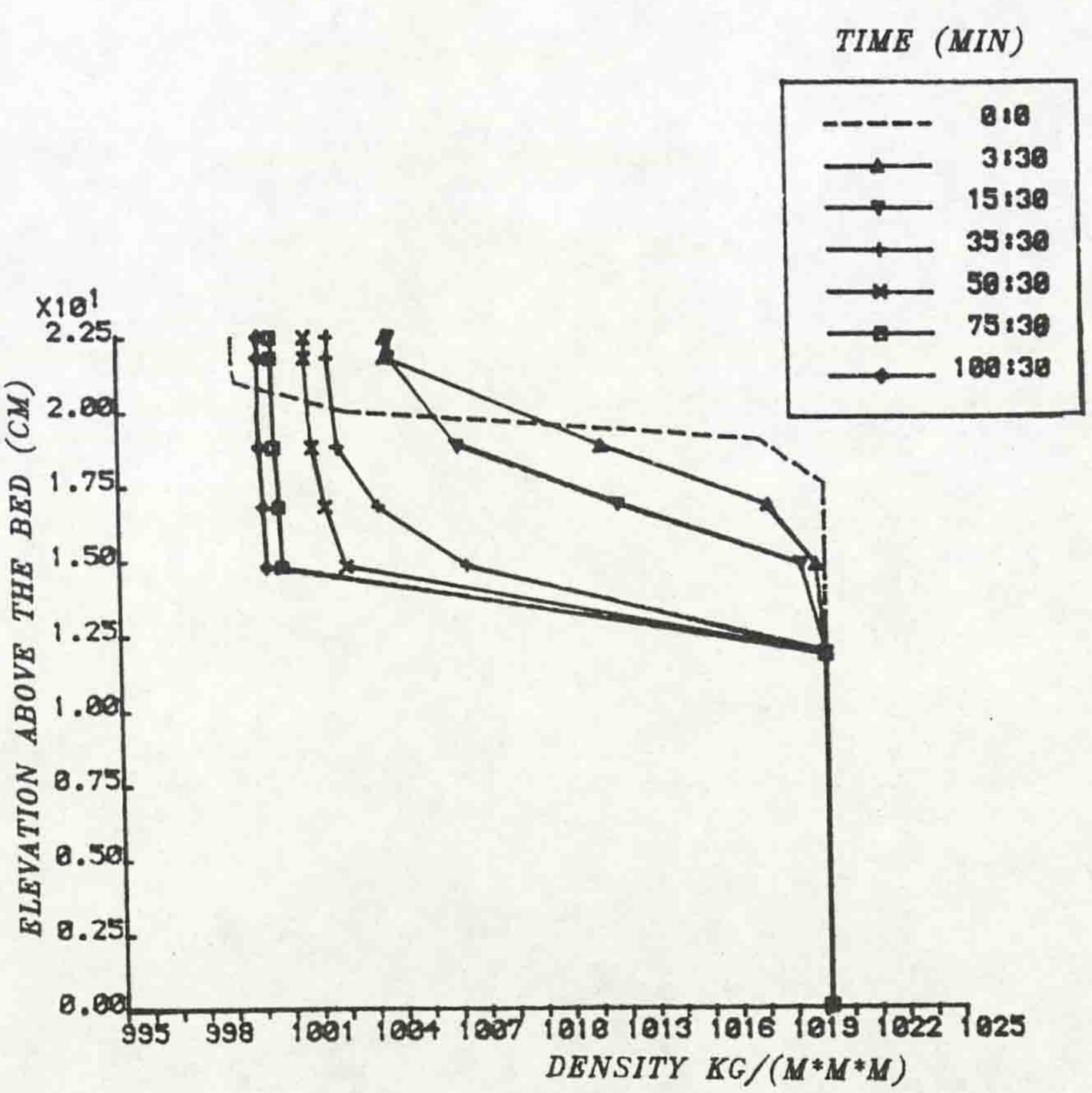

Fig. (6.26) Variation of density with elevation above the bed for station number 1, experiment number 4, Table (6.2), (Q_o = 19.66 cc/sec, ε = 2.1%, h_1 = 2.5 cm).

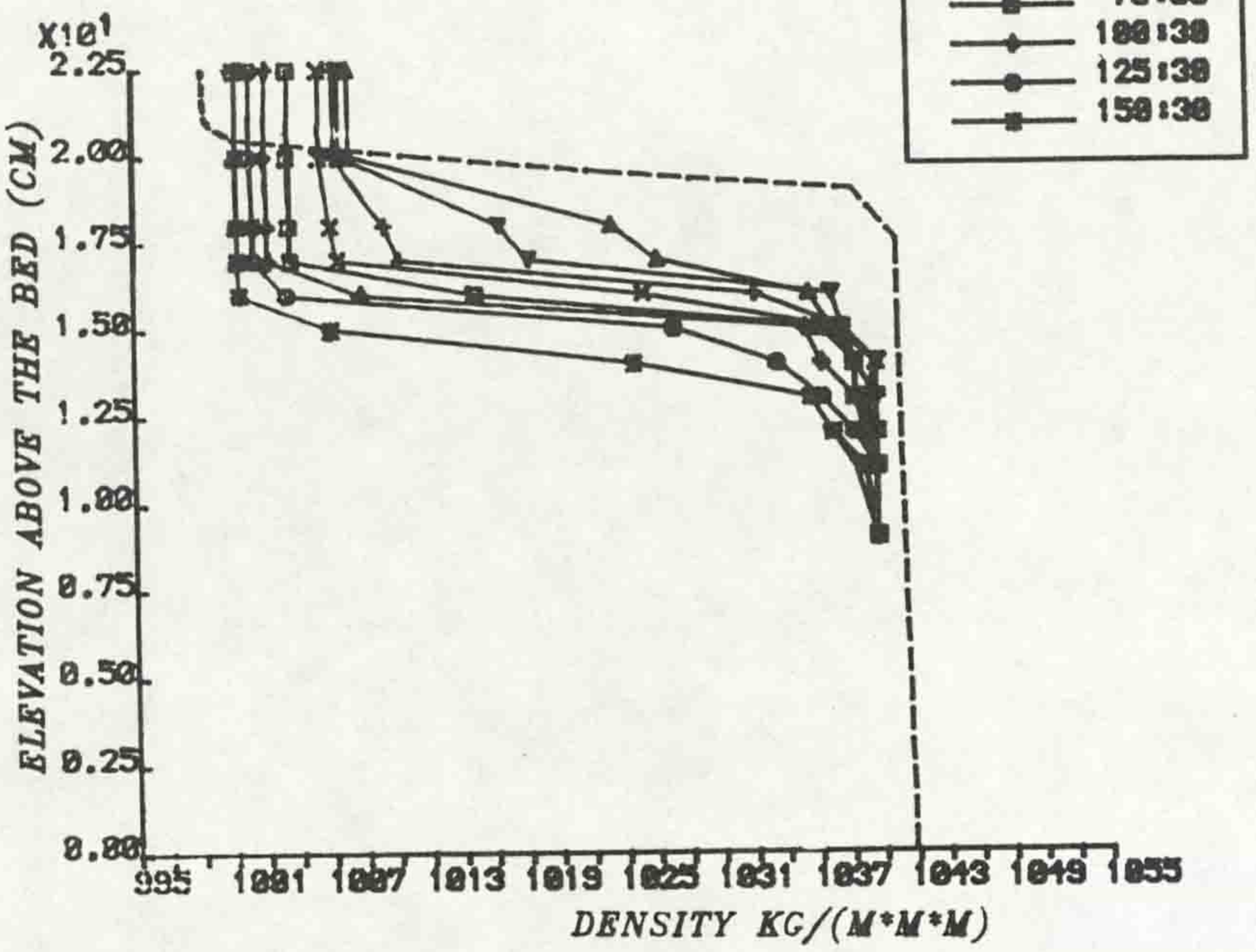

Fig. (6.27) Variation of density with elevation above the bed for station number 8, experiment number 5, Table (6.2), (Q_o = 19.66 cc/sec, ε = 4.35%, h_1 = 2.5 cm).

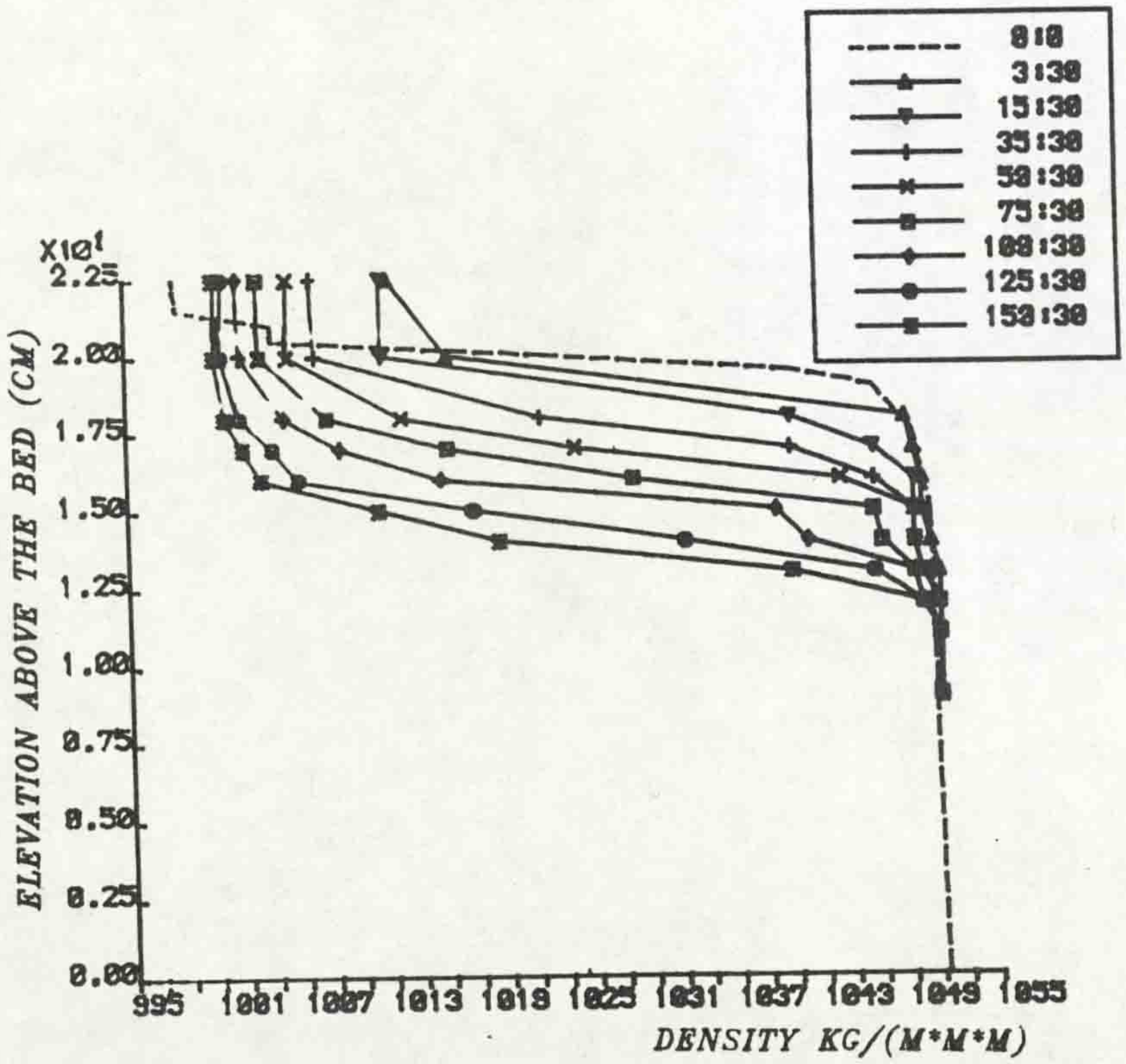

Fig. (6.28) Variation of density with elevation above the bed for station number 1, experiment number 6, Table (6.2), (Q_o = 19.66 cc/sec, ε = 5.3%, h_1 = 2.5 cm).

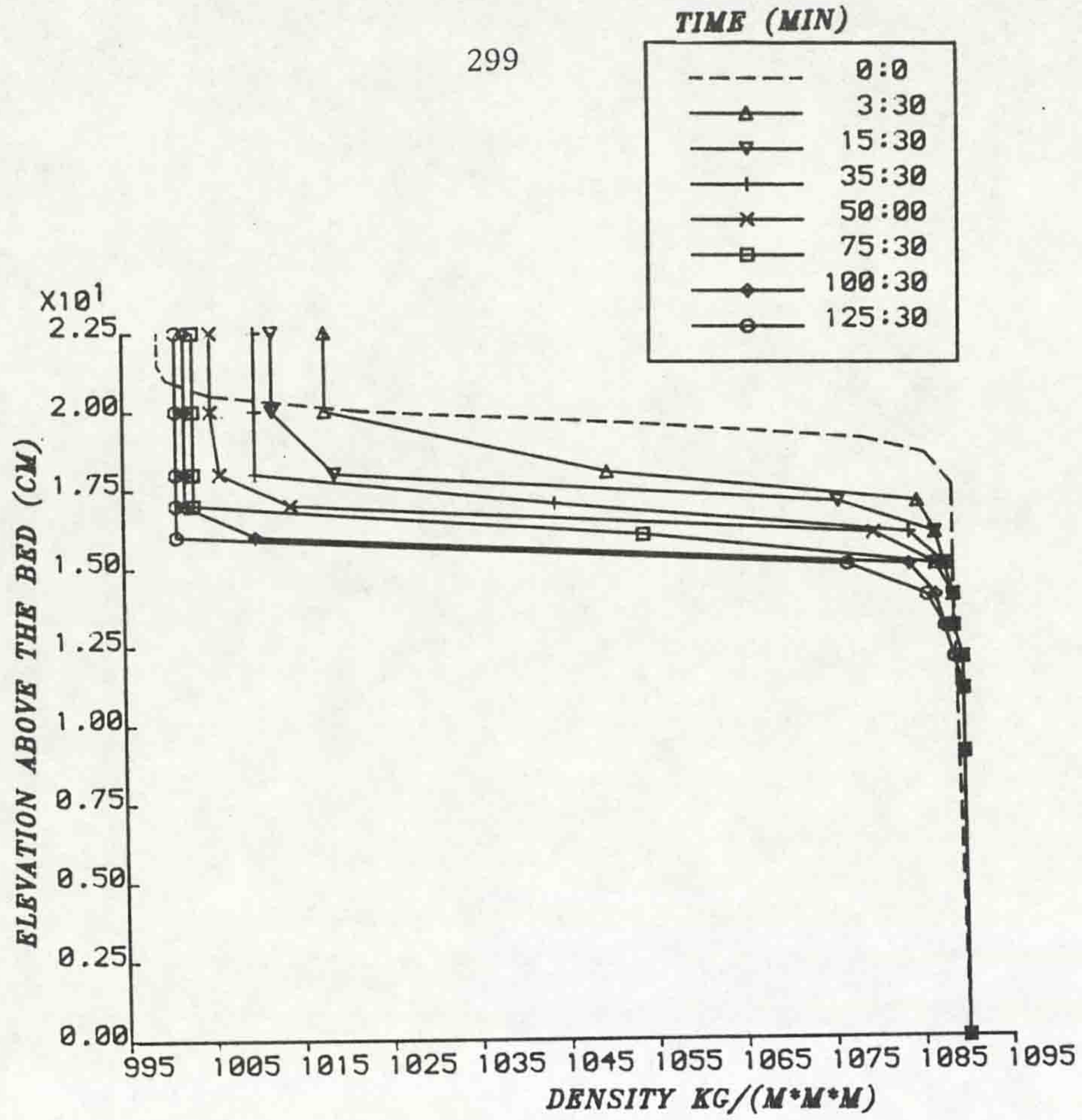

Fig. (6.29) Variation of density with elevation above the bed for station number 8, experiment number 7, Table (6.2), (Q_o = 19.66 cc/sec, ε = 9.11%, h_1 = 2.5 cm).

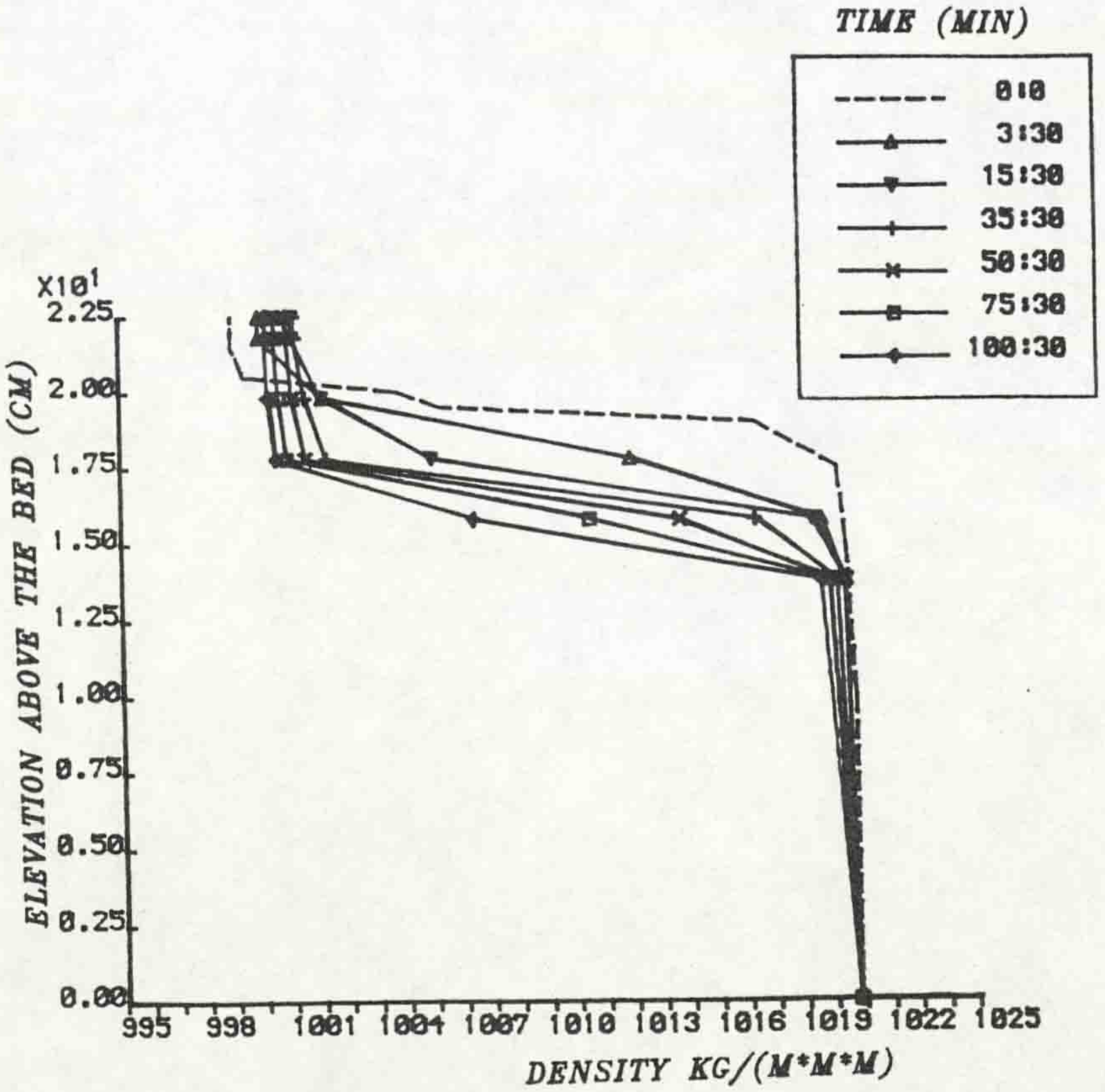

Fig. (6.30) Variation of density with elevation above the bed for station number 1, experiment number 8, Table (6.2), (Q_o = 12.38 cc/sec, ε = 2.2%, h_1 = 2.5 cm).

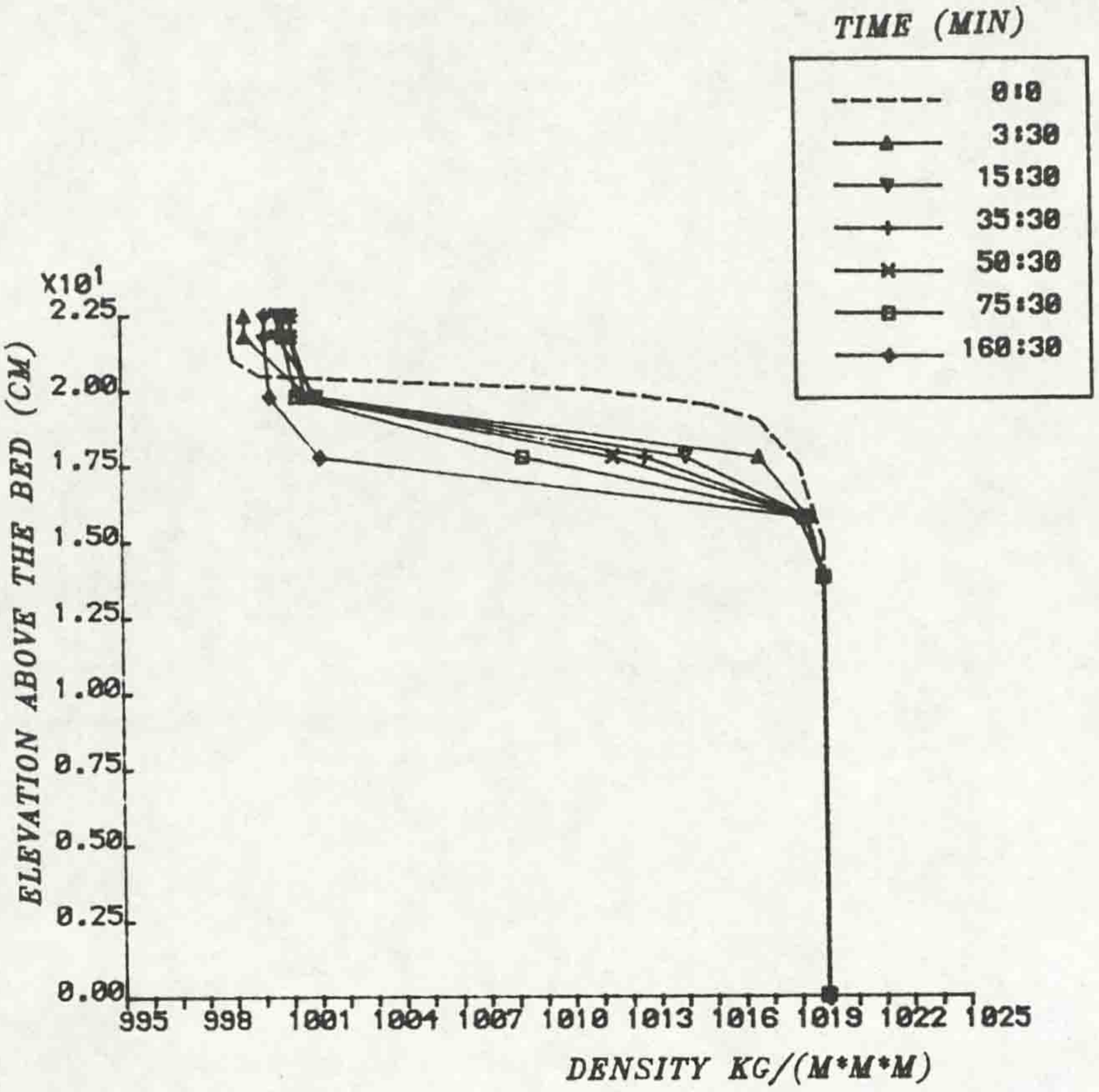

Fig. (6.31) Variation of density with elevation above the bed for station number 1, experiment number 9, Table (6.2), (Q_o = 9.71 cc/sec, ε = 2.1%, h_1 = 2.5 cm).

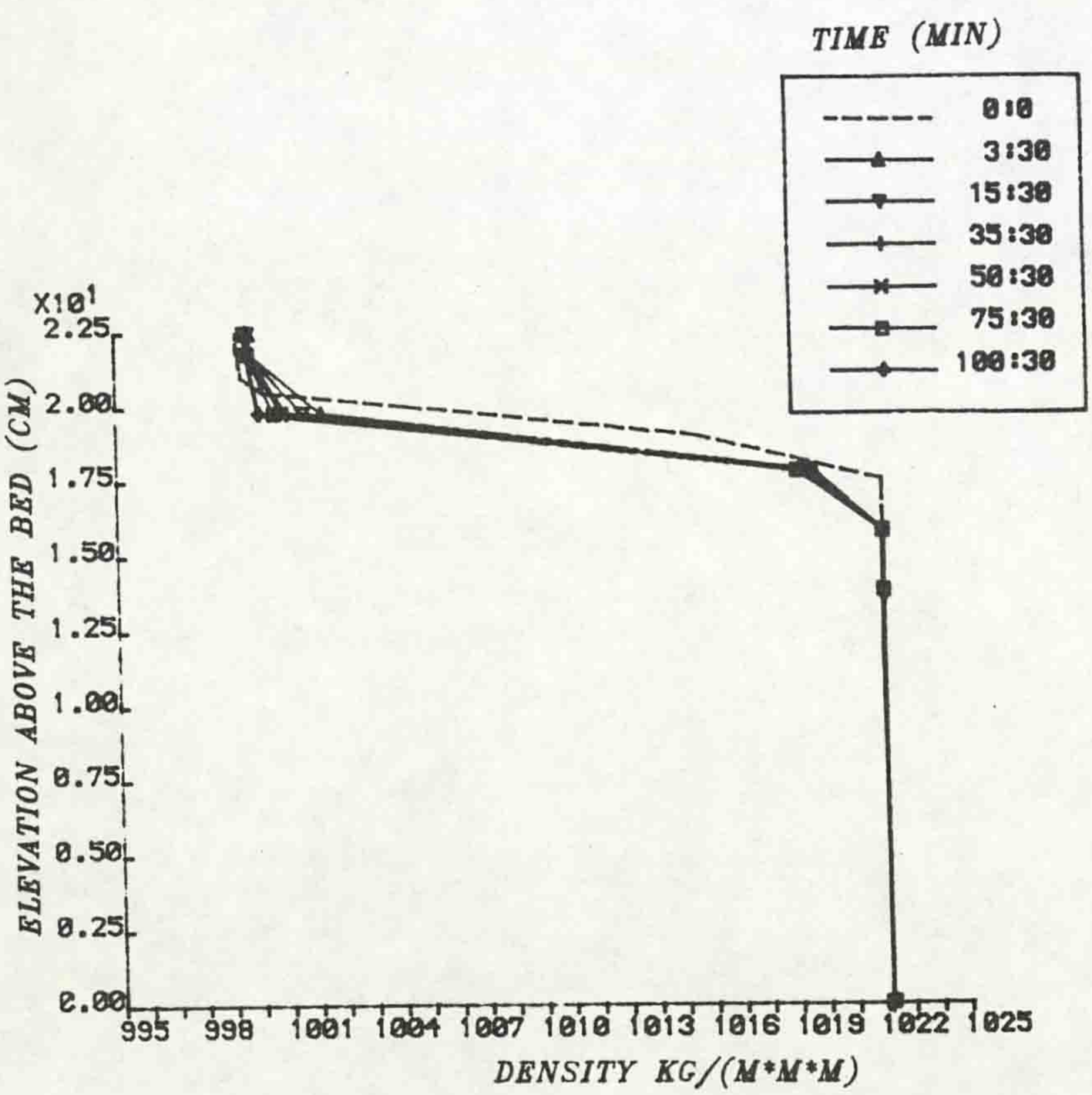

Fig. (6.32) Variation of density with elevation above the bed for station number 1, experiment number 10, Table (6.2), (Q_o = 5.75 cc/sec, ε = 2.3%, h_1 = 2.5 cm).

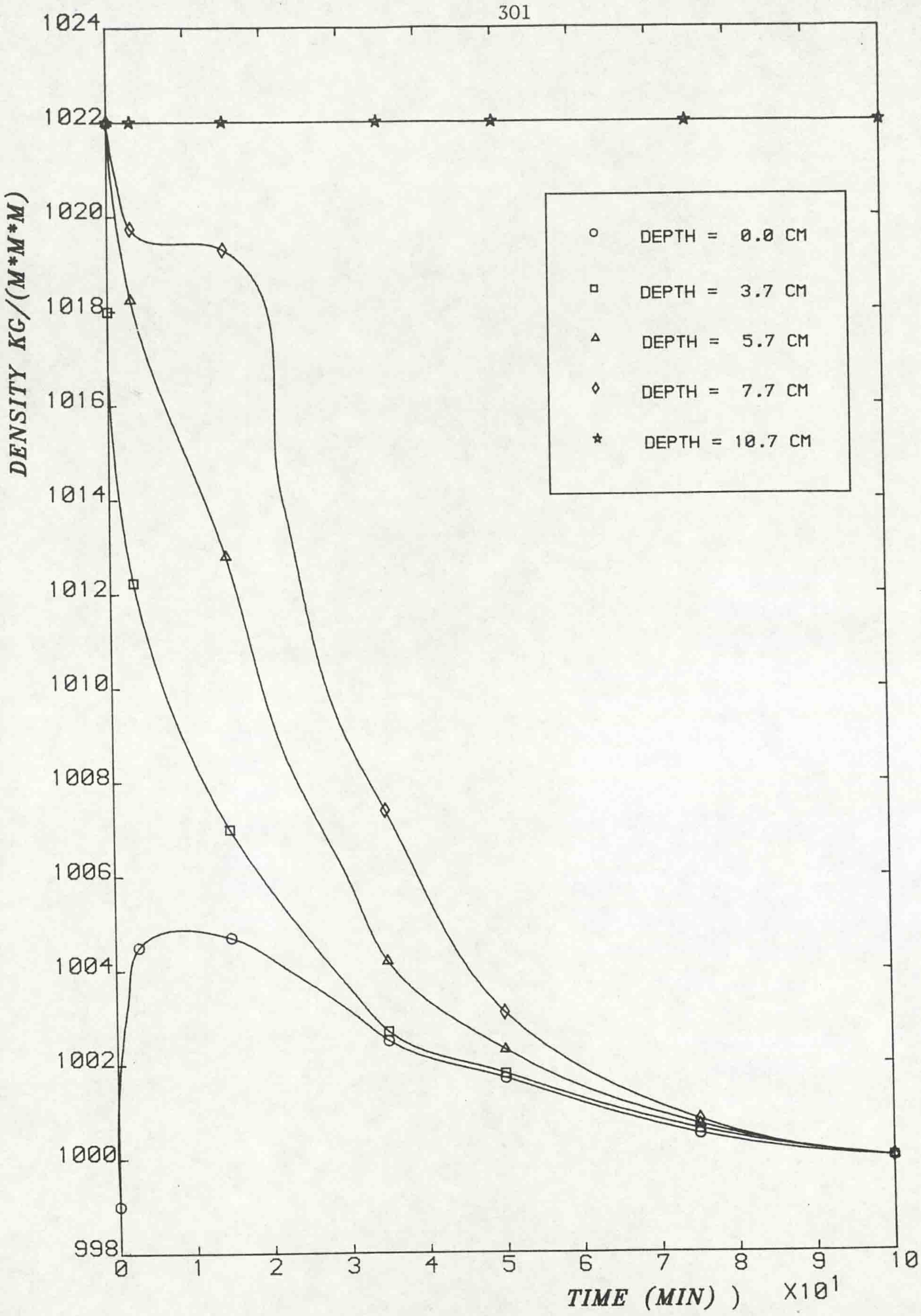

Fig. (6.33) Variation of density with time at different depths from the surface for station number 1, experiment number 4, Table (6.2), (Q_o = 19.66 cc/sec, ε = 2.1%).

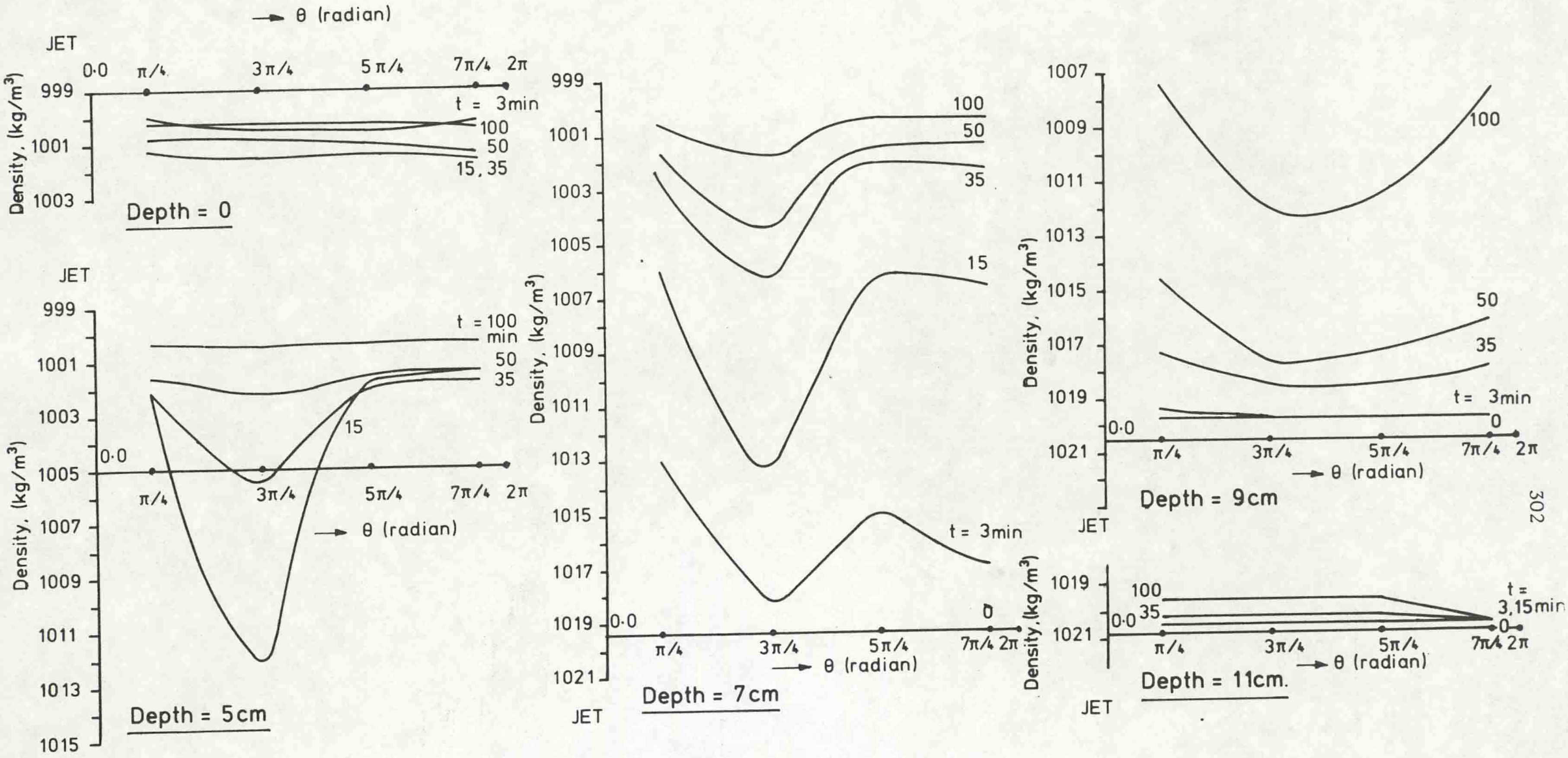

Fig. (6.34) Variation of density with θ for various depths and at different times, experiment number 8, Table (6.2), (Q_o = 12.383 cc/sec, ε = 2.2%, distance from the wall = 3 cm).

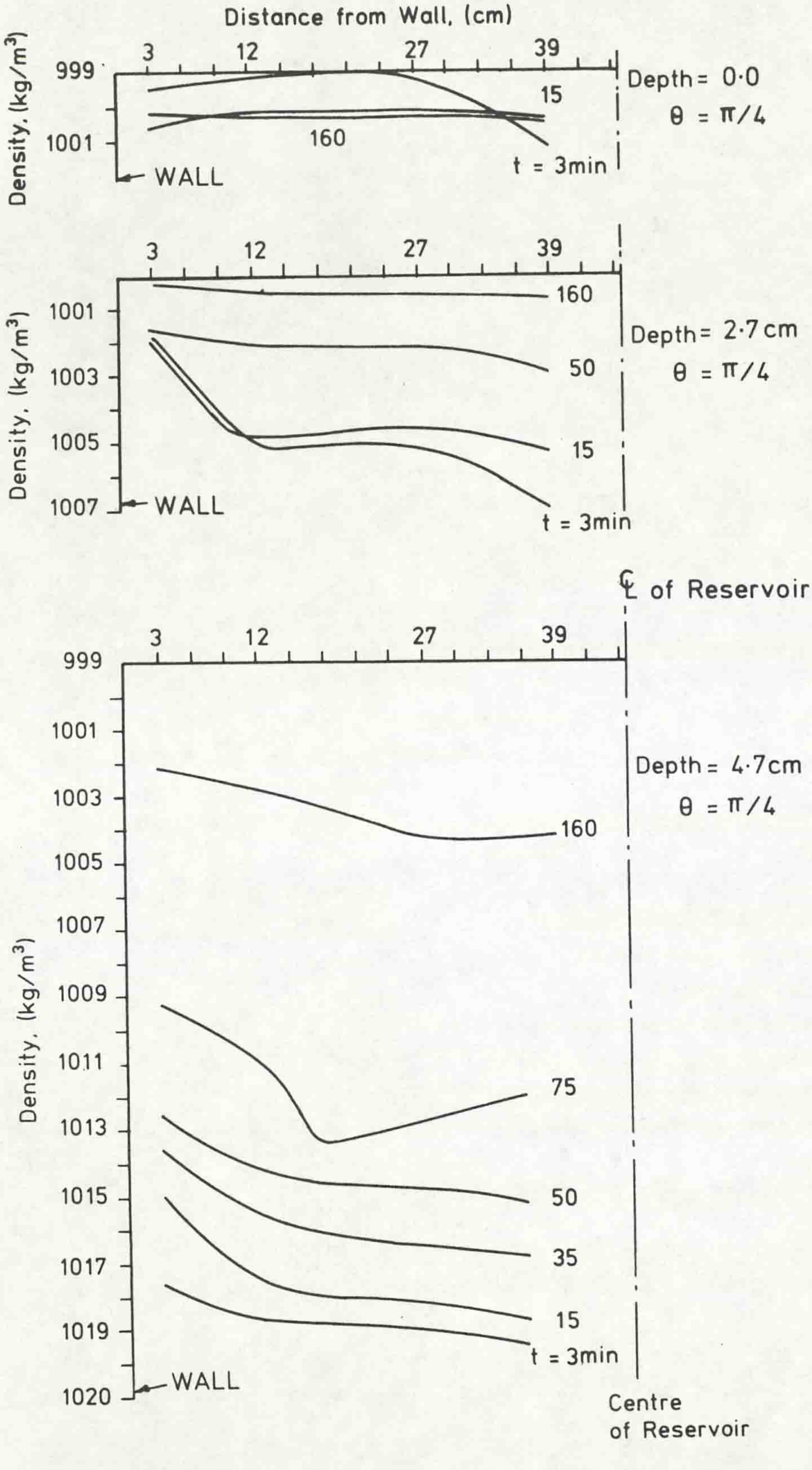

Fig. (6.35) Variation of density with distance from the wall for $\theta = 45^0$, for various depths and at different times, experiment number 9, Table (6.2), (Q_o = 9.71 cc/sec, ε = 2.1%).

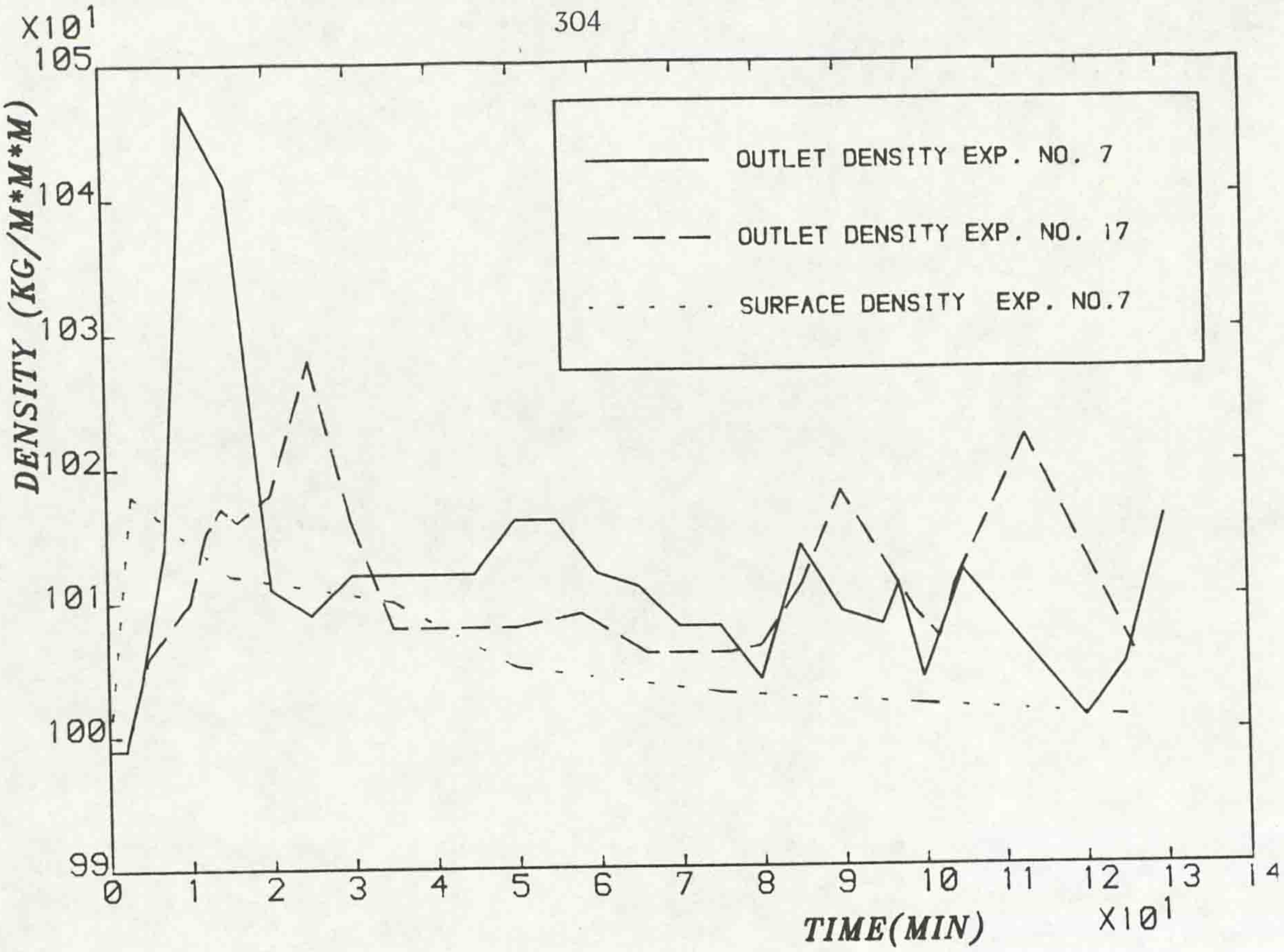

Fig. (6.36) Variation of outlet density with time for experiment number 7, Table (6.2) and experiment number 17, Table (6.3) and for a point near to the wall at $\theta = 45^0$, (Q_o = 19.66 cc/sec, ε = 9.11%).

Fig. (6.37) Bi-log velocity profile for two experiments, Table (6.3), ($\theta = 315^0$, Q = 8.83, ε = 4.3% and 9%).

Experiment No.	Discharge cc/sec	Depth of Fresh Layer before Experiment cm	Depth of Saline before Experiment cm	Depth of Upper Layer in Experiment cm	Density of Fresh Layer kg/m^3	Density of Saline kg/m^3	Hydrogen Bubbles	Wall Velocity	Velocity in Depth	Time Lapse Photography
11	8.83	11.5	11	11.5	999.3	1042.8	✓			
12	8.83	10.5	12	10.5	999	1089	✓			
13	7.15	10.5	12	10.5	999	1088	✓			
14	19.66	12.	10.5	12.	999	1088	✓			✓
15	12.383	12.	10.5	12.	999	1088				✓
16	19.66	2.5	20.	9.	999	1020		✓	✓	
17	19.66	2.5	20.	4.5	999	1090		✓		✓
18	12.383	2.5	20.	6.8	1000	1022		✓		✓
19	5.75	2.5	20.	4.7	999	1090				✓
20	19.66	10.5	12.	10.5	999	1088				✓

Table (6.3) Details of Velocity Measurement Experiments in Stratified Reservoir

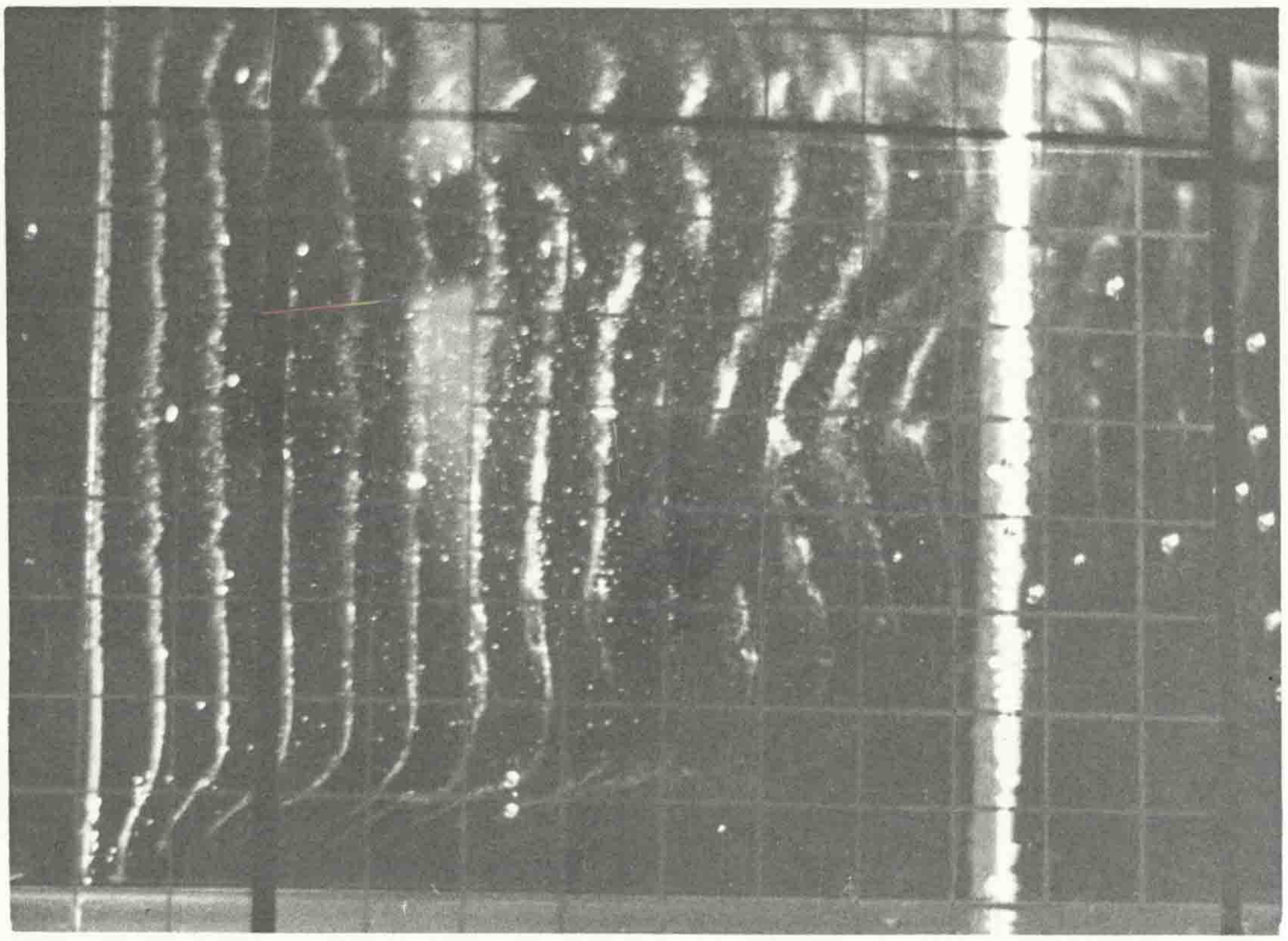

a) $\varepsilon = 4.3\%$

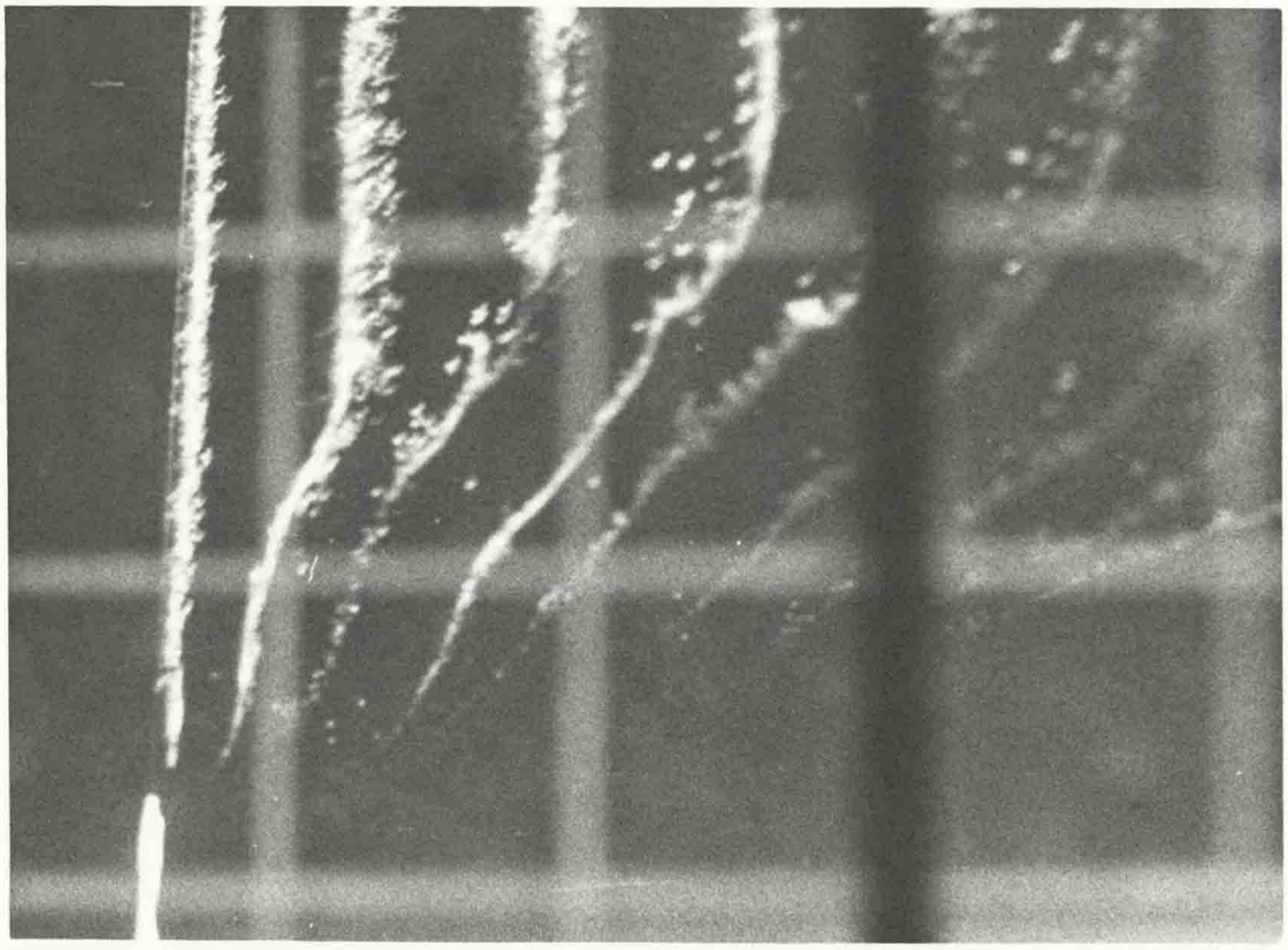

b) $\varepsilon = 9\%$

Fig. (6.38) Hydrogen bubble results ($\theta = 315^0$, $Q_o = 8.83$ cc/sec).

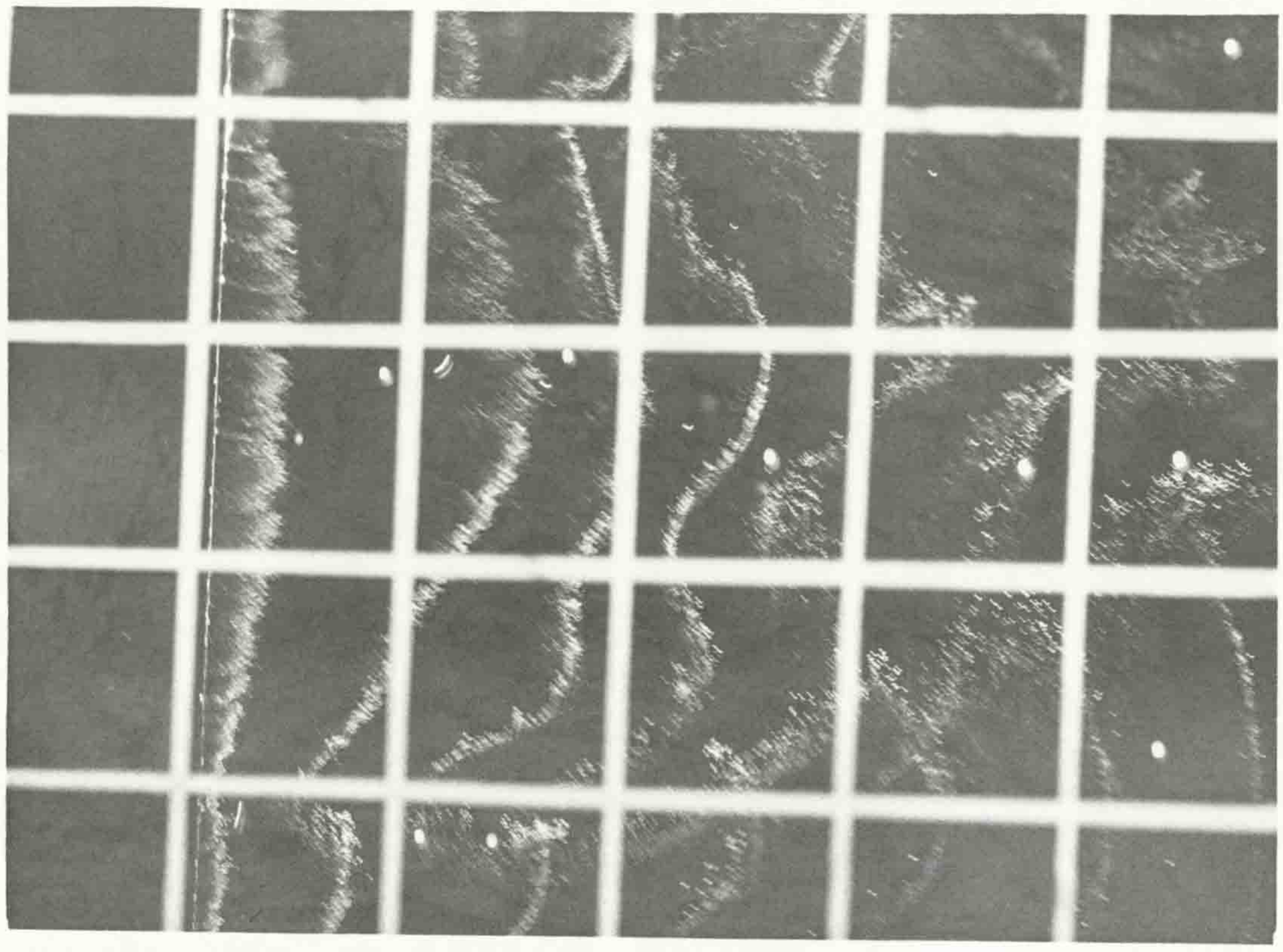

Fig. (6.39) Hydrogen bubble results ($\theta = 45^0$, $Q_o = 7.15$ cc/sec, $\varepsilon = 8.9\%$).

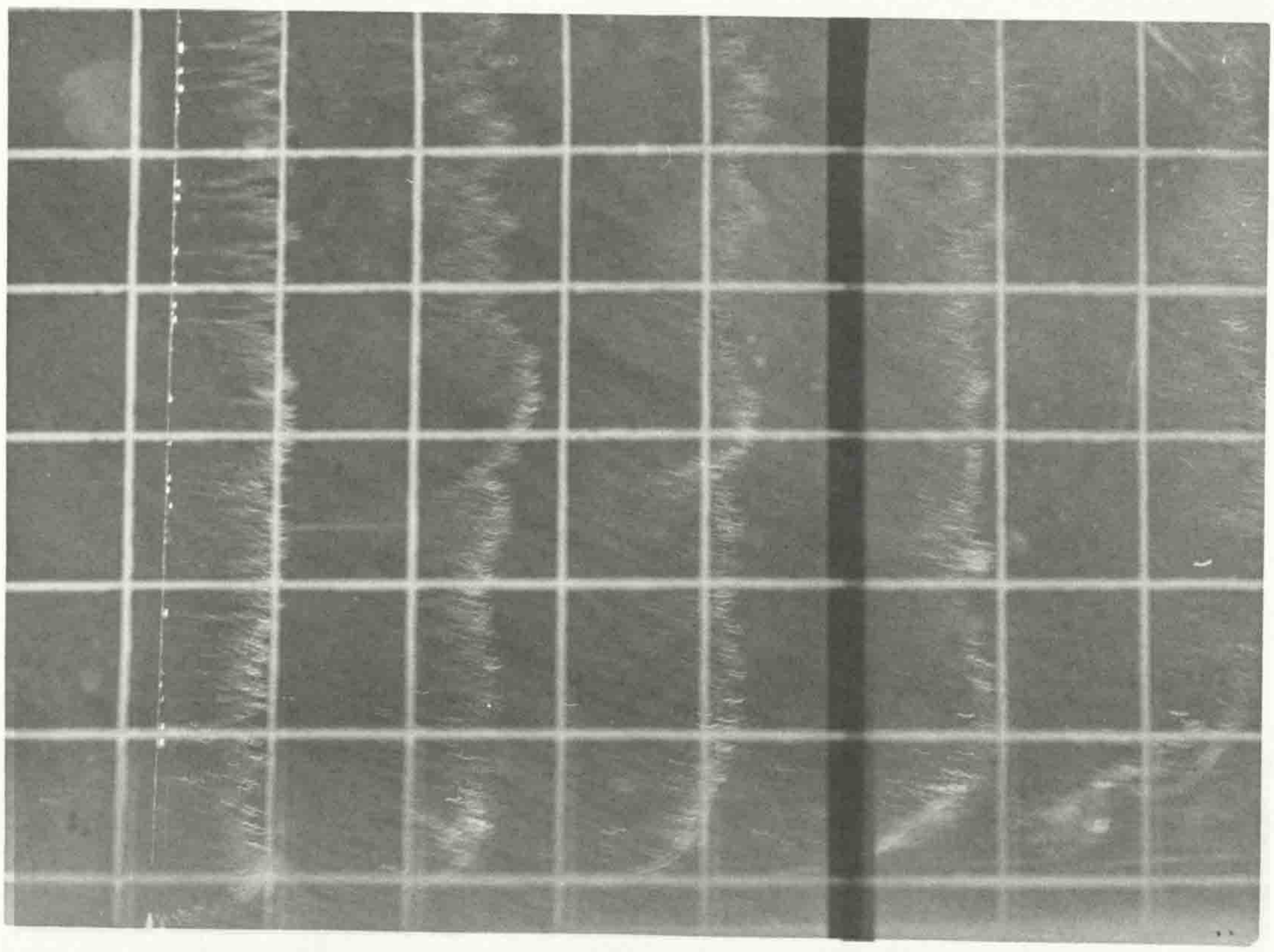

Fig. (6.40) Hydrogen bubble results ($\theta = 315^0$, $Q_o = 19.66$ cc/sec, $\varepsilon = 8.9\%$).

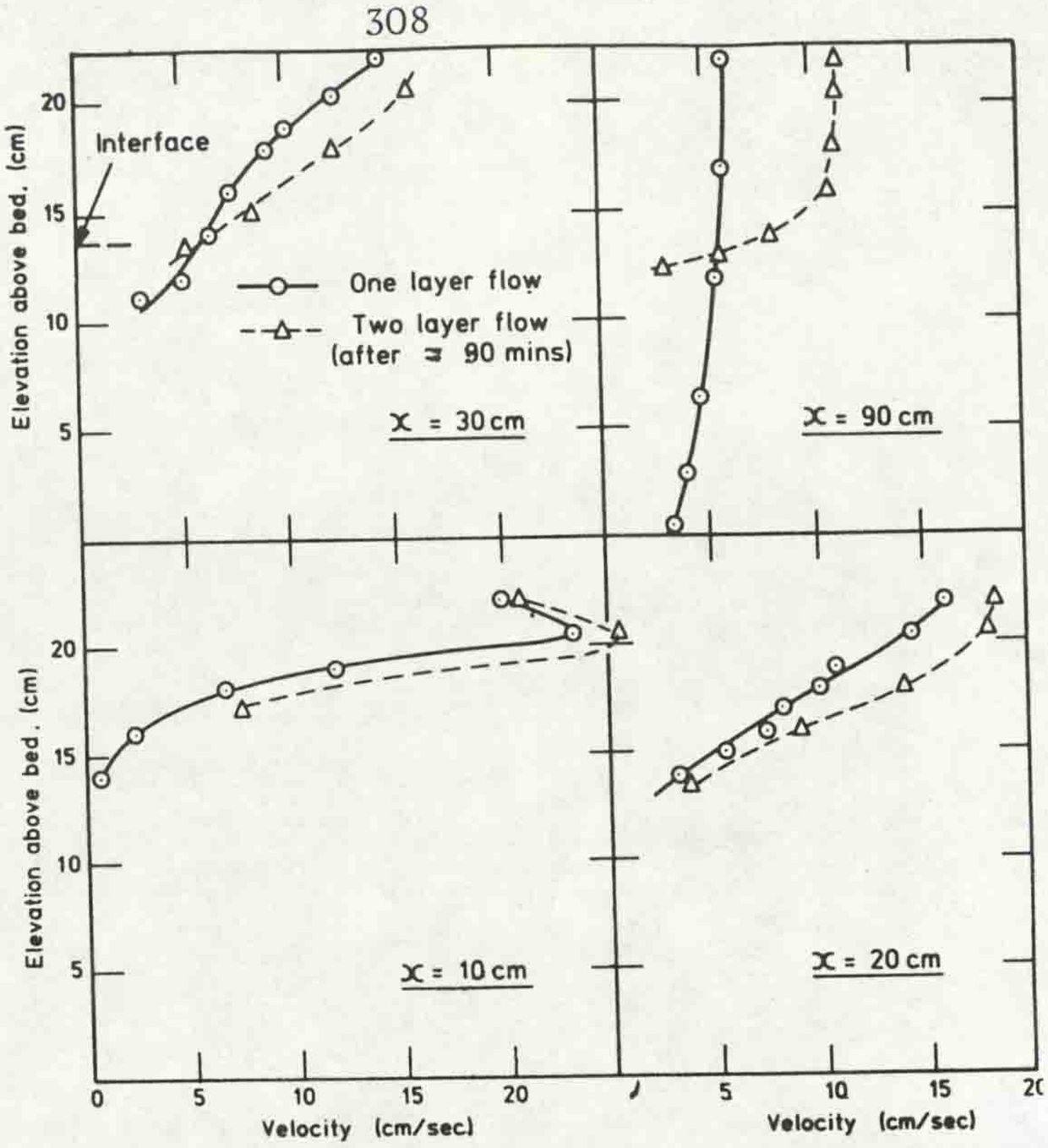

Fig. (6.41) Wall velocity distribution in depth for stratified and homogeneous reservoirs, (Q_o = 19.66 cc/sec, ε = 2.1%).

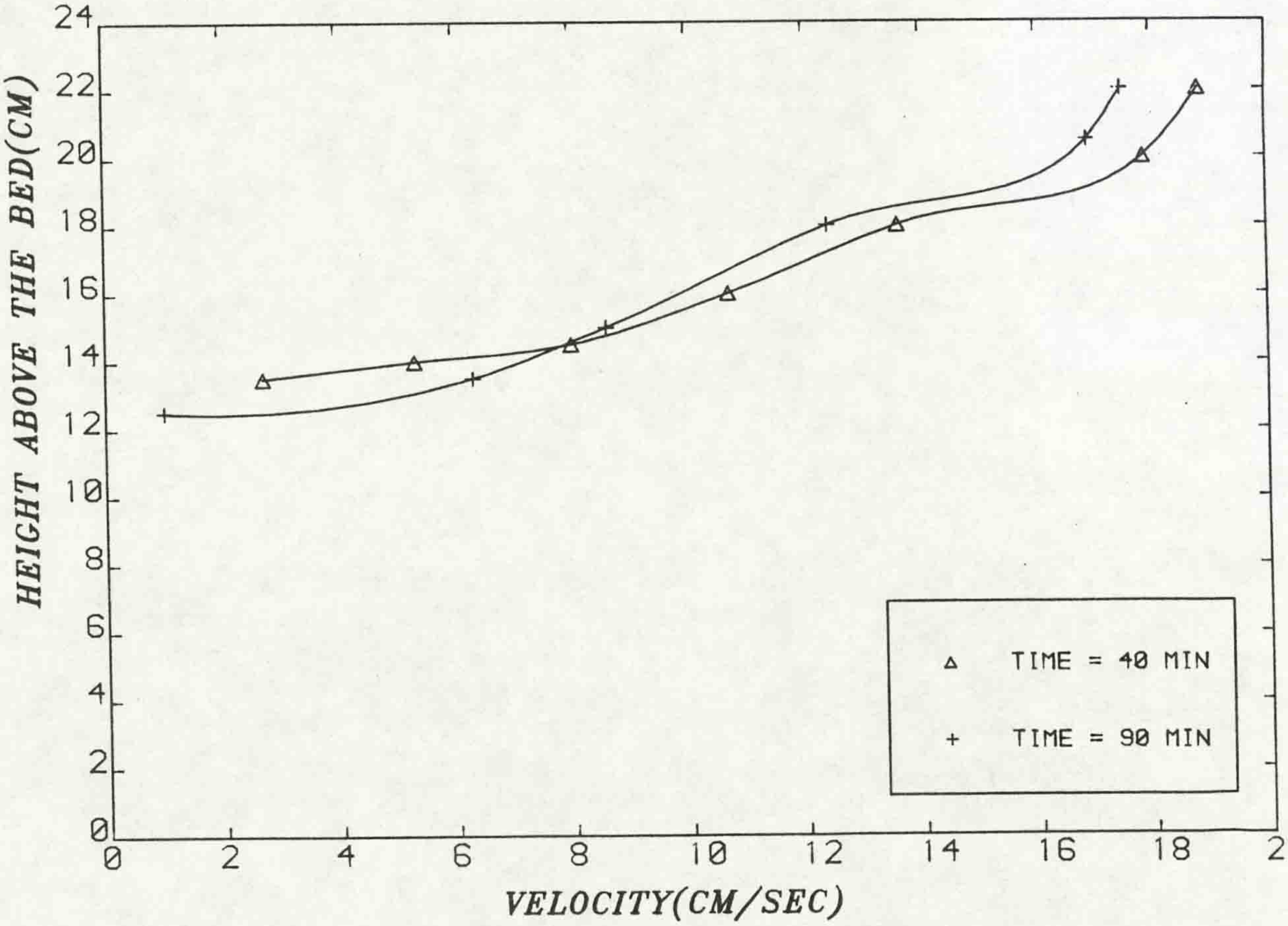

Fig. (6.42) Variation of wall velocity in stratified reservoir at two different times, (x = 30 cm, Q_o = 19.66 cc/sec, ε = 2.1%).

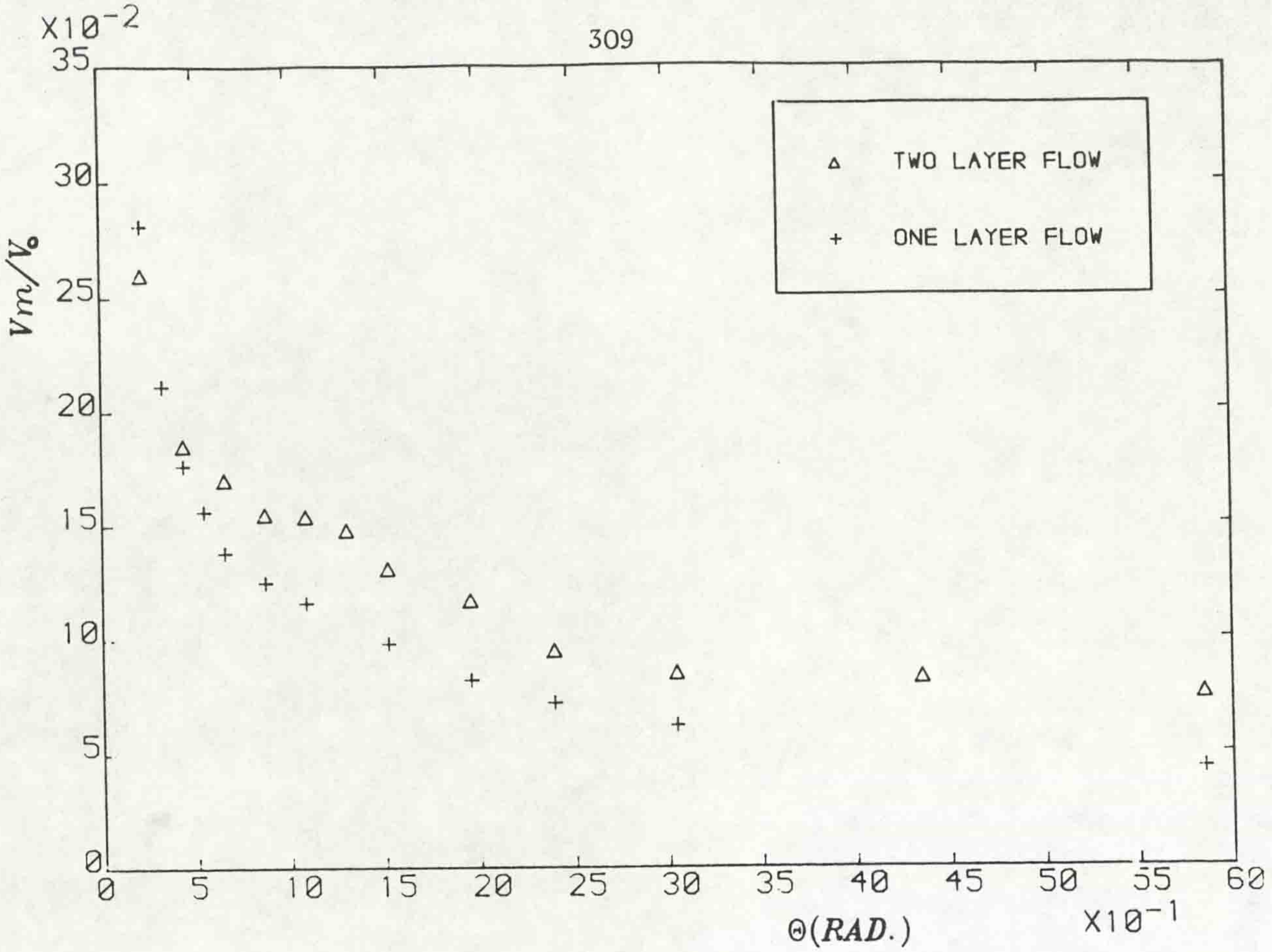

Fig. (6.43) Variation of wall velocity with θ for stratified and homogeneous reservoirs, (Q_o = 19.66 cc/sec, ε = 2.1%).

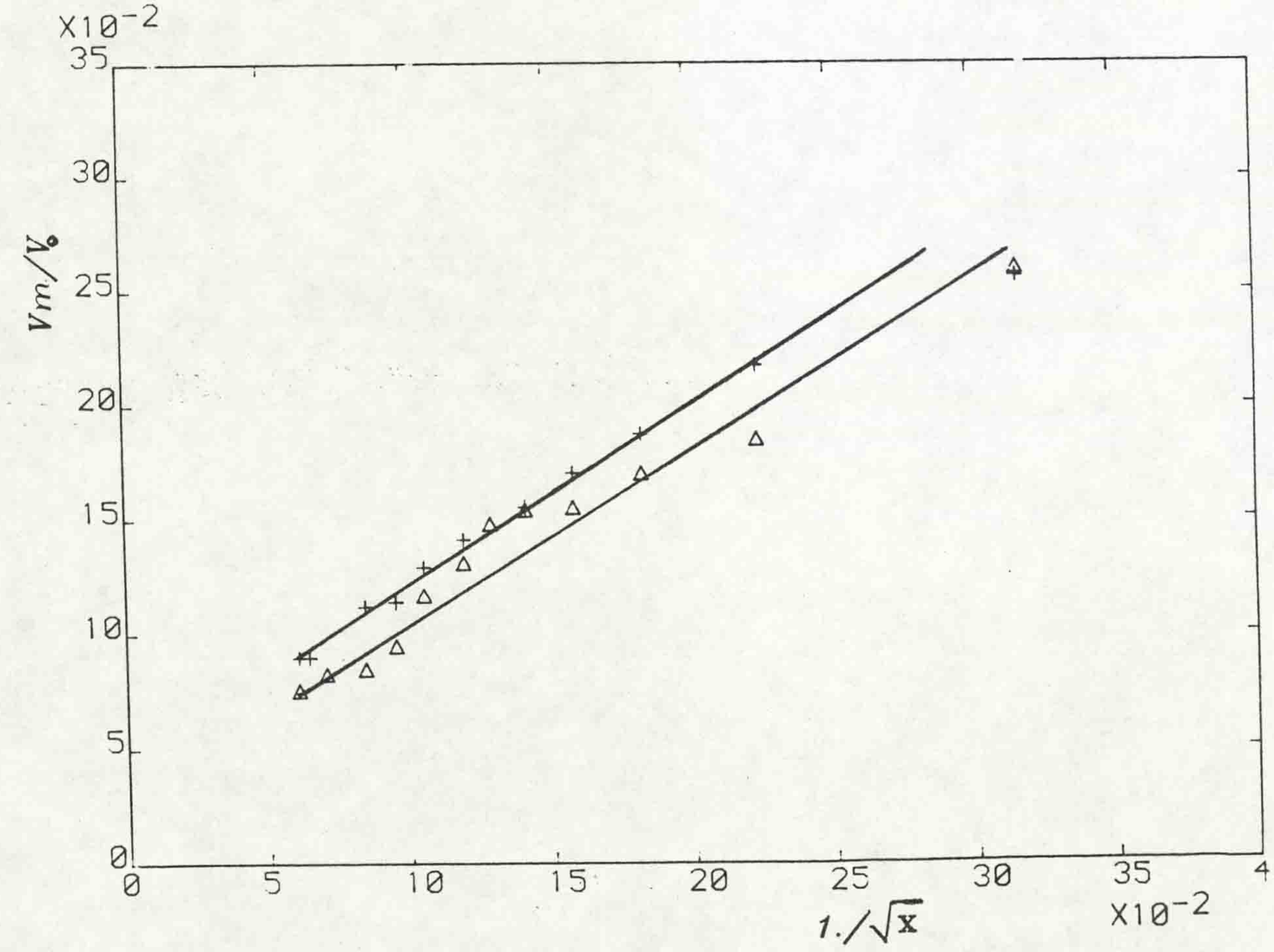

Fig. (6.44) Variation of wall velocity with $1/\sqrt{x}$ for stratified and homogeneous reservoirs, (Q_o = 19.66 cc/sec, ε = 2.1%).

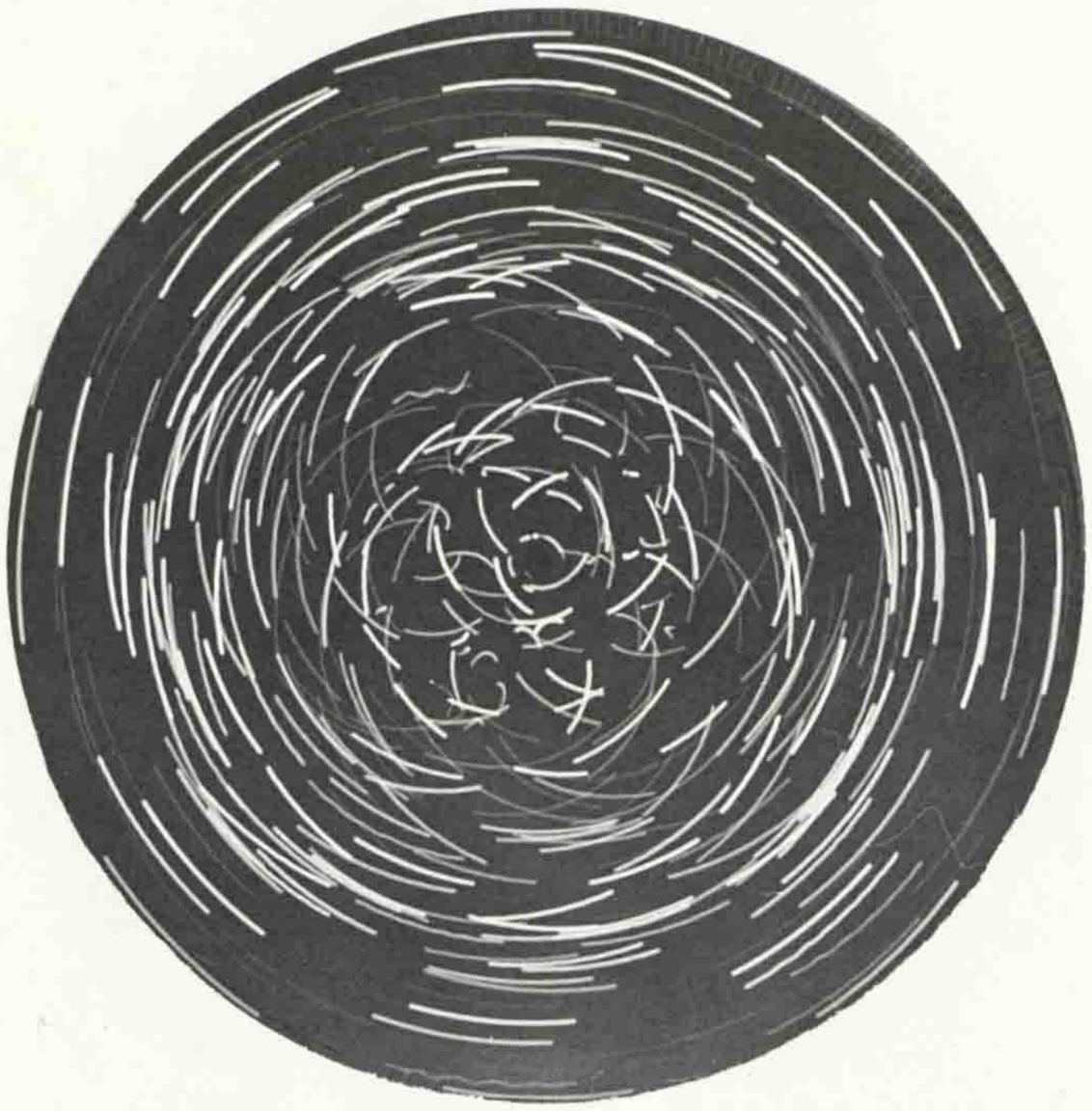

Q_o = 12.383 cc/sec, ε = 2.2%, h_1 = 6.8 cm

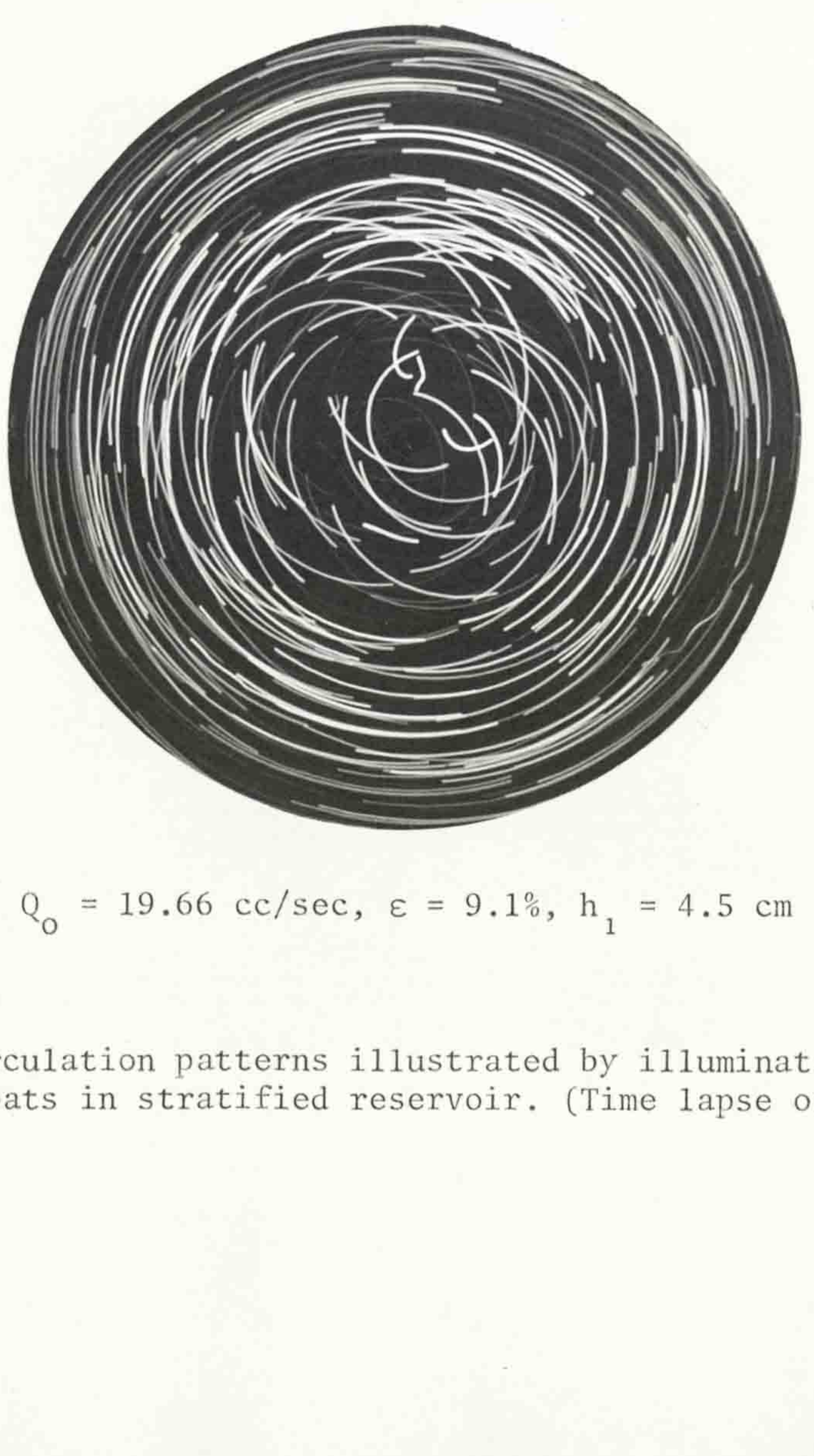

Q_o = 19.66 cc/sec, ε = 9.1%, h_1 = 4.5 cm

Fig. (6.45) Circulation patterns illustrated by illuminated surface floats in stratified reservoir. (Time lapse of 3 seconds).

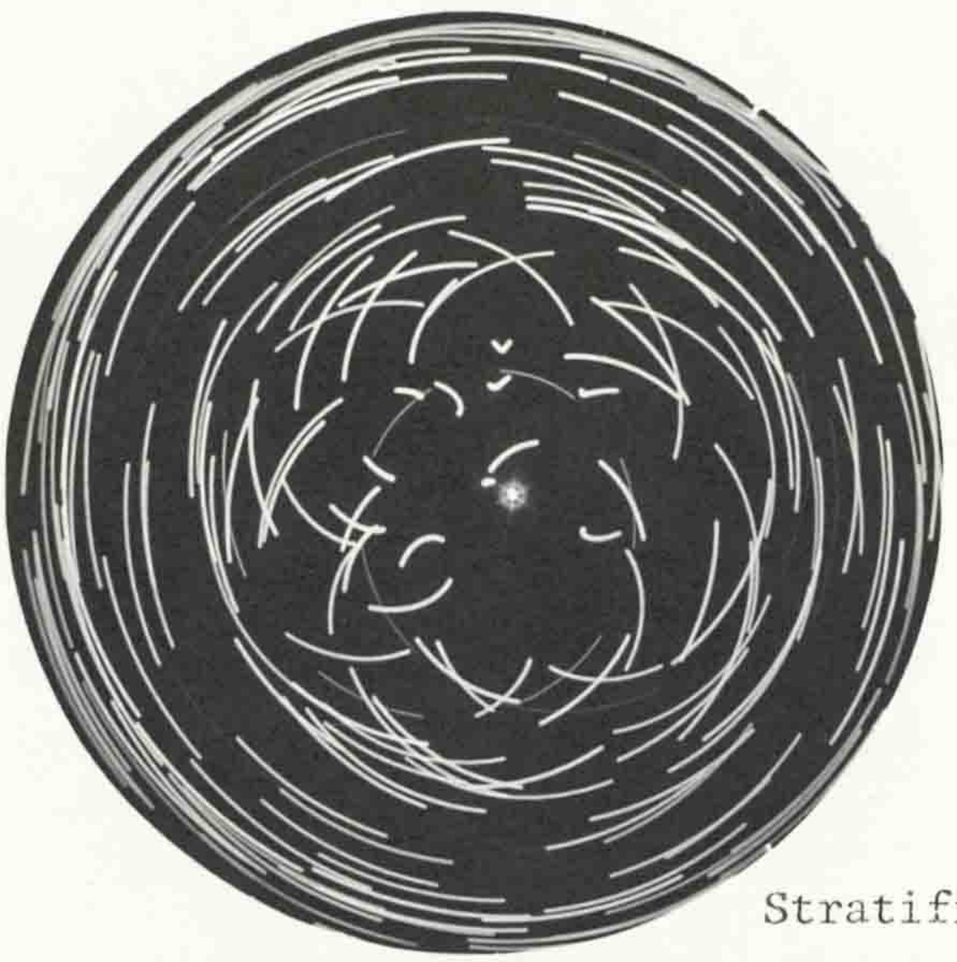

Stratified reservoir

Q_o = 12.383 cc/sec, ε = 8.9%
h_1 = 12 cm
Time lapse = 5 seconds

Q_o = 19.66 cc/sec, ε = 8.9%
h_1 = 12 cm
Time lapse = 5 seconds

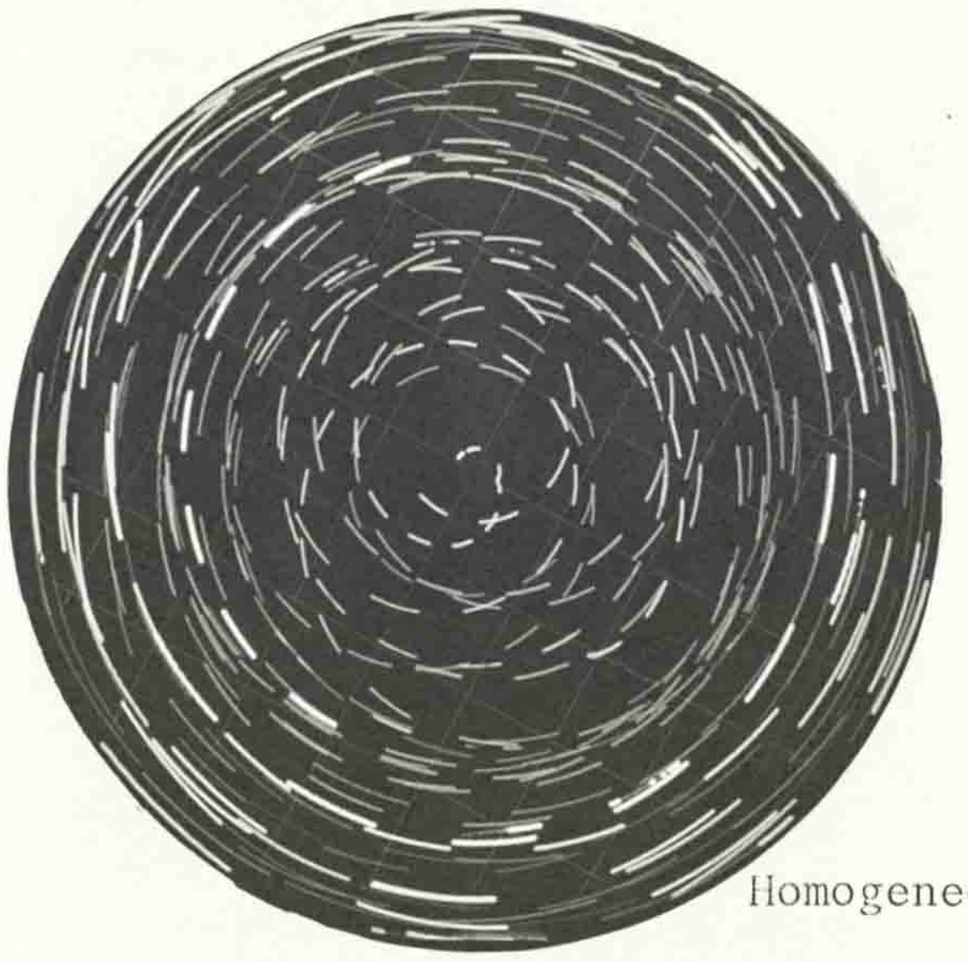

Homogeneous reservoir

Q_o = 12.383 cc/sec, h = 12 cm
Time lapse = 5 seconds

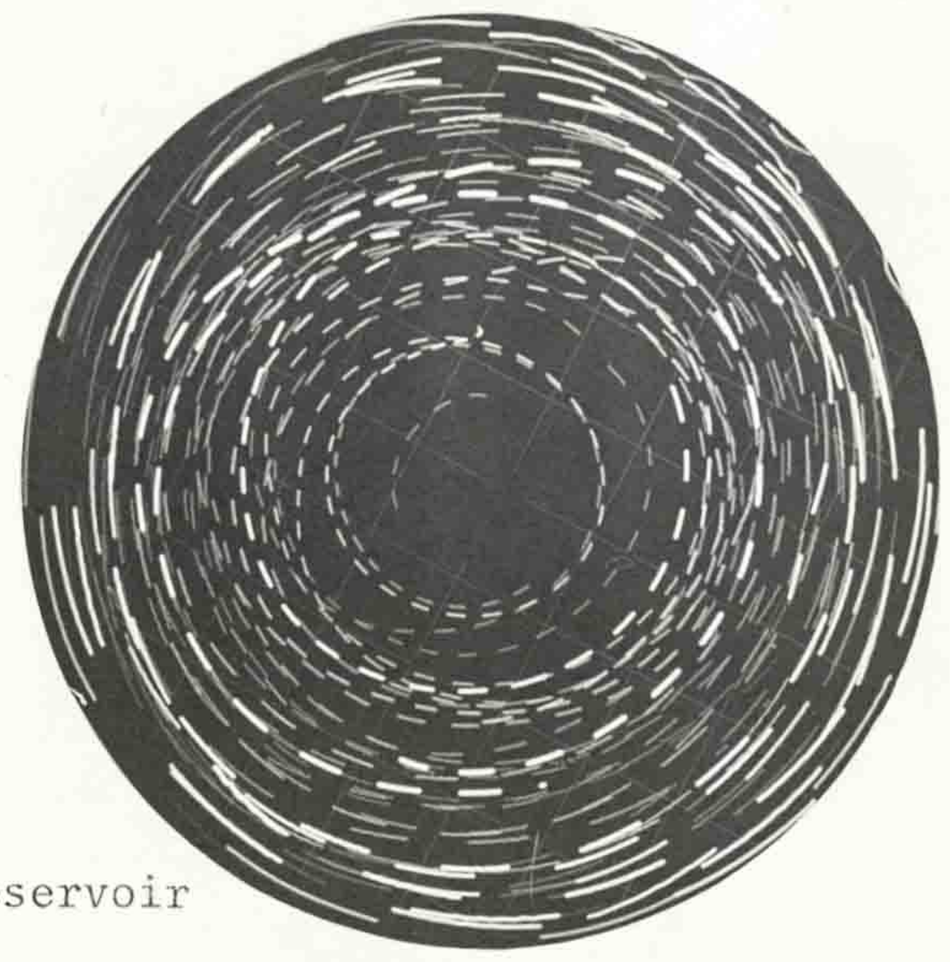

Q_o = 19.66 cc/sec, h = 12 cm
Time lapse = 3 seconds

Fig. (6.46) Circulation patterns illustrated by illuminated surface floats in stratified and homogeneous reservoirs.

Stratified
reservoir

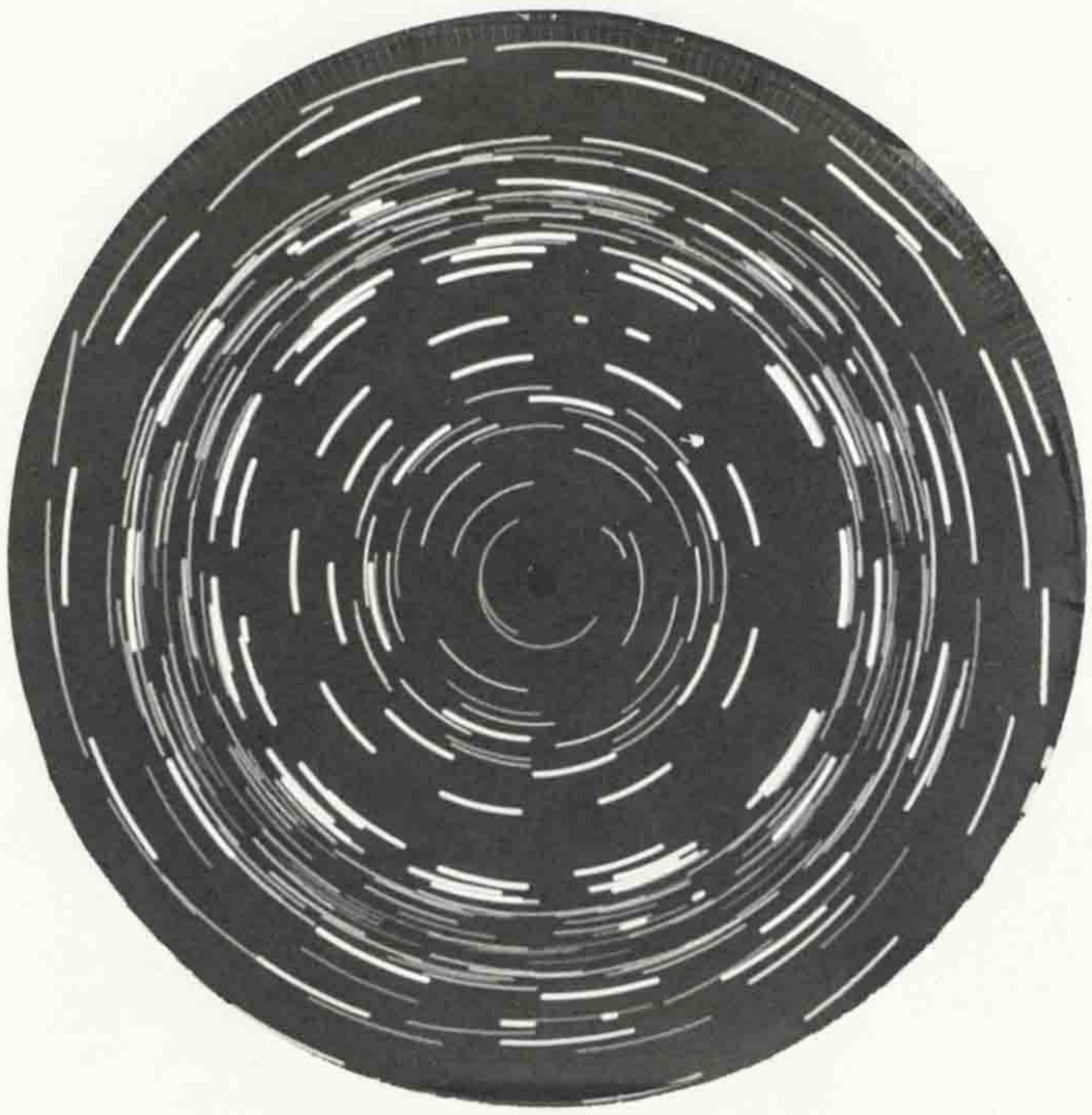

Q_o = 5.75 cc/sec, ε = 9.1%, h_1 = 4.7 cm

Homogeneous
reservoir

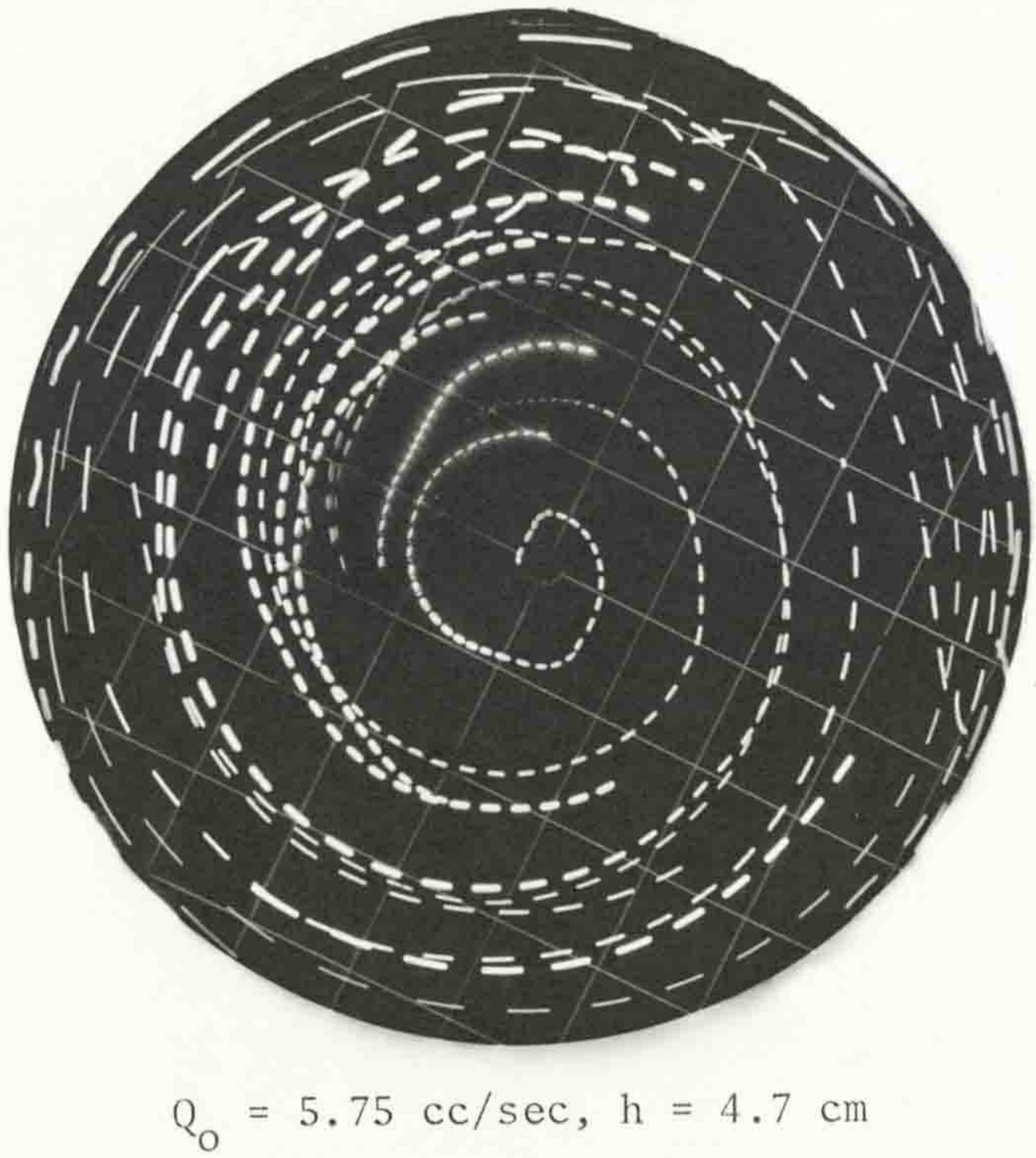

Q_o = 5.75 cc/sec, h = 4.7 cm

Fig. (6.47) Circulation patterns illustrated by illuminated surface floats in stratified and homogeneous reservoirs. (Time lapse of 5 seconds).

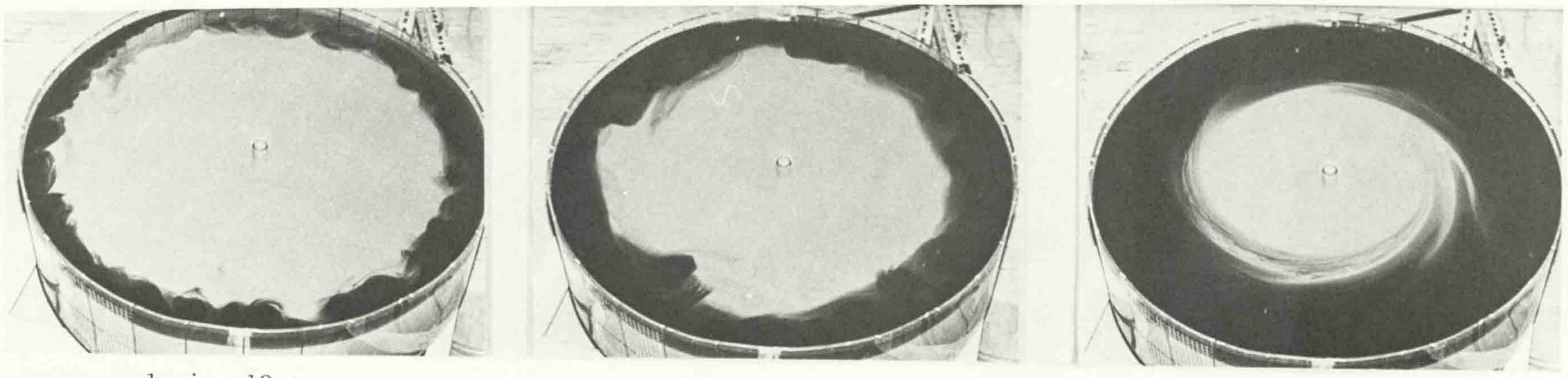

1 min. 10 sec. 4 min. 7 min.

(a)

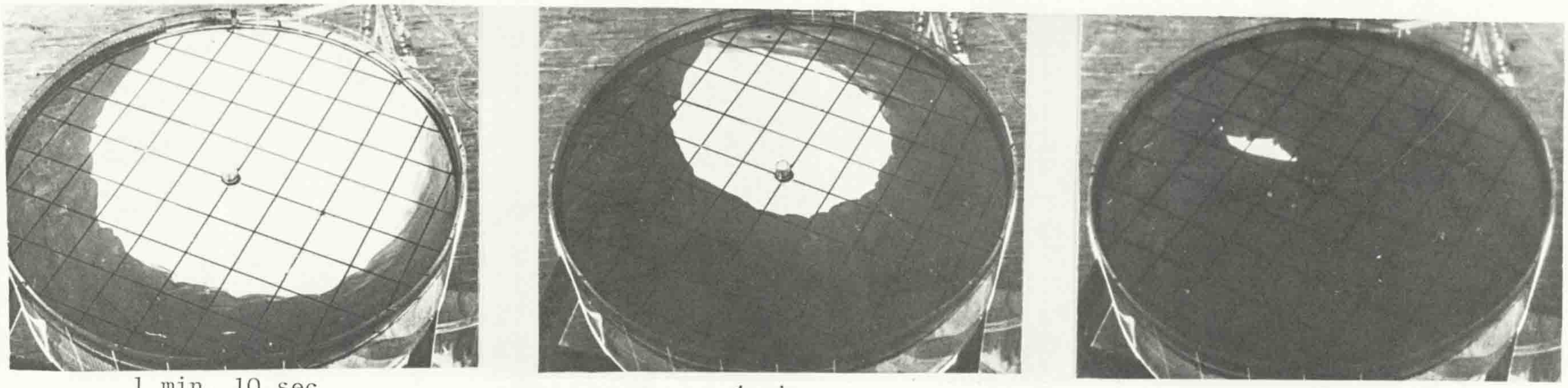

1 min. 10 sec. 4 min. 6 min. 30 sec.

(b)

Fig. (6.48) (a) Circulation produced by a surface jet in a stratified reservoir with interface at 4.7 cm from the free surface.

(b) Circulation produced by a surface jet in a homogeneous reservoir with a solid bottom (water depth = 4.7 cm).

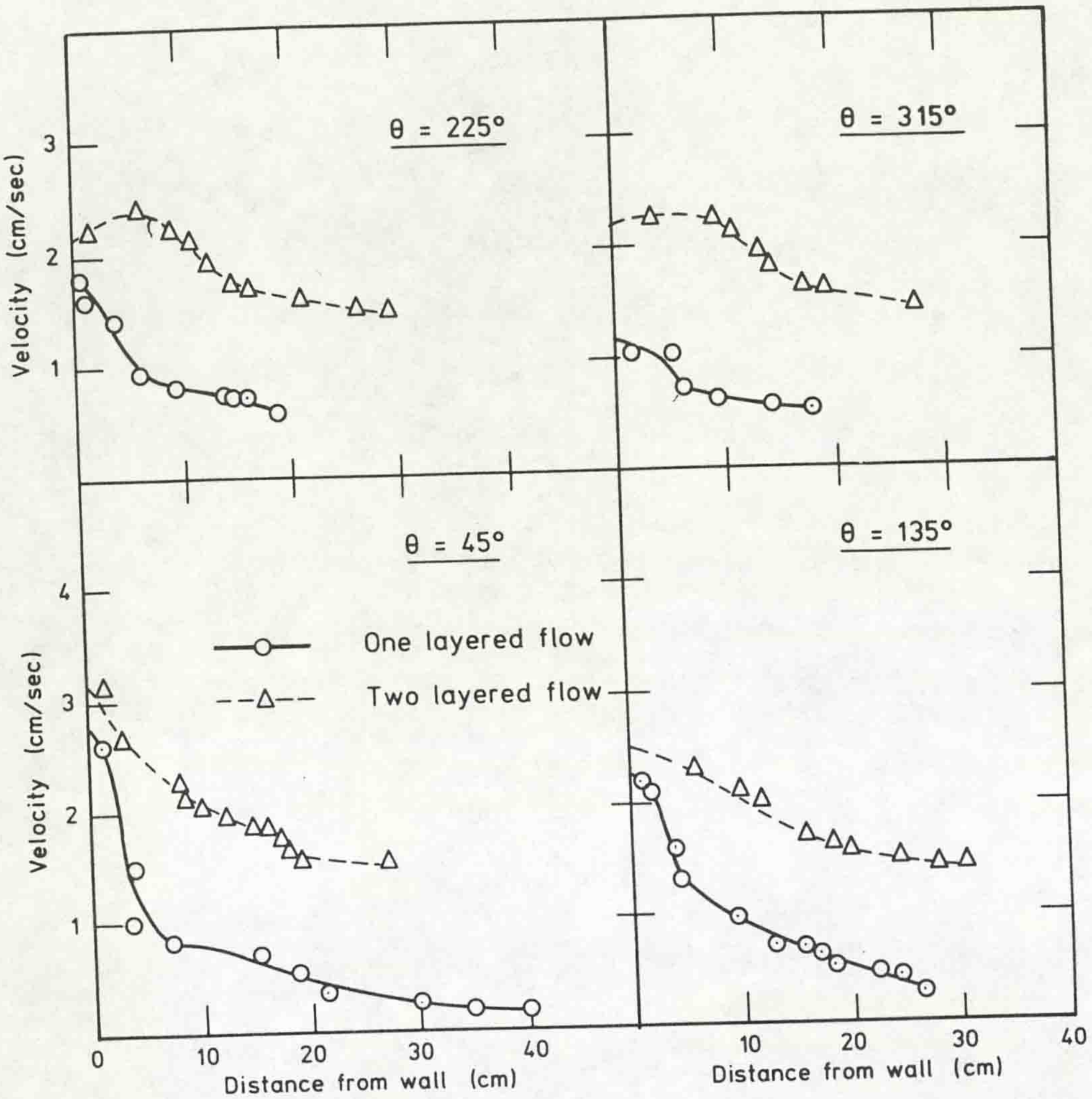

Fig. (6.49) Velocity distribution for one and two layered flows (Q_o = 5.75 cc/sec, total depth for homogeneous reservoir = 4.7 cm, depth of interface for stratified reservoir = 4.7 cm, ε = 9.1%).

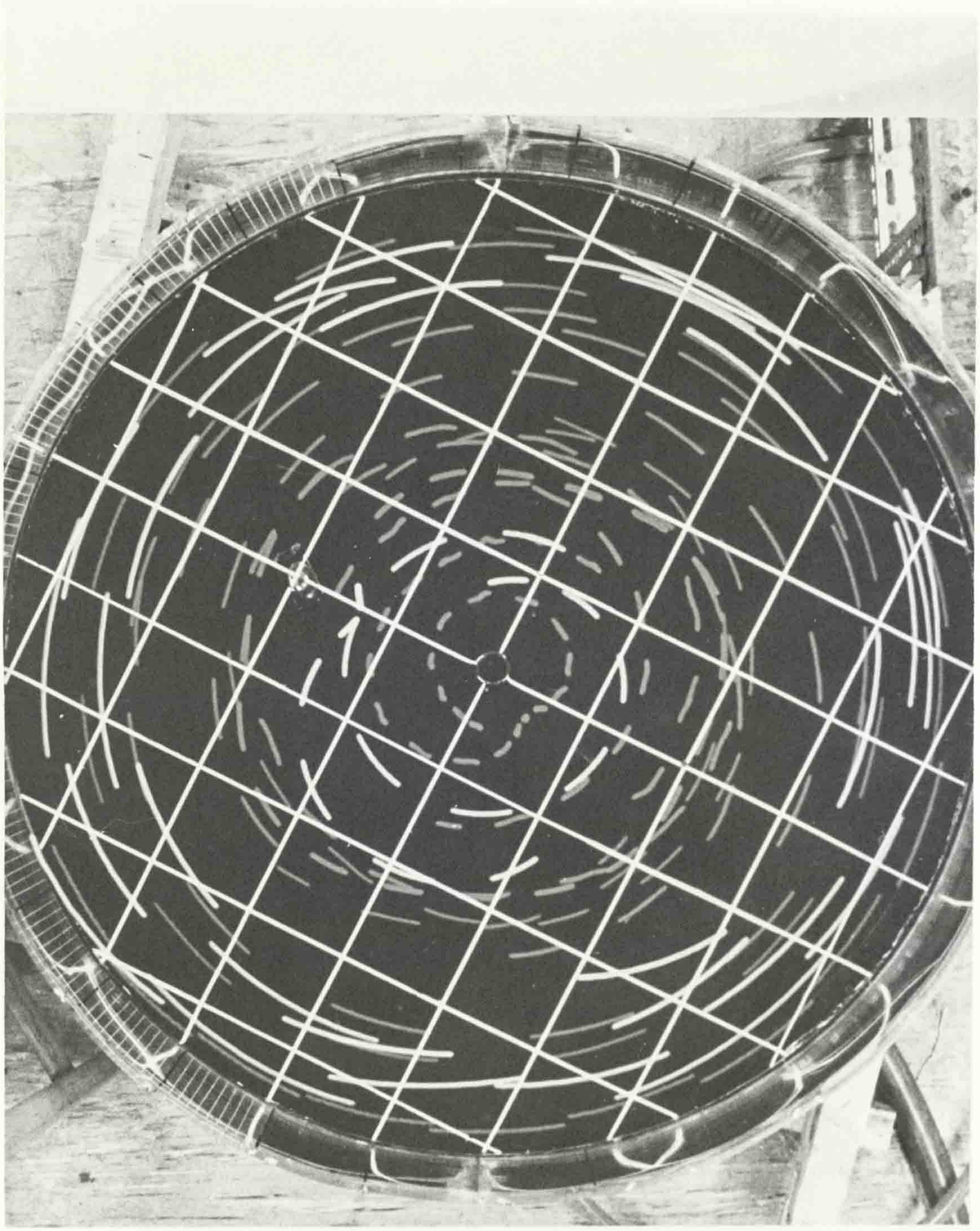

Fig. (6.50) Float tracks at upper (white) and lower (grey) layers of stratified reservoir, (Q_o = 19.66 cc/sec, ε = 8.9%, h_1 = 10.5 lapse time of 3 seconds).

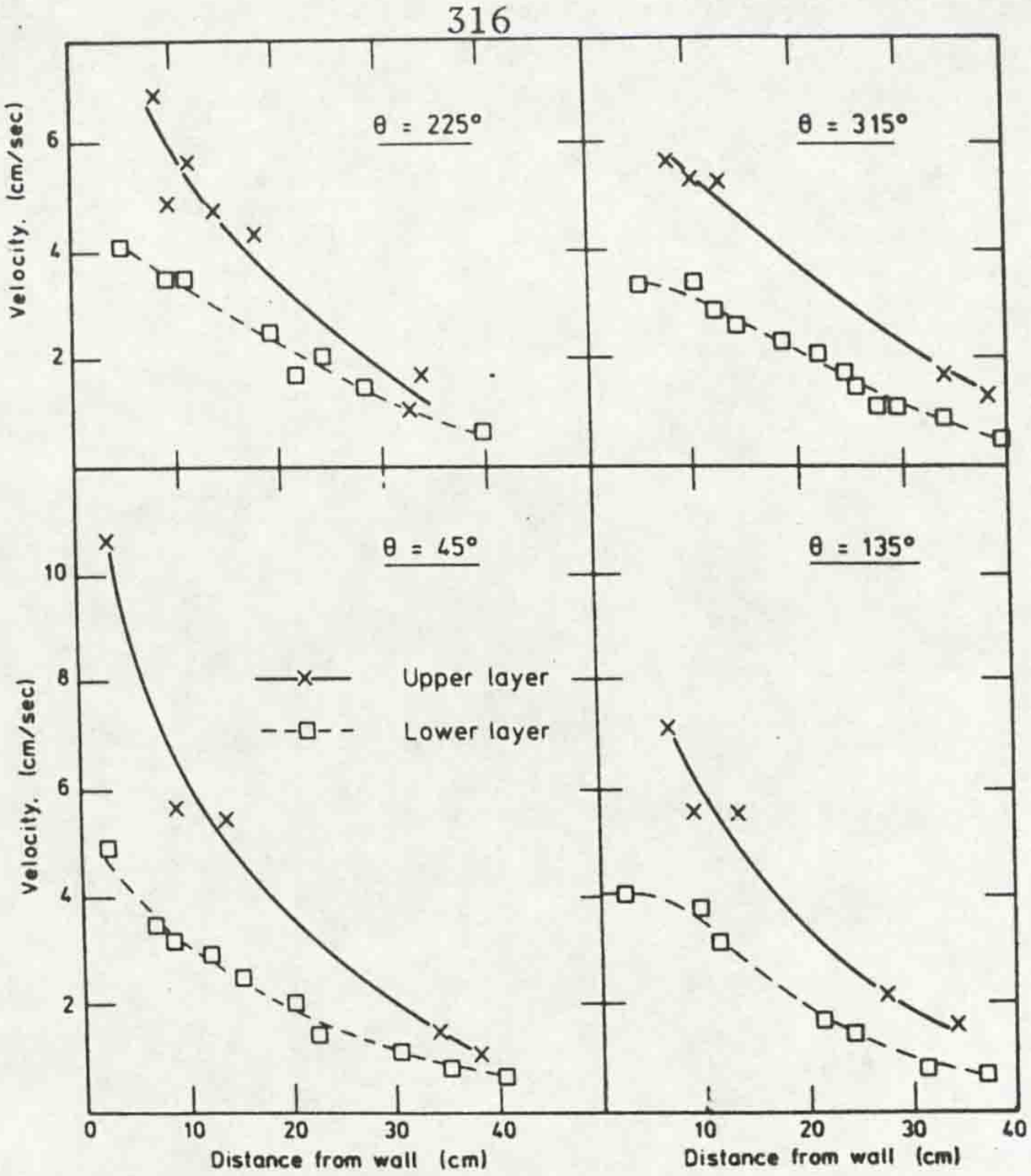

Fig. (6.51) Velocity distribution for upper and lower layers of stratified reservoir, (Q_o = 19.66 cc/sec, ε = 8.9%, h_1 = 10.5 cm).

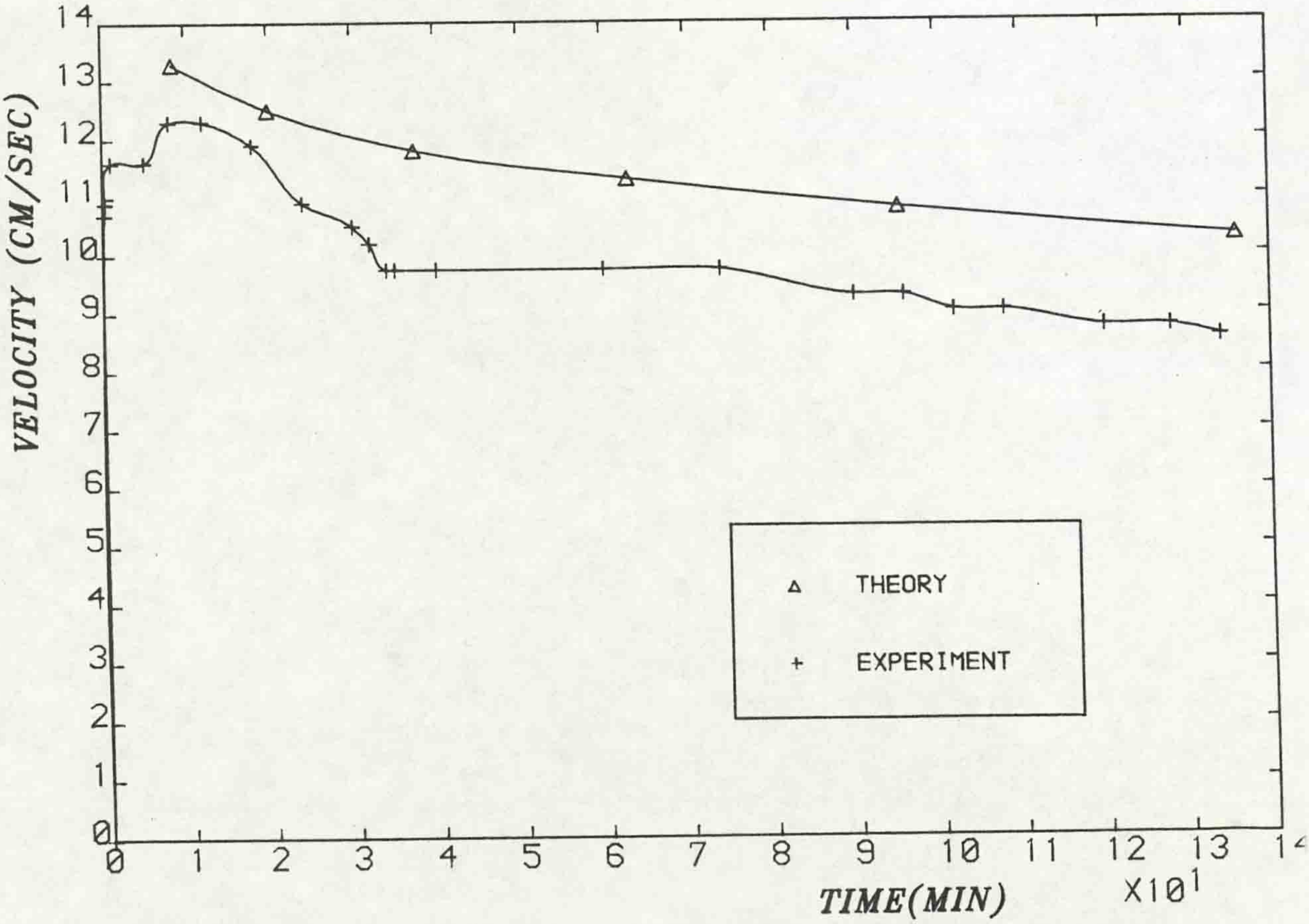

Fig. (6.52) Theoretical and experimental variation of velocity with time in a stratified reservoir at station 1, (Q_o = 12.383 cc/sec, ε = 2.2%).

Author		State of Flow	U_i/U_r
Keulegan	(1966)	Upper Flow	$\frac{u_i}{U_{max}} = 0.63$
椿・小松・下田	(1981)	" "	$u_i/\bar{U} = 0.35 - 0.6$
日野ほか	(1980)	" "	$u_i/\bar{U}_{max} = 0.38 \sim 0.62$
松永ほか	(1984)	" "	$u_i/U_* = 6.4$
Ippen, Harelman	(1951)	Lower Flow	$u_i/U_{max} = 0.6$
Georgiev Borislav	(1972)	" "	$u_i/U_{max} = 0.6$
Nakano et al.		" "	$u_i/\bar{U} = 0.5 - 0.8$ $u_i/U_* = 5.6 \sim 14$

Table (6.4)

Ratio of the Interfacial Velocity to the Upper (Lower) Velocity in Different Experiments (after Susumu Nakano et al 1985)

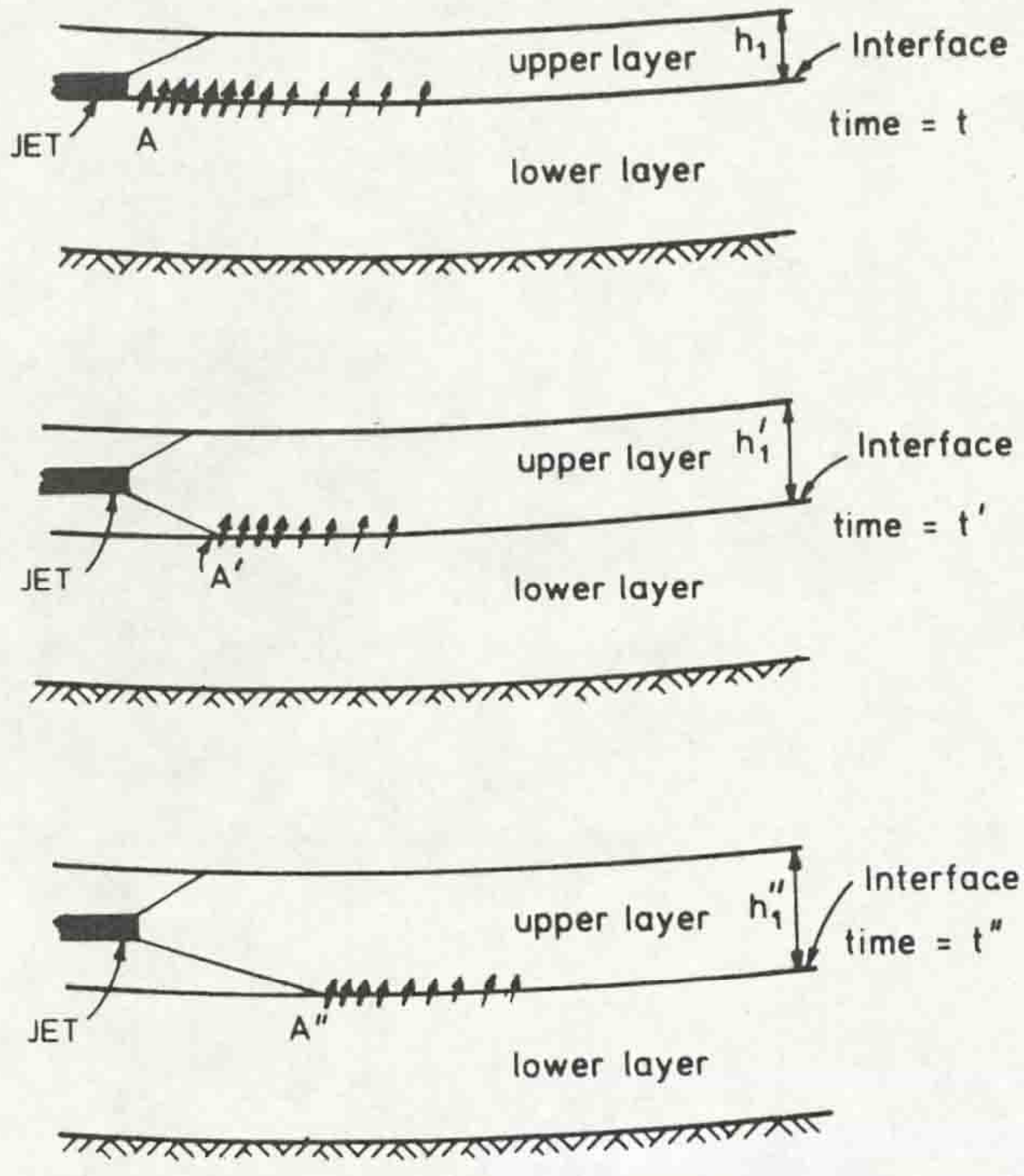

Fig. (6.53) Mechanism of mixing near the inlet.

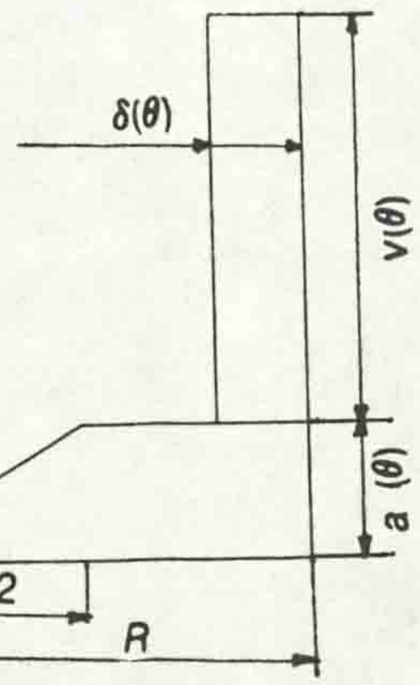

Fig. (6.54a)
Assumed azimuthal velocity profile.

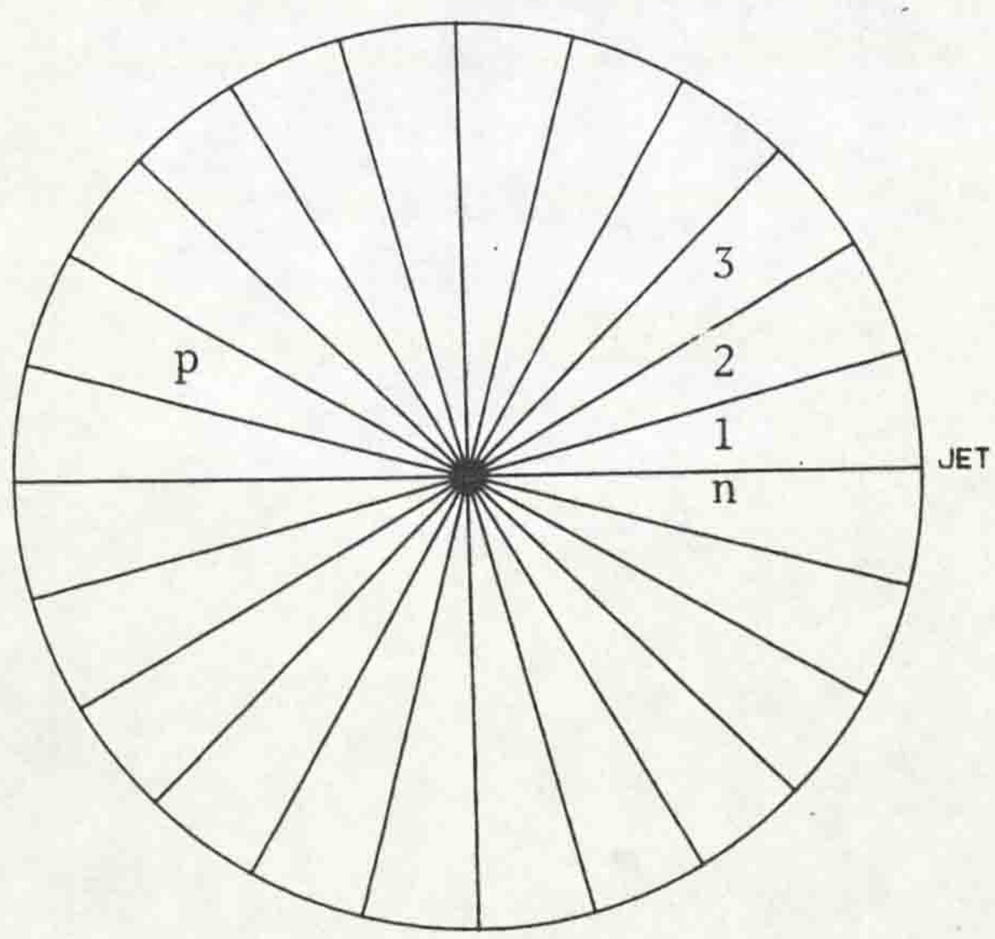

Fig. (6.54b) Discretisation of reservoir plan.

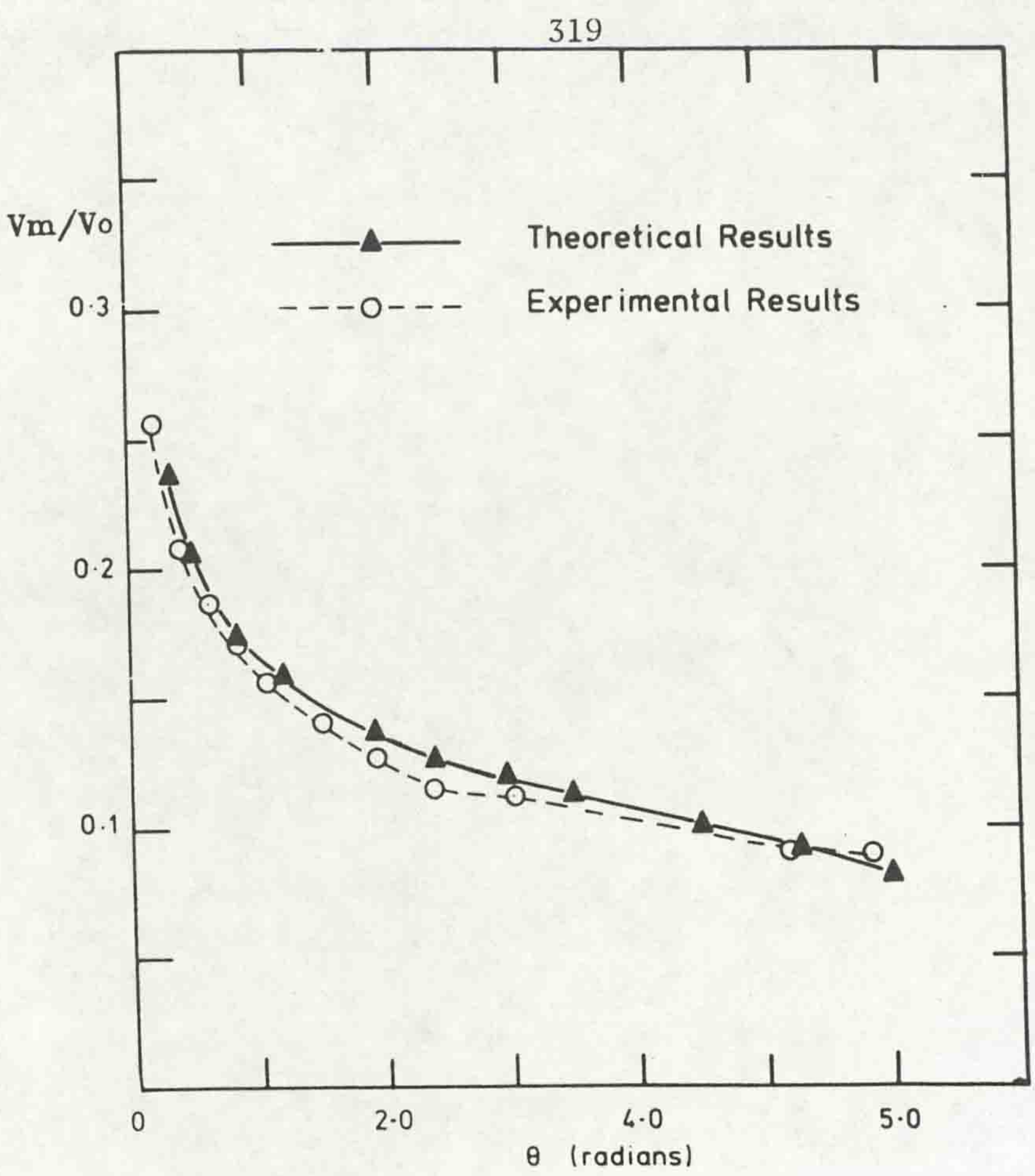

Fig. (6.55) Comparison between theoretical and experimental velocities near the wall, (Q_o = 19.66 cc/sec, ε = 9.1%, h_1 = 4.5 cm).

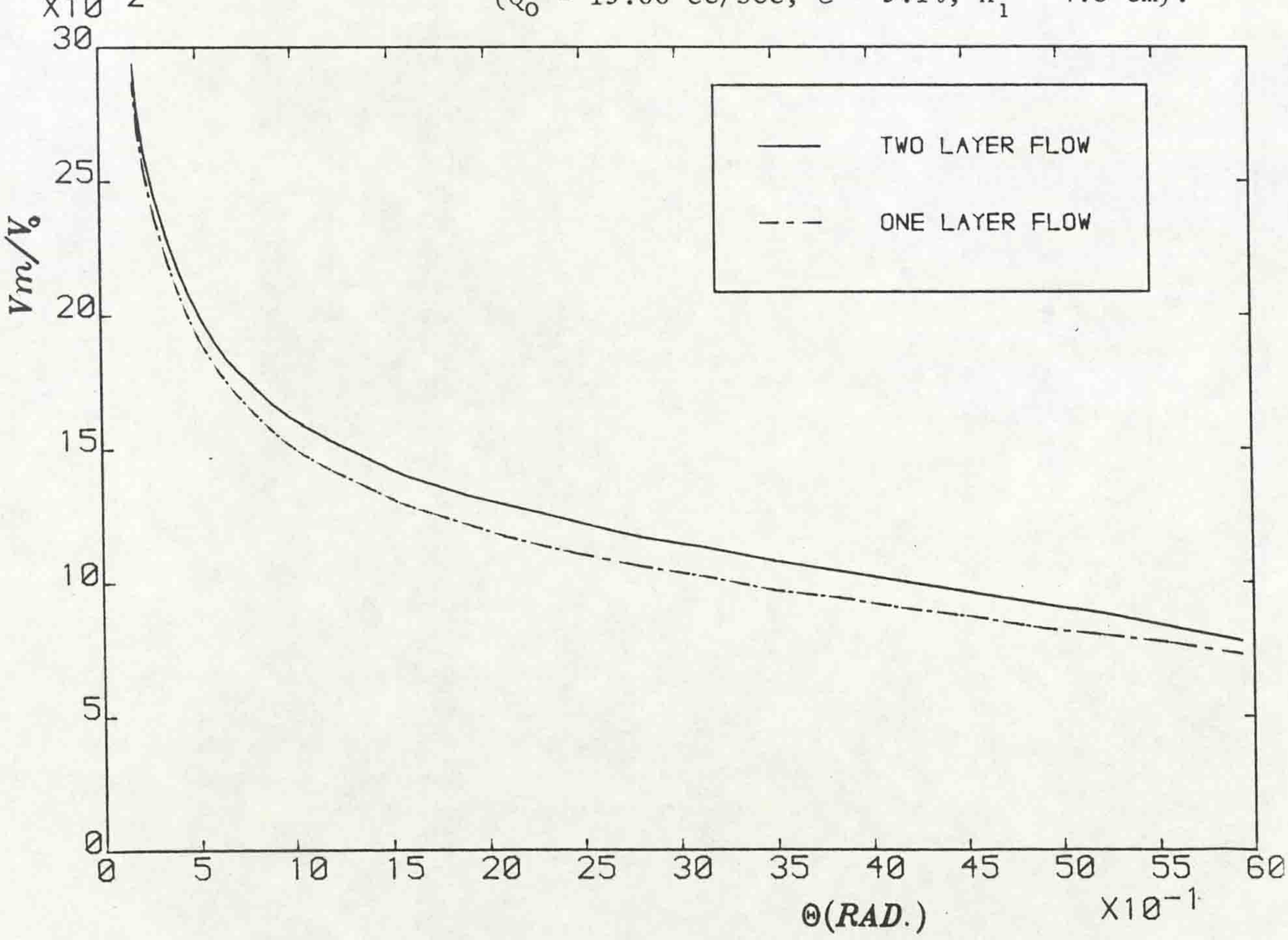

Fig. (6.56) Comparison between theoretical velocities for a homogeneous and stratified reservoir near the wall, (Q_o = 19.66 cc/sec, ε = 9.1%, h_1 = 4.5 cm).

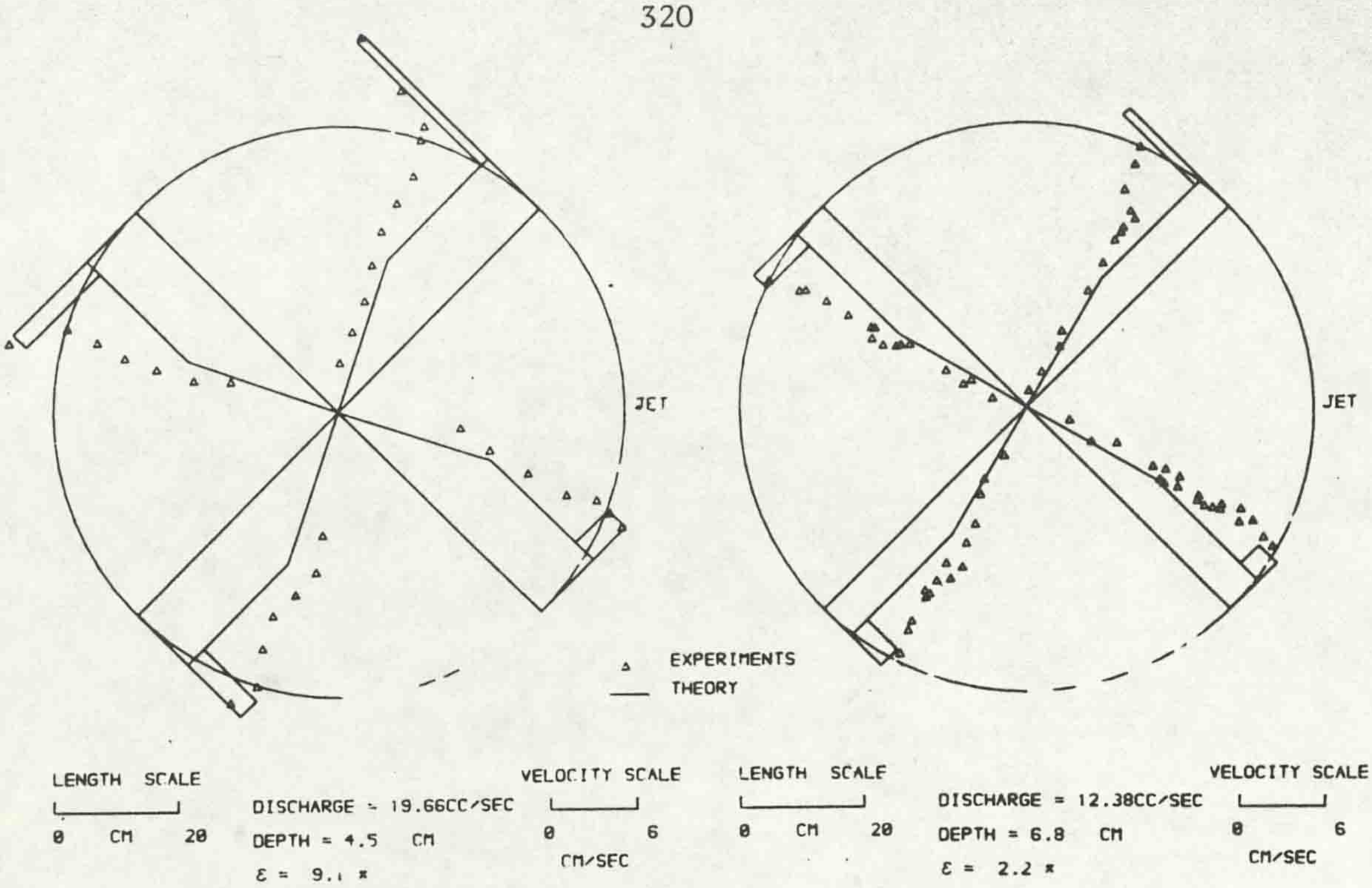

FIG. (6.57) COMPARISON BETWEEN THEORETICAL AND EXPERIMENTAL VELOCITIES FOR UPPER LAYER OF STRATIFIED RESERVOIR

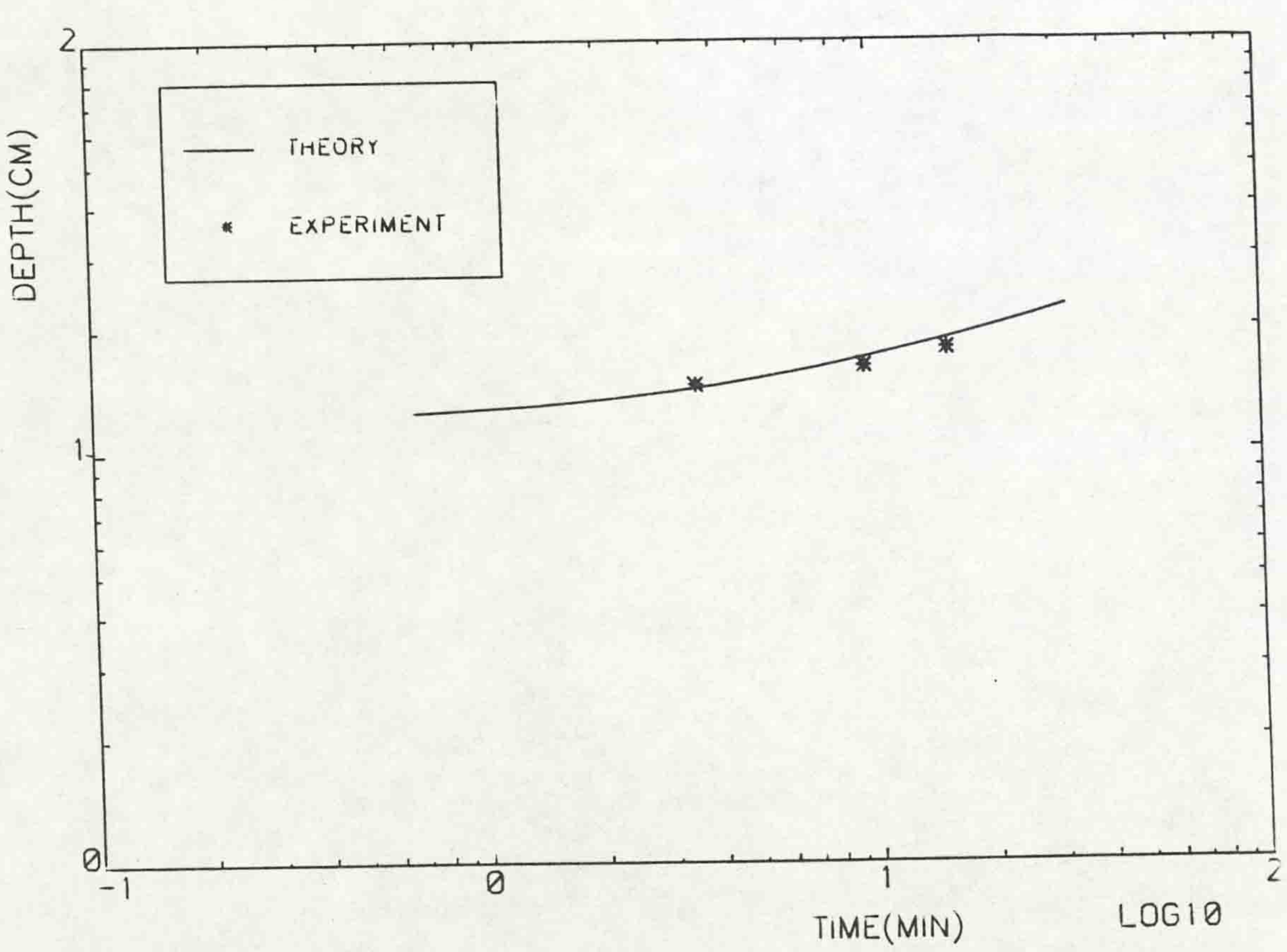

Fig. (6.58) Variation of depth of upper layer with time, (Q_o = 49.5 cc/sec, ε = 1.23%).

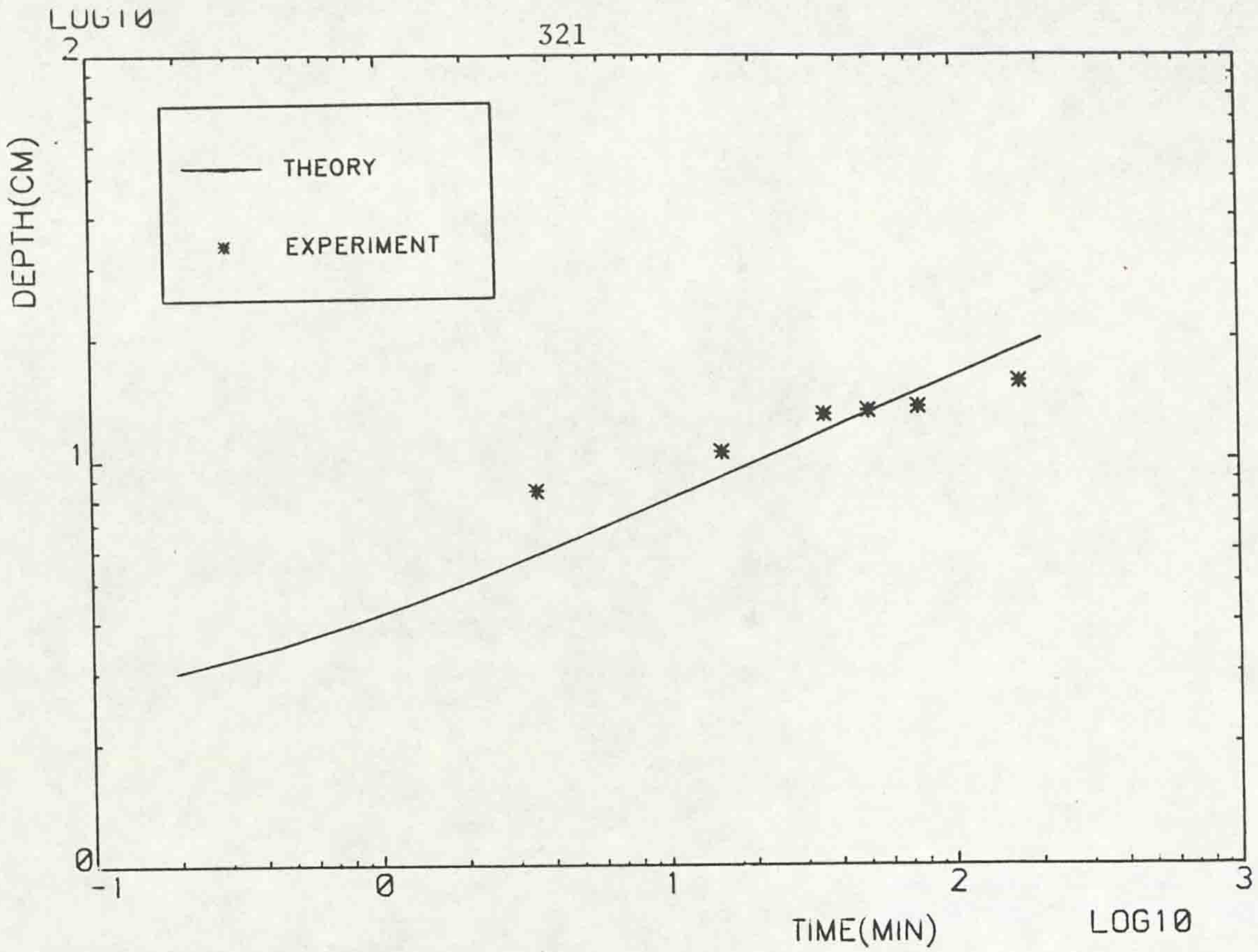

Fig. (6.59) Variation of depth of upper layer with time, (Q_o = 30.88 cc/sec, ε = 2%).

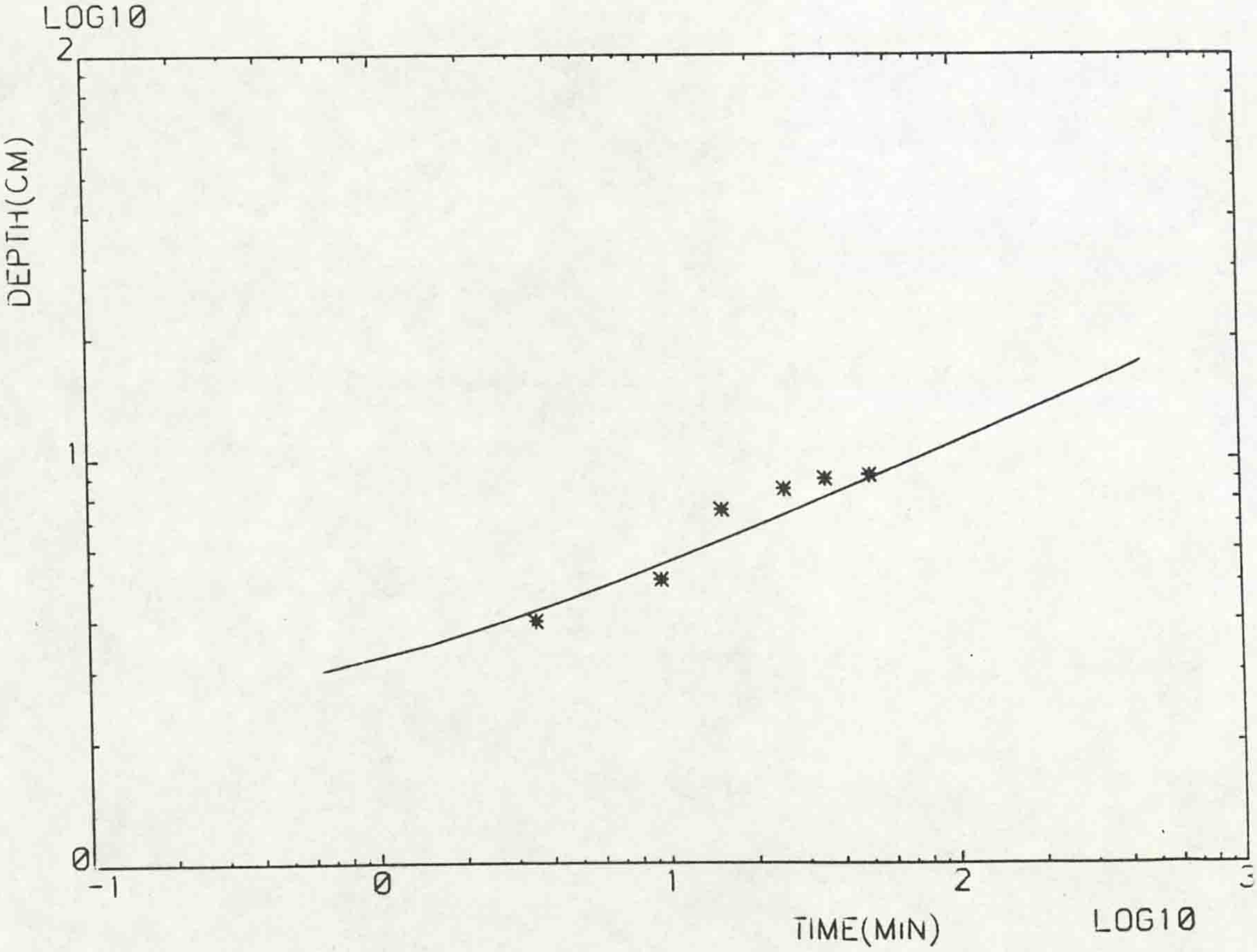

Fig. (6.60) Variation of depth of upper layer with time, (Q_o = 19.66 cc/sec, ε = 1.28%).

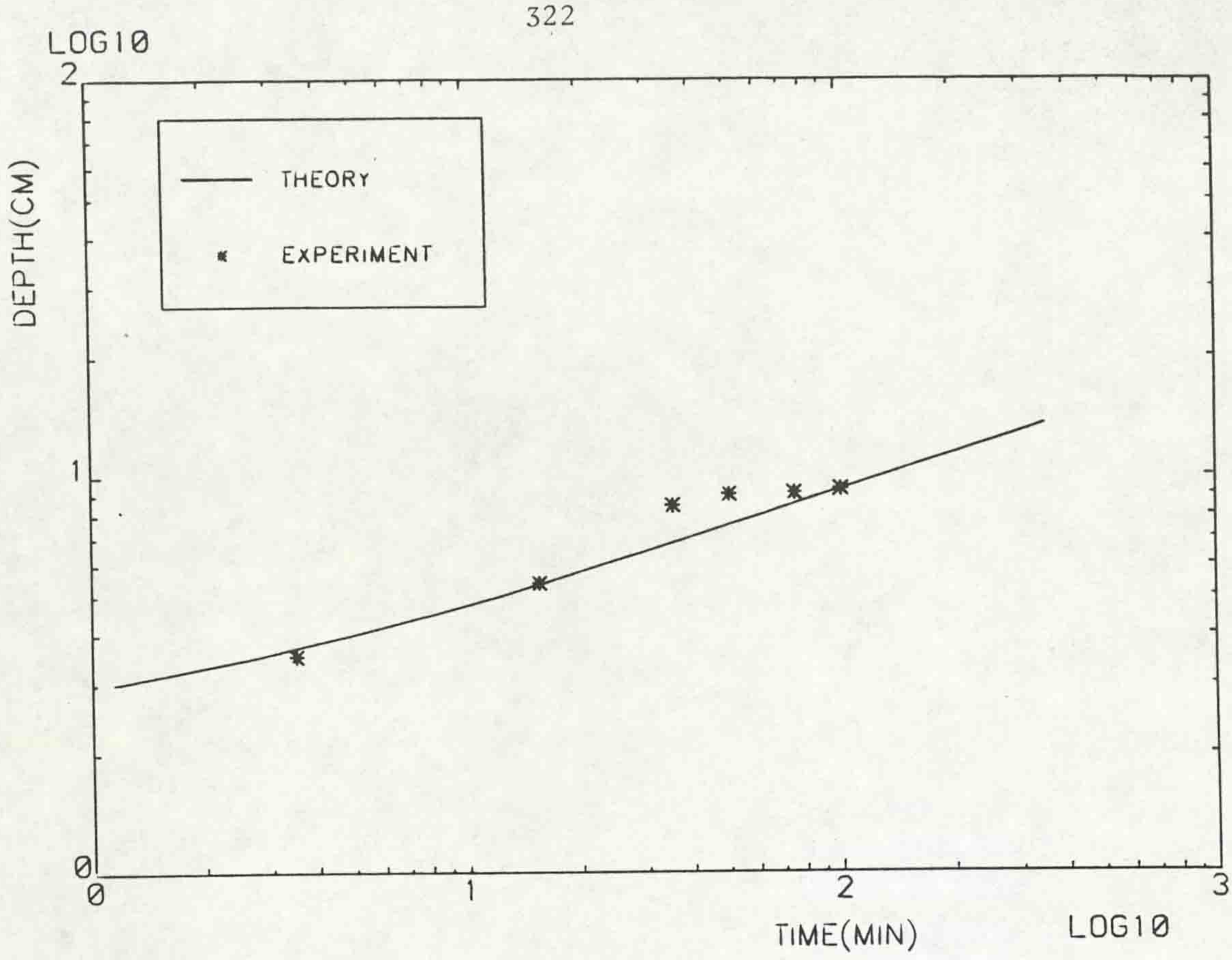

Fig. (6.61) Variation of depth of upper layer with time, (Q_o = 19.66 cc/sec, ε = 2.11%).

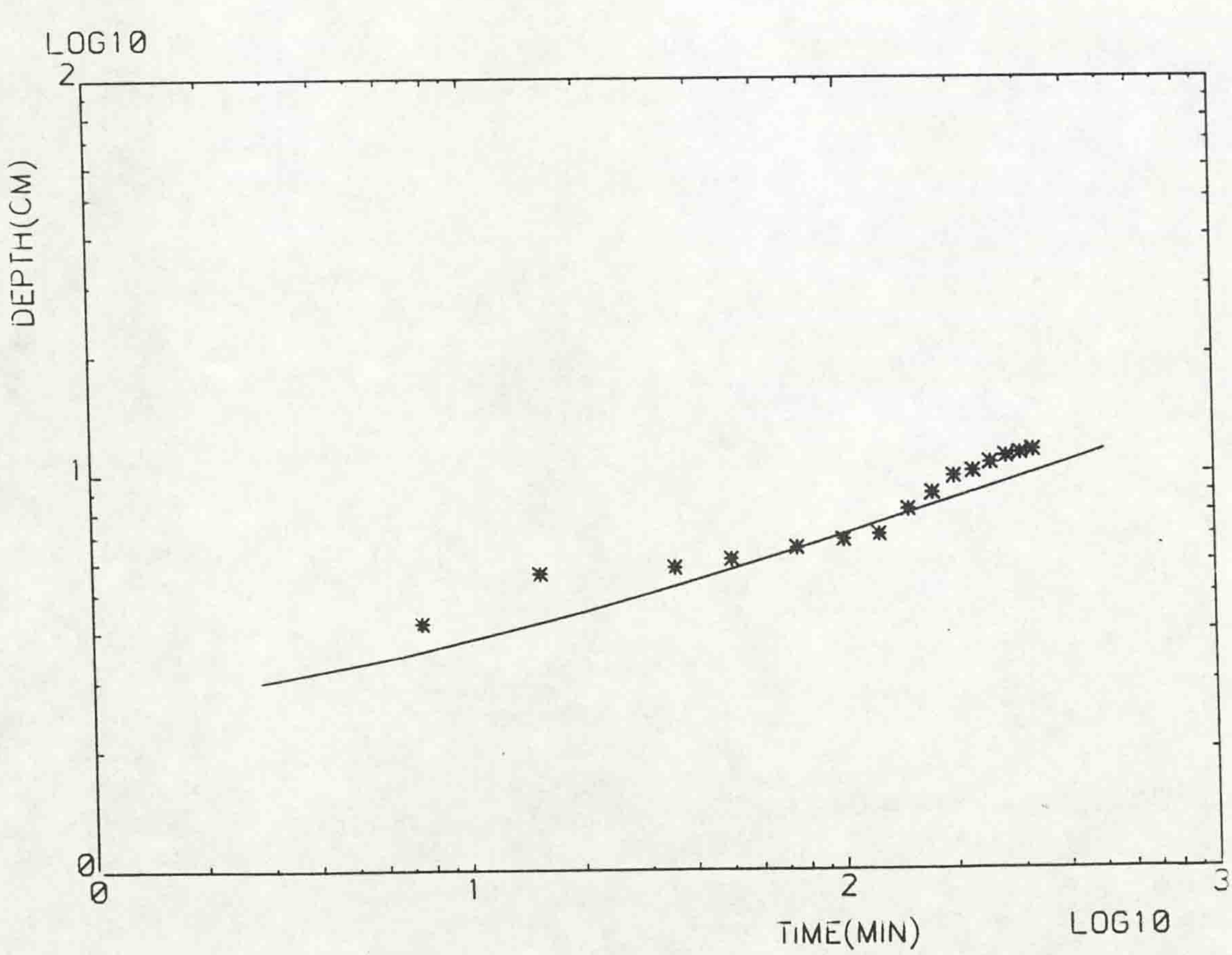

Fig. (6.62) Variation of depth of upper layer with time, (Q_o = 19.66 cc/sec, ε = 4.35%).

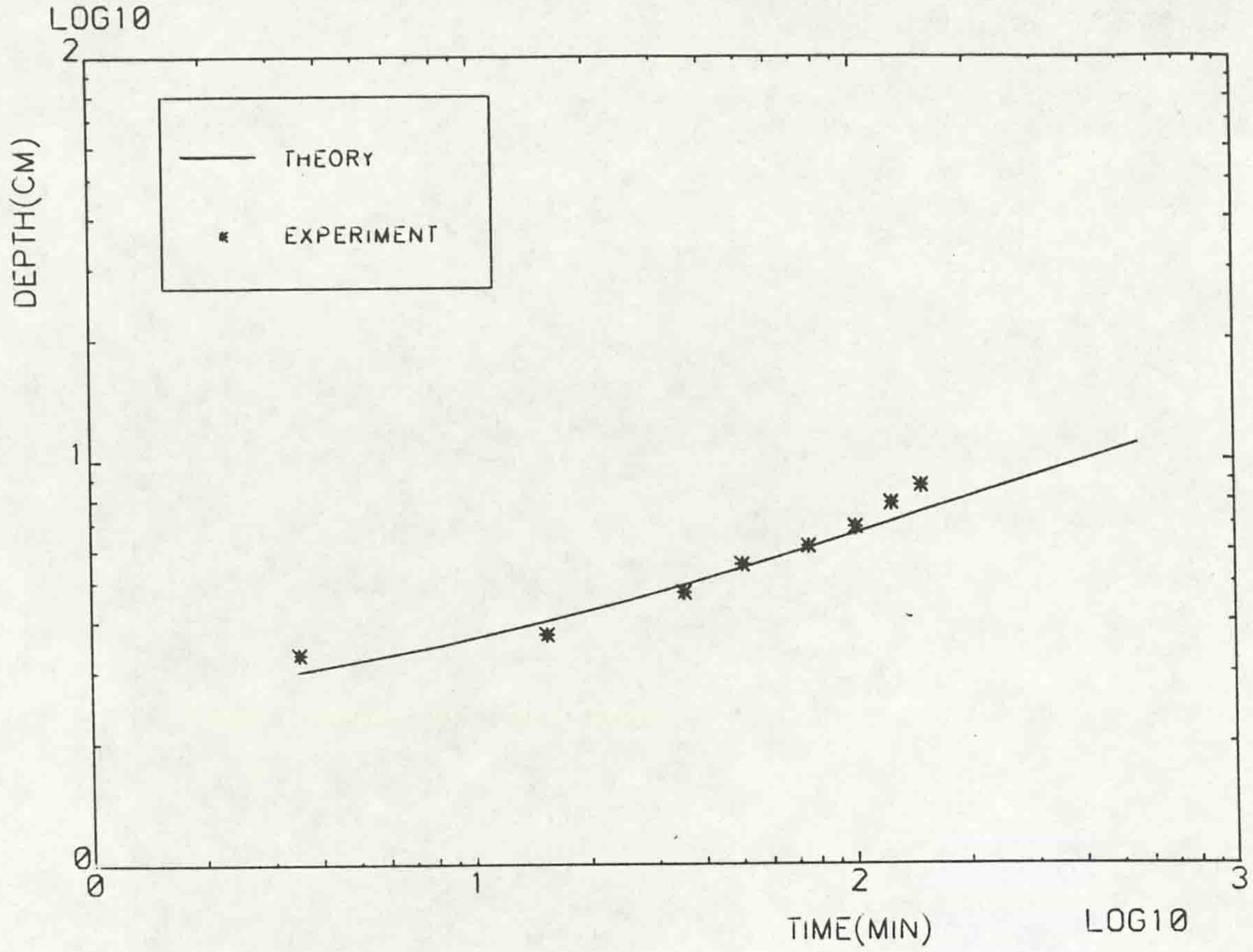

Fig. (6.63) Variation of depth of upper layer with time, (Q_o = 19.66 cc/sec, ε = 5.3%).

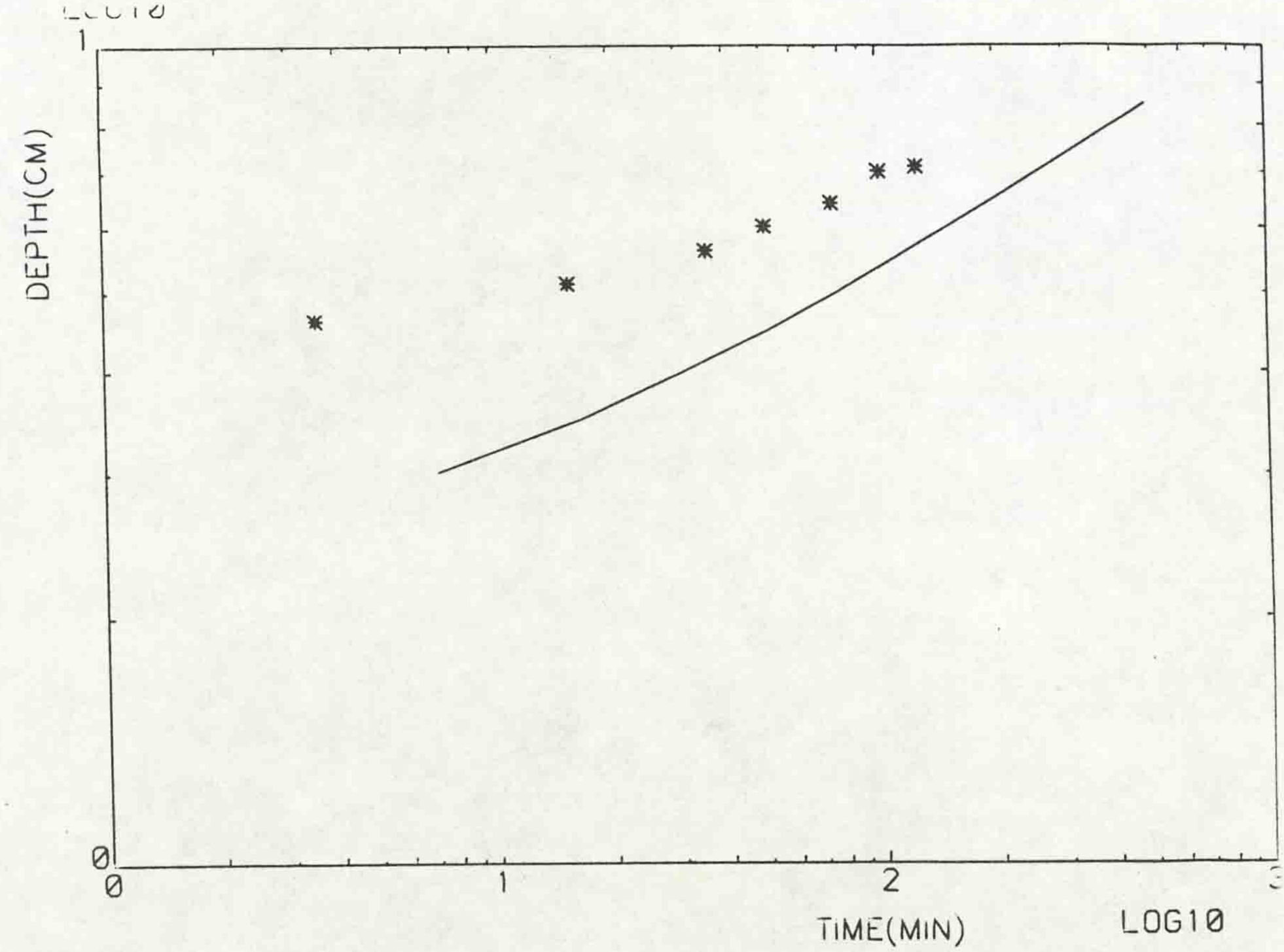

Fig. (6.64) Variation of depth of upper layer with time, (Q_o = 12.383 cc/sec, ε = 9.1%).

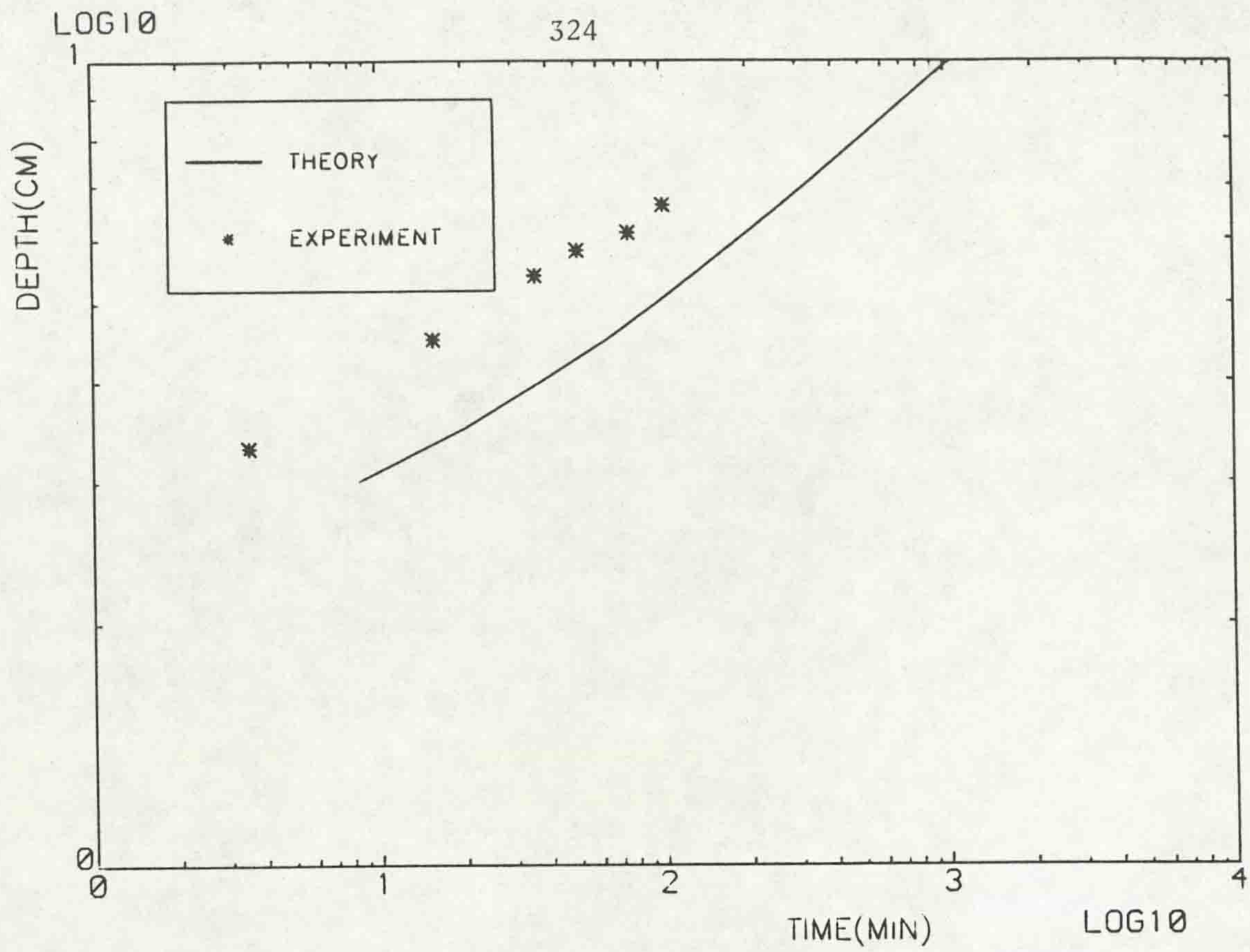

Fig. (6.65) Variation of depth of upper layer with time, (Q_o = 9.71 cc/sec, ε = 2.2%).

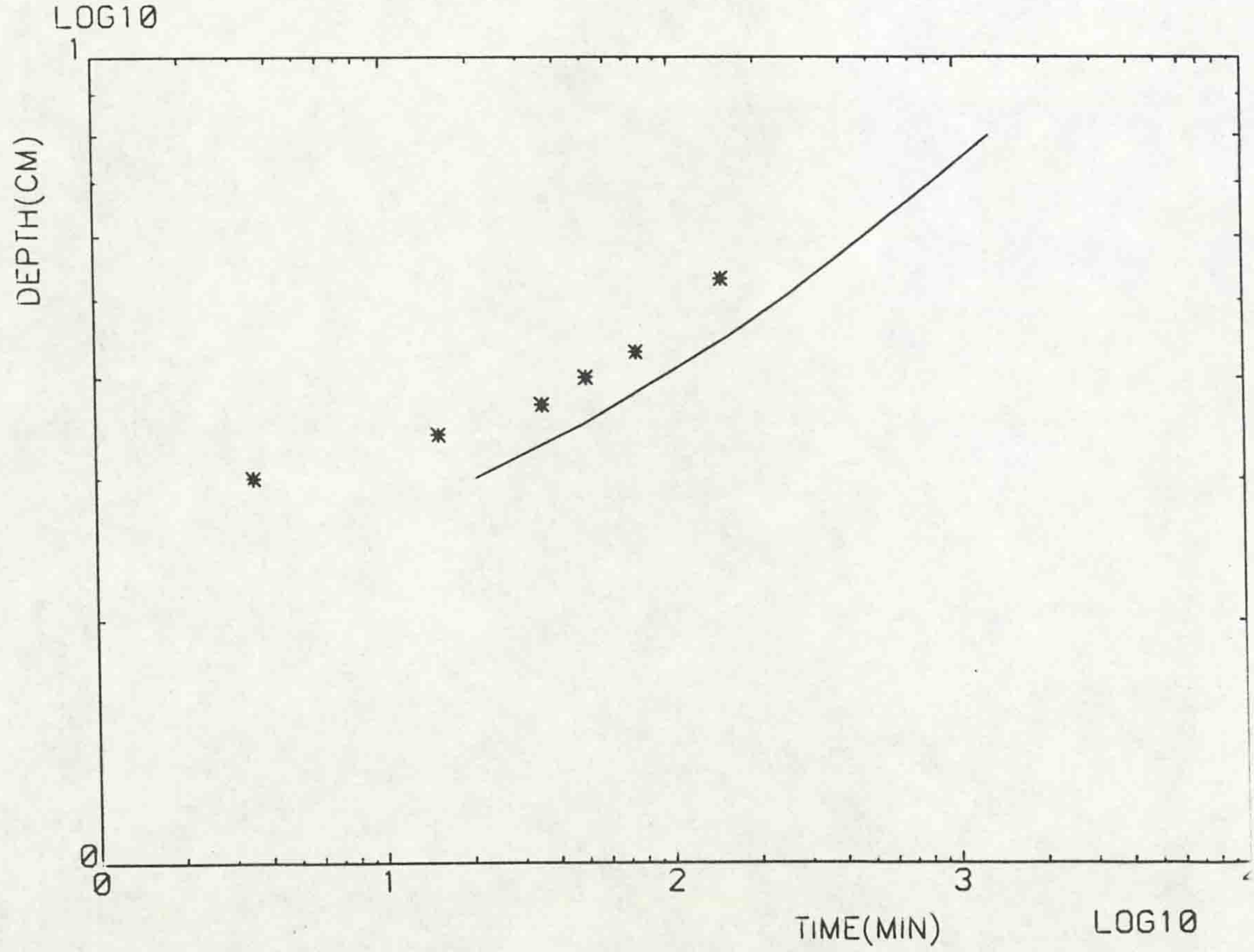

Fig. (6.66) Variation of depth of upper layer with time, (Q_o = 5.75 cc/sec, ε = 2.1%).

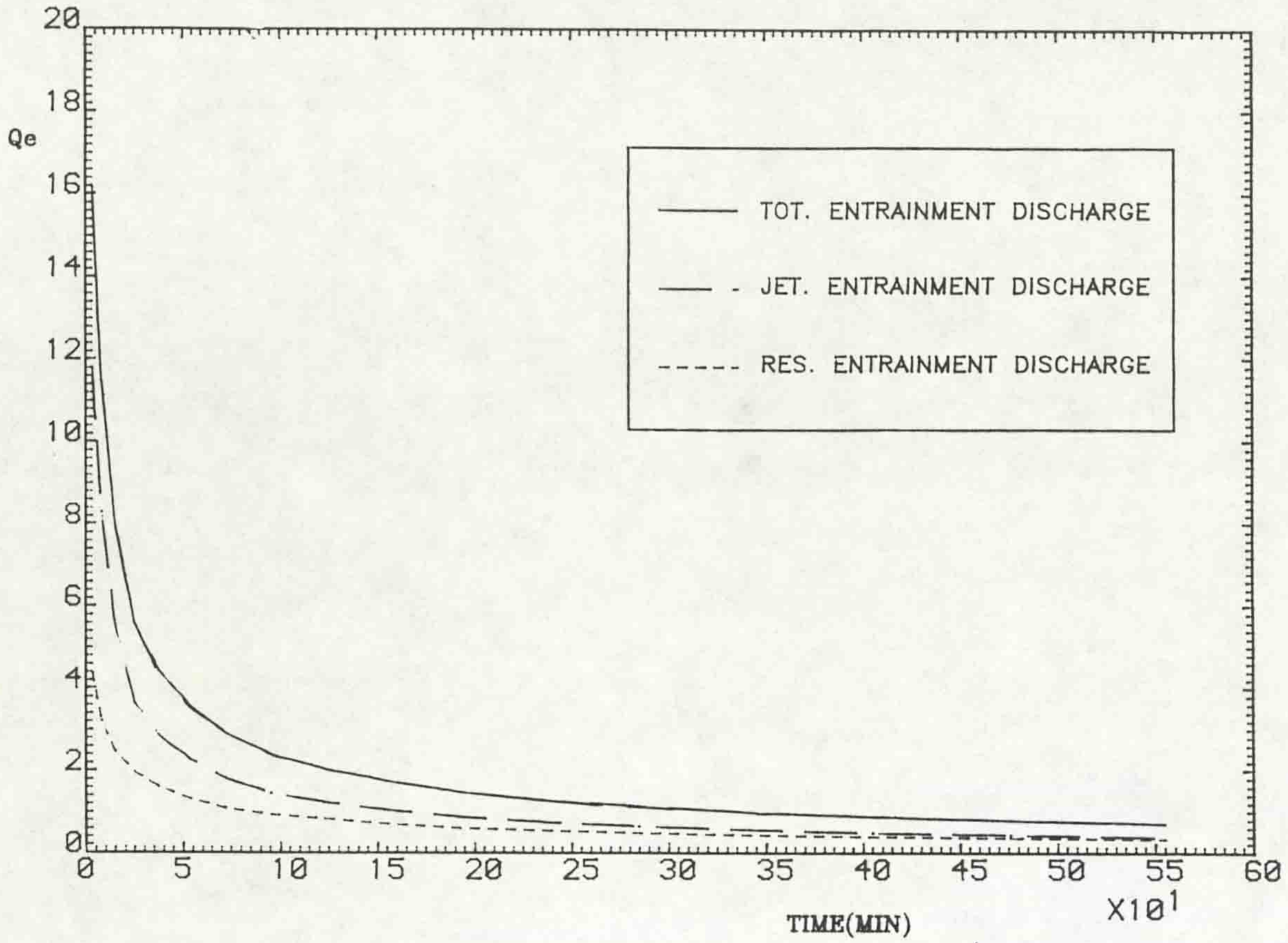

Fig. (6.67) Variation of theoretical entrainment discharge with time, (Q_o = 19.66 cc/sec, ε = 5.3%).

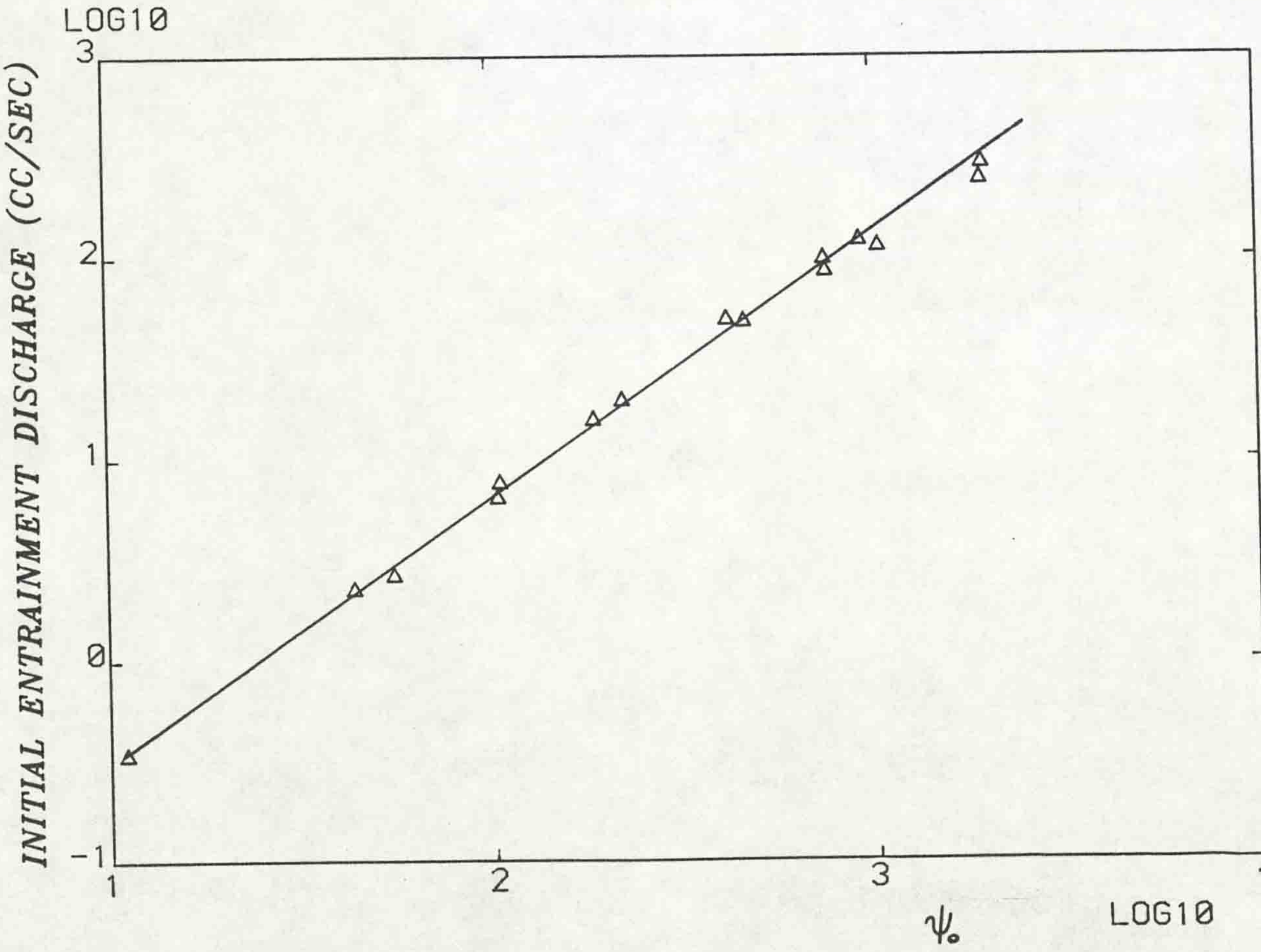

Fig. (6.68) Variation of initial entrainment discharge with ψ_o.

No.	Mark	Q_0 cc/sec	V_0 cm/sec	ϵ %	$Q_e(t_0)$ cc/sec	ψ_0
1	A	30.88	154.4	1.91	298.5	1964.43
2	B	19.66	98.33	0.5	248.2	1938.3
3	C	28.	140.	3.	124.4	932.39
4	D	16.	80.	0.5	116.	1043.8
5	E	30.88	154.4	5.	100.5	750.4
6	F	19.66	98.33	1.28	87.38	757.1
7	G	30.88	154.4	9.	50.54	416.9
8	H	19.66	98.33	2.1	49.28	461.5
9	I	19.66	98.33	4.395	20.11	220.5
10	J	19.66	98.33	5.24	16.16	184.96
11	K	19.66	98.33	9.21	7.908	105.3
12	L	12.38	61.9	2.33	6.646	103.8
13	M	9.71	48.55	2.112	2.72	55.2
14	N	16.	80	12.	2.32	43.5
15	O	12.	60	20.	0.35	11.01

Table (6.5) Details of Numerical Experiments

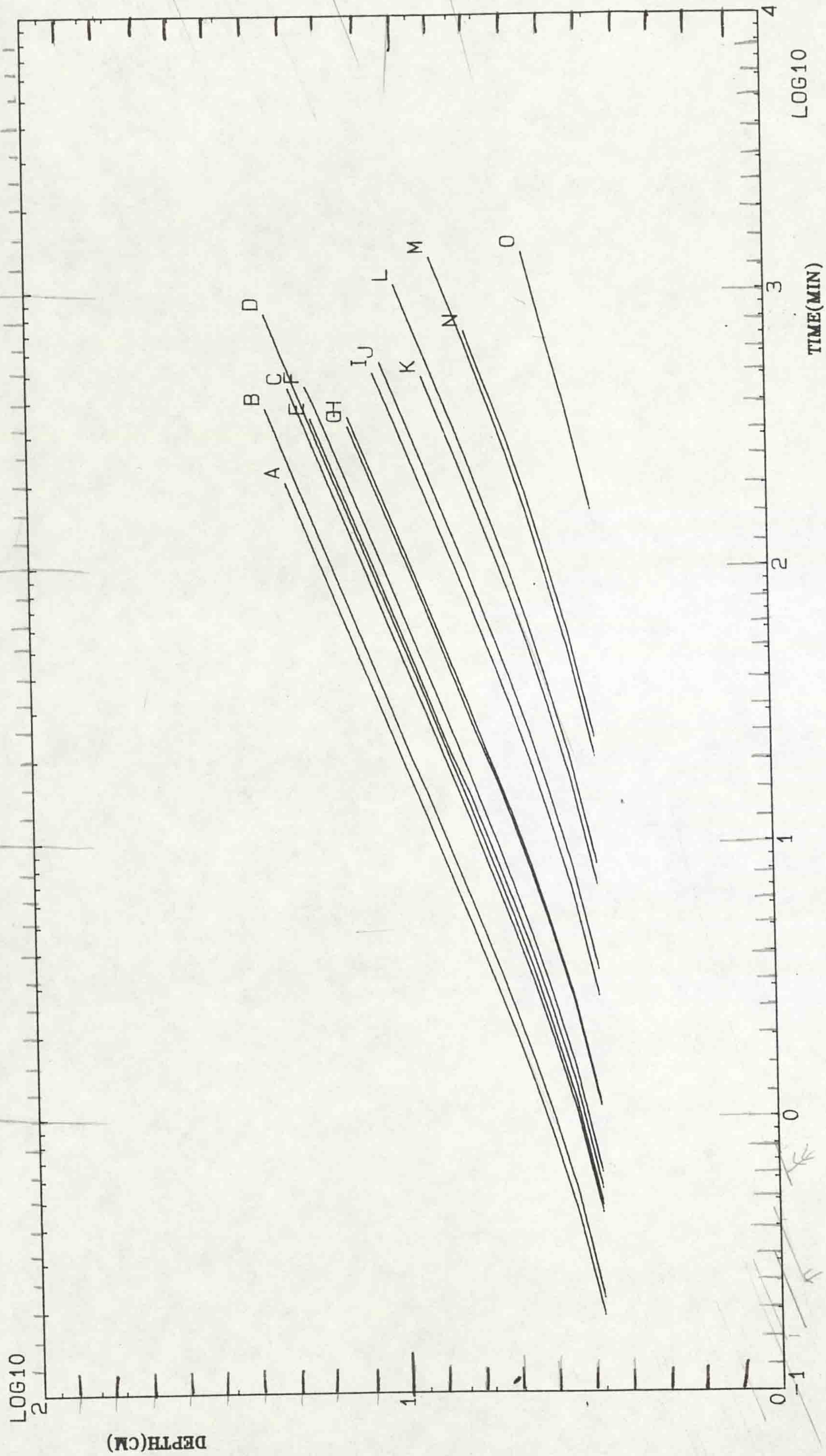

Fig. (6.69) Variation of depth of upper layer with time for the data of Table (6.5).

REFERENCES

1. Abbott et al (1981) "Numerical Modelling of Free-surface Flows that are Two-Dimensional in Plan", in "Transport Models for Inland and Coastal Waters", Fischer H.B. (ed.), Academic Press.

2. Abbott, M.B., Larson, J. and Jianhua, T. (1985) "Modelling Circulation in Depth Averaged Flows", Part I : The Accumulation of the Evidence", J. of Hyd. Research, Vol. 23, No. 4.

3. Abbott, M.B. and Rasmussen, C.H. (1977) "On the Numerical Modelling of Rapid Expansions and Contractions in Models that are Two-Dimensional in Plan", Paper A104, 17th Congress of the Int. Assoc. for Hydraulic Res., Baden-Baden, Germany, Vol. 2, pp. 229-237.

4. Abramovich, G.N. (1963) "The Theory of Turbulent Jets", English Translation published by M.I.T. Press, Massachusetts.

5. Ali, K.H.M., Hedges, T.S. and Whittington, R.B. (1978) "A Scale-Model Investigation of the Circulation in Reservoirs", Proc. ICE, Pt. 2, Vol. 65, March, pp. 129-61.

6. Ali, K.H.M. and Pateman, D.R. (1981) "Prediction of the Circulation in Reservoirs", Proc. Instn. Civ. Engrs., Part 2, 71, June, pp. 427-461.

7. Ali, K.H.M. and Pateman, D.R. (1982) "Reservoir Circulation Induced by Turbulent Jets", 4th European Conf. on Mixing, Paper C3, pp. 81-107.

8. Ali, K.H.M. and Whittington, R.B. (1979) "Liquid-Liquid Mixing in Tanks and Reservoirs", Third Conference on Mixing, York, England, pp. 37-60.

9. Ashford, G. (1979) "An Experimental Study of Jet Forced Circulation Patterns", M.Sc. Thesis, Univ. of London.

10. Ashida, K. and Egashira (1977) "Hydraulic Characteristics of Thermocline in Reservoirs", Proc. 17th Congress of I.A.H.R., Baden-Baden, Vol. 2, Paper A80, pp. 33.

11. Bata, G.C. and Knezevich, B. (1953) "Some Observations on Density Currents in the Laboratory and in the Field", Proc. Minn. Intern. Hydr. Conv., pp. 387-400.

12. Batchelor, G.K. (1951) "Note on a Class of Solutions of the Navier-Stokes Equations Representing Steady Rotationally-Symmetric Flow", Quart J. Mech. Appl. Math., 4, pp. 29.

13. Bodonyi, R.J. (1975) "On Rotationally Symmetric Flow Above an Infinite Rotating Disk', J. Fluid Mech., 67, pp. 65.

14. Boedwadt, U.T. (1940) "Die Drehströmung Über Festem Grund", ZAMM 20, 241-253.

15. Bradbury, L.J.S. (1965) "The Structure of a Self-Preserving Turbulent Jet", J. Fluid Mech., Vol. 23, pp. 31-64.

16. Bradbury, L.S. and Reily (1967) "The Spread of a Turbulent Plane Jet into a Parallel Moving Air Stream", J. Fluid Mech., Vol. 27, pp. 381-394.

17. Brush, L.M. and Rutgers, J.R. (1970) "Artificial Mixing of Stratified Fluids Formed by Salt and Heat in a Laboratory Reservoir", The State Univ., New Brunswick, N.J. Water Resources Research Inst.

18. Chu, V.H. and Vanvari, M.R. (1976) "Experimental Study of Turbulent Stratified Shearing Flow", Proc. ASCE, J. Hydraulic Division, ASCE, Vol. 102, No. HY6, pp. 691.

19. Cochran, W.G. (1934) "The Flow Due to a Rotating Disk", Proc. Cambridge Phil. Soc., 30, pp. 365.

20. Cooley, P. and Harris, S.L. (1954) "The Prevention of Stratification in Reservoirs", J. of Inst. of Water Engineers, Vol. 8, pp. 517-53.

21. Crapper, P.F. and Linden, P.F. (1974) "The Structures of Turbulent Density Interfaces", J. Fluid Mech., Vol. 65, pt. 1, pp. 45-63.

22. Cromwell, T. (1960) "Pycnoclines Created by Mixing in an Aquarium Tank", J. Mar. Res. 18, pp. 73-82.

23. Csanady, G.T. (1978) "Turbulent Interface Layers", J. Geophysical Research, Vol. 83, No. C5, pp. 2329-2342.

24. Delft Hydraulic Laboratory (1974) "Momentum and Mass Transfer in Stratified Flows", Report on literature study R880, Delft, Netherlands.

25. Derby, R.L. (1956) "Chlorination of Deep Reservoirs for Taste and Odour Control", J. of AWWA, Vol. 48, pp. 775.

26. Dermissis, V. and Partheniades, E. (1984) "Interfacial Resistance in Stratified Flows", ASCE, J. of Waterway, Port, Coastal and Ocean Engineering, Vol. 110, No. 2, pp. 231-250.

27. Elder, J.W. (1959) "The Dispersion of marked Fluid in Turbulent Shear Flow", J. Fluid Mech., Vol. 5, pp. 544-60.

28. Ellison, T.H. and Turner, J.S. (1959) "Turbulent Entrainment in Stratified Flows', J. Fluid Mech. 6, pp. 423-48.

29. Engelund, F. (1974) "Flow and Bed Topography in Channel Bends", Proc. ASCE., J. Hydr. Div., 100, HY11.

30. Evan, D.J. (1969) 'The Rotationally Symmetric Flow of a Viscous Fluid in the Presence of an Infinite Rotating Disc with Uniform Suction", Quart. J. Mech. Appl. Math., 22, pp. 467.

31. Falconer, R.A. (1977) "Mathematical Modelling of Jet-Forced Circulation in Reservoirs and Harbours", Ph.D. Thesis, Imperial College, Univ. of London.

32. Flokstra, C. (1976) "Generation of Two-Dimensional and Horizontal Secondary Currents", Report No. S163, Part II, Delft Hydraulic Laboratory, Delft, The Netherlands.

33. Flokstra, C. (1977) "The Closure Problem for Depth Averaged Two-Dimensional Flow", Paper A106, 17th International Association for Hydraulic Research Congress, Baden-Baden, Germany, pp. 247-256.

34. Georgiev, B. (1972) "Some Experimental Investigation on Turbulent Characteristics of Stratified Flows", IAHR Symposium on Stratified Flows, Novosibrisk.

35. Gill, A.E., Smith, J.M., Cleaver, R.P., Hide, R. and Jonas, P.R. (1979) "The Vortex Created by Mass Transfer Between Layers of a Rotating Fluid", Geophys. Astrophys, Fluid Dynamics Vol. 12, pp. 195-220.

36. Goldstein, S. (1931) "On the Stability of Superposed Streams of Fluids of Different Densities", Proc. Roy. Soc. A132, pp. 524-48.

37. Greenspan (1969) "The Theory of Rotating Fluids", Camb. Univ. Press.

38. Guitton, D.E. (1964) "Two-Dimensional Turbulent Wall Jets Over Curved Surfaces". Rep. Mechanical Engineering Research Laboratories, McGill University.

39. Hansen, W. (1962) "Hydrodynamic Methods Applied to Oceanographic Problems", Proceedings of the Symposium on Mathematical-Hydrodynamical Methods of Physical Oceanography, Institute für Meereskunde der Universität Hamburg, Hamburg, West Germany, pp. 25-34.

40. Harleman, D.R.F. (1961) "Stratified Flow", Sect. 26, 'Hand-Book of Fluid Dynamics', Streeter, V. (ed.), McGraw-Hill.

41. Harleman, D.R.F. and Stolzenbach, K.D. (1972) "Fluid Mechanics of Heat Disposal from Power Generation", Annual Review of fluid Mechanics, Vol. 4, 1972, pp. 7-32.

42. Hayashi, T. and Shuto, N. (1967) "Diffusion of Warm Water Jets Discharged Horizontally at the Water Surface", Proc. IAHR Congress, Fort Colins, Vol. 4, pp. 47-59.

43. Hazel, P. (1972) "Numerical Studies of the Stability of Inviscid Stratified Shear Flows", J. Fluid Mech. 51, pp. 39-61.

44. Henderson, F.M. (1966) "Open Channel Flow", McMillan Company, New York.

45. Hino, M. and Nguyen, S.H. (1983) "Velocity Distribution, Interfacial Friction and Entrainment in Two-Layered Stratified Flows", J. Hydroscience and Hydraulic Engineering, Vol. 1, No. 1, pp. 9-36.

46. Hutchinson, G.E. (1957) "A Treatise on Limnology", Vol. 1, John Wiley and Sons, New York.

47. Imberger, J. (1980) "Selective Withdrawal: A Review", Strafitied Flows, Second IAHR Symposium, Trondheim, Vol. 1, pp. 381-400.

48. Ippen, C.M. and Harleman, D.R.F. (1952) "Steady-State Characteristics of Subsurface Flow", Nat. Bur. Standards (U.S.) Circ., S21, pp. 29-93.

49. Irwin, W.H., Symons, J.M., and Robeck, G.G. (1966) "Impoundment Destratification by Mechanical Pumping", ASCE, J. of the Sanitary Engineering Div., Vol. 92, No. SA6.

50. Iwasaki, T., Kishida, S. and Tomoika, R. (1962) "Mixing of Density of a Two-Layered Flow", Proc. 17th Annual Meeting, JSCE, Part II, pp. 129-132 (in Japanese).

51. Jen, Y., Wiegel, R.L. and Mobarek, I. (1966) "Surface Discharge of Horizontal Warm-Water Jet", ASCE, J. of Power Division, Proc. Paper 4801, Vol. 92, PO2, pp. 1-30.

52. Johnson, B.H. (1980) "VAHM A Vertically Hydrodynamic Model using Boundary-Fitted Coordinates", MPHL-80, 3, U.S. Army Engineer Waterways Experiment Station, Vicksburg, Miss.

53. Kaneko, Y. (1966) "An Example of the Interfacial Drag Coefficient of Two-Layered Flow", Proc. 16th Japanese Conf. on Coastal Eng., JSCE, 263-267 (in Japanese).

54. Kanta, L.H., Phillips, O.M. and Azad, R.S. (1977) 'On Turbulent Entrainment at a Stable Density Interface", J. Fluid Mech., 79, pp. 753-68.

55. Kato, H. and Phillips, O.M. (1969) "On the Penetration of a Turbulent Layer into Stratified Fluid", J. Fluid Mech. 37, pp. 643-665.

56. Keulegan, G.H. (1966) "The Mechanism of an Arrested Saline Wedge, in Estuary and Coastaline Hydrodynamics", Ippen, A.T. (ed.), McGraw-Hill, pp. 546-576.

57. Keulegan, G.H. (1949) "Interfacial Instabilities and Mixing in Stratified Flows", J. Res. Nat. Bur. Standard, 43, pp. 487-500.

58. Keulegan, G.H. (1944) "Laminar Flow at the Interface of Two Liquids", J. of Research of the National Bureau of Standards, Vol. 32, June 1944, pp. 303.

59. Kobayashi, R. and Fujisawa, N. (1983) "Turbulence Measurements in Wall Jets Along Strongly Concave Surfaces", Acta Mechania, 47 : pp. 39-52.

60. Koh, R.C.Y. (1971a) "On Buoyant Jets", Proc. 14th I.A.H.R., Vol. 1, pp. A18-1-A18-12.

61. Koh, R.C.Y. (1971b) "Two-Dimensional Surface Warm Jet", ASCE, Journal of Hydraulic Division, Vol. 97, No. HY6, Proc. Paper 8186, pp. 819-836.

62. Kruka, V. and Eskinazi E.S. (1964) "The Wall Jet in a Moving Stream", J. Fluid Mech., 20, pp. 555-579.

63. Kuipers, J. and Vreugdenhil, C.B. (1973) "Calculations of Two-Dimensional Horizontal Flow", Report No. S163, Part I, Delft Hydraulic Laboratory, Delft, The Netherlands.

64. Lamb, H. (1932) "Hydrodynamics", Cambridge University Press.

65. Larsen, J., Rugbjerg, M., Warren, I.R. and Kej. A. (1986) "Abstracts of the 20th Int. Conf. on Coastal Engineering", ASCE.

66. Launder, B.E. and Spalding, D.B. (1972) "Lectures in Mathematical Models of Turbulence", Acad. Press, London, New York.

67. Lean, G.H. and Weare, T.J. (1979) "Modelling Two-Dimensional Circulating Flow", Proc. ASCE, J. of Hydraulic Div., Vol. 105, No. HY1, Proc. Paper 14312, pp. 17-26.

68. Leendertse, J.J. (1984) "Verification of a Model of the Eastern Scheldt", The Rand Corporation, R-3108-NETH.

69. Leendertse, J.J. (1970) "A Water-Quality Simulation Model for Well-Mixed Estuaries and Coastal Seas", Vol. I, Principles of Computation", RM-6230-RC, The Rand Corporation, Santa Monica, Calif.

70. Leendertse, J.J. (1967) "Aspects of a Computational Model for Long-Period Water Wave Propagation", RM-5294-PR, The Rand Corporation, Santa Monica, Calif.

71. Lilly, D.K. (1966) "On the Application of the Eddy Viscosity Concept in the Internal Sub-Range of Turbulence", NCAR-123, National Center for Atmospheric Research, Boulder, Colorado.

72. Lofquist, K. (1960) "Flow and Stress Near an Interface Between Stratified Liquids", Phys. of Fluids, 3, pp. 158-175.

73. Long, R.R. (1975) "The Influence of Shear on Mixing Across Density Interfaces", J. Fluid Mech., Vol. 70, Part 2, pp. 305-320.

74. Love, M.D. and Leslie, D.C. (1977) "Studies of Subgrid Modelling with Classical Closures and Burgers Equation" in "Turbulent Shear Flow I", Selected Papers from the 1st International Symposium on Turbulent Shear Flow, Durst, Launder, Schmidt, Whitelaw (eds.), Penns., U.S.A., Springer-Verlag, 1979, pp. 353.

75. Mardapitta-Hadjipandeli L. (1985) "Numerical Modelling of Tide-Induced Circulations", Ph.D. Thesis, University of Birmingham.

76. Maxwell, W.H.C. and Pazwash, H. (1967) "Basic Study of Jet Flow Patterns Related to Stream and Reservoir Behaviour", Res. Rep. Water Resources Center, Univ. of Illinois, Nolo.

77. Meyer, Z. (1982) "Vertical Circulation in Density Stratified Reservoir", ASCE, J. of Hydraulic Div., Vol. 108, No. HY7, pp. 853.

78. Miles, J.W. and Howard, L.N. (1964) "Note on a Heterogeneous Shear Flow', J. Fluid Mech., 20, pp. 331-6.

79. Moore, M.N. and Long, R. (1971) "An Experimental Investigation of Turbulent Stratified Shearing Flow", J. Fluid Mech., Vol. 49, Pt. 4, pp. 635-655.

80. Mortimer, C.H. (1941) "The Exchange of Dissolved Substances Between Mud and Water in Lakes", J. Ecol., 1941, 19(2), pp. 280-329.

81. Mortimer, C.H. (1942) "The Exchange of Dissolved Substances Between Mud and Water in Lakes", J. Ecol., 1942, 30(1), pp. 197-201.

82. Myers, G.E., Schauer, J.J. and Eustis, R.H. (1961) "The Plane Turbulent Wall Jet I", Jet Development and Friction Factor, Tech. Rep. 1, Dept. of Mech. Engineering, Stanford University, (Also published in Trans. A.S.M.E., J. Basic Eng. 1963).

83. Nachtsheim, P.R. and Swigert, P. (1965) "Satisfaction of Asymptotic Boundary Conditions in Numerical Solution of Systems of Nonlinear Equations of Boundary-Layer Type", NASA TND-3004.

84. Nakano, S., Tsuruya, H. and Ichinohe, H. (1985) "Friction and Entrainment at the Interface of Two-Layered Stratified Flow", Report of the Port and Harbour Research Institute, Vol. 24, No. 2.

85. Newman, B.G. (1967) "The Jets and Wakes in a Pressure Gradient", in Fluid Mechanics of Internal Flow, edited by Sovran, Elsevier.

86. Ockenden, H. (1972) "An Asymptotic Solution for Steady Flow Above an Infinite Rotating Disk with Suction", Quart, J. Mech. Appl. Math. 25, pp. 291.

87. Pande, B.B.L. and Rajaratnam, N. (1977) "An Experimental Study of Bluff Buoyant Turbulent Surface Jets", J. of Hydraulic Research, Vol. 15, No. 3, pp. 261-275.

88. Patel, R.P. (1971) "Turbulent Jets and Wall Jets in a Uniform Streaming Flow", Aeronaut. Q. 22, pp. 311-32.

89. Pateman, D.R. (1982) "Circulation and Mixing in Reservoirs", Ph.D. Thesis, Univ. of Liverpool.

90. Pearson, C.E. (1965) "A Computational Method for Viscous Flow Problems", J. of Fluid Mechanics, Vol. 21, No. 4, pp. 611-612.

91. Philips, N.A. (1959) "An Example of Non-Linear Computational Instability", The Atmosphere and Sea in Motion, Rockefeller Institute Press, New York, N.Y., pp. 501-504.

92. Pollard, R.T., Rhines, P.B. and Thompson, R.O.R.Y. (1973) "The Deepening of the Wind-Mixed Layer", Geophys. Fluid dyn. 3, pp. 381-404.

93. Ponce, V.M. and Yabusaki, S.B. (1981) "Modelling Circulation in Depth-Averaged Flow", J. of Hydraulic Division, ASCE, Vol. 107, No. HY11, pp. 1501-1518.

94. Price, J.F. (1979) "On the Scaling of Stress Driven Entrainment Experiments", J. Fluid Mech., Vol. 90, Part 3, pp. 509-529.

95. Rajaratnam, N. (1984) "Non-Buoyant and Buoyant Circular Surface Jets in Co-Flowing Streams", J. Hydraul. Res., Vol. 22, No. 2, pp. 117-140.

96. Rajaratnam, N. (1976) "Turbulent Jets", Elsevier Scientific Publishing Company.

97. Rajaratnam, N. (1969) "Diffusion of a Supercritical Stream on a Stagnant Pool", Trans. Engrg. Inst. of Canada, Vol. 12, No. A-1, pp. 1-5.

98. Rajaratnam, N. and Humphries, J.A. (1984) "Turbulent Non-Buoyant Surface Jets", J. of Hydraulic Res., Vol. 22, No. 2, pp. 103-115.

99. Rajaratnam, N. and Pani, B.S. (1974) "Three-Dimensional Turbulent Wall Jets", Proc. ASCE, J. Hydraul. Div., Vol. 100, pp. 69-83.

100. Rajaratnam, N. and Subramanya, K. (1967) "Diffusion of Rectangular Wall Jets in Wider Channels", J. Hydraul. Res., 5 : pp. 281-294.

101. Richtmyer, R.D. and Morton, K.W. (1967) "Difference Methods of Initial-Value Problems", 2nd Edition Interscience Publishers, J. Wiley and Sons.

102. Ridley, J.E. (1964) "Thermal Stratification and Thermocline Control in Storage Reservoirs", Proc. Soc. Water Treat. Exam., 13, pp. 275-296.

103. Roache, P.J. (1976) "Computational Fluid Dynamics", Hermosa Publishers.

104. Robinson, S.J. (1979) "Hydraulic Modelling of Circulation in Reservoirs: An Experimental Study of Jet-Induced Circulation in Water Supply Reservoirs", M.Phil. Thesis, Univ. of London.

105. Robinson, S.J. and Minton, P. (1979) "A Method for Measuring Low Water Velocities in Large Hydraulic Models", Tehcnical Note, Proc. Inst. of Civil Engineers, Part 2, March, Vol. 67, pp. 203-211.

106. Rodi, W. (1980) "Turbulence Models and Their Application in Hydraulics", I.A.H.R. Publication.

107. Rogers, M.H. and Lance, G.N. (1964) "The Boundary Layer on a Disk of Finite Radius in a Rotating Fluid", Quar. J. Mech. Appl. Math., 17, pp. 319-30.

108. Rogers, M.H. and Lance, G.N. (1960) "The Rotationally Symmetric Flow of a Viscous Fluid in the Presence of an Infinite Rotating Disk", J. Fluid Mech., 7, pp. 617-31.

109. Rouse, H. and Dodu, J. (1955) "Diffusion Turbulente a Traverse une Discontinuite de Densite", La Houille Blanche 10, pp. 522-532.

110. Rozovskii, I.L. (1957) "Flow of Water in Bends of Open Channels", Academy of Sciences of the Ukranian SSR, Kiev, U.S.S.R., (available from the Office of Technical Services United States Dept. of Commerce, Washington D.C.).

111. Schijf, J.B. and Schoenfeld, J.C. (1953) "Theoretical Considerations on the Motion of Salt and Freshwater", Proc. Minn. Int. Hydraulic Convention, pp. 321-333.

112. Schilichting, H. (1979) "Boundary Layer Theory", McGraw-Hill Book Co., New York, 7th ed.

113. Schwarz, W.H. and Cosart W.P. (1961) "The Two-Dimensional Turbulent Wall Jet", J. Fluid Mech., 10 : 481-495.

114. Sharp, I.J. (1981) "Hydraulic Modelling", Butterworths.

115. Shi-Igai, H. (1965) "On the Resistance Coefficient at the Interface Between Salt and Freshwater", Transactions, Japan Society of Civil Engineers, No. 123, pp. 27-31.

116. Sigalla, A. (1958) "Measurements of Skin Friction in a Plane Turbulent Wall Jet", J.R. Aeronaut. Soc. 62 : 873-877.

117. Smagorinsky, J. (1963) "General Circulation Experiments with the Primitive Equations", Mon. Weather Review, 91/3, 99.

118. Sobey, R.J. (1973) "Flow Patterns in Lakes and Reservoirs", Ph.D. Thesis, Univ. of London.

119. Sobey, R.J. and Savage, S.B. (1974) "Jet-Forced Circulation in Water-Supply Reservoirs", J. Hydraul. Div. Am. Soc. Civ. Engrs., 100, HY12, Dec., pp. 1809-1828.

120. Steel, J.A. (1975) "The Management of Thames Valley Reservoirs", Water Research Center Symposium, Paper 14, Proc. of Symposium on "The Effects of Storage on Water Quality", Reading Univ., pp. 371-397.

121. Steel, J.A. (1972) "The Application of Fundamental Limnological Research in Water Supply System Design and Management" in "Conservation and Productivity of Natural Waters", Edwards, R.W. and Garrod, D.J. (eds.), Symp. Zool. Soc. Lond., (29), pp. 41-67.

122. Stefan, H. (1972) "Dilution of Buoyant Two-Dimensional Surface Discharges", Journal of the Hydraulic Division, ASCE, Vol. 98, No. HY1, pp. 71-86.

123. Stefan, H. and Scheibe, F.R. (1970) "Heated Discharge from Flume into Tank", J. of Sanitary Engineering Division, ASCE, Vol. 96, SA6, Proc. Paper 7762, pp. 1415-1453.

124. Stefan, H. and Scheibe, F.R. (1968) "The Measurement of Low Fluid Velocities with the Aid of a Tethered Sphere", Water Resrouces Res., Vol. 4, No. 6, Dec., pp. 1351-1357.

125. Stewartson, K. (1957) "On Rotating Laminar Boundary Layers", Freiburg Symposium Boundary Layer Research, 59-71.

126. Stuart, J.T. (1954) "On the Effects of Uniform Suction on the Steady Flow Due to a rotating Disk", Quart. J. Mech. Appl. Math., 7, pp. 446-57.

127. Suga, K. and Takahashi, A. (1976) "Entrainment Coefficient of Fresh and Salt Two-Layered Flows", Proc. 31st Annual Meeting, JSCE, Part II, pp. 383-384 (in Japanese).

128. Symons, J.M. (1969) "Water Quality Behaviour in Reservoirs", a compilation of published research papers, Publ. Hlth. Serv. Publs. 1930.

129. Symons, J.M., Carswell, J.K. and Robeck, G.G. (1970) "Mixing of Water Supply Reservoir for Quality Control", J. of AWWA, pp. 324.

130. Tamai, N., Wiegel, R.L. and Tornberg, G.F. (1969) "Horizontal Surface Discharges of Warm Water Jets", ASCE, J. of Power Division, Proc. Paper 6847, Vol. 95, PO2, pp. 253-276.

131. Tani, I. and Kobashi, U. (1951) "Experimental Studies on Compound Jets", Proc. 1st Japan Natl. Congr. Appl. Mech., pp. 465-468.

132. Thompson, R.O.R.Y. (1979) "A Re-Interpretation of the Entrainment Process in Some Laboratory Experiments, Dyn. Atmos. Oceans, 4, pp. 45-56.

133. Thompson, R.W.S. (1954) "Stratification and Overturn in Lakes and Reservoirs", J. Instn. Water Engrs., 8, 1, pp. 1-18.

134. Thompson, S.M. (1969) "Turbulent Interfaces Generated by an Oscillating Grid in a Stably Stratified Fluid", Ph.D. Thesis, Univ. of Cambridge.

135. Thompson, J.F., Thames, F.C. and Wayne Mastine, C. (1977) "TOMCAT - A Code for Numerical Generation of Boundary-Fitted Curvilinear Coordinate System on Fields Containing any Number of Arbitrary Two-Dimesnional Bodies", J. of Computational Phys., 24, pp. 274-302.

136. Townsend, A.A. (1976) "The Structure of Turbulent Shear Flow", Cambridge University Press.

137. Turner, J.S. (1979) "Buoyancy Effects in Fluids", Cambridge University Press.

138. Turner, J.S. (1973) "Geophysical Examples of Layering and Micro-Structure Interpretation and Relation to Laboratory Experiments", Memoires Societe Royale des Science de Liege, 6e Serie, Tom IV.

139. Turner, J.S. (1968) "The Influence of Molecular-Diffusivity on Turbulent Entrainment Across a Density Interface", J. Fluid Mech., 33, pp. 639-656.

140. Ura, M., Tsubaki, T. and Matsunaga, N. (1984) "Characteristics of Flow and Turbulence Near Interfacial Waves in Upper-Layer Flow", J. of Hydroscience and Hydraulic Engineering, Vol. 2, No. 1, pp. 27-45.

141. Verhoff, A. (1963) "The Two-Dimensional Turbulent Wall Jet With and Without an External Stream", Rep. 626, Princeton Univ.

142. Viets, H. and Sforza, (1966) "An Experimental Investigation of a Turbulent Incompressible Three-Dimensional Wall Jet", Rept. 968, Dept. of Aerospace Engineering, Polytechnic Institute of Brooklyn, New York.

143. Von Karman, T. (1921) "Laminar und Turbulente Reibung", Z. Angew, Math. Phys., 1, pp. 233.

144. Vreugdenhil, C.B. (1973) "Secondary-Flow Computations", Delft Hydraulics Laboratory Report No. 114.

145. Vreugdenhil, C.B. and Voogt, (1975) "Hydrodynamic Transport Phenomena in Estuaries and Coastal Waters: Scope of Mathematical Models", Proc. of the Symp. on Modelling Tech., Waterways, Harbours and Coastal Eng. Div. of ASCE, San Francisco.

146. Washburn, E.W. (1929) "International Critical Tables of Numerical Data Physics, Chemistry and Technology", prepared under the auspices of the Inst. Res. Council and National Academy of Sciences, Nat. Res. Council of U.S.A.

147. Weare, T.J. (1979) "Errors Arising from Irregular Boundaries in ADI Solutions of the Shallow-Water Equations", International J. for Numerical Methods in Engineering, Vol. 14, pp. 921-931.

148. Weare, T.J. (1976) "Instability of Tidal Flow Computational Schemes", ASCE, J. of Hydraulic Div., Vol. 102, No. HY5, Proc. Paper 12100.

149. Weinstein, A.S. (1955) "Diffusion of Momentum from Free and Confined Slot Jets into Moving Secondary Streams", Dissertation, Carnegie Inst. of Technology.

150. White, C.M., Harris, S.L. and Cooley, P. (1955) "The Hydraulic Aspect of Stagnation in Reservoirs", Private Report Submitted to the Metropolitan Water Board, London.

151. Wilkinson, D.L. and Wood, I.R. (1971) "A Rapidly Varied Flow Phenomenon in a Two-Layer Flow", Journal of Fluid Mechanics, Vol. 47, pp. 291-256.

152. Williams, J.M. and Holmes, D.W. (1974) "Marker-and-Cell Technique, a Computer Program for Transient Stratified Flows with Free Surfaces", Report No. 134, Hydraulics Research Station, Wallingford, England.

153. Wolanski, E. (1972) "Turbulent Entrainment Across Stable Density-Stratified Liquids and Suspensions", Ph.D. Thesis, The John Hopkins University.

154. Wu, J. (1973) "Wind Induced Turbulent Entrainment Across a Stable Density Interface", J. Fluid Mech., Vol. 61, pp. 275-287.

155. Wurtele, M.G., Peagle, J. and Sielecki, A. (1971) "The Use of Open Boundary Condition with Storm Surge Equations", Monthly Weather Review, Vol. 99, No. 6, pp. 537-544.

156. Yevdjevich, V.M. (1966) "Diffusion of Slot Jets with Finite Orifice Length-Width Ratios", Hydraul. Pap., 2, Colorado STate Univ., Fort Collins.